

IAEA TECDOC SERIES

IAEA-TECDOC-1935

Modern Neutron Detection

Proceedings of a Technical Meeting



IAEA

International Atomic Energy Agency

MODERN NEUTRON DETECTION

The following States are Members of the International Atomic Energy Agency:

AFGHANISTAN	GEORGIA	OMAN
ALBANIA	GERMANY	PAKISTAN
ALGERIA	GHANA	PALAU
ANGOLA	GREECE	PANAMA
ANTIGUA AND BARBUDA	GRENADA	PAPUA NEW GUINEA
ARGENTINA	GUATEMALA	PARAGUAY
ARMENIA	GUYANA	PERU
AUSTRALIA	HAITI	PHILIPPINES
AUSTRIA	HOLY SEE	POLAND
AZERBAIJAN	HONDURAS	PORTUGAL
BAHAMAS	HUNGARY	QATAR
BAHRAIN	ICELAND	REPUBLIC OF MOLDOVA
BANGLADESH	INDIA	ROMANIA
BARBADOS	INDONESIA	RUSSIAN FEDERATION
BELARUS	IRAN, ISLAMIC REPUBLIC OF	RWANDA
BELGIUM	IRAQ	SAINT LUCIA
BELIZE	IRELAND	SAINT VINCENT AND THE GRENADINES
BENIN	ISRAEL	SAN MARINO
BOLIVIA, PLURINATIONAL STATE OF	ITALY	SAUDI ARABIA
BOSNIA AND HERZEGOVINA	JAMAICA	SENEGAL
BOTSWANA	JAPAN	SERBIA
BRAZIL	JORDAN	SEYCHELLES
BRUNEI DARUSSALAM	KAZAKHSTAN	SIERRA LEONE
BULGARIA	KENYA	SINGAPORE
BURKINA FASO	KOREA, REPUBLIC OF	SLOVAKIA
BURUNDI	KUWAIT	SLOVENIA
CAMBODIA	KYRGYZSTAN	SOUTH AFRICA
CAMEROON	LAO PEOPLE'S DEMOCRATIC REPUBLIC	SPAIN
CANADA	LATVIA	SRI LANKA
CENTRAL AFRICAN REPUBLIC	LEBANON	SUDAN
CHAD	LESOTHO	SWEDEN
CHILE	LIBERIA	SWITZERLAND
CHINA	LIBYA	SYRIAN ARAB REPUBLIC
COLOMBIA	LIECHTENSTEIN	TAJIKISTAN
COMOROS	LITHUANIA	THAILAND
CONGO	LUXEMBOURG	TOGO
COSTA RICA	MADAGASCAR	TRINIDAD AND TOBAGO
CÔTE D'IVOIRE	MALAWI	TUNISIA
CROATIA	MALAYSIA	TURKEY
CUBA	MALI	TURKMENISTAN
CYPRUS	MALTA	UGANDA
CZECH REPUBLIC	MARSHALL ISLANDS	UKRAINE
DEMOCRATIC REPUBLIC OF THE CONGO	MAURITANIA	UNITED ARAB EMIRATES
DENMARK	MAURITIUS	UNITED KINGDOM OF GREAT BRITAIN AND NORTHERN IRELAND
DJIBOUTI	MEXICO	UNITED REPUBLIC OF TANZANIA
DOMINICA	MONACO	UNITED STATES OF AMERICA
DOMINICAN REPUBLIC	MONGOLIA	URUGUAY
ECUADOR	MONTENEGRO	UZBEKISTAN
EGYPT	MOROCCO	VANUATU
EL SALVADOR	MOZAMBIQUE	VENEZUELA, BOLIVARIAN REPUBLIC OF
ERITREA	MYANMAR	VIET NAM
ESTONIA	NAMIBIA	YEMEN
ESWATINI	NEPAL	ZAMBIA
ETHIOPIA	NETHERLANDS	ZIMBABWE
FIJI	NEW ZEALAND	
FINLAND	NICARAGUA	
FRANCE	NIGER	
GABON	NIGERIA	
	NORTH MACEDONIA	
	NORWAY	

The Agency's Statute was approved on 23 October 1956 by the Conference on the Statute of the IAEA held at United Nations Headquarters, New York; it entered into force on 29 July 1957. The Headquarters of the Agency are situated in Vienna. Its principal objective is "to accelerate and enlarge the contribution of atomic energy to peace, health and prosperity throughout the world".

IAEA-TECDOC-1935

MODERN NEUTRON DETECTION
PROCEEDINGS OF A TECHNICAL MEETING

INTERNATIONAL ATOMIC ENERGY AGENCY
VIENNA, 2020

COPYRIGHT NOTICE

All IAEA scientific and technical publications are protected by the terms of the Universal Copyright Convention as adopted in 1952 (Berne) and as revised in 1972 (Paris). The copyright has since been extended by the World Intellectual Property Organization (Geneva) to include electronic and virtual intellectual property. Permission to use whole or parts of texts contained in IAEA publications in printed or electronic form must be obtained and is usually subject to royalty agreements. Proposals for non-commercial reproductions and translations are welcomed and considered on a case-by-case basis. Enquiries should be addressed to the IAEA Publishing Section at:

Marketing and Sales Unit, Publishing Section
International Atomic Energy Agency
Vienna International Centre
PO Box 100
1400 Vienna, Austria
fax: +43 1 26007 22529
tel.: +43 1 2600 22417
email: sales.publications@iaea.org
www.iaea.org/publications

For further information on this publication, please contact:

Physics Section
International Atomic Energy Agency
Vienna International Centre
PO Box 100
1400 Vienna, Austria
Email: Official.Mail@iaea.org

© IAEA, 2020
Printed by the IAEA in Austria
December 2020

IAEA Library Cataloguing in Publication Data

Names: International Atomic Energy Agency.
Title: Modern neutron detection / International Atomic Energy Agency.
Description: Vienna : International Atomic Energy Agency, 2020. | Series: IAEA TECDOC series, ISSN 1011-4289 ; no. 1935 | Includes bibliographical references.
Identifiers: IAEAL 20-01366 | ISBN 978-92-0-126520-3 (paperback : alk. paper) | ISBN 978-92-0-126620-0 (pdf)
Subjects: LCSH: Neutrons — Measurement. | Neutron counters. | Detection.

FOREWORD

Neutrons play an essential role in fission in nuclear reactors, and their charge neutrality, finite mass and high penetration, as well as their interactions with both the nucleus and magnetic spins, have given them many applications in science. Nevertheless, they are not trivial to detect, and their energies span a large spectrum. From terrestrial sources, neutrons can be produced in spallation sources with energies up to the order of a GeV and can be studied down to the ultracold range in the hundreds of neV in fundamental physics. The greatest demand for experimental and dosimetric measurement is in a smaller but still vast range: from cold neutrons commonly used in neutron scattering research for materials and solid-state physics through fission to neutrons with energies of the order of 14.1 MeV typical of deuterium–tritium fusion applications.

The different energy ranges and applications require slightly different detector designs and materials, and detectors may have to function in mixed very high radiation and pulsed radiofrequency fields. Furthermore, the workhorse helium-3 detector that has been widely used over several decades has suffered in recent years from uncertainty and restrictions in supply, and from a rise in cost — the so-called helium-3 crisis. This has led to a surge in demand for detectors with competitive efficiency at lower prices. New materials, such as new classes of scintillators, are being developed. Efforts are also being made to mitigate the use of and demand for helium-3 — particularly in neutron scattering, which requires large area coverage — by developing replacement technologies that can meet the challenging performance requirements for the new generation of instruments. Another field in which demand for different capabilities of neutron detection is rising is fusion, where the challenges for materials and electronics are relevant. This publication offers an overview of many of the current developments in this wide field, with an outlook on some future technologies.

The papers included in this publication arose from a technical meeting held at the IAEA in Vienna on 4–8 September 2017, with 42 participants from 20 Member States and an international organization. This meeting brought together a diverse group of experts from standards laboratories and regulatory bodies, and the fields of neutron scattering and fusion, who use a wide variety of different detection technologies to measure neutrons over many orders of magnitude of energies.

The IAEA would like to thank all the participants for their contributions, in particular H. Ing (Canada), L. Packer (United Kingdom) and R. Hall-Wilton (Sweden), who served as scientific chairs of the meeting. The IAEA officer responsible for this publication was I. Swainson of the Division of Physical and Chemical Sciences.

EDITORIAL NOTE

This publication has been prepared from the original material as submitted by the contributors and has not been edited by the editorial staff of the IAEA. The views expressed remain the responsibility of the contributors and do not necessarily represent the views of the IAEA or its Member States.

Neither the IAEA nor its Member States assume any responsibility for consequences which may arise from the use of this publication. This publication does not address questions of responsibility, legal or otherwise, for acts or omissions on the part of any person.

The use of particular designations of countries or territories does not imply any judgement by the publisher, the IAEA, as to the legal status of such countries or territories, of their authorities and institutions or of the delimitation of their boundaries.

The mention of names of specific companies or products (whether or not indicated as registered) does not imply any intention to infringe proprietary rights, nor should it be construed as an endorsement or recommendation on the part of the IAEA.

The authors are responsible for having obtained the necessary permission for the IAEA to reproduce, translate or use material from sources already protected by copyrights.

The IAEA has no responsibility for the persistence or accuracy of URLs for external or third party Internet web sites referred to in this publication and does not guarantee that any content on such web sites is, or will remain, accurate or appropriate.

CONTENTS

1.	INTRODUCTION	1
1.1.	BACKGROUND	1
1.2.	OBJECTIVES	1
1.3.	SCOPE	2
1.4.	STRUCTURE	2
2.	SUMMARY OF THE TECHNICAL MEETING	3
2.1.	DETECTOR MATERIALS AND SPECIAL DETECTION TECHNIQUES	3
2.2.	NEUTRON METROLOGY AND CALIBRATION	4
2.3.	SPECTRAL UNFOLDING	4
2.4.	FRONT END ELECTRONICS	6
2.5.	NEUTRON SPECTROSCOPY	6
2.6.	THERMAL NEUTRON DETECTORS FOR NEUTRON SCATTERING	9
2.6.1.	HELIUM-3 DETECTORS	11
2.6.2.	SCINTILLATOR DETECTORS	12
2.7.	NEUTRON DETECTORS FOR FUSION ENERGY	14
3.	CONCLUSIONS	18
	REFERENCES	19

PAPERS PRESENTED AT THE TECHNICAL MEETING

TOPICAL SESSION 1: DETECTOR MATERIALS AND SPECIAL DETECTION TECHNIQUES

DIAMOND DETECTORS FOR NEUTRONS	25
<i>M. ANGELONE</i>	

SILICON CARBIDE (SiC) NEUTRON DETECTOR FOR POWER RANGE NEUTRON FLUX MONITORING	39
<i>C.P. NAGARAJ, S. TRIPATHI, C. UPADHYAY, A. VENKATESAN, B.K. PANIGRAHI</i>	

NEXT GENERATION NEUTRON DETECTORS	51
<i>K.S. SHAH, M.R. SQUILLANTE, E. VAN LOEF, J. GLODO, L. CIRIGNANO, H. HONG, A. GUEORGUIEV, J. TOWER, A. KARGAR, H. KIM</i>	

NEW SOLID-STATE ORGANIC SCINTILLATORS FOR WIDE-ENERGY NEUTRON DETECTION	65
<i>N. ZAITSEVA, A. GLENN, L. CARMAN, A. MABE, S. PAYNE</i>	

TOPICAL SESSION 2: NEUTRON METROLOGY AND CALIBRATION

NEUTRON METROLOGY – MEASUREMENT STANDARDS AND THEIR APPLICATIONS	77
<i>V. GRESSIER, D.J. THOMAS</i>	
NEUTRON STANDARD FACILITIES IN INDIA	89
<i>SATHIAN, S. GHODKE, M. SEN, Y. SINGH, M.S. KULKARNI</i>	

TOPICAL SESSION 3: SPECTRAL UNFOLDING

SPECTRAL UNFOLDING: A MATHEMATICAL PERSPECTIVE	97
<i>M. KOSLOWSKY</i>	

NEUTRON SPECTRUM ADJUSTMENT AND CROSS-SECTION VALIDATION ACTIVITIES AT THE JOŽEF STEFAN INSTITUTE 117
V. RADULOVIĆ, B. KOS, A. TRKOV, L. SNOJ

USE OF A PRIORI INFORMATION IN BONNER SPHERE UNFOLDING 131
D.J. THOMAS

NEUTRON SOURCE CONDITION IN THE SOLUTION OF THE DIFFUSION EQUATION 137
H.R. VEGA-CARRILLO, E. GALLEGO, A LORENTE, K.A. GUZMAN-GARCIA, L. HERNÁNDEZ-ADAME, S.A. MARTINEZ-OVALLE, L. SAJO-BOHUS, C. LETECHIPÍA-DE LEON, V.M. HERNANDEZ-DAVILA, M.A. SALAS-LUEVANO, B.G. PULIDO-CERVANTES

TOPICAL SESSION 4: FRONT END ELECTRONICS

COMPENDIUM OF FRONT-END ELECTRONICS 147
F. MESSI

TOPICAL SESSION 5: NEUTRON SPECTROSCOPY

RECENT NEUTRON DETECTION WORK AT CANADIAN NUCLEAR LABORATORIES 159
B.M. VAN DER ENDE

RECENT FIRMWARE AND HARDWARE UPGRADES TO THE HPI2080 PULSED NEUTRON REM METER 167
A.L. JUSTUS, M.A. DURAN, R.E. MONTOYA, D.T. SEAGRAVES, J.R. BLAND, T.D. MCLEAN

NEUTRON SPECTROMETERS FROM THERMAL ENERGIES TO GEV BASED ON SINGLE MODERATORS 177
R. BEDOGNI, A. POLA, J.M. GOMEZ-ROS

MEASUREMENTS OF NEUTRON SOURCE USING NESTED NEUTRON SPECTROMETER IN PULSE AND CURRENT MODE 183
A. LICEA, J. DUBEAU, J. KILDEA, M. EVANS, R. MAGLIERI

NEUTRON SPECTROMETRY AROUND LINACS USING PASSIVE BONNER SPHERE SPECTROSCOPY IN PLANETARY MODE 191
H.R. VEGA-CARRILLO, J.L. DENITIES-RENGIFO, E. GALLEGO, A. LORENTE, K.A. GUZMAN-GARICA, M.A.S. LACERDA, R. MENDEX, L. HERNÁNDEZ-ADAME

ABSOLUTE NEUTRON COUNTING. THE INFLUENCE METHOD 201
R.E. MAYER, I.J. RIOS

TOWARDS A NEW COMPACT SCINTILLATION SPECTROMETER FOR 100 MEV NEUTRONS: A CASE STUDY FOR REFERENCE NEUTRON BEAMS 209
A. BUFFLER, A.C. COMRIE, T. HUTTON, F.D. SMIT, R. NOLTE

ROSPEC - A UNIQUE FAST NEUTRON SPECTROMETER 219
H. ING

TOPICAL SESSION 6: THERMAL NEUTRON DETECTORS FOR NEUTRON SCATTERING

DEVELOPMENT OF AREA DETECTORS FOR NEUTRON BEAM INSTRUMENTATION AT THE BUDAPEST NEUTRON CENTRE 237
J. ORBÁN, J. FÜZI, L. ROSTAI, G. KISS

STRATEGY OF EQUIPPING THE PIK REACTOR EXPERIMENTAL STATIONS WITH DETECTION SYSTEMS	251
<i>A. KRIVSHICH, D. ILYIN, R. HALL-WILTON</i>	
STATUS AND PROGRESS IN NEUTRON IMAGING DETECTION SYSTEMS	261
<i>E.H. LEHMANN</i>	
MODERN NEUTRON DETECTORS WITH FAST TIMING RESOLUTION.....	273
<i>B. SEITZ, J.R.M. ANNAND, L. BOYD, K. FISSUM</i>	
DEVELOPMENT OF NEUTRON DETECTORS FOR THE SPECTROMETERS OF THE IBR-2 REACTOR	279
<i>S.A. KULIKOV, A.V. CHURAKOV, V.V. KRUGLOV, A.A. BOGDZEL, V.M. MILKOV, V.V. ZHURAVLEV, S.M. MURASHKEVICH, E.I. LITVINENKO, TS.TS. PANTELEEVA</i>	
THE NEUTRON-TAGGING FACILITY AT LUND UNIVERSITY	287
<i>F. MESSI, H. PERREY, K. FISSUM, D.D. DIJULIO, E. KARNICKIS, V. MAULEROVA, N. MAURITZSON, E. ROFORS, A. HUUSKO, T. ILVES, A. JALGÉN, S. KOFIGAR, H. SÖDERHJELM, D. SÖDERSTRÖM, R. HALL-WILTON, P.M. BENTLEY, C.P. COOPER-JENSEN, J. FREITA-RAMOS, F. ISSA, K. KANAKI, A. KHAPLANOV, G. MAURI, F. PISCITELLI, I. STEFANESCU, J. SCHERZINGER, R. AL JEBALI, J.R.M. ANNAND, L. BOYD, M. AKKAWI, W. PEI</i>	
TOPICAL SESSION 7: NEUTRON DETECTORS FOR FUSION ENERGY	
NOVEL NEUTRON ACTIVATION DETECTOR FOR FUSION	301
<i>I.E. STAMATELATOS, M.I. SAVVA, T. VASILOPOULOU, K. TRIANTOU, K. MERGIA, S. MESSOLORAS, L.W. PACKER, C.R. NOBS, Z. GHANI, P. BATISTONI, M. PILLON, S. LORETI</i>	
NEUTRON DETECTION TECHNOLOGIES AND MEASUREMENT CHALLENGES AT JET AND ITER	313
<i>L.W. PACKER, Z. GHANI, M.R. GILBERT, S. POPOVICHEV, V. KRASILNIKOV, M. CECCONELLO, M. TARDOCCHI, M. REBAI, D. RIGAMONTI</i>	
ACTIVATION FOIL CANDIDATES FOR INTENSE D-LI NEUTRON MEASUREMENT UP TO 60 MeV	337
<i>S. KWON, M. OHTA, K. OCHIAI, H. SUZUKI</i>	
LIST OF ABBREVIATIONS	345
CONTRIBUTORS TO DRAFTING AND REVIEW	349

1 INTRODUCTION

1.1 BACKGROUND

Of the common terrestrial radiations, neutrons have always been regarded as the most difficult to detect. One of the reasons is that neutrons are uncharged and can only be detected via the secondary charged products produced by neutron interactions with matter. While gamma rays are also uncharged, their interactions are adequately covered by the three well-known processes: the photoelectric effect, Compton scattering and pair production, whose theoretical bases are well understood and quantitatively predictable over the common energy range for terrestrial radiation. On the other hand, neutron cross sections with matter are not quantitatively predictable and are based on empirical data that are often inadequate to cover the desired energy range. Another factor that makes neutron detection difficult is that terrestrial neutron radiation covers an energy span of over 8 decades (sub-thermal to over 10 MeV) compared to approximately 3 decades for gamma rays (about 10 keV to 10 MeV). To further complicate the detection of neutrons, neutron spectra in the sub-thermal region are heavily influenced by the molecular structure of the materials that are near the source, while in the high-energy region, many reaction channels are possible and existing interaction models are well known to be poor. So, neutron detection remains very much an empirical science.

In the period following the discovery of the neutron by Chadwick in 1932 [1], significant research went into instrumentation for detection of neutrons, driven mainly by the discovery of fission, which led to the development of the atomic bomb and nuclear reactors for peaceful uses. By 1943, neutrons were detected using elastic collisions with light nuclei, neutron absorption that led to the emission of charged particles and neutron-induced fission. The secondary charged particles from these processes were detected with conventional instrumentation such as electroscopes, ionization chambers, Geiger-Muller counters, cloud chambers, photographic emulsions, and scintillators [2]. Incremental developments in these detection technologies over the next two decades, to establish the basis for neutron detection, are contained in early reference books; e.g., [3–7].

Subsequent developments in neutron detection tend to focus on particular applications such as: neutron dosimetry, e.g. [8, 9], neutron spectroscopy, e.g. [10], and neutron scattering, e.g. [11, 12]. A good summary of neutron detection (excluding neutron scattering) up to about 2005 is given in the popular book by Glen Knoll [13]. More recent developments in neutron detection can be found in numerous conferences including those by SORMA, ANIMMA, IEEE, ACNS, and ISRD, as well as specialized workshops such as those on position sensitive detectors [14], solid state detectors [15], neutron scattering [16], and fusion [17]. There are also many publications in radiation related journals on various aspects of neutron detectors.

Many of the new technologies for neutron detection have been driven by recent funding for homeland security applications (especially by the US Department Homeland Security, Domestic Nuclear Detection Office). The new technologies are beginning to find applications in other neutron related fields, generating new scientific excitement in a field that has seen somewhat sluggish innovation for several decades.

1.2 OBJECTIVES

The objective of this report is to bring together experience and opinions from experts from various fields in which neutron detection is used, as well as to publish an IAEA report that will

cover the current state of the art in neutron detection and provide a 5–10-year outlook on technologies in this field.

1.3 SCOPE

The scope includes new materials and detector electronics, in fields such as metrology, dosimetry, spectroscopy, fusion and scattering applications. The publication excludes applications for security, as these are dealt with under other IAEA activities.

1.4 STRUCTURE

The publication consists of an overview of the technical meeting and the papers that have arisen out of it. The individual papers described are published in full in the Annex.

2 SUMMARY OF THE TECHNICAL MEETING

2.1 DETECTOR MATERIALS AND SPECIAL DETECTION TECHNIQUES

Topical Session 1 contains four papers that describe recent developments in detector technology. The first paper covers diamond detectors that have excellent properties for detection and spectroscopy of fast neutrons above 5.7 MeV, especially under harsh environmental conditions ($>150^{\circ}\text{C}$) as encountered inside fusion reactors. By the deposition of a thin layer of material (fraction of a μm to a few μm) such as LiF, B or a fissile material, diamond detectors can be made to be sensitive to neutrons down to sub-thermal energies, extending its breadth of applications. However, diamond detectors are not yet fully commercial ‘off-the-self’ detectors because of variability in the properties of the diamond wafers. Improvements to reproducibility of wafer properties are needed to bring diamond detectors to a commercial product. As the market expands for diamond detectors, such technological advancements will likely occur.

The second paper describes another interesting solid-state detector based on SiC, which can also be used in harsh environmental conditions. The work is focused primarily on fast neutron detectors for flux monitoring of the power of a fast reactor core, to replace current detectors based on bulky fission chambers and self-powered neutron detectors. The detector described consists of an HDPE conversion layer adjacent to a $1\text{ cm} \times 1\text{ cm}$ SiC wafer. Monte Carlo simulations were done to determine the optimum converter layer thickness and neutron and gamma pulse-height distributions from a single and a stack of such detectors of up to 50 layers. Angular response data are also given. A further study was done to investigate the use of SiC as an alpha spectrometer that would be usable in harsh radiation environments. The studies led to an optimized design for the HDPE/SiC detector for an Am-Be source, yielding a detection efficiency of $\sim 3.85\%$ with the 50-layer stack. The SiC detector when used as an alpha spectrometer yields a resolution of $\sim 22.8\text{ keV}$. More development is required to bring the technology to a mature enough state to be used for neutron detection inside nuclear reactors.

The third paper provides a snapshot of current and next generation neutron detectors that are under development in a leading commercial company known for novel neutron detectors. It covers novel inorganic scintillators that detect gamma rays as well as neutrons, new organic scintillators for fast neutrons, plastics scintillators loaded with heavy metal compounds for increased gamma detection efficiency as well as fast neutron detection, plastics scintillators containing certain inorganic compounds to allow gamma spectroscopy as well as neutron detection and a couple of novel semiconductor neutron detectors. The paper is loaded with data for an enormous variety of novel neutron detectors, some of which will likely become common neutron detectors in the near future. This paper reflects the current active state of neutron detection research mainly supported by funding for applications in homeland security.

The last paper in this Topical Session describes the current development of neutron detectors in a renowned national laboratory that has had a major impact on fast neutron detection through their successful development of pulse shape discrimination (PSD) plastic to replace the conventional PSD liquid scintillator, which has been the standard for fast neutron spectroscopy for over four decades. The paper describes ongoing improvements to this exciting product as well as other new detectors such as trans-stilbene crystals, and crystals that incorporate Li salts to enable both fast and thermal neutron detection (as well as gamma detection) as well as plastics scintillators that are loaded with B-10 or Li-6 compounds to achieve similar

functionalities. All the scintillators use PSD to separate fast neutrons, thermal neutron, and gamma radiations.

The new PSD plastic is already commercially available from a company that is licensed by the national laboratory. Trans-stilbene is now available from another commercial company. As the other scintillators approach a certain level of maturity, they will likely also be commercially available.

2.2 NEUTRON METROLOGY AND CALIBRATION

Topical Session 2 contains two papers on neutron standards and calibration. All quantitative measurements of neutrons require a method to validate their detection efficiency based on accepted standards to yield absolute values of neutron spectra or neutron dose. This type of calibration is particularly important when the instrument is used in connection with the radiation protection of personnel, where prescribed limits of neutron exposure over a particular period are specified by the regulatory authorities of various countries.

The first paper is jointly prepared by renowned experts in the field and discusses the fundamentals of neutron metrology as well as the facilities and services available from one of the most well-equipped standards laboratories in the world. This paper can be regarded as a tutorial on neutron metrology, providing insight into the difficulties of neutron calibration, the reference documents that form the basis of neutron calibration, the various areas of applications where calibration is needed and the type of reference fields that can be used for calibration. Methodologies for performing calibration and ancillary data that may be needed as part of the calibration process are described as finer points that have to be addressed to achieve good accuracy for fluence and dose values. This paper is an excellent reference for all who may be interested in neutron metrology.

The second paper is from a well-known laboratory in India. Many facilities mentioned in the first paper are also discussed here. Of particular interest are the devices that perform secondary calibration using mobile devices that are used for offsite calibration at users' facilities. This laboratory also has an array of neutron detectors for measurement of neutrons fluences and neutron spectra along with an array of neutron sources that meet the requirements for neutron calibration.

2.3 SPECTRAL UNFOLDING

Topical Session 3 deals with the challenge of spectral unfolding, a mathematical process for deriving the energy spectrum of neutrons that impinge a neutron detector (or detectors) that lead to the measured signals from the detector itself. This process is an intrinsic part of neutron spectrometry. When mono-energetic neutrons, such as 2.5 MeV D-D or 14.5 MeV D-T neutrons, strike a neutron detector, the response of the detector rarely gives a mono-energetic peak (unlike gamma spectrometers). The few exceptions are the CLYC detector [18] and the diamond detector (Topical Session 1). Most other 'fast neutron' spectrometers give rise to an energy distribution of pulses (such as observed with hydrogenous scintillators), or a measure of the intensity of a thermal neutron peak (as with Bonner Spheres) whose energy is unrelated to the energy of the impinging neutrons (while its intensity contains the energy information). The relationship between the incident neutron spectrum and the measured quantity is commonly referred to as the response function. A measurement of an incident neutron spectrum

(mono-energetic or continuous) yields a set of data, which has to then be de-convoluted or 'unfolded' to yield the desired incident spectrum.

Around the mid-1960s, significant advancements were made in neutron spectral unfolding, aided by the development of early computers. The early codes included SAND-II [19] for neutron-activation detectors, the work by Burrus et al. [20] that eventually led to the development of the FERDOR code, distributed by RSIC as the FORIST code [21], for unfolding recoil-proton scintillators and the SPEC 4 code [22], for the unfolding of hydrogenous gas counters. The state-of-the-art on spectral unfolding in the early years can be found in the proceedings of a workshop, held by RSIC in 1976 [23], which brought together 60 specialists from 6 countries.

This workshop was quickly followed by another workshop [24], held by the IAEA in 1977 also at the Oak Ridge National Laboratory, on spectral unfolding with particular emphasis on the multiple foil activation technique for reactor dosimetry, addressing accuracy of cross section libraries, selection of foils and methods for evaluation of unfolded spectra.

No such concerted efforts on spectral unfolding have since then taken place. Occasional developments of more recent codes have followed similar techniques as used in the earlier codes, as discussed in an article on neutron spectroscopy in 1987 [10].

The present Topical Session on spectral unfolding presents a brief overview on the status of spectral unfolding. The first paper provides a mathematical description of the unfolding problem and mathematical approaches to the solution of such a problem using modern computational capabilities along with strengths and limitations of such mathematical techniques. It also examines the FERDOR code from a modern computational view point to highlight the approximations that were made originally and that can now be relaxed for a more rigorous solution. In addition, it examines the iterative method of minimization, used by SAND II and a few subsequent codes, to point out the mathematical similarities among them.

Tentative conclusions from this mathematical analysis is that for over-determined data, such as from scintillators, the use of maximum likelihood estimation or the FERDOR type method are good, rigorous methods. However, for under-determined data, such as for Bonner Spheres and activation detectors, where a reasonable estimate of the true spectral result is needed as a guess spectral input, the use of maximum entropy is the most rigorous.

The second paper describes an unfolding code, called GRUPINT, developed at the Jožef Stefan Institute originally for neutron activation analysis but now extended to more general unfolding applications. It fits neutron spectra with three terms for thermal, epithermal and fast, using 19 possible parameters and adjusts these parameters using least squares to generate neutron spectrum covariance matrices by the Monte Carlo method. Results of the fit to data obtained in the central irradiation channel of a TRIGA reactor are presented to demonstrate the reliability of the unfolding code. The results for unfolding Bonner Sphere data provided by Eurodos as part of an inter-comparison are also shown. These seem to be in reasonable agreement with accepted results.

The third paper in this Topical Session provides a condensed guide to the unfolding of data obtained with the popular Bonner Sphere Spectrometer (BSS). Since BSS uses a set of different size spheres with a thermal neutron detector at the centre (normally) and one is attempting to derive a complete neutron spectrum (usually) from thermal to above 10 MeV, the unfolding of BSS data is an underdetermined problem mathematically. For such problems, the use of other

information is highly desirable if not essential. Also, the experience of the unfolders in rejecting unlikely results and steering the unfolding to give the desired spectrum is important. As an example, the author shows that the unfolded results for a particular BSS measurement using a simple guess spectrum as spectral input and using the result of a Monte Carlo calculated spectrum as input, yield two completely different spectral results, with the calculated input providing the correct result. Thus, the author wishes to emphasize that a good spectral guess as input to the unfolding of BSS data greatly enhances the validity of the spectral measurements.

The fourth paper discusses a computational technique that can be used to provide spectral data that could be utilized as input for the unfolding of moderator data such as provided by Bonner Spheres. While most spectroscopists would now resort to Monte Carlo calculations to provide such spectral data (as illustrated in the preceding paper) or use published spectral data [25-27] if they are applicable, there may be laboratories that do not have the computational resources to perform such Monte Carlo calculations. This paper discusses the solving of neutron transport equations to provide spectral data, a mathematical technique that preceded the development of modern Monte Carlo codes. This paper discusses only a 2-group approximation for the solution of the transport equation, rather than the more sophisticated ‘multi-group’ solution, as utilized in codes such as ANISN [28]. Nevertheless, the authors show that the results of the calculations using the mathematical solutions of the transport equations were in good agreement with those obtained using the MCNP Monte Carlo code and with experimental measurements. Readers who are interested in the use of transport codes for their own reasons are advised to read available literature on such a topic.

2.4 FRONT END ELECTRONICS

Topical Session 4 provides the basics of the electronics used with neutron spectrometers and detectors. It divides the electronics into the detector (or sensor), the front-end electronics and read-out electronics that present the data in a particular display form for any data acquisition system. The basic properties of signal processing, such as impedance matching, signal to background noise (S/N) and signal integration to optimize S/N and differences between digital and analogue signals are explained. The main functions of the front-end electronics are listed. The processing and shaping of the signals from the front-end-electronics to suit the readout electronics are described, which often involve digitizing the analogue signals from the sensor. Common ‘logic families’ are described along with conventional read-out signals using different converters (e.g. Analogue-to-Digital) to display the data in a particular form (e.g. radiation energy spectrum). The purpose of this paper is not to serve as a reference for electronic designers, but merely to provide enough technical understanding for the reader to be able to select commercially available electronics appropriately for his/her scientific experiment. Further description of nuclear electronics can be found in Ref. [13].

2.5 NEUTRON SPECTROSCOPY

Topical Session 5 contains eight papers that provide a snapshot of the broad range of neutron detectors for various applications. The first five are on broad-energy detectors based on the use of thermal neutron detectors embedded within neutron moderators of various designs to achieve desired responses to neutrons of different energies, while the last two papers describe high-resolution neutron spectrometers. The sixth paper describes an interesting technique for measuring the neutron fluence with any detector without knowledge of its detection efficiency. These papers are not intended to be exhaustive, since it would be nearly impossible to cover

the enormous range of applications involving neutrons. For example, there is no mention of neutron detectors particularly utilized in radiation therapy, battlefield dosimetry, space dosimetry, cosmic ray research, or oil-well logging. There are no papers on bubble detectors or commercial fast neutron spectrometers based on hydrogen recoil. With regard to fast neutron spectrometers, the development of the PSD plastic scintillator (Topical Session 1) has led to several new products that have been developed in connection with homeland security applications, but not intended for general neutron monitoring around reactor environments or hospital environments, where neutrons extend down to thermal energies. The seventh paper on a high-resolution spectrometer uses the new PSD plastic but only for high-energy (> 1 MeV) neutron measurements.

The first paper in Topical Session 5 describes work done in a national laboratory in response to the recognized need for neutron detectors that do not use He-3 gas, which has been the most common thermal neutron gas-filled detector for decades. This need for 'He-3 alternative' detectors resulted from the large projected number of neutron detectors required by the U.S. Homeland Security Program such that the global He-3 gas supply would be inadequate. Such neutron detectors for Homeland Security do not need to be spectroscopic. The main requirement was to be inexpensive and to detect neutrons (of all energies) as efficiently as possible.

This paper describes the testing of three alternative technologies called 'boron-coated straw', 'boron-loaded liquid scintillator' and 'liquid argon' detectors. Various properties of these detectors such as detection efficiency, gamma insensitivity and rejection of gamma rays signals relative to neutron signals were investigated by experiment and by Monte Carlo simulations. The capabilities and limitations of these technologies for various potential applications, including Homeland Security, were summarized.

The second paper describes recent upgrades to a moderator type, broad-energy, neutron rem meter called HPI 2080. This is an Ag-wrapped GM tube in a polyethylene moderator, that can operate reliably in a pulsed neutron field, often found in accelerator laboratories. A brief history of this instrument and past upgrades are described. Recent upgrades to hardware and firmware are described in detail along with testing of the latest version in reference radiation fields and experience with the instrument in various operational venues.

The third paper describes a single moderator version of the conventional Bonner Sphere Spectrometer that usually consists of six or more polyethylene moderators of different sizes. This proposed spectrometer, called SP², consists of 31 thermal neutron detectors arranged in symmetrical positions along three axes at five radial distances inside a 30 cm diameter polyethylene sphere. The thermal neutron detectors can be passive (e.g. TLDs) or active (e.g. Li-6 radiator on a silicon diode). Monte Carlo simulations were done to determine the relative response of the embedded detectors to various mono-energetic neutrons to establish the detector response functions. Measurements of neutron spectra are done by reading the 31 detectors and performing spectral unfolding. Tests of the SP² were done using mono-energetic neutron beams at NPL (facility described in Topical Session 2).

Another version of this spectrometer is called CYSP. This is a cylindrical moderator 65 cm high \times 50 cm diameter. It has a collimator 30 cm long \times 15 cm diameter, centrally located inside. Numerous thermal neutron detectors are strategically placed inside the moderator. Its mode of operation is similar to the SP².

The authors claim that these new moderator spectrometers have responses similar to the Bonner Sphere spectrometers and offer new opportunities for real-time spectroscopic monitoring of neutron fields in a variety of venues.

The fourth paper describes yet another version of the Bonner Sphere Spectrometer. Here, the authors replace the many spheres of the traditional spectrometer by concentric, nesting, cylindrical shells that can be sequentially stacked to increase the size of the moderator, like a matryoshka doll. This configuration obviously reduces the size and weight of the traditional spectrometer and makes it less cumbersome to manipulate. Monte Carlo calculations were done to determine the response functions of this Nested Neutron Spectrometer and measurements were made in reference neutron fields as well as in operational venues where such spectrometers might be used. Results similar to the traditional Bonner Sphere Spectrometer were obtained.

The fifth paper describes a new way of using a Bonner Sphere Spectrometer, especially applicable for measuring secondary neutron fields associated with high-energy linacs used in medical applications. The idea is to use all the spheres at the same time in a ‘planetary mode’, reducing the measurement time significantly relative to sequential measurements using one sphere at a time.

The authors recognized that the use of all the spheres simultaneously could suffer from ‘cross-talk’, or the effect of one sphere on the rest. They performed Monte Carlo calculations under a typical operational scenario, including a phantom to represent a patient, and found that the cross-talk was negligible. They performed measurements inside a therapy room using the spectrometer and obtained good agreement with spectral results using Monte Carlo simulation.

The sixth paper in this Topical Session describes a unique way to determine the neutron (or gamma) fluence using any detector that does not completely absorb the impinging neutrons, without detailed knowledge of the detector detection efficiency; the method can in fact be used to determine its detection efficiency. This method, called ‘the influence method’ is explained using two identical detectors and making measurements of counts in each detector with one detector shielding the second detector in the line of the beam. In essence, the two measurements provide two known quantities, which can be utilized to determine two unknowns: the incident neutron fluence and the detection efficiency (assumed identical for both detectors in this case). The expressions for incident fluence and detection efficiency are explicitly given in relation to the two measured count rates. The authors also provide expressions for estimations of uncertainty for such determinations, as well as expressions for more complex situations such as for detectors having different detection efficiencies, accounting for detector scattering effects as well as the case of using multiple detectors, when stacks of detectors are needed to achieve desired detection efficiencies. The method is illustrated by using an Am–Be neutron source, which itself is a statistical emitter of neutrons, and the use of two He-3 counters at different distances from the source. The impact of multiple measurements on the uncertainty of the emission rate was examined. These measurements yielded an emission rate that agreed with the quoted value to within 0.2%.

The seventh paper is one of only two papers on high-resolution (in energy) neutron spectrometers. It describes a spectrometer under development at the iThemba laboratory, which produces mono-energetic beams up to 100 MeV as reference fields, well-known to those doing research in space radiation and in high-energy laboratories. The paper describes the neutron facility at the laboratory, which may be useful for readers not familiar with this facility. The

spectrometer under development, called the ‘compact neutron spectrometer’ is based on the new PSD plastic viewed with silicon photomultipliers (SiPMs), making use of digital pulse-shape discrimination to reject gamma rays. The final spectrometer is intended to cover the energy range 1–100 MeV. The current scintillators consist of four slabs of plastic scintillator $6 \times 6 \times 50 \text{ mm}^3$ (each viewed separately), separated by a polyethylene cross 15 mm thick. Illustration of its performance is made using an Am-Be source and comparison of electronic signals and unfolded spectral results made previously using a traditional liquid scintillator viewed with a fast PMT. Pulse-shape discrimination performance and spectral results of the new scintillator are comparable to the traditional spectrometer. The authors intend to enlarge the scintillator to $6 \times 6 \times 150 \text{ mm}^3$ with similar changes to the polyethylene cross to enable the spectrometer to extend up to 100 MeV. Tests are underway to assess the performance of the larger compact neutron spectrometer.

The eighth paper describes a spectrometer called ‘ROSPEC’ that is currently regarded by many as the state-of-the-art neutron spectrometer. It was originally built for the NATO military and was adopted as the NATO reference spectrometer. However, it is now in common use in many national laboratories world-wide that are interested in fast neutron spectrometry. ROSPEC is certified by NIST for use in radiation measurements associated with radiation protection applications. ROSPEC consists of four spherical hydrogenous counters, filled with different pressures, each spanning a particular range of neutron energies. These ranges overlap and so the four counters together span the energy range 50 keV to 4.5 MeV. To cover the energy range below 50 keV, two more spherical counters filled with He-3 are used. One of these counters is embedded inside a special boron shell to alter its response to mimic the dosimeter response (of tissue) from 1 eV to 50 keV, while the second measures the thermal neutron fluence. For measurement of neutrons above 4.5 MeV, a second small spectrometer, called SSS, is used. It measures neutrons using an array of tiny plastic scintillators that enable pulse-height rejection of gamma rays above 4.0 MeV in neutron energy. Thus, ROSPEC plus SSS measures neutron spectra from thermal to 16 MeV.

The great appeal of ROSPEC is that it is a proven commercial product. Its operation requires no expertise in terms of neutron spectroscopy. When SSS is used along with ROSPEC, no input spectrum (unlike Bonner Spheres) is required. The operation of the system requires ‘start’ of the measurement, ‘end’ of measurement and ‘unfold’ of data. The spectral data from all the detectors are merged to produce one continuous spectrum as the ROSPEC output. The paper provides a brief history of ROSPEC over an evolutionary period of about 30 years and shows representative data from reference sources as well as spectra taken in various operational venues such as critical facilities, nuclear fuel processing plants, nuclear reactor environments, and shipment of radioactive materials.

2.6 THERMAL NEUTRON DETECTORS FOR NEUTRON SCATTERING

Neutron scattering science is at a pivotal point; it is both a time of worry about a significant capacity decline and a time of hope for a renaissance in its future.

The worry about the decline in capacity comes from the current general trend in closing research reactors; e.g., in 2019, the BER-II reactor in Helmholtz Zentrum Berlin (HZB), Germany, the ORPHEE reactor at Laboratoire Léon Brillouin (LLB), Saclay, France and the JEEP-II reactor at IFE in Norway have closed, with a large number of instruments becoming unavailable for use. The HZB and LLB are amongst the world’s leading neutron research centres.

The hope for a renaissance comes from two quarters.

1. First, there are four new, advanced neutron sources which among them plan to build more than 90 new, beyond state-of-the-art instruments within the next decade: (i) The Chinese Spallation Source in Dongguan near Hong Kong, China; (ii) the PIK Reactor near St Petersburg, Russia; (iii) the second target station at the Spallation Neutron Source at Oak Ridge, USA; and (iv) the European Spallation Source in Lund, Sweden.

These new instruments will ensure neutron science remains at the cutting edge; however, an overall drop in capacity is foreseen due to the large number of sources closing. Advances in the past couple of decades in instrumentation and neutron transport modelling have enabled a second hope for the future:

2. Smaller compact neutron sources (mostly accelerator based) for which there has been a surge of design studies recently [29]. Their comparatively moderate costs may allow them to be regional alternatives to the generation of research reactors now closing.

An overview and forecast for neutron instrumentation in Europe is given in the recent ESFRI report on the neutron landscape [30].

Neutron scattering science deals with the investigation of materials using thermal and cold neutrons. This has impact on many areas of materials science from finding new materials and developing tailor-made materials to medicines and bio-science. This in turn is an interrogative tool in addressing the grand challenges of society, and neutron science has its role to help solve all of these issues [31].

The Nobel Prize in Physics of 1994, awarded to Clifford Schull and Bertram Brockhouse, summarizes succinctly neutron scattering: it is about interrogations as to where the atoms are and what the atoms do. The measurements made are of differential cross sections, where:

- *Elastic measurements*: the single differential cross section as a function of solid angle for a specific incoming neutron energy. The measurements (diffraction) correspond to determining where the atoms are; i.e., their relative location.
- *Inelastic measurements*: the double differential cross sections as a function of solid angle and scattered neutron energy, for a specific incoming neutron energy. The measurements (spectroscopy) correspond to determining what the atoms do; i.e. their dynamics.

The design of a neutron scattering instrument is in principle simple: it defines a phase space flux incident on a sample, and measures the rate of scattering into a particular scattering angle. As the energy of the neutron is not directly measurable, it will need to be determined either by selection by (i) a mechanical device (such as a velocity selector), (ii) diffraction from a monochromator, or (iii) using time-of-flight techniques, where the neutron speed's and its interaction time in the detector determine its energy. At the heart lie the detectors.

Neutron scattering relies principally on thermal neutron detection. This is dependent upon a nuclear interaction between the neutron and a target atom in the converter material inside the detector. As the neutron's energy is so low (in the meV range), it is not possible to register the collisions of the neutron itself inside a material directly. There are two implications of this:

- First, the products of this neutron interaction in the converter material have to be readily detectable, and distinguishable from other particles in the environment.

- Second, the cross section of the nuclear interaction should be larger than the elastic or inelastic interaction cross sections, so that the position of detection of the neutron is comparable to its outgoing direction from the sample being probed by the neutrons.

Detectable products of the neutron interaction are photons or charged particles (ions or electrons). These can be subsequently detected with common radiation detection technology (Figure 1). As these detectors are well developed elsewhere, discussions of neutron detectors nearly always concentrate on the most optimal application of the neutron converter material – and use the detection techniques from other disciplines.

Currently, over 80% of neutron detectors used in neutron scattering worldwide are He-3 based. The remainder are mostly Li-6 based scintillator detectors, with some BF₃ gaseous detectors (with B-10 as the active materials) from the 1970’s and 1980’s.

Given the constraints above, in terms of suitable isotopes to use as a convertor for thermal neutron detection, there are only a few that are realistic: He-3, Li-6, B-10, Gd-157 and U-235 (Table 1). Additionally, the cross sections of these convertor materials vary roughly by $1/v$ in the region of energies of interest.

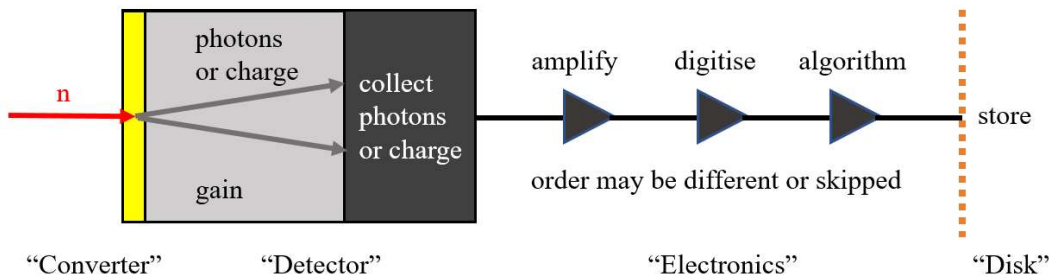


FIG. 1. Schematic of a neutron detector and its components.

TABLE 1. COMMONLY USED ISOTOPES FOR THERMAL NEUTRON DETECTION, REACTION PRODUCTS AND THEIR KINETIC ENERGIES. FROM THE ILL BLUE BOOK [32]

Reaction	Energy (MeV)	Particle	Energy (MeV)	Particle	Energy (MeV)
$n(^3\text{He}, p)^3\text{H}$	+0.77	p	0.57	^3H	0.19
$n(^6\text{Li}, \alpha)^3\text{H}$	+4.79	α	2.05	^3H	2.74
93%: $n(^{10}\text{B}, \alpha)^7\text{Li} + 2.3 \text{ MeV} + \gamma$	(0.48)	α	1.47	^7Li	0.83
7%: $n(^{10}\text{B}, \alpha)^7\text{Li}$	2.79	α	1.47	^7Li	1.01
$n(^{235}\text{U}, \text{Lfi})\text{Hfi}$	+~100	Lfi		Hfi	≤ 60
$n(^{157}\text{Gd}, \text{Gd})e^-$	+ ≤ 0.182	Conversion electron			0.07–0.182

where Lfi and Hfi are the light and heavy fission fragments

2.6.1 Helium-3 detectors

Helium-3 detectors are gaseous, with He-3 as both the convertor medium and counting gas. They exist in two broad forms:

One dimensional: Most commonly these are in the form of tube-shaped detectors, which act as a proportional counter. Diameters of 850 mm are common. Originally, He-3 detectors were truly one dimensional, i.e., there was no position resolution within the tube length. However, nowadays nearly all He-3 detectors use a resistive wire to give a position sensitivity, by using charge division along the wire. With suitable electronics and data treatment, this can give a position sensitivity of ca. 1%, or slightly better, along the wire.

Two dimensional: Helium-3 detectors also exist as area detectors. These use the principle of a multiwire proportional counter (MWPC) [33] to cover a specific active sensitive area without dead space, but have a well-known limitation in rate capability. The first micro pattern gaseous detector was the Micro-Strip Gaseous Chamber (MSGC), which was invented by Anton Oed from the ILL in 1988 [34]. This design takes advantage of micro production techniques; e.g., those commonly used in printed circuit board fabrication, to create a cheap high-performance detector design. Numerous He-3 MSGCs are in operation in neutron scattering instruments.

2.6.2 Scintillator detectors

Scintillator detectors rely on the detection of scintillation light from the interaction of the ions produced in the nuclear interaction with the scintillator material. The light is detected typically in photomultiplier tubes, or with charge-coupled devices (CCDs). They are divided into two categories:

- *Directly coupled scintillator detectors* where the scintillator material is directly coupled to the light detecting devices.
- *Indirectly coupled scintillator detectors* where the light from the scintillator material is directed into light guides or thin fibres which transport the light to the light detecting devices. These materials sometimes shift the wavelength of the light, to enable the light detecting devices to detect it with a higher quantum efficiency per photon.

The motivation for using indirectly coupled scintillator detectors is typically to save cost, and to cover larger sensitive areas with the detectors by combining channels to reduce both the number of light sensitive devices needed and the subsequent electronics and processing.

At the European Spallation Source (ESS), which is currently under construction in Lund, the increase in source brightness, transformative improvements in moderator design combined with better instrument design has led to detector requirements being far beyond the existing state of the art. The instantaneous rate capability of the neutron detectors being developed is between a factor of 10 and 1000 better than that needed for today's top-performing instruments. Similarly, the position resolution and active area covered by the detector system are increased by several fold. One of the main emphasis of the detector development programme from ESS is to concentrate in developing He-3 replacement detector technologies. ESS has chosen to specialise in B-10 thin film technologies, where the convertor is a thin film of boron carbide, enriched in B-10. The ions from the nuclear reaction escape into a gaseous detector and are subsequently detected. It is possible to deposit boron carbide cheaply over large areas; ESS has such a facility, which more than satisfies its needs of several 1000 square metres of thin film. The progress in these technologies is such that the performance is matching that of the requirements for ESS instruments; demonstrator detectors have been mounted on existing neutron scattering instruments and have been shown to be able to match or outperform existing He-3 detectors. With half the instruments at ESS based upon detectors designed around B-10 thin films as a convertor, this is now very much an emerging technology.

New developments in the Monte Carlo simulation of thermal neutron scattering processes in condensed matter have been made. The goal is to be able to have a complete detector and experiment simulation. The Monte Carlo package GEANT4 is the working horse in many disciplines for detector simulation and design. However, the applicability to thermal neutrons is limited due to its highly imperfect description of thermal neutron interactions, which in turn means that it is not possible to reproduce well the behaviour of the detector to neutrons. The most obvious examples of this is not modelling crystalline materials, in particular coherent scattering, i.e. diffraction is not modelled, and also not modelling neutron-phonon scattering. A new library, NCRYSTAL, has been written to be able to model thermal neutron transport in crystals. This in turn enables complete detector and experiment simulation, which allows future neutron detectors to be optimised by design with simulation. V1.0 has been released [35].

Additional work has gone on to be able to lower the barrier to entry and simplify simulation neutron detector and instrument performance. An overview of these is given here [36]. This includes visualisation tools, a framework for the simulations and MCPL [37], which allows simple particle exchange between Monte Carlo packages. This particle exchange between Monte Carlo packages has the benefit that different Monte Carlo codes have been optimised and tuned for specific purposes. By allowing these codes to be used together, the best package can be chosen for the task in hand – and several packages used in 1 simulation.

The Paul Scherrer Institute in Switzerland houses several large-scale facilities, one of which is the neutron spallation source SINQ, where there are currently about 20 neutron instruments. Most of the recent effort in development has focussed on ZnS scintillator material mixed with Li-6F as the convertor medium, where the light is transported with wavelength shifting fibres. The light detection is done with silicon photomultipliers (SiPMs). SiPMs are widely used in other disciplines, but not so widely yet in neutron detection. By analysing the temporal distribution of the SiPM pulses, the neutron signal can be extracted. Both 1D and 2D arrangements of detectors are possible. The detector performance is very good, comparable or better than that from He-3 detectors, and this is a good design for neutron diffractometers.

The papers that have been contributed to this Topical Session cover several developments of detector technologies for neutron scattering.

The first paper describes a typical regional neutron scattering centre and its history. The Budapest Neutron Centre (BNC) has a history with the reactor dating back to 1959, with significant upgrades in 1967 and 1992. Over this time the development of the instrumentation has meant that large position sensitive detectors need to be factors up to 1 million times better performing, because of improved instrument performance.

The detectors installed on the neutron instruments at the BNC are a mixture of He-3 tubes and area detectors; since the early 2000's they have produced area detectors in-house. These detectors are available through technology transfer with spin-off companies close to the facility, and BNC have been involved in EU projects relating to the development of high rate detectors.

The second paper describes the development of the detection system dedicated for the PIK reactor at the St Peterburg Nuclear Physics Institute (PNPI). It deals with an historical analysis of detectors at different facilities around the world, including J-PARC, ESS, ILL, and attempts to come to a global trend. Due its merits, and to the relatively easy access to He-3 in Russia, PIK has chosen to base many of their detectors on He-3 systems (c.f. the situation with ESS described above).

The third paper describes the recent status and progress in neutron imaging detection systems. Imaging, i.e. radiography and tomography, with neutrons is often treated differently than

neutron scattering. The key properties of the neutron for imaging are its highly penetrating nature, due to its neutral charge, allowing it to penetrate quite thick samples under study, as well as its very different contrast properties compared to X-rays, making X-ray and neutron imaging very complementary techniques.

The progress in the past 30 years in detectors for imaging has been immense. Time-resolved images at kHz are now possible with advanced cameras, and even faster with discrete event detectors. The detector resolutions can be as high as 10 μm . With detector developments currently ongoing, there is an aspiration for achieving 1 μm resolution, and time resolution in the 100 μs range. One promising detector is the Gd-doped micro-channel plate coupled with a Timepix time-resolved ASIC (application-specific integrated chip), which offers excellent time- and position-resolution, with reasonable detection efficiency. The workhorse detector for neutron imaging is a neutron sensitive scintillator coupled to a CCD camera.

The fourth paper describes recent work on pixellated neutron detectors with excellent timing resolution that are also promising for imaging. Here the pixellation is achieved by using multi-anode photomultiplier tube photo detectors, coupled to GS-20, a Li-6 doped cerium aluminosilicate glass optimized for thermal neutron response. Better pixellation can also be achieved with solid state silicon photomultiplier (SiPM) arrays. It is possible to etch chevroned microchannel plates. The Timepix ASIC makes an excellent match to these detectors to optimize their performance.

The fifth paper describes the development of neutron detectors for spectrometers at the pulsed IBR-2 reactor in Dubna. The IBR-2 reactor is currently the highest instantaneous brightness neutron source. Dubna builds 1D and 2D position-sensitive He-3 detectors, ring detectors for full axial coverage, as well as wavelength-shifting fibre-based scintillator detectors. One feature of note here is that for a couple of instruments, the detector geometry is time focusing, which means that the scintillator screen itself has to be curved. In this geometry, optimised for time-of-flight diffraction, neutrons of various energies scattered at different angles from the same d -spacing will be recorded at the same time-of-flight.

The final paper presents what is involved in a radioactive source-based facility for testing detectors and detector development. Understanding backgrounds at the same time as understanding signals is important, and so an array of gamma, fast neutrons and thermal neutrons (by moderations) is needed. One useful addition is the ability to tag fast neutrons from the prompt photon simultaneously released, allowing tagged fast neutrons of 1–6 MeV to be used in such a facility allows event-by-event energy determination and optimizes the use of a broad-spectrum neutron source.

2.7 NEUTRON DETECTORS FOR FUSION ENERGY

Neutron diagnostics have been essential to the study of controlled thermonuclear fusion since the early developments in the 1940s and 50s, importantly providing the primary evidence of thermonuclear fusion reactions in such devices from the two most studied reactions involving deuterium–deuterium (DD) and deuterium–tritium (DT) plasmas, which release characteristic 2.45- and 14.1-MeV neutrons in those reactions, respectively. Various types of fusion power technologies are being pursued, either via government-funded international or domestic research, and increasingly via private technology investments. The majority of the approaches are based on magnetic or inertial plasma confinement techniques, or a combination of these. The contributed papers from this session largely focus on detectors for magnetic confinement

fusion, although many of the technologies that are discussed here are relevant, and in many cases are already deployed, in alternative fusion approaches such as inertial confinement.

Broadly speaking, there are two main categories of magnetic confinement devices being pursued today in fusion energy research: i) tokamak devices and ii) stellarator devices. Both concepts operate with a toroidal plasma configuration and aim to provide equilibrium between the pressure in the plasma with the forces in the magnetic field by the introduction of a ‘twist’ in the toroidal magnetic field, which essentially serves to reduce the drift of plasma particles towards the first wall, leading to undesirable cooling of the plasma and hence the fusion reaction rate. In a tokamak, the rotation in the magnetic field is provided by the introduction of a strong toroidal electric current within the plasma, whereas in a stellarator device the twisting is introduced by highly complex, non-axisymmetric magnetic field coils. The Joint European Torus (JET), based in the UK, is an example of a tokamak device – currently the world’s largest, and the only device that is currently able to operate using tritium fuel. Several other devices are in operation around the world such as ASDEX (Axially Symmetric Divertor Experiment, Garching, Germany), KSTAR (Korea Superconducting Tokamak Advanced Research, Daejeon, Republic of Korea), EAST (Experimental Advanced Superconducting Tokamak, Hefei, China), NSTX (National Spherical Torus Experiment, Princeton, USA) to name a few of the approximately 30 or so. Wendelstein 7-X (Greifswald, Germany) is an example of a stellarator machine, currently the world’s largest.

A wide range of neutron diagnostics are used to support experimental diagnostics for magnetic confinement fusion. Neutron measurements provide a direct determination of fusion power, since 80% of the energy released in a DT reaction is by the neutron itself. In addition, spatial neutron emissivity from the plasma, the fuel ion ratio and ion interactions in plasma instabilities may be determined from appropriate neutron diagnostics. An extensive range of diagnostics are foreseen for ITER (International Thermonuclear Experimental Reactor), an international experimental programme to construct a large tokamak device in Cadarache in France. ITER aims to produce significant fusion power, 500 MW for sustained periods of time, and a fusion gain of 10, i.e. 10 times more energy will be produced than the energy required to heat the plasma. A key factor for neutron detection technologies to be deployed is resilience to the extreme radiation environment, with 14-MeV neutron fluxes of up to 1×10^{14} n cm⁻² s⁻¹ in locations near the first wall components of ITER.

Three extended papers are contained in this Topical Session of this publication. The first gives background on the current status of tokamak fusion research at JET, an EU facility located at Culham in the UK, and for ITER. The paper compares the neutron spectra and fluxes predicted in fusion experiments in both facilities and outlines the role of neutron transport and activation simulations in supporting and optimizing the diagnostics for deployment in those fields. The range of instruments either currently deployed in JET or under development are discussed with key details on each of the systems provided. The discussion broadly divides systems into those that operate with specific nuclear reactions such as fission chambers, activation foils and diamond-based wide band-gap instrument and on those relying on elastic neutron scattering such as scintillators, GEM, He-4 gas filled chambers detectors, and superheated bubble detector types, for example. Neutron spectrometers are also discussed, in particular, time-of-flight or magnetic spectrometry techniques such as TOFOR and MPR instruments along with new developments for vertical compact neutron spectrometers including a detector array consisting of a matrix of 12 independent, single-crystal diamond detectors. ITER detection systems are

described which include a description of the following systems: neutron flux monitors installed in radial diagnostic ports; divertor neutron flux monitors; micro-fission chambers; a neutron activation system with irradiation ends at various locations inside the vacuum vessel; radial and vertical neutron cameras; a high-resolution neutron spectrometer and other neutron spectrometers. Besides the nuclear conditions the paper discusses a number of additional environmental factors for detection systems at ITER, which presents a range of challenges for operation of such systems, many experienced in combination. Included in the discussion are the high temperature environments, high and transient magnetic fields, high radiation fields, intense RF fields and low vacuum conditions.

The second paper, focuses on a particularly resilient, activation-based neutron detector concept, targeted towards demonstration fusion reactor environments, such as those proposed in DEMO concepts, particularly for use within tritium breeding blankets where monitoring of the nuclear conditions is needed to predict breeding performance and the conditions within the blanket. A concept is proposed in the paper which utilizes a novel, low-activation matrix compound capsule which contains a range of metallic elements. The requirement for the detector is to accurately measure neutron fluence under high and variable neutron count rates, high gamma background, high temperature, and high and variable magnetic fields. The paper discussed the selection criteria for the choice of activation foils and associated reactions along with the carbon and SiC capsule design and some additional mechanical tests that have been performed. Pre-analysis calculations to predict activities and reaction rates associated with the specific reactions utilized which were performed using the MCNP and FISPACT-II codes. These results were compared with experimental results for tests performed at a 14-MeV neutron irradiation facility based at Frascati, Italy.

The third paper reports on the development of multiple threshold activation foils for the future liquid-Li target Advanced Fusion Neutron Source in Japan with an eye also towards DEMO. The detection range has to cover up to 60 MeV. The needs for accurate cross section measurements are discussed.

A summary of neutron detector technologies and parameters covered in this Topical Session are detailed in a summary, see Table 2 below.

TABLE 2. SUMMARY OF KEY NEUTRON DETECTION TECHNOLOGIES DEPLOYED IN NUCLEAR FUSION DEVICES

Detector Type	Nominal operational detection range (n cm ⁻² s ⁻¹)	Typical deployment systems	Quantities derived
Activation foils	10 ⁵ –10 ¹⁵	Integrated neutron flux monitoring for absolute neutron yield	Fusion power
		Neutron spectrometry	Neutron energy spectra
Scintillator-based systems (Spectrometers)	10 ² –10 ⁸	Time-of-flight systems	Neutron energy spectra
		NE213, BC301, BC309,	Fuel ion temperature
		EJ200, BC418, Stilbene (and others)	Fuel ion velocity distribution Fuel ratio: n_d/n_t

Detector Type	Nominal operational detection range (n cm⁻²s⁻¹)	Typical deployment systems	Quantities derived
		Magnetic proton recoil spectrometers	Plasma heating and rotation
Scintillator-based systems (Cameras)	10 ² –10 ⁸	Neutron profile monitors (2D cameras)	Neutron emission tomography, triton burnup, fast particle confinement
Fission counter-based systems	10 ⁵ –10 ¹⁵ (dynamic range is extended through pulse mode, Campbell mode and current mode)	Time-resolved total emission rate Pairs of U-235 and U-238-based systems	Fusion power Magneto-hydrodynamic instabilities and fast particle interactions
Diamond detector systems, Si diodes, proton recoil counter, SPND	10 ⁵ –10 ¹¹	Tritium breeding modules	Diamond detector systems, Si diodes, proton recoil counter, SPND
Gas proportional counters	10 ¹ –10 ⁶	Delayed neutron counting systems e.g. using Th-232 and U-238	

SPND: self-powered neutron detector

3 CONCLUSIONS

The detection of neutrons is essential in many fields. However, the materials used and the design of detectors vary greatly depending on the field of application. Specialization has developed within the various communities, such as primary metrology, spectroscopy, neutron scattering, fission and fusion. The result has been that many developments have occurred within these fields, but there has been little chance for the different communities to exchange information and share experiences.

The Technical Meeting on Modern Neutron Detection was convened specifically to allow representatives from these communities to come together in one common forum. This resulting TECDOC provides an overview of several of the currently deployed materials and technologies for measuring neutrons in different fields of application, and a summary of several of the new approaches that are under active research and development around the world.

It is hoped that the broad overview of technologies, materials and applications contained in this TECDOC will prove useful for Member States when appraising possible neutron detection technologies for specific applications within existing or future facilities.

REFERENCES

- [1] CHADWICK, J., Possible existence of a neutron, *Nature* **129** (1932) 312.
- [2] SMYTH, H.D.W., “Appendix 1. Methods of Observing Fast Particles from Nuclear Reactions”, *Atomic Energy for Military Purposes, The Smyth Report*, Princeton, NJ: Princeton University Press (1946).
- [3] BIRKS, J.B., *Scintillation Counters*, Pergamon Press, London (1953).
- [4] MARION, J.B., FOWLER, J.L., *Fast Neutron Physics, Part 1*, Interscience Publishers, New York (1960) Ch. II–IV.
- [5] SOODAK, H. (Ed) *Reactor Handbook*, Interscience Publisher, New York, (1962) Ch. 2.
- [6] YEATER, M.L., *Neutron Physics*, Academic Press, New York, (1962) 318 pp.
- [7] SNELL, A.H., *Nuclear Instruments and Their Uses*, John Wiley, New York (1962) 494 pp.
- [8] ING, H., PIESCH, E., Status of neutron dosimetry, *Radiat. Prot. Dosim.* **10** (1985).
- [9] SHANI, G., *Radiation Dosimetry Instrumentation and Methods*, CRC Press, Boca Raton (1991).
- [10] CROSS, W.G., ING, H., “Neutron Spectroscopy”, *The Dosimetry of Ionizing Radiation Vol. II* (KASE, K.R., BJARNGARD, B.E., ATTIX, F.H., Eds), Academic Press, New York (1987) 374 pp.
- [11] PRICE, D.L., SKOLD, K., Introduction to neutron scattering, *Methods Exp. Phys.* **23A** (1986) 1–97.
- [12] SIDIS, Y., “Introduction to neutron spectroscopy”, paper presented in Ecole d’été Mico-Aussois, Laboratoire Léon Brillouin, CEA-CNRS, Saclay, France (2010).
- [13] KNOLL, G., *Radiation Detection and Measurements*, 4th edn, Wiley & Sons, U.K., (2010) 830 pp.
- [14] International Workshop in Position Sensitive Neutron Detectors, May 15–17, 2018. Forschungszentrum Julich GmbH, Germany.
- [15] GUARDIOLA, C., LOZANO, M., PELLEGRINI, G., Neutron Detection with Silicon Devices. (Proc. Spanish Conf. on Electron Devices, 2009) 54–56 IEEE, Santiago de Compostela, Spain (2009).
- [16] 7th Design and Engineering of Neutron Instruments Meeting (DENIM), Paul Scherrer Institute, Switzerland (2018).
- [17] 31st RD 50 Workshop on Radiation hard semiconductor devices for very high luminosity colliders, CERN. November 20–22, 2017, Geneva, Switzerland.
- [18] SMITH, M. B., et al., Fast neutron spectroscopy using Cs₂LiYCl₆: Ce (CLYC) scintillator, *IEEE Trans. Nucl. Sci.* **60** (2013) 855–859.
- [19] MCELROY, W.N., BERT, S., CROCKETT, T., HAWKINS, R.G., SAND II – A Computer-Automated Iterative Method for Neutron Flux Determination by Foil Activation, AFWL-TR-67-41 (1967).
- [20] REPLOGLE, J., HOLCOMB, B.D., BURRUS, W.R., The use of mathematical programming for solving singular and poorly conditioned system of equations, *J. Math. Anal. Appl.* **20** 2 (1967) 310–324.
- [21] RADIATION SAFETY INFORMATION COMPUTATIONAL CENTRE, RSIC Computer Code Collection, FERDOR and COOLC Spectra Unfolding Codes, contributed by Oak Ridge National Laboratory and Gulf Radiation Technology, San Diego, CA, PSR-17 (1975).
- [22] BENJAMIN, P.W., KEMSHALL, C.D., BRICKSTOCK, A., The Analysis of Recoil Proton Spectra, AWRE Report No. 09/68 (1969).

- [23] RADIATION SAFETY INFORMATION COMPUTATIONAL CENTRE, “Workshop on Unfolding Radiation Energy Spectra”, Oak Ridge National Laboratory, April 12–13 (1976); A Review of Radiation Energy Spectra Unfolding, compiled by D.K. Trubey, ORNL/RSIC – 40 (1977).
- [24] INTERNATIONAL ATOMIC ENERGY AGENCY, Current Status of Neutron Spectrum Unfolding, IAEA–TECDOC–221 (1979).
- [25] INTERNATIONAL ATOMIC ENERGY AGENCY, Compendium of Neutron Spectra in Criticality Accident Dosimetry, Technical Reports Series No. 180, IAEA, Vienna (1978).
- [26] INTERNATIONAL ATOMIC ENERGY AGENCY, Compendium of Neutron Spectra and Detector Responses for Radiation Protection Purposes, Technical Reports Series No. 318 (1990).
- [27] INTERNATIONAL ATOMIC ENERGY AGENCY Compendium of Neutron Spectra and Detector Responses for Radiation Protection Purposes Supplement to Technical Reports Series No. 318, Technical Reports Series No. 403 (2001).
- [28] EAGLE, W.W., Jr., A User Manual for ANISN, Oak Ridge National Laboratory Report K-1693 (1967).
- [29] MARCHIX, A., et al., Saclay Compact Accelerator-driven Neutron Sources (SCANS), J. Phys. Conf. **1046** (2018) 012009.
- [30] CARLILE, C., PETRILLO, C., CARPINETI, M., DONZELLI, M., (Eds), ESFRI Physical Sciences and Engineering Strategy Working Group—Neutron Landscape Group, Neutron scattering facilities in Europe —Present status and future perspectives, ESFRI Scripta **1** (2016) Dipartimento di Fisica - Università degli Studi di Milano.
- [31] WILLIS, B.T.M., CARLILE, C.J., Experimental Neutron Scattering, Oxford University Press (2013).
- [32] DIANOUX, A.J., LANDER, G., ILL Neutron Data Booklet, OCP Science (2003).
- [33] CHARPAK, G., et al., The use of multiwire proportional counters to select and localize charged particles, Nucl. Instrum. Methods **62** (1968) 262.
- [34] OED, A., Position-sensitive detector with microstrip anode for electron multiplication with gases, Nucl. Instrum. Methods A **263** (1988) 351.
- [35] CAI, X.X., KITTELMANN, T., NCrystal: A Library for thermal neutron transport, submitted to Computer Physics Communications (2019), arXiv:1901.08890, <http://mctools.github.io/ncrystal>
- [36] KANAKI, K., et al., Simulation tools for detector and instrument design, Physica B: Condens. Matter **551** (2018) 386.
- [37] KITTELMANN, T., et al., Monte Carlo Particle Lists: MCPL, Comput. Phys. Commun. **218** (2017) 17.

PAPERS PRESENTED AT THE TECHNICAL MEETING

TOPICAL SESSION 1
DETECTOR MATERIALS AND SPECIAL DETECTION TECHNIQUES

DIAMOND DETECTORS FOR NEUTRONS

M. ANGELONE

Dipartimento Fusione e Tecnologie per la Sicurezza Nucleare

ENEA C.R. Frascati

Via E. Fermi, 45, 00044 Frascati (Italy)

e-mail : maurizio.angelone@enea.it

Abstract: For many years, diamond has been studied and used for detection of direct and indirect ionizing particles because it exhibits many outstanding properties which make feasible the realization of fast and low noise radiation detectors suited for withstanding harsh environments. Furthermore, its low atomic number ($Z = 6$), close to that of tissue, render diamond very interesting to radiation dosimetry. Besides, diamond has low sensitivity to gammas. The latter property can be helpful in mixed neutron–gamma fields to enhance the neutron response. The development and commercial availability of high-quality homoepitaxial diamond films allowed a quick and impressive improvement on the detection performances of diamond-based detectors. One of the most deeply studied applications of diamond is for neutron detection, which is of primary importance when dealing with fusion or fission reactors, as well as accelerators, high-energy physics and dosimetry. In this paper we will focus on the use of diamond neutron detectors made by single-crystal films (SCD) grown by the RF-assisted CVD technique. The paper recalls the basic working principle of the diamond detector and discusses its advantages and draw-backs. Examples of diamond detector applications are presented including some recent studies and tests in harsh environments (e.g. $T > 500$ K).

1 INTRODUCTION

For many years, diamond (both natural and artificial) has been studied and used for detection of direct and indirect ionizing particles because it exhibits many outstanding properties which make this material very attractive for realizing fast, low noise, active radiation detectors [1–4] suited to withstand harsh environments. Amongst the many diamond properties are a) high band-gap (5.3 eV); b) high break-down field (10^7 V/cm); c) high carrier mobility (the highest for holes, 2200 cm²/Vs at room temperature); d) low dielectric constant; e) high fusion temperature (4100 °C), high thermal conductivity (20 W/cm K) and good radiation hardness [5–9]. Furthermore, its low atomic number ($Z = 6$), close to that of tissue, renders diamond very interesting also for radiation dosimetry [10–12]. Besides, diamond has low sensitivity to gammas. The latter properties can be helpful in mixed neutron–gamma fields to enhance the neutron response. Low Z also has some drawbacks, since the reduction of the stopping power of the radiation of interest, in turn, means a reduction of the sensitivity of the detector.

One of the most studied application of diamond is for neutron detection. Application of natural diamond to high-resolution, 14-MeV neutron spectrometry have been reported since 1995 [13]. However, the use of natural diamond was impractical. Large differences in the response of natural diamond films were observed because each natural diamond is almost unique requiring ‘*ad hoc*’ selection and characterization and thus is costly.

The use of diamond in radiation detection has been possible thanks to the development of the radiofrequency-assisted (RF) chemical vapour deposition (CVD) technique [1,14] for producing polycrystalline (pCVD) and, more recently, homoepitaxial (single-crystal diamond (SCD)) films.

The development and commercial availability of high-quality single SCD films allowed a quick and impressive improvement in the detection performances of diamond-based detectors (100% charge collection efficiency, energy resolution comparable to that of silicon, good reproducibility, etc.), and consequently use of diamond detectors in different applications fields was possible (e.g. UV and extreme UV detection, minimum ionizing particle (MIP) detection, beam monitoring, dosimetry for radiology and radiotherapy, boron neutron capture therapy (BNCT), microdosimetry [26]).

An ideal neutron detector would be compact, have low sensitivity to gamma-rays, able to discriminate neutrons from gamma-rays, fast in the response and both radiation- and temperature-hard (to allow operation in harsh environments). It would also be sensitive to both thermal and fast neutrons. Diamond meets almost all the above criteria; however, it is not sensitive to thermal neutrons and scarcely sensitive (via elastic scattering) to low-energy neutrons (< 5 – 6 MeV). The sensitivity to thermal neutrons can be achieved using a thin layer of ⁶LiF (or B [24] or fissile materials [27]). Detectors based upon this principle were used in fission reactors, and in fusion tokamak JET [28, 29]. Besides, in a sandwich configuration diamond detector with lithium has been proposed for measuring in-core fast neutron spectra [30]. The discussion above clearly shows the many reasons to study and use diamond-based detectors. To this respect, it ought to be mentioned that one issue is with the difficulty of finding reliable and reproducible diamond detectors and/or films on the market. Presently, the diamond films used for radiation

detection are classified as ‘*electronic grade*’ which means diamond films having a very low content (of the order of a few ppb) of contaminants (e.g. N).

In this paper we will focus mainly on the use of diamond neutron detectors made by single-crystal films grown by RF assisted CVD technique.

The paper first recalls the basic working principle of diamond detectors and discusses their advantages and drawbacks (Section 2 below). In Section 3, the n–carbon interactions are briefly reviewed, while in Section 4 some applications of SCD diamond detectors to neutron detection will be presented including some recent studies and applications in harsh environments e.g. characterized by high temperature. To conclude, a discussion about the outstanding issues and possible further development are both addressed.

2 THE DIAMOND DETECTOR

A diamond detector in its simplest form is a two-terminal electronics device formed by an intrinsic diamond layer (semiconductor) sandwiched by two (metal) contacts and can be considered a ‘*solid state ionization chamber*’. A biasing voltage is applied between the two electrodes, its magnitude depending upon the application and the film quality (Fig. 1a).

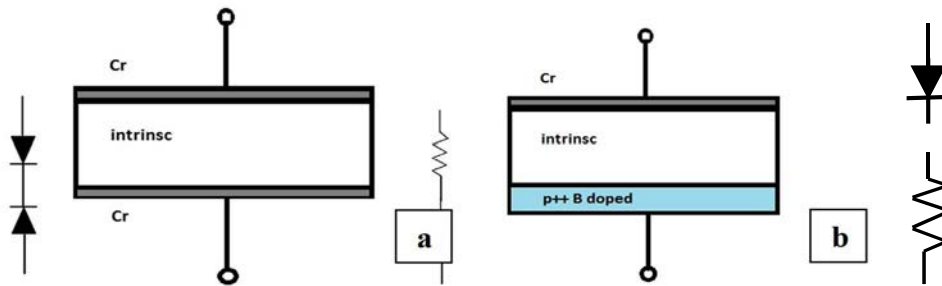


FIG. 1. a) Lay-out of diamond detector with two metallic contacts. The two types of electrical contacts are shown by their electrical equivalence: double rectifying diode (double-Schottky) or the double ohmic contacts (resistors). See text; b) Lay-out of the ‘layered’ diamond detector realized with one heavily borated carbon layer ($> 10^{20}$ atom/cm³) and one metallic contact. On the left, the electrical equivalence (diode and resistor respectively) for the two-contact diamond interfaces are shown.

Different metals (e.g. Ag, Au, Cr, Ni, Pt, Ti, W) can be used to deposit the contacts (the so-called metallization procedure [31]). The metal layer has typical thickness in the range 30–200 nm. Often, two (or even three) layers of different metals are used to form *layered metal electrical contacts* (e.g. Ti/Pt, Cr/Au etc.).

Depending on the fabrication procedure, the metal–diamond junction forms either *Schottky* or *ohmic* contacts. The former is usually formed when a metal layer is just deposited (either by sputtering or evaporation technique) on a diamond surface. In this case a rectifying junction is formed at the metal–diamond interface (the physical dimensions are of a few atomic layers) characterized by a typical electrical potential (Schottky barrier) due to the difference between the work functions of metal and diamond. The magnitude of the barrier depends on the metal used, and typically ranges from 0.5 to 1 eV. For a detailed analysis of the Schottky barrier properties see [32, 34].

A classical approach to study the metal–diamond contacts is based upon the measurements of the I–V characteristics at various biasing voltages. Figure 2 shows a typical I–V curve for a 500- μ m-thick detector made with two layered Ti/Pt–Ti/Pt Schottky contacts (see Fig. 1a, left side). The curve shows the typical (double) diode (rectifying) shape. The ohmic contact, in turn, can be produced after a proper treatment at high temperature of the metal–diamond junction. The procedure and the annealing temperatures are depending upon the metal used. A very thin layer of the so-called *carbon-like* structure is formed at the interface between the diamond and the metal which is assumed to improve the electrical properties of the detector. In general, an ohmic contact should have low resistivity, good adhesion, high thermal stability, high corrosion resistance, bondable top-layer and suitability for micro-patterning [31]. All these properties but the first apply also to Schottky contacts which are, indeed, characterized for having high resistivity.

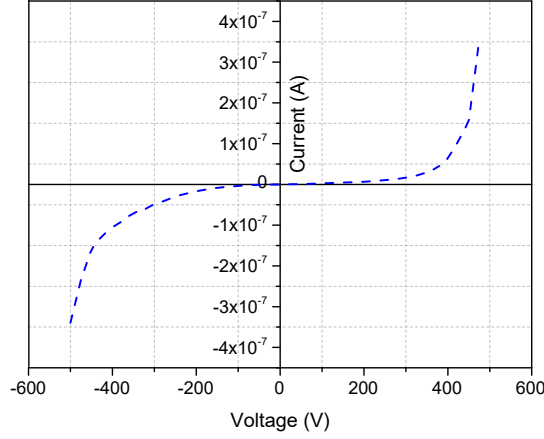


FIG. 2. Typical ‘double’ diode rectifying I - V curve measured with a diamond detector 500- μm thick and equipped with two metallic Ti/Pt-Ti/Pt metal contacts.

Ohmic contacts can be realized also by using a diamond-like carbon (DLC) film (1–3 nm) [35]. DLC is a form of amorphous carbon between diamond and graphite, containing significant portion of sp^3 bonded atoms in the matrix. The DLC contact consists of a very thin (1–3 nm) diamond-like carbon film. This layer allows for the injection of both holes and electrons in the diamond substrate. In the past the Diamond Detector Ltd company (DDL, no longer in the market) was commercializing detectors based on this contact deposition technique which were showing excellent properties in terms of time dependent stability and energy resolution (see Section 4).

There is another method to get ohmic contacts which is based upon the deposition, by the RF-assisted CVD technique, of a layer of SCD diamond highly enriched in boron ($> 0.5 \times 10^{20} \text{ cm}^{-3}$) on top of an intrinsic SCD film [36]. Detectors having on one side this ohmic contact and on the other side a standard metal–diamond Schottky contact (Fig. 1b) are used for X-ray detection and dosimetry since the built-in potential due to the Schottky barrier allows for the use of the detector without the need of any external bias. The properties of such a detector, also named ‘layered’ diamond detector, are addressed in detail in [37]. This type of detector is also suited for neutron detection [38].

2.1 BASIC DETECTION MECHANISM AND ELECTRICAL SIGNAL

Diamond is a semiconductor with band gap of 5.48 eV and thus the electric charge is carried both by electrons (e^-) and holes (h^+) produced either by direct or indirect ionizing radiation impinging on the detector. Under an external electric field \mathbf{E} these charges move away from each other and during the drifting they can either be trapped in the defects intrinsic to the diamond or move toward the electrodes. It is important to note that the movement of charges throughout the diamond generates the *induced current* measured in the external circuit to which the detector is connected. Here it is pointed out that it is not necessary that the carriers will actually reach the electrodes to generate the induced current since the Ramo–Shockley’s theorem applies [39–40]. The total current flowing in the external circuit, as in any other semiconductor, is thus the sum of the *electron* and *hole* induced currents. In the case of two plane parallel electrodes, by applying the Ramo–Shockley’s theorem, the instantaneous charge dQ induced at the electrodes in a detector of thickness L by a charge q (e.g. electron) generated at a distance dx from one of the electrodes (see Fig. 3) can be calculated as:

$$dQ = idt = q \frac{\Delta x}{L} \quad (1)$$

It is interesting to consider the case of a *minimum ionizing particle* (MIP) passing through the diamond detector. This particle produces in diamond 36 pairs of e^- and h^+ per μm . Let’s call this quantity q_0 . The charge produced by a minimum ionizing particle in a distance L is thus $Q_0 = q_0 L$. This is the *maximum total charge* we can expect to be produced in a perfect diamond detector of thickness L by a MIP. However, it could happen that the charges are trapped in the detector after moving a distance $d_T < L$, called the *charge-collection distance* (ccd). In this case the effective *collected charge* Q_C is:

$$Q_C = Q_0 \frac{d_T}{L} \quad (2)$$

And thus :

$$d_T = L \frac{Q_C}{Q_0} \quad (3)$$

Thus, by measuring Q_C we can get the ccd of the detector.

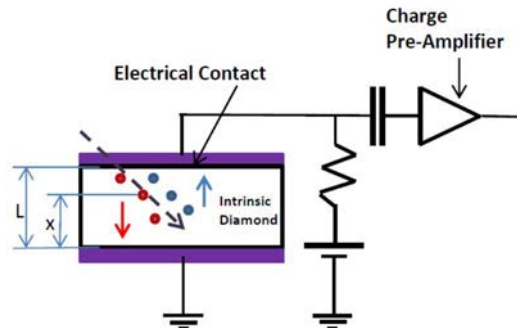


FIG. 3. Schematic representation of the particle–diamond interaction and charge generation inside the diamond crystal.

The increase of the ccd value has represented one of the main goals of past work on diamond detectors (especially for pCVD), as the ccd is directly correlated to the diamond film quality (reduction of impurities and defects and thus of trapping levels).

The electrical signals produced by a diamond device are characteristically ‘very fast’, i.e. the rising time of the electrical pulse is of the order of hundreds of ps (depending upon the film thickness and applied voltage). The *rise time* of the measured pulse (t_c) can be defined as the time required for the free charge carriers to move (drift) toward the electrodes in the electric field E . The product $i \times t_c$ is thus the total charge Q deposited in the diamond detector by a single ionizing effect. The current i is thus proportional to the deposited energy (which in turn depends on the energy of the ionizing particles) and this is fundamental to realize any neutron detector. For a detailed analysis of the current induced in the diamond detector see Refs. [4, 41].

3 NEUTRON DETECTION WITH DIAMOND

3.1 NEUTRON–CARBON INTERACTION

Natural carbon (99% ^{12}C and 1% ^{13}C) interacts with (fast) neutrons through a number of reactions which, for $E_n < 20$ MeV, are listed in Table 1 [13]. However, elastic scattering occurs also at low energy with a cross section that is almost constant up to high neutron energy.

TABLE 1. n-CARBON REACTIONS FOR NEUTRON ENERGY UP TO 20 MeV.

Reaction	Q -value (MeV)
$^{12}\text{C}(n,\alpha)^9\text{Be}$	-5.701
$^{12}\text{C}(n,n')3\alpha$	-7.275
$^{12}\text{C}(n,n')^{12}\text{C}$	0
$^{12}\text{C}(n,p)^{12}\text{B}$	-12.587
$^{12}\text{C}(n,d)^{11}\text{B}$	-13.732
$^{13}\text{C}(n,\alpha)^{10}\text{Be}$	-3.835

The most important n-C reaction for neutron energy greater than about 5.7 MeV is the $^{12}\text{C}(n,\alpha)^9\text{Be}$ reaction. The produced α and ^9Be ions are simultaneously detected producing the isolated and sharp peak in the pulse height spectrum (PHS), as shown in Fig. 4a. Considering the PHS at 13.8 MeV, it can be stated that this spectrum features

a complex shape in which the structures are due to three main reactions in ^{12}C : elastic scattering, $^{12}\text{C}(n,n')3\alpha$ and $^{12}\text{C}(n,\alpha)^9\text{Be}$. The most energetic peak centred at ~ 8.1 MeV is due to the $^{12}\text{C}(n,\alpha)^9\text{Be}$ reaction, the shape of this peak is due to two independent contributions, namely the broadening due to the intrinsic resolution of the diamond detector itself and an additional kinematic broadening that depends on the energy distribution of the incoming neutron beam (about 14 MeV in Fig. 4a). When the kinematic contribution dominates over the intrinsic broadening, the shape of this peak becomes a diagnostic of the incoming neutron energy spectrum. This is why it is used for neutron spectrometry especially in fusion reactors as well as with monoenergetic neutrons.

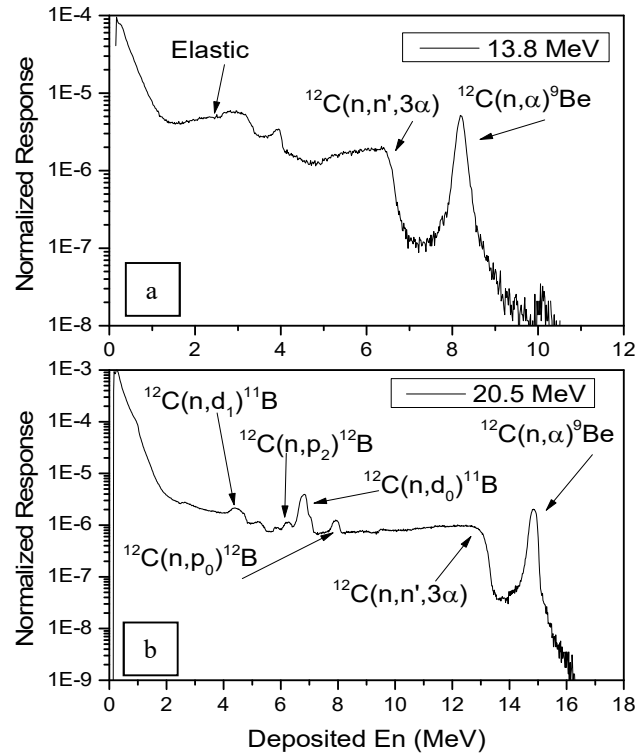


FIG. 4. Pulse Height spectra (PHS) measured with a 500- μm -thick single crystal diamond detector irradiated with 13.8 MeV (a) and 20.5 MeV (b) monoenergetic neutrons. The identified n -C reactions are indicated.

The total energy of the reaction products is $E_\alpha + E_{\text{Be}} = E_n - 5.701$ MeV, where E_n is the energy of the impinging neutron (Table 1). The direct relationship between E_n and the reaction products' energy allows spectroscopic measurements of the incident neutrons thanks to the already discussed property that in diamond the produced signal is proportional to the deposited energy. However, by increasing the neutron energy other nuclear reactions channels are possible and this reflects in the number of other peaks emerging in the PHS as shown in Fig. 4b.

A point to be discussed is whether the thickness of the diamond film can affect the performances of the detector in terms of energy resolution. For small intrinsic diamond layer thickness some of the produced α 's and ^9Be particles can escape from the detection volume thus releasing only a fraction of their kinetic energy inside the diamond volume. This edge effect would be more evident for diamond thicknesses comparable to the penetration length of the produced α and ^9Be fragments (of the order of 20 μm and 5–6 μm for α and ^9Be ions, respectively). However, when the film thickness is reduced to a few μm many reaction events produce low signals which are acquired in the low energy part of the PHS leading to reduced intensity of the $^{12}\text{C}(n,\alpha)^9\text{Be}$ peak and thus of the detection efficiency for 14 MeV neutrons.

3.2 THERMAL NEUTRON DETECTION

Diamond does not respond to thermal neutrons and this limits its application to detection of fast neutrons. However, as already said, this limit can be overcome by depositing a thin layer (ranging from a fraction of μm to

several μm) of materials having high cross section to thermal neutron. Usually ${}^6\text{LiF}$, B or fissile materials are deposited by an *evaporation technique* on top of the diamond film (Fig. 5a).

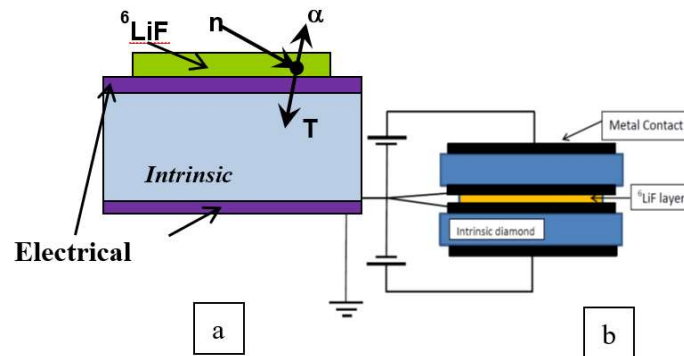


FIG. 5. a) Layout of a SCD + ${}^6\text{LiF}$ (LiDia) detector; b) Layout of a 'sandwich' detector in which the ${}^6\text{LiF}$ layer is in between the two diamond films.

The working principle of these detectors is the same regardless of the type of the deposit. For example, in the case of ${}^6\text{Li}$ and B the following reactions are produced by thermal (and low energy) neutrons, n_{th} :



Since (6) and (7) are two-body reactions, for the momentum conservation the produced ions move in opposite directions. For example, considering reaction (6), for each reaction *either α or T can enter the diamond film and release its kinetic energy* (Fig. 5a). Depending on the thickness of the ${}^6\text{LiF}$ layer and thanks to the excellent energy resolution of the diamond, both α and T peaks can be observed in the PHS (Fig. 6). It can be noticed that the 2.07 MeV α peak is broader than the 2.73 MeV T peak and consequently less intense because the two peaks have the same area. This effect is due to the higher stopping power of α particles in ${}^6\text{LiF}$ compared to the tritium ions. This effect becomes more evident increasing the ${}^6\text{LiF}$ layer thickness to allow the formation of a single peak due to the overlapping of the α and T peaks. The ${}^6\text{LiF}$ -covered diamond detectors are also referred to as Lithium diamond detectors or LiDia.

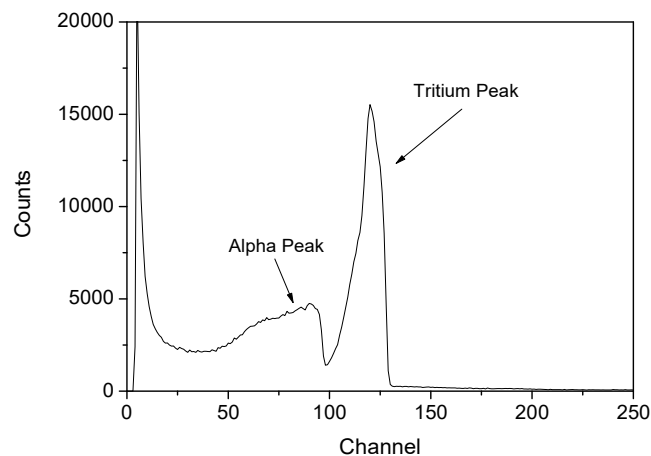


FIG. 6. Typical PHS recorded with a LiDia detector showing the α -T peaks (${}^6\text{LiF}$ layer thickness $0.5 \mu\text{m}$).

A boron-covered detector was, in turn, proposed for the boron neutron capture therapy (BNCT) [24]. In this case a 'sandwich' configuration (Fig. 5b) was used to allow the total energy produced in the ${}^{10}\text{B}(n,\alpha){}^7\text{Li}$ reaction to be fully absorbed in the detector. The sandwich configuration is particularly suited for neutron dosimetry and spectrometry since it allows for the full energy deposition inside the detector. For the same reason, this configuration was also proposed for measuring the fast neutron spectrum in ADS systems [30]. However, such a spectrometer is limited in applications for neutrons in the energy range of 6–7 MeV. As already said, at greater

neutron energy other n–C reaction channels are open up, which produce peaks in the PHS and which can interfere and/or overlap with the ones produced by the n–⁶Li of the n–B reactions.

4 APPLICATIONS

To conclude this short review on diamond neutron detectors we present three applications covering different topics. This is intended just to outline the wide range of applications possible with diamond detectors which are very versatile detectors. The reader is encouraged to refer to the wide bibliography available (some interesting applications are addressed in the References at the end of this paper).

4.1 NEUTRON DETECTION IN THERMAL REACTORS

One of the earliest applications of SCD detectors covered with ⁶LiF was the measurement of neutrons in the 1 MW TRIGA RC-1 fission research reactor of ENEA-Casaccia [38] (Italy). In such an experimental environment, both high neutron flux and intense fluxes of gamma-rays are present, and the detector operated at very high counting rate. The diamond detector was of the ‘layered’ type [37] that is with one ohmic diamond–boron enriched contact. The diamond film, the ohmic contact and the detector were produced at Rome Tor Vergata University. The detector was connected to a 10-m long cable and positioned 80 cm above the reactor core mid-plane. The electronics chain consisted of an Ortec 142A charge preamplifier, a shaping amplifier with 1-μs shaping time and a multichannel scaler (MCS). A ²³⁵U fission chamber was also installed in the reactor and used as a reference. During the irradiation the reactor power was varied from 10 kW up to its maximum power of 1 MW through several steps (inset Fig. 7).

In Fig. 7, the measured counting rate for the LiDia detector is compared to the one obtained by the reference ²³⁵U fission chamber (data in Fig. 7 corrected for the pile-up). An excellent linearity was observed demonstrating the possible use of diamond in nuclear fission reactors even at high count rates (up to about 150,000 cps).

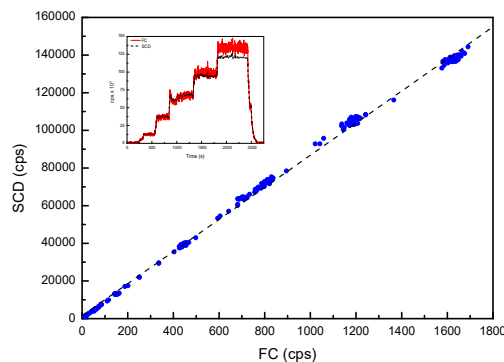


FIG. 7. Counting rate of the LiDia detector vs. ²³⁵U fission chamber counting rate as measured in the TRIGA reactor (data corrected for the pile-up). The inset shows the whole irradiation from 10kW up to 1 MW TRIGA reactor power.

4.2 NEUTRON EMISSION MEASUREMENT AT THE JET TOKAMAK

Neutron detection is one of the most important diagnostics of the fusion process since the total and time dependent neutron emission as well as the neutron energy yield fundamental information about the burning plasma parameters (e.g. plasma temperature, burn-up ratio, plasma density etc. [42]). For this reason, a long-term test of CVD diamond detectors was performed at the Joint European Torus (JET) in the period 2006-2010 [43, 44].

Three single crystal diamond detectors produced at Rome Tor Vergata University were installed inside the JET torus hall in April 2006 and left in operation until the end of 2010. All three detectors were of the layered type [37]. Two detectors (SCD-1 and SCD-2) were of the LiDia type (thickness 105 and 75 μm respectively). To enhance the response to neutrons, SCD-1 and SCD-2 were enclosed in a small box of polyethylene. The third one (SCD-3) was a 200-μm thick, intrinsic diamond film, which was used to measure the 14-MeV emission from the triton burn-up (see below).

Each detector was directly connected to a charge preamplifier ORTEC Mod. 142A and both detector and preamplifier were located inside a metallic box installed in the torus hall (TH) at about 4 m from the plasma centre (in Octant-1). The connection to shaping amplifier and threshold discriminators, located in the diagnostic area outside the TH, was obtained by means of about 100-m long, 50- Ω coaxial cables (RG-58 type). The logic signals produced by the discriminators were acquired in terms of count rate versus time by the JET acquisition system (CODAS). Both the time-dependent response and the Pulse Height Spectra (PHS) were recorded for every JET pulse.

In the period 2006–2010, JET operated with DD plasmas thus 2.5-MeV neutrons were mainly produced. However, 14-MeV neutrons were also produced by means of the so-called Triton burn-up [45]. The 14-MeV neutron burn-up yield is very low, about 1% of the total, the latter in JET usually ranges from 10^{15} to $7\text{--}8 \times 10^{17}$ n/s per pulse, depending upon the plasma scenario and conditions.

Two discrimination thresholds were set for all the detectors. The lowest (THR-1) was able to detect all the signals produced by the neutrons regardless of their energy; the second threshold (THR-2) was set well above the first one in order to detect only the signals due to 14-MeV neutrons produced by the $^{12}\text{C}(n,\alpha)^9\text{Be}$ reaction. The response of the SCD diamond detectors was compared to the official JET total neutron yield measured by JET-KN1 diagnostic system which consists of a three sets of fission chambers arranged around the machine. Each set comprises a ^{235}U and ^{238}U chamber operating in pulse counting and current mode [46]. The 14-MeV neutrons data measured by the SCD-3 detector were, in turn, compared to the ones routinely measured by three Silicon diodes.

Figure 8 shows an example of the time-dependent neutron emission measured by the SCD-2 detector during a single JET pulse. Both total and 14-MeV emission are reported and compared with the same quantities measured by KN1 total yield monitor as well as with ones over the three silicon diodes available at JET for measuring the 14-MeV neutron emission. Good agreement is observed despite the low statistics of the SCD-2 detector due to the small diamond dimensions and the low yield of 14-MeV neutrons. Note that the 14-MeV neutron emission is delayed with respect to the 2.5-MeV neutron emission from the D–D plasma of about 200–300 ms. This is due to the Tritium slowing time in the plasma (200–300 ms) before its interaction with deuterium for producing 14-MeV neutrons. Figure 8 shows as this time delay is properly measured using the LiDia detector. To note that for measuring the total and tritium burn-up neutron yield, two different and independent detectors are routinely used at JET. These tests demonstrated that using a single LiDia detector it is possible to discriminate between the total and the 14-MeV neutrons produced by the triton burn-up. This allowed the first contemporary measurement at JET of both the total and 14-MeV neutron yields as well as their time dependency with very good reliability and stability using a single detector [43].

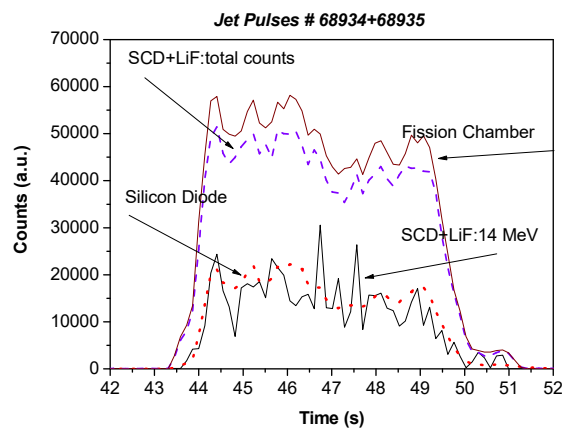


FIG. 8. The total and 14 MeV neutron emission as recorded at JET with the diamond detector and compared to the official neutron monitors of JET.

The linearity and the stability over the long lasting experimental period was also demonstrated. For example, the total number of counts measured by the SCD-1 and SCD-2 detectors for each JET pulse is reported in Fig. 9 as a function of the JET neutron yield (measured by KN1). In the plot more than 500 JET pulses acquired during the whole JET experimental campaign are reported. The SCD-1 and SCD-2 detectors show a good linearity demonstrating the possibility of reliable use of diamond detectors in large fusion facility.

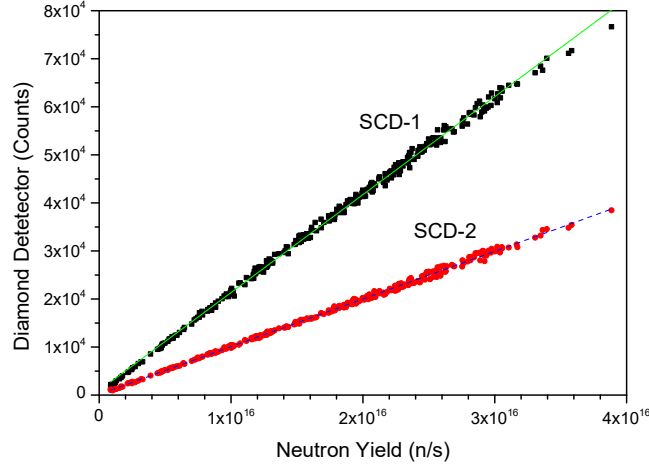


FIG. 9. Correlation between diamond detectors (SCD-1 and SCD-2) counting and the total JET neutron yield measured by ^{235}U fission chamber (the plot refers to more than 500 JET pulse acquired during the whole JET experimental campaign).

Last, but not least, in Fig. 10 the correlation for the 14-MeV neutron emission from triton burn-up measured by the SCD-3 and one of the silicon diodes routinely used at JET is shown. Also in this case, despite the very low statistics of the diamond counter (note the large error bars), good agreement is observed.

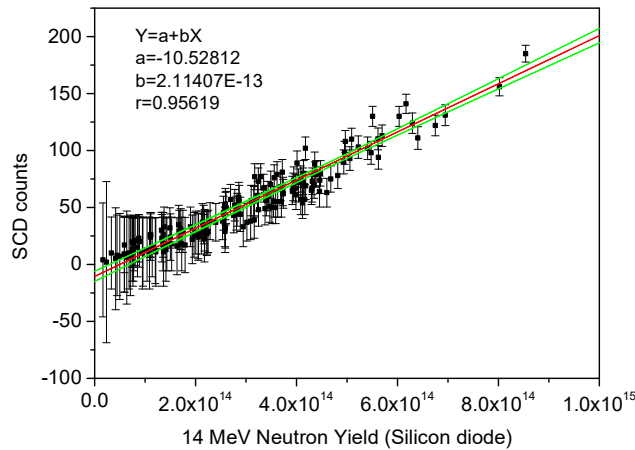


FIG. 10. Correlation between SCD-3 and one of the silicon diodes used at JET for recording the 14 MeV neutron production from the Triton burn-up. More than 200 JET pulses are reported. The statistical error bars are shown as well as the linear fit of the data.

4.3 APPLICATION OF DIAMOND DETECTORS TO N-C CROSS SECTION MEASUREMENT

The very high energy resolution makes diamond detectors suited as fast neutron spectrometer. Since the neutron spectrum is obtained by unfolding procedures using the response matrix of the detector, a fundamental requirement is the knowledge of these response functions at several neutron energies. The first response function for a type-IIA artificial single crystal diamond detector was measured by Kaneka [47]. More recently, response functions of an artificial single crystal diamond detector were measured in an energy range of 5–20.5 MeV by Pillon and co-workers [48] by using quasi-monoenergetic neutrons. The measurements were performed at the Van de Graaff neutron generator of the EC-JRC-IRMM as part of the EUFRAT program supported by the European Commission.

In Fig. 11, some of the measured response functions (PHS) are plotted. An important consequence of the data presented in Fig. 11 is that for each measured PHS, after identifying the reaction responsible for the peaks produced at a given neutron energy, each peak can be used to extract the neutron cross-section for this specific

reaction channel at the given neutron energy. This is feasible via a proper procedure based upon the peak fitting and the knowledge of the neutron fluence as well as of the volume of the detector (as detailed discussed in [48]). This method allowed the measurement, for the first time, of the $^{12}\text{C}(n,\alpha)^9\text{Be}$ and of other cross sections in the 5–20.5 MeV neutron energy range. An example of the results for the $^{12}\text{C}(n,\alpha)^9\text{Be}$ reaction is shown in Fig. 12 [48]. More details and other measured cross sections data are in [49].

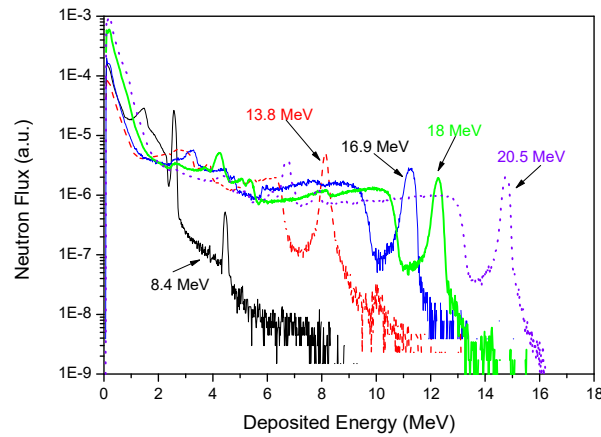


FIG. 11. PHS at different neutron energies measured during the Geel experiment discussed in Ref. [48].

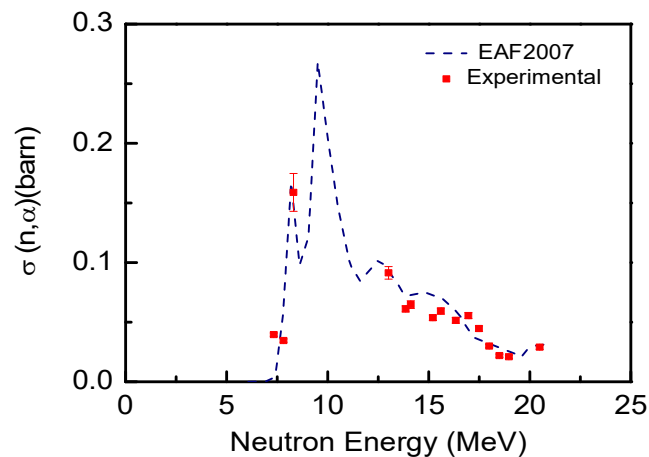


FIG. 12. Measured $^{12}\text{C}(n,\alpha)^9\text{Be}$ cross section (points) compared to theoretical data from the EAF-2007 compilation (dotted line).

4.4 HIGH-TEMPERATURE OPERATION

In the last years an increasing interest in testing and operating diamond neutron detectors in harsh environment characterized by high radiation level and high temperature ($>150\text{ }^\circ\text{C}$) has emerged. The application of diamond detectors in harsh environments represents one of the most promising activities for the future. Indeed, although theoretically diamond can withstand very high temperature, presently available detectors can operate (both in pulse and spectrometric mode) up to about $230\text{--}240\text{ }^\circ\text{C}$ [50]. It has been already pointed out that for operating at high temperature the diamond detectors need a specialized design. The latter makes use of mineral cables [51], which in turn can withstand temperatures up to $800\text{ }^\circ\text{C}$ as well as high radiation doses: The use of glue or other adhesives to realize the electrical contacts is to be avoided for reasons linked to long lasting operation. Some authors proposed the use of ‘mechanical’ connections to realize the electrical contacts [51]. In Fig. 13 a proposed layout of a diamond detector designed for operating at high temperature is shown [50].

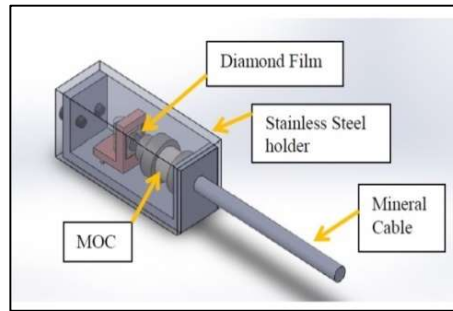


FIG. 13. Layout of a prototype diamond detector designed for operation at high temperature.

With such a configuration, stable and reproducible operation in spectrometric mode were reported up to 240 °C using Ag metal contacts. Similar results were also obtained with other metallic contacts (e.g. Cr). Layered detectors with one borated contact and one metallic contact were tested too and always the operational limit was around 240 °C (Fig. 14). Polarization effects which quickly degrade the performances of the detector were observed for all detectors for $T > 240$ °C. However, once the detector is cooled down below the ‘critical temperature’ of 240 °C the performances of the detector are restored. The reasons for not operating in a stable mode for $T > 240$ °C are not fully understood – studies are ongoing. To conclude we state that some, not yet reproduced, operation at $T > 240$ °C was realized—the reason for the irreproducibility is under investigation.

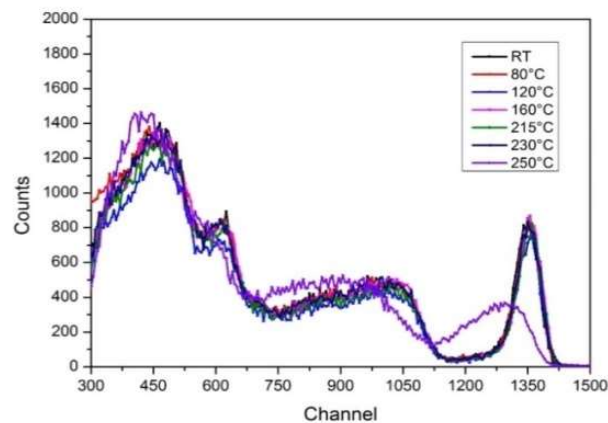


FIG. 14. PHS as function of the temperature recorded for a layered diamond detector with Cr–B contacts irradiated with 14-MeV neutrons at the Frascati neutron generator (FNG).

5 DISCUSSION AND CONCLUSION

Most of the studies and applications of diamond neutron detectors are based upon the use of ‘self-made’ detectors which vary due to the diamond film production methodology and producer (often diamond is produced by the user himself), the volume, type of the electrical contacts etc. rendering difficult to inter-compare the results even if obtained under similar conditions and applications. The lack of a reproducible, agreed upon and shared procedure to produce artificial CVD diamond represents the main limiting reason for a more extensive (and reproducible) use of diamond detectors.

Probably the main issue is with the availability of good quality and reproducible ‘electronics grade’ diamond films. In the market there is just one (perhaps two–three) producers which can guarantee the needed quality of the diamond films, even if always in very limited quantity. These films show a good reproducibility (on the average) of their physical and electronics performances. However, presently it is very difficult, if not impossible, to produce a large number of detectors which can guarantee exactly the same performance.

Another problem limiting widespread use of diamond detectors is their small dimensions. For monocrystalline diamond a typical film is about 4-mm side and 500- μm thick. More rarely (and at higher cost) thinner films, e.g. 100–300 μm , can be available. For many applications, thin films (e.g. < 100 μm) would also be sufficient, but these films are almost impossible to find on the market.

More serious is the situation if we look at 'off the shelf' detectors. Presently there are perhaps just a few companies which can provide commercial detectors for neutrons. However, also in this case, the reproducibility of the performances among different detectors is not always observed.

Another problem concerns the radiation hardness of the detector when exposed to intense neutron fluxes. Long-lasting neutron (and gamma) irradiation can affect the performances of the detector. This problem has been investigated in the past by several authors and for different types of radiation; however, a clear answer is still missing as it depends on the radiation and also on the working conditions (e.g. flux rate, temperature, etc.). For the case of neutrons, monocrystalline diamond can survive with good performances up to fluences of 2×10^{14} n.cm⁻² of 14-MeV neutron [52]. Other measures using lower energy neutrons seem indicate that higher fluences can be withstood [53]. No data were so far reported about the effect of high gamma doses to detector performances.

A dedicated discussion is necessary for neutron dosimetry. A number of promising applications have been proposed so far; however, apart from commercial application for gamma dosimetry in medical physics, to the author's knowledge, no other applications have been developed at a level to which it can be stated that diamond detectors are well suited for neutron dosimetry applications. However, it is worth mentioning the attempt to use diamond detectors, specifically designed, to microdosimetry [26,54].

REFERENCES

- [1] PAOLETTI, A., TUCCIARONE, A. (Eds), The Physics of Diamond, Proc. Int. School Phys. "Enrico Fermi", Course CXXXV, Varenna (Italy), 23 July–2 August 1996, IOS Press (1997).
- [2] KOIZUMI, S., NEBEL, C.E., NESLADEK, M. (Eds), Physics and Application of CVD Diamond, Wiley-VCH Verlag GmbH Co. KGaA, Weinheim (2008).
- [3] TRAPPER, R.J., Diamond detectors in particle physics, Rep. Prog. Phys. **63** (2000) 1273.
- [4] PERNEGGER, H., High mobility diamonds and particle detectors, Phys. Status Solidi **203** 13 (2006) 3299.
- [5] ALLERS, L., HOWARD, A.S., HASSARD, J.F., MAINWOOD, A., Neutron damage of CVD diamond, Diamond Relat. Mater. **6** 2–4 (1997) 353.
- [6] OH, A., MOLL, M., WAGNER, A., ZEUNER, W., Neutron irradiation studies with detector grade CVD diamond, Diamond Relat. Mater. **9** 11 (2000) 1897.
- [7] ALEKSEYEV, A., et al., Study of natural diamond detector spectrometric properties under neutron irradiation, Nucl. Instrum. Methods Phys. Res. A **476** (2002) 516.
- [8] ANGELONE, M., et al., Radiation hardness of a polycrystalline chemical-vapor-deposited diamond detector irradiated with 14 MeV neutrons, Rev. Sci. Instrum. **77** (2006) 023505.
- [9] TANAKA, T., et al., Radiation tolerance of type IIa synthetic diamond detector for 14 MeV neutrons, Diamond Relat. Mater. **14** 11–12 (2005) 2031.
- [10] VITTONI, E., et al., Thermoluminescence in CVD diamond films: application to radiation dosimetry, Diamond Rel. Mater. **8** (1999) 1234.
- [11] BUTTAR, C.M., et al., A study of radiotherapy dosimeters based on diamond grown by chemical vapour deposition, Diamond Rel. Mater. **9** (2000) 965.
- [12] GUERRERO, M.J., et al., Requirements for synthetic diamond devices for radiotherapy dosimetry applications, Diamond Rel. Mater. **13** (2004) 2046.
- [13] PILLON, M., ANGELONE, M., KRASILNIKOV, A., 14 MeV neutron spectra measurements with 4% energy resolution using a type IIa diamond detector, Nucl. Instrum. Methods Phys. B **101** (1995) 473.
- [14] WERNER, M., LOCHER, R., Growth and application of undoped and doped diamond films, Rep. Prog. Phys. **61** (1988) 1665.
- [15] SCHMID, G.J., KOCH, J.A., LERCHE, R.A., MORAN, M.J., A neutron sensor based on single crystal CVD diamond, Nucl. Instrum. Methods Phys. A **527** (2004) 554.
- [16] KANEKO, J.H., et al., Response function measurement of layered type CVD single crystal diamond radiation detectors for 14 MeV neutrons. Rev. Sci. Instrum. **75** 10 II, (2004) 3581.
- [17] PILLON, M., et al., Neutron detection at JET using artificial diamond detectors, Fusion Eng. Des. **81** (2007) 1174.
- [18] PACE, E., DE SIO, A., Diamond detectors for space applications, Nucl. Instrum. Methods Phys. A **514** (2003) 93.
- [19] THE RD42 COLLABORATION, Development of CVD diamond radiation detectors, Report CERN/EP 98-80, April 20 (1988).
- [20] ANGELONE, M., et al., Time dependent 14 MeV neutron measurement using a polycrystalline chemical vapour deposited diamond detector at the JET tokamak, Rev. Sci. Instrum. **76** (2005) 013506.

- [21] BUCCIOLINI, M., et al., Diamond dosimetry: Outcomes of the CANDIDO and CONRAD INFN projects, *Nucl. Instrum. Methods Phys. Res. A* **552** 1–2 (2005) 189.
- [22] KOIDE, Y., LIAO, M., ALVAREZ, J., Thermally stable solar-blind diamond UV photodetector, *Diamond Relat. Mater.* **15** (2006) 1962.
- [23] BERGONZO, P., et al., Diamond-based semi-transparent beam-position monitor for synchrotron radiation applications, *J. Synchrotron Rad.* **6** (1999) 1.
- [24] ALMAVIVA, S., et al., Improved performance in synthetic diamond neutron detectors: Application to boron neutron capture therapy, *Nucl. Instrum. Methods Phys. Res. A* **612** (2010) 580.
- [25] ANGELONE, M., et al., Thermal and fast neutron dosimetry using artificial single crystal diamond detectors, *Rad. Meas.* **46** (2011) 1686.
- [26] ROLLET, S., et al., A novel microdosimeter based upon artificial single crystal diamond, *IEEE Trans. Nucl. Sci.* **59** 5 (2012) 2409.
- [27] PIETROPAOLO, A., et al., A single crystal diamond based neutron beam monitor for instrumentation at pulsed neutron source, *Nucl. Instrum. Methods Phys. Res. A* **610** (2009) 677.
- [28] MARINELLI, M., et al., High performance ^6LiF -diamond thermal neutron detectors *Appl. Phys. Lett.* **89** (2006) 143509.
- [29] PILLON, M., et al., Development of on-line tritium monitor based upon artificial diamond for fusion applications, *IEEE Trans. Nucl. Sci.* **58** 3 (2011) 1141.
- [30] OSIPENKO, M., et al., Neutron spectrometer for fast nuclear reactors, *Nucl. Instrum. Methods Phys. Res. A* **709** (2015) 207.
- [31] WERNER, M., Diamond metallization for device applications, *Semicond. Sci. Technol.* **18** (2003) S41.
- [32] TUNG, R.T., The physics and chemistry of Schottky barrier height, *Appl. Phys. Rev* **1** (2014) 011304.
- [33] TATSUMI, N., IKEDA, K., UMEZAWA, H., SHIKATA, S., Development of diamond Schottky barrier diode, *SEI Tech Rev* **68** (2009) 54.
- [34] TERAJI, T., KOIDE, Y., ITO, T., Schottky barrier height and thermal stability of p-diamond (100), *Thin Solid Films* **557** (2014) 241.
- [35] GALBIATI, A., et al., Performance of monocrystalline diamond radiation detectors fabricated using TiW, Cr/au and a novel ohmic DLC/Pt/Au electrical contact, *IEEE Trans. Nucl. Sci.* **56** 4 (2009) 1863.
- [36] PRINS, J.F., Preparation of ohmic contacts to semiconducting diamond, *J. Phys. D. Appl. Phys.* **22** (1989) 1562.
- [37] ALMAVIVA, S., et al., Chemical vapor deposition diamond based multilayer radiation detector: physical analysis of detection properties, *J. Appl. Phys.* **107** (2010) 014511.
- [38] MARINELLI, M., et al., Synthetic single crystal diamond as a fission reactor neutron flux monitor, *Appl. Phys. Lett.* **90** (2007) 183509.
- [39] RAMO, S., Current induced by electron motion, *Proc. IRE* **27** (1939) 684.
- [40] SHOCKLEY, W., Currents to conductors induced by a moving point charge, *J. Appl. Phys.* **9** (1938) 635.
- [41] WEISS, C., Ionization signals from diamond detectors in fast-neutron field, *Eur. Phys. J. A* **52** (2016) 269.
- [42] JARVIS, O.N., Neutron spectrometry at JET (1983-1999), *Nucl. Instrum. Methods Phys. Res. A* **476** 1–2 (2002) 474.
- [43] ANGELONE, M., et al., Development of single crystal diamond neutron detectors and test at JET tokamak, *Nucl. Instrum. Methods Phys. Res. A* **595** (2008) 616.
- [44] LATTANZI, D., et al., Single crystal CVD diamonds as neutron detectors at JET, *Fusion Eng. Des.* **84** (2009) 1156.
- [45] HEIDBRINK, W.W., CHRIEN, R.E., STRACHAN, J.D., Burn-up of fusion produced tritons and ^3He ions in PLT and PDX, *Nucl. Fus.* **23** 7 (1983) 917.
- [46] SWINHOE, M.T., JARVIS, O.N., Calculation and measurement of ^{235}U and ^{238}U fission counter assembly detection efficiency, *Nucl. Instrum. Methods Phys. Res.* **221** (1984) 460.
- [47] KANEKA, J., IKEDA, Y., NISHITANI, T., KATAGIRI, M., Response function measurement of a synthetic diamond radiation detector for 14 MeV neutrons, *Rev. Sci. Instrum.* **70** (1999) 1100.
- [48] PILLON, M., et al., Experimental response functions of a single-crystal diamond detector for 5–20,5 MeV neutrons, *Nucl. Instrum. Methods Phys. Res. A* **640** (2011) 185.
- [49] PILLON, M., et al., High-resolution measurements of the excited states (n,pn), (n,dn) C-12 cross sections, *EPJ Web of Conferences* **146** (2017) 11005.
- [50] PILOTTI, R., et al., Development and high temperature testing by 14 MeV neutron irradiation of single crystal diamond detectors, *J. Instrum.* **11** (2016) c06008.
- [51] ANGELONE, M., et al., Spectrometric performances of monocrystalline artificial diamond detectors operated at high temperature, *IEEE Trans. Nucl. Sci.* **59** (2012) 2416.

[52] PILLON, M., et al., Radiation tolerance of a high quality synthetic single crystal chemical vapor deposition diamond detector irradiated by 14.8 MeV neutrons, *J. Appl. Phys.* **104** (2008) 054513.

[53] ALMAVIVA, S., et al., Characterization of damage induced by heavy neutron irradiation on multi-layered ${}^6\text{LiF}$ -single crystal chemical vapor deposition diamond detectors, *J. Appl. Phys.* **106** (2009) 073501.

[54] VERONA, C. et al. Toward the use of single crystal diamond based detectors for ion-beam therapy microdosimetry, *Rad. Measurements* **110** (2018) 25.

SILICON CARBIDE (SiC) NEUTRON DETECTOR FOR POWER RANGE NEUTRON FLUX MONITORING

C.P. NAGARAJ¹, S. TRIPATHI², C. UPADHYAY¹, A. VENKATESAN¹, B.K. PANIGRAHI¹

¹Indira Gandhi Centre for Atomic Research, Department of Atomic Energy, Kalpakkam- 603102, India

²Homi Bhabha National Institute, Anushakti Nagar, Mumbai-400094, India

Email: ncp@igcar.gov.in

Abstract: The potential of Silicon Carbide (SiC) for use in semiconductor nuclear radiation detectors has been long recognized. The wide band-gap of SiC (3.25 eV) makes it an attractive semiconductor for use in high dose rate and high ionization nuclear environments. SiC is also attractive because it can operate stably at elevated temperature (up to 700 °C). Because of high-temperature and radiation resistance, SiC radiation detector can be utilized in diverse applications, including ex-core neutron flux monitoring in nuclear reactors, measurement of spent nuclear fuel neutron emission to determine burn-up, nuclear materials safeguards monitoring. Although bare SiC can detect fast neutrons, it was demonstrated that its detection efficiency can be improved by juxtaposing a conversion layer. Based on Monte Carlo simulation studies, High Density Poly Ethylene (HDPE) material has been selected to be used as a converter because of high concentration of hydrogen. The present work focused on the study of the enhancement in the efficiency of SiC fast neutron detector with a stacked structure. The simulations have been performed to optimize the converter layer thickness for different mono-energetic and Am-Be neutron sources. The fabrication of single and stacked detectors will be taken up for demonstration of improvement in efficiency with experimental results in nuclear reactors.

1 INTRODUCTION

Neutron detectors are employed for nuclear applications such as high-energy physics experiments, special nuclear material detection [1], monitoring of nuclear reactor core [2], fuel reprocessing plants, fast neutron radiation therapy [3], and several other applications including space [4–8]. In most of the occasions, the generated neutrons are of high energy, for example, in nuclear reactors, neutrons generated through fission are born as fast neutrons with high kinetic energy [9, 10]. Also, neutron interaction with matter is strongly dependent on the energy, as the energy increases the probability of interaction goes down due to the rapid reduction in cross section [11, 12]. Knoll [12] has quoted that in principle, almost all techniques of slow neutron detection can be applied for fast neutron detection as well. But the detection efficiency will be very poor due to the cross section, and such a low efficiency limits practical applications. Thus, fast neutron devices have to incorporate a revamped or different detection scheme to achieve acceptable detection efficiency. Contrary to slow neutron detection, the detection of fast neutrons could provide additional information associated with the energy of the incident neutron, vital in some applications [13, 14]. Information on neutron kinetic energy is lost in conversion for slow neutrons, as the energy liberated in the conversion reaction itself (Q-value) is extremely large compared to the neutron energy. However, the energy of fast neutrons is not negligible compared to the reaction Q-value. In principle, subtracting the reaction Q-value from the reaction product energies can yield the incident neutron energy. Various methods have been developed for fast neutron spectroscopy and detection [4, 12].

This work is primarily focused towards the development of a fast neutron detection system for neutron flux monitoring of the power of a fast reactor core. Fission Chambers and Self-Powered Neutron Detectors (SPND) are generally preferred owing to their high resistance to radiation-induced damage [15–17]. Fission Chambers are quite good at gamma discrimination due to the high energy associated with the resultant fission fragments. However, it is a gas-filled detector which requires a high-voltage supply to collect the generated charge pairs and costly fissile material enrichment to achieve high efficiency. Therefore, there is a need to develop a detection system which could be employed as an alternative or diverse sensor of neutron detection having the following features: operability in harsh environments, wide neutron spectrum response, and compact size in comparison to bulky gas-filled detectors.

With the above objective, we have modelled a fast neutron detector, which can be exposed in the ex-vessel location of a fast reactor operating at power. A wide band-gap semiconductor, Silicon Carbide (SiC) (3.25 eV for 4H-SiC polytype), has been chosen as a charged particle detector to detect recoil protons from hydrogenous converter materials. High-density polyethylene (HDPE) (C₂H₄)_n is used as a converter material for fast neutrons that generates recoil protons [18–22]. Details the proton recoil method of neutron detection and model validation by analytical methods can be found Ref. [14] and references therein. Ref. [14] also reports on the efficiency improvement of stacked structures of planar SiC-based semiconductor fast neutron detectors. Monte-Carlo simulations have been used to model the detector and optimize the converter layer thickness for different mono-

energetic and Am–Be neutron sources. In order to discriminate the background events, a low-level discriminator (LLD) is applied and its effect on detection efficiency is demonstrated.

2 DETECTOR SIMULATION

A computational or analytical model is useful to understand the particle transport mechanism through converter and detector materials before fabricating a detector. This allows optimization of the thickness of the converter layer. A comparative review of Monte Carlo based codes is given in Ref. [23]. We use the Geant4 [24] simulation toolkit package, which includes tracking, geometry, physics models, and hits, and can in any geometry track secondary particles created via any reaction. It models the physics of electromagnetic, hadronic, and optical process from the low- to very high-energy range [25]. The software was developed in an object-oriented approach and implemented in the C++ programming language.

2.1 DETECTOR MODEL DESCRIPTION

Both a planar and a stacked detector geometry are shown in Fig. 1 as modelled in Geant4. The system consists of a $1\text{ cm} \times 1\text{ cm}$ converter layer and a similar dimension detector. The converter layer thickness is varied to obtain the optimized thickness.

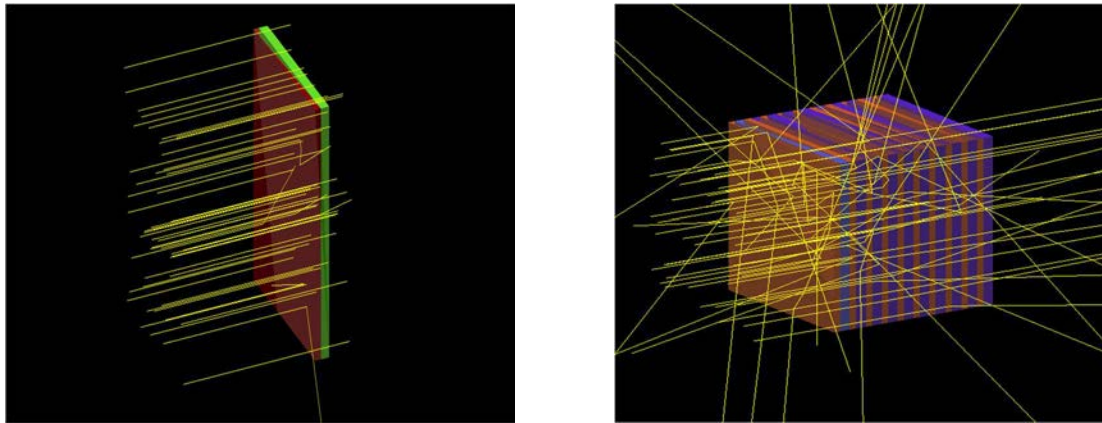


FIG. 1. (a) Planar detector model (b) Stacked detector model in Geant4.

The particle source is set such that all the particles would fall randomly and perpendicularly on the front face of the converter material, and is modelled as 1 cm away from the detector. 10^9 neutrons have been simulated for each event in the HPC clusters facility available in IGCAR. The standard physics model “QGSP_BERT_HP” was used in this simulation [26]. The Am–Be source was taken from the ISO Report 8529-1 [27]. The effects of dead layers and temperature were not considered in this simulation work.

3 RESULTS AND DISCUSSION

3.1 OPTIMIZATION OF HDPE THICKNESS FOR DIFFERENT ENERGY NEUTRON SOURCES

SiC can directly interact with fast neutrons and generate Si and C recoils. But these recoils would have low kinetic energy at the time of generation [11]. Fast neutrons have relatively high cross-sections for elastic scattering reactions with low- Z converter materials. If we employ a hydrogenous converter material in juxtaposition with a SiC detector, better efficiency can be achieved [28]. If we keep on increasing HDPE converter thickness, more interactions will take place and a larger number of recoil protons would be generated. But these recoils would have a certain energy which they will continuously lose within the material during transport, through ionization and excitation phenomena. If the thickness of the converter approaches or exceeds the maximum range of highly energetic recoil protons, there is a probability that many of the generated recoils would be lost in converter itself. Therefore, we have used Monte Carlo Geant4 simulations to optimize the HDPE converter thickness such that the maximum number of recoil protons can penetrate the converter region to induce a signal in the SiC detector.

Figure 2 depicts the range of recoil protons as a function of their energy in HDPE and SiC materials.

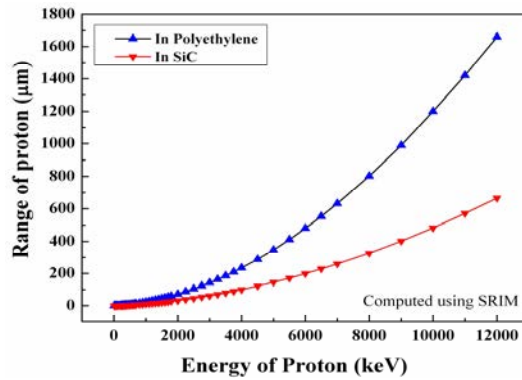


FIG. 2. Range of recoil proton in HDPE and SiC materials.

Figure 3 shows detector efficiencies for different energy neutrons and converter thicknesses. After a certain converter thickness, efficiency begins to decrease, due to self-absorption of the proton energy within the converter itself. This effect limits the efficiency of the planar detector. As different thicknesses provide maximum efficiencies for different neutron energies, a thickness efficient for the energy range of 0.5–11 MeV (in the context of this work) has to be selected, and 400 μm was chosen as optimal. Figure 3 can be used to select different optimal HDPE converter thicknesses for different mono-energetic neutron sources; e.g., 100 μm is optimal for a 2.5 MeV D–T neutron source. The optimal HDPE thickness for an Am–Be neutron source, illustrated in Fig. 4, ranges between 400 μm and 1000 μm, where the detector will provide maximum efficiency of 0.112–0.117%, which is approximately constant. There are few neutrons significantly higher than 6 MeV in the ²⁴¹Am–Be spectrum, and a larger thickness would reduce the recoil protons that reach the detector. Thus, 400 μm could be regarded as an optimum for the ²⁴¹Am–Be spectrum.

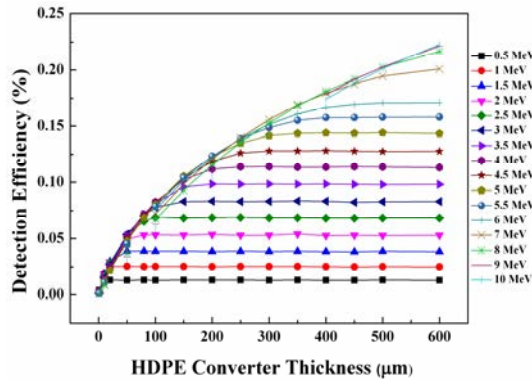


FIG. 3. Optimization of HDPE converter material for different mono-energetic neutrons.

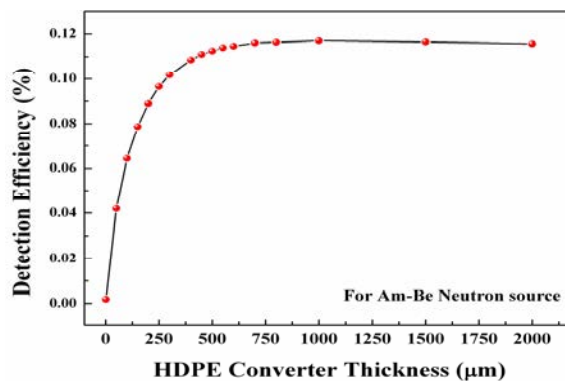


FIG. 4. Optimization of HDPE for Am–Be neutron source.

3.2 GAMMA BACKGROUND EFFECT ON DETECTOR

In general, neutrons are accompanied by a gamma-ray background. In order to understand the effect of gamma background on neutron detection, we have simulated the detector in a mixed environment. For this study, we have generated a mixed neutron–gamma source (ratio 1:1) of energies ranging over 0.1–10 MeV with 10^9 particles as shown in Fig. 5(a). Figure 5(b) shows the energy spectrum in the SiC detector which contains events due to both neutrons and gamma rays. It can be deduced that the gamma-induced events are dominating or comparable to neutron-generated events in the lower-energy region below 1 MeV. Between 1 MeV and 2 MeV, background events could be troublesome for some applications. Beyond 2 MeV, the effect is almost negligible. Further, to eliminate the gamma and other background charged particles, a low-level discriminator can be employed. Figure 6 illustrates the effect of different values of LLD on the neutron detection efficiency.

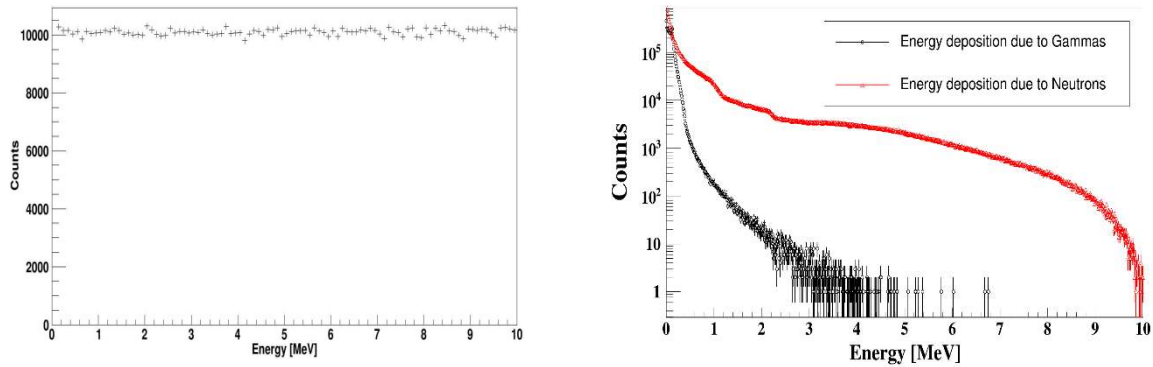


FIG. 5. (a) Incident energy spectrum of mixed neutron and gamma-rays. (b) Comparison of neutron and gamma induced events in SiC detector.

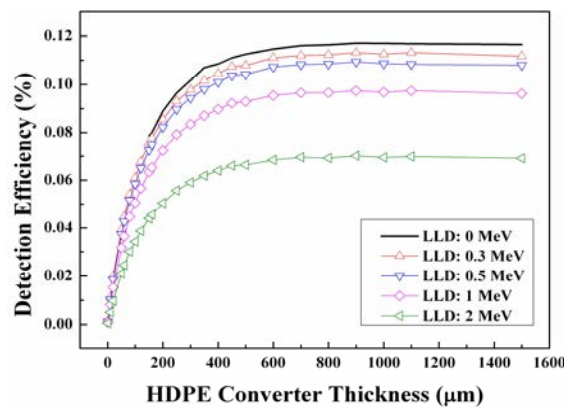


FIG. 6. Effect of LLD on neutron detection efficiency of SiC detector.

3.3 STACKED DETECTOR SIMULATION

Using G4 Replica Class of Geant4, the converter and detector volume is regarded as a single layer and is replicated to generate a stacked structure (Fig. 1(b)). The optimum thickness for a single layer is 400 μm for polyethylene and 600 μm for SiC. Simulations for 10^9 neutron events and up to 10 layers have been performed and efficiency estimated as a function of the number of layers in the stack.

Figure 7 shows that efficiency does not increase linearly with number of layers. As we increase the number of layers from 1 to 2, the efficiency almost doubles i.e. $\sim 99\%$, but from 2 to 3 layers the increment is reduced to 50%. Similarly, going from 9 to 10 layers, the increment is just 10%. At a certain number of layers, efficiency saturates; it is possible that the probability of interaction for a neutron with polyethylene saturates at certain thicknesses. Furthermore, each layer of polyethylene attenuates some fraction of the incident neutrons and decreases the incident flux for subsequent converter layers. Ref. [29] shows a similar effect for a thermal neutron

detector with ^{10}B and LiF converters. Thus, a stacked structure has to have an optimized number of detectors, power supply and processing electronics: 1.04% can be achieved with a 10-layer stacked detector.

Furthermore, the converter thickness corresponding to 5, 10, 15, 20, and 50 stacks was modelled, and maximum efficiency of $\sim 3.85\%$ could be achieved at ca. $400\ \mu\text{m}$ (Fig. 8). Altering the thickness of converter of individual layers may further enhance efficiency but requires further detailed study.

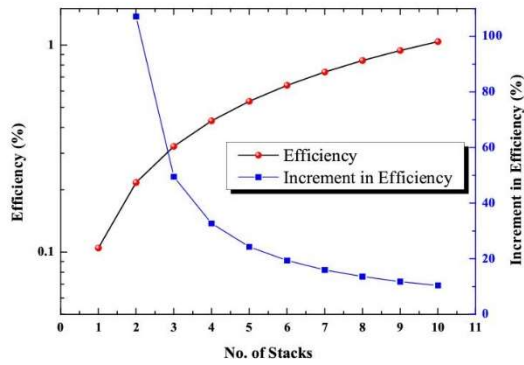


FIG 7. Increment in efficiency with stacked configuration.

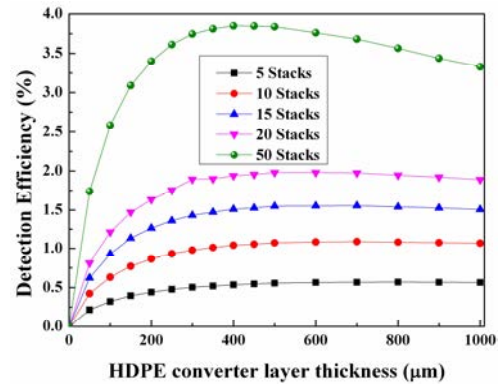


FIG 8. Efficiency vs HDPE thickness with different number of layers in a stack.

Figure 9 illustrates the effect of different energies of gamma rays on the 10-layer stack detector. Note that the gamma-induced events are dominant below the 1 MeV energy region. Beyond 1 MeV, the effect is quite minimal.

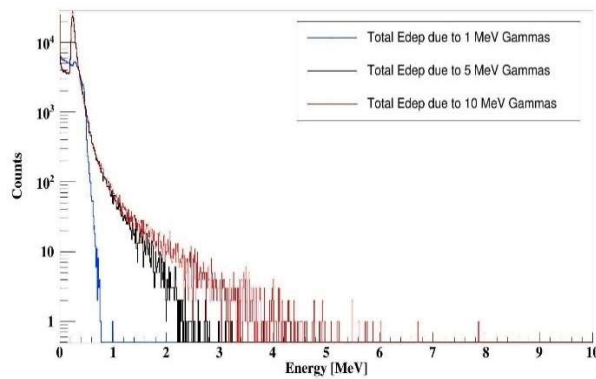


FIG 9. Gamma-induced events in a SiC stacked detector.

3.4 NEUTRONS IMPINGING AT DIFFERENT ANGLES

In a practical scenario such as in a reactor environment, neutrons would not always fall perpendicularly onto the detector surface; rather, they will fall with different angles as explained by the solid angle concept [12]. As we know, the recoil proton energy depends on the scattering angle and a neutron will generate the recoil proton with maximum energy in the case of a head-on-collision i.e., $\theta = 0^\circ$. At angles greater than 0° , the recoil energy decreases. To study the angle effect, we have generated neutrons at different angles with respect to the detector surface and recorded the spectrum.

Figure 10 shows the spectrum due to neutrons impinging on the detector surface with different angles. It is evident that the angles near to 0° offer a slightly better spectrum. Therefore, in this study the efficiency obtained is the maximum since all the neutrons are impinging perpendicularly.

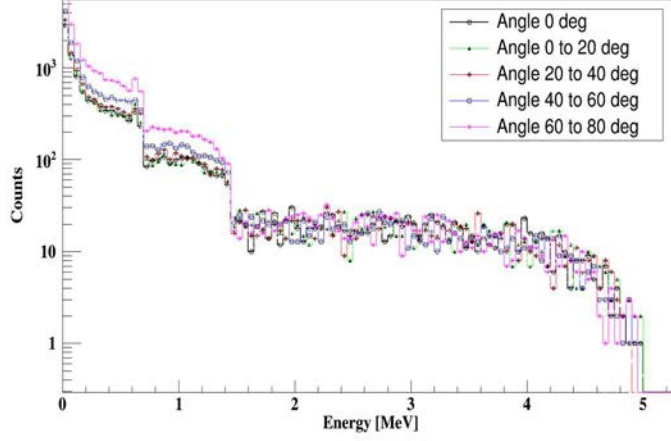


FIG. 10. Angle-dependent neutron-induced spectrum in a SiC detector.

3.5 ALPHA SPECTROSCOPIC CAPABILITY

A further study has been carried out to investigate the feasibility of silicon carbide (SiC) based wide band-gap semiconductor detector to work as an alpha particle spectrometer in a harsh radiation environment. The Geant4 simulation toolkit has been employed for simulating the transport of α particles through the SiC-based radiation detector. The effect on Full Width at Half Maximum (FWHM) of the detector due to energy straggling of the alpha particles while traversing through the contact layers has been assessed by TRIM and Geant4 simulations.

An ^{241}Am -alpha source of 5.486 MeV will continuously lose its energy while traversing the active layer of the detector via ionization and excitation phenomena. These ionizations will result in the generation of electron-hole pairs in the depletion region of the detector. The applied electric field across the diode will encourage the electrons and holes to move in opposite directions to induce current at the electrodes, which can be considered as a charge collection process. The better the charge collection process, the better would be the resolution of the spectrometer. The range of an α particle of 5.486 MeV in SiC is $\sim 18 \mu\text{m}$, calculated using SRIM package. In this simulation, we have assumed that the detector is fully depleted and that therefore an α particle impinging normally would be completely stopped in the detector's active region. Figure 11 illustrates a plot of α particle counts as a function of energy. A sharp peak can be observed for a ^{241}Am α -emitter. Furthermore, Fig. 11 also represents a FWHM for a Gaussian fit to ^{241}Am peak in SiC for a Au contact. The FWHM measured for a semiconductor spectrometer encompasses several independent components [12] in the form of quadrature sum (Eq. 1):

$$\begin{aligned} (\text{FWHM}_{\text{Total}})^2 &= (\text{FWHM}_{\text{Elec/Noise}})^2 + (\text{FWHM}_{\text{Leakage}})^2 + (\text{FWHM}_{\text{Statistical}})^2 \\ &+ (\text{FWHM}_{\text{SiC}})^2 + (\text{FWHM}_{\text{other}})^2 \end{aligned} \quad (1)$$

where,

$\text{FWHM}_{\text{Total}}$:	observed FWHM of full energy peak
$\text{FWHM}_{\text{Elec/Noise}}$:	noise from front-end electronics
$\text{FWHM}_{\text{Leakage}}$:	detector leakage current
$\text{FWHM}_{\text{Statistical}}$:	charge generation statistics by the alpha particles
FWHM_{SiC}	:	charge collection properties of SiC semiconductor
$\text{FWHM}_{\text{Other}}$:	other sources such as variation in energy loss in the contact or other protective layers in semiconductor detector due to differences in angle of incidence of the alpha particle, loss of energy in the environment between detector and source etc.

The pulse height variation due to fluctuations in the leakage current will be negligible because of the very low leakage current in SiC (nanometer range). According to Ref. [30] the spectrum broadening due to front-end electronics is $\sim 8 \text{ keV}$ which can be attributed as a practical limit of electronics that cannot be minimized further

with the technology presently available. Broadening due to charge generation statistics can be estimated by following equation:

$$(\text{FWHM}_{\text{Statistics}})^2 = 2.3552 (\varepsilon.F.E_\alpha) \quad (2)$$

where ε is the energy required to generate an electron–hole pair in SiC, i.e. 7.75 eV [14]; F is the Fano factor which has been reported to be < 0.04 [10] and E_α is the energy of alpha particle. A calculation from the expression above using a Fano-factor of 0.04 and ε of 7.75 eV predicts a value of $\text{FWHM}_{\text{Statistics}}$ to be 3.071 keV for a 5.486 MeV alpha from an ^{241}Am source.

If we keep the detector and source in vacuum, then the energy loss other than in the detector could be made negligible. However, Schottky contacts and other protective materials which comprise the entrance window to the detector active volume could result in significant broadening of spectrum due to the energy loss in there while traversing. Also, differences in angles of incidence of α -particles in the case of a point source would further increase the energy straggling due to the extra path length of travel of α -particles in that material. In this work, our main emphasis is to estimate the contribution of energy straggling due to contacts; i.e. peak broadening in FWHM of a SiC alpha spectrometer due to other sources as mentioned above using Geant4 Monte-Carlo simulation model. Figure 11 has the FWHM of ~ 22.8 keV for a Gaussian fit to ^{241}Am alpha source with Au contact on SiC spectrometer, which is in good agreement with the value reported in Ref. [30] using an alternate method. The value for FWHM_{SiC} component is reported as ~ 20 keV in the literature [30]. The quadrature sum of all the FWHM components will result in the overall FWHM of ~ 45 keV which is in agreement with the experimental value reported in the literature [31].

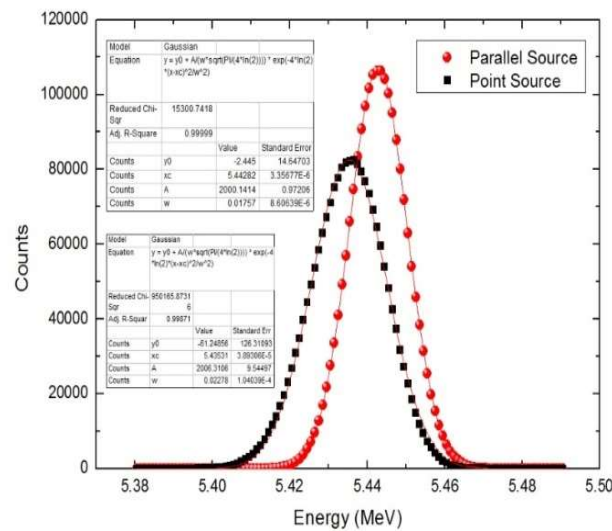


FIG. 11. FWHM for a Gaussian fit to ^{241}Am parallel and point source in SiC spectrometer with Au contact.

3.6 DETECTOR DEVICE OPTIMIZATION USING TCAD

A TCAD simulation study has been carried out to assess the performance of a silicon carbide (SiC) based fast neutron detector in a harsh environment. A 3D-structure of a 4H–SiC based Schottky diode reported in literature [32] has been created using the DevEdit3D module of SILVACO and is shown in Fig. 12. The n-type 4H–SiC diode structure is partitioned into two uniformly doped layers: (1) a lightly doped (10^{15} cm^{-3}) epitaxial layer (10 μm) for Schottky contact, and (2) a heavily doped (10^{19} cm^{-3}) lower active layer (20 μm) for ohmic contact. The lightly doped top layer is good for charge carrier mobility, as with increasing doping concentration the mobility degrades and subsequently the charge collection time increases. The highly doped SiC layer was used for ohmic contact formation as it creates a very thin depletion region at the interface of the ohmic contact–semiconductor junction. Table 1 lists the important material and model parameters, extracted from recent experimental work [33], for 4H–SiC device simulation and modelling.

TABLE 1. MODEL PARAMETER VALUES FOR SiC DEVICE MODELING IN SILVACO TCAD (VALUES MENTIONED WITHOUT UNITS ARE UNITLESS QUANTITIES)

Model	Parameter	Value
Band-gap variation with temperature	EGALPHA	0.033 eV/K
	EGBETA	10 ⁵ K
	EG300	3.265 eV
Band-gap variation with doping	BGN.LIND.ANC	-1.5 × 10 ⁻² eV
	BGN.LIND.BNC	-2.93 × 10 ⁻³ eV
	BGN.LIND.ANV	1.9 × 10 ⁻² eV
	BGN.LIND.BNV	8.74 × 10 ⁻³ eV
Mobility	MU1N.CAUG	28 cm ² /(V.s)
	MU2N.CAUG	950 cm ² /(V.s)
	ALPHAN.CAUG	0
	BETAN.CAUG	-2.4
	GAMMAN.CAUG	0.73
	DELTAN.CAUG	-0.61
	NCRITN.CAUG	1.94 × 10 ¹⁷ cm ⁻³
	D.CONWELL	6.9 × 1020 [cm.V.s] ⁻¹
	F.CONWELL	7.425 × 10 ¹³ cm ⁻²
SRH Recombination	VSATN	2.2 × 10 ⁷ cm/s
	TAUN0	1 × 10 ⁻⁹ s
	TAUP0	6 × 10 ⁻⁷ s
Auger Recombination	TMUN	2.25
	AUGN	5 × 10 ⁻³¹ cm ⁶ /s
Impact Ionization Model	AUGP	2 × 10 ⁻³¹ cm ⁶ /s
	AN1	3.44 × 10 ⁶ cm ⁻¹
	BN1	2.58 × 10 ⁷ V/cm

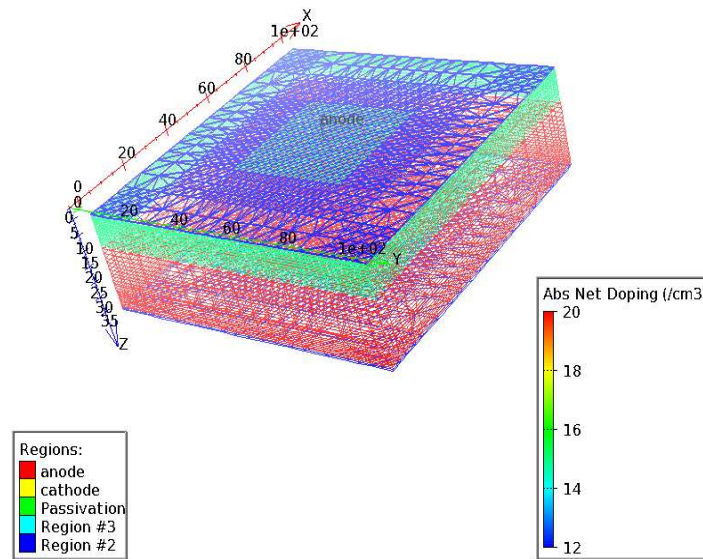


FIG. 12. SiC based Schottky Diode structure using DevEdit3d

Current voltage simulations on SiC Schottky diodes as a function of temperature (0–500 °C) have been performed. Figures. 13 and 14, respectively, show the forward and reverse bias IV -curves. Figure 13 shows that the forward voltage decreases at high temperature, due to the reduction in external force required to drive the charge carriers in the conduction process. This current–voltage relationship of a Schottky diode is described by thermionic emission theory:

$$I = I_s \{1 - \exp(qV/nkT)\} \quad (3)$$

where

$$I_s = A.A^* T^2 \exp\left(-\frac{q\phi_B}{kT}\right) \quad (4)$$

is the reverse saturation current, n is the ideality factor, A is area, A^* is the Richardson constant, T is the temperature, ϕ_B is the barrier height, and k is the Boltzmann constant. The increase in reverse saturation current with temperature is shown in Fig. 14. The leakage current increases with temperature due to tunnelling through the surface and bulk states.

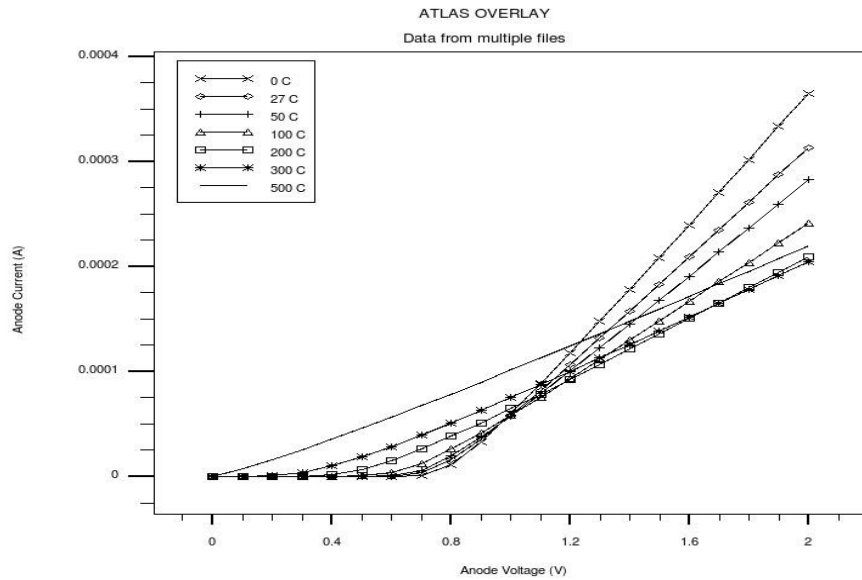


FIG. 13. Forward IV-characteristics at different temperatures.

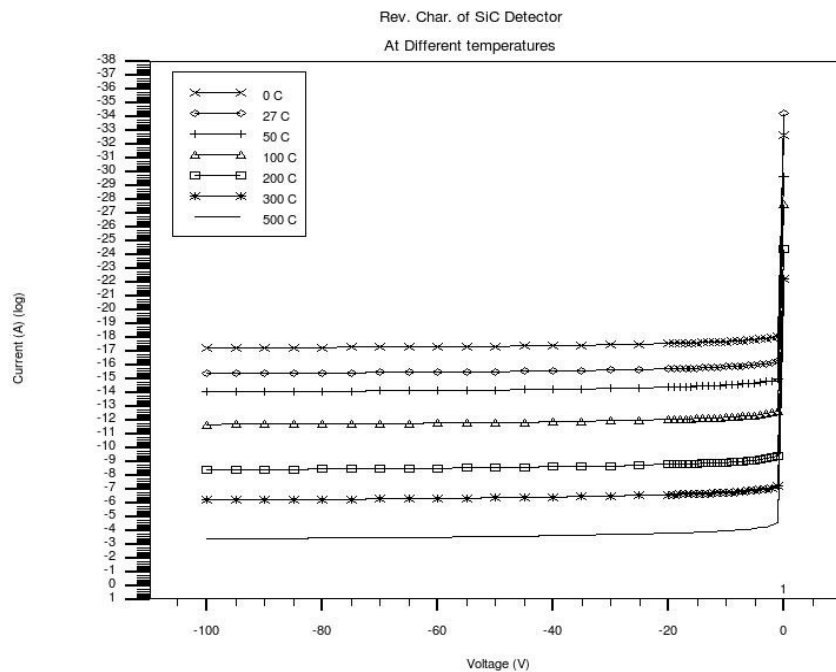


FIG. 14. Reverse IV-characteristics at different temperatures.

Figure 15 shows the Capacitance–Voltage (CV) curve. The CV characteristic shows capacitance in the order of 100 pF, which is equivalent to that of Si-based detectors. The capacitance of the detector should be 10 times of the preamplifier. Preamplifier capacitance is generally in the range of 1–10 pF.

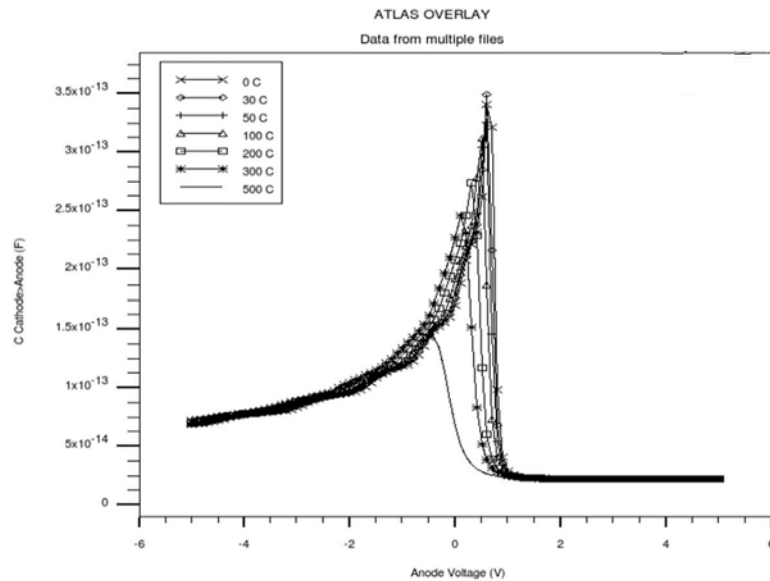


FIG. 15. CV-characteristics at different temperatures.

4 CONCLUSIONS

We have presented a proton recoil neutron detector modelled using Geant4. Our detector consists of an HDPE converter layer to generate recoil protons upon interaction with neutrons and a SiC detector to detect the energetic recoil protons. We have optimized the HDPE thickness for different mono-energetic neutrons (1–10 MeV) and a standard neutron source (Am–Be) and it is found to be $\sim 400 \mu\text{m}$. Simulation of the detector in a mixed neutron–gamma environment reveals the requirement of LLD. The effect of LLD on the neutron detection efficiency is demonstrated. The stacked structure of the detector is simulated in order to determine the increase in efficiency. We could achieve efficiency of $\sim 3.85\%$ with 50 layers in a stack. Alpha spectroscopic capability of SiC was presented and contribution of $\text{FWHM}_{\text{Other}}$ component is estimated to be $\sim 22.8 \text{ keV}$. Furthermore, detector device characteristics are demonstrated in TCAD at elevated temperatures. Future work will be focused on the radiation damage study and fabrication of SiC-based detector and testing the detector in nuclear reactors.

REFERENCES

- [1] RUNKLE, R.C., BERNSTEIN, A., VANIER, P.E., Securing special nuclear material: Recent advances in neutron detection and their role in nonproliferation, *J. Appl. Phys.* **108** 11 (2010) 111101.
- [2] SIVARAMAKRISHNA, M., NAGARAJ, C.P., MADHUSOODANAN, K., CHELLAPANDI, P., Neutron flux monitoring system in prototype fast breeder reactor, *Int. J. Eng. Innov. Technol. IJEIT* **3** 10 (2014).
- [3] COHEN, L., AWSCHALOM, M., Fast neutron radiation therapy, *Ann. Rev. Biophys, Bioeng.* **11** 1 (1982) 359.
- [4] TSOULFANIDIS, N., *Measurement and Detection of Radiation*, Hemisphere Publishing Corporation (1983) 600 pp.
- [5] AGARWAL, J.H., Electronic aids for enhancement of agricultural production, *IETE Tech. Rev.* **10** 1 (1993) 57.
- [6] KALRA, N., DAS, D.K., SARKAR, T.K., Electronics in water management, *IETE Tech. Rev.* **8** 6 (1991) 348.
- [7] FELDMAN, W.C., AUCHAMPAUGH, G.F., BYRD, R.C., A novel fast-neutron detector for space applications, *Nucl. Instrum. Methods Phys. Res. Sect. Accel. Spectrometers Detect. Assoc. Equip.* **306** 1 (1991) 350.
- [8] CHEN, G., LANZA, R.C., Fast neutron resonance radiography for elemental imaging: theory and applications, *IEEE Trans. Nucl. Sci.* **49** 4 (2002) 1919.
- [9] VERBINSKI, V.V., BOKHARI, M.S., A fast-neutron spectrometer for reactor environments, *Nucl. Instrum. Methods* **46** 2 (1967) 309.
- [10] CORTESI, M., et al., Concept of a novel fast neutron imaging detector based on THGEM for fan-beam tomography applications, *J. Instrum.* **7** 2 (2012) C02056.

- [11] GLASSTONE, S., Nuclear Reactor Engineering: Reactor Design Basics, 4th edn, Vol. 1, cbspd, New Delhi (2004) 495 pp.
- [12] KNOLL, G.F., Radiation Detection and Measurement, 4th edn, John Wiley and Sons (2010) 860 pp.
- [13] STROMSWOLD, D.C., HANSEN, R., REEDE, P., PEURRUNG, A., Direct Fast- Neutron Detection PNNL-13068, Pacific Northwest National Laboratory, Richland, Washington (2000) (Available at: <https://www.osti.gov/servlets/purl/750259>).
- [14] TRIPATHI, S. et al., Geant4 Simulations of Semiconductor Detectors (SiC) for Fast Neutron Spectroscopy, 2015 Annual IEEE India Conference (INDICON), IEEE, New Delhi (2015) 1–6.
- [15] DUCHENE, J., High temperature fission chambers, IRE Trans. Nucl. Sci. **9** 1 (1962) 123.
- [16] JAMMES, C., et al., Assessment of the high temperature fission chamber technology for the French fast reactor program, IEEE Trans. Nucl. Sci. **59** 4 (2012) 1351.
- [17] GOLDSTEIN, N.P., TODT, W.H., A survey of self-powered detectors—Present and future, IEEE Trans. Nucl. Sci. **26** 1 (1979) 916.
- [18] HARRIS, Jr, L., KNOLL, G.F., KING, J.S., Proton-recoil spectrometer for fast neutron spectra, Trans. Am. Nucl. Soc **8** (1965) 73.
- [19] FLAMMANG, R.W., SEIDEL, J.G., RUDDY, F.H., Fast neutron detection with silicon carbide semiconductor radiation detectors, Nucl. Instrum. Methods Phys. Res. Sect. Accel. Spectrometers Detect. Assoc. Equip. **579** 1 (2007) 177.
- [20] SEDLAČKOVÁ, K., et al., MCNPX Monte Carlo simulations of particle transport in SiC semiconductor detectors of fast neutrons, J. Instrum. **9** 5 (2014) C05016.
- [21] DENNIS, J.A., Neutron flux and energy measurements, Phys. Med. Biol. **11** 1 (1966) 1.
- [22] MCGREGOR, D.S., KLANN, R.T., GERSCH, H.K., YANG, Y.H., Thin-film-coated bulk GaAs detectors for thermal and fast neutron measurements, Nucl. Instrum. Methods Phys. Res. Sect. Accel. Spectrometers Detect. Assoc. Equip. **466** 1 (2001) 126.
- [23] McKINNEY, G., et al., “Review of Monte Carlo all-particle transport codes and overview of recent MCNPX features.” International Workshop on Fast Neutron Detectors and Applications (FNDA2006). Proc Sci. (2006), 2007, <https://doi.org/10.22323/1.025.0088>
- [24] AGOSTINELLI, S., et al., Geant4—a simulation toolkit, Nucl. Instrum. Methods Phys. Res. Sect. Accel. Spectrometers Detect. Assoc. Equip. **506** 3 (2003) 250.
- [25] Geant4 Collaboration: Physics Reference Manual, http://geant4.web.cern.ch/support/user_documentation.
- [26] ALLISON, J., et al., Geant4 developments and applications, IEEE Trans. Nucl. Sci. **53** 1 (2006) 270.
- [27] INTERNATIONAL ORGANIZATION FOR STANDARDIZATION, ISO 8529-1:2001(en), Reference Neutron Radiations — Part 1: Characteristics and Methods of Production (2001) <https://www.iso.org/obp/ui/#iso:std:25666:en>.
- [28] FRANCESCHINI, F., RUDDY, F.H., Silicon Carbide Neutron Detectors, INTECH Open Access Publisher (2011).
- [29] MCGREGOR, D.S., et al., Design considerations for thin film coated semiconductor thermal neutron detectors—I: basics regarding alpha particle emitting neutron reactive films, Nucl. Instrum. Methods Phys. Res. Sect. Accel. Spectrometers Detect. Assoc. Equip. **500** 1–3 (2003) 272.
- [30] RUDDY, F.H., et al., High-resolution alpha-particle spectrometry using 4H silicon carbide semiconductor detectors, IEEE Trans. Nucl. Sci. **53** 3 (2006) 1713–1718.
- [31] PULLIA, A., et al., An SiC/GaN detector/front-end detection system for high-resolution alpha-particle spectroscopy, IEEE Trans. Nucl. Sci. **55** 6 (2008) 3736–3740.
- [32] DAS, A., DUTTAGUPTA, S.P., TCAD simulation for alpha-particle spectroscopy using SiC Schottky diode, Radiat. Prot. Dosimetry **167** (2015) 443–452.
- [33] STEFANAKIS, D., ZEKENTES, K., TCAD models of the temperature and doping dependence of the bandgap and low field carrier mobility in 4H–SiC, Microelectron. Eng. **116** (2014) 65–71.

NEXT GENERATION NEUTRON DETECTORS

K.S. SHAH, M.R. SQUILLANTE, E. VAN LOEF, J. GLODO, L. CIRIGNANO, H. HONG,
A. GUEORGUIEV, J. TOWER, A. KARGAR, H. KIM
Radiation Monitoring Devices, Inc. ('RMD')
Watertown, MA 02472 USA
E-mail: KShah@RMDInc.com

Abstract: This article discusses advances in neutron detection technologies, focusing on scintillation. Inorganic scintillators incorporating ${}^6\text{Li}$, such as $\text{Cs}_2\text{LiYCl}_6:\text{Ce}$ and other related elpasolites, are covered in detail. Thermal neutron detection efficiency, and the ability to separate gamma-rays and thermal neutrons using pulse height and pulse shape analysis, are addressed. Crystal fabrication and optical readout issues, as well as new instrumentation based on these novel scintillators, which combine neutron and gamma-ray detection in a single detector, are also discussed. In addition, this article describes new organic scintillators, including recent advances in loading organometallic compounds into plastic scintillators to enhance their gamma-ray efficiency while providing fast neutron detection with good neutron/gamma pulse shape discrimination. Composite scintillators that incorporate inorganic scintillators in an organic scintillating host are also discussed. Finally, results from a polycrystalline diamond detector and a new semiconductor neutron detector, ${}^6\text{LiInSe}_2$, are presented.

1 INTRODUCTION

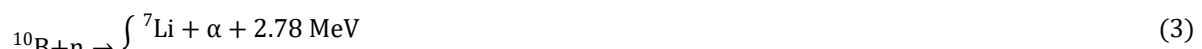
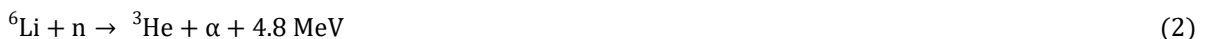
Neutrons are uncharged particles that penetrate dense, high atomic number materials relatively easily compared to gamma rays, but are readily absorbed or scattered by various lighter elements, such as hydrogen, deuterium, or lithium. Since neutrons are not generated from any naturally occurring radioactive decay, and the neutron background rate is reasonably constant and low ($\sim 0.007 \text{ cm}^{-2}\text{sec}^{-1}$), detection of neutrons can indicate the presence of isotopes (such as plutonium and californium) that undergo spontaneous fission, as well as induced fission as in uranium [1]. In addition to spontaneous and induced fission, neutrons can also be emitted by mixing transuranic alpha emitters with certain light nuclei such as Be, in particular. Since (α, n) reactions produce neutrons randomly in time and fission produces neutrons in bursts, coincidence measurements can distinguish between neutrons produced by (α, n) reactions and neutrons produced by fission. Passive neutron measurements can be used to verify the ${}^{240}\text{Pu}$ content of plutonium metal and to verify the contents of UF_6 cylinders. For natural UF_6 , 80% of the neutrons are due to (α, n) reactions and the rest to spontaneous fission [2].

1.1 THERMAL NEUTRON DETECTION

Detection of neutrons is generally performed indirectly by measuring the signal from secondary ionizing particles that are produced during the interaction of a neutron with matter. For detecting neutrons, the most important interactions of neutrons with matter are:

- 1) the reaction with ${}^6\text{Li}$ or ${}^{10}\text{B}$, which produces alpha radiation
- 2) the reaction with ${}^3\text{He}$, which produces a proton and a triton (${}^3\text{H}$)
- 3) elastic scattering by nuclei.

The first two interactions are most likely to occur for neutrons with energies of up to about 0.5 eV. These neutrons fall in the slow or thermal neutron range. For low-energy neutrons, techniques have been developed to detect them by measuring the protons, tritons, and alpha particles that are produced by the reaction of neutrons with isotopes such as ${}^3\text{He}$, ${}^6\text{Li}$, ${}^{10}\text{B}$, or ${}^{157}\text{Gd}$ (Eqs 1–5), which have large cross sections for thermal neutron absorption. Each interaction of a thermal neutron with ${}^3\text{He}$, ${}^6\text{Li}$, ${}^{10}\text{B}$, or ${}^{157}\text{Gd}$ can be characterized by its cross-section for thermal neutron absorption and a Q value. The Q value determines the total energy of the reaction products.



1.2 FAST NEUTRON DETECTION

There are basically three general types of devices for fast neutron detection: (1) counters based on neutron moderation; (2) detectors based on the ${}^3\text{He}(n,p)$, ${}^6\text{Li}(n,\alpha)$, and ${}^{35}\text{Cl}(n,p){}^{35}\text{S}$ reactions, and (3) detectors based on fast neutron scattering. For counters based on neutron moderation the incident fast neutrons are thermalized by a hydrogen-rich moderator and the thermal neutrons are then detected using a thermal neutron detector. The moderating process eliminates information on the incident neutron energy. Solid state detectors that incorporate ${}^6\text{Li}$, ${}^{10}\text{B}$, or ${}^{157}\text{Gd}$ have the advantage of size and ruggedness compared to gas-filled detectors.

The two reactions traditionally used for fast neutron spectroscopy are ${}^3\text{He}(n,p)$ and ${}^6\text{Li}(n,\alpha)$ [3]. Elastic scattering, whereby a fast neutron transfers energy to a recoil nucleus, can also be used to detect epithermal and fast neutrons. Recently, detectors have been developed based on the interaction with ${}^{35}\text{Cl}$:



Neutron detection by carbon-based detectors, such as SiC and diamond, includes both neutron interactions and scattering. For higher sensitivity, they can be combined with a layer of a hydrogen-containing material to detect the protons scattered from that layer. Diamond is a very promising material for a solid-state fast neutron detector. Table 1 shows calculated estimates of linear attenuation coefficients for some promising fission neutron detection materials [4]. From the calculations, diamond has the highest intrinsic efficiency per unit thickness for arbitrary shape of the fission neutron spectrum. Cubic boron nitride (c-BN) has an attenuation coefficient similar to diamond, but the film growth technology is not as well established as for diamond.

TABLE 1. LINEAR ATTENUATION COEFFICIENTS FOR FISSION NEUTRON DETECTION MATERIALS

Material	$N(\text{atoms}/\text{cm}^3)$	$\langle\sigma\rangle$ (barns)	$\langle\mu_n\rangle$ (%/mm)
Diamond	17.6×10^{22}	2.32	4.10
c-BN	17.3×10^{22}	2.16	3.70
BC517p	11.1×10^{22}	3.19	3.50
BC400	10.0×10^{22}	3.00	3.00
SiC	9.6×10^{22}	2.65	2.50

Cross sections averaged over an unmoderated fission spectrum with a T parameter of 1.6 MeV. BC517p is a liquid scintillator and BC400 is plastic (data from Schmid [4]).

2 SCINTILLATION DETECTORS

Other than ${}^3\text{He}$, the most common neutron detectors are based on scintillators. There are two typical modes of operation utilizing scintillators, which we could call extrinsic and intrinsic. In the extrinsic mode, a scintillator is matched with neutron-absorbing medium (a converter) such as Li or Gd that produces particles under neutron excitation to be detected by the scintillator. The scintillator itself does not need to be neutron sensitive. In a typical mode of operation, a flat scintillator screen, such as CsI:Tl, can be coated with either isotope and used for neutron imaging when coupled to a CCD camera [5]. An extension of this model are perforated silicon devices [6] and coated silicon devices, which are not discussed here.

The intrinsic mode is based on the scintillator containing a neutron sensitive element. One of the first such scintillators is LiI:Eu, where the capture of neutrons by Li produces charged particles that create a full energy peak in the pulse height spectra [7]. In the case of Li, the deposited energy is 4.8 MeV. Due to the fact that charged particles have higher quenching factors than gamma-rays, the equivalent energy in the gamma type spectrum is lower than the full deposited energy. In the case of LiI it is ~ 4 MeV [8]. LiI, and later Li-glass, for many years were the only major scintillators used for neutron detection. This changed at the beginning of the 21st century with the discovery of elpasolites.

2.1 ELPASOLITE SCINTILLATORS

$\text{Cs}_2\text{LiYCl}_6$ (CLYC) was discovered by Delft University [9,10] and further developed by RMD [11]. Originally the material was thought to be a good thermal neutron scintillator with relatively high equivalent energy of >3 MeV and, more exciting, excellent pulse shape discrimination (PSD). An example of the energy spectra is shown in Fig. 1.

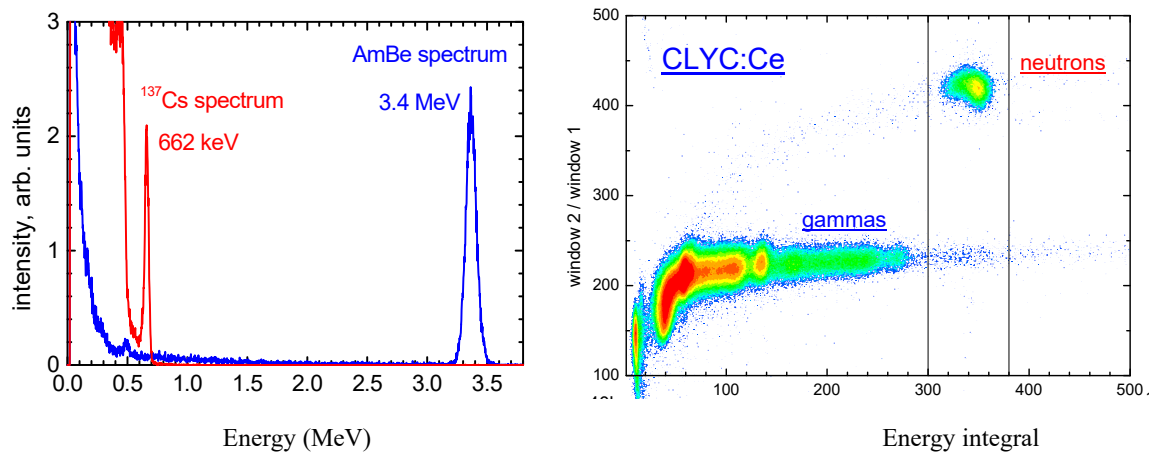


FIG. 1. Example of energy spectra of the CLYC scintillator. Red line shows a ^{137}Cs spectrum with the 662 keV line and blue line AmBe spectrum with thermal neutron peak at 3.4 MeV gamma equivalent energy. The right graph shows pulse shape discrimination data, where the x-axis is proportional to the light yield (energy) and the y-axis is the PSD factor. The gamma and neutron signals are very well separated.

Compared to the current scintillators, CLYC allows for effective differentiation between gamma-rays and neutron signals based on their pulse shapes, thereby increasing reliability of gamma-ray rejection. An example of PSD data is also shown in the figure (right). This feature is lacking in the other two major materials that rely only on pulse height discrimination. Further discoveries showed that CLYC also has quite good energy resolution, 5% at 662 keV, and excellent proportionality, making this material a dual mode scintillator (neutron/gamma). The main properties of CLYC and other Li-based scintillators are shown in Table 2. Please note that the best neutron attenuation length is still provided by LiI, since it contains the highest amount of Li per cm^2 .

TABLE 2. BASIC PROPERTIES OF LI-BASED NEUTRON SCINTILLATORS

Scintillator	LY (ph/MeV)	Decay (ns)	ER @ 662keV (%)	Density, (g/cm^3)	Neutron LY, (ph/n)	Neutron Att. Length	PSD, Fig. of Merit
LiI(Eu)	15 000	1,200	7.5	4.08	60 000	0.06	No, –
Li-glass	4 000	75	–	2.5	6 000	~0.13	No, –
CLYC:Ce	20 000	1, 50, 1 000	4	3.3	65 000	0.26	Yes, ~4
CLLBC:Ce	45 000	130, 600	3	~4	135 000	0.38	Yes, ~3
TLYC	30 000	57, 460, 1 050	4	4.5	57 000	0.24	Yes, 2.4

$\text{Cs}_2\text{LiLa}(\text{Br},\text{Cl})_6$ scintillators (CLLB, CLLBC) are the structural analogs of CLYC, but provide increased light yield and significantly better gamma-ray energy resolution. In terms of neutron detection, there are small differences. First, the neutron detection is slightly higher than in the case of CLYC. While the total attenuation length for CLYC is shorter, that is due to Cl, which has a meaningful cross-section for thermal neutron detection. In CLYC only 78% of neutrons are stopped by ^6Li , while CLLB and CLLBC stop about 92%. While CLLB and CLLBC are comparable, the latter is characterized by better PSD (~2 vs. ~3 FOM value). Examples of CLLBC data are shown in Figure 2. Currently, the development of elpasolites is turning towards increased density for better gamma detection, and materials such as $\text{Tl}_2\text{LiYCl}_6$ are being investigated [12].

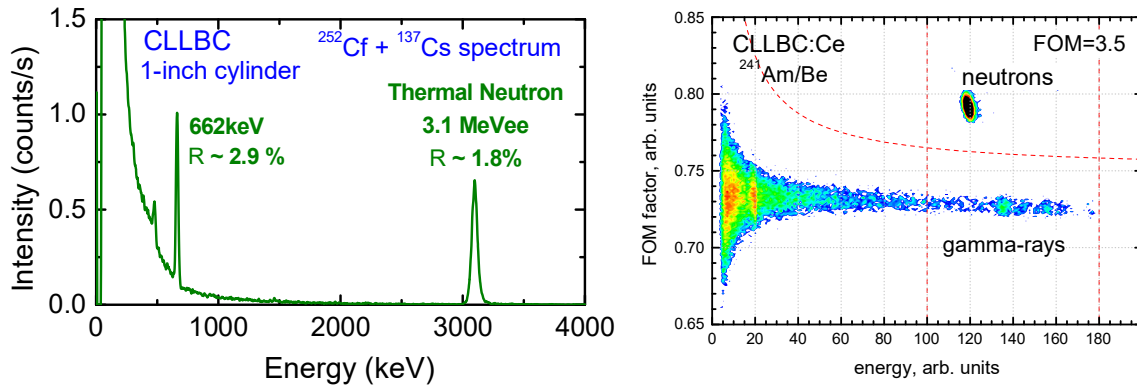


FIG. 2. Example of a mixed ^{137}Cs and ^{252}Cf energy spectrum measured with a CLLBC scintillator: The thermal neutron peak appears at 3.1 MeV gamma equivalent energy. The right graph shows pulse shape discrimination data, where the x-axis is proportional to the light yield (energy) and the y-axis PSD factor. The gamma and neutron signals are also very well separated.

2.2 GADOLINIUM-BASED SCINTILLATORS

In addition to Li, Gd is another ion that is often used as a scintillator constituent. While Gd has a very high cross-section for thermal neutron detection (48,890 barns for natural isotope), its products are high-energy gamma-rays and conversion electrons. The former are relatively useless, therefore, the main signal comes from the latter. The energy deposited in the scintillator from the conversion electrons is rather low, typically about 80 keV. Low energy and lack of PSD make scintillators based on Gd useful mainly in the form of thin films, where the gamma-ray absorption is minimized by low thickness. The electrons are also produced in about 80% of captures (branching), limiting scintillator efficiency. Figure 3 shows neutron attenuation curves and an example of the pulse height spectra measured with the $\text{GdI}_3:\text{Ce}$ scintillator under ^{252}Cf excitation [13]. The neutron peak appears at 86 keV, as calibrated by the 60 keV photopeak from ^{241}Am .

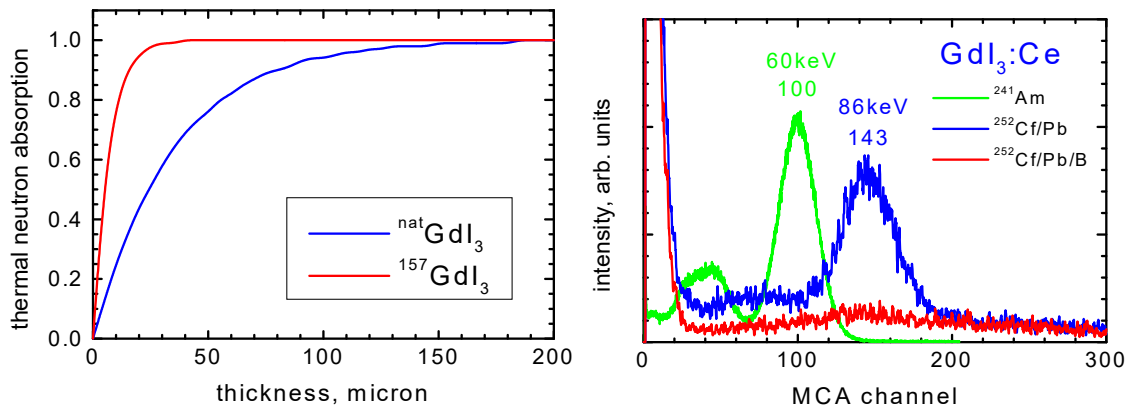


FIG. 3. Left shows absorption of thermal neutron vs. thickness for different versions of GdI_3 . Right shows pulse height spectra measured under ^{252}Cf with ^{241}Am (60 keV) for a reference.

2.3 FAST NEUTRON DETECTION

Coming back to the difference in the detection between CLYC and CLLB, we pointed out Cl. Indeed, it not only competes with Li for neutron absorption but also produces useful signals. Bubble Technology Industries, Ontario, Canada, discovered that Cl has meaningful cross-section to capture not only thermal neutrons but also fast neutrons [14,15]. This reaction, as stated in the Introduction, produces a proton of energy proportional to the incident energy of the neutron. To a certain extent this allows for fast neutron spectroscopy. Figure 4 shows the absorption cross section as a function of energy of the active isotopes (left) and data obtained using CLLBC in a mixed radiation field (right).

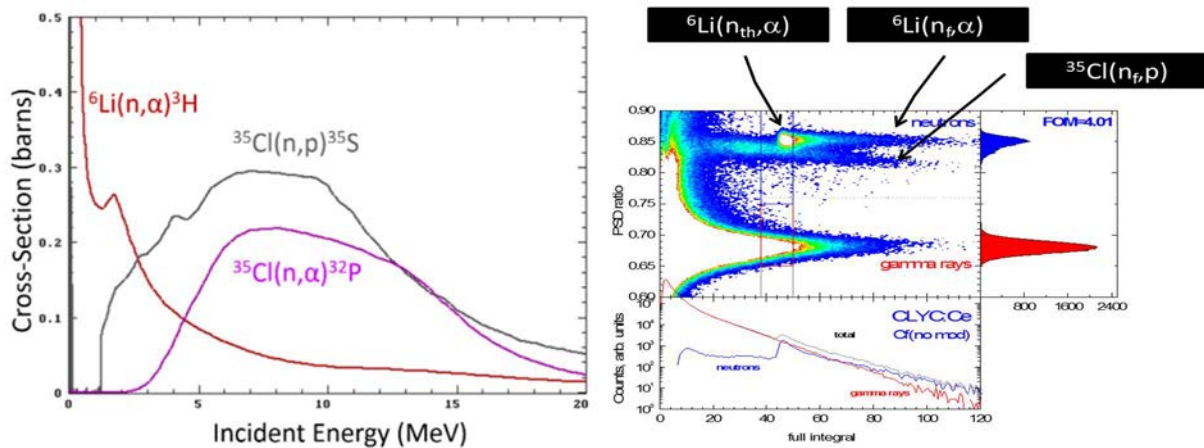


FIG. 4. Example of a mixed ${}^{137}\text{Cs}$ and ${}^{252}\text{Cf}$ energy spectrum measured with a CLLBC scintillator. The right graph shows pulse shape discrimination data, where the x-axis is proportional to the light yield (energy) and the y-axis PSD factor.

3 PLASTIC AND ORGANIC SCINTILLATORS

3.1 PLASTIC SCINTILLATORS

The fast neutron signature of special nuclear materials is an important component of current and future radiation detection systems for nuclear non-proliferation [16]. Commercial liquid scintillators detect fast neutrons efficiently, at low cost, and using pulse shape discrimination (PSD) can distinguish neutrons from gamma rays [17]. However, as they are based on volatile organic compounds and have relatively low flash points, they are not readily transported, handled, or installed. Traditional plastic scintillators are, in contrast, handled with ease, can detect fast neutrons efficiently, often suffer from low light yields and do not provide efficient PSD [18].

A research initiative focused on fabrication of advanced plastic scintillators that possess higher light yields and enhanced PSD was begun that built on the pioneering work of Zaitseva et al. [19]. These new plastic scintillators, based on novel and standard polymer hosts, are doped with tailored wavelength shifters and additives to improve light transmission.

Typically, the plastic scintillators with PSD, now being developed, are made from styrene wherein a large amount of PPO is dissolved. The monomer solution is then sealed in a container under reduced pressure and polymerized over the course of several weeks. Figure 5 shows a typical pulse height spectrum of the PSD plastic scintillator under ${}^{137}\text{Cs}$ 662 keV gamma-ray excitation. The spectrum from a BGO crystal is shown for comparison. The light yield of this plastic scintillator is estimated to be ca. 13,000 ph/MeV, based on BGO's light yield (8,200 ph/MeV), the Compton edges of the plastic scintillator and BGO, and the system's spectral response.

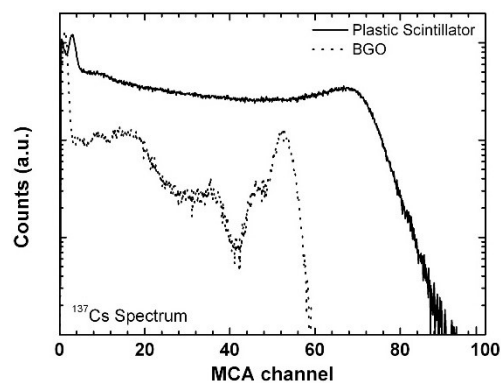


FIG. 5. Pulse height spectrum of a polystyrene plastic scintillator doped with PPO fabricated at RMD. To compare, the spectrum of a BGO crystal is shown as well.

The figure of merit (FOM) for a typical polystyrene plastic scintillator is shown in Figure 6. The FOM is defined as the separation between the centroids of the gamma-ray (C_γ) and neutron (C_n) event distributions, divided by the sum of the widths of the gamma-ray (W_γ) and neutron (W_n) event distribution, as shown in Equation 8.

$$FOM = \frac{|C_\gamma - C_n|}{W_\gamma + W_n} \quad (8)$$

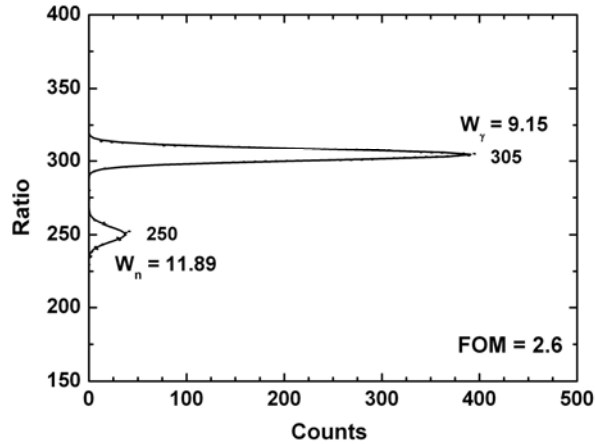


FIG. 6. Figure of merit (FOM) for a polystyrene plastic scintillator fabricated at RMD.

Considering that in traditional plastic scintillators, PSD is either absent or negligible while the FOM for the thermal neutron scintillator $\text{Cs}_2\text{LiYCl}_6:\text{Ce}$ is close to 4 [20], a measured FOM of about 2.6 for these plastic scintillators is very good.

3.2 ORGANIC SCINTILLATORS FOR FAST NEUTRON DETECTION

In addition to the plastic scintillators, single crystal organic scintillators that have high light yields, fast scintillation decay, and very good neutron/gamma pulse shape discrimination (PSD), have been investigated. One of these is 9-phenylcarbazole (PCz).

Typically, PCz powder is obtained from commercial sources and purified before use. Large crystals of PCz are then grown from solution, dissolving the purified powder in an appropriate solvent, and slowly evaporating it. An example of a PCz crystal is shown in Figure 7.



FIG. 7. Single crystal PCz.

Figure 8 shows a typical pulse height spectrum of a PCz crystal. To compare, the spectrum of the reference BGO crystal is shown as well. Using the known light output of BGO crystal as the calibration standard, the light output of doped PCz is estimated at 25,000 ph/MeV. Figure 9 shows the PSD FOM plot of PCz at 120 keVee with a FOM of 1.9. At 1 MeVee the FOM is 2.7.

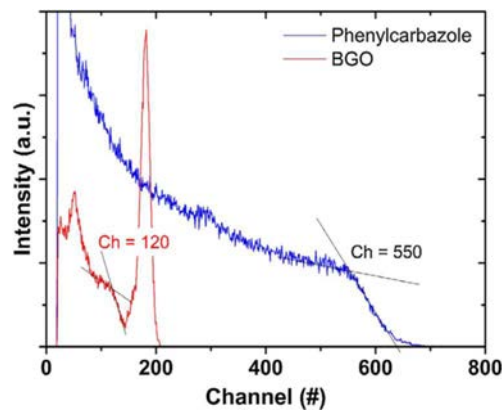


FIG. 8. Pulse height spectrum of a PCz crystal.

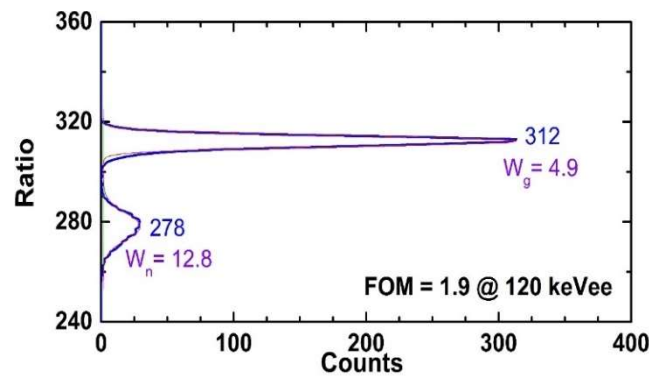


FIG. 9. PSD FOM plot of PCz at 120 keVee with a FOM of 1.9.

3.3 PLASTIC SCINTILLATORS FOR DUAL FAST-NEUTRON/GAMMA-RAY DETECTION

A new concept being explored with respect to plastic scintillators is to incorporate heavy metal compounds. The idea is that these heavy metal compounds will increase the density and effective Z of the plastic scintillators, thereby increasing the photoelectric fraction of the pulse height of the plastic scintillators as well, which will lead to a more visible photopeak in the pulse height spectra. Figure 10 shows an example of such a plastic scintillator containing an organotin compound.

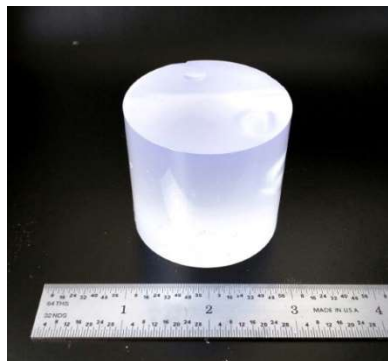


FIG. 10. Plastic scintillator containing an organotin compound.

Typically, these organometallic-loaded plastic scintillators are made similarly to ‘standard’ PSD neutron plastic scintillators: styrene is mixed with PPO and an organometallic compound to obtain a monomer mixture that is subsequently polymerized into a plastic scintillator.

Figure 11 shows the pulse height spectrum of a 1”-diameter tin-loaded plastic scintillator under 662 keV gamma-ray excitation using a ^{137}Cs source. The spectrum features a clearly resolved photopeak with an energy resolution of about 10% (FWHM). As far as we know, this is the best ever energy resolution obtained (at 662 keV) with a plastic scintillator. Using BGO as a reference, the estimated light yield is about 10,000 ph/MeV. The PSD FOM plot for this plastic scintillator is shown in Figure 12.

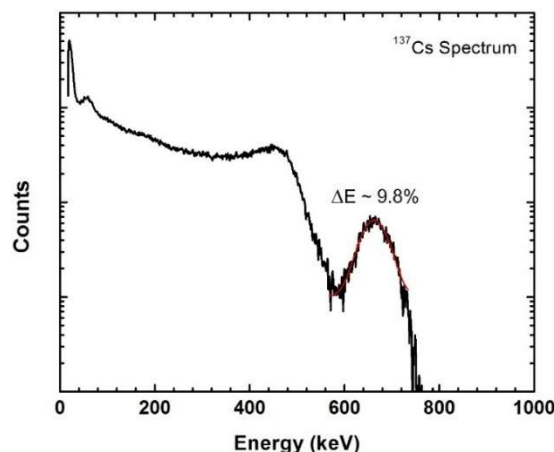


FIG. 11. Pulse height spectrum obtained with a 1” diameter tin-loaded plastic scintillator under 662 keV gamma-ray excitation. Note the excellent energy resolution of about 9.8%.

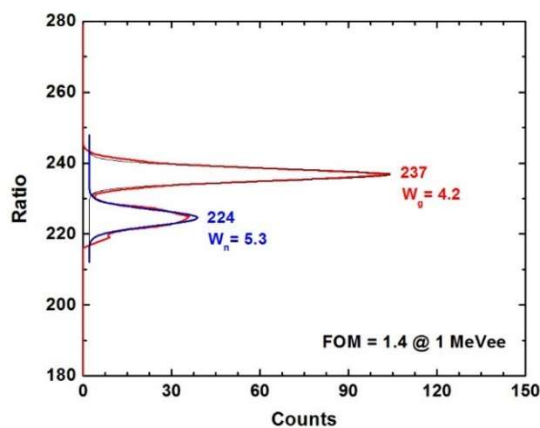


FIG. 12. PSD Figure of Merit (FOM) plot, at 1 MeVee, of a tin-loaded plastic scintillator fabricated at RMD.

4 COMPOSITE DETECTORS

Multi-modal operation afforded by simultaneous detection of gamma-rays and neutrons with a single scintillator such as CLYC, and related compositions in the elpasolite family, have exciting properties and the potential to significantly enhance the capabilities of nuclear detection instrumentation. High sensitivity is critical in the handheld and wearable instruments, most often achieved through large detection volumes. Crystal growth, however, is a slow process and large inorganic scintillators are expensive due to yield issues. The recent progress in plastic scintillator materials with PSD that have good γ -ray/neutron discrimination capability leads to a solution for achieving the goals of larger, more sensitive detectors with discrimination capability at a much lower cost than single crystals. Combining CLYC and plastic scintillators in a composite structure provides the benefits of both inorganic and organic scintillator types. The approach involves suspending inorganic scintillator elements within an organic matrix.

Composite scintillators were formed by pre-casting the plastic incorporating CLYC crystals of different sizes viz. 5mm cube in 1" × 1" plastic cylinder, 4 pillars of CLYC (5mm × 5mm × 20 mm) in 1" × 1" plastic, 4 pillars of CLYC (12.5 mm × 12.5 mm × 31 mm - up to 20% CLYC loading) in 2" × 2" plastic shown in Fig. 13 (left). Pulse height spectra measured using a ¹³⁷Cs source for the four individual CLYC pillars are shown in Fig. 13 (right).

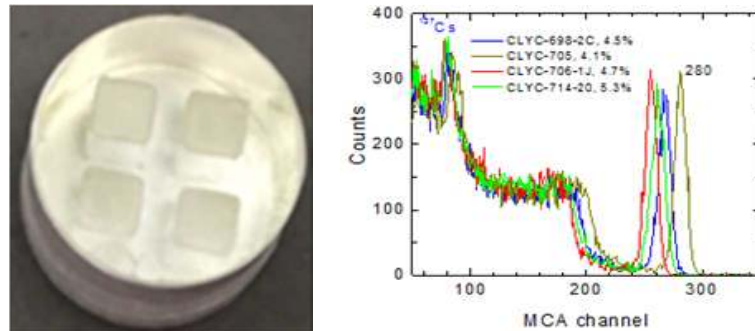


FIG. 13. Photograph of a CLYC-plastic composite scintillator with CLYC pillars (12.5 mm × 12.5 mm × 31 mm) inserted into Ø2" × 2" PSD-capable plastic (left). Pulse height spectra of 4 CLYC pillars measured using a ¹³⁷Cs source (right).

CLYC provides high gamma-ray photopeak efficiency, efficient thermal neutron detection, and excellent neutron/gamma discrimination, whereas a plastic scintillator provides fast neutron detection, adds further to total gamma-ray sensitivity and acts as a light guide for the scintillation light generated in the inorganic CLYC material. A complete packaged scintillation detector was constructed using this sample coupled to a R6233-100 PMT. A photograph of the detector is shown in Figure 14 (left).

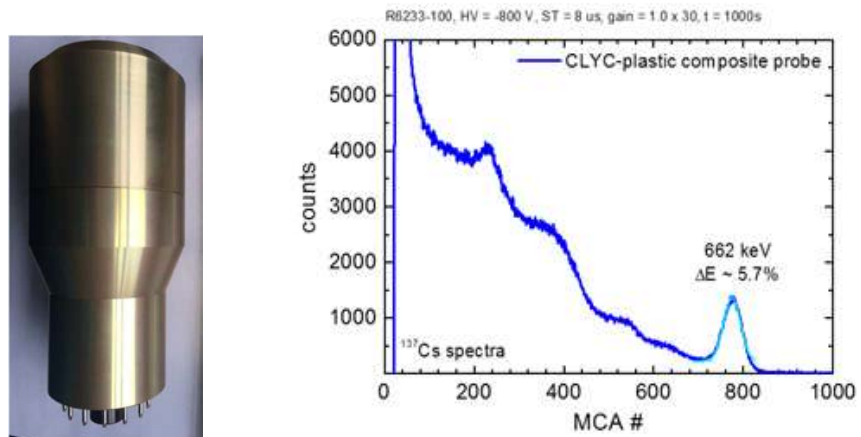


FIG. 14. CLYC-plastic composite detector probe (left); pulse height spectrum of the probe measured using a ¹³⁷Cs source.

The experimental results demonstrate high performance, multi-signature detection. The 2" × 2" CLYC-plastic composite detector provided a single photopeak with gamma resolution of ~5.7% at 662 keV. The non-proportionality of the 2" × 2" composite was measured with ~5% deviation in the range of 60 keV to 1.2 MeV. For the thermal neutron peak we obtained energy resolution of 4.8% FWHM at 3 MeVee (Fig. 15 left). Excellent separation between the gamma-rays, fast and thermal neutron events, was observed with the new composite detector. Figure 15 (right) shows a PSD scatter plot recorded with the same detector using simultaneous ¹³⁷Cs and ²⁵²Cf excitations.

Table 3 shows a comparison of the scintillation properties of 2" × 2" samples of a CLYC-plastic composite and a CLYC crystal. Although, with 20% loading the PE of the composite was lower, it was comparable to a 1" × 1" NaI:Tl detector. Note that the gamma-ray PE of the composite is proportional to the amount of CLYC loading in the sample. For 60% CLYC loading the efficiency is about 3 times higher. The technology was expanded to cover the newer members of the elpasolite family—CLLBC and TLYC. The main advantage of these materials is higher light yield and gamma efficiency, respectively.

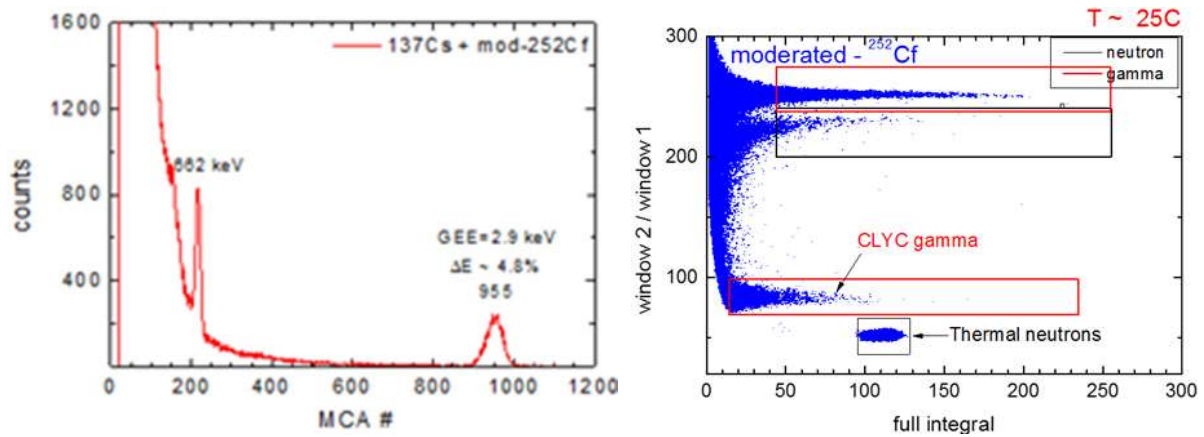


FIG. 15. CLYC-plastic composite detector probe: Pulse height spectrum (left), PSD scatter plot (right,) measured using ^{137}Cs and ^{252}Cf .

TABLE 3. COMPARISON OF THE SCINTILLATION PROPERTIES OF THE COMPOSITE TO CLYC

Scintillation Properties	CLYC Crystal (2" × 2")	CLYC-plastic composite (20% CLYC loading in 2" × 2" plastic)
Energy resolution @ 662 keV	4%	5.7%
Light yield (ph/MeV)	20 K	16 K
Gamma efficiency (Total g/s)	537	470
Photopeak efficiency (662 keV cts/s)	80.2	17
PSD FOM @ 1 MeVee	2.6	1.5 (plastic), 2.2 (CLYC)
Cost (\$/cc)	30	10 (load factor dependent)

5 SEMICONDUCTOR DETECTORS

5.1 CVD DIAMOND FOR FAST NEUTRON DETECTION

Due to its high atom packing density and low atomic number, diamond has a high neutron linear attenuation coefficient and very low gamma-ray linear attenuation coefficient. In addition, diamond is chemically very stable and exhibits excellent radiation hardness. Diamond also has a wide band gap for low noise operation at elevated temperature, high electron and hole mobility and breakdown voltage for fast response, and high charge collection efficiency.

Polycrystalline diamond wafers were grown by chemical vapor deposition (CVD). This method has the advantage that large areas are possible and films can be deposited on arbitrarily shaped substrates. Diamond films grown by CVD typically consist of columnar microcrystals where the grains increase in size as the film grows thicker. Since grain boundaries degrade charge transport, the strategy is to grow thick films and remove the heavily polycrystalline material near the substrate surface. A growth rate of $\sim 1 \mu\text{m/hr}$ is typical for detector quality material.

5.2 FAST NEUTRON DETECTION MECHANISM

Since the energy threshold for inelastic scattering ($^{12}\text{C}(n,n')^{12}\text{C}^*$) and (n,α) reactions is $> 4.8 \text{ MeV}$, the primary interaction mechanism for fission neutron detection is via elastic scattering. A neutron scatters off a ^{12}C nucleus transferring a fraction of its kinetic energy to the nucleus (recoil nucleus). The recoil nucleus creates electron-hole pairs which drift under an applied electric field creating a current pulse in the detector. Note that the energy transferred to a ^{12}C nucleus depends on the scattering angle. Therefore, a mono-energetic beam of neutrons will produce a distribution of energy deposited in the detector (for single scatter events) depending on the scattering angle. Also note that for ^{12}C ($A = 12$), the maximum energy that a neutron can transfer to the nucleus is 28% of the incident neutron energy. The energy deposition spectrum (ignoring charge collection effects) would be approximately rectangular for a mono-energetic input neutron spectrum.

5.3 EXPERIMENTAL RESULTS

A diamond wafer was grown at Coating Technology Solutions, Inc., Somerville, MA (CTS) by plasma enhanced chemical vapor deposition (peCVD). Parallel plate detectors were fabricated at RMD by depositing Au/Cr contacts by thermal evaporation. Figure 16 shows a 2-inch diameter \times \sim 0.5 mm thick polycrystalline diamond wafer with three pairs of Au/Cr contacts.

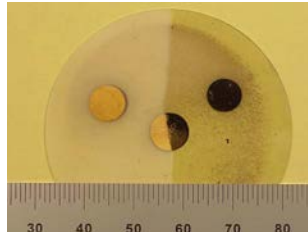


FIG. 16. Photograph of CVD diamond wafer with three pairs of Au/Cr contacts. The wafer was grown at approximately 1 $\mu\text{m/hr}$. The wafer thickness is \sim 0.5 mm.

Figure 17 shows an I(V) curve (left) and charge collection distance versus bias voltage (right) for one device on the diamond wafer. The response to an Am/Be source (left) and mono-energetic source (right) are shown in Fig. 18.

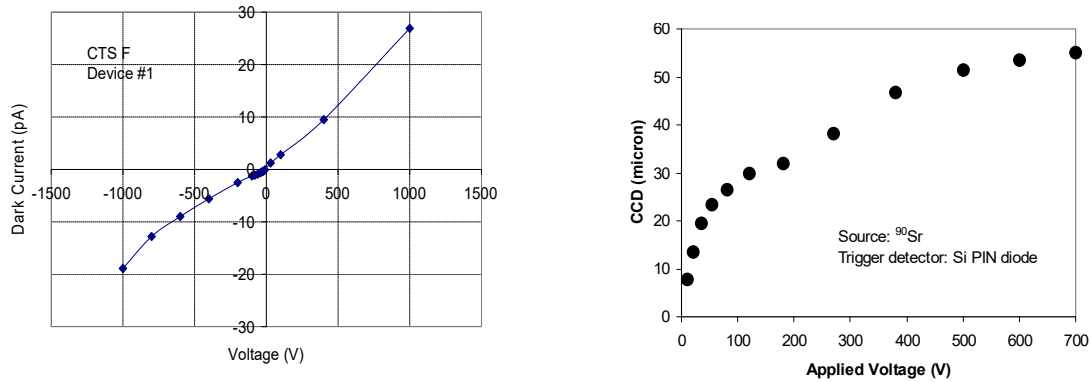


FIG. 17. Left: Current versus voltage curve. From the detector geometry and slope of the curve near the origin, a resistivity value of $3 \times 10^{14} \Omega\text{cm}$ was obtained. Right: Charge collection distance (CCD) versus applied bias voltage.

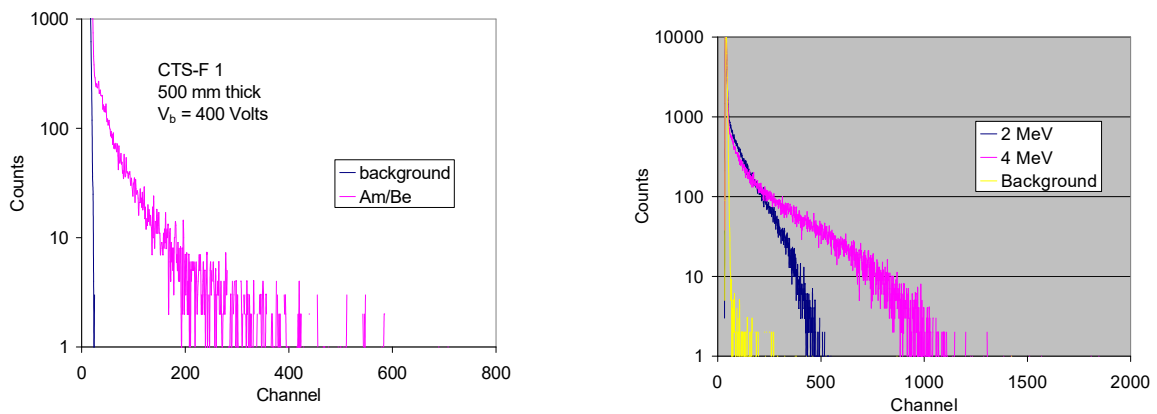


FIG. 18. Left: Am-Be neutron spectrum from 0.5mm thick diamond detector. Right: Pulse height spectra of mono-energetic neutrons at the accelerator facility at the University of Kentucky. Note that the maximum channel number approximately doubles when the incident neutron energy doubles.

5.4 ${}^6\text{LiInSe}_2$ SEMICONDUCTOR NEUTRON DETECTOR

As stated above, ${}^6\text{Li}$ is one of several isotopes that have affinity for thermal neutrons. In recent years, ${}^6\text{LiInSe}_2$ semiconductor technology has progressed and recently $\varnothing 17$ mm crystals have been grown [21,22]. The synthesis process is a separate first step before crystal growth, using starting elements of the highest obtainable purity. The material is grown using the vertical Bridgman method. An example of a LiInSe_2 crystal ingot with a diameter of $\varnothing 17$ mm \times 55 mm length is shown in Figure 19. The ingots range in colour from red to greenish or yellow, depending on the precise stoichiometry. Figure 20 shows multiple wafers cut from the ingot shown in Figure 19. The colour and bandgap of the wafers are almost identical indicating that the stoichiometry along the crystal growth axis is uniform.

The fabrication processes include wafer slicing and polishing, followed by the deposition of electrical contacts, and finally attaching wires to the detector. The wafers are mounted on white ceramic substrates with copper foil strips on the sides that allow electrical connection to the detector electronics, as shown in Figure 21.



FIG. 19. Single crystal ingot of LiInSe_2 , 55mm long \times 17mm diameter.

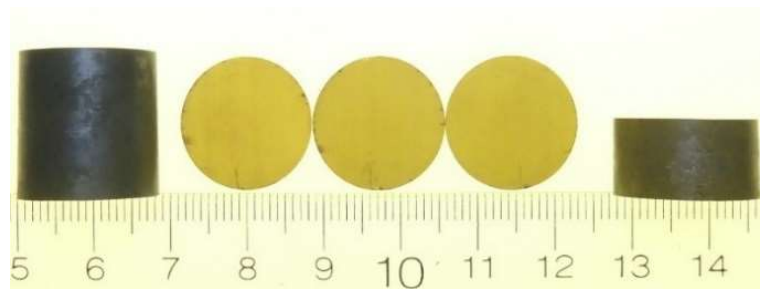


FIG. 20. Multiple wafers with 17mm diameter cut from the LiInSe_2 ingot shown in Figure 19.

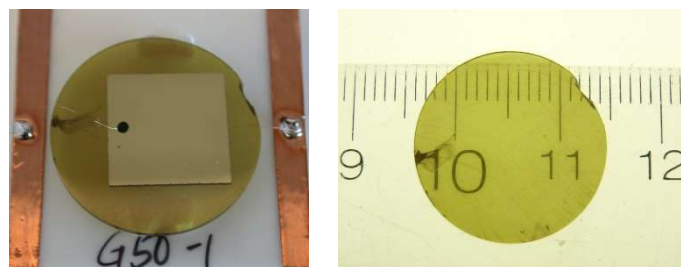


FIG. 21. Left: LiInSe_2 $\varnothing 17$ mm wafer; right: assembled detector with 300/300 Å Cr/Au contacts deposited through thermal evaporation.

Figure 22 shows the gamma-ray and neutron response of the same detector. We measured background (black curve), ${}^{60}\text{Co}$ gamma-ray response (green curve) and moderated Am-Be neutron response (red curve). The neutron response is clearly separated from the gamma-ray events.

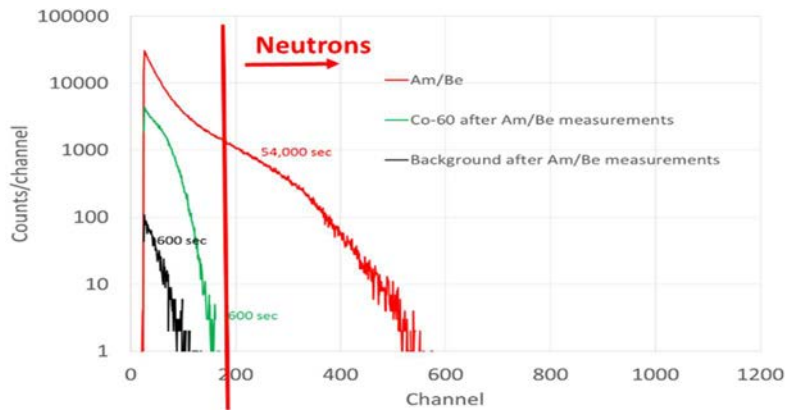


FIG. 22. Gamma-ray and neutron spectra obtained with LiInSe_2 .

Detectors of more than 100 mm² active area have been fabricated with efficiency and gamma-ray rejection ratio comparable to a ^3He tube at 10 atm. Calculations show that a LiInSe_2 detector with 1.5 mm thickness will have at least 25% higher sensitivity and obtain 0.75 cps/nv/cm², which number will be almost identical to the specific sensitivity of a ^3He tube with 10 atm gas pressure. The gamma-ray rejection ratio of LiInSe_2 detector and ^3He tube were comparable in the low 10^{-7} range. Both parameters, sensitivity and gamma-ray rejection, are satisfying the performance requirements for successful replacement of ^3He tubes in handheld radiation instruments.

6 SUMMARY

The past few years have seen a dramatic increase in the research and development of neutron detector technology, partly spurred by the decreased availability of, and increased demand for, ^3He . As a result, there have been numerous significant advances in the field, including advances in neutron detection in application areas beyond finding a viable alternative for ^3He . Research in the technologies described, and on many other device types, continues and further advancements are expected.

ACKNOWLEDGEMENTS

The authors greatly appreciate the support received from the U.S. Department of Homeland Security, Domestic Nuclear Detection Office, the Defense Threat Reduction Agency, and the U.S. Department of Energy. This support does not constitute an express or implied endorsement on the part of the Government.

REFERENCES

- [1] Y12 NUCLEAR SECURITY COMPLEX, www.y12.doe.gov/orsens/neutron.html.
- [2] REILLY, D., ENSSLIN, N., SMITH, H., KREINER, S., Passive Nondestructive Assay of Nuclear Materials, U.S. Nuclear Regulatory Commission, pp 11–18, (1991).
- [3] KNOLL, G., Radiation Detection and Measurement, 4th edn, John Wiley and Sons, (1999)
- [4] SCHMID, G.J., et al., “A neutron sensor based on synthetic single crystal diamond”, UCRL-Conf-200447, October 21, 2003.
- [5] NAGARKAR, V.V., OVECHKINA, E.E., BHANDARI, H.B., New structured scintillator for neutron radiography, Phys. Proc. **69** (2015) 161–168.
- [6] MCGREGOR, D.S., et al., Development of compact high efficiency microstructured semiconductor neutron detectors, Rad. Phys. Chem. **116** (2015) 32–37.
- [7] MURRAY, R.B., Use of $^6\text{LiI}(\text{Eu})$ as a scintillation detector and spectrometer for fast neutrons, Nucl. Instrum. **2** 3 (1958) 237.
- [8] SYNTFELD, A., et al., $^6\text{LiI}(\text{Eu})$ in neutron and γ -ray spectrometry—a highly sensitive thermal neutron detector, IEEE Trans. Nucl. Sci. **52** (2005) 3151–3156.
- [9] COMBES, C.M., et al., Optical and scintillation properties of pure and Ce^{3+} -doped $\text{Cs}_2\text{LiYCl}_6$ and $\text{Li}_3\text{YCl}_6:\text{Ce}^{3+}$ crystals. J. Lumin. **82** (1999) 299–305.
- [10] VAN LOEF, E.V.D., et al., Scintillation and spectroscopy of the pure and Ce^{3+} -doped elpasolites: Cs_2LiYX_6 ($\text{X}=\text{Cl},\text{Br}$). J. Phys.: Condens. Matter **14** (2002) 8481–8496.
- [11] GLODO, J., HAWRAMI, R., SHAH, K.S., Development of $\text{Cs}_2\text{LiYCl}_6$ scintillator. J. Crystal Growth **379** (2013) 73–78.

- [12] HAWRAMI, R., et al., $\text{Ti}_2\text{LiYCl}_6\text{:Ce}$: A new elpasolite scintillator, *IEEE Trans. Nucl. Sci.* **63** 6 (2016) 2838–2841.
- [13] GLODO, J., HIGGINS, W.H.C., LOEF, E.V.D., SHAH, K.S., $\text{GdI}_3\text{:Ce}$ —A new gamma and neutron scintillator. 2006 IEEE NSS Conf. Records, (2006) 1574–1577.
- [14] SMITH, M.B., et al., Fast neutron spectroscopy using $\text{Cs}_2\text{LiYCl}_6\text{:Ce}$ (CLYC) scintillator. *IEEE Trans. Nucl. Sci.* **60** (2013) 855–859.
- [15] SMITH, M.B., et al., Fast neutron measurements using $\text{Cs}_2\text{LiYCl}_6\text{:Ce}$ (CLYC) scintillator. *Nucl. Instrum. Methods Phys. Res. A* **784** (2015) 162–167.
- [16] RUNKLE, R.C., Nuclear sensors and their role in nuclear nonproliferation, *Nucl. Instrum. Methods Phys. Res. A* **652** (2011) 37–40.
- [17] RANUCCI, G., GORETTI, A., LOMBARDI, P., Pulse-shape discrimination of liquid scintillators, *Nucl. Instrum. Methods Phys. Res. A* **412** (1998) 374–386.
- [18] BROOKS, F.D., PRINGLE, R.W., FUNT, B.L., Pulse shape discrimination in a plastic scintillator, *IRE Trans. Nucl. Sci.* **7** (1960) 35–38.
- [19] ZAITSEVA, N., et al., Plastic scintillators with efficient neutron/gamma pulse shape discrimination, *Nucl. Instrum. Methods Phys. Res. A* **668** (2012) 88–93.
- [20] LEE, D.W., et al., Pulse-shape analysis of $\text{Cs}_2\text{LiYCl}_6\text{:Ce}$ scintillator for neutron and gamma-ray discrimination, *Nucl. Instrum. Methods Phys. Res. A* **664** (2012) 1–5.
- [21] KARGAR, A., et al., “Lithium and boron based semiconductors for thermal neutron counting”, in *Hard X-Ray, Gamma-Ray, and Neutron Detector Physics XIII 2011 Sep 28* (Vol. 8142, p. 81421P). International Society for Optics and Photonics
- [22] STOWE, A.C., et al., Crystal growth in LiGaSe_2 for semiconductor radiation detection applications, *J. Cryst. Grow.* **379** (2013) 111.

NEW SOLID-STATE ORGANIC SCINTILLATORS FOR WIDE-ENERGY NEUTRON DETECTION

N. ZAITSEVA, A. GLENN, L. CARMAN, A. MABE, S. PAYNE

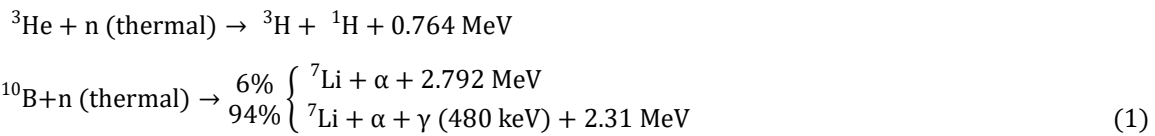
Lawrence Livermore National Laboratory,
California, USA

Email: zaitseval@llnl.gov

Abstract: Detection of special nuclear materials (SNM) requires instruments which can detect and characterize uranium and plutonium isotopes, having at the same time the ability to discriminate among different types of radiation. For many decades, neutron detection has been based on ^3He proportional counters sensitive primarily to thermal neutrons. The most common methods for detection of fast neutrons have been based on liquid scintillators with pulse shape discrimination (PSD). The shortage of ^3He and handling issues with liquid scintillators stimulated a search for efficient solid-state PSD materials. Recent studies conducted at LLNL led to development of new materials, among which are organic crystals with excellent PSD and first PSD plastics for fast neutron detection. More advantages have been introduced by plastics doped with neutron capture agents, such as ^{10}B and ^6Li , that can be used for combined detection of both thermal and fast neutrons, offering, in addition, a unique ‘triple’ PSD for signal separation between fast neutrons, thermal neutrons, and gamma-rays. Among commercially produced materials are large-scale (>10 cm) stilbene crystals grown by the inexpensive solution technique, and different types of PSD plastics which, due to the deployment advantages and ease of fabrication, create a basis for the widespread use as large-volume and low-cost neutron detectors.

1. INTRODUCTION

Most common methods used in current neutron detectors are based on nuclear capture reaction with low energy (thermal) neutrons. Examples are well-known ^3He proportional counters or more recently developed boron-coated straw (BCS) detectors that utilize the capture reactions:



The biggest advantage of these detectors is the negligible sensitivity to the background gamma radiation. However, since they enable the direct detection of only thermal neutrons, high-energy (fast) neutrons produced by most radioactive materials have to be thermalized prior to the detection. Thermalization requires use of moderation (typically through the interaction with high density polyethylene, HDPE) that in most cases leads to the loss of information about the origins of the fast neutrons and leads to efficiency loss for neutrons already near thermal energies.

Direct detection of fast neutrons has been traditionally done using organic scintillators comprised of fluorescent aromatic molecules. The process is based on elastic scatter of fast neutrons on hydrogen atoms. Excitation of organic molecules by any ionizing radiation leads to formation of excited singlet (S_1) and triplet (T_1) states, recombination of which produces two-decay scintillation pulses consisting of the prompt and delayed components (Fig. 1 A). The prompt light is produced by fast de-excitation of individual S_1 states, while the delayed component results mostly from annihilation of pairs of T_1 - T_1 states [1]. Recoil protons, being heavier than electrons, produce more localized excitation, leading to a higher probability of T_1 - T_1 interaction and therefore an increased fraction of delayed light compared to gamma-induced pulses.

The difference in the pulse shapes gives basis for the Pulse Shape Discrimination (PSD) techniques [2–4] implemented to separate pulses based on the delayed light fraction $R = \int B_{\text{slow}} / \int A_{\text{total}}$ corresponding to slow and total integrals defined by time gates of Fig. 1A. Using standard characterization setup and modern digitisers (Fig. 1B) mixed field scintillation pulses can be separated into groups corresponding to neutrons and gammas (Fig. 1C). The ability of a detector to perform neutron/gamma signal discrimination is quantified by the Figure of Merit, FOM, defined by the schematic of Fig. 1 D.

Although PSD phenomena were first discovered and studied with crystals [2, 5], organic liquid scintillators had become dominant materials for fast neutron detection. Liquid scintillators have efficient scintillation and PSD and are easily available in large volumes at low cost. However, they have many disadvantages related to toxicity, flammability, possible environmental hazards, that result in restricted use in field conditions. The required expansion volume, generally in the form of a nitrogen bubble left in the liquids, can also be problematic. Few initially known organic crystals with PSD, such as stilbene, p-terphenyl, and anthracene, became practically

unavailable, due to the difficulties of growth by traditionally applied melt-growth techniques. And finally, numerous attempts to obtain efficient PSD in plastic scintillators in the past resulted in unstable materials [6] or inability to achieve neutron/gamma discrimination of any practically useful level.

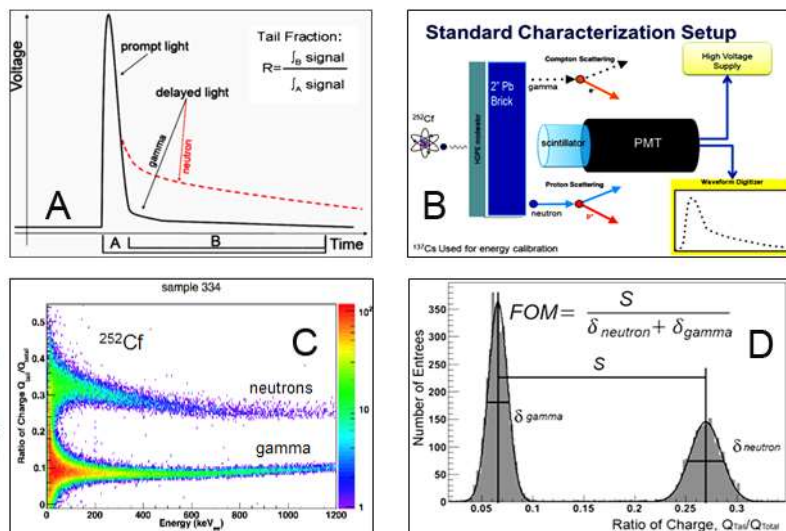


FIG. 1. A – Schematic representation of two-component decay pulses containing prompt and delayed light components; the fraction of the delayed light is defined by the tail fraction ratio R ; B – Standard experimental setup used for scintillator characterization; C – A typical experimental PSD plot showing separated distributions for neutron and gamma pulses; D – definition of the PSD Figure of Merit.

2. NEW SOLID-STATE SCINTILLATORS FOR FAST NEUTRON DETECTION

2.1. ORGANIC CRYSTALS

2.1.1 Stilbene single crystals

The current work has been focused on development of solid state scintillators for replacement of liquid scintillators. To identify materials capable of neutron detection through neutron/gamma discrimination, about 150 types of organic crystals were tested in initial studies. Good PSD properties were found in many hydrocarbon-based crystals, some of which, like 9,10-diphenylanthracene or 1,1,4,4-tetraphenylbutadiene [7], showed PSD properties useful for efficient neutron detection. However, previously known *trans*-stilbene crystal was still proven to be the best material for practical application. In addition to high light output (LO) and excellent PSD, stilbene revealed good potential for large-scale production because of relatively inexpensive raw material and adequate growth and mechanical properties. To produce large-scale stilbene crystals, a new method of growth from organic solvents (Fig. 2) has been developed and applied [8] instead of the previously used melt (Bridgman) technique [9].

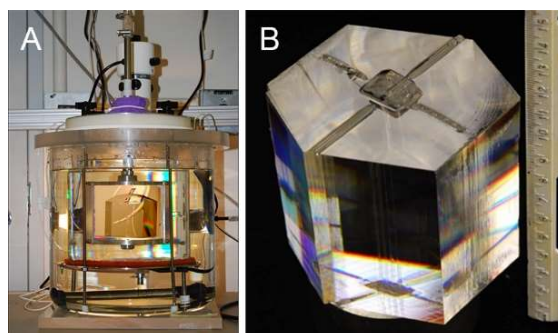


FIG. 2. A – A double-vessel crystallizer used for growth of neutron-detection crystals from organic solvents; B – A 10-cm scale faceted stilbene crystal grown at 20 mm/day rate in 10 days duration.

The developed technology for stilbene crystal growth has been transferred to industry for commercial production in the US by Inrad Optics [10] that now offers crystals up to 17 cm in linear sizes, as well as detection elements of different sizes and shapes (Fig. 3). Studies of new single crystals revealed that solution-grown stilbene has high structural performance of real single crystals compared to less homogeneous melt-grown crystals, which contain visible grain boundaries scattering the light [11]. The structural perfection resulted in higher LO and PSD, especially pronounced at increasing size and lower energy ranges. Tests conducted with 10-cm-scale solution-grown stilbene crystals showed LO about twice higher compared to commonly used EJ-309 liquid scintillators and about 50% higher than LO of melt-grown stilbene crystals of the same length and shape. Even more impressive results were obtained from comparison of stilbene to liquid scintillators. As illustrated by Fig. 4, stilbene crystals exhibit much better PSD in wide energy ranges compared to the commonly used commercial scintillators EJ-309. The corresponding LO of stilbene crystals is about factor of 2 higher than that of the liquid scintillators.

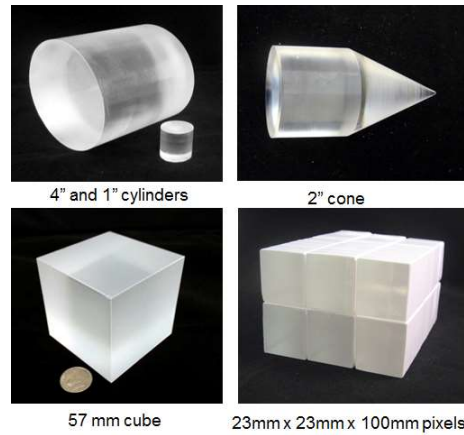


FIG. 3. A – Stilbene scintillator parts produced by Inrad Optics with custom sizes and shapes for different neutron detection applications.

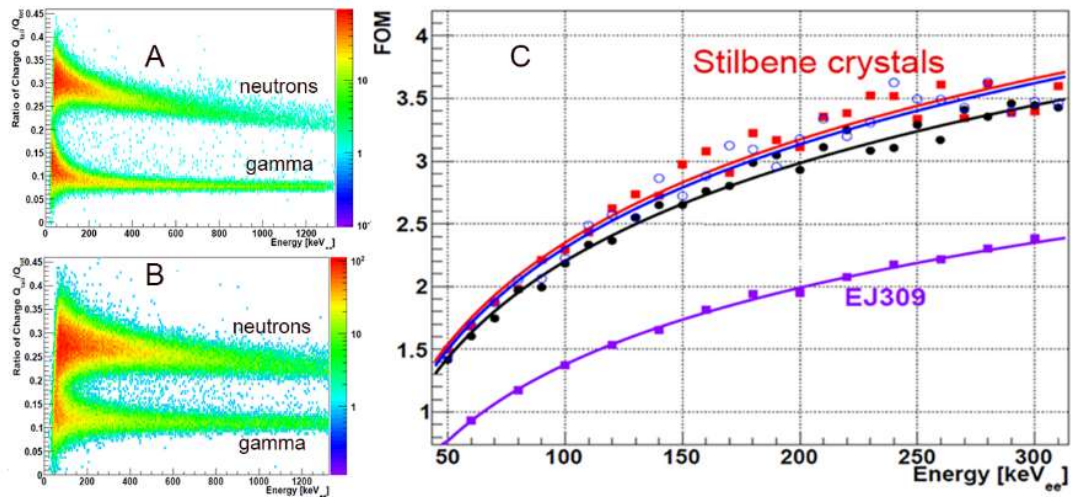


FIG. 4. A – Experimental PSD plot of neutron/gamma discrimination obtained with a stilbene detector of 51 cm diameter and 76 mm long; B – PSD measured with same size and shape commercial EJ-309 liquid scintillator; C – Energy dependence of PSD FOMs of several stilbene crystals in comparison to liquid scintillators of 51 cm diameter and 76 mm long. ^{252}Cf source used for measurements.

One more development was made with deuterated stilbene never before grown as a single crystal. As shown in a previous publication [12], replacement of hydrogen by deuterium in the composition of organic scintillators leads to the appearance of the monoenergetic peaks useful for neutron spectroscopy without a need in time-of-flight technique applications. Interaction of neutron with heavier-than-hydrogen deuterons produces larger density of local excitation, leading to higher probability of T_1 - T_1 interaction and better PSD compared to regular stilbene (Fig. 5). Tests for neutron spectroscopy properties of first deuterated crystals are currently being conducted at University of Michigan that initiated the idea of the d-stilbene growth and tests.

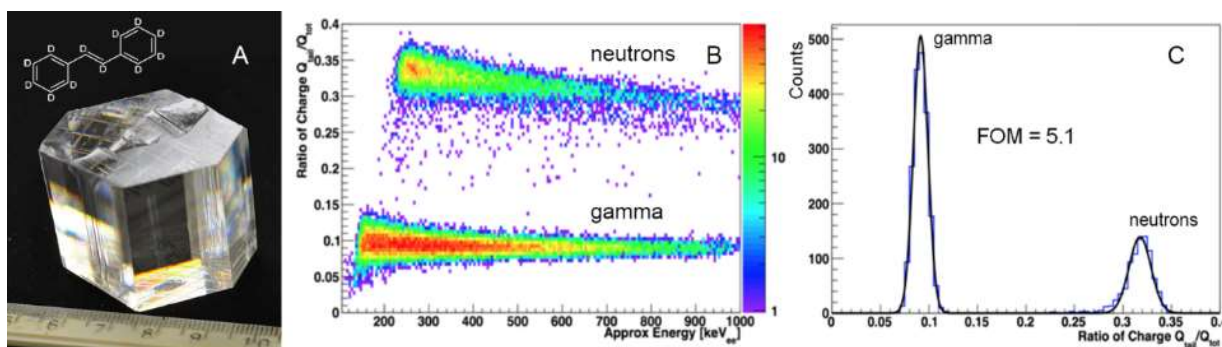


FIG. 5. A – First deuterated stilbene d-12 single crystal of 35 mm in height; B – experimental PSD plot; C – Gaussian fit of neutron and gamma peaks separated with FOM=5.1 in the energy range 450–500 keVee. ^{252}Cf source used for measurements.

2.1.2 Mixed crystals with controlled fraction of delayed light in scintillation pulses

Studies conducted with stilbene and other new crystals led to better understanding of scintillation mechanisms in organic scintillators. One of the most important result of these studies was obtained with mixed diphenylacetylene-stilbene (DPAC-stilbene) and bibenzyl-stilbene (BB-stilbene) crystals. Test of numerous mixed crystals showed that the fraction of the delayed light in scintillation pulses of multi-component organic systems can be controlled by the concentrations of different bandgap constituents. The concentration dependence of PSD presented in Fig.6 shows that low concentrations of stilbene in mixed DPAC-stilbene crystals leads to the practical suppression of the delayed light and PSD that suddenly rises to high levels at about 20% of stilbene additions. The detailed mechanism of the phenomenon has been reported previously [13]. Briefly, it can be explained by efficient excitation energy transfer from DPAC to the narrower bandgap stilbene molecules. At low concentration, widely separated stilbene molecules serve as traps holding excited triplet energy without a possibility of the interaction due to large separations. At some point, increasing concentration of stilbene leads to the decreased average distance needed for the efficient T_1-T_1 interaction and production of the delayed light (Fig. 6).

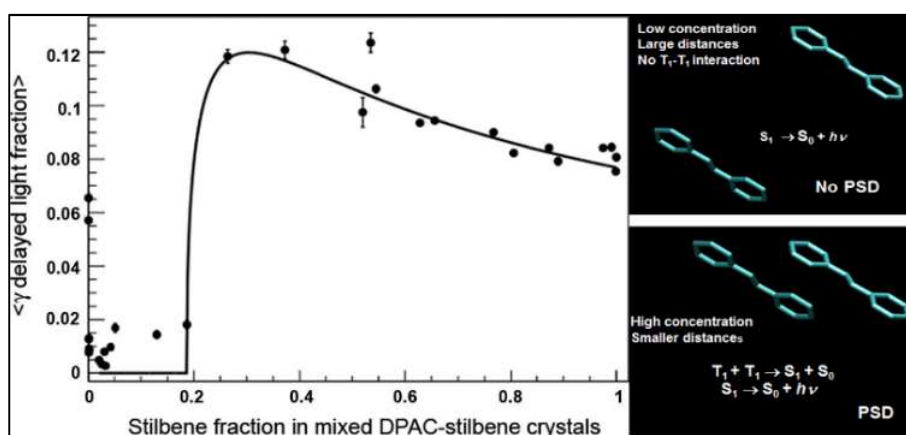


FIG. 6. Change of PSD in mixed DPAC-stilbene crystals. Right schematics illustrate suppression and sudden rise of PSD at changing concentration of stilbene molecules that, due to the narrower bandgap, hold excitation transferred from the initially excited DPAC. © [2011] IEEE. Reprinted, with permission, from [13].

The discovered mechanism was used for growth of new types of organic crystals with suppressed delayed light (low afterglow). The use of scintillators with very low afterglow is beneficial for ion and neutron spectroscopy in high intensity laser facilities when separation of temporally close signals is required. One such application includes the separation of 14 MeV neutrons produced in the fusion reaction $\text{D} + \text{T} \rightarrow {}^4\text{He} + \text{n}^0$ and the 10–12 MeV neutrons scattered in the high-density compressed laser targets. With a temporal separation of only 30 ns, the intensity of the scattered neutrons can be a thousand times lower than that of the 14 MeV neutrons, leading to a need for organic scintillators with a fraction of delayed light not exceeding 10^{-3} . Comparison of DPAC-stilbene

and BB-stilbene decay characteristics (Fig. 7) showed that the new single crystals have a much smaller fraction of delayed light in the scintillation pulses than oxygen-quenched liquid scintillators or the fastest commercial plastics. Note that the suppression of delayed light in single crystals, achieved by the minimization of T_1-T_1 interactions, does not affect the efficiency of the LO determined mainly by the de-excitation of the excited singlet S_1 states. As a result, the LO of the of crystals with suppressed delayed light can be equal or even higher than the LO of pure stilbene, which is different from liquid and plastic scintillators in which the suppression of the delayed light by oxygen leads to the quenching of both prompt and delayed components [14]. DPAC and BB crystals doped with low concentration of stilbene (~1 wt %) are now being used in diagnostic experiments of the world largest laser National Ignition Facility (NIF) [15] for the detection of neutrons via time-of-flight spectrum [16].

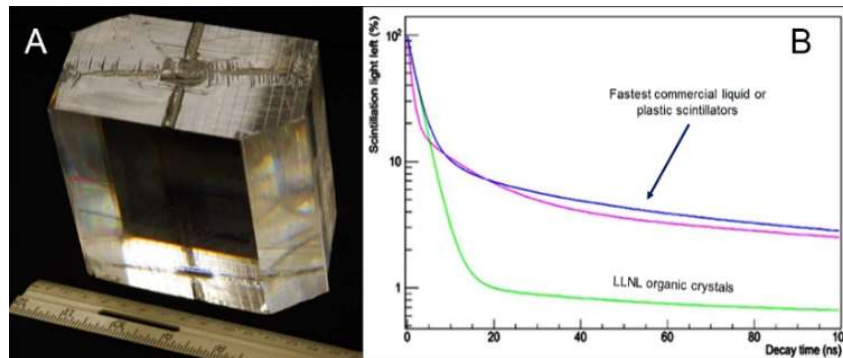


FIG. 7. A – 10 cm scale bibenzyl-stilbene mixed crystal used in NIF time-of-flight diagnostic experiments; B – sharp scintillation decay without the delayed light component enables separation of 14 MeV neutrons from 10–12 MeV neutrons scattered in the high-density compressed target.

2.2. PLASTIC SCINTILLATORS WITH PULSE SHAPE DISCTIMINATION

Plastic scintillators present mixed systems composed of one or two organic dyes dissolved in a polymer matrix. In comparison to single crystals, plastics have many advantages. They can be manufactured at large variations of sizes and shapes at lower cost as non-toxic, non-hazardous, non-hygroscopic materials. However, for many decades plastics have been known as scintillators not capable of PSD, because of traditionally used low concentrations of scintillating dyes on the level of about 1–5 wt %, that, according to the dependence shown in Fig. 6, falls to the region of no delayed light production. To develop first plastic scintillators with efficient PSD [17], the dye loads were shifted into the range of higher concentrations of 20–30 wt %, using a highly soluble scintillation dye 2,5-diphenyloxazole, PPO (Fig. 8). Reports following the first publication confirmed that a similar approach can be used with other scintillating dyes [18]. In 2012 the developed technology was licensed by Eljen Technology [19] for commercial production under the trade name EJ-299.

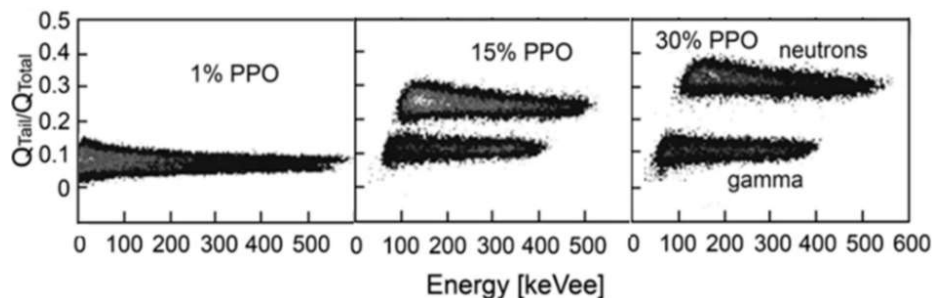


FIG.8. Experimental PSD patterns showing increase of neutron/gamma peak separation at increasing PPO concentration in a PVT polymer matrix. Reprinted from [17], Copyright (2012), with permission from Elsevier.

However, when first commercially produced plastics became available at large scale, most users reported inferior scintillation performance compared to liquid scintillators the plastics intended to replace [20,21]. In addition, new plastics loaded with high dye concentration tend to be physically unstable, eventually revealing softness, shape

deformation, dye leaching, with the resulting loss of transparency within a year of use. More recent developments corrected these initial problems. Chemical compositions and polymerization procedures have been modified to achieve temporal stability, so that improved plastics could remain stable at PPO concentrations up to $\sim 40\%$ without physical degradation (Fig. 9 A). The LO of the modified plastics is now similar to that of the commonly used liquid scintillator, EJ-309 (Fig. 9B) and equal to the LO of the brightest traditional (non-PSD) plastics, such as EJ-200. Increase of scintillating dye loads also enable substantial improvement of PSD. As indicated by the results shown in Fig. 10A, at relatively high energy, plastics perform similar to liquid scintillators, while in at lower energies they exhibit even higher PSD that potentially may approach stilbene PSD levels (Fig. 10B).

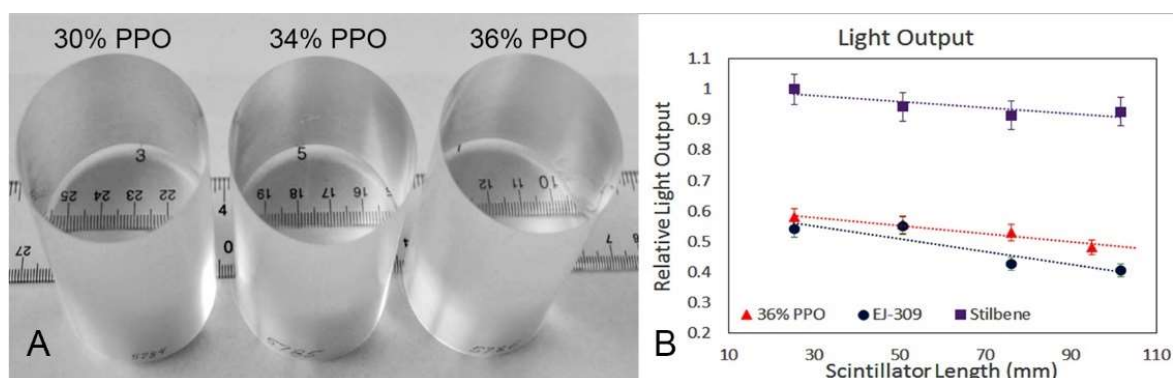


FIG. 9. A – PSD plastics of high optical transparency prepared with different concentration of the primary dye. The plastics height is 76 mm. Plastics remain physically stable during three years of observation; B – LO of 51 mm diameter plastic cylinders containing 36% PPO in comparison to the LO of same sizes stilbene and liquid scintillators EJ-309.

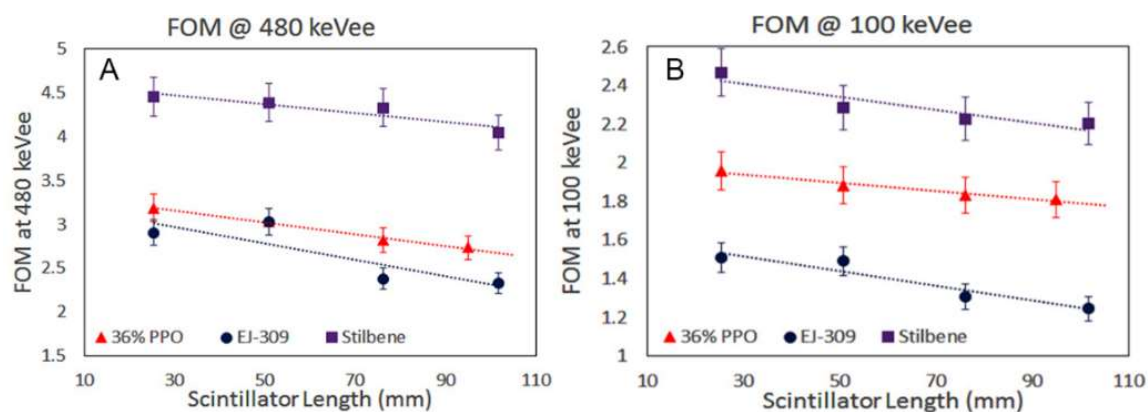


FIG. 10. A – PSD FOMs of 51 mm diameter 36% PPO plastics vs length in comparison to liquid scintillators EJ-309 and stilbene crystals of same sizes and shape. A – similar PSD in the energy range of ^{137}Cs Compton edge; B – better PSD compared to liquid scintillators at lower energies. ^{252}Cf source used for measurements.

Noticeable progress has been also achieved in development of commercial PSD plastics. According to the Eljen Technology website, previous EJ-299 plastics have been replaced by a new version of PSD plastics EJ-276. Comparison of the $3'' \times 3''$ commercial EJ-276 and EJ-309 scintillators shows equal LO and similar PSD [22]. In addition, the new plastics offer improved physical hardness and long-term stability and can be produced in variety of sizes and shapes requested by users for different applications (Fig. 11).

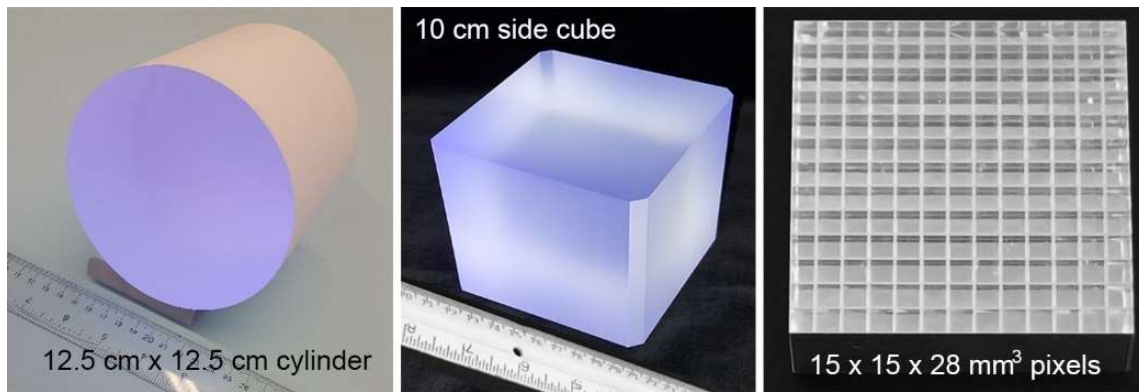


FIG. 11. PSD plastics with improved physical stability and scintillation performance produced by Eljen Technology in different sizes and shapes for fast neutron detection applications.

3. NEW SCINTILLATORS FOR DETECTION OF FAST AND THERMAL NEUTRONS

3.1. ${}^6\text{Li}$ CONTAINING CRYSTALS

Solid-state scintillators described above can be used only for detection of fast (high energy) neutrons. Wider energy neutron detection can be achieved by the addition capture nuclei, such as ${}^6\text{Li}$, that facilitates detection of thermal neutrons through the nuclear reaction ${}^6\text{Li} + n^0 = {}^3\text{H} + \alpha + 4.8 \text{ MeV}$. The reaction products do not contain gamma rays that can interfere with the discrimination process. A number of ${}^6\text{Li}$ -containing organic crystals found to have unique properties that can be used for simultaneous detection of both fast and thermal neutrons. Examples of crystals are represented by ${}^6\text{Li}$ salts of salicylic acids, such as previously described ${}^6\text{Li}$ -3-PSA [23] or later studied ${}^6\text{Li}$ -4-MeSA (${}^6\text{Li}$ salt of methylsalicylic acid). As illustrated by Fig. 12, crystals of these compounds produce signatures of both thermal and fast neutrons, due to the capture and elastic scatter interactions, respectively. The crystals have a remarkably good PSD comparable to or even exceeding that of stilbene. They also exhibit a unique property of discrimination between fast and thermal neutrons ('triple PSD'). A new and important feature of these materials is that they do not need use of moderation to detect fast or thermal neutrons. Due to the high content of hydrogen and ${}^6\text{Li}$ (up to 4.2%), the crystals have a potential to provide high overall efficiency for wide energy neutron detection. A relatively low LO (~30–50% of commercial EJ-309 liquids or EJ-200 plastics) can be attributed to insufficiently developed techniques of Li-salts synthesis and low purity of commercial raw materials. Current studies are being conducted to develop appropriate methods for purification of raw materials, synthesis, and growth of large defect-free crystals to the sizes required for practical applications.

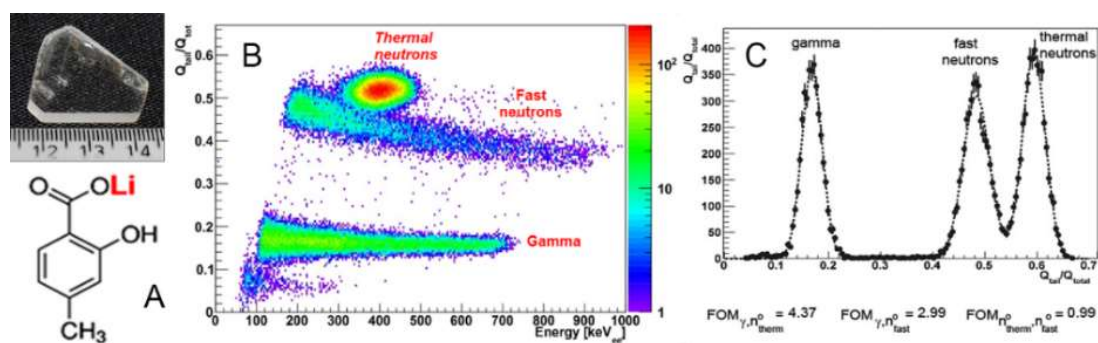


FIG. 12. A – Crystal of Lithium salt of 4-methylsalicylic acid with the corresponding molecular formula; B – Experimental PSD plot showing signatures of both fast and thermal neutrons well separated from gamma rays; C – 'triple' PSD profile with FOMs corresponding to discrimination between fast and thermal neutrons separated for gamma radiation. ${}^{252}\text{Cf}$ source used for measurements.

3.2. ${}^6\text{Li}$ -LOADED PLASTIC SCINTILLATORS

The major problem in the preparation of plastic scintillators relates to the extremely low solubility of highly polar Li-organic compounds in non-polar aromatic polymers. First reported [24, 25] ${}^6\text{Li}$ -loaded PSD plastics were prepared by dissolution of ${}^6\text{Li}$ -organic salts complexed with specific organic ligands to decrease the polarity of ${}^6\text{Li}$ ions. Plastics can be easily scaled to large sizes as optically transparent, stable in air materials with high degree of discrimination from gamma rays (Fig. 13). Similar to ${}^6\text{Li}$ containing crystals, ${}^6\text{Li}$ -loaded plastics can be used for combined detection of fast and thermal neutrons without need for moderation, simplifying designs and decreasing weights of the final detectors. Current plastics may be loaded with $\sim 0.4\%$ of ${}^6\text{Li}$ allowing for more than 50% thermal capture efficiency at the scintillator length ~ 5 cm [24]. Developments continue for searching new lithium compounds soluble in aromatics to increase concentration of ${}^6\text{Li}$ in plastics without loss of scintillation performance and PSD.

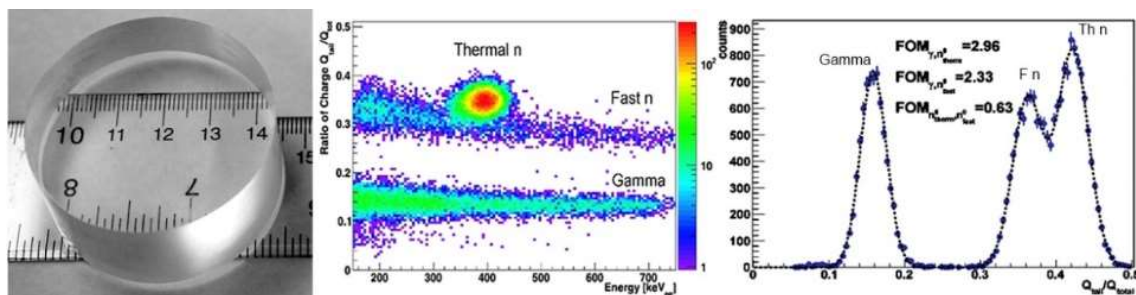


FIG. 13. ${}^6\text{Li}$ -loaded plastic with corresponding PSD measured using ${}^{252}\text{Cf}$ source.

3.3. ${}^{10}\text{B}$ -LOADED PLASTICS

The ${}^{10}\text{B}$ capture reaction with thermal neutrons produces monoenergetic alpha particles of lower energy (2.310 MeV) compared to ${}^6\text{Li}$ (4.8 MeV). In addition, the products of reaction contain gamma rays (*see reaction 1 in Introduction section*). However, ${}^{10}\text{B}$ has a big advantage of the high neutron capture cross section (Fig. 14 B) that makes it possible to obtain high detection efficiency with scintillators of smaller thicknesses (Fig. 14 C, [23]) allowing for the escape of the large fraction of gamma rays produced in the reaction. High neutron detection efficiency and high gamma rejection of ${}^{10}\text{B}$ -loaded PSD plastics has been demonstrated in first prototype devices designed for detection of both fast and thermal neutrons without moderation. Current developments continue with smaller and lighter handheld ${}^{10}\text{B}$ detectors based on the use of PMTs and SiPMs. Less expensive ${}^{10}\text{B}$ -containing molecules, alternative to the currently used carboranes, are studied in other groups for future applications [26].

4. SUMMARY

New solid-state organic scintillators with efficient neutron/gamma discrimination (PSD) have been developed with a purpose to replace liquid scintillators traditionally used fast neutron detection. Developed materials include *trans*-stilbene single crystals grown by the application of solution growth technique and first plastics with PSD capabilities. The developed technologies have been transferred to industry for commercial production in the US. More than 10 cm scale stilbene crystals are now commercially produced by Inrad Optics. Stilbene crystals have superior light output and PSD compared to liquid scintillators. Improved formulations of PSD plastics tested at large scale up to 10 cm show performance equal to that of the commonly used liquid scintillators EJ-309. New PSD plastics are commercially available from Eljen Technology as EJ-276 product replacing initial EJ-299 scintillators. Improved properties and availability of new materials provide basis for widespread replacement of liquid scintillators in small and large area neutron detectors. More research is being conducted with ${}^6\text{Li}$ - and ${}^{10}\text{B}$ -loaded PSD materials that can be used for the combined detection of fast and thermal neutrons without the need for neutron moderation. New scintillators demonstrate increased efficiency of wide energy neutron detection that have potential for use in compact PMT and SiPM handheld devices.

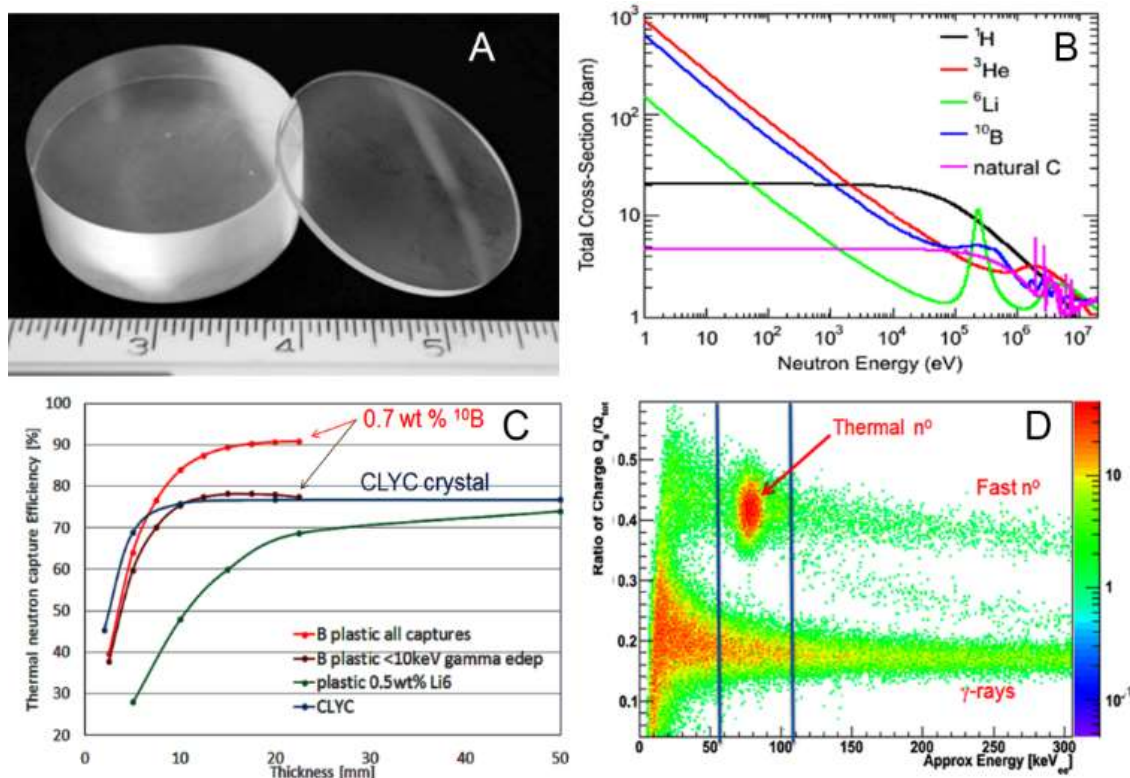


FIG. 14. A – ^{10}B -loaded plastics of different thickness prepared for combined detection of fast and thermal neutrons; B – ^{10}B thermal neutron capture close of that of ^3He ; C – GEANT simulation results showing thermal neutron capture probability of ^{10}B -loaded plastics in comparison to ^6Li plastics and CLYC crystals; D – Experimental PSD plot obtained with a 0.7 wt % ^{10}B -loaded plastic with signatures of fast and thermal neutrons separated from gamma rays.

ACKNOWLEDGEMENTS

The work performed under the auspices of the U.S. Department of Energy by Lawrence Livermore National Laboratory under Contract DE-AC52-07NA27344. This work has been supported by the U.S. Department of Energy, NA-22 and DTRA offices, and by the US Department of Homeland Security, DNDO, under competitively awarded IAA HSHQDC-09-X-00743. This support does not constitute an express or implied endorsement on the part of the Government.

REFERENCES

- [1] BIRKS, J.B., The Theory and Practice of Scintillation Counting, Pergamon Press, London, (1964).
- [2] BROOKS, F.D., A scintillator counter with neutron and gamma-ray discrimination, Nucl. Instrum. Methods **4** (1959) 151–163.
- [3] MORRIS, C.L., A digital technique for neutron-gamma pulse shape discrimination, Nucl. Instrum. Methods **137** (1976) 397.
- [4] KASCHUCK, Y., ESPOSITO, B., Neutron/ γ -ray digital pulse shape discrimination with organic scintillators, Nucl. Instrum. Methods A **551** (2005) 420–428.
- [5] OWEN, R.B., The decay times of organic scintillators and their application to the discrimination between particles of different specific ionization, IRE Trans. Nucl. Sci. **NS-5** (1958) 198–201.
- [6] BROOKS, F.D., PRINGLE, R.W., FUNT, B.L., Pulse shape discrimination in a plastic scintillator, IRE Trans. Nucl. Sci. **NS-7**, 2–3 (1960) 35–38.
- [7] FRABONI, B., FRALEONI-MORGERA, A., ZAITSEVA, N., Ionizing radiation detectors based on solution-grown, Adv. Funct. Mater. **26** (2016) 2276–2291.
- [8] CARMAN, L. et al., The effect of material purity on the optical and scintillation properties of solution-grown *trans*-stilbene crystals, J. Cryst. Growth **368** (2013) 56–61.

- [9] BUDAKOVSKY, S.V., et al., New effective organic scintillators for fast neutron and short-range radiation detection, *IEEE Trans. Nucl. Sci.* **54** (2007) 2734–2740.
- [10] INRAD OPTICS, <http://www.inradoptics.com>.
- [11] ZAITSEVA, N., et al., Scintillation properties of solution-grown trans-stilbene single crystals, *Nucl. Instrum. Methods A* **789** (2015) 8–15.
- [12] BECETTI, F., et al., Deuterated-xylene (xylene-d10; EJ301d): A new, improved deuterated liquid scintillator for neutron energy measurements without time-of-flight, *Nucl. Instrum. Methods A* **820** (2016) 112–120.
- [13] ZAITSEVA, N., et al., Pulse shape discrimination in impure and mixed single-crystal organic scintillators, *IEEE Trans. Nucl. Sci.* **58** (2011) 3411–3420.
- [14] LAUCK, R., et al., Low-afterglow, high-refractive-index liquid scintillators for fast-neutron spectrometry and imaging applications, *IEEE Trans. Nucl. Sci.* **56** (2009) 989–993.
- [15] SPAETH, M.L., et al., Description of the NIF laser, *Fusion Sci. Technol.* **69** (2016) 25–145.
- [16] GLEBOV, V.Yu., et al., Testing a new NIF neutron time-of-flight detector with a bibenzyl scintillator on OMEGA, *Rev. Sci. Instrum.* **83** (2012) 10D309.
- [17] ZAITSEVA, N., et al., Plastic scintillators with efficient neutron/gamma pulse shape discrimination, *Nucl. Instrum. Methods A* **668** (2012) 88–93.
- [18] ZHMURIN, P.N., et al., Polystyrene-based scintillator with pulse-shape discrimination capability, *Nucl. Instrum. Methods A* **761** (2014) 92.
- [19] ELJEN TECHNOLOGY, <http://eljentechnology.com>.
- [20] POZZI, S.A., BOURNE, M.M., CLARKE, S.D., Pulse shape discrimination in the plastic scintillator EJ-299-33, *Nucl. Instrum. Methods A* **723** (2013) 19–23.
- [21] LAWRENCE, C.C., et al., Neutron response characterization for an EJ299-33 plastic scintillation detector, *Nucl. Instrum. Methods A* **759** (2014) 16–22.
- [22] ZAITSEVA, N.P., et al., Recent developments in plastic scintillators with pulse shape discrimination, *Nucl. Instrum. Methods A* **889** (2018) 97–104.
- [23] ZAITSEVA, N., et al., Pulse shape discrimination with lithium-containing organic scintillators, *Nucl. Instrum. Methods A* **729** (2013) 747–754.
- [24] MABE, A., et al., Transparent plastic scintillators for neutron detection based on lithium salicylate, *Nucl. Instrum. Methods A* **806** (2016) 80–86.
- [25] PAWELCZAK, I.A., et al., Boron-loaded plastic scintillator with neutron- γ pulse shape discrimination capability, *Nucl. Instrum. Methods A* **751** (2014) 62–69.
- [26] MAHL, A., ^{10}B enriched plastic scintillators for application in thermal neutron detection, *Nucl. Instrum. Methods A* **880** (2018) 1–5.

TOPICAL SESSION 2
NEUTRON METROLOGY AND CALIBRATION

NEUTRON METROLOGY—MEASUREMENT STANDARDS AND THEIR APPLICATIONS

V. GRESSIER

Institut de Radioprotection et de Sûreté Nucléaire (IRSN),
F-13115 Saint-Paul-lez-Durance,
France
E-mail: vincent.gressier@irsn.fr

D. THOMAS

National Physical Laboratory
Teddington, Middlesex, TW11 0LW
UK

E-mail: david.thomas@npl.co.uk

Abstract: The neutron measurement standards provided by calibration laboratories at all levels, from primary laboratories to those providing routine testing, are essential in underpinning accurate measurements and providing facilities for testing new devices whether they involve completely novel neutron detecting mechanisms or older detection methods in new configurations. The paper outlines the types of calibrations required to characterise a device, and describes the fields available commenting on their advantages, disadvantages and some of the problems associated with performing reliable calibrations.

1 INTRODUCTION

1.1 DEFINITION

Neutron metrology is concerned with research into techniques for determining the number of free neutrons, i.e. neutron not bound in a nucleus, in various situations. The quantities of interest are the fluence, i.e. the number of neutrons crossing a defined area, or the number of neutrons emitted from a source [1]. These are usually determined per unit time leading then to fluence rate or source emission rate.

Determination of these quantities is complicated by the very large range of energies and intensities encountered in neutron fields. Neutron energies can vary from very low values (thermal neutrons with energies around 25 meV or ‘cold neutrons’ with even lower energies) up to the GeV range, as encountered around high-energy accelerators, and as produced in the atmosphere by cosmic rays. Fluence rates can vary from a few neutrons per square centimetre per second, when dealing with radiation protection for the public, up to $10^{15} \text{ cm}^{-2} \cdot \text{s}^{-1}$ or higher in the core of a high-flux reactor, or near high intensity neutron sources. To fully characterize a neutron field not only does the number of neutrons need to be determined, but the energy distribution and the directional characteristics of the field also need to be taken into consideration. For these reasons energy and angular spectrometry are important elements of neutron metrology.

1.2 NEUTRON MEASUREMENT STANDARDS

Neutron metrology labs provide standardized neutron fields, i.e. neutron fields with well-known characteristics, for determining the response of neutron-measuring devices and for measuring cross sections. They are a vital prerequisite for characterizing novel neutron detecting instruments. An important feature of these fields is that they can be produced at more than one lab so that they can be validated by intercomparisons. The most common reference neutron fields are those produced using radionuclide neutron sources. Their usefulness is, however, restricted by their fixed energy spectrum. Because device responses and cross sections tend to vary markedly with neutron energy measurements in a single fixed spectrum tend to be of only limited use. Monoenergetic, or quasi-monoenergetic, neutron fields, produced in the main with accelerators, are thus very important, but unfortunately cannot at present cover the full range of energies of interest. Standard fields with spectra matching those in which responses or cross sections need to be determined are also important. Examples are simulated workplace fields, well-characterized thermal fields, and high intensity fields with a moderated fission spectrum.

The production of neutron fluence standards is an example of a classic metrology problem. To derive standard fields requires instruments with well-known characteristics, but the determination of instrument characteristics depends on the availability of standardized fields. (Instruments with 100% detection efficiency tend not to be available.) The problem is overcome by various means, e.g. the use of radionuclide sources whose emission rates can be

determined accurately using, for example, the manganese bath technique, the use of reactions such as n-p scattering where the cross section can be measured precisely without recourse to instruments of known response, or the detection of the associated charged particles that are emitted in some neutron-producing reactions, the T(d,n)⁴He reaction being a classic example. These techniques are used to a greater or lesser extent in all the energy regions.

A number of different types of measurement standards are defined in metrology, depending on how they are produced and on their uncertainties [2]. The highest level is a primary standard established using a primary reference measurement procedure, or created as an artefact chosen by convention, e.g. the kilogram. A primary reference measurement procedure is one that does not involve measuring with a detector calibrated for the quantity of interest. In the neutron area the use of a manganese bath for determining source emission rate falls in this category, as does the associated particle technique. National standards are provided by National Metrological Institutes (NMIs) or Designated Institutes (DIs) and in the neutron area are not necessarily all derived using primary procedures. Secondary standards tend to be held by calibration labs, their validity being verified by their traceability to a primary standard. A reference measurement standard is simply one designated for the calibration of other measurement standards for quantities of a given kind. A working standard is one used routinely to calibrate or verify measuring instruments or systems.

1.3 STANDARDS DOCUMENTS

There are international standards that describe the production and use of neutron calibration fields, and others describing test methods for measuring devices such as area survey instruments and personal dosimeters.

The International Organization for Standardization, ISO, published the 8529 series of three standards covering accelerator-based fields, radionuclide source fields, and reactor filtered beams. These documents describe production [3] and standardization [4] of neutron calibration fields of energies up to 20 MeV, and how they should be used [5]. Currently, there are no standards for higher energy neutron fields.

The ISO 8529 series does not cover simulated workplace neutron calibration fields where different issues have to be considered. ISO 12789 [6] uses a different approach and is applicable to this situation.

The International Electrotechnical Commission has developed standards for radiation protection devices, e.g. IEC 61005 [7] for area survey instruments, and IEC 61526 [8] for active personal dosimeters. These describe recommended test methods, while recognizing the difficulties of producing neutron standards for testing in certain circumstances, e.g. monoenergetic neutrons in the range from thermal energies to approximately 1 keV where measurement standards are not available.

1.4 ORGANIZATION OF THE METROLOGY SYSTEM

Users of neutron measuring devices need information about the reliability (uncertainty) of the device readings. They may, for example, require traceability to national measurement standards. Direct calibrations at national labs, or transfer devices calibrated at these labs can both provide traceability.

Neutron secondary laboratories using radionuclide sources for calibration can achieve reasonably direct traceability to national standards by using sources with emission rates measured at a national lab, e.g., with the manganese sulphate bath technique [9]. Using a well-characterized source or calibrated transfer device in a secondary lab does not on its own ensure traceability. It is also essential that appropriate calibration techniques, based on sound metrological practice, are used.

For the traceability chains outlined above to function correctly the standards at national labs should themselves be correct within their quoted uncertainties. To demonstrate this national labs participate in international comparison exercises overseen by the International Committee for Weights and Measures (CIPM). Comparisons to validate standards in the area of ionizing radiation are organized by the Consultative Committee for Ionizing Radiation (CCRI) [10]; Section III of CCRI is responsible for neutron metrology.

1.5 APPLICATIONS

All users of neutron measuring devices who need to make an absolute rather than a relative measurement can benefit from the availability of standard neutron fields, however, there are a number of technical areas where calibration and testing is particularly important as detailed in reference [1] and outlined below.

Cross section measurements: All neutron transport calculations, including those for nuclear reactors, depend on reliable cross sections. An enormous amount of effort has gone into the measurement of these cross sections,

particularly at the start of the nuclear age. This effort has decreased over the years although there is now renewed interest for next generation reactors and for fusion. Cross section measurements probably present neutron metrology with its biggest challenge in terms of accuracy requirements. Metrology labs tend not to be involved in routine measurements, which are usually done relative to an accurately known standard cross section, but work on improving these standard cross sections clearly falls within the remit of metrology labs [11].

Radiation protection: The problem in this technical area is that the response functions of survey instruments and personal dosimeters do not match the required dose equivalent quantities, ambient and personal dose equivalent, over the whole energy range of interest, and a device calibrated very precisely in a standard calibration field may still over- or under-read by large amounts in real workplace fields. A large proportion of the work of metrology labs, particularly national labs is the characterisation of radiation protection instrument responses as a function of energy and direction of incidence.

Criticality dosimetry: Dose measurements for criticality accidents differ from those for routine radiation protection in several ways. The doses are likely to be in the range from 100 mGy to 10 Gy (the quantity of interest is absorbed dose, measured in grays, rather than dose equivalent measured in sieverts). Decisions have to be made quickly on the basis of the results and so rapid processing is important. With regard to accuracy: 'The dosimetry system used has to be capable of giving the neutron and gamma-ray components of the dose with an uncertainty of less than $\pm 50\%$ within 48 h and less than $\pm 25\%$ four days later' [12]. In principle the metrology requirement is simply a facility with a fission spectrum, with possibly the option of some moderation and shielding to replicate the conditions at an accident. Appropriate facilities are, however, in short supply since very high fluence rates are required.

Therapy level neutron dosimetry: Early trials of the efficacy of fast neutrons in cancer therapy in the 1930s were curtailed by World War II. Clinical research began again in 1965 at the Hammersmith Hospital in London where patients were irradiated with neutron beams from a cyclotron. It became clear that for certain tumours, better local control could be achieved using neutrons than with photons. Significant effort was put into therapy level neutron dosimetry, which involves measuring absorbed dose at high intensities, and work was undertaken to provide protocols and standards [13]. However, some poor results and the greater cost compared to photons has meant that fast neutrons have never developed into a commonly used treatment modality. A technique known as, boron neutron capture therapy (BNCT) where slow neutrons are captured by boron incorporated in the tumour producing charged particles which irradiate and kill the tumour cells is undertaken at some facilities. The complexity of the technique and difficulty of getting the boron into the tumour mean it is not widely used at present, although there are interesting recent developments using accelerators coupled to moderators as neutron source [14].

Reactor instrumentation — fission and fusion: Neutron detectors used in the control circuitry of fission reactors detect predominantly thermal neutrons. Calibrations are usually provided by research reactors and the chief requirement is that any new instrument has the same response as others of the same type already in use. For future fusion reactors the ability to measure neutron fluences will be critical for monitoring the state of the plasma and for demonstrating control of the whole system [15]. Various neutron monitors will be used, two of the more important types being fission chambers with surrounding moderator material and activation foils. Activation measurements are important since activation samples can cope with very high fluences and pulsed fields. The metrological need is for more accurately known cross sections for the activation materials [16]. Because of the nature of these monitor systems calibrations have to be performed with the monitors in-situ with appropriate neutron sources. Approaches to achieving this are being investigated [17]. There are also direct applications at fusion research facilities for neutron measuring devices such as scintillators, diamond detectors and proton recoil devices developed for metrology at NMIs.

Reactor dosimetry: This is a term used to describe measurements made using a number of activation samples placed in the vicinity of the reactor core. The aim is to determine the spectrum and intensity of the neutrons incident on critical constructional components. The main metrological needs are good cross section data and an ability to determine the activity accurately.

Cosmic-ray neutron fields: Measurements of cosmic-ray neutrons are subject to most of the problems that make neutron metrology difficult, including a very wide energy range (thermal to GeV energies), and the presence of other types of radiation. For measurements in aircraft, an area where considerable effort has been expended over recent years, there is the problem of relatively low dose rates so that it is difficult to make good measurements in a single flight. Several different types of measuring devices, both passive and active, have been used to characterize the field, the one considered the 'reference' device is the tissue equivalent proportional counter because it has the most appropriate response function over the high energy region where most of the dose occurs. It can also measure the photon dose. All these devices need to be calibrated. The usual approach is to use the

simulated cosmic ray field CERF available at CERN [18], but quasi-monoenergetic neutron reference beams with energies up to 400 MeV are also available [19].

Radiation effects in electronics and material testing: Neutrons are the major source of single event effects (SEEs) induced by radiation. The term SEE describes the corruption of digital information and/or the production of damage in an electronic device by charge injection arising from a single incident particle. SEEs can be induced by high-energy neutrons in the MeV to GeV region (reactions with silicon or tungsten in metallization) or by thermal and epithermal neutrons (reactions with ^{10}B used as dielectric over-layers and a dopant in silicon). Several standards, for example reference [20], have been published requiring tests in various neutron fields including: thermal fields, intense 2.5 MeV fields, 14 MeV fields, quasi-monoenergetic fields, and broad high energy spectra from spallation sources without moderator assembly.

High neutron fluence rates with energies above a few MeV induce cascade processes and nuclear reactions in irradiated materials generating structural defects by displacement of atoms. They also introduce impurities such as helium and hydrogen isotopes. Quantifying radiation damage of this type will be critical not only for future fusion reactors but also for the materials around spallation source targets and possibly in the future high-power laser-based neutron sources [21]. To support these activities, neutron metrology has to provide neutron standards from thermal up to ~ 1 GeV with high fluence rates, i.e. with fluence rates of at least $10^6 \text{ cm}^{-2} \cdot \text{s}^{-1}$ at the calibration point. That is beyond most of the facilities available at NMIs. That is why dedicated material testing facilities are required with a link to neutron metrology standards.

2 NEUTRON STANDARDS AND REFERENCE FIELDS

The main role of a national laboratory is to act as the pinnacle of the calibration chain. It is likely to have one or more of a number of different neutron standards.

2.1 THERMAL NEUTRON STANDARDS

Thermal neutron fields [22] can be produced in a number of ways, using a reactor, using radionuclide sources in a moderator, or using the neutron-producing target of an accelerator in a graphite pile (see Figure 1). The standard is almost invariably the activation of gold, in principle a relatively easy measurement. Because the fields are produced in different ways, and depend on the moderation of fast neutrons so that they are likely to contain epithermal neutrons, no two thermal facilities are exactly alike. The fields tend to be a combination of a thermal Maxwellian peak at some temperature, which needs to be determined, plus epithermal neutrons. Fluence defining conventions, such as the Westcott convention, make it possible to inter-compare cross sections, particularly $1/v$ cross sections measured in different facilities, but protection devices need a knowledge of the ‘true’ neutron spectrum, i.e. spectrometric information is needed.



FIG. 1. Left hand side thermal facility based on radionuclide sources in a moderator; right hand side thermal facility based on an accelerator.

2.2 SOURCE EMISSION RATE STANDARDS

The total emission rate from an encapsulated radionuclide source, such as ^{252}Cf or $^{241}\text{Am-Be}$, is the most accurate neutron standard presently available. The manganese bath technique is now the predominant method of measuring this quantity [9]. It is a primary technique, not depending on a calibrated neutron detector. Neutrons are detected by their activation of the manganese in a manganese sulphate bath (see Figure 2). Comparison exercises have shown good agreement between different national labs, but some corrections, e.g. that for neutron losses in the manganese sulphate solution in the bath to $^{16}\text{O}(n,\alpha)$ reactions, require further work. To use the neutrons from a source the anisotropy of the emission needs to be measured and this is usually done with using an instrument with a near flat energy response such as a long counter.



FIG. 2. Manganese baths for neutron source emission measurement. The smaller bath is used for low energy sources where neutron escape from the bath is less likely.

2.3 SOURCE BASED FLUENCE STANDARDS

Because the fluence at a given distance from a source of accurately known emission rate can be known with high precision, and the spectra of several commonly-used radionuclide sources have been measured, and the spectrum-averaged dose equivalent per unit fluence can thus be well known, source-based fields provide the most accurate neutron dose equivalent standards available [9], but only for a specific energy distribution. They are therefore used for routine calibrations of dosimetry devices. They are also used for calibrating specialist devices, e.g. those used for monoenergetic neutron measurements, in a well-known broad energy distribution. The spectra have been measured by various means: time-of-flight for ^{252}Cf where the spontaneous fission can provide a start signal, scintillators, hydrogen recoil spectrometers, ^3He spectrometers, and Bonner spheres. Because a number of different sources with different, albeit broad range spectra, are available some information on the energy dependence of devices can be obtained by using different sources.

2.4 ACCELERATOR BASED FLUENCE STANDARDS

Free neutrons are only produced in nuclear reactions and an obvious way of inducing these reactions is by using a charged particle accelerator. An accelerator capable of producing particles in the energy range from about 100 keV to 3 or 4 MeV can be used to produce a whole range of monoenergetic neutrons from a few keV up to 20 MeV (although there is a gap between 7 MeV and 13 MeV) by using a number of different reactions and the range of particle energies [23]. There are four reactions that produce most of these energies. They are: $^7\text{Li}(p,n)^7\text{Be}$, $\text{T}(p,n)^3\text{He}$, $\text{D}(d,n)^3\text{He}$ and $\text{T}(d,n)^4\text{He}$. ISO standard 8529 recommends a number of energies that scan this energy range. These are listed in Table 1 together with some details of the targets used, the charged particle energy E_p required, the angle of the neutrons relative to the charged particle beam, the energy width ΔE_n of the neutrons for the listed target thicknesses, and the neutron yield per steradian and per μC of beam. Standards above 20 MeV require a very much bigger (and more expensive) accelerator [18].

TABLE 1. ISO RECOMMENDED MONOENERGETIC ENERGIES AND PROPERTIES

Energy	Reaction	Target	Mass ($\mu\text{g}/\text{cm}^2$)	E_p (MeV)	Angle	ΔE_n (keV)	Yield ($\text{sr}^{-1}\mu\text{c}^{-1}$)
24 keV	$^{45}\text{Sc}(\text{p},\text{n})^{45}\text{Ti}$	Sc	20	2.93	40°	<0.4	6.0×10^2
24 keV	$^7\text{Li}(\text{p},\text{n})^7\text{Be}$	LiF	70	1.94	76.5°	8	1.3×10^5
144 keV	$^7\text{Li}(\text{p},\text{n})^7\text{Be}$	LiF	70	1.94	0°	12	6.8×10^6
250 keV	$^7\text{Li}(\text{p},\text{n})^7\text{Be}$	LiF	70	2.02	0°	11	3.4×10^6
565 keV	$^7\text{Li}(\text{p},\text{n})^7\text{Be}$	LiF	70	2.30	0°	8	1.5×10^7
1.2 MeV	$\text{T}(\text{p},\text{n})^3\text{He}$	T in Ti	1000	2.10	0°	107	7.9×10^6
2.5 MeV	$\text{T}(\text{p},\text{n})^3\text{He}$	T in Ti	1000	3.36	0°	76	1.4×10^7
5.0 MeV	$\text{D}(\text{d},\text{n})^3\text{He}$	D in Ti	1000	2.50	0°	191	5.1×10^6
5.0 MeV	$\text{D}(\text{d},\text{n})^3\text{He}$	D ₂ gas	500	2.40	0°	190	9.2×10^6
14.8 MeV	$\text{T}(\text{d},\text{n})^4\text{He}$	T in Ti	1000	0.21	0°	407	1.3×10^7
19 MeV	$\text{T}(\text{d},\text{n})^4\text{He}$	T in Ti	1000	2.69	0°	375	3.7×10^6

2.5 SIMULATED WORKPLACE NEUTRON FIELDS

Although calibrations in monoenergetic fields are ideal for determining device response functions, i.e. the response as a function of energy and/or angle, these devices are not usually intended for use in monoenergetic monodirectional fields. Because most neutron measuring devices do not have the required response functions enabling them to measure the quantity of interest, whether it be fluence or dose equivalent, at all energies and angles, the availability of simulated workplace calibration fields offers another approach to calibration [6]. Many workplace fields have significant numbers of intermediate energy neutrons, and monoenergetic standards are not available in this region, so simulated workplace fields are often designed to have a large number of neutrons in this energy region [24]. Another problem area is energies above 20 MeV where no NMI is yet able to offer standards. The CERN CERF [18] field provides a reasonably realistic field for cosmic ray neutron fields in the atmosphere.

2.6 CALIBRATION FACILITIES

The manner in which neutron calibrations are performed means that neutron metrology labs need particular specialist features. Thermal neutron calibration facilities require either a reactor or a large moderating structure. For the latter approach calibrations can be performed in a beam extracted from the moderator, or in a cavity within the moderator. The requirement is thus for space for these structures. Simulated field facilities also usually require a significant area for the moderating materials usually present, but in these types of standards there is no attempt to correct for unwanted scattered neutrons—they are part of the simulated field.

This differs completely from the usual situation when realising standard neutron fields based on radionuclide sources or neutrons from a target bombarded by particles from an accelerator. The premise in both these cases is that the calibration field is that from the source of neutrons with no contaminant neutrons produced by scattering in the environment, i.e. from the walls, floors and ceiling of the lab, in the air, and from all other equipment in the area. Because the number of scattered neutrons seen by a device depends on the size of the room, neutron calibration facilities using radionuclide sources or an accelerator tend to be large. The need for thick shielding walls, or an exclusion zone around the building, mean that these large facilities are expensive to set up. For radionuclide sources calibration rooms tend, if possible, to be at least $7\text{m} \times 7\text{m} \times 7\text{m}$. For monoenergetic neutron facilities they are usually even larger – see Figure 3. Corrections for scatter still need to be made and various techniques are employed based on the variation of the ratio of scattered to direct neutrons with distance or the use of a shadow cone to cut out the direct neutrons and hence measure the scattered component. The few NMIs with accelerator based standards tend to have even larger low-scatter experimental areas.



FIG. 3. Low scatter experimental hall of accelerator-based facility for monoenergetic reference fields.

Secondary radiations such as photons always accompany the neutrons and their characteristics need to be known. The complete description of a reference radiation field therefore includes directional information and the energy distribution of the fluence for each type of ionizing radiation present. Any point in the reference field having such a complete description can be used as a point of test for calibration of any neutron sensitive device, regardless of any response to non-neutron radiation.

Thermal neutron reference fields should have a very low, ideally zero, fast neutron component. Because the fluence to dose equivalent conversion coefficients are significantly higher for fast neutrons than thermal ones a contribution of just a few % of contaminant fast neutrons in the total fluence may constitute the majority of the total dose equivalent [22].

In the case of accelerator-based neutron sources, there are additional problems that come from the neutron producing target such as: parasitic (p,n) or (d,n) reactions, reactive layer diffusion into the target backing (a particular problem for Li targets), etc. As a consequence, the neutron field characteristics have to be regularly experimentally checked by means of fast neutron spectrometers and the neutron fluence rate has to be constantly monitored.

3 CALIBRATION PROCEDURES

3.1 DEFINITION AND GOAL

A calibration is a set of operations that establish, under specified conditions, the relationship between values indicated by a device, and the corresponding known (i.e. conventionally true) values of the quantity to be measured. The calibration of a neutron sensitive device can range from a simple calibration factor at a single neutron energy, or energy distribution, to a full response characterization over the entire range of energy and angle of incidence of any particles to which the device is sensitive. As the responses of neutron sensitive devices and the fluence to dose equivalent conversion coefficients can vary dramatically with neutron energy and incident angle [25], both simulation and experiments in standard neutron fields are required for a full characterization.

3.2 DIFFERENCE BETWEEN CALIBRATION FACTOR AND FULL CHARACTERIZATION

The calibration factor, N , is the end result of the simplest form of calibration. It is simply the factor by which the reading M of the device is multiplied in order to obtain the value of the quantity to be measured in a given reference field [26].

To be precise, such a calibration factor is only valid for an instrument used in the same radiation field as the reference field, or to one with the correct energy response and, when relevant, angular response, to the quantity of interest. Very few, if any, neutron instruments possess these properties over their whole working range so, in the absence of a reference neutron field representative of the workplace in which the device will be used, a simple calibration factor is of limited use other than to verify the device's response stability as a function of time.

Ideally, a full calibration would determine the energy and angular response functions using as many reference fields as appropriate, possible, or affordable. Such a calibration, called a full response characterization, requires a substantial measurement programme if based solely on experimental measurements. This is usually impractical for time and cost reasons. The most effective calibration/characterization is by modelling of the detectors' response function/matrix using widely available Monte Carlo radiation transport codes. The importance of validation by measurements in as many neutron reference fields as is feasible is illustrated in Figure 4.

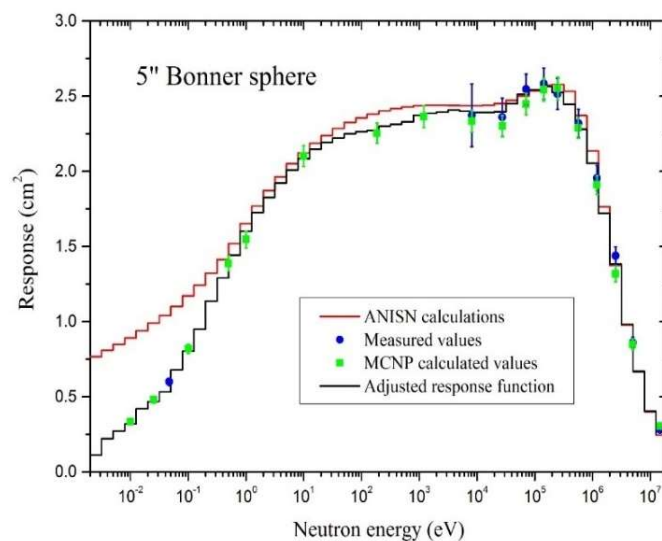


FIG. 4. Example of device response function determination. Calculated and measured responses for a Bonner sphere.

3.3 RECOMMENDED CALIBRATION PROCESS

3.3.1 Full calculation of device response

A device response should be calculated in terms of energy and direction not only for neutrons but also, if discrimination between different radiation types is not possible, for all the other ionizing radiations (mainly photons) that the device is sensitive to. This calculation is fundamental a priori information that should be given by manufacturers!

If the device reading is a single value (a number of counts, a dose equivalent, etc.) there is just one energy response function for the device (e.g. a Bonner Sphere, or an area survey instrument). If the device reading is a distribution (a pulse height spectrum) varying with energy or/and angle, then the response matrix has to be determined, i.e. the set of the pulse height response functions for the neutron energies to which the detector responds (e.g. a proton recoil counter). The response function or response matrix are calculated with radiation transport codes, in most cases Monte Carlo codes such as MCNP, Geant, or dedicated codes.

Spherical detectors (e.g. some survey meters and gaseous proton recoil devices, or Bonner sphere type spectrometers) can be considered as having nearly isotropic fluence/ $H^*(10)$ responses. Only an energy response function is required for these devices and they can be used in neutron fields with any directional properties. In all other cases, (e.g. survey instruments with other geometries or equipped with electronics that result in their response not being isotropic) and for all $H_p(10)$ measuring devices where the quantity depends on neutron direction, an angular response function also has to be determined; the calculation using Monte Carlo codes providing a first step.

3.3.2 Optimization of the number of measurements

The number of measurements required in both energy and direction can be reduced when using the a priori information from the calculation. A limited number of points are indeed enough in most of cases to validate experimentally the simulated responses.

3.3.3 Experimental characterization for other ionizing radiation responses

In neutron calibration fields there are always secondary radiations (particularly gamma radiation) present, produced with, or induced by, the neutrons. This is also true of any neutron field that needs to be measured. If a device is sensitive to these secondary radiations, and has no discrimination capabilities, then the response due to these radiations also has to be determined. There are two options depending on the degree of knowledge that has to be achieved for the instrument. The first one is to fully characterize its response to the secondary radiations. However, to use this information the full energy and angular distribution of the radiations in the calibration field need to be known or determined. That is why, where possible, the contribution of these secondary radiations is estimated by producing a similar field, but without neutrons (possible for some monoenergetic neutron fields, for example). However, the best solution by far is to have a device insensitive to other radiations, or with discrimination capabilities.

3.3.4 Experimental characterization of neutron responses at selected reference fields

The experimental characterization of the neutron response of a device has to be performed in monoenergetic or quasi-monoenergetic fields (from a few keV up to several hundreds of MeV), in thermal neutron fields for the low energy range, and in well characterized realistic neutron fields for the epithermal neutron range.

Several parameters have to be determined/known to correctly determine the device response and its uncertainty [25]:

- a) **Stability/reproducibility:** radionuclide sources, for examples, can be used to check this regularly.
- b) **Dead time/linearity:** several methods can be applied, for example the use of the same monoenergetic fields with different beam currents. In recent years, due to the increasing number of facilities producing pulsed radiation fields, especially in the medical domain, the problems of calibrations in such fields have become increasingly important, in particular those caused by dead time during the pulse.
- c) **Effective centre:** this is the point in the detector, often called the reference point, that determines the reference calibration distance. For 'spherical' devices the geometric centre can be considered as the effective centre. However, the effective centre of any non-spherical device should be systematically studied. (Dosimeters on a phantom, are a special case where the effective centre is usually taken to be on the front face of the phantom although a defined point in the dosimeter is also sometimes used.) In order to determine the effective centre, measurements (with geometry and neutron scattering corrections applied) are performed at several distances in the same neutron field. Simulation of these measurements, including the instrument and a detailed description of the environment, can also be performed to calculate the integrated response at several distances. The variation of experimental or simulated integrated responses with the distance d are then fitted by an equation of the form $A/(d+r)^2$ leading to the value, r , of the effective centre. If this determination is performed in several monoenergetic fields, then it is possible to obtain the variation of the effective centre as a function of the energy. If the effective centre is not known or cannot be properly determined, large calibration distances should be used to reduce, to a reasonable level, the uncertainty induced by lack of information on this parameter.
- d) **Effect of the instrument in the field:** the presence of the instrument modifies the neutron field, increasing the scattered neutron level and shadowing some areas. This is of particular importance in thermal fields and should then be taken into account using Monte Carlo calculation to estimate the corrections to be applied.
- e) **Geometry correction factor:** At very short distances from a point neutron source the neutron field may no longer be uniform over the whole front face of the detector, inducing readings that will exceed those expected from the inverse square law. In addition, calibrations performed with dosimeters placed far from the centre point of the front face of a phantom generate problems for the proper definition of $H_p(10, \alpha)$ when a phantom is exposed in a field that is not homogeneous over the whole surface. The fluence, and in the case of monoenergetic fields also the energy, will vary with the angle of incidence α . For spherical devices in isotropic neutron fields, a geometry correction factor can be calculated using the method described in the ISO 8529 standards. This geometry correction can generally be neglected beyond

1 m from the source. For calibrations in non-isotropic neutron fields or of non-spherical devices, the geometry correction has to be calculated. This requires accurate knowledge of the detector geometry as well as of the neutron field. If not possible, the calibration has to be performed in a neutron field as near as possible to a broad and parallel beam (i.e. with calibration distances of at least 1 to 2 m with the consequent problem of an increasing contribution from scattered neutrons).

- f) **Scatter correction factor:** At short distances, the neutron scattering correction is small compared to the geometry correction, but increases with distance whereas the geometry correction decreases. In-scattered neutrons come from the walls, floor, and ceiling of the room, and also from the air. Scatter from the walls etc. decreases as the size of the room increases, and for very large rooms, such as those often available at several facilities using an accelerator to produce monoenergetic neutrons, the air in-scatter can become larger than that from the room boundaries. To correct for neutron scattering, the shadow cone technique should be considered as the reference experimental method due to strong limitations of the other methods outlined in ISO 8529. Corrections for air out-scatter from the solid angle defined by the device being calibrated are performed using simple air attenuation calculations. Finally allowance has to be made for neutrons scattered in the target assembly, and this is done using Monte Carlo calculations. When none of the experimental methods are applicable, simulations have to be performed requiring detailed knowledge of both the calibration field and instrument to be calibrated. If information is missing, and such calculations are not possible, then the neutron field should be considered as a realistic one, comprising a defined amount of scattered neutrons, using methods described in ISO12789.
- g) **Fluence to dose equivalent conversion coefficients:** Values for $h^*(10)$ and $h_p(10,\alpha)$ (the conversion coefficients are written with lower case letters) are taken from international recommendations, the most recent being in reference [27] where they are published as a function of energy between 1 meV and 20 MeV, and also of angle, α , for $h_p(10,\alpha)$. They are considered to be exact, i.e. can be applied without uncertainties, however, where the neutron spectrum or the monoenergetic neutron energy have uncertainties a contribution is included for the effect of this uncertainty. To derive spectrum averaged values the spectrum obviously needs to be known. Coefficients for some radionuclide source spectra (^{252}Cf , $^{241}\text{Am-Be}$, and $^{241}\text{Am-B}$) are given in ISO standards [5] together with uncertainty values deriving from uncertainties in the spectra. In a scatter-corrected measurement, e.g. one where a shadow cone is used, or one where scatter is negligible, and the field is unidirectional or from a point source, determination of the appropriate conversion coefficient is relatively straightforward both for $h^*(10)$ and $h_p(10,\alpha)$. However, where the field includes scatter, e.g. some realistic fields, and the quantity of interest is $h_p(10,\alpha)$ not only the spectrum needs to be known but also the variation of the spectrum with the angle of incidence on the device.

3.3.5 Tests before use

The poor energy and angular responses of neutron measuring instruments means that they would ideally be calibrated in a field that is exactly the same as the one in which they will be used. The huge variety of possible neutron fields makes this practically impossible. However, before use in an actual workplace field an intermediate step is recommended whereby a device calibrated in the laboratory is tested in a field representative of the one where the device will be used. This 'test' field should have the same kind of neutron energy distribution as the one that the instrument will be required to measure, several incident angles, and an important level of photon contamination, if possible with a field representative of the one it will be exposed to. These test fields could be radionuclide sources, in particular the heavy water moderated ^{252}Cf source or/and realistic fields.

The alternative approach, and the best way forward if reliable measurements are particularly important, for example if neutron doses in an area approach statutory limits, is to undertake field measurements of the spectrum and angle dependence of the field. The performance of a device can then be validated by comparison with dose values derived from the field measurements.

In Germany a system of codifying calibration fields for albedo personal dosimeters in terms of four different application areas has been developed [28, 29]. Each area has a different calibration field, each one involving a different degree of moderation. The application area is determined from simple field measurements. This approach does not provide completely correct calibration fields, but ones that are at least reasonably appropriate.

4 CONCLUSIONS

Neutron metrology offers the developers of neutron measuring devices and the end users a number of important capabilities. One obvious one is the routine quality checking of instruments to ensure their response characteristics do not change with time.

If a measuring device is to be used in a field for which a calibration source exists, e.g. a thermal field or a radionuclide source field with minimum scattering, directly relevant calibrations can be performed.

Probably the most important service offered by neutron metrology labs with a range of irradiation capabilities, particularly those with where monoenergetic neutrons are available, is that of characterising the response functions of newly developed instrument (or in some cases old instruments which have been in use for years without their response functions being measured accurately). Without this capability validation of improvements in neutron measuring devices are impossible.

Many challenges for neutron metrology exist in areas where standards are presently unavailable including: high energies above 20 MeV, energies between thermal and about 1 keV, pulsed fields, and very intense fields such as those which will be encountered in future fusion facilities. Some areas exhibit a combination of problems, an example being neutron contamination at proton therapy facilities where there are: high energies, a pulsed field, and in the treatment beam other radiations. Work on new measurement standards that address the needs in these areas is underway, but there are significant difficulties. High energies, for example, require a high energy accelerator, intense fields require specialist accelerators and extensive shielding. These are things that tend to be beyond the scope of individual metrology laboratories so that collaboration between national metrology labs is the obvious way forward.

REFERENCES

- [1] THOMAS, D.J., NOLTE, R., GRESSIER, V., What is neutron metrology and why is it needed? *Metrologia* **48** (2011) S225–S238.
- [2] BUREAU INTERNATIONAL DES POIDS ET MESURES, JCGM 200:2012 International vocabulary of metrology – Basic and general concepts and associated terms (VIM) 3rd edn (2012)
- [3] INTERNATIONAL ORGANIZATION FOR STANDARDIZATION, Reference Neutron Radiations—Part 1: Characteristics and Methods of Production, International Standard 8529-1 (Geneva, Switzerland: ISO) (2001).
- [4] INTERNATIONAL ORGANIZATION FOR STANDARDIZATION, Reference Neutron Radiations—Part 2: Calibration Fundamentals of Radiation Protection Devices Related to the Basic Quantities Characterizing the Radiation Field, International Standard 8529-2 (Geneva, Switzerland: ISO) (2000).
- [5] INTERNATIONAL ORGANIZATION FOR STANDARDIZATION, Reference Neutron Radiations—Part 3: Calibration of Area and Personal Dosimeters and Determination of their Response as a Function of Neutron Energy and Angle of Incidence, International Standard 8529-3 (Geneva, Switzerland: ISO), (1998).
- [6] INTERNATIONAL ORGANIZATION FOR STANDARDIZATION, Reference Neutron Radiations—Characteristics and Methods of Production of Simulated Workplace Neutron Fields, International Standard 12789 (Geneva, Switzerland: ISO) (2000).
- [7] INTERNATIONAL ELECTROTECHNICAL COMMISSION, Radiation Protection Instrumentation — Neutron Ambient Dose Equivalent (Rate) Meters, IEC Standard 61005 (Geneva, Switzerland: IEC) (2003).
- [8] INTERNATIONAL ELECTROTECHNICAL COMMISSION, Radiation Protection Instrumentation — Measurement of Personal Dose Equivalents Hp(10) and Hp(0,07) For X, Gamma, Neutron and Beta Radiations—Direct Reading Personal Dose Equivalent Meters and Monitors, IEC Standard 61526 (Geneva, Switzerland: IEC) (2010).
- [9] ROBERTS, N.J., MOISEEV, N.N., KRÁLIK, M., Radionuclide neutron source characterization techniques, *Metrologia* **48** (2011) S239–S253.
- [10] BUREAU INTERNATIONAL DES POIDS ET MESURES, Consultative Committee for Ionizing Radiation (CCRI), <https://www.bipm.org/en/committees/cc/ccri/>.
- [11] CARLSON, A.D., The neutron cross section standards, evaluations and applications, *Metrologia* **48** (2011) S328–S345.
- [12] MÉDIONI, R., DELAFIELD, H.J., Criticality accident dosimetry: an international intercomparison at the Silene reactor, *Radiat. Prot. Dosim.* **70** (1997) 445–454.
- [13] INTERNATIONAL ATOMIC ENERGY AGENCY, Advances in dosimetry for neutrons and heavy charged particles for therapy applications, Proceedings of an Advisory Group Meeting, IAEA, Vienna (1984).

- [14] KREINER, A.J., et al., Present status of accelerator-based BNCT, *Rep. Pract. Oncol. Radiother.* **21** 2 (2016) 95–101.
- [15] BERTALOT, L., et al., Fusion neutron diagnostics on ITER tokamak, *JINST* **7** (2012) C04012.
- [16] PROKOPOWICZ, R., et al., Measurements of neutrons at JET by means of the activation methods, *Nucl. Instrum. Methods Phys. Res. A* **637** (2011) 119–127.
- [17] BATTISTONI, P., et al., 14 MeV Calibration of JET neutron detectors – Phase 1: calibration and characterization of the neutron source, *Nucl. Fusion* **8** 2 (2017) 026012.
- [18] MITAROFF, A., SILARI, M., The CERN-EU high-energy reference field (CERF) facility for dosimetry at commercial flight altitudes and in space, *Radiat. Prot. Dosim.* **102** (2002) 7–22, see also <http://tis-div-rp-cerf.web.cern.ch/tis-div-rp-cerf/>.
- [19] HARANO, H., NOLTE, R., Quasi-monoenergetic high energy neutron standards above 20 MeV, *Metrologia* **48** (2011) S292–S302.
- [20] JOINT ELECTRON DEVICE ENGINEERING COUNCIL, Measurement and Reporting of Alpha Particles and Terrestrial Cosmic Ray-Induced Soft Errors in Semiconductor Devices, JEDEC Standard JESD89A (JEDEC Solid State Technology Association, Arlington, VA.: USA) (2006).
- [21] GRESSIER, V., Review of neutron calibration facilities and monitoring techniques: new needs for emerging fields, *Radiat. Prot. Dosim.* **161** (2014) 27–36.
- [22] WILLIAMS, J.G., GILLIAM, D.M., Thermal neutron standards, *Metrologia* **48** (2011) S254–S262.
- [23] NOLTE, R., THOMAS, D.J., Monoenergetic fast neutron reference fields: I. Neutron production, *Metrologia* **48** (2011) S263–S273.
- [24] LACOSTE, V., TAYLOR, G., RÖTTGER, S., Simulated workplace neutron fields, *Metrologia* **48** (2011) S301–S312.
- [25] GRESSIER, V., TAYLOR, G.C., Calibration of neutron-sensitive devices, *Metrologia* **48** (2011) S313–S327.
- [26] BARTLETT, D.T., et al., Concepts and quantities in spectrometry and radiation protection, *Radiat. Prot. Dosim.* **107** (2003) 23–35.
- [27] INTERNATIONAL COMMISSION ON RADIOLOGICAL PROTECTION, Conversion Coefficients for use in Radiological Protection against External Radiation, ICRP Publication 74 (1997), also published by the International Commission on Radiation Units and Measurements as ICRU Report 57 (1998).
- [28] DIN, DIN 6802 Neutron Dosimetry – Part 4: Measurement Technique For Individual Dosimetry Using Albedo Dosimeters (1998).
- [29] CHEVALLIER, M.-A., et al., EURADOS IC2012n: Further information derived from a EURADOS international comparison of neutron personal dosimeters, *Radiat. Prot. Dosim.* **170** (2016) 78–81.

NEUTRON STANDARD FACILITIES IN INDIA

V. SATHIAN, S. GHODKE, M. SEN, Y. SINGH, M. S. KULKARNI
Radiation Safety Systems Division
Bhabha Atomic Research Centre, Trombay, Mumbai-400085.
India
E-mail: sathian@barc.gov.in

Abstract: Many reactors and accelerators are under development in the country, so neutron measurement has become very important. All neutron measurements within India are traceable to the national laboratory for ionising radiation, Bhabha Atomic Research Centre. This paper gives an overview of the facilities established in the centre to ensure the traceability of all neutron measurements in the country. The centre has established Primary Standards, Secondary Standards and different field standards for neutron source yield measurement and neutron fluence rate measurements.

1 INTRODUCTION

Bhabha Atomic Research Centre (BARC), India is developing and maintaining various standards for ionising radiation measurement to ensure the traceability of all radiation measurement in the country to the national laboratory. Different primary standards, secondary standards and transfer standards for neutron source yield and fluence rate measurement are developed and maintained here. The manganese sulphate bath system is the primary standard for neutron source yield measurement, and a Precision Long Counter is the secondary standard. A Proton Recoil Telescope has been established as a primary standard for fast neutron fluence rate measurement. A Standard Thermal Assembly in Graphite (STAG) has been established as a primary standard for thermal neutron fluence rate measurement. A light-weight transfer standard has been developed for onsite standardization of neutron sources. The national lab is providing calibration services to various users in the country using the standards established.

2 MANGANESE SULPHATE BATH SYSTEM

The manganese sulphate bath system, see Figure 1, is the primary standard for neutron source yield measurement. This system is of the highest metrological quality. It permits the determination of neutron yield of the source from basic quantities like number of atoms of different element present in the tank, the absorption cross section, and the efficiency of the detecting system. The accuracy of the measurement has been verified by comparisons with comparable standard of other institutions participated in an international intercomparison.



FIG. 1. Manganese sulphate bath system.

The BARC manganese sulphate bath system consists of a spherical steel tank of 1-m diameter filled with 200kg of manganese sulphate in 500 litres of doubly distilled water. The induced activity in the solution is measured

using a detecting assembly and correlated to the neutron source yield. There is a concrete wall separating the tank and detection assembly. The detection assembly consists of a 3" × 3" NaI(Tl) scintillator placed inside a re-entrant type hollow metallic box. This box is kept inside a lead shield. This lead shield is made of small interlocking type lead bricks. The solution is circulated to the detecting assembly by a quarter HP centrifugal pump kept on the interposing wall. The scintillator is connected to a photomultiplier tube. This is connected to a pre-amplifier and amplifier. An MCA is used for data acquisition. The neutrons emitted by the source are moderated in the solution and are absorbed by the manganese present inside the tank. The induced activity is measured and correlated to the neutron source strength through the cross sections and number of atoms. All neutron sources in India of yield 10^4 to 10^8 are standardized using this system.

3 THERMAL STAG

The Standard Thermal Assembly in Graphite (STAG), shown in Figure 2, is the primary standard for thermal neutron fluence rate. It consists of six Am-Be neutron sources embedded in a graphite assembly of 122 cm × 156 cm × 163 cm. There is a cavity of 4 cm × 4 cm × 15 cm at the centre of the assembly. The thermal neutron fluence rate at this cavity is 6400 n/cm²/sec and is uniform in the entire length of the cavity. This value has been established in terms of gold and manganese cross sections. There are two portals for calibration of thermal neutron detectors with thermal neutron fluence rate of 150 n/cm²/sec and 250 n/cm²/sec. This facility is extensively used for the calibration of neutron detectors used in our reactors. This facility is being used for many R&D activities using thermal neutron.



FIG. 2. Standard Thermal Assembly in Graphite (STAG).

4 PRECISION LONG COUNTER

A Precision Long Counter (PLC), see Figure 3, is the secondary standard for neutron source yield measurement, and it is traceable to the manganese sulphate bath system, the primary standard. The principle of operation of a PLC is based on the use of a slow neutron detector within a carefully designed moderating medium. It has a boron trifluoride (BF₃) proportional counter positioned inside two concentric high-density polythene cylindrical moderators separated by an annular thermal neutron shield made up of 5% boron-loaded polyethylene. At both the front and the back there is a thin sheet of cadmium. The whole assembly is enclosed in an aluminium outer casing. The reaction involved in the BF₃ neutron detector is $^{10}\text{B}(n,\alpha)^7\text{Li}$ which has a large cross section for thermal neutrons and follows the $(1/v)$ law up to 1 MeV. The outer annulus of high-density polyethylene and the 5% boron-loaded polythene layer act as a shield ensuring that neutrons hitting the sides of the long counter have a low probability of being detected. Only those striking the front face have a high probability of reaching the slow neutron detector. So basically it is a unidirectional system. The position of the BF₃ detector, thicknesses of the inner and outer moderator, and the absorber layer were adjusted in such a way that it has a near constant efficiency for a long range of neutron energies. The efficiency is measured using standard sources.



FIG. 3. Precision Long Counter.

5 NEUTRON TRANSFER STANDARD [1]

The primary standard and secondary standards of neutron source yield measurement are very heavy and sensitive system which requires controlled laboratory conditions. To meet the requirement from various universities for standardization of neutron sources a transfer standard has been designed and developed for onsite standardization of neutron sources. This is a portable, light-weight system. It is shown in Figure 4 and consists of a BF_3 counter placed inside a moderating assembly of high-density polyethylene. The thickness of the moderating assembly is optimized by simulation to give a constant efficiency up to 10 MeV. This system is also calibrated using a neutron source standardised by the manganese sulphate system.

6 NEUTRON SOURCE IDENTIFIER [2,3]

Neutron sources are used in various fields such as research activities, industries and in medical applications. For proper use, these sources should be identified and standardized accurately so that the type and yield of a neutron source is known to the user. Presently the MnSO_4 bath system, the primary standard, and a Precision Long Counter, the secondary standard, are used for standardization, having accuracy within $\pm 1\%$ and $\pm 5\%$ respectively. These standards are very heavy and bulky, cannot be transferred to the field for source standardization, and they cannot identify the source.

Most of the commonly used methods for the identification of a neutron source are very tedious, time consuming and are not always accessible to many laboratories and usually include unfolding procedures. Therefore, it is necessary to have a portable transfer standard for in-situ standardization as well as identification of neutron sources. Fast and reliable identification and standardization of neutron sources is very important for personal protection in nuclear industries and also in the public domain. This paper presents a new technique for identification and standardization of laboratory neutron sources based on the ratio of the response of two thermal neutron detectors placed at different distances from the source, all placed inside the moderating assembly. Based upon the ratio of responses of neutron detectors, the unknown neutron source can be identified without employing energy-spectrum unfolding techniques and can be standardized. The system was designed using the FLUKA code. The system, shown in Figure 5, is a portable one made of high-density polythene discs which can be easily dismantled and transported, and can be reassembled at the site without any difficulties. Fluka simulation was used to optimize various design parameters in such a way, that there is wide difference in the ratio of counts of two detectors placed at two different distances for different types of sources. This ratio is used as a signature of the source for the commonly available laboratory neutron sources. The ratio varies between 13 and 38. The weight of the system is about 20 kg.

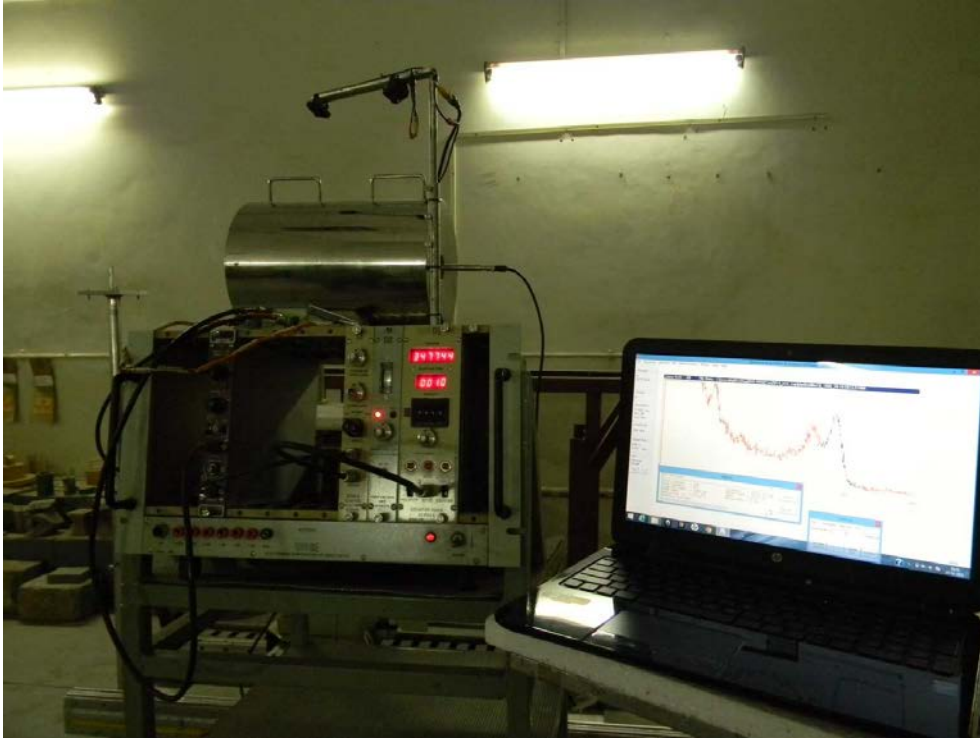


FIG. 4. Newly developed Transfer Standard.



FIG. 5. Neutron source identifier.

This system has been designed to identify various neutron sources based on the ratio of counts of two BF_3 counters kept at two different distances from the source inside a moderating assembly. The ratio for different sources has been obtained using simulation as well as using standard sources available in the lab.

The system consists of HDP moderating assembly in the form of a right circular cylinder made up of circular discs of 3 cm thickness, 40 cm diameter, and 30 cm total height incorporating two BF_3 detectors at a distance of 22 cm and 6 cm from the neutron source cavity. The measurements are carried out using the two BF_3 counters, each one having a thermal neutron sensitivity of 10 cps/(n/cm²/sec). When the source's neutron spectrum is similar, the identification is done based on the gamma spectrum of the source.

7 PROTON RECOIL NEUTRON TELESCOPE

The Proton Recoil Neutron Telescope shown in Figure 6 is a primary standard for fast neutron fluence rate measurement in the MeV range. The neutron fluence rate is measured in terms of the $n-p$ scattering cross-section. The principle of operation is that, neutrons incident on a thin polyethylene film called a 'proton radiator' knock protons out by elastic collisions. The proton radiator and a CsI(Tl) detector are enclosed inside a vacuum chamber. The proton recoil neutron telescope consists of a polyethylene radiator (C_2H_2)_n about 15 mg/cm² having diameter 4 cm, and a CsI(Tl) scintillation crystal of thickness 1.5 mm and 4 cm diameter. The radiator and crystal are kept in a stainless-steel chamber of wall thickness 0.1 cm, 12.5 cm diameter and 37.5 cm long under vacuum. A 0.3 mm tantalum sheet lines the inside wall and entrance window to avoid the charged particle background. The vacuum of 1×10^{-3} Torr is achieved with a rotary pump.



FIG. 6. Neutron Telescope.

For the given geometry, the efficiency of telescope is theoretically calculated for 14 MeV neutrons, $\epsilon = 5.59 \times 10^{-6}$ counts per neutron per steradian

8 NEUTRON SPECTROMETERS

Energy information is very important for neutron dosimetry. BARC has different neutron spectrometers such as Bonner spheres, threshold detectors, NE-213 based spectrometer, bubble detector based spectrometer (Fig. 7).



FIG. 7. Bonner sphere spectrometer and NE-213 based neutron spectrometer.

9 THERMAL NEUTRON FACILITIES

In addition to the thermal STAG, the primary standard for thermal neutron fluence rate, there are different thermal neutron facilities for the testing and calibration of neutron detectors. They include a Neutron Howitzer and a Water Jig—see Figure 8. These facilities are used for testing and calibration of neutron detectors used in the reactor. In-situ calibration of neutron detectors used in regulatory and protection channels of reactors before criticality are performed using the water jig.



FIG. 8. Water Jig and Neutron Howitzer.

10 CALIBRATION FACILITIES

Protection level neutron instruments are calibrated in the Neutron Calibration Facility—Figure 9. The Radiation Standards Section, RSS, has different kinds of neutron sources such as Am–Be, ^{252}Cf , D_2O -moderated ^{252}Cf , Am–B, Am–F, Am–Li, and also different moderated spectra. An automatic system is used for the adjustment of the instruments to reduce the radiation exposure of operating personnel.



FIG. 9. Neutron calibration facility

REFERENCES

- [1] SEN, M. et al., Development of a portable transfer standard for the neutron source yield measurement using Fluka simulation, Nucl. Instrum. Methods Phys. Res., Sect. B **360** (2015) 145–149.
- [2] GHODKE, S. et al., “Measurement of gamma spectrum and neutron yield of $^9\text{Be}(\alpha, n)^{12}\text{C}$ sources using indigenously developed BGO detector”, paper presented at NUCAR-2015, TSH, Mumbai (2015).
- [3] SINGH, Y. et al., Modelling of neutron source identifier using Fluka technique and its experimental verification, paper presented at NUCAR-2015, TSH, Mumbai (2015).
- [4] AXTON, E.J., Intercomparison of neutron source emission rates (1978–1984) Metrologia, **23** (1987) 129–144.

TOPICAL SESSION 3
SPECTRAL UNFOLDING

SPECTRAL UNFOLDING: A MATHEMATICAL PERSPECTIVE

M. KOSLOWSKY

Bubble Technology Industries

Chalk River, Ontario

Canada, K0J 1J0

Email: koslowskym2@bubbletech.ca

Abstract: Given a set of measurements from a set of one or more neutron detectors, the ability to determine the energy spectrum of the incident radiation field is of great value for a number of applications. We address the problem of calculating this spectrum, known as spectral unfolding. Several different methods of spectral unfolding are considered, including maximum likelihood estimation, maximum a posteriori probability, and maximum entropy, as well as a handful of other methods.

1 INTRODUCTION

A common problem in neutron detection is to have a set of measurements, typically in the form of counts, from a set of detectors, or from channels in a spectrometer. The challenge is to compute the best neutron spectrum that fits the data; computation of such a spectrum is referred to as *spectral unfolding*. We assume that m such measurements have been taken by a set of m different detectors, and that $\{y_j, j = 1, \dots, m\}$ is the resulting set of measurements. Since each y_j is a certain number of counts from the j^{th} detector, we assume that y_j is the outcome of a Poisson random variable Y_j .

Let φ represent the fluence per unit energy, so that $\varphi: [0, \infty) \rightarrow \mathbb{R}$. We may then compute the expected value of Y_j using

$$\mathcal{E}[Y_j] = \int_0^{\infty} K_j(E) \varphi(E) dE \quad (1)$$

A function K_j satisfying this relation is assumed to exist for each detector (or spectrometer channel); this function is called the *response function for detector j* . The value of $K_j(E)$ may be determined for any energy E by measuring using a mono-energetic spectrum; in other words, by selecting $\varphi(\varepsilon) = \delta(\varepsilon - E)$ in Equation 1. Accomplishing this task for arbitrary energies can be difficult experimentally; in any case, response functions are often calculated using Monte Carlo simulations, for which the use of mono-energetic input spectra is trivial. Examples of response functions are shown in Figures 1 and 2. Note that response functions, especially in the case of spectrometers, frequently refer to pulse-height distributions from mono-energetic sources. We eschew this definition and work instead with response functions that represent channel sensitivity, as implied by Equation 1.

The response functions for the detectors are usually employed using an approximation, the purpose of which is to reduce the fluence φ to an element of \mathbb{R}^n for finite n . This approximation is commonly referred to as *discretization*, in spite of the fact that the purpose of the approximation is actually finitization. The procedure used is as follows. Select a basis set $\{u_k, k = 1, \dots, n\}$ and approximate φ with

$$\varphi(E) = \sum_{k=1}^n x_k u_k(E)$$

where $x \in \mathbb{R}^n$, and define the *response matrix* R using

$$R_{jk} = \int_0^{\infty} K_j(E) u_k(E) dE \quad (2)$$

We may then reduce Equation 1 to the form

$$\mathcal{E}[Y] = Rx \quad (3)$$

where Y is now a vector of random variables corresponding to the set of detectors. By far the most ubiquitous method of selecting a basis is to choose delta functions centred at a set of predetermined energies $\{E_k, k = 1, \dots, n\}$, which reduces R to the familiar form

$$R_{jk} = K_j(E_k)$$

The ubiquitous method of discretization is the only one we consider here. We also assume that the basis set has been chosen in such a way as to produce a response matrix of maximum rank.

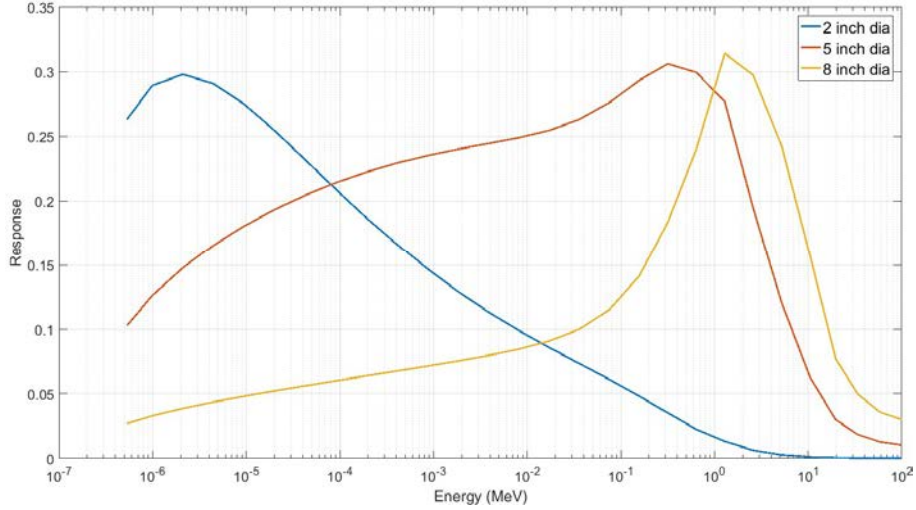


FIG. 1. Response functions for Bonner spheres of different diameters [1].

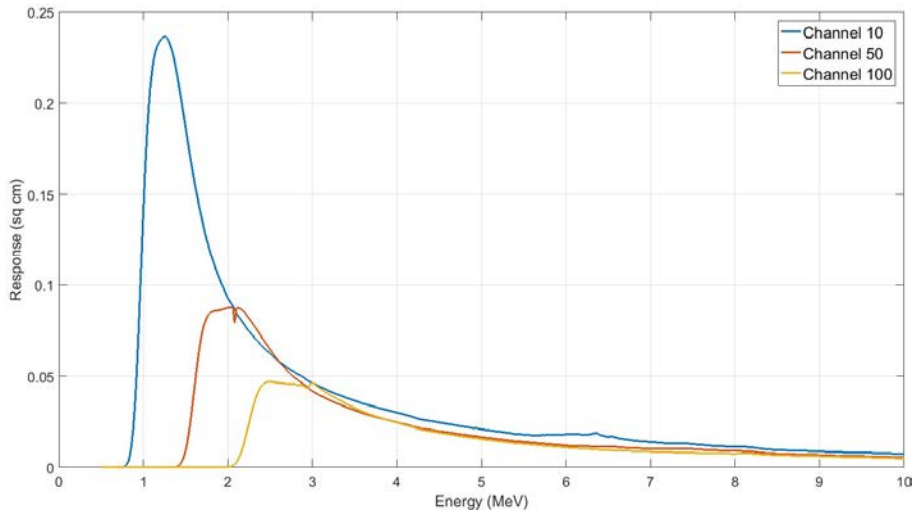


FIG. 2. Response functions for different channels of an NE-213 scintillator. The response functions are in this case dependent on the photomultiplier and electronics, as well as the properties of the scintillator.

Having selected a method of discretization, we have to also be able to determine if one possible discretized spectrum x is better than another possible spectrum. We therefore consider a map $F: \mathbb{R}^n \rightarrow \mathbb{R}$, that maps the discretized spectrum to a real number that quantifies how good the candidate spectrum is. The form of F would ideally take into account the measured data, as well as the expected value of Y given in Equation 3. We may therefore wish to consider F instead as a function mapping x , R , and y to a real number, so that

$$F: \mathbb{R}^n \times \text{Hom}(\mathbb{R}^n, \mathbb{R}^m) \times \mathbb{R}^m \rightarrow \mathbb{R}$$

The aim is to find global maximizers of F , perhaps subject to some constraints. The most general form of this type of unfolding problem is therefore

$$x^* = \underset{x}{\operatorname{argmax}} F(x, R, y) \quad (4)$$

Subject to inequality and equality constraints

$$G(x, R, y) \leq 0, \quad H(x, R, y) = 0$$

Any x satisfying these constraint conditions is called a *feasible point*. In practice, the solution of the unfolding problem is also considerably simplified by the selection of an F that is concave with respect to the spectrum x , and the selection of constraint conditions to produce a convex set of feasible points.

To summarize, there are essentially three steps to devising an unfolding program of this type. One has to select a method of discretization, select an objective function and constraint conditions, and finally decide on a method of solving the resulting optimization problem. We now consider some particular examples of unfolding problems, including maximum likelihood estimation, maximum a posteriori probability, and maximum entropy.

2 MAXIMUM LIKELIHOOD ESTIMATION

The first type of unfolding problem we consider is Maximum Likelihood (ML) estimation, in which the objective function F is set equal to the log-likelihood function, so that

$$F(x, R, y) = \log P(y|R, x) \quad (5)$$

where P is a probability density function. This choice for the objective function is of course subject to Equation 3; namely, if z is a possible outcome of Y , and Ω is the set of possible outcomes, then

$$\int_{\Omega} zP(z|R, x)dz = Rx$$

By choosing F in this manner, we are therefore attempting to maximize the likelihood function with respect to the discretized spectrum x . Naturally, the use of maximum likelihood estimation leads to different methods depending on the type of probability density chosen in Equation 5.

2.1 NORMAL MAXIMUM LIKELIHOOD ESTIMATION

Beginning with the normal distribution, the objective function becomes

$$F(x, R, y) = -(y - Rx)^T \Sigma^{-1} (y - Rx) \quad (6)$$

where Σ is a covariance matrix, often set to be diagonal with entries equal to the variance of y . A non-negativity constraint is frequently applied, in which case F can be maximized using methods in quadratic programming. Solutions to the normal maximum likelihood estimation problem are also called least squares solutions.

If no constraint is applied, then the least squares solution can be trivially written down in explicit form. Since we are assuming that R is of maximum rank, we have to consider only three possibilities. If R is overdetermined,

$$x^* = (R^T \Sigma^{-1} R)^{-1} R^T \Sigma^{-1} y \quad (7)$$

If R is invertible (equivalent to being a square matrix with maximum rank), then the previous equation still holds, but can be further simplified to

$$x^* = R^{-1} y \quad (8)$$

Finally, if R is underdetermined, then x^* is a (non-unique) solution of

$$Rx^* = y \quad (9)$$

One has to therefore use a set of conditions other than maximum likelihood estimation in order to obtain a unique solution in the underdetermined case.

Since, in the absence of constraints, the normal maximum likelihood solution can be written explicitly, we may more easily perform an analysis of its performance from a theoretical point of view. Note that, if x^* is given by Equation 7, then it is an outcome of the random variable X given by

$$X = (R^T \Sigma^{-1} R)^{-1} R^T \Sigma^{-1} Y$$

Furthermore, from Equation 1, the expected value of X is given by

$$\mathcal{E}[X] = \int_0^{\infty} g(E) \varphi(E) dE \quad (10)$$

where

$$g(E) = (R^T \Sigma^{-1} R)^{-1} R^T \Sigma^{-1} K(E) \quad (11)$$

We call g the *sensitivity function* [2], so called because $g(E)$ represents the sensitivity of $\mathcal{E}[X]$ to radiation of energy E . Note that g is vector-valued, with the k^{th} value being the sensitivity of the k^{th} bin in the unfolded spectrum. Some sample sensitivity functions for different bins of an NE-213 scintillator are shown in Figure 3.

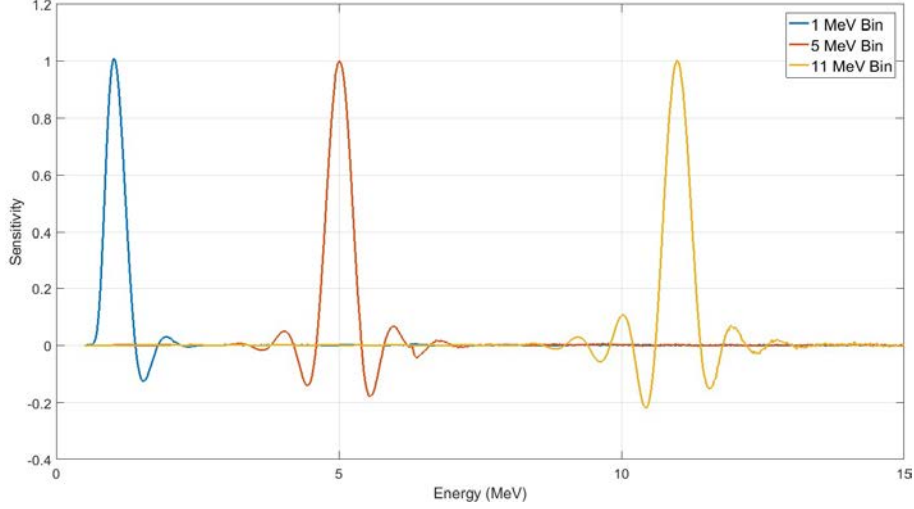


FIG. 3. Sensitivity functions corresponding to three bins of a 48-bin unfolding scheme using an NE-213 scintillator: Note that at the preselected energies used for the discretization, the sensitivity is always either one or zero.

We may now take a known theoretical spectrum, and integrate it using Equation 10. The resulting unfolded spectrum $\mathcal{E}[X]$ represents the unfolded spectrum using unconstrained least squares, in the case where the measurement consists entirely of the expected values of Y . Therefore, the unfolded spectrum should converge to $\mathcal{E}[X]$ as the uncertainty in the measurement becomes small; thus, $\mathcal{E}[X]$ is the ideal unfolded spectrum. Deviations of $\mathcal{E}[X]$ from the theoretical spectrum therefore represent artefacts of the unfolding process due to discretization. Figure 4 illustrates the result of this process for a ^{252}Cf source. For comparison, Figure 5 shows an unfolded spectrum from measured data using a ^{252}Cf source. Note that the artefacts seen at low energy in the expected result (in Figure 4) show up in the unfolded spectrum from the measured data. Additionally, Figure 6 illustrates an unfolded spectrum from measured data using an Am-Be source.

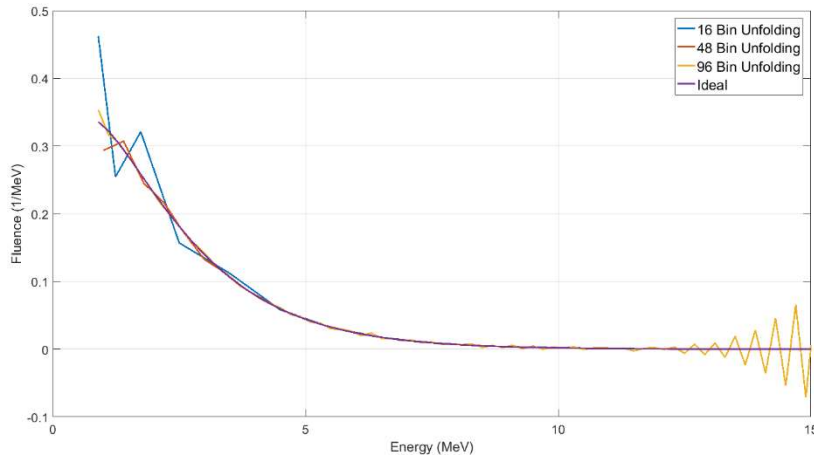


FIG. 4. The predicted unfolded spectrum for ^{252}Cf , assuming an ideal spectrum without statistical fluctuation. The features on the graph are artefacts.

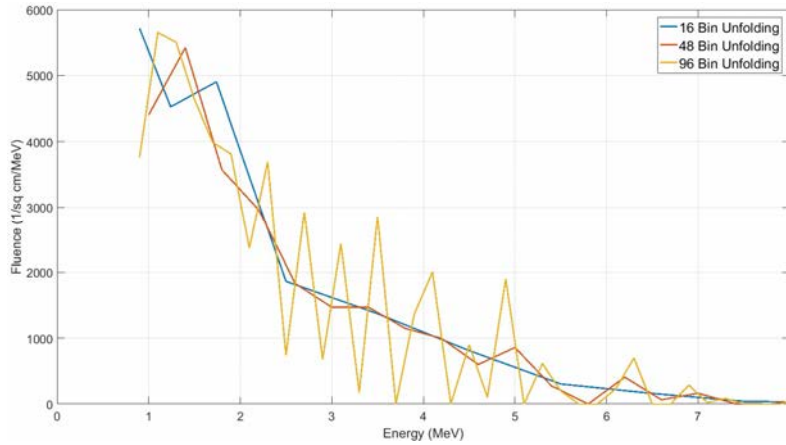


FIG. 5. An unfolded spectrum from a ^{252}Cf measurement. The optimization has been done with a non-negativity constraint. Note that the noise is amplified by moving to a greater number of bins in the unfolded spectrum.

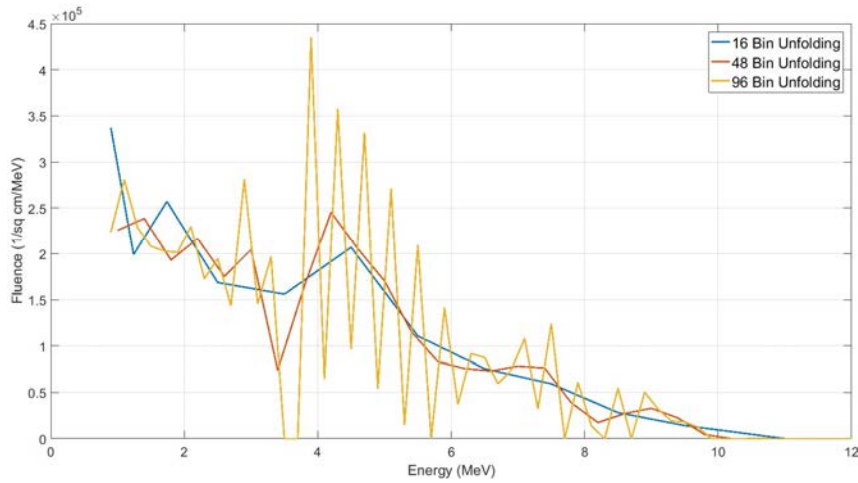


FIG. 6. An unfolded spectrum from an Am-Be measurement, using a non-negativity constraint. Using many bins results in greater noise, whereas a coarse binning is unable to illustrate the features of an Am-Be spectrum effectively.

These two Figures, showing unfolded spectra from ^{252}Cf and Am-Be measurements, also highlight the two chief drawbacks of using normal maximum likelihood estimation. As can be seen, the unfolding is highly susceptible to statistical noise, which is amplified by the unfolding process due to the very large condition number of the response matrix. The result is that one has to bin very coarsely in order to minimize statistical effects, with the result that rather significant artefacts can be introduced to the unfolded spectrum. Naturally, a coarse binning scheme also has the disadvantage of negating the ability to discriminate any finer features in the spectrum that is subjected to this method. To summarize, normal maximum likelihood estimation suffers from noise amplification and artefacts, as well as having no mechanism to deal with underdetermined problems, while its principle advantage is merely its ease of implementation. The choice of normal rather than Poisson statistics is also not theoretically correct, although we will see below that the difference between the two is often negligible.

2.2 POISSON MAXIMUM LIKELIHOOD ESTIMATION

Turning now to Poisson maximum likelihood estimation, the log-likelihood function (and hence the objective function) is given by

$$F(x) = \sum_{j=1}^m \left[y_j \log \left(\sum_{k=1}^n R_{jk} x_k \right) - \sum_{k=1}^n R_{jk} x_k \right]$$

As with normal statistics, if there exists x^* such that $y = Rx^*$, then x^* is a maximizer of F ; however, if R is overdetermined then we employ an iterative approach rather than seeking an explicit solution. One iterative method that can be used for Poisson maximum likelihood estimation is the Maximum Likelihood Expectation Maximization (MLEM) algorithm [3,4]. MLEM begins with an initial guess $x^{(0)}$ and iterates using the relation

$$x_i^{(p+1)} = \frac{\sum_{j=1}^m y_j \frac{R_{ji} x_i^{(p)}}{\sum_{k=1}^n R_{jk} x_k^{(p)}}}{\sum_{j=1}^m R_{ji}} \quad (12)$$

until some convergence criteria is met. Note that a non-negativity condition is implicit in this approach, since if $x_i^{(0)} > 0$ then $x_i^{(p)} > 0$ for all p , and similarly if $x_i^{(0)} = 0$ then $x_i^{(p)} = 0$. Some examples of ^{252}Cf and Am–Be spectra unfolded using MLEM are shown in Figures 7–8.

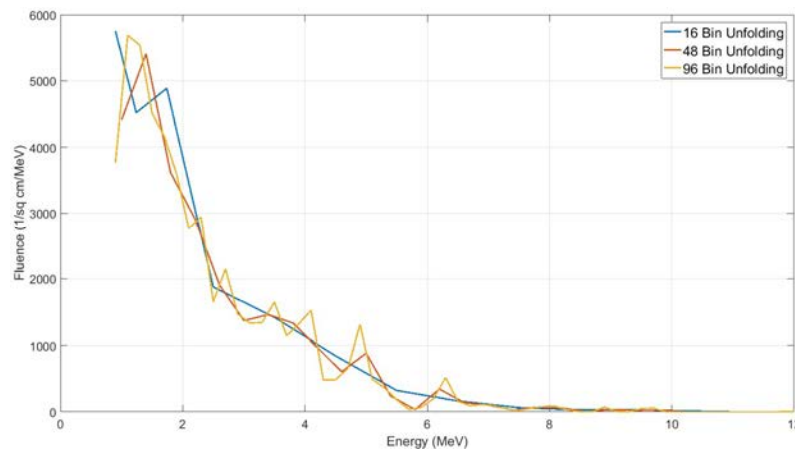


FIG. 7. An unfolded spectrum from a ^{252}Cf measurement. The result shows similar behaviour to unfolding with normal statistics, with the same artefacts and the same tendency towards increasing noise as the binning becomes finer.

As Poisson maximum likelihood estimation is quite similar to normal maximum likelihood estimation, it tends to suffer from the same problems. Namely, as can be seen in Figures 7 and 8, the statistical uncertainty is amplified by the unfolding, and the same discretization artefacts are still visible. In fact, the Poisson unfolded spectra look and behave almost identically to the normal unfolded spectra. Therefore, if the choice of a Poisson statistical model is more correct, then it is a correction that changes very little of importance. Application of the MLEM algorithm to an underdetermined problem will of course be heavily dependent on the choice of an initial guess spectrum, and the behaviour of this algorithm in these situations is not something that we have tested at present.

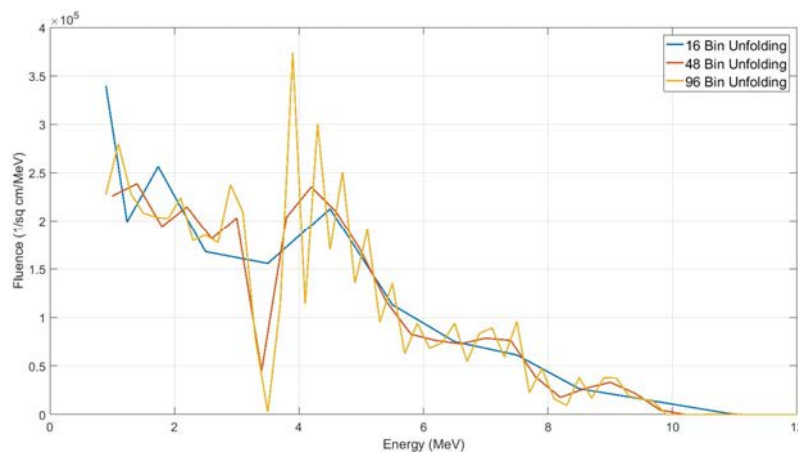


FIG. 8. An unfolded spectrum from an Am–Be measurement. The result illustrates the same behaviour as with normal statistics, particularly regarding the trade-off between features and noise as the binning is refined.

3 MAXIMUM A POSTERIORI PROBABILITY

The two main issues with maximum likelihood estimation are the amplification of statistical noise, and the presence of artefacts. One method of mitigating these problems is to smooth the unfolded spectrum. Another method is to introduce an extra term to the objective function that improves the behaviour of the solution. These latter types of methods are called *regularization* methods, and one approach to formulating them is Maximum A Posteriori Probability, or MAP.

Given measured data y and parameters x , the approach of MAP is to consider x as the outcome of a random variable. Consider Bayes' Theorem

$$P(x|R, y) = \frac{P(y|R, x)P(x)}{P(y, R)} \quad (13)$$

Then we aim to find the most likely value of x given the measurement y , by maximizing $\log P(x|y)$, so that the objective function F becomes

$$F(x, R, y) = \log P(y|R, x) + \log P(x) \quad (14)$$

Here $P(x)$ is called the prior distribution, and $P(x|R, y)$ is called the posterior distribution, which is why the method is called maximum a posteriori probability. This approach is, of course, dependent on the choice of prior distribution, which is selected beforehand.

The choice of prior is supposed to reflect prior knowledge of the spectrum, allowing us to bias the maximum likelihood estimate in favour of one that maximizes $P(x)$. Typically, the prior is selected to encourage a smooth solution. To that end, we use prior distributions of the form

$$\frac{1}{C} \exp(-\lambda \| Ax \|^2) \quad (15)$$

where A is a linear operator, and λ is a positive real number. To enforce a smoothness condition, A could be a difference operator (of first or second order). The ideal choice of parameter x^* now becomes

$$x^* = \underset{x}{\operatorname{argmax}} (\log P(y|R, x) - \lambda x^T A^T A x) \quad (16)$$

In other words, we are maximizing an objective function that is the sum of the log-likelihood function and a regularization term. The parameter λ can then be adjusted to give the regularization different relative weight in the unfolding.

3.1 NORMAL MAXIMUM A POSTERIORI PROBABILITY

If we adopt a log-likelihood function based on a normal statistical model, the optimization problem becomes

$$x^* = \underset{x}{\operatorname{argmax}} \{- (Rx - y)^T \Sigma^{-1} (Rx - y) - \lambda x^T A^T A x\} \quad (17)$$

Typically, a non-negativity constraint is also applied. This problem is an example of Tikhonov regularization [5]. In the unconstrained case, the solution is

$$x^* = (R^T \Sigma^{-1} R + \lambda A^T A)^{-1} R^T \Sigma^{-1} y \quad (18)$$

As with normal maximum likelihood estimation, the constrained solution can be found using quadratic programming. Note also that x^* changes depending on the choice of λ .

Naturally, the introduction of a parameter such as λ that can influence the unfolding necessitates the determination of an 'ideal' value for λ . There are two relatively crude methods of doing so that are immediately obvious. The crudest method is to simply adjust λ experimentally to something that gives reasonable results for some unfolded spectrum. This approach may work well if one is measuring the same or similar spectra, but is likely to result in either oversmoothing or undersmoothing if one then attempts to unfold a different type of spectrum.

The second relatively crude method is to set either the residual term

$$(Rx^* - y)^T \Sigma^{-1} (Rx^* - y)$$

or the regularization term

$$(x^*)^T A^T A x^*$$

equal to some constant value. This approach is equivalent to maximizing whichever term is not fixed, subject to an equality constraint on the term that is fixed, since then λ represents a Lagrange multiplier (or its reciprocal). One could, for example, set the residual term equal to unity, meaning that the deviation of Rx^* from y is set to a single standard deviation. However, the appropriate constraint is $(Rx^* - y)^T \Sigma^{-1} (Rx^* - y) \leq 1$, not an equality constraint, and therefore fixing a term in the objective function can lead to an inappropriate degree of smoothing.

Another approach to determining λ is to examine the so-called L-curve [5]. The L-curve is a plot of the regularization term versus the residual term, as λ changes. In many cases, this curve is roughly L-shaped (hence the name), and since we are attempting to determine λ that keeps both the residual and regularization terms relatively small, the ideal choice of λ is one that corresponds approximately to the corner of the 'L'. One method of selecting the corner is to choose the point of maximum curvature on the L-curve. An example of an L-curve used for unfolding is shown in Figure 9; in this case, A is a second order difference operator.

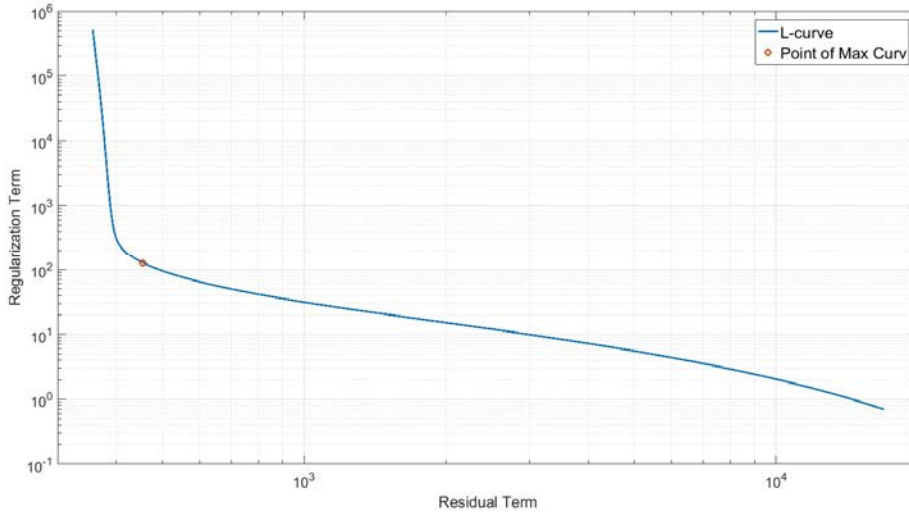


FIG. 9. The L-curve for a ^{252}Cf measurement. The parameter λ has been selected to correspond to the point highlighted in red on the L-curve, which is the point of maximum curvature.

Having selected λ , we may repeat our previous work on sensitivity functions in the context of normal MAP. Defining the random variable X this time as

$$X = (R^T \Sigma R + \lambda A^T A)^{-1} R^T \Sigma^{-1} Y$$

then, as in Equation 10, the expected value of X is

$$\mathcal{E}[X] = \int_0^\infty g(E) \varphi(E) dE$$

where in this case the regularized sensitivity function is given by

$$g(E) = (R^T \Sigma^{-1} R + \lambda A^T A)^{-1} R^T \Sigma^{-1} K(E) \quad (19)$$

Figure 10 shows an example of a sensitivity function for a ^{252}Cf measurement. Unlike maximum likelihood, the experimental data is relevant to the sensitivity function for MAP since it influences the selection of λ , which then impacts the sensitivity. The corresponding predicted unfolded spectrum for ^{252}Cf is shown in Figure 11, and an unfolded spectrum using measured data is shown in Figure 12.

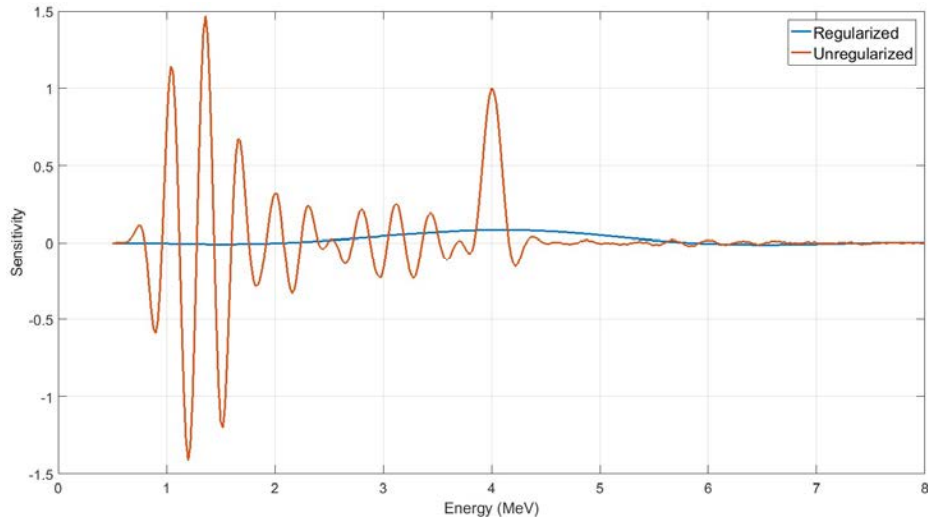


FIG. 10. A sensitivity function for ^{252}Cf unfolding using normal MAP (regularized), compared to a sensitivity function for normal maximum likelihood (unregularized) estimation. The normal ML sensitivity looks much worse than those previously shown due to the much larger number of bins. As can be seen, the regularization employed acts to smooth the spectrum.

Unfortunately, the use of the L-curve for selection of λ is not infallible. In particular, the L-curve method is prone to error when the L-curve is not very 'L'-shaped. As an example, we consider measured data from an Am-Be source. The L-curve for this set of measured data is shown in Figure 13. As can be seen, the shape of the curve is not particularly ideal, and in fact there are three points of local maximum curvature. Use of the point of global maximum curvature unfortunately leads to over-smoothing, whereas use of the other local maxima can begin to show some of the features of the Am-Be spectrum. Unfolded Am-Be spectra are shown in Figure 14.

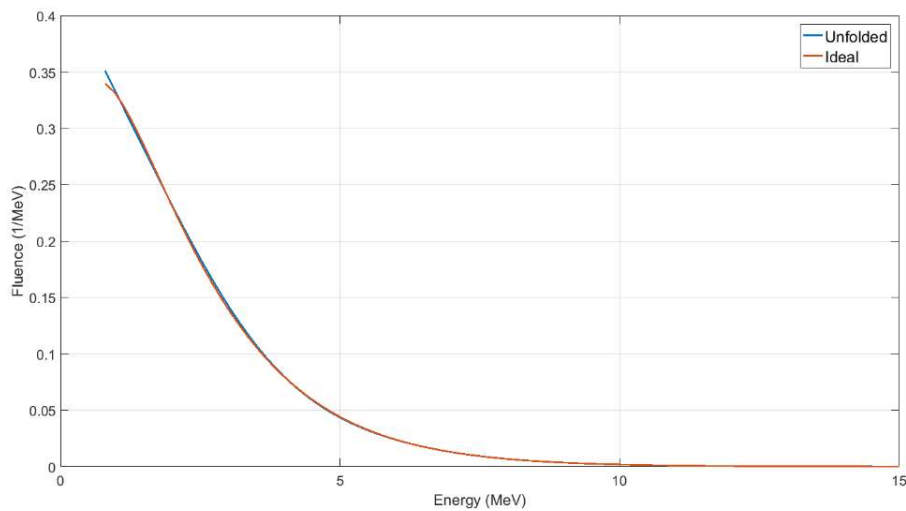


FIG. 11. The predicted unfolded spectrum for ^{252}Cf using normal MAP, assuming an ideal spectrum without statistical fluctuation. Note that the artefacts seen when using normal ML have been smoothed out by the regularization.

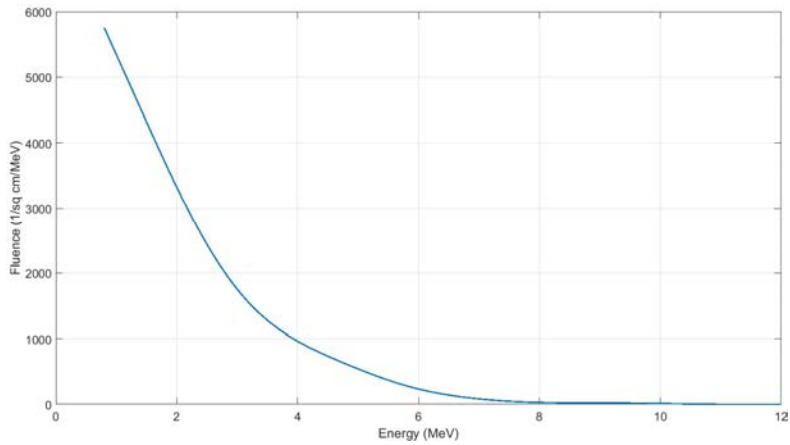


FIG. 12. An unfolded spectrum from a ^{252}Cf measurement using normal MAP. Unlike normal ML, the artefacts and noise have been aggressively smoothed.

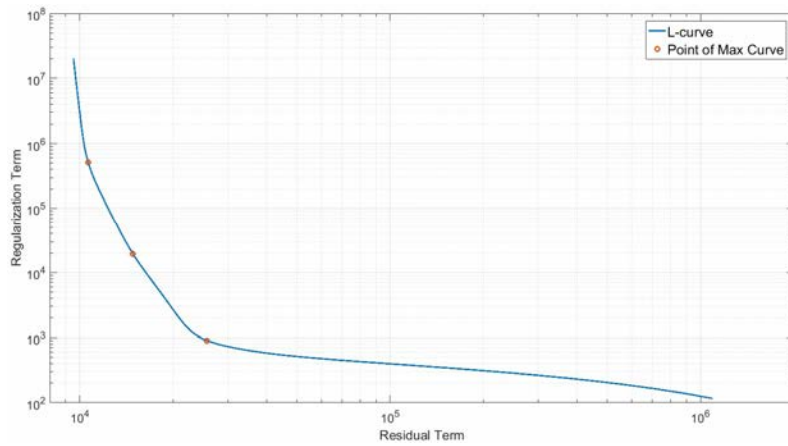


FIG. 13. The L-curve for an Am-Be measurement. The curvature of the L-curve in this case has three local maxima, which are highlighted in red.

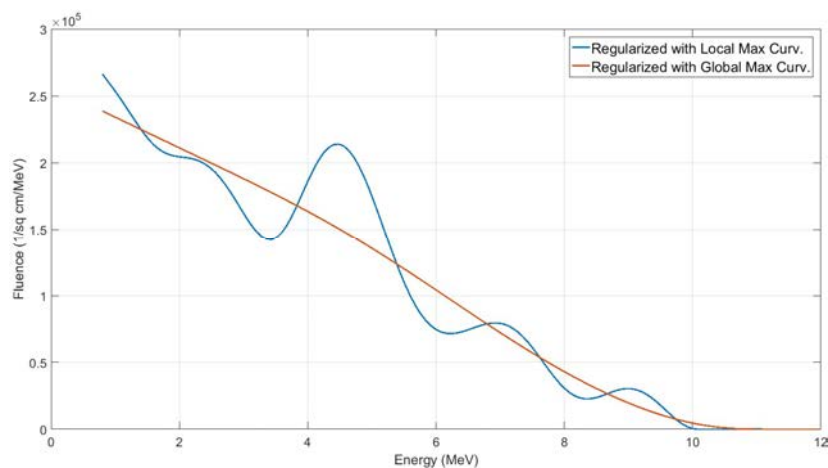


FIG. 14. An unfolded spectrum from an Am-Be measurement using normal MAP. The over-regularized curve uses the point of maximum curvature in order to select λ , whereas if one selects on of the local maxima, some of the features of the Am-Be spectrum become visible.

The chief advantage to regularization using MAP, compared to normal maximum likelihood estimation, is the ability to smooth noise and artefacts. The ability to tackle statistical noise is the chief application of this technique, which has been in use for decades. One may also increase the number of bins in the unfolded spectrum, and count on the regularization to prevent the unfolding problem from becoming singular. However, if the unfolding problem is very under-determined due to a very low number of measurements, then using a smoothness condition to choose an unfolded spectrum may not result in an appropriate answer. Additionally, some care has to be taken to choose an ideal weight for the regularization.

3.2 POISSON MAXIMUM A POSTERIORI PROBABILITY

Using a Poisson statistical approach to the maximum a posteriori probability method yields the following objective function:

$$F(x) = \sum_{j=1}^m \left[y_j \log \left(\sum_{k=1}^n R_{jk} x_k \right) - \sum_{k=1}^n R_{jk} x_k \right] - \lambda x^T A^T A x \quad (20)$$

This objective function is more difficult to optimize using the expectation maximization algorithm than the objective function for Poisson maximum likelihood estimation; we therefore instead use a variant called a Generalized Expectation Maximization (or GEM) algorithm [6]. The operator A has been selected to be a difference operator, which penalizes the difference between the fluence in adjacent bins.

Examples of unfolded spectra using Poisson MAP-GEM are shown in Figure 15 and 16. As with normal MAP, the regularization smooths out statistical noise and artefacts, at the expense of requiring a choice for the weight λ . The number of unfolded bins can still be high, while counting on the regularization to pick a smooth solution. As before, the use of Poisson statistics is expected to have a minimal effect.

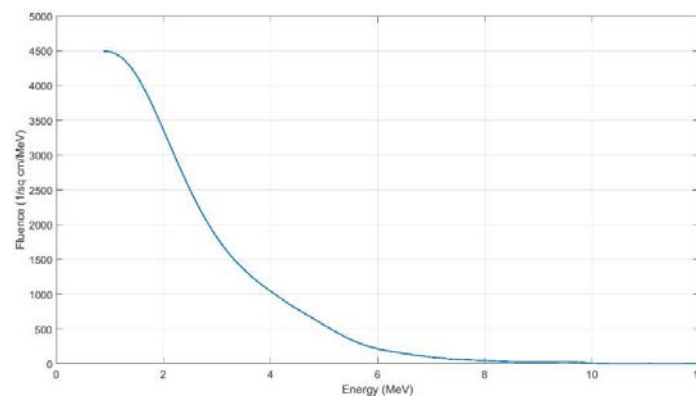


FIG. 15. An unfolded spectrum from a ^{252}Cf measurement, using Poisson MAP-GEM. Similar to the case of normal MAP, the unfolded spectrum exhibits little in the way of artefacts or noise.

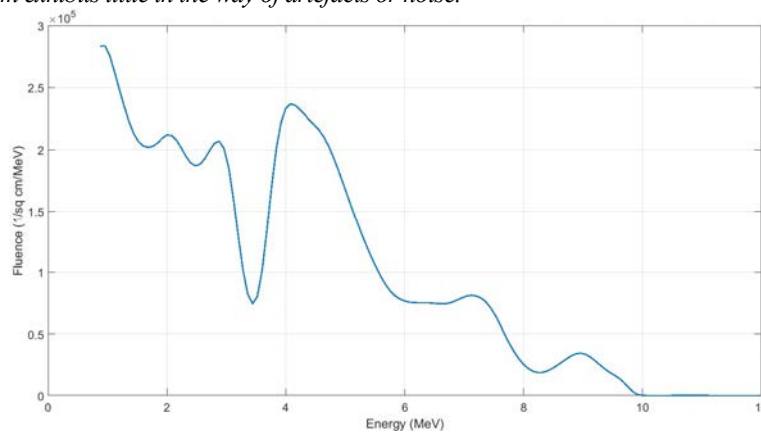


FIG. 16. An unfolded spectrum from an Am-Be measurement, using Poisson MAP-GEM. Again, as in the case of normal MAP, the spectrum is much smoother than the maximum likelihood solution.

4 MAXIMUM ENTROPY

Suppose that we expect the neutron spectrum for a measurement to be close to some known spectrum, and we wish to bias the unfolded spectrum towards this known spectrum. In order to encourage the solution to be closer to the known spectrum, some method of determining how close two spectra are to each other is required. In order to find such a method, one might start with a set of axioms regarding how a method of determining the proximity of two spectra ought to behave [7,8]. One result is to define the functional

$$H(\varphi, \psi) = \int_{\Omega} \left(\varphi(x) \log \frac{\varphi(x)}{\psi(x)} + \psi(x) - \varphi(x) \right) dx$$

which can be regarded as a generalization of Kullback's notion of directed divergence [9]. Here φ and ψ are two different spectra, which are nonzero at the same set of energies. This set of energies, at which the spectra are nonzero, is called the supporting set of φ and ψ , which we denote by Ω . Skilling [8] then defines the *cross entropy* as

$$S(\varphi, \psi) = -H(\varphi, \psi) \quad (21)$$

However, since S is not symmetric, a better definition might be to call S the *cross entropy of φ with respect to ψ* . We then choose ψ to be the prior known spectrum, and maximize S with respect to φ . Note that the measured data is not included in the cross entropy, and is incorporated into the optimization problem using a constraint. In fact, in the absence of this constraint, the maximum entropy solution is $\varphi = \psi$.

Taking into account discretization, the final form of the problem becomes

$$F(x, R, y) = F(x) = - \sum_{k=1}^n \left(x_k \log \frac{x_k}{z_k} + z_k - x_k \right) \quad (22)$$

where z is a discrete form of the prior distribution, subject to the constraint (for normal statistics)

$$(Rx - y)^T \Sigma^{-1} (Rx - y) \leq \kappa^2 \quad (23)$$

where κ is related to the confidence level of the constraint.

One method that has been employed to tackle this optimization problem is to use Lagrange multipliers, which is the approach of unfolding code MAXED [10]. It can be shown that solving the maximum entropy problem with an equality constraint is equivalent to solving

$$\lambda^* = \max_{\lambda \in \mathbb{R}^m} \left\{ - \sum_{k=1}^n \left[z_k \exp \left(\sum_{j=1}^m \lambda_j R_{jk} \right) \right] - \kappa \sqrt{\lambda^T \Sigma^{-1} \lambda} - y^T \lambda \right\} \quad (24)$$

with

$$x_k^* = z_k \exp \left(\sum_{j=1}^m \lambda_j^* R_{jk} \right) \quad (25)$$

We have therefore essentially traded the constrained optimization problem for an unconstrained optimization problem, which can then be solved using some method of nonlinear programming (MAXED uses simulated annealing or pre-conditioned conjugate gradient algorithms, depending on the case).

Unfolded spectra using maximum entropy are shown in Figures 17 and 18. The results look quite good, as they should, since the priors chosen for the unfolding are ideal forms of the source spectra. Ultimately, the maximum entropy method lives or dies based on the quality of the prior, and a poorly chosen prior distribution can produce hideous results. The main advantage of the maximum entropy method is its ability to tackle very underdetermined unfolding problems – as the problem becomes less underdetermined, the constraint condition makes more of an impact on the unfolding, and the choice of prior matters less. In fact, if R is not underdetermined at all, and κ is small, then we are left with the least squares (normal maximum likelihood) solution.

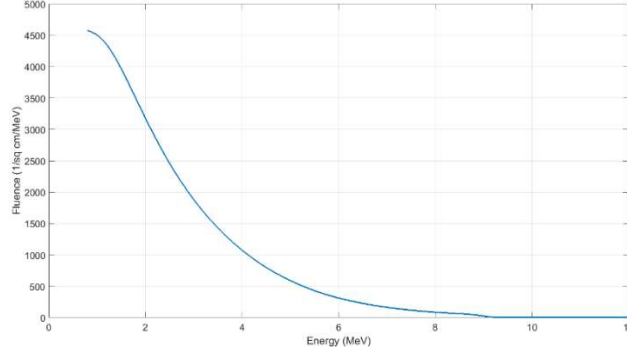


FIG. 17. An unfolded spectrum from a ^{252}Cf measurement, using maximum entropy. A Maxwell–Boltzmann distribution was used as the prior. The spectrum has also been smoothed after unfolding.

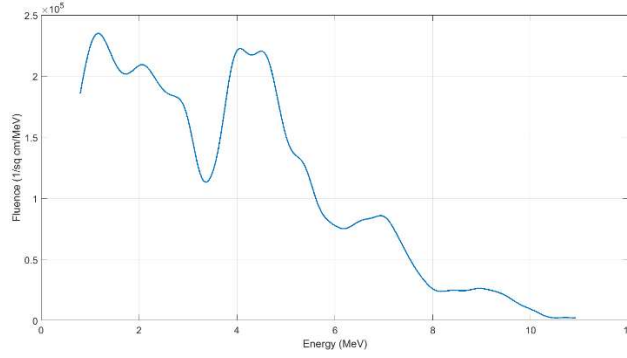


FIG. 18. An unfolded spectrum from an Am–Be measurement, using maximum entropy. The ISO recommended Am–Be spectrum was used as the prior. The spectrum has also been smoothed after unfolding.

5 OTHER METHODS

5.1 FERDOR

The approach of FERDOR [2,11,12] is, rather than solving for the fluence φ directly, to instead estimate the value of

$$\psi(\varphi) = \int_0^{\infty} w(E)\varphi(E)dE \quad (26)$$

where w is a function called a *window function*. While w can, in principle, be any arbitrary function such that the integral in Equation 26 exists, it is typically selected to smooth the solution. For this reason, the usual choice of w is a normal distribution.

Now, we may use a linear combination of the response functions to bound w , so that

$$\sum_{j=1}^m u_j^{\text{lo}} K_j(E) \leq w(E) \leq \sum_{j=1}^m u_j^{\text{up}} K_j(E) \quad \forall E \quad (27)$$

Integrating Equation 27 with φ , and taking advantage of Equation 1, results in

$$(u^{\text{lo}})^T \mathcal{E}[Y] \leq \psi(\varphi) \leq (u^{\text{up}})^T \mathcal{E}[Y]$$

Assuming that Y is a normal random variable, it follows that

$$(u^{\text{lo}})^T y - \kappa \sqrt{(u^{\text{lo}})^T \Sigma (u^{\text{lo}})} \leq \psi(\varphi) \leq (u^{\text{up}})^T y + \kappa \sqrt{(u^{\text{up}})^T \Sigma (u^{\text{up}})}$$

where y is the data (as usual), Σ is the covariance of y , and κ is selected to achieve a confidence level that ψ lies within the interval.

Now we wish to choose u^{lo} and u^{up} to provide the narrowest possible bounds for ψ . Therefore, we define

$$\psi^{\text{lo}} = \max_{u \in \mathbb{R}^m} \{u^T y - \kappa \sqrt{u^T \Sigma u} \mid u^T K(E) \leq w(E) \forall E\} \quad (28)$$

and

$$\psi^{\text{up}} = \min_{u \in \mathbb{R}^m} \{u^T y + \kappa \sqrt{u^T \Sigma u} \mid u^T K(E) \geq w(E) \forall E\} \quad (29)$$

so that

$$\psi^{\text{lo}} \leq \psi(\varphi) \leq \psi^{\text{up}} \quad (30)$$

with confidence determined by κ . The aim of FERDOR is to solve for ψ^{lo} and ψ^{up} . FERDOR is therefore a technique that is developed using probability theory with normal statistics, though not conventionally portrayed as a maximum likelihood problem. Note as well that no approximations regarding discretization have been made in Equations 28 and 29, and in fact the confidence interval has been constructed in such a way as to take into account the difficulty of approximating the window function with response functions.

Of course, the optimization problems in Equations 28 and 29 are not as easy to solve as they could be, and FERDOR therefore makes a handful of approximations in order to work instead with a set of problems that is more tractable. The first approximation made is regarding discretization. We test the inequality constraint in the optimizations only at a finite number of points, and assume that these points are sufficiently close together to accurately capture the behaviour of the window and response functions. Therefore, Equation 27 is replaced with

$$(u^{\text{lo}})^T R \leq w \leq (u^{\text{up}})^T R$$

Here w is a vector, with entries given by $w(E_k)$, where E_k are energies selected for the discretization of the response matrix R . The new discretized optimization problems are therefore

$$\psi^{\text{lo}} = \max_{u \in \mathbb{R}^m} \{u^T y - \kappa \sqrt{u^T \Sigma u} \mid u^T R \leq w\} \quad (31)$$

and

$$\psi^{\text{up}} = \min_{u \in \mathbb{R}^m} \{u^T y + \kappa \sqrt{u^T \Sigma u} \mid u^T R \geq w\} \quad (32)$$

with the confidence interval still given by Equation 30.

Now, the discretized optimization problems are still inconvenient to use, and therefore we invoke a modified version of Wolfe duality [2,12]. The dual problems are

$$\psi^{\text{lo}} = \min_{x \in \mathbb{R}^n} \{w^T x \mid (Rx - y)^T \Sigma^{-1} (Rx - y) \leq \kappa^2, x \geq 0\} \quad (33)$$

and

$$\psi^{\text{up}} = \max_{x \in \mathbb{R}^n} \{w^T x \mid (Rx - y)^T \Sigma^{-1} (Rx - y) \leq \kappa^2, x \geq 0\} \quad (34)$$

These dual optimization problems are now linear programming problems, subject to an elliptical and a non-negativity constraint.

The FERDOR method, however, makes further approximations with respect to the dual formulation, with the aim of producing a problem with an explicit solution. In particular, the constraint region of the dual problems is inconvenient to work with, since its boundary is usually not differentiable due to the non-negativity constraint. We therefore relax the non-negativity constraint by approximating it with a second elliptical constraint. Set

$$q_k = \min_{1 \leq j \leq m} \left\{ \frac{y_j + \kappa \sigma_j}{R_{jk}} \right\}, \quad 1 \leq k \leq m$$

where σ_j is the j^{th} diagonal element of Σ . We call the set of points x satisfying $0 \leq x \leq q$ the Q-box. Note that the feasible set for the dual formulation lies within the Q-box. We may therefore replace the non-negativity constraint with $0 \leq x \leq q$. We now replace the Q-box with the smallest ellipse containing the Q-box, called the Q-ellipse,

and finally take a convex combination of the original constraint ellipse with the Q-ellipse. The final feasible region therefore becomes

$$\frac{1}{\tau^2 + \kappa^2} \left[(Rx - y)^T \Sigma^{-1} (Rx - y) + \frac{\tau^2}{n} (x - p)^T Q^{-2} (x - p) \right] \leq 1 \quad (35)$$

where $Q = \text{diag}(p)$ with $p = \frac{q}{2}$, and n is the dimension of the problem (equal, as usual, to the number of energies used for the discretization). This constraint acts as a compromise between the Q-ellipse (itself representing a relaxed non-negativity condition), and the original constraint ellipse. The parameter τ plays the role of a weight, in choosing how much the Q-constraint matters compared to the original elliptical constraint. A sample geometry of the various constraint regions is shown in Figure 19.

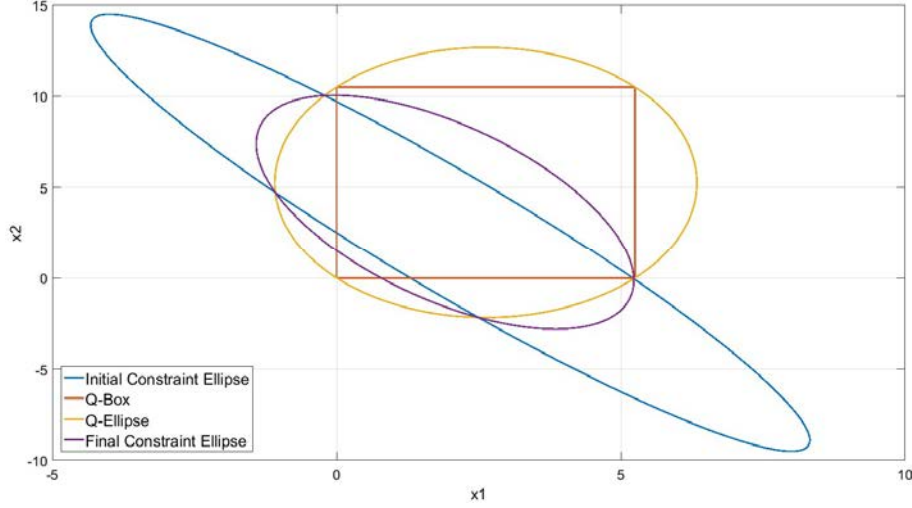


FIG. 19. A typical geometry for a 2-dimensional unfolding problem. Note how the Q-box contains the original constraint ellipse in the first quadrant.

The dual optimization problems, subject to the simplified constraint condition in Equation 35, can be solved using Lagrange multipliers. The solution is

$$\psi^{\text{lo}} \geq w^T \tilde{x} - \left(\sqrt{\tau^2 + \kappa^2} - \rho \right) \sqrt{w^T \left(R^T \Sigma^{-1} R + \frac{\tau^2}{n} Q^{-2} \right)^{-1} w} \quad (36)$$

and

$$\psi^{\text{up}} \leq w^T \tilde{x} + \left(\sqrt{\tau^2 + \kappa^2} - \rho \right) \sqrt{w^T \left(R^T \Sigma^{-1} R + \frac{\tau^2}{n} Q^{-2} \right)^{-1} w} \quad (37)$$

where

$$\tilde{x} = \left(R^T \Sigma^{-1} R + \frac{\tau^2}{n} Q^{-2} \right)^{-1} \left(R^T \Sigma^{-1} y + \frac{\tau^2}{n} Q^{-2} p \right) \quad (38)$$

and

$$\rho = (R\tilde{x} - y)^T \Sigma^{-1} (R\tilde{x} - y) + \frac{\tau^2}{n} (\tilde{x} - p)^T Q^{-2} (\tilde{x} - p) \quad (39)$$

Some examples of unfolded spectra using FERDOR are shown in Figures 20 and 21. Of note is the fact that the amount of smoothing, as determined by the width of the window functions, is problem-dependent—a feature that FERDOR has in common with regularization-based methods. The original approach of FERDOR was simply to pick a width to the window functions and live with the consequences; other implementations have endeavoured to adjust the amount of smoothing in order to meet a pre-determined level of uncertainty for each ψ [13]. In any case, FERDOR attempts to deal with the problems of artefacts and poor conditioning by smoothing with window functions, and is therefore a more robust method than maximum likelihood estimation.

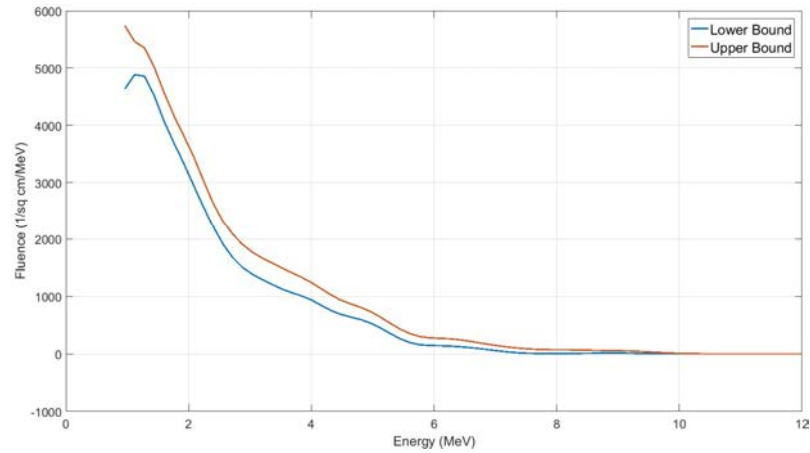


FIG. 20. An unfolded spectrum from a ^{252}Cf measurement, using FERDOR. The window functions are normal distributions with standard deviation corresponding to triple the instrument resolution, with $\kappa = 3$, and $\tau = 0.1$.

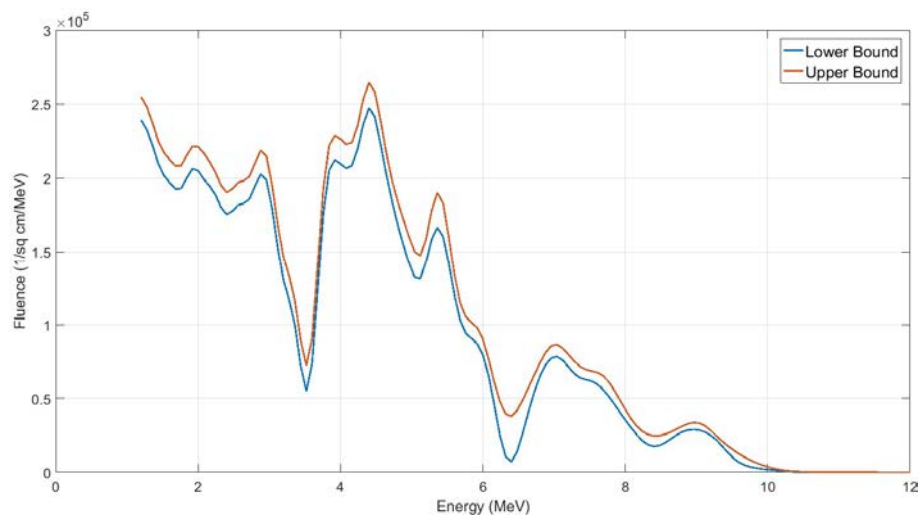


FIG. 21. An unfolded spectrum from an Am–Be measurement, using FERDOR. The window functions are normal distributions with standard deviation corresponding to the instrument resolution, with $\kappa = 3$ and $\tau = 0.1$.

5.2 ITERATIVE METHODS

One class of methods that has commonly been used to tackle unfolding problems (esp. very under-determined problems), are so-called iterative methods. In general, these methods are quite ubiquitous, and it may seem somewhat disingenuous to treat them separately when they are used as part of most of the previously mentioned unfolding methods (quadratic programming for constrained least squares, MLEM, MAP-GEM, PCG and simulated annealing are all iterative methods, or classes of iterative methods, that have been previously mentioned). However, two applications of iterative methods to unfolding are worth mentioning, and we will also cover a class of iterative methods that has seen historical use for neutron spectral unfolding.

One use of iterative methods is related to regularization. An observation that has been made in the past, is that the unfolded spectrum after a low number of iterations is relatively free of noise, whereas the amount of noise in the unfolded spectrum becomes much greater as the iterations converge. Certain authors have remarked upon this behaviour [14], with some advocating the practice of terminating the iterations early in order to suppress statistical noise. However, determining the ideal termination point leads to a similar problem to finding the regularization parameter in MAP-style problems, and any algorithm that simply terminates early at a pre-designated point has to therefore be *ad hoc*.

Also of interest is the use of iterative methods to tackle very under-determined problems. The typical procedure is similar in some ways to the maximum entropy method, in which one uses an initial guess, or prior, spectrum. An iterative approach to the under-determined problem, rather than setting up an objective function to choose between different solutions that are consistent with the measurement (as the maximum entropy method does), instead uses the prior as the initial spectrum for the iteration, and iterates until $y = Rx$. The assumption is that, if the prior is reasonably close to the actual spectrum, then the iterations will merely tweak unfolded spectrum to make it more consistent with the measured data. One class of methods that has been used to solve $y = Rx$, subject to a non-negativity constraint, is as follows. Let $x^{(l)}$ be the (discretized) unfolded spectrum after l iterations, and set

$$A_j^{(l)} = \frac{y_j}{\sum_{k=1}^n R_{jk} x_k^{(l)}}$$

Then the iterations are defined by

$$x_k^{(l+1)} = x_k^{(l)} \Theta^{-1} \left(\frac{1}{\sum_{j=1}^m W_{jk}^{(l)}} \sum_{j=1}^m W_{jk}^{(l)} \Theta(A_j^{(l)}) \right) \quad (40)$$

where Θ is an invertible function, and the $W_{jk}^{(l)}$'s represent weights, which may change with each iteration. It is not our intention to delve into the properties that Θ and W have to have in order for the iterations in Equation 40 to be useful as an unfolding algorithm, but merely to introduce two different implementations—SPUNIT [15,16] (used by the BUNKI code) and SAND II [17].

If, in Equation 40, Θ is the identity map and $W_{jk}^{(l)} = \frac{R_{jk}}{y_j}$, then we have the SPUNIT algorithm. Doroshenko, et al. [16], in their article in which they introduce this algorithm, introduce it as a method based on information theory. This assertion is misleading. The approach is to compare two distributions using directed divergence (or what we have previously termed cross entropy). The two distributions that are compared are the measured response, and the expected response given the current estimate of the unfolded spectrum. The conclusion is that the unfolded spectrum from which the measured data diverges the least is a solution of $y = Rx$, and most of the effort in the article is expended pursuing this solution. SPUNIT is therefore not based on information theory in the same sense as the maximum entropy method discussed previously.

Similarly, SAND II uses the logarithm for Θ , and weights defined by

$$W_{jk}^{(l)} = \frac{R_{jk} x_k^{(l)} + R_{j(k-1)} x_{k-1}^{(l)}}{2 \sum_{i=1}^n R_{ji} x_i^{(l)}}, k = 2, \dots, n$$

and

$$W_{j1}^{(l)} = \frac{R_{j1} x_1^{(l)}}{\sum_{k=1}^n R_{jk} x_k^{(l)}}$$

$$W_{j(n+1)}^{(l)} = \frac{R_{jn} x_n^{(l)}}{\sum_{k=1}^n R_{jk} x_k^{(l)}}$$

Unfolded spectra using SPUNIT and SAND-II are shown in Figures 22 and 23.

The iterative methods shown here are designed for application to problems similar to those for which maximum entropy is intended. Overall, the unfolded spectra from the maximum entropy approach appear to better reflect the expected unfolded spectra for the sources used in the measurements, at least in the case of an NE-213 scintillator. Maximum entropy also offers a quantitative way of comparing how close a spectrum is to the prior, something which could be lacking in the formulation of iterative methods based on Equation 40.

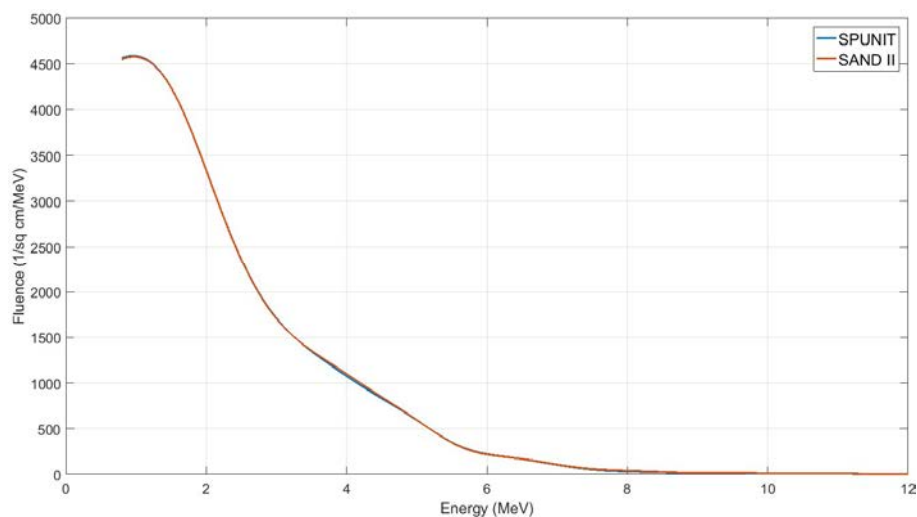


FIG. 22. An unfolded spectrum from a ^{252}Cf measurement, using SAND II and SPUNIT. The unfolded spectrum has been smoothed.

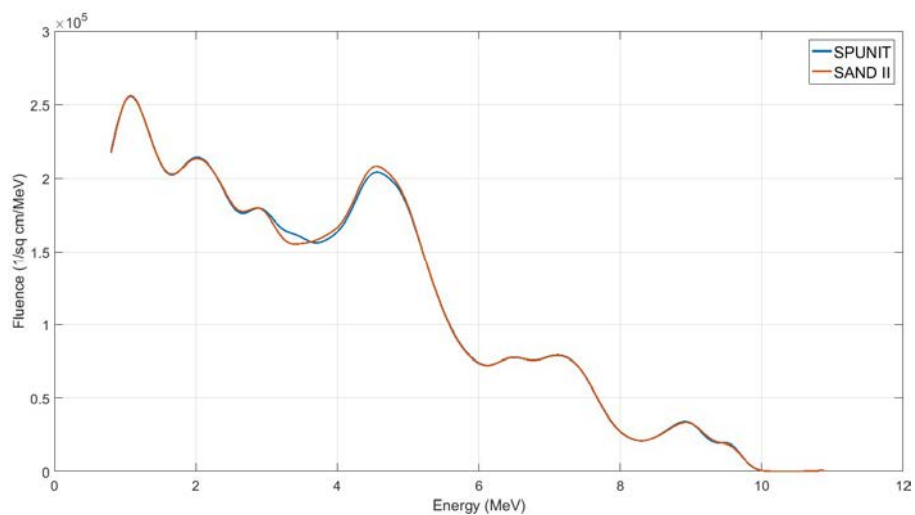


FIG. 23. An unfolded spectrum from an Am-Be measurement, using SAND II and SPUNIT. The unfolded spectrum has been smoothed.

6 CONCLUSIONS

To summarize, the simplest method to implement for an over-determined (or exactly determined) problem is maximum likelihood estimation, either normal or Poisson, with normal being a more trivial method than Poisson. However, maximum likelihood methods tend to suffer from large statistical errors in the unfolded spectrum due to the poor conditioning of the response matrix, as well as being unable to cope with artefacts introduced due to

discretization. In fact, one may have difficulty ascertaining whether the features in such an unfolded spectrum are actually real.

The typical method of dealing with these drawbacks is to smooth. We have covered two methods of smoothing that can be used to deal with poor conditioning and artefacts—regularization and window functions. These approaches, however, add a second problem—namely, deciding on the degree of smoothing required. The ideal amount of smoothing is barely sufficient to erase the idiosyncrasies of the maximum likelihood estimate, without smoothing more, so as to preserve as much as possible the characteristics of the unfolded spectrum. Unfortunately, automating the selection of the ideal level of smoothing, in a fashion that works in all cases, is nontrivial.

In order to tackle under-determined unfolding problems, two types of techniques have been discussed – maximum entropy and iterative methods. Of these methods, maximum entropy is recommended due to its more rigorous approach to the unfolding problem.

REFERENCES

- [1] AWSCHALOM, M., SANNA, R.S., Applications of Bonner Sphere detectors in neutron field dosimetry, *Radiat. Prot. Dosimetry* **10** 1–4 (1985) 89–101.
- [2] BURRUS, W.R., “Utilization of A Priori Information by Means of Mathematical Programming in the Statistical Interpretation of Measured Distributions”, Oak Ridge National Lab. Report ORNL-3743 (1965).
- [3] DEMPSTER, A.P., LAIRD, N.M., RUBIN, D.B., Maximum likelihood from incomplete data via the EM algorithm, *J. Royal. Statist. Soc. B (Methodol.)* **39** 1 (1977) 1–38.
- [4] SHEPP, L.A., VARDI, Y., Maximum likelihood reconstruction for emission tomography, *IEEE Trans. Med. Imaging* **1** 2 (1982) 113–122.
- [5] HANSEN, P.C., O’LEARY, D.P., The use of the L-Curve in the regularization of discrete ill-posed problems. *SIAM J. Sci. Comput.* **14** 6 (1993) 1487–1503.
- [6] HEBERT, T., LEAHY, R., A generalized EM algorithm for 3-D Bayesian reconstruction from Poisson data using Gibbs priors. *IEEE Trans. Med. Imaging* **8** 2 (1989) 194–202.
- [7] SHORE, J.E., JOHNSON, R.W., Axiomatic derivation of the principle of maximum entropy and the principle of minimum cross-entropy. *IEEE Trans. Inf. Theory* **26** 1 (1980) 26–37.
- [8] SKILLING, J., “Classical Maximum Entropy”, *Maximum Entropy and Bayesian Methods*. Springer, Dordrecht, Netherlands (1989), ISBN: 978-0-7923-0224-7.
- [9] KULLBACK, S., *Information Theory and Statistics*. Dover, New York, USA (1968).
- [10] REGINATTO, M., GOLDHAGEN, P., MAXED, A computer code for maximum entropy deconvolution of multisphere neutron spectrometer data, *Health Phys.* **77** (1999) 579–583.
- [11] RUST, B.W., BURRUS, W.R., “Suboptimal Methods for Solving Constrained Estimation Problems”, *Tennecomp Systems Report TPR-0145, DASA 1604* (1971).
- [12] RUST, B.W., BURRUS, W.R., *Mathematical Programming and the Numerical Solution of Linear Equations*. Elsevier, New York, USA (1972), ISBN: 0-444-00119-0.
- [13] JOHNSON, R.H., WEHRING, B.W., “The FORIST Unfolding Code”, *A Review of Radiation Energy Spectra Unfolding*, Oak Ridge National Lab. ORNL/RSIC-40 (1976) 33–39.
- [14] VEKLEROV, E., LLACER, J., Stopping rule for the MLE algorithm based on statistical hypothesis testing, *IEEE Trans. Med. Imaging* **6** 4 (1987) 313–319.
- [15] MILLER, S.C., Thesis: AFITBUNKI: A Modified Iterative Code to Unfold Neutron Spectra from Bonner Sphere Detector Data, Air Force Institute of Technology (1993).
- [16] DOROSHENKO, J.J., et al., New methods for measuring neutron spectra with energy from 0.4 eV to 10 MeV by track and activation detectors, *Nucl. Technol.* **33** 3 (1977) 296–304.
- [17] MCELROY, W.N., BERG, S., CROCKETT, T., A Computer-Automated Iterative Method for Neutron Flux Spectra Determination by Foil Activation, Air Force Weapons Lab Report AFWL-TR-67-71, Vol. 1 (1967)

NEUTRON SPECTRUM ADJUSTMENT AND CROSS-SECTION VALIDATION ACTIVITIES AT THE JOŽEF STEFAN INSTITUTE

V. RADULOVIĆ, B. KOS, A. TRKOV, L. SNOJ

Jožef Stefan Institute

Jamova 39

1000 Ljubljana

Slovenia

Abstract: This paper presents the recent activities at the Jožef Stefan Institute in neutron spectrum characterization and cross-section validation using the GRUPINT spectrum adjustment code, developed at the Jožef Stefan Institute (JSI) in Ljubljana, Slovenia. GRUPINT is a complex code package, which was originally developed for the calculation of constants relevant to Neutron Activation Analysis (NAA) from neutron spectra and cross sections in standard SAND-II 640 energy group structure. Over time the original code has been extensively upgraded and numerous features have been added, such as the fitting of input neutron spectra obtained from Monte Carlo calculations with an analytical expression and fitting the function parameters to measured reaction rate ratios. Results of a recent study aimed at determining the applicability of boron nitride filters to shift the sensitivity of a particular set of capture reactions to the epithermal range, for neutron spectrum characterization and cross-section validation, are presented. Finally, an application of the GRUPINT code to Bonner Sphere Spectrometry in the framework of a recent EURADOS intercomparison exercise, is described.

1 INTRODUCTION

Accurate knowledge of the neutron spectrum inside irradiation channels in nuclear reactors and around various irradiation facilities is necessary for integral nuclear cross-section measurements and validation in support of experimental campaigns (primarily in research reactors and around neutron sources) and neutron fluence determination (primarily around nuclear power plants). Moreover, it allows for the verification and validation of computational methods, in particular Monte Carlo particle transport codes (e.g. MCNP [1], TRIPOLI [2], etc.), which are extensively used for the characterization of radiological properties of irradiation facilities. Therefore, considerable effort has been dedicated to the development of codes which adjust neutron spectra based on a priori information, to sets of measurements - reaction rates or Bonner sphere signals. There are numerous adjustment (unfolding) codes in existence, mostly based on Least Squares algorithms [3–5]. Over the last decade, adjustment codes based on neural networks have gained considerable popularity [6–9]. To our knowledge there are only two unfolding codes based on the parametrization of the neutron spectrum with an analytical function: FRUIT [10], a code designed to unfold the neutron spectrum from measurements with Bonner spheres, and GRUPINT for classical dosimetry measurements.

This paper presents the GRUPINT neutron spectrum adjustment code, developed at the Jožef Stefan Institute (JSI) in Ljubljana, Slovenia. GRUPINT is a complex code package, which was originally developed for the calculation of constants relevant to Neutron Activation Analysis (NAA) from neutron spectra and cross sections in standard SAND-II 640-energy group structure. Over time the original code has been extensively upgraded and numerous features have been added. The neutron spectrum in GRUPINT is parametrized by an analytical function based on physical models, described by a maximum of 19 parameters. The parameters of the analytic function can be fitted by GRUPINT, firstly to reproduce input spectra from Monte Carlo calculations and secondly, to adjust the neutron spectra, on the basis of sets of measured reaction rate ratios or ratios of the same reaction rate, bare and under cover (e.g. Cd-ratios). Another important feature of the GRUPINT code is the possibility of generation of the neutron spectrum covariance matrix through a Monte Carlo algorithm, in which selected parameters of the analytic function are sampled uniformly and the covariances are computed by definition. The covariance matrix thus generated is one of the inputs for a final adjustment step using the ZOTT99 code [11], implemented into GRUPINT, which yields physical uncertainties and correlations in the neutron spectrum.

The first part of the paper details the general features of the code, in particular the implemented function used to parametrize the neutron spectrum and the code fitting abilities. The process of fitting a typical input neutron spectrum is presented for the spectrum in the Central Channel (CC) of the JSI TRIGA reactor. The second part of the paper focuses on the characterization of the spectra in three irradiation channels of the JSI TRIGA reactor with different spectral characteristics, based on measured reaction rate ratios for nuclear reactions with well-known cross-sections. Subsequently the validation of the nuclear data for a selection of nuclear reactions is presented.

The final part of the paper presents the results obtained using the GRUPINT code in the context of a recent Bonner sphere spectrometry unfolding exercise organized by EURADOS.

2 THE GRUPINT CODE

GRUPINT is a complex code package whose primary purpose was the calculation of constants relevant to Neutron Activation Analysis (NAA) from input neutron spectra and cross-section libraries in 640-energy group structure. The constants are as follows: σ_0 (cross section value at 0.0253 eV), I (resonance integral), F_{Cd} (cadmium transmission factor), g (generalized Westcott g-factor), σ_{th} (thermal spectrum averaged cross section) and σ_f (fission spectrum averaged cross section).

These capabilities of the GRUPINT code have been exploited in the past in the context of NAA [12] for the assessment of capture cross-sections from evaluated nuclear data files [13] and for the experimental determination of activation constants for the $^{27}Al(n, \gamma)$ reaction [14], taking into account the fission spectrum contribution to the reaction rate.

The first version of the code dates back to April 2000. Over time the code has been developed extensively and has become a versatile package which, in addition to its original purpose, allows the user to parametrize the neutron spectrum with an analytic function, fit the analytic function parameters to general input neutron spectra (e.g. obtained by Monte Carlo calculations) by the Least-Squares method, adjust the neutron spectrum parameters in order to best reproduce a set of measured reaction rate ratios (or cadmium ratios), by the Least-Squares method and to generate neutron spectrum covariance matrices by the Monte Carlo method.

2.1 NEUTRON SPECTRUM PARAMETRIZATION

The neutron spectrum is parametrized by an analytic function, defined by a 19 possible parameters. It consists of three terms: the thermal (Ψ_t), epithermal (Ψ_e) and fast term (Ψ_f). The thermal term Ψ_t is defined as:

$$\Psi_t = C_t E^l \left[e^{-\frac{E}{kT}} + C_{t1} e^{-\frac{E}{kT_1}} + C_{t2} e^{-\frac{E}{kT_2}} \right], \quad (1)$$

where C_t is a normalization constant, which ensures continuity and k is the Boltzmann constant. The term is a superposition of three Maxwellian distributions, the main Maxwellian around temperature T and two distributions around temperatures T_1 and T_2 , usually of far lesser magnitude (controlled by the constants C_{t1} and C_{t2}) which allow for an adequate representation of possible distortions in the upper thermal region. The superposition is multiplied by an E^l term, where l is the thermal slowing-down parameter.

The epithermal term Ψ_e is defined by three slope parameters, as:

$$\Psi_e = E^{-[1+\alpha_0+\alpha_1 \log(E)+\alpha_2(\log(E))^2]}, \quad (2)$$

where α_0 gives the general deviation of the spectrum from pure $\frac{1}{E}$ behaviour, the higher order terms α_1 and α_2 , multiplied by $\log(E)$ and $(\log(E))^2$, account for distortions in the epithermal part of the spectrum.

The fast part can be modelled either by a Watt distribution (with parameters W_a and W_b), multiplied by a slowing-down term or a Maxwellian distribution around energy E_f , again multiplied by a slowing-down term:

$$\Psi_f = \begin{cases} C_f e^{-\frac{E}{W_a}} \sinh(\sqrt{EW_b}) \frac{1}{E^{m_0+m_1 E}} \\ C_f \sqrt{E} e^{-\frac{E}{E_f}} \frac{1}{E^{m_0+m_1 E}}, \end{cases} \quad (3)$$

where C_f is a normalization constant which ensures continuity. The complete spectrum is a weighted sum of the three terms:

$$\Phi = K_t \Psi_t + K_e \Psi_e + K_f \Psi_f, \quad (4)$$

where the parameters K_t , K_e and K_f defined as follows:

$$K_e = \begin{cases} 1 & \text{for } E_t < E < E_f \\ 0 & \text{otherwise} \end{cases} \quad (5)$$

$$K_t = 1 + O_t - K_e$$

$$K_f = 1 + O_f - K_e$$

The parameters E_t and E_f are the thermal and fast region energy breakpoints, O_t and O_f are the thermal and the fast overlap parameters, which determine the fractions of the thermal and fast contributions above E_t and below E_f , respectively.

The fitting algorithm in the GRUPINT code is based on a direct search for a minimum of a functional by a systematic variation of parameters, one at a time, one after another. The parameters which can be fitted in the GRUPINT code are: $E_t, E_f, \alpha_0, \alpha_1, \alpha_2, O_t, O_f, W_a, W_b, l, m_0, m_1, T, C_{t1}, T_1, C_{t2}, T_2$. The normalization constants C_t and C_f , which ensure continuity between the different energy regions of the spectrum are computed automatically.

2.2 FITTING OF THE SPECTRUM PARAMETERS – INPUT SPECTRUM

This section serves as an illustration of the meaning of the parameters of the analytical function used to parametrize the neutron spectrum and to demonstrate the fitting capabilities of GRUPINT. The starting point is an input neutron spectrum, typically obtained by Monte Carlo calculations (e.g. with the MCNP code). In the present case, the neutron spectrum in the Central irradiation channel (CC) of the JSI TRIGA reactor is considered. Figure 1 displays the input neutron spectrum and four analytically defined neutron spectra. The spectra in Figure 1 and all the following Figures are displayed in lethargy representation. The spectra in Figure 1 labelled ‘User defined’ consist of a thermal Maxwellian at temperature $T = 352$ K, a pure $\frac{1}{E}$ epithermal component and a fast Maxwellian at mean energy $W_a = 2.2$ MeV, the thermal and fast energy breakpoints being $E_t = 0.05$ eV and $E_f = 2$ MeV. The spectra are defined with different values of the thermal and fast overlap parameters O_t and O_f ; all other parameter values are default. The O_t and O_f parameters determine the relative magnitudes of the thermal and fast component.

Typically, the fitting procedure is started with the thermal component parameters E_t, O_t, T and l . The spectrum in Figure 1 labelled ‘Fit-1’ was obtained by fitting these three parameters simultaneously, while leaving all others default. The fitted spectrum describes very well only the thermal part.

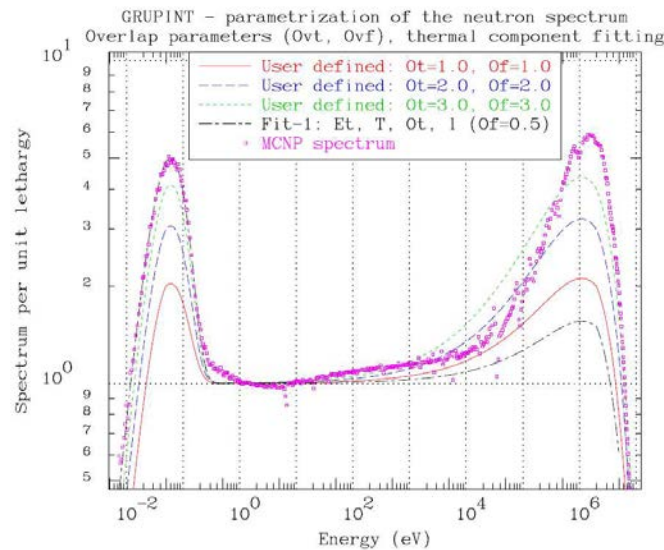


FIG. 1. Fitting the parameters of the thermal part to an input spectrum.

Figure 2 displays the fitting of the epithermal slope parameters. The two spectra labelled ‘User defined’ have α parameter values of -0.03 and 0.03 respectively, the remaining parameters are the same as in the spectrum labelled ‘Fit-1’, also shown in Figure 2.

The spectrum in Figure 2 labelled ‘Fit-2’ was obtained by fitting the α and α_1 parameters simultaneously. Overall this spectrum describes well the thermal part and the epithermal slope. The α_1 and α_2 parameters are meant for fine-tuning the slope in the epithermal region and in most cases are not required (i.e. they are left default).

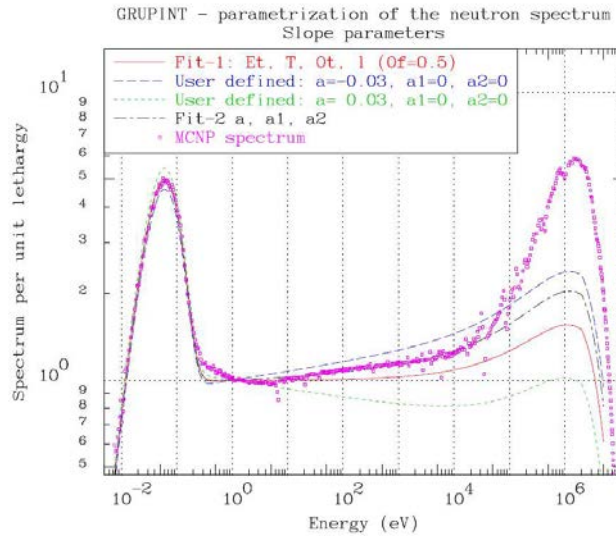


FIG. 2. Fitting the epithermal slope parameters to an input spectrum.

Figure 3 displays the final steps in the GRUPINT fitting sequence. As seen previously in Figures 1 and 2 and indicated in Figure 3, there is a distortion in the spectrum between the thermal and epithermal regions (from around 0.1 eV to around 1 eV), which is common. The spectrum labelled ‘Fit-3’ was obtained by fitting the parameters O_t , C_{t1} and C_{t2} ; the latter two govern the strengths of two additional Maxwellian distributions in the spectrum, at pre-set temperatures of 700 K and 1000 K. These temperatures can be fitted automatically by GRUPINT, however as a general rule, if too many parameters (> 3–4) are allowed to vary simultaneously, the fitting algorithm may fail.

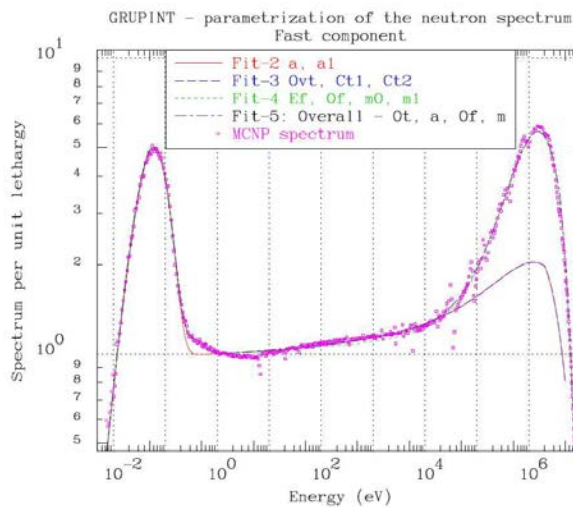


FIG. 3. Fitting the parameters of the fast part to an input spectrum, overall fit.

In the next step (spectrum labelled ‘Fit-4’) the parameters of the fast spectrum component E_f , O_f , m_0 and m_1 were fitted. The spectrum thus obtained describes the input spectrum from the Monte Carlo calculation well, however a small deviation in the epithermal region is introduced. To refine the fit, another step is made in which the main spectrum parameters O_t , α and O_f and additionally the fast slowing-down parameter m is fitted. The final result of the analytic function fitting labelled ‘Fit-5’.

2.3 FITTING OF THE SPECTRUM PARAMETERS – MEASUREMENTS

After the input spectrum has been sufficiently well reproduced, a similar fitting sequence is performed, where the parameters of the neutron spectrum are fitted to measured reaction rate ratios, either ratios of one nuclear reaction

to another or the same nuclear reaction, measured with and without cover—e.g. Cd ratios. It is possible for the latter ratios to be determined with a lower uncertainty than the absolute reaction rate values.

2.4 NEUTRON SPECTRUM COVARIANCE MATRIX GENERATION

An important feature of GRUPINT is the ability to generate the covariance matrix of the reaction rate ratios, spectrum parameters and the neutron spectrum by a Monte Carlo algorithm. A user-defined subset of the analytic neutron spectrum parameters is sampled uniformly within ranges around the initial parameter values (obtained from the previous fitting procedures). The covariances are computed by definition:

$$\text{cov}(x_i, x_j) = \frac{1}{n} \sum_{l=1}^n (x_i^0 - x_i^l)(x_j^0 - x_j^l)$$

where x is a vector composed of the reaction rate ratios R , the 19 parameters of the neutron spectrum and the neutron spectrum in 640 energy group structure. The covariance matrix thus generated defines the correlations between the energy groups of the neutron spectrum. It is used in the final step, in which the neutron spectrum is adjusted using the ZOTT99 code, implemented into GRUPINT.

3 CHARACTERIZATION OF THE SPECTRA IN THE JSI TRIGA REACTOR

Here we present the results of the characterization of the neutron spectra for three routinely used irradiation channels in the JSI TRIGA reactor, namely the Central Channel (CC), located in the centre of the reactor core, the Pneumatic Tube (PT), located in the outer ring of fuel element positions and the IC40 irradiation position, part of the carousel. For the characterization the following measured reaction rate ratios have been used: $^{197}\text{Au}(n, \gamma) R_{\text{Cd}}$, $^{238}\text{U}(n, \gamma) R_{\text{Cd}}$, $^{27}\text{Al}(n, p)$ vs. $^{197}\text{Au}(n, \gamma)$, $^{27}\text{Al}(n, \alpha)$ vs. $^{197}\text{Au}(n, \gamma)$. Nuclear data from the IRDFF-v1-02 library [15] was used.

Figures 4, 5 and 6 display the input neutron spectra obtained from Monte Carlo calculations, the fitted analytic functions, and the final spectra obtained by fitting the spectrum parameters to the measured reaction rate ratios and Cd-ratios, and additionally, the Cd-filtered spectra. In order to visualize the differences in the spectra (which are often quite small), in the bottom parts of the figures the ratios of the spectra vs. the initial fitted analytic functions are displayed.

A positive correction in the thermal region is observed in all the fitted spectra. The magnitude of the thermal peak is increased by around 20 % in the CC, 10 % in the PT and 5 % in the IC40. The spectral shapes in the epithermal and fast energy regions remain practically unaltered. The goodness-of-fit can be judged on the basis of the relative differences between the measured and calculated reaction rate ratios. For the fitted spectra, the agreement is generally within the experimental uncertainties, i.e. within 5 % for the R_{Cd} values for the $^{197}\text{Au}(n, \gamma)$ and $^{238}\text{U}(n, \gamma)$ reactions and generally within 10 % for the reaction rate ratios $^{27}\text{Al}(n, p)$ vs. $^{197}\text{Au}(n, \gamma)$ $^{27}\text{Al}(n, \alpha)$ vs. $^{197}\text{Au}(n, \gamma)$. Figures 7, 8 and 9 display the relative differences between the measured and calculated R_{Cd} values for the $^{197}\text{Au}(n, \gamma)$ and $^{238}\text{U}(n, \gamma)$ reactions and the reaction rates ratios $^{27}\text{Al}(n, p)$ vs. $^{197}\text{Au}(n, \gamma)$ $^{27}\text{Al}(n, \alpha)$ vs. $^{197}\text{Au}(n, \gamma)$, with the final fitted spectra.

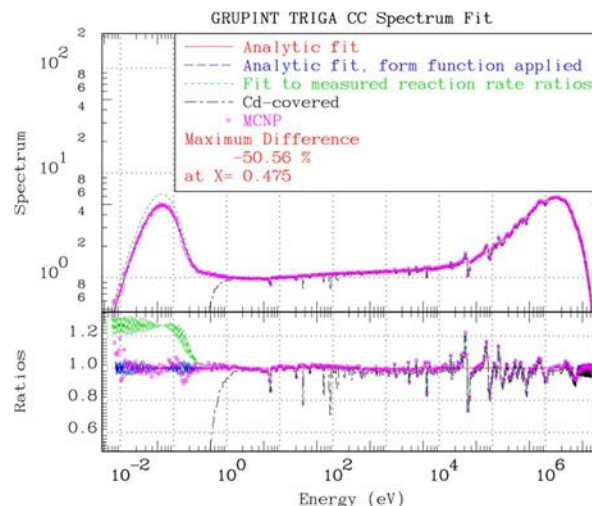


FIG. 4. JSI TRIGA Central Channel spectrum fitting.

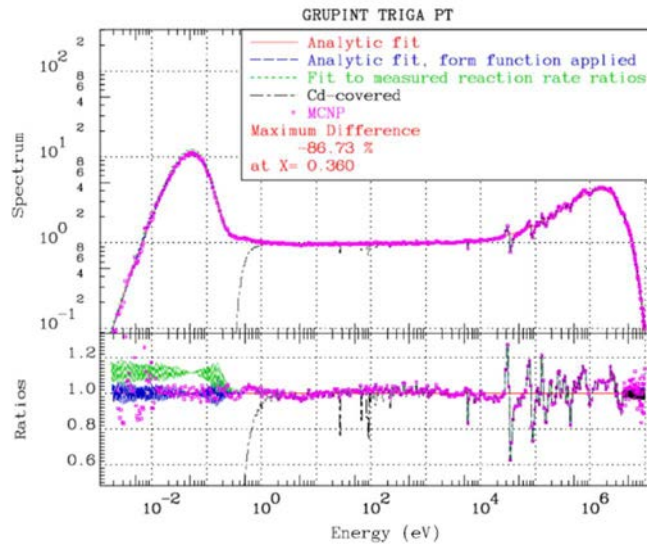


FIG. 5. JSI TRIGA Pneumatic Tube (PT) spectrum fitting.

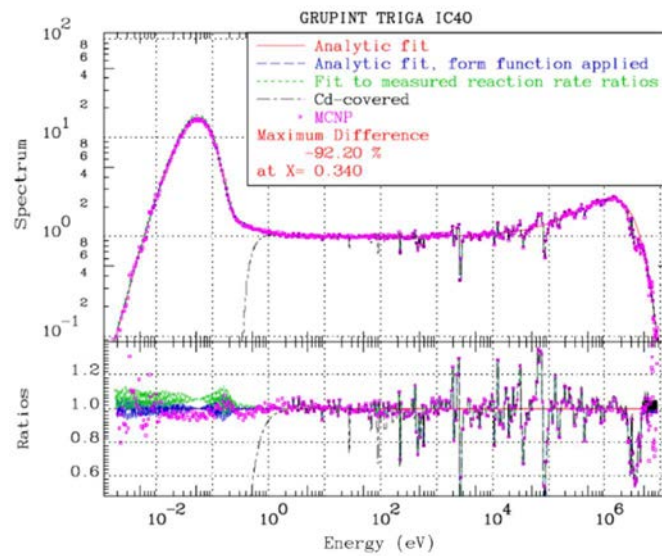


FIG. 6. JSI TRIGA IC40 channel spectrum fitting.

Spectrum adjustment - CC - reaction rate ratio comparison

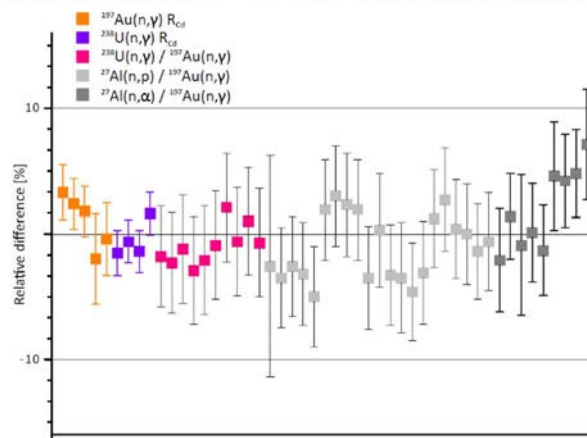


FIG. 7. JSI TRIGA Central Channel – relative differences between measured and calculated reaction rate ratios for nuclear reactions used to characterize the neutron spectrum.

Spectrum adjustment - PT - reaction rate ratio comparison

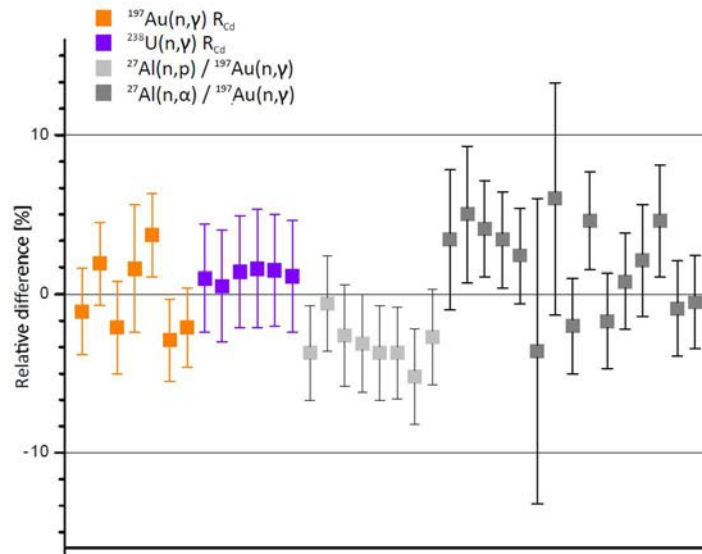


FIG. 8. JSI TRIGA Pneumatic Tube (PT) – relative differences between measured and calculated reaction rate ratios for nuclear reactions used to characterize the neutron spectrum.

Spectrum adjustment - IC40 - reaction rate ratio comparison

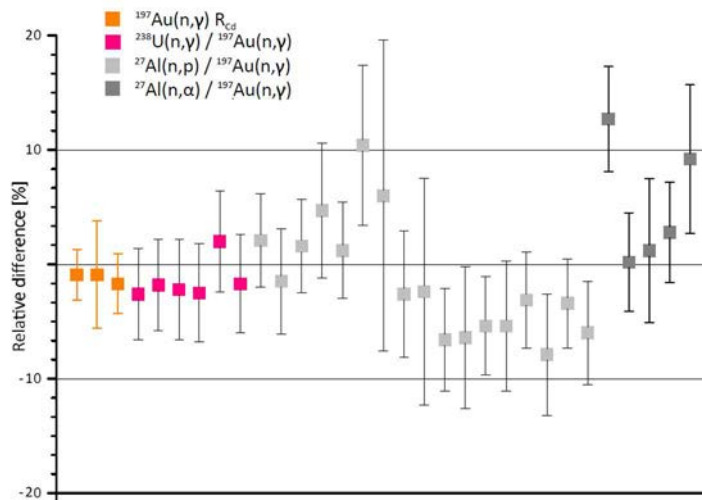


FIG. 9. JSI TRIGA IC40 channel – relative differences between measured and calculated reaction rate ratios for nuclear reactions used to characterize the neutron spectrum.

3.1 JSI TRIGA PT CHANNEL - CROSS SECTION VALIDATION

In the experimental campaign in the PT channel of the JSI TRIGA reactor, measurements were performed for a selection of nuclear reactions in order to obtain experimental indications of the quality of the nuclear data. Table 1 lists the sample materials and the measured nuclear reactions. Measured R_{Cd} and reaction rate ratio values were compared to calculated values using the final fitted spectrum and the IRDFF-v1-02 cross section library, except for the $^{117}\text{Sn}(n, n')$ reaction, in which case data from the ENDF/B-VII.1 library was used.

TABLE 1: SAMPLE MATERIALS AND MEASURED NUCLEAR REACTIONS

Sample material	Nuclear reaction
Al-1%Th	$^{232}\text{Th}(n,\gamma)$
Al-1%Mn	$^{55}\text{Mn}(n,\gamma)$
Al-0.1%Co	$^{59}\text{Co}(n,\gamma)$
Al-2%Sc	$^{45}\text{Sc}(n,\gamma)$
Fe	$^{58}\text{Fe}(n,\gamma)$
Sn enriched in Sn-117	$^{117}\text{Sn}(n,n')$

Figure 10 displays the relative differences between the measured and calculated reaction rate ratios.

The results of the measurement campaign in terms of the nuclear data quality can be summarized as follows:

- Good agreement was observed for the $^{232}\text{Th}(n,\gamma)$ and the $^{55}\text{Mn}(n,\gamma)$ reactions, which confirms the quality of the nuclear data and the usability of the reactions for neutron spectrum characterization.
- Disagreement was observed for the $^{58}\text{Fe}(n,\gamma)$ reaction, consistent with results from previous experimental campaigns, which indicates the need for improvements in the nuclear data.
- Strong consistent disagreement was observed for the $^{117}\text{Sn}(n,n')$ reaction, which is unfortunate, since this reaction is of particular interest for the characterization of the epithermal spectrum component, on account of its low threshold.
- The results for the $^{59}\text{Co}(n,\gamma)$ and $^{45}\text{Sc}(n,\gamma)$ reactions are inconclusive on account of the very low induced activities.

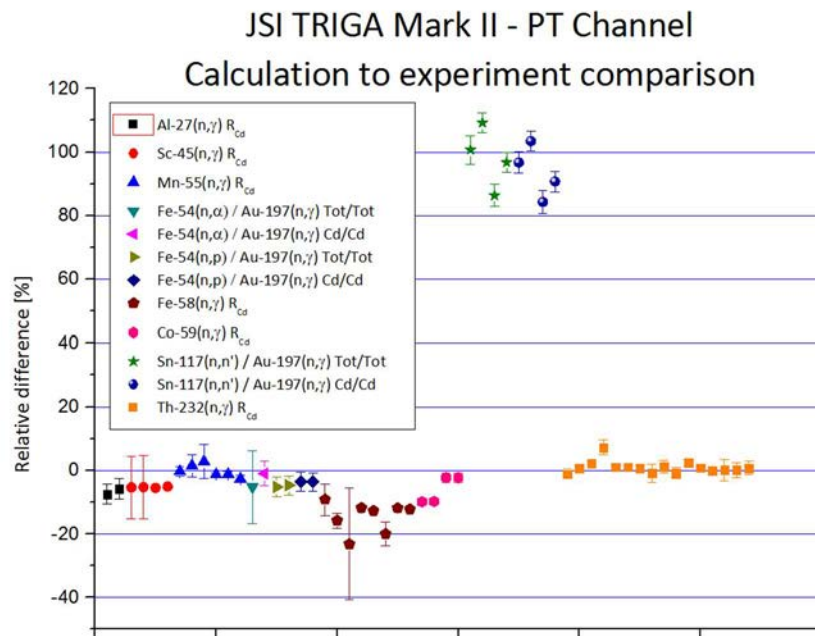


FIG. 10. Relative difference in the measured and calculated R_{Cd} values and reaction rate ratios.

4 SPECTRUM CHARACTERIZATION AND CROSS-SECTION VALIDATION IN THE EPITHERMAL RANGE

Activation measurements have been performed in the experimental campaign in the PT channel of the JSI TRIGA reactor using boron nitride filters. The motivation behind the measurements was to shift the sensitivity of capture reaction measurements to the epithermal range, with the objectives of spectrum characterization and cross-section validation. Boron nitride filters with a wall thickness of 4 mm were used. The filter transmission functions were determined through Monte Carlo calculations. GRUPINT incorporates an exponential parametrization of the filter transmission function $t(E)$ given as:

$$t(E) = \exp\left(-nd_{\text{eff}}(\sigma_a(E) + \xi\sigma_s(E))\right), \quad (6)$$

where n is the atom density of the material, d_{eff} is an effective filter thickness, $\sigma_a(E)$ is the material absorption cross-section, ξ is a scattering fraction and $\sigma_s(E)$ is the material scattering cross-section. Material cross-sections for boron nitride were generated and the transmission function parameters d_{eff} and ξ were fitted, firstly to the Monte Carlo transmission function and subsequently to the measured $^{197}\text{Au}(n,\gamma)$ and $^{238}\text{U}(n,\gamma)$ boron nitride ratios. Figure 11 displays a boron nitride filter used in the experimental campaign and the filter transmission function.

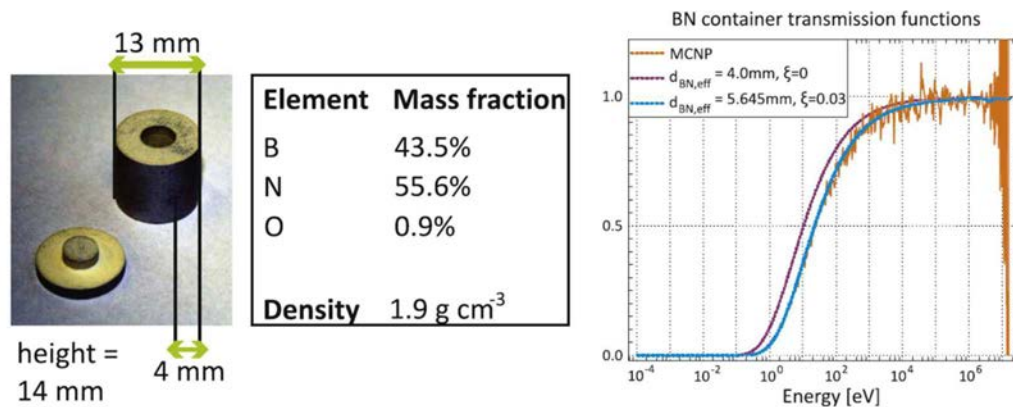


FIG. 11. Boron nitride filter used in the experiments and its transmission function.

Measured boron nitride ratios for other nuclear reactions were compared to calculated ones, using the characterized neutron spectrum and boron nitride transmission function. Figure 12 displays the relative differences and uncertainties in the boron nitride ratios.

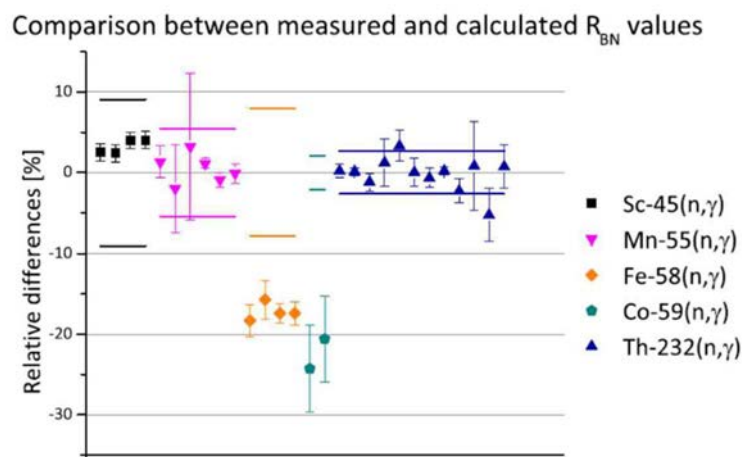


FIG. 12. comparison between the measured and calculated boron nitride ratios

Consistency was observed between the comparison for the measurements using boron nitride and cadmium filters.

A table of capture reactions from the ENDF/B-VII.1 library was made, sorted by the $E_{50\%}$ value (energy where the cumulative reaction rate reaches 50% of the total), in the JSI TRIGA PT spectrum, filtered by available boron nitride filters. The table includes comments and a final verdict on the suitability of the reactions for activation measurements [16]. As the available boron nitride filters have an effective cut-off energy at around 10–20 eV, the applicability of boron nitride, boron carbide and ^{10}B enriched boron carbide was studied with the objective to increase the effective cut-off energy and shift the sensitivity of capture reaction measurements to higher energies.

5 APPLICATION TO BONNER SPHERE SPECTROMETRY

An inter-comparison of different unfolding techniques was proposed by EURADOS [17]. Four different scenarios that cover a wide range of neutronics applications were proposed:

- Scenario 1: Medical accelerator

The scenario is comprised of a medical linear accelerator used for radiotherapy. The source beam is moderated by a water phantom. Bonner sphere measurements were performed at two locations, P1 and P2. A schematic of the scenario is given in Figure 13 (left).

- Scenario 2: A simulated workplace field

The scenario is aimed to simulate a metrology laboratory room with a moderated neutron source. The source was a standard ^{241}Am –Be source suspended in a steel tube clad by lead. The actual room was covered by wood and neutron absorbent material (borated concrete) to reduce neutron scattering off the walls. Between the source and the measurement position a container filled with water was placed to moderate the neutrons. A schematic of the scenario is given in Figure 13 (right).

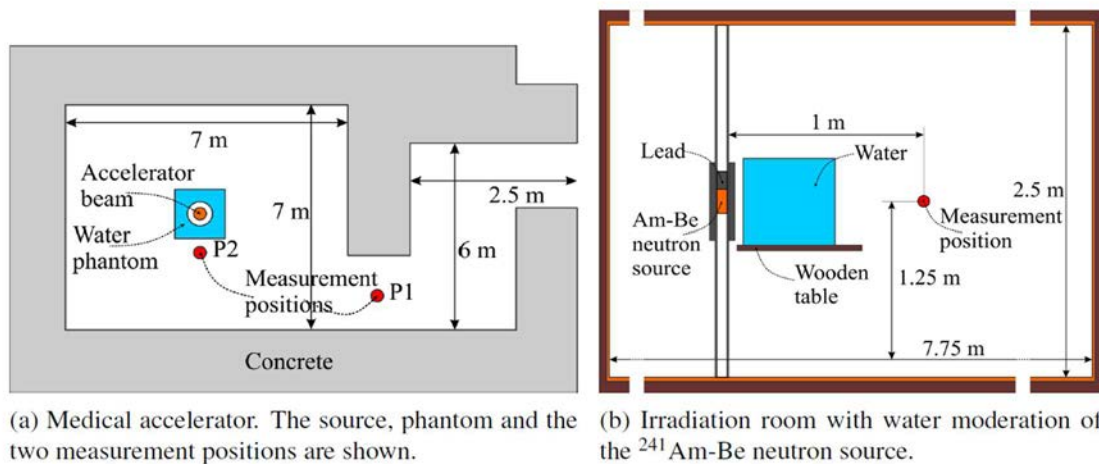


FIG. 13. Medical accelerator scenario and the water moderated irradiation room scenario schematics.

- Scenario 3: An irradiation room with a radionuclide source

This scenario closely resembles the previous one. The source was once again a ^{241}Am –Be source, but it was placed in an iron sphere with a radius of 10 cm. The source in the iron sphere was placed in the centre of a concrete room. The measurement position was 4 m away from the source along one of the diagonals of the room's horizontal plane. A schematic of the scenario is given in Figure 14 (left).

- Scenario 4: A sky-shine scenario

The last scenario was aimed to approximate a sky-shine situation. Environmental Bonner sphere measurements were performed 100 m from a nuclear power plant. The power plant was a simple concrete structure. The walls of the plant were thick enough to absorb most of the neutrons and ensure that the main contribution to the measurements came from air scattered neutrons. The source was specified as (α,n) source so the ^{241}Am –Be source was used once again. A schematic of the scenario is given in Figure 14 (right).

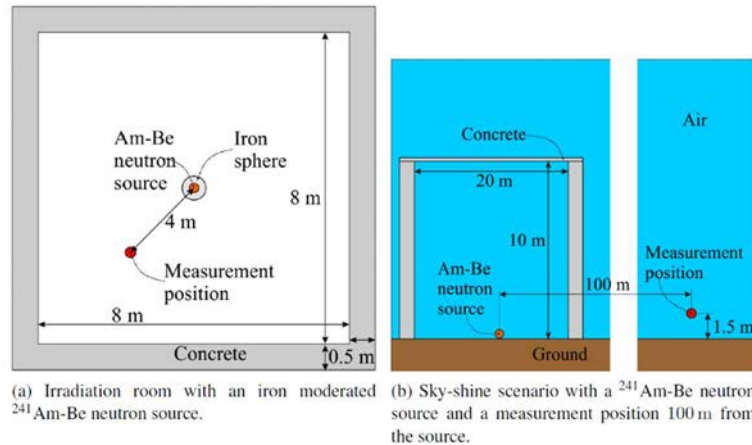


FIG. 14. Iron-moderated source in irradiation room and sky-shine scenario schematics.

EURADOS provided all of the input data needed for the unfolding procedure. The response functions of each of the Bonner spheres were given in a 104 energy group structure. GRUPINT uses a standard SAND-II 640 energy group structure. The ANGELO-2.3 [18] code was used to convert the response functions to the 640 energy group structure. The response functions were then reformatted to the ENDF6 format and were used instead of nuclear reaction cross-section files in GRUPINT. The response functions, given in units per neutron fluence, in the original 104 energy structure and in the 640 group structure are shown in Figure 15. The different Bonner spheres are designated by the thickness of polyethylene that covered them (2" = 2 inch polyethylene cover).

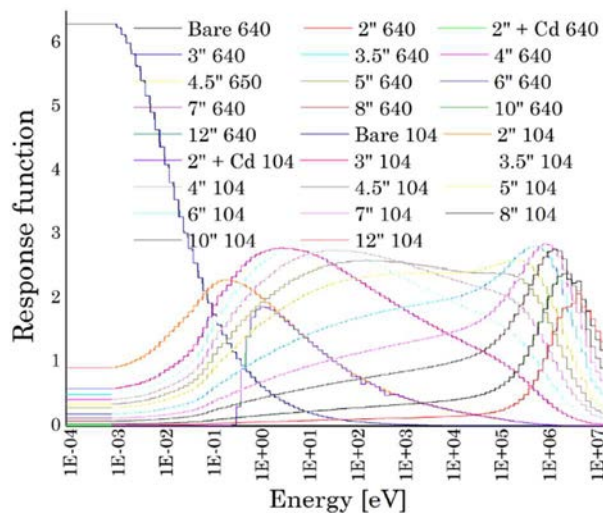


FIG. 15. Response functions of the Bonner spheres in the original 104 and the standard SAND-II 640 energy group structures.

The measurements, number of counts, of each Bonner sphere measurement were written in the appropriate GRUPINT input format. GRUPINT uses relative reaction rate measurements for the spectrum adjustment. Because of this, all measurements were normalized to the measurement with the bare Bonner sphere. All normalized measurements were used in the GRUPINT adjustment procedure except the measurement with the 6 inch Bonner sphere in the sky-shine scenario. The measurement was deemed physically inconsistent compared to measurements for Bonner spheres with different polyethylene thicknesses.

Model information retrieved from the scenario descriptions was used to construct simple MCNP models. MCNP was used to calculate the initial guess spectra which GRUPINT uses in the first part of the fitting procedure. GRUPINT's output, the fitted neutron spectra based on the measurements and the response functions, served as input for the ZOTT99 code [11]. ZOTT99 produced the uncertainties of the fitted parameters as a covariance matrix. The result of the unfolding procedure were the adjusted spectra and their covariance matrices. These results were normalized to the absolute values given in the EURADOS documentation.

The resulting unfolded spectra for the first scenario are given in Fig. 16. The black line represents the unfolded spectrum in measurement position P1 and the red line in position P2. The flux units are given per Gy because the original data was normalized to a medical accelerator burst equivalent to 1 Gy. No specific data was given on the medical accelerator source spectrum. The resulting spectra differ from a typical reactor spectra, in that the slope in the epithermal energy range is more pronounced, however they reproduce very well the measurement data, as can be seen in the comparison between the experimental and calculated count rate ratios, given in Table 1.

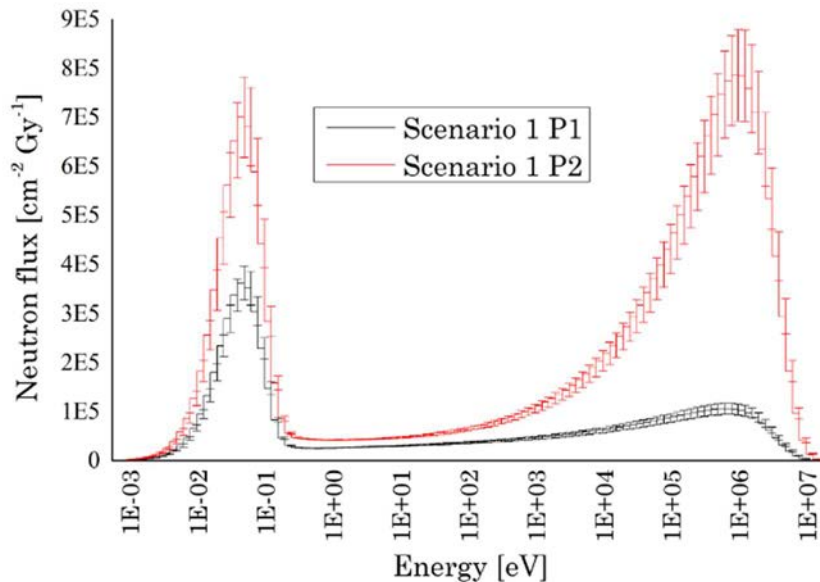


FIG. 16. Unfolded neutron spectra with uncertainties for measurement locations P1 and P2 of scenario 1—the medical accelerator.

The unfolded neutron spectra for scenarios 2 and 3 are given in Fig. 17. The higher thermal peak for scenario 2 is clearly seen which is the result of moderation of neutrons in water. The unfolded spectrum for scenario 4 is given in Fig. 18. A larger fast neutron peak can be observed which is to be expected in a sky-shine scenario [19].

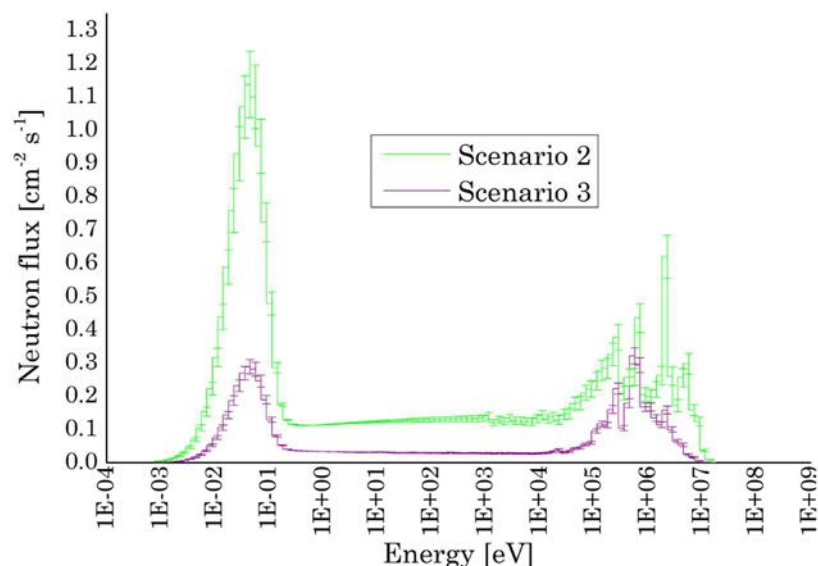


FIG. 17. Unfolded neutron spectra with uncertainties for scenario 2—a simulated workplace field and scenario 3—an irradiation room with a radionuclide source.

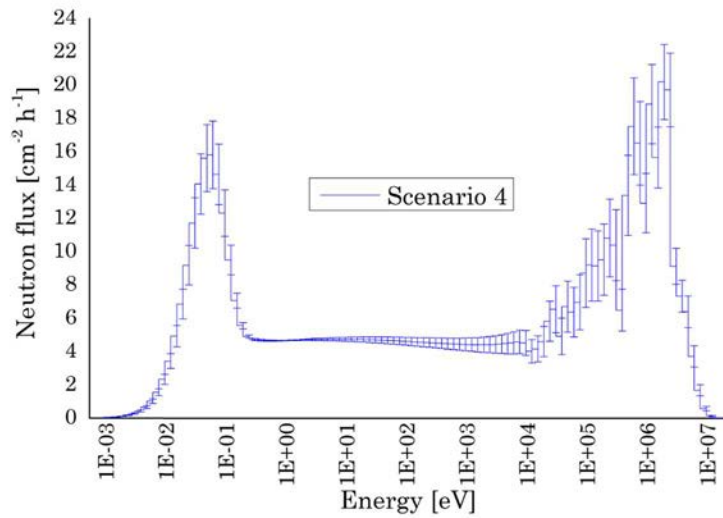


FIG. 18. Unfolded neutron spectra with uncertainties for scenario 4—a sky-shine scenario.

To test the quality of the unfolded spectra, the spectra were convoluted with the Bonner sphere response functions to calculate the activity of each of the Bonner spheres for all scenarios. We compared the calculated activity to the original measured activities supplied by EURADOS. Table 2 reports the ratio between the measured and calculated count rates (C/E values, where C stands for calculated and E stands for the measured count rate). It can be seen that the C/E quantity is for most cases within the uncertainty.

TABLE 2. COMPARISON OF THE CALCULATED AND EXPERIMENTAL COUNT RATES (C/E) FOR EACH BONNER SPHERE AND EXPERIMENTAL SCENARIO

Bonner sphere	Scenario 1 P1		Scenario 1 P2		Scenario 2		Scenario 3		Scenario 4	
	C/E	unc.	C/E	unc.	C/E	unc.	C/E	unc.	C/E	unc.
2"	1.00	0.03	0.99	0.03	0.92	0.04	1.00	0.03	0.85	0.05
2" + Cd	1.07	0.02	0.91	0.02	1.13	0.04	0.97	0.02	0.93	0.05
3"	1.02	0.02	1.02	0.02	1.03	0.04	1.00	0.02	1.07	0.05
3.5"	1.03	0.02	0.99	0.02	1.00	0.04	1.01	0.02	1.04	0.05
4"	1.01	0.02	1.05	0.03	0.98	0.04	1.00	0.02	1.07	0.05
4.5"	0.99	0.02	1.00	0.03	0.97	0.04	1.00	0.02	0.94	0.05
5"	1.02	0.02	1.01	0.03	1.03	0.04	0.99	0.02	1.04	0.05
6"	1.03	0.03	0.96	0.02	1.01	0.05	1.04	0.02	1.24	0.05
7"	1.00	0.03	0.97	0.03	1.05	0.04	1.01	0.03	0.94	0.06
8"	1.02	0.03	0.98	0.03	0.96	0.04	0.98	0.03	0.97	0.06
10"	0.99	0.03	1.02	0.03	0.89	0.05	0.98	0.03	0.97	0.06
12"	1.01	0.03	1.03	0.04	1.05	0.05	0.98	0.03	1.01	0.06

6 CONCLUSIONS

The aim of this paper is to present the GRUPINT neutron spectrum adjustment code package, developed at the Jožef Stefan Institute in Ljubljana, Slovenia. The role and meaning of the parameters in the neutron spectrum parametrization and the fitting procedure are illustrated on the case of the neutron spectrum in the Central Channel of the JSI TRIGA reactor, obtained by a Monte Carlo calculation with the MCNP code. The characterization of the neutron spectrum has been performed for three routinely used irradiation channels of the JSI TRIGA reactor with different spectral characteristics. The final fitted spectra reproduce the measured reaction rate ratios within the experimental uncertainties.

REFERENCES

- [1] GOORLEY, T., et al., Features of MCNP6, *Ann. Nucl. Energy* **87** (2016) 772–783.
- [2] BRUN, E. et al., TRIPOLI-4, CEA, EDF and AREVA reference Monte Carlo code, *Ann. Nucl. Energy* **82** (2015) 151–160.
- [3] PEREY, F.G., Least Squares Dosimetry Unfolding: The Program STAY-SL", ORNL/TM-6062, ENDF-254 (1977).
- [4] MCELROY, W.N., BERG, S., A Computer-Automated Iterative Method for Neutron Flux Spectra Determination by Foil Activation, Vol. II: SAND II (Spectrum Analysis by Neutron Detectors II) and Associated Codes, AFWL, Technical Report AFWL-TR-67-41 (1967).
- [5] MATZKE, M., Unfolding of pulse height spectra: the HEPRO program system. Report PTB-N-19. (Braunschweig: Physikalisch-Technische Bundesanstalt) (1994).
- [6] BRAGA, C., DIAS, M., Application of neural networks for unfolding neutron spectra measured by means of Bonner spheres, *Nucl. Instrum. Methods Sect. A* **476** (2002) 252–255.
- [7] AVDIC, S., POZZI, S.A., PROTOPODESCU, V., Detector response unfolding using artificial neural networks, *Nucl. Instrum. Methods Sect. A* **565** (2006) 742–752.
- [8] MARTINEZ-BLANCO, M.R., et al., A neutron spectrum unfolding code based on generalized regression artificial neural networks, *Appl. Rad. Isot.* **117** (2016) 8–14.
- [9] HOSSEINI, S.A., Neutron spectrum unfolding using artificial neural network and modified least square method, *Rad. Phys. Chem.* **126** (2016) 75–84.
- [10] BEDOGNI, R., DOMINGO, C., ESPOSITO, A., FERNÁNDEZ, F., FRUIT: An operational tool for multisphere neutron spectrometry in workplaces, *Nucl. Instrum. Methods Phys. Res. Sect. A* **580** (2007) 1301–1309.
- [11] MUIR, D.W., Evaluation of Correlated Data Using Partitioned Least Squares: A Minimum-Variance Derivation, LA-UR-2365 (Rev.) also published in *Nucl. Sci. Eng.* **101** (1989) 88–93.
- [12] ŞAHIN, D., RADULOVIĆ, V., LINDSTROM, R.M., TRKOV, A., Re-evaluation of neutron flux characterization parameters for NIST RT-2 facility, *J. Radioanal. Nucl. Chem.* **300** (2014) 499.
- [13] TRKOV, A., et al., Supplementary Data for Neutron Activation Analysis, INDC(NDS)-0693, IAEA, Vienna, 2015.
- [14] RADULOVIĆ, V., TRKOV, A., JAĆIMOVIĆ, R., JERAJ, R., Measurement of the neutron activation constants Q_0 and k_0 for the $^{27}\text{Al}(n,\gamma)^{28}\text{Al}$ reaction at the JSI TRIGA Mark II reactor, *J. Radioanal. Nucl. Chem.* **298** (2013) 1791–1800.
- [15] CAPOTE, R., ZOLOTAREV, K.I., PRONYAEV, V.G., TRKOV, A., Updating and Extending the IRDF-2002 Dosimetry Library, *J. ASTM International* **9** 4 (2012) 1–9.
- [16] RADULOVIĆ, V., et al., Use of boron nitride for neutron spectrum characterization and cross-section validation in the epithermal range through integral activation measurements, *Nucl. Instrum. Methods Phys. Res. Sect. A* **840** (2016) 5–14.
- [17] GÓMEZ-ROS, J.M., et al., Exercise on neutron spectrum unfolding in Bonner sphere spectrometry, EURADOS, <https://www.researchgate.net/project/EURADOS-International-comparison-on-neutron-spectra-unfolding-in-Bonner-spheres-spectrometry>, 2017.
- [18] KODELI, I., SARTORI, E., "ANGELO-LAMBDA, Covariance matrix interpolation and mathematical verification", <https://www.oecd-nea.org/tools/abstract/detail/nea-1798>, Feb 2010.
- [19] DIKAREVA, O.F., KARTASHEV, I.A., NETECHA, M.E., ZHARKOV, V.P., Baikal-1 Skyshine Experiment, NEA/NSC/DOC/(95)03/VIII, ALARM-REACAIR-SKY-1, Sep. 30 (2009), revision 1, NEA ICSBEP Database.

USE OF A PRIORI INFORMATION IN BONNER SPHERE UNFOLDING

D.J. THOMAS

Nuclear Metrology Group
National Physical Laboratory
Teddington
TW11 0LW
UK

Abstract: The problem of unfolding measured Bonner sphere data to derive a neutron spectrum is outlined and the use of a priori information, derived either from neutron transport calculations or measurements with other instruments, is discussed. Examples are given of cases where this a priori information greatly increases the confidence in the final spectrum. Neutron transport calculations can also help in understanding Bonner sphere measurements in particular if unexpected features are seen.

1 INTRODUCTION

Bonner spheres have been one of the most commonly used neutron spectrometry systems since their properties were first outlined in 1960 [1]. A Bonner sphere set consists of a thermal neutron sensor used at the centre of a number of moderating spheres of different diameter ranging typically from 5 cm to 30 cm or possibly even larger. Each sphere has a different response as a function of energy, the small spheres being most sensitive to low energy neutrons and the larger ones being more sensitive to the high energy neutrons. From the measured responses of the spheres in a neutron field the spectrum can be unfolded.

The characteristics, advantages and disadvantages, and developments of Bonner spheres over the years have been outlined in several review articles, for example reference [2]. Briefly, their advantages are: the energy range over which they can be used, which is from thermal to about 20 MeV for conventional polyethylene sphere sets, and to the GeV region if metal shells are included in some of the polyethylene spheres; an isotropic response so the directional properties of the field do not need to be known; they are easy to operate; and the fact that different central thermal neutron sensors can be used means they can have a range of sensitivities, including high neutron sensitivity, insensitivity to photons and, when activation foils are used as the sensor, they can be used in pulsed fields. Their disadvantages are: measurements usually have to be taken sequentially which can be time consuming and relies on the field remaining constant, the resolution is poor, they are heavy, and the bulk of the larger spheres can introduce scattering problems if used in confined spaces. Attempts have been made to speed up the data acquisition process, for example by having thermal sensors at different depths within a cylindrical moderator, but this approach results in the device having a direction dependence.

A review of the literature on neutron field spectrometry will reveal the large number of measurements that have been made over the years, and exercises to investigate their results have provided data on the reliability of the derived spectra and on the important features of a good Bonner sphere set [3]. The availability of reliable validated response functions, i.e. the responses of the individual spheres as a function of neutron energy, is important. These can be derived from calculations or measurements, or ideally from a combination of both. The process of unfolding the spectrum is dependent on ratios of sphere responses, so any inaccuracies in individual response functions can result in artificial features in the spectrum.

2 UNFOLDING

2.1 USE OF CALCULATED A PRIORI INFORMATION

Most of the disadvantages of Bonner spheres are simply inconveniences, but there is one aspect that introduces significant uncertainties into the results, and this is the process of unfolding the spectrum from the measured sphere responses. Bonner spheres are essentially integral detectors. Each sphere in the set provides a single number, M_i , which is an integral of its response function over the spectrum from zero to the maximum relevant energy, E_{\max} , as shown in Eq. (1)

$$M_i = \int_0^{E_{\max}} r_i(E) \cdot \Phi(E) dE \quad (1)$$

where:

$r_i(E)$ is the response function for the i^{th} detector,

and

$\Phi(E)$ is the neutron spectral fluence as a function of energy E .

Provided the response functions are sufficiently different, each detector provides information about the spectrum, and from the set of M_i values information can be unfolded about $\Phi(E)$. Neutron spectra are, however, usually expressed as histograms, and Eq. (1) is conventionally approximated by Eq. (2) which, if there are m detectors, represents a set of m equations:

$$M_i = \sum_{j=1}^n r_{ij} \cdot \Phi_j \quad (2)$$

where:

Φ_j is the fluence averaged over a channel extending from energy E_j to E_{j+1} and

r_{ij} is the response function of the i^{th} sphere averaged over this energy interval.

In principle any number of channels can be used for the spectrum, but to get some reasonable level of detail the usual choice is 5 or 10 channels per decade, with equal-width on a logarithmic scale, resulting in of the order of 50 or 100 channels for spectrometry up to 20 MeV, and even more if higher energies are considered. In such cases m is clearly smaller than n , and this means that the problem is underdetermined mathematically. Various unfolding methods have been applied to this problem, and the available techniques have been extensively studied [4], contrasted [5], and also compared [6] over the years. Nevertheless, it is impossible to get away from fact that $m > n$ and the use of some other information is highly desirable, if not essential.

Commonly used approaches are to impose restrictions on the spectrum, e.g. that the number of neutrons in a channel has to be non-negative and the spectrum reasonably smooth, although this latter requirement is not necessarily correct if there is the possibility of sharp peaks or dips in the spectrum, e.g. the well-known window at 24 keV in iron which results in a peak in the spectrum of neutrons through iron shielding.

Evidence that Bonner Spheres can provide reasonable results on their own can be found in a comparison exercise held at a simulated workplace field [3]. However, the participants were aware of how the neutrons were produced (a 14 MeV generator, a ^{238}U converter and moderating material) and so would have some idea if an unfolded spectrum was likely to be drastically wrong. It is clear that the experience of the unfolders in rejecting unlikely results and steering the unfolding in the direction of more likely results can be important. This is a help in most situations, but can result in genuine features being rejected because the reason for their presence is not known.

The best approach to improving the credibility of Bonner sphere spectra is the use of reliable a priori information. Most unfolding codes use it in some form or other, it is sometimes referred to as the start spectrum. This can come either from experiment or calculation, or simply be a guess. The way in which this information is used varies between codes, but its importance is often overlooked.

If a priori information is available with uncertainties the unfolding problem can then have a unique mathematical solution. Techniques are available that allow for the use of this information and unfolding codes based on these techniques provide in principle an exact answer. Two such codes [7,8] in fact require not only a priori spectrum information with uncertainties, but also uncertainties for the response functions, and covariance terms for both these data sets. This reflects their origin in reactor dosimetry, where the unfolding equation is the same, but the response functions of the Bonner spheres are replaced by activation cross sections where covariance information is increasingly becoming available. The difficulty applying this approach to Bonner sphere unfolding is that the a priori spectral information is very rarely known with uncertainties, even less so with covariance information, and although covariance terms have to be present in the response functions, whether derived from measurements or calculations, they tend not to be known. Also, the handling of these large data sets is a problem, particularly converting the response function data to the channel structure used in the a priori information, or vice versa.

Even if uncertainty information is not available, the use of a priori data in spectrum unfolding can greatly improve the validity of the resulting spectrum.

2.2 USE OF CALCULATED A PRIORI INFORMATION

Bonner spheres are often used to determine spectra from which radiation protection operational quantities are derived. An example of this is given in reference [9]. The measurements were performed at a uranium enrichment plant, and

in addition to measurements at the site boundary for protection of the general public, measurements were made close to a large flask of uranium hexafluoride, UF₆, shown in Fig. 1, where radiation workers may be exposed.

Neutron production within the flask occurs primarily via the ¹⁹F(α ,n) reaction the alpha particles coming from the decay of the various uranium isotopes. There are also neutrons from the spontaneous fission of ²³⁸U, and a small component from delayed neutron emission due to radioactive decay. The program SOURCES 4C [10] was used to calculate the neutron production rate and energy spectrum from unit volume of material. The total mass of UF₆ was approximately 12,500 kg, so a large amount of scatter occurred within the flask. There is also a substantial wall thickness. The flask was modelled in MCNP5 [11] using a simplified version of the geometry of the cylinder, and this was surrounded by a 3 m radius sphere of dry air. No walls, floor or any other external material was included, the surroundings being relatively scatter free. A uniform distribution of UF₆ on the inside walls of the cylinder was assumed, with the layer thickness chosen to match the total mass of UF₆. In the MCNP calculation neutrons corresponding to the SOURCES 4C energy spectrum were sampled uniformly throughout the UF₆ volume.



FIG. 1. A Bonner sphere set up to measure the spectrum from a flask of UF₆.

The results of unfolding with and without the calculated a priori information are shown in Figure 2, and the implications for the total fluence and ambient dose equivalent are indicated in Table 1.

TABLE 1. COMPARISON OF INTEGRAL QUANTITIES OBTAINED USING THE SIMPLE AND CALCULATED A PRIORI SPECTRA

A priori spectrum used in unfolding	Total fluence (cm ⁻² s ⁻¹)	Total ambient dose equivalent H*(10) (μSv h ⁻¹)
Simple guess	5.41	3.63
Calculated a priori	5.45	3.25
(Simple/Calculated) -1	-0.8%	+11.5%

The unfolding was performed with the Maxed code [12,13], with the ‘simple a priori guess’ being performed with a rough estimate of where a peak might be expected in the fast neutron region. A small thermal and epithermal (1/E) component was added to the a priori data for both unfolding attempts to allow for scatter especially from the floor.

The difference in the two unfolded spectra is very evident from Fig. 2. Both spectra, however, had acceptable χ^2 values when the measured responses are compared with those obtained by integrating the unfolded spectrum with the response functions. Both spectra give very similar values for the total fluence, but the derived ambient dose equivalents are rather different. The fact that the unfolding process barely changed the a priori spectrum gives much greater confidence in this spectrum than the one from the simple guess.

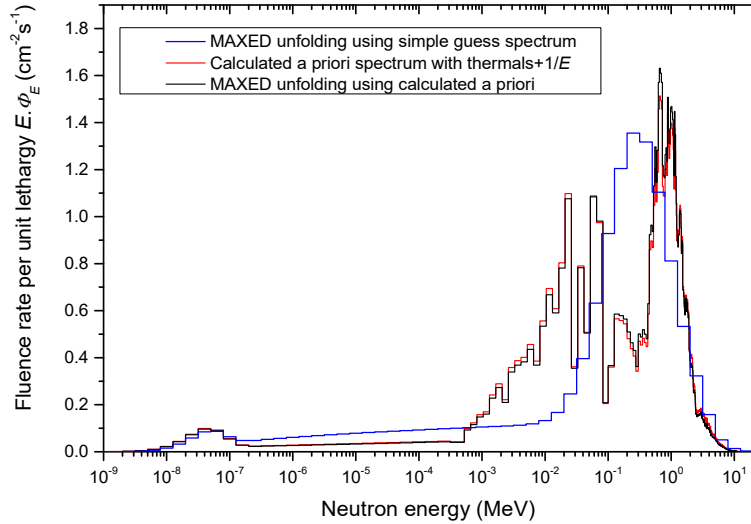


FIG. 2. Unfolded spectra from Bonner sphere measurements near a flask of UF_6 .

Another good example of the use of calculated a priori data can be found in the work of Campo et al. [14] to determine the spectra at various locations around a cask for dry storage of spent fuel. The determination of the source term for the transport calculation, i.e. the spectrum of neutrons from the spent fuel, requires precise information about the fuel such as enrichment, cooling time, specific power and burn up profile. This was derived using the ORIGEN module of the SCALE 6.1 code package and the final spectral calculations, which require detailed information about the geometry of the cask, were performed with the MAVERIC module from this package [15].

The unfolded spectrum, derived using codes from the UMG 3.3 package [13], is compared with the a priori data in Fig. 3. They highlight the benefits of the combined calculation plus Bonner sphere measurement approach. The changes introduced by the unfolding to the calculated data in the region above roughly 1 MeV are minimal. At lower energies the unfolding changes the fluence, but not the shape of the spectrum. The features of the calculation are retained including a peak in the 24 keV region, probably due to the iron window, and peaks at higher energies due to features in the cross sections of the various materials present including oxygen present in the UO_2 .

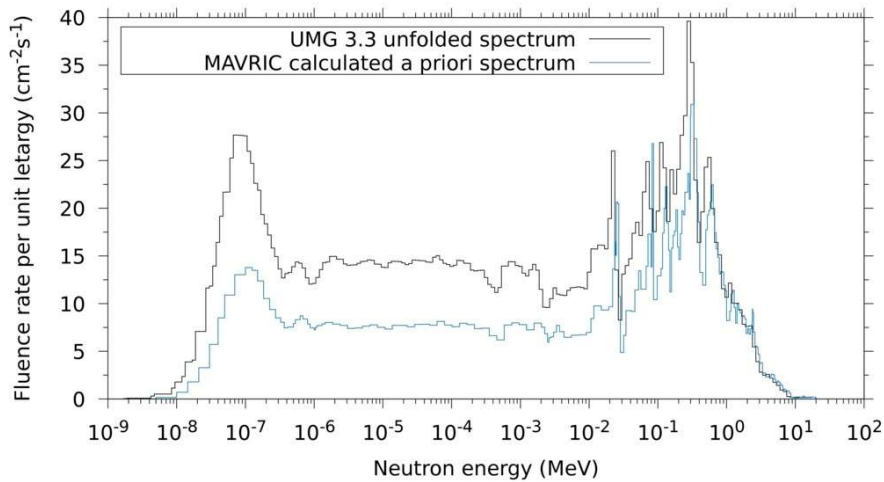


FIG. 3. Neutron spectrum near a spent fuel storage cask based on unfolding of Bonner sphere measurements using a priori information from calculations with the MAVERIC code. Reproduced with the kind permission of the author [14].

2.3 USE OF MEASURED A PRIORI DATA

High resolution neutron spectrometers, such as hydrogen recoil counters, 3He spectrometers, and scintillators, are available for the energy region above about 50 keV. Below this energy spectrometry is difficult. Bonner spheres can fill the gap between this energy and thermal, and the fact that the response functions tend to be derived in

terms of equal-width groups on a logarithmic scale, means that the resolution in this region is good. Measurements of radionuclide source spectra with Bonner spheres, using high resolution a priori information for the higher energy region, have provided data to confirm the dose equivalent per unit fluence from these sources that are used regularly for dosimeter and survey instrument calibrations. Examples are measurements for $^{241}\text{Am}\text{-Be}$ [16] and for $^{241}\text{Am}\text{-B}$ and $^{241}\text{Am}\text{-F}$ [17]. The Bonner sphere results helped to confirm the high energy data as well as providing the low-energy spectrum. As expected the low-energy component was small in all these cases.

The results of Bonner sphere measurements on radionuclide sources have, however, not always given the expected result. Measurements of the low energy spectrum of an $^{241}\text{Am}\text{-Li}$ source showed a completely unexpected feature [18]. High-resolution data were available from measurements with ^3He spectrometers and proton recoil counters and gave a broad spectrum extending down to about 50 keV. Below this energy the spectral intensity was expected to decrease, as it did with the other radionuclide sources measured. However, the Bonner sphere measurements while not changing the high-resolution data, thus going some way to confirming the spectrum in this energy region, indicated an unexpected number of low energy neutrons – see Fig. 4.

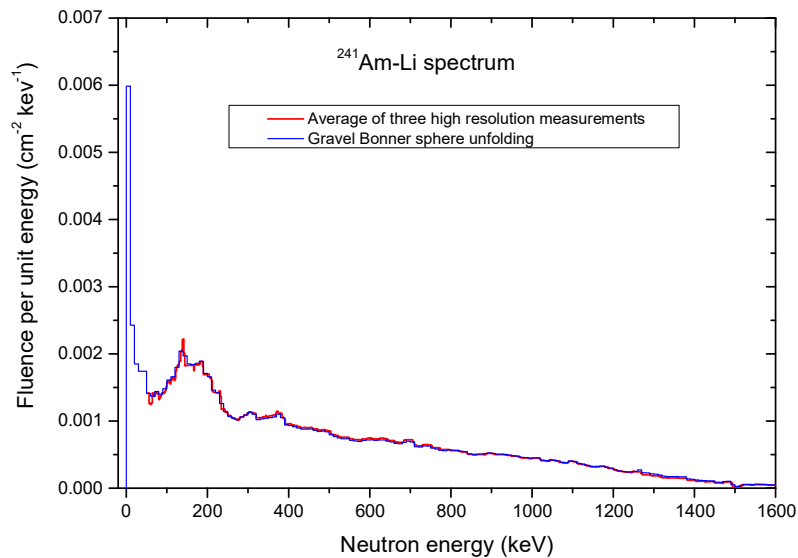


FIG. 4. Result of Bonner sphere unfolding for an $^{241}\text{Am}\text{-Li}$ radionuclide source.

This occasioned a review of how the source was made. It consisted of a mixture of 1.8 g of $^{241}\text{AmO}_2$ mixed with a lithium compound, all doubly encapsulated in a steel cylinder with outer dimensions of 30 mm diameter and a height of 60 mm. The origin of the low energy component only became clear when it was realised that the lithium compound was 14.8 g of lithium hydride (LiH). The presence of this amount of hydrogen, and the fact that a neutron can lose a large amount of energy in a single collision with a hydrogen atom, was the explanation of the low energy component. A calculation with MCNP, modelling the capsule construction and using the high-resolution data for the spectrum of neutrons from the primary $^7\text{Li}(\alpha, n)$ reactions, gave a low energy component in good agreement with the measurement, and it could be shown that removing the hydrogen from the calculation removed the low energy component.

3 CONCLUSIONS

Over the years improved data on response functions, and better understanding of unfolding techniques, have meant that the Bonner sphere approach has increasingly become a reliable spectrometry technique for obtaining information about neutron fields in a variety of locations for radiological protection and other purposes. The use of additional measurements or of neutron transport calculations to provide a priori information helps considerably with the unfolding problem and greatly enhances the validity of the measurements. Calculations can also be used to explain and confirm unexpected features.

REFERENCES

- [1] BRAMBLETT, R.L., EWING, R.I., BONNER, T.W., A new type of neutron spectrometer, *Nucl. Instrum. Methods* **9** (1960) 1–12.
- [2] ALEVRA, A.V., THOMAS, D.J., Neutron spectrometry in mixed fields: Multisphere spectrometers, *Radiat. Prot. Dosim.* **107** (2003) 37–72.
- [3] THOMAS, D.J., et al., Results of a large scale neutron spectrometry and dosimetry comparison exercise at the Cadarache moderator assembly, *Radiat. Prot. Dosim.* **70** (1997) 313–322.
- [4] MATZKE, M., Propagation of uncertainties in unfolding procedures, *Nucl. Instrum. Methods Phys. Res. A* **476** (2002) 230–241.
- [5] REGINATTO, M., Overview of spectral unfolding techniques and uncertainty estimation, *Radiation Measur.* **45** (2010) 1323–1329.
- [6] ALEVRA, A.V., et al., Unfolding Bonner-Sphere Data: A European Intercomparison of Computer Codes, *Physikalisch Technische Bundesanstalt Laboratory PTB-7.22-90-1*, (1990).
- [7] SCHMITTROTH, F.A., Method for Data Evaluation with Log-Normal Distributions, HEDL-SA-1742, Hanford Engineering Development Laboratory, Richland, WA (December 1978).
- [8] PEREY, F.G., Least Squares Dosimetry Unfolding: the Program STAY'SL. Oak Ridge National Laboratory Report ORNL/TM-6062, ENDF-254 (1977).
- [9] ROBERTS, N.J., THOMAS, D.J., VISSER, T.P.P., Improved Bonner sphere neutron spectrometry measurements for the nuclear industry, *Radiat. Phys. Chem.* **140** (2017) 319–321.
- [10] SHORES, E.F., SOURCES 4C: A Code for Calculating (α ,n), Spontaneous Fission, and Delayed Neutron Sources and Spectra, LA-UR-02-1839 (2002)
- [11] X-5 MONTE CARLO TEAM, MCNP—A General Monte Carlo N-Particle Transport Code, Version 5, Vol. I: Overview and Theory, LA-UR-03-1987, April 2003 revised Oct. 2005 (2005).
- [12] REGINATTO, M., GOLDHAGEN, P., NEUMANN, S., Spectrum unfolding, sensitivity analysis and propagation of uncertainties with the maximum entropy deconvolution code MAXED. *Nucl. Instrum. Methods Phys. Res. A* **476** (2002) 242–246.
- [13] NUCLEAR ENERGY AGENCY DATA BANK, code package NEA-1665 UMG 3.3, Analysis of Data Measured with Spectrometers using Unfolding Techniques.
- [14] CAMPO, X., et al., Monte Carlo neutron evaluation of dual purpose ENSA-DPT spent fuel casks. Poster presented at Neutron and Ion Dosimetry Symposium, Krakow (2017).
- [15] BOWMAN, S.M., SCALE 6: Comprehensive Nuclear Safety Analysis Code 331 System. *Nucl. Technol.* **174** (2007) 126–148.
- [16] BEDOGNI, R., et al., Investigation of the neutron spectrum of americium–beryllium sources by Bonner sphere spectrometry, *Nucl. Instrum. Methods Phys. Res. A* **763** (2014) 547–552.
- [17] ROBERTS, N.J., et al., Bonner sphere measurements of ^{241}Am -B And ^{241}Am -F neutron energy spectra unfolded using high-resolution a priori Data, *Radiat. Prot. Dosim.* **161** (2014) 225–228.
- [18] TAGZIRIA, H., ROBERTS, N.J., THOMAS, D.J., Measurement of the ^{241}Am -Li radionuclide neutron source spectrum, *Nucl. Instrum. Methods Phys. Res. A* **510** (2003) 346–356.

NEUTRON SOURCE CONDITION IN THE SOLUTION OF THE DIFFUSION EQUATION

H.R. VEGA-CARRILLO

Unidad Academica de Estudios Nucleares y Unidad Academica de Ingenieria Electrica

Universidad Autonoma de Zacatecas

Mexico

E-mail: fermineutron@yahoo.com

E. GALLEGO, A LORENTE, K.A. GUZMAN-GARCIA

Departamento de Ingenieria Energetica – ETSI Industriales

Universidad Politecnica de Madrid

Spain

L. HERNÁNDEZ-ADAME

CONACyT-Centro de Investigaciones Biológicas del Noroeste

Mexico

S.A. Martinez-Ovalle

Grupo de Fisica Nuclear Aplicada y Simulacion

Universidad Pedagogica y Tecnologica de Colombia – Tunja

Colombia

L. SAJO-BOHUS

Universidad Simon Bolivar

Venezuela

C. LETECHIPÍA-DE LEON, V.M. HERNANDEZ-DAVILA, M.A. SALAS-LUEVANO, B.G. PULIDO-CERVANTES

Universidad Autonoma de Zacatecas

Mexico

Abstract: The neutron transport equation describes neutrons throughout phase-space; however, exact, analytical solutions can only be obtained for highly idealized problems. In its application to real world problems, approximations to the neutron transport equation are used: some require numerical methods, while others, like the diffusion equation, can be solved obtaining exact solutions used as a first approach to transport theory. In the neutron diffusion equation, boundary conditions are applied to the general solution to obtain a particular solution. One of these conditions is known as the source condition. In this work, a general and formal expression for the source condition is used, where neutron leakage from finite media and neutron absorption in infinite media are included. In this work, the diffusion equation in three coordinate systems for two energy groups was solved in order to determine the radial distribution of neutrons in water. This distribution was compared with the measured neutron flux along the radius of a water-filled cylindrical container with a $^{241}\text{AmBe}$ neutron source at its centre and with the results obtained using Monte Carlo methods. The solution obtained compares well with both.

1 INTRODUCTION

The origin of environmental neutrons is due to anthropogenic activities and natural processes. Some of the human activities where neutrons are produced include electric power production, oil and coal industries, analytical procedures [1] such as the neutron activation analysis using radioisotopic neutron sources or a research reactor, and the production of radioisotopes for medical, industrial, research, and teaching uses. Around medical facilities, neutrons are produced in linear accelerators for radiotherapy [2] and during the radioisotope production in cyclotrons for positron emission tomography. Also, neutrons are produced in learning processes for the training of human capital [3] or as a tool for research [4]. In nature, neutrons are produced during the interaction between cosmic rays and the nuclei in the atmosphere, or through the decay of some radioisotopes [2].

In order to use neutrons in applications, proper handling, shielding, and radiation protection protocols are required. In the design of such protocols, it is important to know the neutrons distribution in energy, time and space. A tool to determine these characteristics is to solve the transport equation which gives the number of neutrons in a

differential volume in space, with energy between E and $E + dE$, moving in the solid angle comprised between Ω and $\Omega + d\Omega$.

Unfortunately, the transport equation cannot be solved exactly. Therefore, under certain assumptions, simplified versions of the transport equation are used that are solved by numerical methods, or a simple version is obtained using diffusion theory. Also, other procedures are used where approximate solutions are obtained, such as performing measurements or using Monte Carlo methods. In Monte Carlo, a model is built including the source, detectors, and surroundings and the transport of source particle by source particle is simulated [5]. The neutron diffusion approximation comes from diffusion theory which states that the solute will diffuse from volumes with high concentrations of neutrons to zones with low concentration. This theory is based on the Fick's law, which for neutrons is defined as,

$$\bar{\mathbf{J}} = -D \nabla \varphi \quad (1)$$

Here, $\bar{\mathbf{J}}$ is the neutron current density vector, D is the diffusion coefficient of neutron in the medium and φ is the neutron fluence rate (neutron flux). This equation implies that neutron current density is a conservative field.

In the solution of the neutron diffusion equation, the spatial distribution of neutrons is obtained in a medium characterized by D and L (diffusion length). In the solution process for a fixed source problem, a condition known as 'jump condition' [6] or 'source condition' [5] has to be applied. The source condition has been formalized [7] through Gauss' theorem, as shown in Eq. (2).

$$Q = \lim_{p \rightarrow 0} \oint_{\text{Sup}} \bar{\mathbf{J}} \cdot d\bar{\mathbf{S}} = \iiint_{\text{Vol}} \nabla \cdot \bar{\mathbf{J}} dV = -D \iiint_{\text{Vol}} \nabla^2 \varphi dV \quad (2)$$

In this equation, Q is the source strength, which is the source's neutron emission rate (s^{-1}), p is a length parameter defined between the closed surface and the source's surface, ∇ is the differential operator containing the directional derivatives (pseudovector) that in combination with the neutron density vector is named the divergence of $\bar{\mathbf{J}}$, and ∇^2 is an operator including the second derivatives with respect to space, also known as the Laplacian. In order to use the formal source condition, you can take just two members of Eq. (2), like,

$$Q = \lim_{p \rightarrow 0} \oint_{\text{Sup}} \bar{\mathbf{J}} \cdot d\bar{\mathbf{S}} \quad (3)$$

The physical meaning of Eq. (3) is the following: if a neutron source is surrounded by a closed surface, totally or partially encompassing the source, neutrons from the source will pass through the surface, which is used as a pseudovector in order to determine those neutrons leaking out from the surface and which becomes the neutron current density vector. Thus, in the limit where the closed surface approaches the neutron source surface, neutrons leaking out accounts for all the neutrons emitted by the source. This meaning is completed by analyzing the divergence of the neutron current density, which will give a scalar: if the scalar is positive it means there are 'sources' in the volume; if is negative it there are 'sinks'; if it is zero it means that in the volume there are no 'sources' or 'sinks' of neutrons.

If the formal source condition is used as is shown in Eq. (4).

$$Q = -D \iiint_{\text{Vol}} \nabla^2 \varphi dV \quad (4)$$

The Laplacian of neutron flux at a particular point represents the degree to which the value of the neutron field at that point differs from the average value of the neutron field in the vicinity of the point. From the diffusion equation in steady state,

$$\nabla^2 \varphi - \frac{1}{L^2} \varphi = 0 \quad (5)$$

Therefore,

$$\nabla^2 \varphi = \frac{\varphi}{L^2} \quad (6)$$

Plugging Eq. (6) into Eq. (4), and recalling that $\Sigma_a = D L^{-2}$, which is the macroscopic absorption cross section, Eq. (4) becomes,

$$Q = -\frac{D}{L^2} \iiint_{\text{Vol}} \varphi dV = -\Sigma_a \iiint_{\text{Vol}} \varphi dV \quad (7)$$

This means that in an infinite medium where neutrons are emitted by a source, those neutrons will eventually be absorbed in the volume.

The diffusion equation does not consider the decay of the free neutron, nor the neutron mass. It also assumes that neutron absorption in the medium is small. Solutions obtained with the diffusion equation can be used as a first approach to know the distribution in space of neutrons.

This equation can be used for simple cases such as monoenergetic neutrons in a single medium [7] as well as more complex cases, including different media and several energy groups. In the design of novel neutron detectors, where a moderator is included the detector, performance can be estimated by using the diffusion approximation. The solutions, although approximate, have exact solutions, where exact is used in the context of having a mathematical function.

The objective of this work was to determine the spatial distribution of neutrons of a $^{241}\text{AmBe}$ isotopic source in a water-filled cylindrical container by solving the diffusion equation using two energy groups. This distribution was compared with results obtained with Monte Carlo calculations and measurements.

2 MATERIALS AND METHODS

2.1 SOLVING THE DIFFUSION EQUATION

The steady-state diffusion equation was solved using two energy groups; in group 1 are neutrons whose energy is larger than 0.1 eV and group 2 contains neutrons whose energy is less than or equal to 0.1 eV (thermal). These diffusion equations are shown in Eqs. (8–9).

$$\nabla^2 \phi_1 - \frac{1}{\tau} \phi_1 = 0 \quad (8)$$

$$\nabla^2 \phi_2 - \frac{1}{L^2} \phi_2 = -\frac{\Sigma_1}{D_2} \phi_1 \quad (9)$$

In Eq. (8), τ is the Fermi Age which is a measure of the distance that neutrons travel during their moderation, so the square root of this parameter is the square root of 1/6 of the quadratic average distance that the neutrons travel from the site they are born as fast neutrons, until they become thermal. In Eq. (9), L represents the diffusion length that is 1/6 of the mean quadratic distance that the neutrons travel from the point where they became thermal to the point where they are absorbed [5]. In this equation, the source term of thermal neutrons is those that slowed down out of the fast group, i.e. $\Sigma_1 \phi_1$. Solutions of Eqs. (8) and (9) were obtained for three coordinate systems: Cartesian rectangular, cylindrical and spherical. In order to estimate the particular solution for ϕ_2 the last constant, being the amplitude, the formal source condition was applied [7].

1.1 MEASUREMENTS

The distribution of the thermal neutrons of the $^{241}\text{AmBe}$ source was measured with a proportional detector of $^{10}\text{BF}_3$. The source was placed in the centre of a 1-cm thick cylindrical container made of methylmethacrylate with 41.25 cm in radius and 107.4 cm in height, shown in Fig. 1.

Along the axis of the container there is a 2-cm radius and 0.3-cm-thick methylmethacrylate tube where the neutron source was inserted. The centre of the detector was aligned with the centre of the source and the position of the detector was varied along the radius. The mixture of ^{241}Am and Be from the source is contained in a hermetic stainless-steel cylinder of type 304L of 0.953 cm radius and 3.556 cm height. The source strength is $5.2 \times 10^6 \pm 3\% \text{ s}^{-1}$.



FIG. 1. Water container.

2.2 MONTE CARLO CALCULATIONS

MCNP5 code [8] was used to build a detailed model of the water container, the $^{10}\text{BF}_3$ detector, and the source. As a source term, the neutron spectrum of ISO [9] was used.

The transport of the neutrons in the water was simulated and the neutron spectra were calculated at the same sites where measurements were carried out. The spectra were integrated over energy to determine the contribution of thermal neutrons ($E \leq 0.1$ eV) and epithermal and fast neutrons ($0.1 \text{ eV} < E \leq 14$ MeV). In the calculations, 10^8 histories were used. The radial distribution of the neutrons of $^{241}\text{AmBe}$ in water obtained by the three methods were compared.

3 RESULTS

3.1 SOLUTIONS OF DIFFUSION EQUATION

In cartesian coordinates the solution of two group diffusion equation gives the neutron flux of energy group 2 (thermal) along the x -axis. This solution is shown in equation 10, where Q_σ is the source strength per cm^2 and D_2 is the diffusion constant of water for thermal neutrons.

$$\Phi_2(x) = \frac{Q_\sigma L^2}{2 D_2 (\tau - L^2)} \left(\sqrt{\tau} \text{Exp} \left[-\frac{|x|}{\sqrt{\tau}} \right] - L \text{Exp} \left[-\frac{|x|}{L} \right] \right) \quad (10)$$

In cylindrical coordinates the solution is shown in Eq. (11), here Q_λ is the source strength per unit length of the source. K_0 is the modified Bessel function of the second kind of order zero.

$$\Phi_2(r) = \frac{Q_\lambda L^2}{\pi D_2 (2\tau - L^2)} \left(K_0 \left[\frac{r}{\sqrt{\tau}} \right] - K_0 \left[\frac{r}{L} \right] \right) \quad (11)$$

In Eq. (12) the solution in spherical coordinates for neutrons along the radius is shown.

$$\Phi_2(r) = \frac{Q L^2}{4\pi D_2 (\tau - L^2) r} \left(\text{Exp} \left[-\frac{r}{\sqrt{\tau}} \right] - \text{Exp} \left[-\frac{r}{L} \right] \right) \quad (12)$$

The plots of Eqs. (10–12) are shown in Fig. 2, which were normalized to the neutron flux at 2.7 cm from the source. In this figure, the L , D_2 , and τ are for water, namely $\tau = 27 \text{ cm}^2$, for group 1, $D_2 = 0.16 \text{ cm}$ and $L = 2.54 \text{ cm}$ for group 2 [10]. In the three solutions the arguments in the functions show the contribution of neutrons from both energy groups.

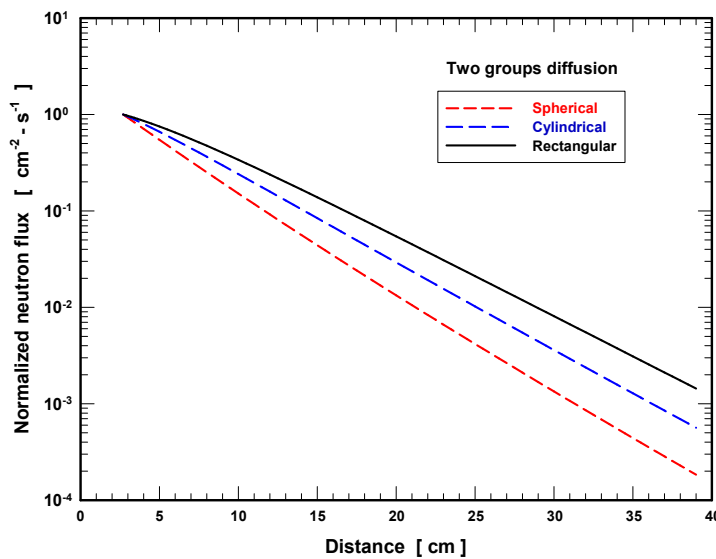


FIG. 2. Thermal neutron flux (group 2) as a function of the distance from the source.

3.2 EXPERIMENTAL RESULTS

Figure 3 shows the results of count rates measured with a $^{10}\text{BF}_3$ which was moved along the radius of water container, in order to compare the count rates were also normalized to count rate measured to 2.7 cm from the source. Approximately, above 7 cm in water the neutron flux decreases exponentially.

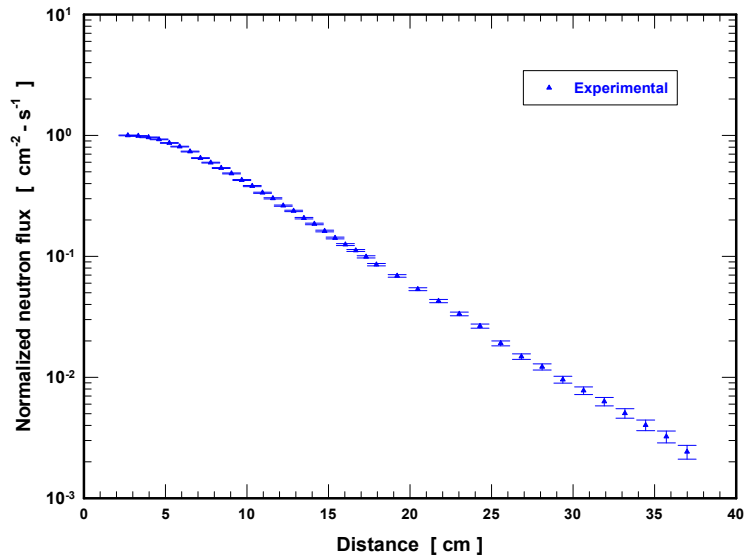


FIG. 3. Neutron flux along the radius, measured with a $^{10}\text{BF}_3$ detector.

Monte Carlo simulation was used to estimate the neutron spectra along the radius at the source height; in Figure 4 some of these spectra are shown. At 2.7 cm from the source the amount of methylmethacrylate and the water between the source and the $^{10}\text{BF}_3$ detector model is enough to produce epithermal and thermal neutrons; however, the distance is too small, and the largest contributions are due to neutrons with $E > 0.5$ MeV.

Also, in Fig. 4 it can be noticed that as the distance is increased the proportion of thermal neutrons also increases due to moderation of epithermal and fast neutrons.

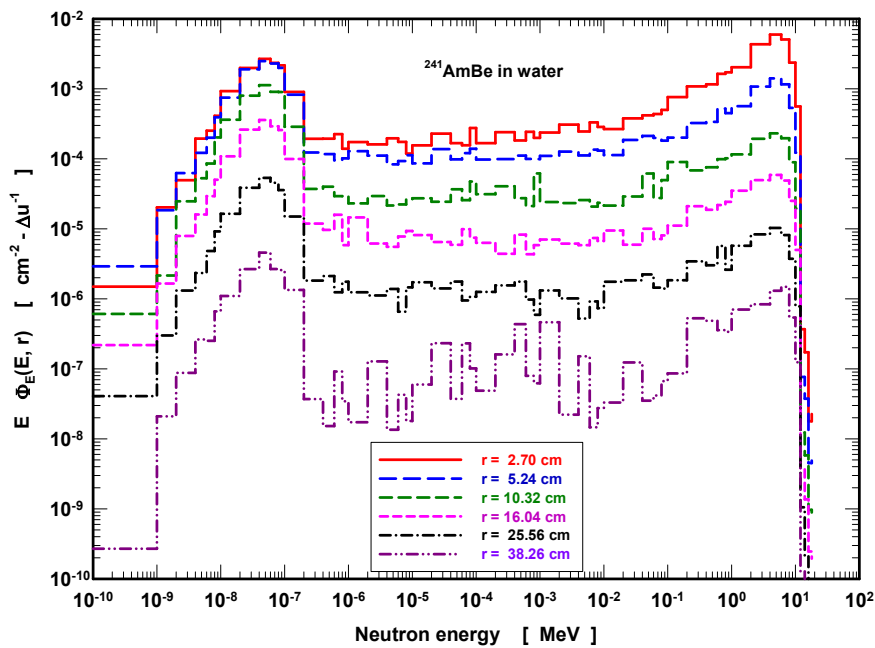


FIG. 4. Neutron spectra of $^{241}\text{AmBe}$ source in water.

3.3 MONTE CARLO CALCULATIONS

The total neutron fluence rate in each position was obtained by integrating the spectrum for all energies, and the thermal neutron flux was obtained by integrating the spectra for neutrons with energy ≤ 0.1 eV.

Total and thermal neutron fluences, normalized to values calculated at 2.7 cm, are shown in Fig. 5. While the total neutron fluence has an exponential decrease as the distance is increased, thermal neutrons reach its maximum value at 3.97 cm, being 4.2% larger than the neutron flux to 2.7 cm. From distances from the source ranging from 9 to 37 cm, the total and thermal neutrons decrease approximately at the same pace.

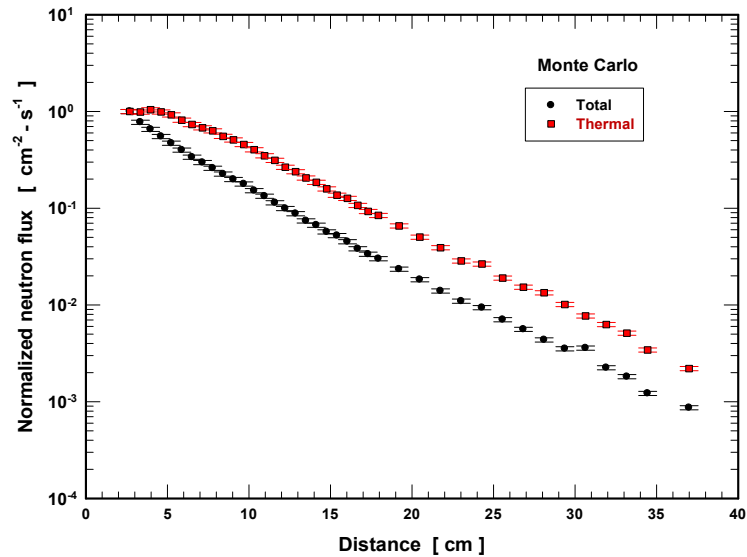


FIG. 5. Normalized, total and thermal, neutron flux calculated with Monte Carlo.

3.4 COMPARING THE NEUTRON FLUX OBTAINED WITH DIFFERENT PROCEDURES

In Fig. 6 is shown the normalized neutron flux distribution along the radius measured with a $^{10}\text{BF}_3$ detector. Also in the figure is the normalized thermal neutron flux estimated with Monte Carlo calculations. There is a good agreement between the measurements and calculations.

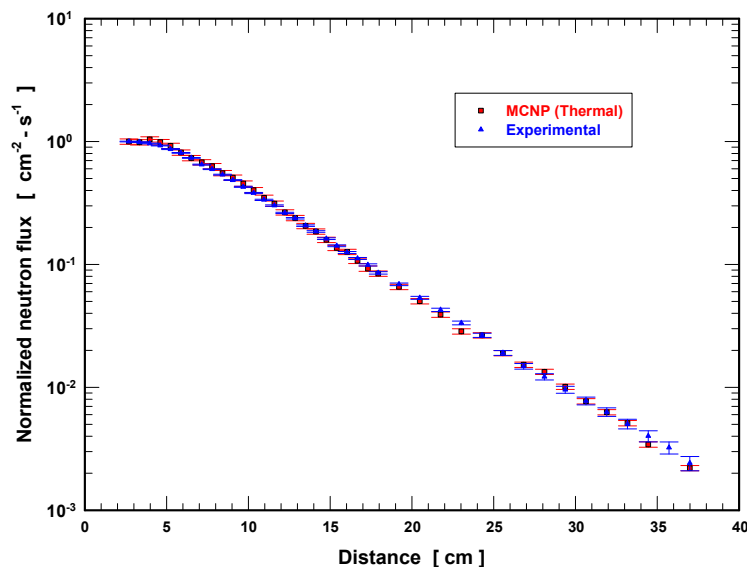


FIG. 6. Neutron flux along the radius.

In Fig. 7 are the solutions of the diffusion equation for two groups for spherical, cylindrical and rectangular coordinates (equations 10, 11 and 12). Here, the $L = 2.85$ cm, $\tau = 27$ cm², and $D_2 = 0.16$ cm [5, 10]. For each

solution is included the total neutron flux estimated with Monte Carlo that was scaled to the amplitude of equations 10, 11, and 12. The solution for cylindrical coordinates is closer to the Monte Carlo calculations than are solutions for Cartesian and spherical coordinates.

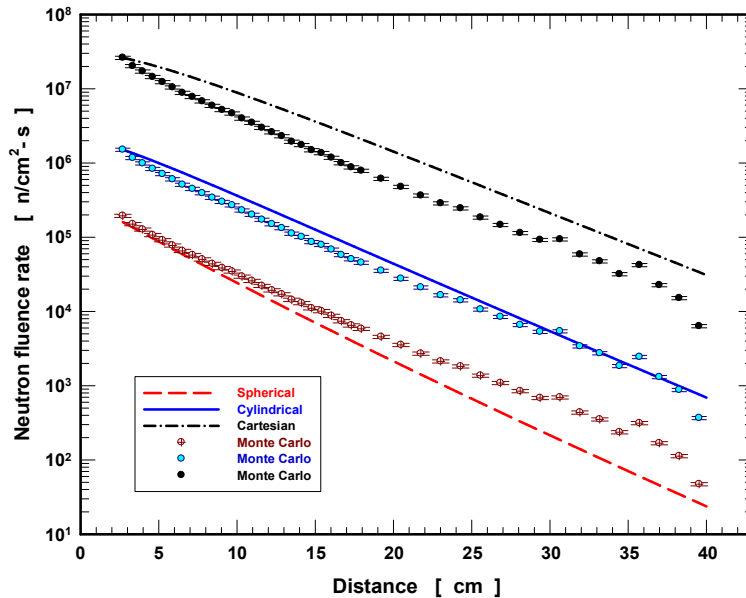


FIG. 7. Neutron flux calculated using two-group diffusion equation and Monte Carlo.

4 CONCLUSION

The radial distribution of the neutron flux from a $^{241}\text{AmBe}$ source in water at the midplane of the source was determined by three methods: Solving the diffusion equation for two energy groups in three coordinate systems, measuring the thermal neutrons with a $^{10}\text{BF}_3$ detector, and using Monte Carlo methods. With the spectra, the thermal ($E < 0.1$ eV) and total neutron fluxes were obtained. Solutions of diffusion equation were obtained by using the formal expression of the source condition. The $^{241}\text{AmBe}$ source produces neutrons from 0.5 to 11.5 MeV and these neutrons are in the calculated neutron spectra in water. Due to neutron moderation and thermalization in water, the spectra include epithermal and thermal neutrons. As the distance from the source increases, total neutron fluence decreases due to neutron absorption and neutron leaking out from the moderator.

Experimental measurements agree well with the thermal neutron flux calculated using Monte Carlo methods. The thermal neutron flux is approximately reduced three orders of magnitude in 37 cm of light water.

The solution for the 2-group diffusion equation in cylindrical coordinates is closer to the Monte Carlo calculations than are solutions for Cartesian and spherical coordinates.

REFERENCES

- [1] SHI, F., MA, J., ZHAO, J., LIU, S., Detection sensitivities of C and O in coal due to a channel in a moderator, *Radiat. Meas.* **46** (2011) 88–91.
- [2] GÓMEZ-ROS, J.M., et al., Designing an extended energy range single-sphere multi-detector neutron spectrometer, *Nucl. Instrum Meth Phys Res A* **677** (2012) 4–9.
- [3] ALI, S., et al., A portable shield for a neutron howitzer used for instructional and research purposes, *Appl. Radiat. Isot.* **103** (2015) 37–42.
- [4] GUZMÁN-GARCÍA, K.A., et al., Performance of $^{10}\text{B}+\text{ZnS}(\text{Ag})$ neutron detectors in RPM for the detection of special nuclear materials, *Radiat. Meas.* **107** (2017) 58–66.
- [5] LAMARSH, J.R., *Introduction to Nuclear Reactor Theory*, Addison-Wesley, Massachusetts (1972) 118–155.
- [6] ZWEIFEL, P.F., *Reactor Physics*, McGraw-Hill, New York (1973) 23–43.
- [7] VEGA-CARRILLO, H.R., The source condition in neutron diffusion theory, *Rev. Mex. Fís.* **47** (2001) 381–385.
- [8] X-5 MONTE CARLO TEAM. MCNP - A General Monte Carlo N-Particle Transport Code, Version 5, Report LA-UR-03-1987, Los Alamos National Laboratory. (2003).
- [9] INTERNATIONAL ORGANIZATION FOR STANDARDIZATION, ISO 8529 Part 1: 2001, Reference neutron radiations: Characteristics and methods of production (2001).

[10] LAMARSH, J.R., Introduction to Nuclear Engineering, Third printing, Addison-Wesley Publishing Co, Reading (1977) 177–181.

[11] NATIONAL COUNCIL ON RADIATION PROTECTION AND MEASUREMENTS (Bethesda, MD). Calibration of survey instruments used in radiation protection for the assessment of ionizing radiation fields and radioactive surface contamination, NCRP Rep. 112 (1991).

[12] VEGA-CARRILLO, H.R., MARTINEZ-OVALLE, S.A., Few groups neutron spectra, and dosimetric features, of isotopic neutron sources, Appl. Radiat. Isot. **117** (2016) 42–50.

TOPICAL SESSION 4
FRONT END ELECTRONICS

COMPENDIUM OF FRONT-END ELECTRONICS

F. MESSI

Division of Nuclear Physics, Lund University and
European Spallation Source ERIC
Lund, Sweden
Email: francesco.messi@nuclear.lu.se

Abstract: Our world is changing fast. On one hand, technological developments provide us with new and powerful electronics devices on almost a weekly basis. On the other hand, the end-user of these electronics is now rarely required to actually configure the devices, as everything is automated. This ‘de-empowerment’ of the end-user may be detrimental to the scientific community. This is because the unique conditions in which a scientific measurement is performed require the end-user to have unrestricted access to every variable of the experimental setup. In this compendium, a general overview of some popular electronic modules is presented, and the different characteristics the end-user should take into consideration when buying/designing electronics systems for a new experimental application are discussed. ¹

1 INTRODUCTION

Modern detectors provide as output electrical signals that encode the information obtained during measurements. These signals may be of very different nature depending upon the detector used. They may take the form of a current, a charge or a potential difference (dpp), to name few. For example, a photomultiplier tube (PMT) provides a signal in the form of current proportional to the amount of scintillation light collected on its photocathode. Regardless of the detector, electronic modules are required to process these signals and to decode the information contained within them. In the example of a scintillator instrumented with a PMT, reading the output current signal over a known resistance will provide a voltage signal (dpp pulse) while determining its amplitude will give a measurement of the current deposited in the detector. In this way, instrumentation electronics are a key component of any experimental setup.

Depending upon the information required from the detector, a precise chain of signal-processing electronics needs to be defined. This electronics chain can be divided into blocks according to the standard function required of them. In the example of Figure 1 the electronics chain is divided into two blocks, a Front-End Electronics (FEE) block and a Read-Out Electronics (ROE) block. FEE is defined as the electronics located immediately downstream of the detector. Usually, dealing with analog signals, FEE are the most delicate part of the electronics chain. Consider first the concept of electronic noise, the signal-to-noise ratio (S:N) is crucial to analog signals. Noise is a random fluctuation of the voltage level and can affect the signal in different ways at different times. As an example, in Figure 2(a), the same pulse is recorded at four different times using a noisy electronic channel. As can be seen, a measurement of the signal, either the integration of the pulse (charge) or the crossing of a fixed threshold value by the pulse (time), will provide four different results. Since analog signals carry all of the information obtained during the measurement in one single pulse, any noise perturbation may very easily compromise the readout.

In terms of signal integrity, a ‘digital signal’ is more insensitive to noise than an ‘analog signal’. A digital signal is, in fact, an analog signal which can have only two voltage levels. One level is assigned digital information ‘0’ (*zero* or *low*) and the other level is assigned digital information ‘1’ (*one* or *high*). The two levels are nonadjacent regions (the coloured bands in Fig. 2(b)). The logical information contained within a digital pulse at a specific time depends whether the voltage level is in one region or in the other. Since each region is of the order of hundreds of millivolts, a noise perturbation needs to be substantially high to compromise the information carried by the pulse.

The purpose of the FEE is to:

1. decouple the detector from the rest of the electronics system and match the impedances;
2. acquire the electrical signal from the detector and prepare the information (shape the signal) for the ROE;
3. digitise the analog signal for the Data Acquisition system (DAQ).

¹ The idea for this compendium came from the IAEA Technical Meeting on Modern Neutron Detection in September 2017, where the alarming trend was noted that neutron scientists are buying detectors and associated electronics like never before, and without actively choosing the later but relying only on the recommendations of the detector supplier.

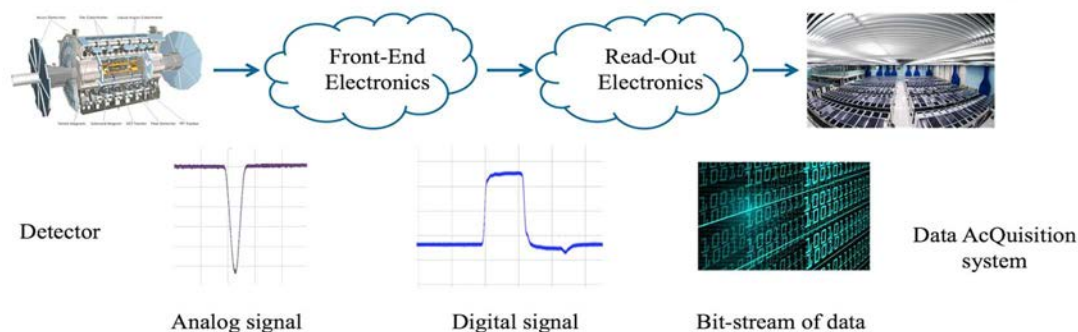


FIG. 1. Detectors of any experimental setup produce analog electrical signals. These analog signals are converted into digital signals by the Front-End Electronics (FEE). Read-Out Electronics (ROE) compress the information carried by the resulting digital signals into a bit-stream of data to be stored on a computer.

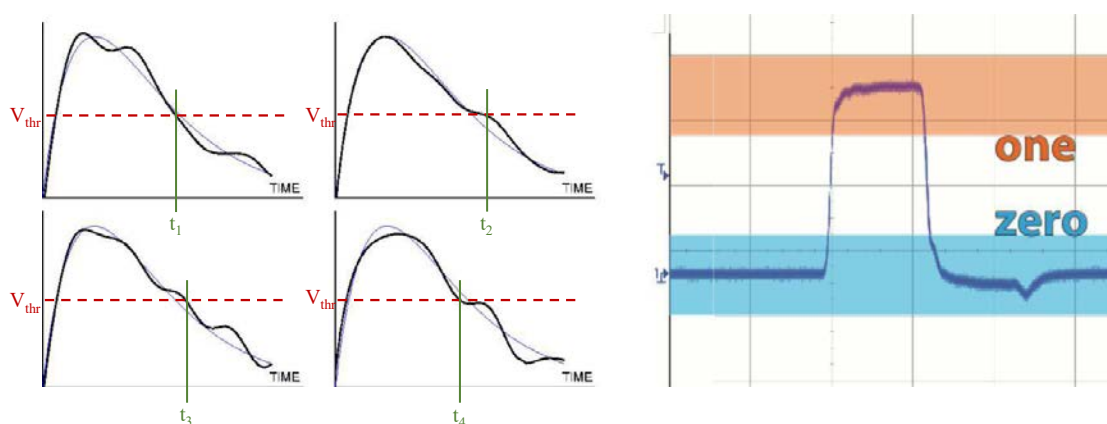


FIG. 2. Analog signals (left) and digital signal (right). Analog signals are extremely sensitive to noise perturbations. The same pulse will cross a fixed threshold at four different times when noise is present. Left: Signal plus noise (thick, black) at four different times. The noiseless signal is superimposed for comparison (thin, blue). The signal-to-noise ratio is about 20. Figure from [1], modified by the author. Right: A digital signal can have only two voltage levels. The first is associated with digital information 'zero' (blue band) and the second to digital 'one' (orange band).

1.1 DECOUPLING AND IMPEDANCE MATCHING

The main task of the FEE is to decouple the detector from the rest of the electronics chain and to match the impedances between the two. This is important to avoid damage both to the detector and to the electronics chain (such as from high-voltage discharges), and to avoid noise contamination in both directions. In fact, any spark resulting in a large transient electric signal from the detector may damage the electronics. For example, a broken wire from a wire chamber may short the connected digitiser to the high-voltage, thus damaging the electronics module and destroying the input stage of that channel. It is also important to protect the detector from any unwanted signal feeding back from the electronics. The majority of modern electronics modules are conceived for a 50 Ohm impedance system. This in general is not the case for the detector in use. If a mismatch in impedance is present, signal reflections may occur and/or an unwanted current may flow back into the detector. Both effects may introduce perturbations into the detector itself. For example, high-frequency noise on one channel may generate an oscillation on the ground plane of the detector, thus compromising all the channels. Moreover, if the impedance mismatch is very large, too much current may flow out of the detector resulting in damage to the detector itself.

There are several ways to decouple a detector. Very often, a solution is already integrated into the detector itself and not user-accessible. The simplest way to decouple a detector is via a resistor, a capacitor, or a combination of the two. This is known as 'passive decoupling'. Sometimes active decoupling is necessary, in order to preserve the integrity of the signal and/or to match the impedances. In this case, an analog buffer or an operational amplifier

(OpAmp) may be used. The decoupling of a system is unique and a specific study needs to be performed for each individual setup. It is responsibility of the user to check that the necessary decoupling is present and correct for the measurement to be performed.

1.2 ACQUISITION AND SHAPING OF THE SIGNAL

Signals from a detector are usually short current pulses $i(t)$ whose time scale may vary from few ps till several hundreds of μs , depending upon the detector technology. These pulses may be invisible to the ROE. In fact, any electronics module needs a minimum amount of time to recognise an input signal and may miss a signal if it is too fast. Further, the pulse can be too small with respect to random noise or a slow discharge pulse and thus lie out of the sensitive range of the input stage of the applied electronics.

The shape of a pulse can be modified without affecting the information it carries. For example, a signal can be stretched in time, conserving its integral or maintaining it proportional to the original. In this way, a fast pulse can be smoothed and acknowledged by the ROE without perturbing the energy measure provided. These devices are known as ‘shapers’. The simplest shaper consists of a series of CR-RC circuits (see Fig. 3).

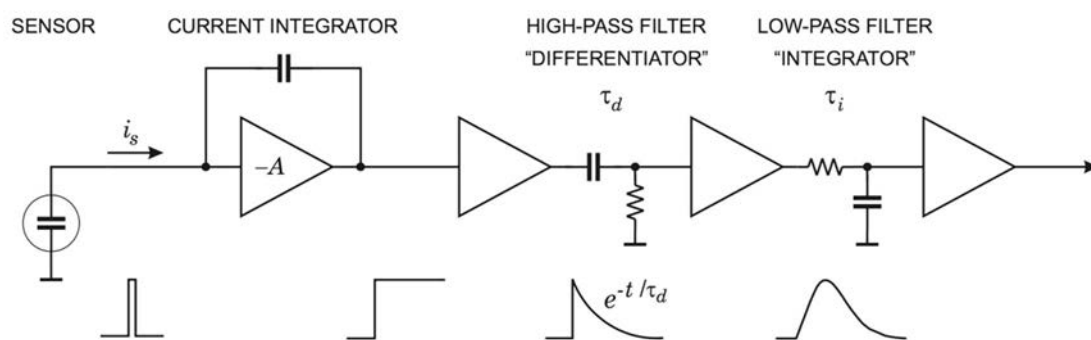


FIG. 3. Components of a pulse-shaping system. The signal current from the sensor, i_s , is integrated to form a step impulse with a long decay. A subsequent high-pass filter (‘differentiator’) limits the pulse width and the low-pass filter (‘integrator’) draws out the rise time to form a cusp-less pulse with a smooth transition. Figure from [1].

When the rate at the detector is high, a subsequent pulse can arrive before the previous pulse has been processed. If the second pulse overlaps with the previous pulse, this is known as ‘pileup’. In this case, the electronics may not recognise the second pulse and its information may be lost (for example, to a discriminator) or erroneously added to the previous pulse (for example, by a Charge-to-Digital Converter, QDC). By constraining the pulse width, this effect can be limited and the second pulse can be fully resolved (see Fig. 4).

Optimum pulse shaping generally depends on the particular application in question.

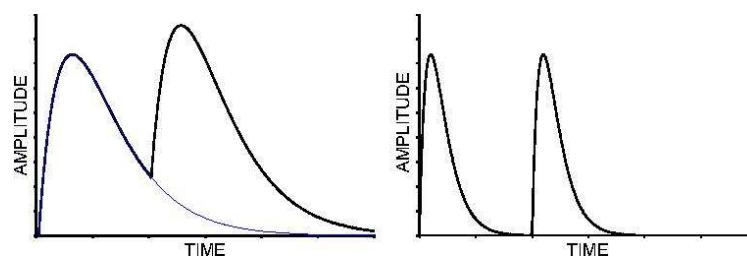


FIG. 4. Amplitude pileup occurs when two pulses overlap (left). Reducing the shaping time allows the first pulse to return to the voltage baseline before the second pulse arrives. Figure from [1].

1.3 DIGITISING: FROM THE ANALOG TO THE DIGITAL WORLD

The ultimate task of the FEE is to prepare the information provided by the detector for the ROE or for the DAQ itself. This means the analog signal from the detector has to be converted into a digital signal that can be passed on to a DAQ. In other words, the purpose of the FEE is to translate the information from the analog world to the digital world.

As mentioned before, a digital signal is an analog signal which can have only two voltage levels. Several different ‘logical families’ exist, according to the different voltages assigned to the digital information. In Table 1, an overview is presented together with the respective corresponding voltages levels.

TABLE 1. FAMILIES OF DIGITAL SIGNALS

Family	One (V)	Zero (V)
TTL	2 to 5	0 to 0.8
NIM	3 to 12	2 to 1.5
ECL	0.81 to 1.13	1.95 to 1.48
LVDS	P	1.27 to 2.40
	N	0.92 to 1.12

NOTE: Not all families are compatible with each other. Intermediate modules that correctly translate from one family to another have to be used to enable level transition

Conversion between the analog and digital world is performed with three different kinds of modules:

Discriminators: determine if a signal exceeds a given threshold.

1. Time-to-Digital Converters (TDCs): convert the time at which a signal is recorded into a digital number.
2. Analog-to-Digital Converters (ADCs): convert the analog value of a signal into a digital number.
3. In particular, a Voltage-to-Digital Converter (VDC) converts an instantaneous voltage level, while a Charge-to-Digital Converter (QDC) the integrated charge.

Any other more complex module is generally a combination or an evolution of these three basic models.

2 BASIC EXAMPLE: PHOTOMULTIPLIER TUBE (PMT)

Since the basic principles of FEE apply to any detector setup, a simple detector setup will be used for illustrative purposes in this paper — a scintillator coupled to a PMT.

Fig. 5 shows a scheme of three possible scenarios for the read-out of such a detector:

In the top case, a time measurement is performed. The signal is passed to a discriminator and a TDC is used to digitize time information. In the middle case, an energy measurement is performed. The signal is passed to a shaper circuit and a QDC is used to digitize the energy deposited in the detector. In the bottom case, the signal is passed to a digitiser. The entire pulse is digitised and, if the digital ‘image’ of the pulse is accurate, all of the information is saved. Subsequent analysis can be performed off-line on the recorded data.

Two important components are common to all the scenarios. One is the first stage of the FEE: the pre-Amplifier (preAmp). The preAmp serves two purposes. The first is to decouple the detector to the rest of the electronics chain and match the impedance of the PMT to the impedance of the cable. The second is to amplify the signal from the detector (that in general can be very small) and to drive the transmission line, or cable. This helps preserving the signal-to-noise ratio (S:N). The second is the cable itself. Cables are crucial for any setup. It is through the cable that the signal travels from one component to another. It is also through the cable that the

majority of noise is introduced. It is important to choose the correct cable for the setup. Different cables have different impedances, dielectric coefficients and can drive different kinds of signals.²

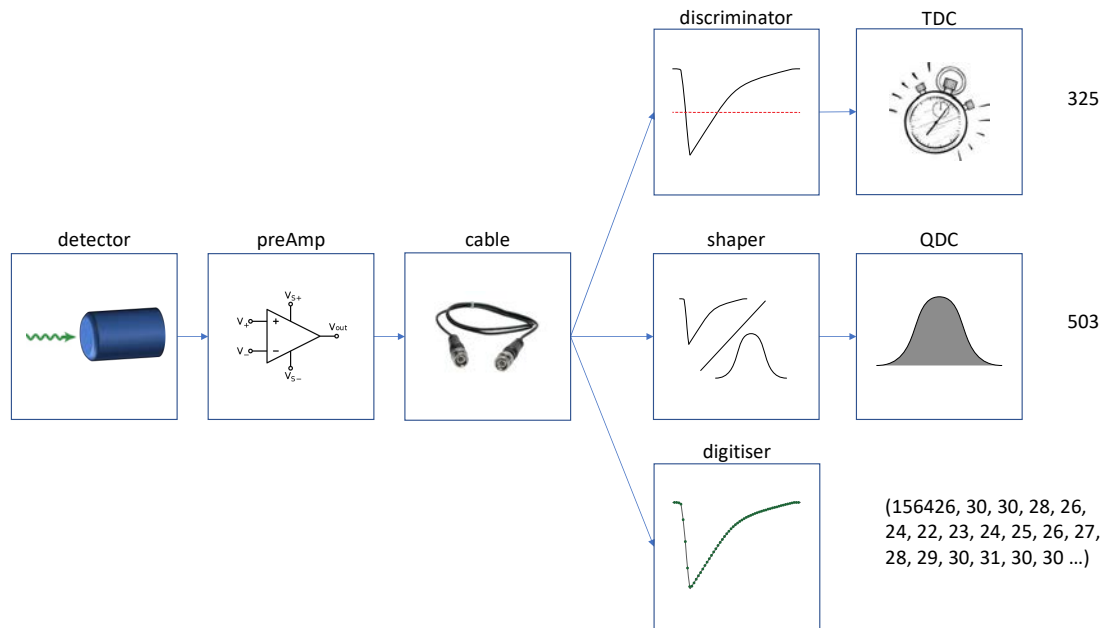


FIG. 5. Example of detector read-out. Three different electronics chain presented for the read-out of a scintillating detector coupled to a PMT.

2.1 POSITION-TIME MEASUREMENT, DISCRIMINATOR AND TDC

Position-sensitive detectors measure the passage of a particle and the time of the detection. In the example of a plastic scintillator coupled to a PMT, the passage of a particle results in an electric pulse. To produce a trigger, the electric pulse needs to be discriminated from electronics noise and/or from signals generated by other particles interacting with the detector. The time of the digital pulse can be measured using a TDC.

2.1.1 Discriminator

A discriminator is a module that compares two signals. One of them is a fixed voltage level, also known as the ‘discrimination threshold’, while the other is the analog pulse from the detector. If the pulse exceeds the threshold, the output of the discriminator will be ‘one’. If the pulse is under threshold, the output is ‘zero’ (refer to Fig. 6). To avoid loss of information, the discrimination threshold needs to be set *as low as possible* as required by the S:N. In fact, the information carried by any signal that does not pass the discriminator is lost forever. Many kinds of discriminators exist, such as leading edge / dual threshold / constant fraction, to name few. A detailed discussion of these various types of discriminators is beyond the scope of this paper. In general, the user has to be aware of the type of discriminator used and how to correctly set it up. The data sheet for the module may be useful.

² For example, a coaxial cable is meant for *single-ended signals*, while a twisted pair ribbon cable is meant for *differential signals*. A detailed discussion on transmission lines in general is out of the scope of this paper. More information can be found in [2] or [3].

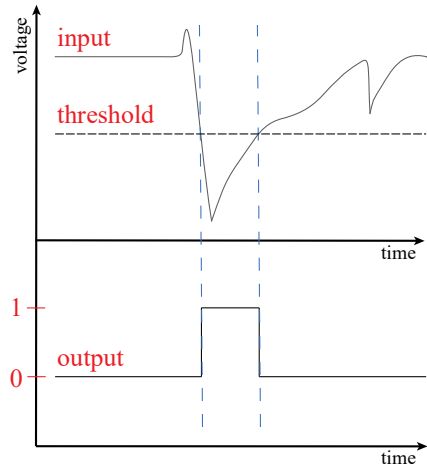


FIG. 6. Signals from a discriminator. On the top panel, an analog signal as function of time shown together with the constant discrimination threshold. On the bottom panel, the corresponding digital output signal from a discriminator.

2.1.2 TDC

A TDC is a device used to digitize the detected time of an event. In general, it requires a shaped signal as input. This is often a digital signal with constant width and very fast rise time, such as that provided by a discriminator. The simplest way to think of a TDC is a chronometer: a start is provided and a counter is increased at regular intervals (e.g. with a clock). When a signal is provided to the channel, the counter stops increasing. The time information relative to the signal is the number stored in the counter multiplied by the period of the clock.

$$T_{\text{measure}} = TDC \times CLK$$

Modern TDCs, also called MultiHit-TDCs, do not stop the counter when the signal is received, but rather store the value of the counter into memory and continue to count. In this way, multiple hits can be recorded in sequence, without losing any events due to read-out and reset operations. There are several ways to generate a TDC and an explanation of them is beyond the scope of this paper.³

2.2 ENERGY MEASUREMENT, SHAPER AND QDC

Calorimeter detectors measure the energy deposited by a particle in the detector. In the example of a scintillator coupled to a PMT, the particle loses some or all its energy in the scintillator. The light emitted by the scintillating material, which is proportional to the deposited energy, is collected by the PMT. The resulting electrical current pulse has an integral that is proportional to the amount of detected light and thus the deposited energy. A QDC module will integrate the electric pulse, providing a digital word with a value proportional to the measured energy. Often, QDC modules require a signal with specific time and shape characteristics to correctly perform the integration. A shaper circuit is almost always needed (recall Section 1.2).

As in mathematics, an integral requires a closed interval, so a conventional QDC needs a well-defined time interval for the integration of the pulse. This is provided with a digital signal called a ‘gate’. The QDC will integrate the analog signal for the time period that the gate signal is ‘one’. Analog delay lines are difficult to avoid in such a configuration as the signal to be measured needs to be placed within the gate. Recall that using cable is not as simple as it can seem. It is not always possible to obtain the necessary analog delay value to place the signal within the gate without compromising the integrity of the signal. The usage of digitiser modules or in general of a sampling ADC (sADC), is one way to reduce the amount of electronics modules in the setup and avoid analog delay lines.

³ Recently, FPGA (Field Programmable Gate Array) technology has been used more and more for TDC development. More information can be found in [4].

2.3 DIGITISER

A digitiser is a module that allows for the conversion of analog signals into digital information that can be directly passed to a DAQ. As shown in Fig. 7, the value of the analog signal is measured at regular steps. Those regular steps are known as the ‘sampling time’. These samples, or relative digital amplitudes, can then be processed. In this way, a digital approximation to any pulse can be stored on a disk and the full measurement can be analysed in real time or off-line. In fact, once the pulse is reconstructed, the time of the interaction can be extrapolated as can the charge integration or the shape identification.

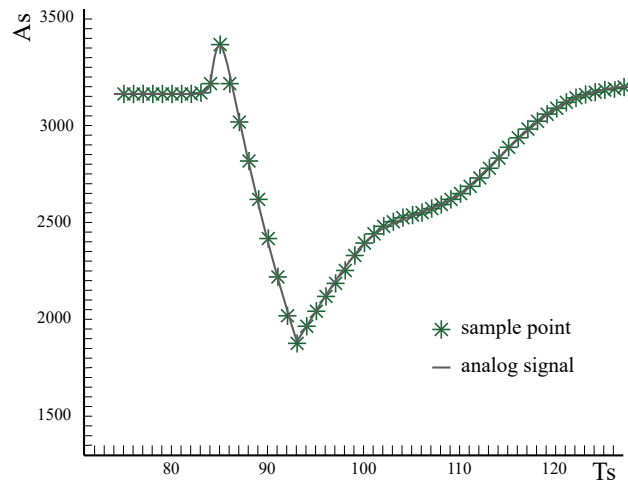


FIG. 7. Digitiser output. In grey the original analog signal from a PMT; in green, the sample points. The ADC channels (A_s) are plotted as a function of their sampling time (T_s).

3 CHARACTERISTICS OF A DIGITISER

Modern electronics are everyday becoming faster and delivering better performance. Today, it is possible to perform all of the discrimination, shaping and digital conversion operations with a digitiser for the majority of applications. In fact, the digital representation of an analog pulse provided by a modern digitiser is so accurate that all the original information enclosed within the original analog signal can be reconstructed offline using mathematical algorithms. For each of the sample points, the digitiser provides a pair of numbers: the *sampling time* (T_s) and the ADC value of the sample (A_s). By plotting these variables against one other, the digitised pulse can be visualised. This is exactly the same process performed by a modern oscilloscope — the input signal is digitised and the sampled points are displayed as function of the time. From such a figure, the main characteristics of many electronics modules can be examined:

Sampling Rate. The Sampling Rate (R_s), expressed often in Gs/s (*giga samples per second*), represents the constant time interval between two consecutive measurements. The higher the sampling rate, the more accurate the reconstruction of the signal. As a consequence, more memory is required to store the data. If the sampling rate is too low, features of the original signal may be lost, as shown in Figure 8(a). If the rate of the sampling is high enough [5], the original signal can be reconstructed without losing any of the information it carried.⁴

Slew Rate. The Slew Rate, expressed often in V/ μ s (*volts per microsecond*), is defined as the maximum change of voltage per unit of time. It represents the number of volts one measurement can differ at maximum from the previous if the sampling rate is 1 μ s. This is a very important characteristic! If the Slew

⁴ It applies also to: sADC.

Rate is not high enough, the digitiser will not be able to follow the signal. Regardless of the sampling rate, the signal will not be reconstructed correctly (see Figure 8(b)).⁵

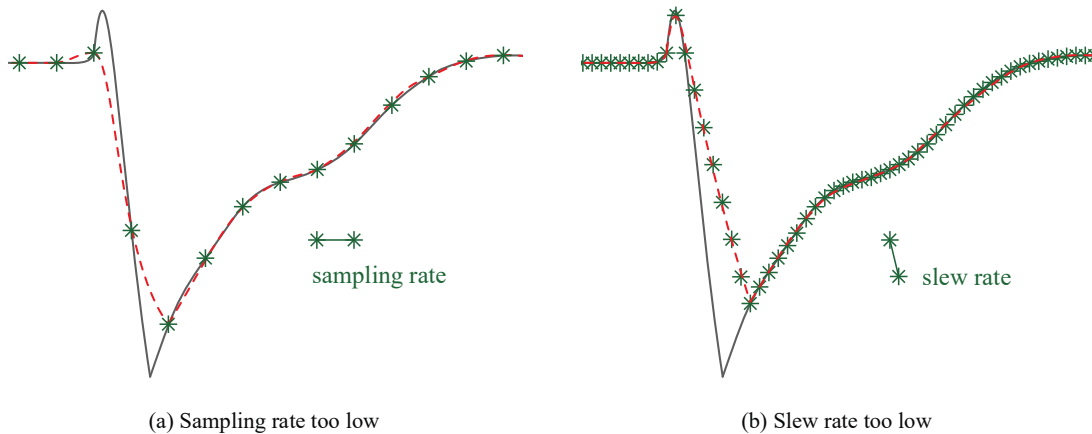


FIG. 8. Non-optimal digitization of an analog pulse. In grey the original analog signal, in green the digitized samples and in red the signal reconstructed from the digitisation. If the Sampling Rate and the Slew Rate are not high enough, important features of the original signal may be lost.

Analog Bandwidth. The analog bandwidth represents the range of frequencies for which the device performs linearly. Any signal can always be decomposed in its Fourier transform. The maximum frequency of this series has to be included within the bandwidth. To avoid distortion, the bandwidth of the digitiser needs to be large enough for the detected signal. On the other hand, if the bandwidth is too large the amount of noise transmitted without increasing the signal will increase.⁶

Input Range. The input range is the maximum amplitude the digitiser can accept as input. If the input signal exceeds this, the digitiser will first saturate and, if the value continues to increase, may be damaged.⁷

Reference Voltage and Analog Resolution. Reference voltage and analog resolution are two characteristics linked to the digitisation process itself. A digital representation of an analog signal cannot have infinite precision. It would require a sampling process with an infinite sampling rate, slew rate and analog bandwidth. A real sampling (discretisation) process occurs with finite voltage range divided into a well-defined number of sub-intervals. The upper limit of the range is called the ‘reference voltage’, while each interval of the range corresponds to an ADC channel (A_s). The analog resolution of a digitiser, expressed in the number of bits, is given by the voltage range divided the total number of ADC channels. In Figure 7, the baseline of the signal is at channel ~ 3150 . In binary, this is equal to 110001001110 and the digitiser used has to have an analog resolution of at least 12 bits. Assuming the reference voltage range from -1 to $+1$ V, each ADC channel corresponds to $2 \text{ V} / 2^{12} \text{ ch} \sim 0.5 \text{ mV}$.⁸

Time Resolution. The time resolution is the depth of the TDC counter register. It is expressed in ‘number of bits’ and provides the number of consecutive samples to which a unique time stamp can be assigned ($\#_s = 2^n$). In the majority of cases, after a time $\#_s \times R_s$, the counter is reset without an intervention from the user.⁹

⁵ It applies also to: OpAmps, analog buffers, discriminators.

⁶ It applies also to: OpAmps, analog buffers.

⁷ It applies also to: any kind of electronics modules.

⁸ It applies also to: ADCs, TDCs.

⁹ It applies also to: TDCs.

Memory. While in principle it is possible to transfer all data as soon as they are measured, this is inconvenient and highly demanding on the hardware in question. Instead, data are often stored inside the module and transferred to the user (to the screen of the oscilloscope or to the DAQ running on a computer for example) in blocks. A large amount of memory may help in protecting against data loss during the transmission stage.¹⁰

4 SUMMARY

Modern electronics are becoming cheaper every day and simultaneously offering better and better performance. Today, it is possible to perform scientific experiments using commercially available electronics, without any need to develop custom modules for individual detectors. Nevertheless, it is very important to choose the correct FEE and to correctly configure it, according to the needs of the experiment to be performed. The FEE are the electronics located as close as possible to the detector. They serve to decouple the detector from the rest of the electronics chain and match the impedances, to shape the analog signal provided by the detector, and to convert this analog signal to a digital signal. Modern digitisers can recreate an accurate digital representation of the analog pulse from a detector. In the majority of cases, this representation is sufficient for all the information carried by the analog pulse can be correctly reconstructed.

REFERENCES

- [1] SPIELER, H., “Analog and Digital Electronics for Detectors” (2006), <https://www.semanticscholar.org/paper/Analog-and-Digital-Electronics-for-Detectors-Spieler/63105332da95e78ced710e605af87185d50ba03c>.
- [2] BOGATIN, E., Signal Integrity—Simplified, Prentice Hall Professional Technical Reference (2004).
- [3] GREEN, L., Understanding the importance of signal integrity, IEEE Circuits Devices Mag. **15** 6 (1999) 7–10.
- [4] ZHENG, J., CAO, P., JIANG, D., AN, Q., Low-cost FPGA TDC with high resolution and density, IEEE Trans. Nucl. Sci. **64** 6 (2017) 1401–1408.
- [5] SHANNON, C.E., Communication in the Presence of Noise, Proc. IRE **37** 1 (1949) 10–21.

¹⁰ It applies also to: ADC and TDC boards.

TOPICAL SESSION 5
NEUTRON SPECTROSCOPY

RECENT NEUTRON DETECTION WORK AT CANADIAN NUCLEAR LABORATORIES

B. M. VAN DER ENDE

Canadian Nuclear Laboratories

Chalk River, ON, K0J 1J0

Canada

Email: bryan.vanderende@cnl.ca

Abstract: In this paper, some recent representative contributions from Canadian Nuclear Laboratories to He-3 neutron detection replacement technologies are presented. This includes a summary of an evaluation of a boron-coated straw neutron detector against radiation portal monitor guidelines, unique features of a patented boron-loaded liquid scintillator, and initial investigations into liquid argon scintillation detection with pulse shape discrimination, for neutron detection applications.

1 INTRODUCTION

Canadian Nuclear Laboratories (CNL), formerly Atomic Energy of Canada Ltd., engages in a wide variety of neutron detection activities: neutron detector evaluations and measurements (including application developments, such as stand-off reactor monitoring), neutron detector development (including (Gas Electron Multiplier) GEM detectors, integrated Special Nuclear Material (SNM) detection schemes, etc.), neutron dosimetry, and development of detector simulation techniques.

This paper presents three particular ventures that have a focus on developments for the replacement of He-3 neutron detection technology with alternatives, to address the current He-3 supply problem [1]. This includes a recent evaluation of a boron-coated straw (BCS) neutron detector, together with a comparison of Geant4 [2] with MCNPX [3] in its evaluation; results on a patented boron-loaded liquid scintillator technology; and developments of a liquid argon neutron detector, focusing on how liquid argon detection coupled with pulse shape discrimination is now a mature detection technology that can be more deeply exploited.

2 EVALUATION OF A BORON-COATED STRAW NEUTRON DETECTOR

2.1 DESCRIPTION OF DETECTOR AND EXPERIMENTAL METHODS

The BCS detector is a commercial off-the-shelf product from Proportional Technologies Inc. (Houston, TX, USA). The detector consists of seven 25.4 mm-diameter Al tubes, arranged in a planar configuration with an active detection area 1 m long and 18 cm wide. Each Al tube contains seven 7.5 mm-diameter copper straws lined with 1 mm thick layer of B₄C, enriched to 95% B-10, and filled with drift gas consisting of Ar and CO₂ mixed in a ratio of 9:1 at a pressure of 0.7 atm. Moderation of neutrons is achieved by surrounding the BCS detector tubes with a high density polyethylene (HDPE) box of inner dimensions 141.5 cm (l) × 18.5 cm (w) × 2.54 cm (h).

Three key parameters were investigated concerning the performance of the BCS detector for radiation portal monitor applications: (1) the absolute neutron detection efficiency, (2) the gamma insensitivity (the intrinsic detection efficiency for detecting gamma radiation as neutron signal), and (3) the gamma absolute rejection ratio in the presence of neutrons. Suggested requirements for each of these quantities in radiation portal monitor applications are defined and recommended in a report from Pacific Northwest National Laboratory (PNNL) [4].

Measurements of absolute neutron detection efficiency of the BCS and its gamma absolute rejection ratio were performed at the Health Physics Neutron Generator Facility (HPNGF) at CNL, using a calibrated Cf-252 neutron source, and an Ir-192 gamma source of known activity. The facility is also equipped with a calibrated Bonner sphere spectrometer, and a rotating proton recoil spectrometer, each of which have been used to carefully characterize the neutron dose and fluence at various distances from the Cf-252 source in the test facility, according to the ISO-8529 standard [5]. Measurements of the absolute rejection ratio were performed with the aforementioned Ir-192 source in a radiography facility at CNL: different gamma exposure rates were emulated through varying the distance between the Ir-192 source and the BCS detector.

2.2 COMPARISON OF GEANT4 WITH MCNP IN BCS DETECTOR EVALUATION

Monte Carlo models of the BCS detector were constructed and utilized to compare with experimental results of the absolute neutron detection efficiency in this detector evaluation. Monte Carlo models were constructed in both Geant4 (version 4.10.00.p2) and MCNPX (version 2.7.0) software packages, and a careful comparison of the results from the two packages was carried out to examine how well Geant4 could be used for detailed thermal

neutron detector characterization against MCNPX. Neutron simulations in the region of thermal energy to 20 MeV are the traditional domain of MCNP, while Geant4 has only recently expanded capabilities to this domain. The absolute neutron detection efficiency was estimated from a pulse height spectrum calculated in MCNPX, and from energy loss due to ionization in the gas detection volume calculated in Geant4. Further details regarding the setup of the simulation models, and comparison of results, can be found in Ref. [6].

2.3 RESULTS OF THE DETECTOR EVALUATION

Experimental measurements of the absolute detection efficiency were carried out using neutron shadow cones designed as per ISO-8529 guidelines [5]. These shadow cones allow one to separate out the direct component of neutron counts from the scattered component in the total neutron count rate. The count rate with no shadow cone in place provides the total neutron count rate, while the count rate with a full shadow cone in place provides the scattered component, largely induced by room return; the difference between the measurements provides the direct component. The largest shadow cone available provided full shadowing for the BCS detector in its moderator box with a source-detector distance of 4 m. Two versions of the moderator box were considered, one with 2" thick HDPE on all sides of the detector, and another version that replaced the incident side of the moderator box with 1" thick HDPE (referred to hereafter as a 1"-2" configuration). Results of the measurement are shown in Table 1 in terms of net count rate per ng of Cf-252, in comparison with Monte Carlo simulation results.

The neutron detection efficiency was deduced from MCNPX simulation data via integration of the calculated pulse height spectra. The simulated pulse height spectra are normalized for source neutron emission rate of 2311 n/s per ng of the Cf-252 source, enabling one to obtain the detection efficiency from direct integration. The pulse height spectra are shown in Figure 1(a), and it can be seen that the spectral shape shown agrees with previously published spectra [7, 8]. The neutron count rate in Geant4 is deduced from counting neutron capture daughter products (α or Li-7 particles) that deposit energy in the proportional gas volume of the BCS detector, above a 100 keV threshold value that excludes low-energy gamma and electron contributions, while simultaneously losing a minimal number of neutron events; the energy distribution of such events is shown in Figure 1(b). In doing so, it is assumed that the Cf-252 point source is a 1 ng source emitting 2311 n/s, so that the time of exposure of the detector is the number of neutrons released by the source in the simulation, divided by the neutron emission rate. By dividing the number of neutron hits in the detector by the exposure time, one arrives at the desired efficiency.

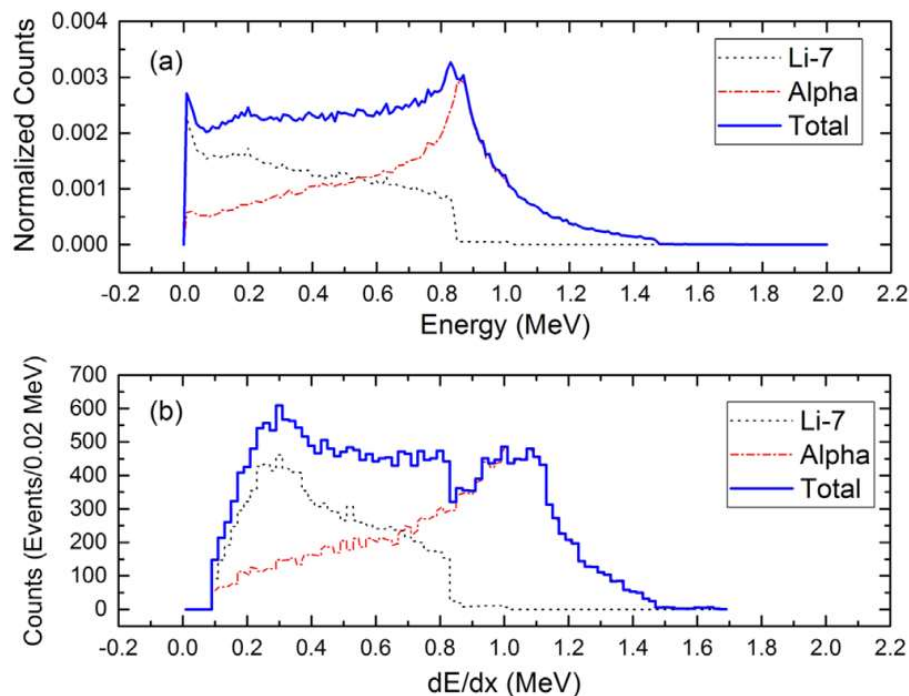


FIG. 1 (a) Pulse height spectra calculated from MCNPX model of the BCS detector. (b) Cumulative deposited energy of B-10 neutron capture decay products, calculated from Geant4 model of the BCS detector.

TABLE 1. NEUTRON COUNT RATE MEASURED AND CALCULATED (CPS/NG OF CF-252) FOR 4 M SOURCE–BCS DETECTOR DISTANCE

Moderator configuration	Measured	MCNPX	Geant4
1”–2” config.	0.166 ± 0.008	0.193 (<i>16%</i>)	0.192 (<i>16%</i>)
2” config.	0.19 ± 0.01	0.212 (<i>11%</i>)	0.219 (<i>15%</i>)

NOTE: Simulation percentage agreement with measurement are indicated in italics within parentheses

The results in Table 1 show that the Geant4 results agree with those of MCNPX within 0.4% to 3%, while the two simulation packages are systematically higher than those from measurement by 11% to 16%. In real measured pulse height spectra for boron-lined neutron detectors, there is strong overlap between the plateau of low energy neutron events, and the low energy gamma and noise peak that appears near zero energy. It is probable that the lower level discrimination of the BCS detector in the experimental measurements was sufficiently high to eliminate gamma and neutron events, at the cost of missing some lower energy neutron events. The results clearly show, however, that Geant4 estimates the neutron detector performance as well as MCNPX. Further cross-comparisons between the software packages using the BCS detector model corroborates this conclusion [6].

Table 1 gives the experimental detection efficiency of the BCS detector as high as 0.191 ± 0.010 cps/ng Cf-252 for a source-detector distance of 4 m. The PNNL guidelines state this efficiency should meet 2.5 cps/ng Cf-252 at 2 m source-detector distance [4]. By correcting for inverse square-law scaling in the detector count rate with source-detector distance, as well as for differences in moderator shielding configurations, one can estimate from measurement this efficiency to be 0.84 cps/ng Cf-252. Applying the same corrections to the simulation results brings this estimate up to as much as 0.96 cps/ng Cf-252. Clearly, the present configuration of the BCS detector does not meet the criteria of 2.5 cps/ng Cf-252, but the BCS detector configuration can easily be scaled up with more detector straws to meet this criterion.

Gamma insensitivity of the BCS detector was measured using an Ir-192 source and varying its distance from the BCS detector to emulate different gamma field strengths. The gamma insensitivity was quantified as the ratio of the measured BCS detector count rate to the predicted total gamma photon rate of incidence. The results are shown in Figure 2 (a), in comparison with a He-3 detector of similar dimensions, employing two 2” diameter tubes filled to 4 atm pressure with He-3, and surrounded by 0.75” thick HDPE. The graph clearly indicates the superior insensitivity to gamma radiation of B-10 against He-3, at all irradiation levels tested, by a factor of 2 or greater, and well within the PNNL recommendation of 1×10^{-6} at 10 mR/hr [4].

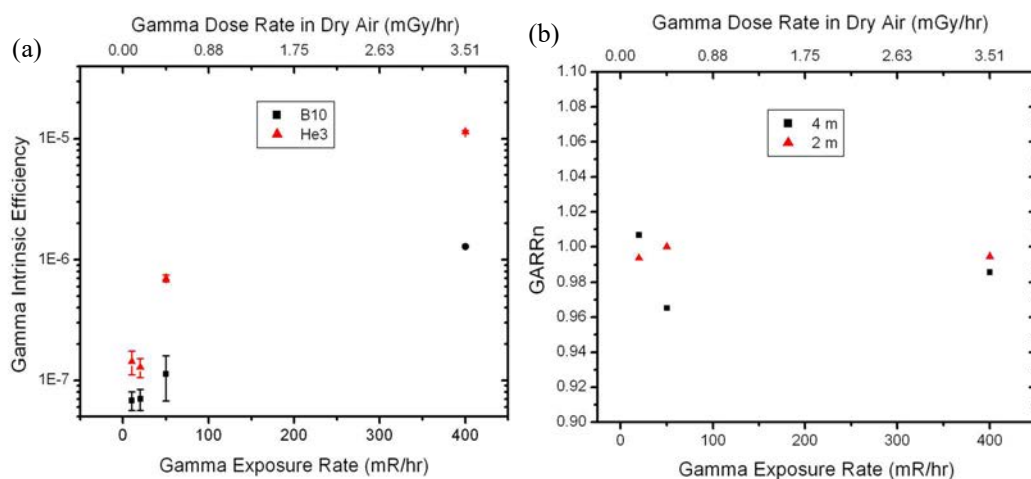


FIG. 2 (a) Gamma insensitivity of the BCS detector versus gamma exposure rate. (b) Gamma absolute rejection ratio for neutrons (GARRn) versus gamma exposure rate, for fixed Cf-252 distance from the detector. Black squares indicate a Cf-252 distance of 4 m, and red circles indicate a Cf-252 distance of 2 m

The gamma absolute rejection ratio was quantified as the ratio of BCS detector count rate when exposed simultaneously to both Ir-192 and Cf-252, divided by the BCS detector count rate when exposed only to Cf-252. This ratio was quantified for various exposures to Ir-192 and Cf-252 by varying the source distances from the BCS detector, and results are shown in Figure 2(b). In all cases, results are well within PNNL guidelines that the ratio stay between 0.9 and 1.1.

3 BORON-LOADED LIQUID SCINTILLATOR

Boron-10-loaded liquid scintillators are an alternative form of neutron detectors using Boron that can be considered. In B-10, an average energy of 2.34 MeV is deposited from neutron capture products, and part of this energy is converted into optical photons that can be detected with photomultiplier tubes (PMTs). While B-10-loaded liquid scintillators are commercially available, they come with drawbacks: they usually come with a high content of trimethyl borate, which is unstable, and decomposes with exposure to moisture, and the scintillator material is often quite flammable, posing a hazard for its use.

At CNL, a boron-loaded liquid scintillator has been developed and patented that is based upon linear alkyl benzene (LAB: $C_6H_5C_nH_{2n+1}$ ($10 \leq n \leq 16$)), which is a stable material that is economically produced with high flash point ($130^\circ C$) that provides enhanced flame resistance. The scintillator light output is also enhanced by adding fluor PPO (2,5-Diphenyloxazole) and wavelength shifter bis-MSB (1,4-Bis(2-methylstyryl)benzene) to the liquid scintillator mixture; optimum light yield is attained with PPO concentration greater than 5 g/L, and bis-MSB concentration of 0.2 g/L [9]. Below are further characterizations carried out concerning this liquid scintillator material.

3.1 ENERGY SPECTRA

B-10 neutron capture leads to the creation of an alpha particle with an average energy of 1.48 MeV. The quenching factor for 1 to 2 MeV alpha particles in LAB is 20 to 25; such B-10 capture should lead to a peak in the range of 60–75 keV. This is demonstrated below in Figure 3, where a peak near 60 keVee (‘electron equivalent’ recoil energy measured by scintillation light) is displayed in the presence or absence of gamma irradiation. The spectra were recorded using a neutron reflectometer at the National Research Universal (NRU) reactor, irradiated by 2.37 Å wavelength (14.37 meV energy) neutrons. Gamma radiation is a natural constituent of the neutron beams emanating from NRU, and this was blocked in ‘gamma off’ acquisitions using 50.8 mm-thick lead bricks. ‘Neutron off’ acquisitions employed 1 mm thick Cd sheets. A Co-60 source was used to calibrate the energy spectrum. Further details concerning the measurement can be found in Ref. [10].

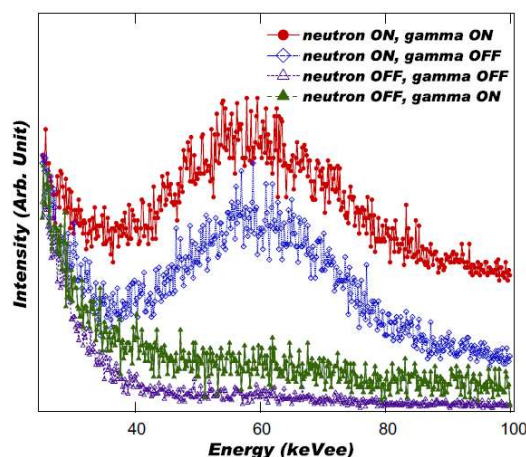


FIG. 3. Energy spectra for the boron-loaded LAB liquid scintillator in neutron and gamma on/off conditions. See text for further details.

3.2 PULSE RESPONSE

Boron-capture of thermal neutrons leads to alpha emission, so detecting alpha particles signals neutron detection. Compton-scattered electrons induced by gamma radiation provide beta pulses. Pb-212, a good alpha and beta emitter, then emulates a mixed radiation field when it is placed in the B-10 liquid scintillator, as if the liquid scintillator is detecting neutrons in a gamma radiation field. Results from such a measurement are shown in Figure

4(a). The rate of energy deposition by alpha particles is larger than for beta particles, leading to higher pulse height, and longer pulse tails – this forms the basis of pulse shape discrimination. Figure 4(b) gives a visual comparison between pulses from alpha and beta particles. A discrimination parameter R can be defined based on the relative areas of total pulse and pulse tail areas as,

$$R = \frac{S_{\text{tail}}(t_Q \rightarrow t_{\text{end}})}{S_{\text{total}}(t = 0 \text{ ns} \rightarrow t_{\text{end}})},$$

where, S_{tail} is the area under the pulse from $t_Q \approx 16$ ns to the end of the pulse, and S_{total} that under the entire pulse.

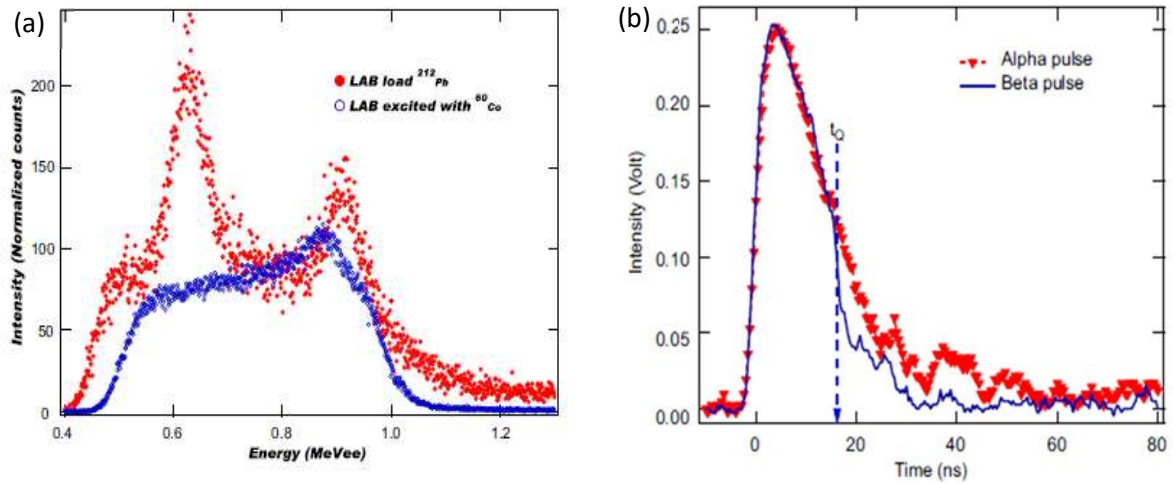


FIG. 4 (a). Pb-212 energy spectrum detected by the boron-loaded LAB liquid scintillator. (b) Comparison of normalized alpha- and beta-induced pulses from the boron-loaded LAB liquid scintillator.

3.3 PULSE SHAPE DISCRIMINATION

Figure 5(a) shows a scatter plot of R versus pulse signal area, for alpha and beta events. Through statistical averaging on raw data, one can classify data into 140 equal-width groups, according to the total area. For each group, average values of R were determined for alpha and beta particles, and plotted at the centre of the group range of the total area.

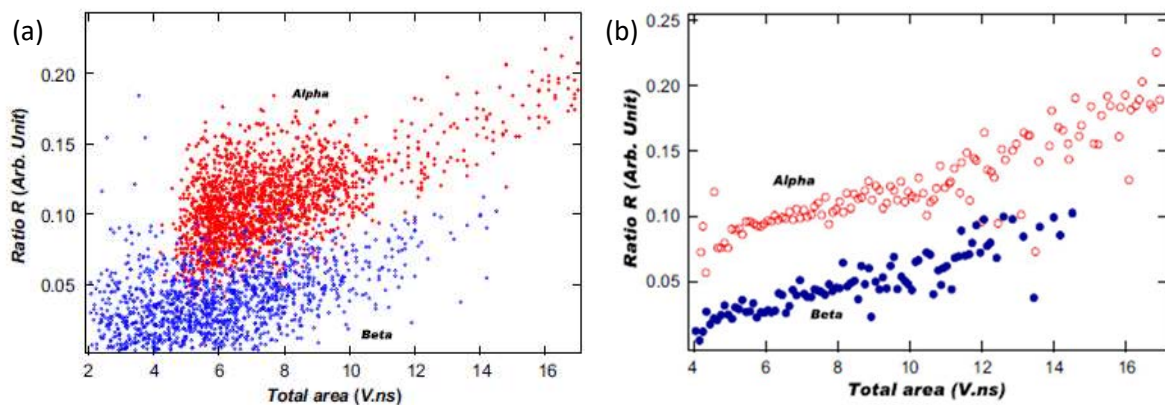


FIG. 5 (a). Ratio R for alpha events (in red) and beta events (in blue). (b) Average of ratio R for alpha events (in red) and beta events (in blue).

As can be seen in Figure 5(b), the bandwidths for alpha and beta averaged R data is ± 0.01 , and the average separation is ~ 0.07 . Based on this, a Figure of Merit (FOM) can be defined as

$$\text{FOM} = \frac{(\text{Alpha-Beta})_{\text{separation}}}{\text{Bandwidth}(R_{\text{alpha}}) + \text{Bandwidth}(R_{\text{beta}})} = 1.75.$$

4 LIQUID ARGON DETECTION

In addition to BCS and B-10-loaded liquid scintillation, work at CNL has also focused on a more novel approach to neutron detection, using liquid argon. Liquid argon detection technology has achieved a mature state in recent years [11]. It is a means of sensitive neutral particle detection in cutting-edge particle physics experiments such as neutrino, double β -decay, and dark matter search experiments. As shown below, the technique offers unprecedented neutral particle sensitivity, as well as other advantages over traditional neutron detection methods.

4.1 LIQUID ARGON SCINTILLATION

Where one can conceive of the viability of maintaining argon in liquid form (between 83.95 K and 87.45 K at standard atmospheric pressure), liquid argon has key advantages: (1) argon is cheaper than other liquefied gases; (2) argon is easier to purify from contaminants; (3) the scintillation light from liquid argon consists of two different decay times, which facilitates discrimination between nuclear recoil background events. In particular, heavily ionizing projectiles such as α particles or nuclear recoils contribute mostly to the fast decaying component, while the contribution from electrons and γ -rays to the slow component is larger.

4.2 DEAP-3600

DEAP-3600 is an acronym name for a particle physics experiment called Dark matter Experiment using Argon Pulse shape discrimination employing 3600 kg of liquid argon [12]. The experiment is situated 2 km underground at SNOLAB (Sudbury, Ontario, Canada), and contains the liquid argon within a 2-inch thick acrylic vessel of 85 cm radius. The apparatus employs 255 inner PMTs and associated light guides, contained within an 8 m diameter ultra-pure water tank. The water tank, itself equipped with 48 muon veto PMTs, is used to discriminate against interfering particle track signals. The sensitivity of the detector volume to the spin-dependent WIMP nucleon cross section is as low as 10^{-46} cm², roughly **20 times** beyond current experiments. The liquid argon detection technology employed in this experiment is being considered for use in a smaller scale neutral particle detector based on liquid argon pulse shape discrimination.

4.3 LIQUID ARGON VS. TRADITIONAL NEUTRON DETECTION

Figure 6 shows a detailed comparison of the energy-dependent neutron interaction cross section of liquid argon, with He-3 and B-10. While it is apparent that He-3 and B-10 provide higher thermal neutron cross sections, argon provides superior interaction cross section with neutrons for energies near 0.1 MeV and beyond. Liquid argon provides further enhancement in neutron interaction probability through its increased mass density in liquid form. Liquid argon thus displays considerable advantage as a fast neutron detector. This is corroborated in Figure 7, which shows a calculated ratio of liquid argon detector efficiency vs. a comparably-sized He-3 detector. From simulation using GEANT4, the figure considers the efficiency of ~ 10 kg of liquid argon relative to a typical HDPE-moderated He-3 tube used in radiation portal monitors (RPMs). For simplicity, the HDPE moderator is assumed to be in a form-fitting cylindrical shape. This moderator configuration is more optimal than for an enclosing rectangular box of the same thickness that is more typically employed in RPMs, so the calculation provides some advantage to the He-3 over the liquid argon in this case. Nevertheless, the liquid argon is seen to out-perform the He-3 for energies beyond 0.575 MeV, by up to a factor of 4. Further work investigating the efficacy of liquid argon for smaller format detectors is ongoing.

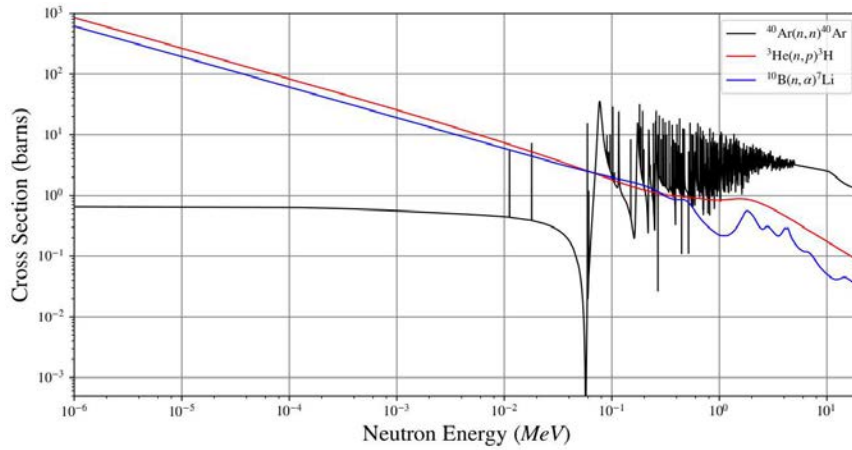


FIG. 6. Neutron cross sections for Ar-40, He-3, and B-10, as a function of incident neutron energy.

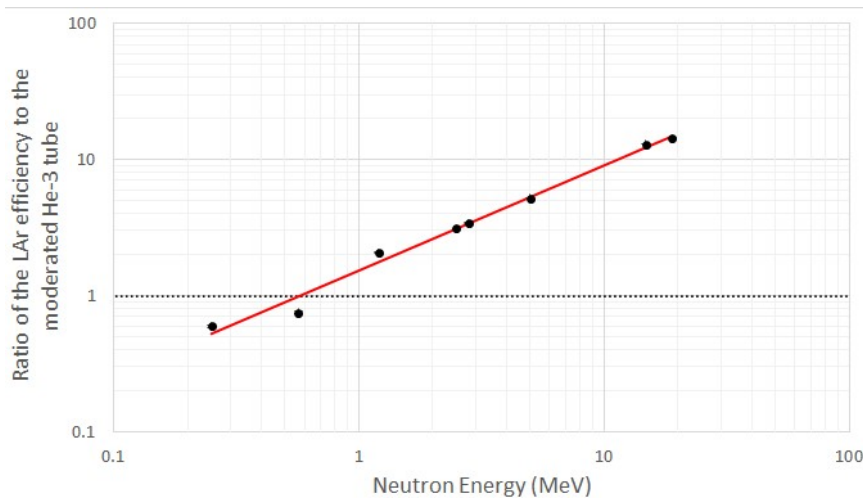


FIG. 7. Comparison of neutron detection efficiency for 10 kg of liquid Ar-40, in comparison to a comparably-sized, HDPE-moderated He-3 detector.

5 CONCLUSIONS

In recent years, CNL has engaged in activities related to efforts to develop and evaluate alternative neutron detection technologies to He-3. In this paper, we have summarized a few representative activities, including an evaluation of a BCS neutron detector against recommended radiation portal monitor performance metrics, development of a patented boron-loaded liquid scintillator, and recent investigation into liquid argon pulse shape discrimination for neutron detection applications.

The BCS neutron detector evaluation demonstrates that the configuration tested yields insufficient detection efficiency for neutron portal monitor applications, but can be readily scaled up to address this deficiency. The BCS detector, however, demonstrates superior gamma insensitivity in comparison to a similar-sized He-3 neutron detector.

The boron-loaded liquid scintillator discussed possesses some unique features in comparison with other available boron-loaded liquid scintillators, by exploiting an economical scintillating material that is more stable against exposure to moisture and offers higher flame resistance. Its pulse shape discrimination capability is also good in comparison with other liquid scintillators.

Pulse shape discrimination using liquid argon, meanwhile, is a mature neutron detection technology that is currently exploited in high-sensitivity cutting-edge particle physics experiments. There is strong potential for using such technology in more compact neutron detector packaging for detecting fast and epithermal neutrons.

REFERENCES

- [1] KOUZES, R.T., The ^3He supply problem, Pacific Northwest National Laboratory report PNNL-18388 (2009).
- [2] AGOSTINELLI, S., et al., Geant4 – a simulation toolkit, *J. Nucl. Instrum. Methods Phys. Res., Sect. A* **506** 3 (2003) 250–303.
- [3] PELOWITZ, D.B., et al., MCNPX User’s Manual Version 2.7.0, Los Alamos National Laboratory LA-CP-11-00438 (2011).
- [4] KOUZES, R.T., ELY, J.R., LINTEREUR, A.T., STEPHENS, D.T., Neutron Detector Gamma Insensitivity Criteria, Pacific Northwest National Laboratory report PNNL-18903 (2009).
- [5] INTERNATIONAL ORGANIZATION FOR STANDARDIZATION Reference Neutron Radiations – Part 2: Calibration Fundamentals of Radiation Protection Devices Related to the Basic Quantities Characterizing the Radiation Field. Geneva: ISO; ISO-8529 (2000).
- [6] VAN DER ENDE, B.M., ATANAKOVIC, J., ERLANDSON, A., BENTOUMI, G., Use of GEANT4 vs. MCNPX for the characterization of a boron-lined neutron detector, *J. Nucl. Instrum. Methods Phys. Res., Sect. A* **820** (2016) 40–47.
- [7] KOUZES, R.T., et al., Neutron detection alternatives to ^3He for national security applications, *J. Nucl Instr Meth Phys Res A*. **623** (2010) 1035–1045.
- [8] SICILIANO, E.R., KOUZES, R.T., Boron-10 line proportional counter wall effects, Pacific Northwest National Laboratory report PNNL-21368 (2012).
- [9] BENTOUMI, G., DAI, X., PRUSZKOWSKI, L., LI, L., SUR, B., A novel boron-loaded liquid scintillator for neutron detection, *AECL Nucl. Rev.* **1** (2012) 57–59.
- [10] BENTOUMI, G., et al., Characterization of a liquid scintillator based on linear alkyl benzene for neutron detection. *J. Nucl. Instrum. Methods Phys. Res., Sect. A* **701** (2013) 221–224.
- [11] CHEPEL, V., ARAJO, H., Liquid noble gas detectors for low energy particle physics, *J. Instrum.* **8** 4 (2013) R04001.
- [12] BOULAY, M.G., DEAP-3600 dark matter search at SNOLAB, *J. Phys.: Conf. Series* **375** (2012) 012027.

RECENT FIRMWARE AND HARDWARE UPGRADES TO THE HPI2080 PULSED NEUTRON REM METER

A.L. JUSTUS, M.A.DURAN, R.E. MONTOYA, D.T. SEAGRAVES, J.R. BLAND, T.D. MCLEAN
Los Alamos National Laboratory,
Los Alamos, NM, 87545
USA
Email: tmclean@lanl.gov

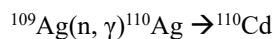
Abstract: The HPI2080 neutron rem meter was developed in the 1970's and was specifically designed for use in pulsed neutron fields. It has recently been upgraded with respect to hardware and firmware both out of necessity (e.g. obsolete components) and the desire to introduce new measurement capabilities. This paper details these upgrades and provides data demonstrating the new operational modes. Additional potential upgrades are also discussed that are designed to further improve the instrument.

1 INTRODUCTION

The focus of the IAEA Technical meeting on modern neutron detection methods was on current state-of-the-art techniques with an eye to future developments over the next 5-10 years. To this end, presentations given at the meeting introduced new instrumentation [1] and/or promising novel detector media [2-3]. But it is also clear that there will be a continuing need for existing tried and true neutron instrumentation for health physics applications over the foreseeable future. In particular, polyethylene-moderated rem meters utilizing thermal neutron detectors will, in all probability, long continue to be deployed as area monitors and for routine radiation surveys. These instruments have proven to be reliable, requiring little maintenance and are moderate in cost. They also provide continuous, albeit not always a dosimetric, response over the range from thermal to fast neutrons. However, there are always room for improvements usually driven by necessity (e.g. obsolete components) or a desire to upgrade the instrument's capabilities. Both of these reasons were behind a recent upgrade of the HPI2080 neutron rem meter conducted at Los Alamos National Laboratory (LANL). These upgrades are described and some preliminary data for this pulsed neutron rem meter are presented.

1.1 HPI2080 BACKGROUND

The initial mention of the instrument that would eventually be known as the HPI2080 appears to have been given by Smith [4] in 1962. He described an instrument based on a Ag-wrapped GM tube in a polyethylene (PE) moderator for use at Lawrence Berkeley National Laboratory's 6.3 GeV Bevatron facility. The instrument relied on the following reactions for neutron detection;



where the GM tube detected the betas (and gammas) emitted by the silver isotopes (Table 1) following thermal neutron capture. The natural abundances of ^{107}Ag and ^{109}Ag are 52% and 48% respectively. At a neutron energy of 2.5E-08 MeV, the respective neutron capture cross-sections are 39 and 90 b for ^{107}Ag and ^{109}Ag [5].

TABLE 1. SELECTED PROPERTIES OF SILVER ISOTOPES

Isotope	t _{1/2} (s)	Maximum beta energy (MeV)
^{108}Ag	143	1.65
^{110}Ag	24.6	2.89

By 1971, the instrument had undergone further refinements and was now known as the Albatross. Awschalom et al. [6] described a number of upgrades to create version III for use at the National Accelerator Laboratory (Batavia, IL). Many of the features in the present instrument were introduced in this version. These included the characteristic octagon-shaped PE moderator and the use of second GM tube to serve as the gamma compensator. This tube was wrapped in tin foil of sufficient thickness to provide the same gamma attenuation properties as the silver foil. The net count rate is converted to neutron dose rate using a calibration factor established using an Am-Be neutron source. Further details on the calibration of the HPI2080 are given later.

The next major upgrade (to the Albatross IV) was described by Brown et al [7]. Improvements included digital processing to give a running average count rate as opposed to the fixed 10s RC time constant used previously. They also revised the setup procedures so that the balance constant that corrects for any gamma sensitivity difference in the two GM tubes and the neutron calibration factor were independently adjustable. These authors also discussed the various processes and their relative contributions to count rates in both GM tubes. This data will be discussed in greater detail below.

The last major instrument upgrade occurred in the early 1990's. By that time the Albatross was available commercially through Health Physics Instruments¹ as the Model 2080. As documented by Frankle [8], several improvements to the instrument were proposed by HPI for deployment at the Los Alamos Meson Physics Facility (LAMPF)². These proposals were accepted and incorporated into the Model 2080. However, perhaps the most significant upgrade was done at LAMPF. It had previously been observed that the GM tubes were paralyzable and in high count rate fields would fail to announce an alarm condition. LAMPF staff modified the pre-amplifier so that in high fields, the instrument would switch to a current mode of operation in order to trigger an alarm condition. Figure 1 shows the HPI2080 following the 1990's upgrades; the preamplifier sits directly on top of the PE moderator while the panel display with the user interface, alarm LEDs and input/output connections is supported above the PE moderator assembly. In Fig.2, the wrapped GM tubes are shown secured to the support paddle which is inserted vertically through the top of the PE moderator.



FIG. 1. HPI2080 prior to current upgrade.



FIG. 2. Ag-wrapped GM (at end) and Sn-wrapped GM tubes mounted on support paddle.

1.2 HPI2080 FLUENCE AND DOSE RESPONSE

The MCNP-calculated [9] fluence response of the Albatross when irradiated from the side is shown in Fig. 3 where it is compared with the $H^*(10)$ curve [10]. At energies above 10 MeV, the Albatross's response increasingly fails to mimic the $H^*(10)$ curve and consequently the dose response declines at energies beyond 10 MeV as indicated in Fig. 4. To address this issue, a companion model, the so-called Eagle, was developed to extend the HPI2080 response to higher energies. The Eagle incorporates a 1.5cm thick Tungsten cup that surrounds the GM tubes and uses a distinctive cylindrically-shaped PE moderator.

A cross-sectional view of the Eagle is shown in Fig. 5. The Tungsten cup serves to increase the neutron population via (n, xn) reactions in the PE moderator to compensate for the rapidly decreasing (n,p) cross-section. This approach of adding high-Z material to bolster a neutron instrument's response at high energies is well-known [11–13]. As

¹ Health Physics Instruments (HPI), Goleta, CA

² Later known as the Los Alamos Neutron Science Centre (LANSCE)

Fig. 3 shows, the fluence response of the Eagle is appreciably enhanced above 10 MeV in relation to the Albatross and is able to better match the H*(10) dose curve at these energies as indicated in Fig. 4.

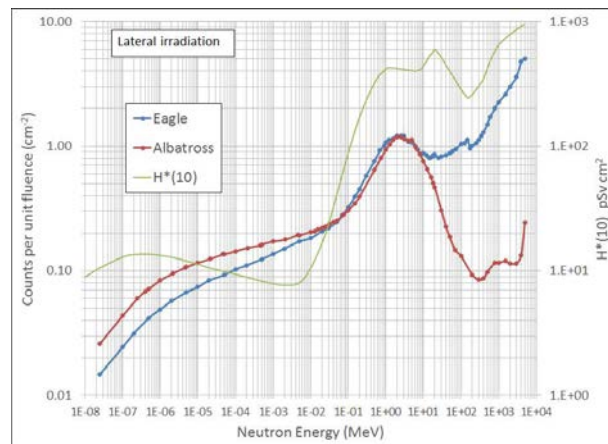


FIG. 3. MCNP-calculated HPI2080 fluence response in comparison with the H*(10) neutron dose curve.

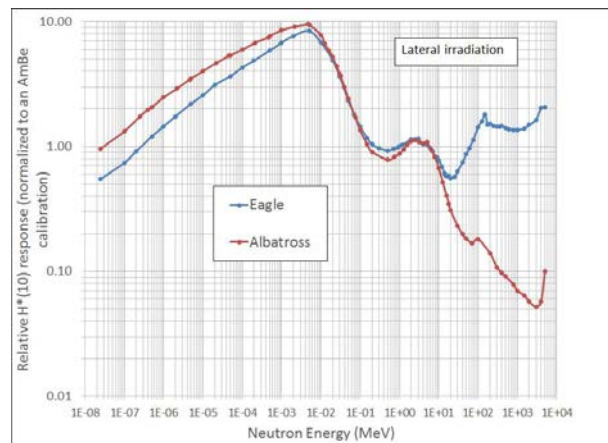


FIG. 4. HPI2080 dose response normalized to an Am-Be calibration.

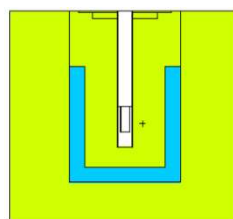


FIG. 5. Cross sectional view of the Eagle version of the HPI2080.

1.3 PROCESSES CONTRIBUTING TO HPI2080 COUNT RATES

There are several processes that contribute to the count rates reported by the GM tubes. For the Ag-wrapped tube these include the beta emissions from both activated Ag isotopes as well as the following gamma source terms: the prompt gammas following activation, gammas associated with the neutron source, secondary gammas produced within the PE moderator and ambient background gammas. The Sn-wrapped tube is also subject to the above-mentioned gamma source terms except for the prompt gamma contribution. These prompt gammas are of particular concern as they cannot be subtracted using the Sn-wrapped GM tube and because their differing detection probability in pulsed and steady-state fields. In a continuous neutron field, the randomness associated with Ag-foil activation maximizes their detection. However, in a pulsed field, notwithstanding the neutron die away time in the PE moderator, thermal neutron activation occurs on a time scale comparable to the resolving time of the GM tube. As a result, these prompt gammas are not detected with

high probability and in some cases are only capable of registering a maximum of a single count per accelerator pulse. Brown [7] recognized this issue and made measurements that indicated in an ^{241}Am -Be calibration (*i.e.* steady-state) field about 18% of the Ag-wrapped counts were due to prompt gammas. As a consequence, the calibration factor was appropriately adjusted in anticipation of lower count rates per unit average dose rate in pulsed fields. He was able to provide nominal count rates for all the other processes and the HPI2080B upgrade was an ideal opportunity to reaffirm some of his reported data.

1.4 HPI2080 CALIBRATION

The HPI2080 instruments are calibrated on a dedicated irradiator shown in Fig. 6. The instrument is centred between guide tubes along which ^{137}Cs and ^{241}Am -Be sources are transported pneumatically from below-grade storage locations. The calibration procedure is semi-automated using custom software and consists of a three-step process; the ^{137}Cs source is used to determine any mismatch in the gamma response of the two GM tubes. If necessary, a correction factor (balance constant) for the Sn-wrapped count rate is stored and subsequently applied when calculating the net count rate. The second step determines the neutron calibration factor (*i.e.* counts per unit dose) using the ^{241}Am -Be source. A final step involves raising both sources to verify that the neutron dose rate remains unchanged.



FIG. 6. HPI2080 calibration range.

2 HPI2080 UPGRADES

The upgrade to the HPI2080B model involved several hardware and firmware updates. The hardware changes included a redesign of the high voltage/pre-amplifier board (including the modifications to invoke a current mode of operation at high count rates), a new main circuit board and an updated front panel. Upgrade kits containing these items (Fig.7) were used to retrofit existing HPI2080 instruments. To date about 30 of the approximately 100 HPI2080 units at LANL have been upgraded to the HPI2080B model including both of the Eagle instruments.



FIG. 7. Hardware upgrade kit for the HPI2080B.

The firmware changes introduced two additional modes of operation. Prior to the upgrade, only rate meter operation was possible where only the averaging time was user selectable. This mode has been retained as the default operating mode in the HPI2080B. The first of the new operating modes was a delayed scaler mode designed to help radiological control technicians (RCTs) conduct routine surveys. When in this mode, the

instrument uses a user-entered build-up time (typically 2 minutes) before starting a timed count (5 minute default). At the end of the count time, an audible beep signals the RCT that the scaler count has finished. In this fashion, an RCT can make an average dose rate measurement without being tethered to the instrument - potentially in a high radiation area. The second new mode was primarily designed to integrate the dose from a single pulse or burst. In this mode, the RCT enters a desired integration time that allows for egress, any time delay time until the pulse and for sufficient count time following the pulse. This mode can also be used to integrate dose over an extended period of time to obtain an average dose rate in repetitive fields. Integration times of up to 60 minutes are allowed. The HPI2080B is capable of integrating dose up to a maximum of 9999.9 μSv but when used in very high instantaneous dose rate fields it is possible that dead time effects could lead to significant counting losses. Limiting the dose per accelerator pulse to a maximum of 1000 μSv is recommended to avoid such losses.

Table 2 presents the selected properties of the HPI2080B many of which remained unchanged following the upgrade. Figure 8 shows the upgraded Albatross and Eagle instruments.

TABLE 2. SELECTED PROPERTIES OF THE HPI2080B

Feature	Description
Dimensions	51cm(high) \times 28cm (wide) \times 23cm (deep)
Weight	Albatross: 11.5 kg , Eagle: 17.3 kg
Foil thickness	Ag = 0.25 mm, Sn = 0.36 mm
Temperature	-20 $^{\circ}\text{C}$ to 50 $^{\circ}\text{C}$
Relative Humidity	10% to 90% @ 35 $^{\circ}\text{C}$ non-condensing
Dose rate range	$\leq 9999 \mu\text{Sv/h}$
Dose range	$\leq 9999 \mu\text{Sv}$ but recommended limit is 1000 μSv (see text)
Max. gamma rate	Manufacturer recommends gamma dose rates be limited to $< 0.5 \text{ Sv/h}$
Response times	Multiples of 16 seconds in rate meter mode.
Alarm thresholds	Low alarm at 40 $\mu\text{Sv/h}$ and high alarm at 200 $\mu\text{Sv/h}$.
Alarm indicators	Green ($\leq 40 \mu\text{Sv/h}$), yellow (40 $\mu\text{Sv/h}$ - 200 $\mu\text{Sv/h}$) and red ($> 200 \mu\text{Sv/h}$) LEDs
Audible alarm	80 dB at 30cm when high alarm or fast trip alarm enunciated
Fast trip alarm	At count rates equivalent to 13 mSv/h (neutron) or 400 $\mu\text{Sv/h}$ (gamma) or if in a current mode of operation
Battery	12 h recharge time and 30 h run time



FIG. 8. The upgraded HPI2080B rem meters: Eagle (left) and Albatross (right) models.

3 RECENT MEASUREMENTS

3.1 REFERENCE FIELD MEASUREMENTS

In a low ambient background environment in the absence of a neutron source, an extended run with a HPI2080B established a background count rate in the neutron channel of 0.1014 ± 0.0012 cps and 0.1294 ± 0.0013 cps in the gamma channel. These count rates and ones stated below are representative of those expected for the HPI2080B.

Figure 9 compares the GM count rates in a 220 mrad/h ^{137}Cs reference field for the same HPI2080 as above. This data was obtained by taking advantage of the HPI2080's RS232 serial port and monitoring the individual GM tubes using separate multichannel analysers operated in multichannel scaler (MCS) mode. Dwell times of one second were used to collect the data. Gross count rates of 337.0 (1.532 cps per mrad/h) and 423.4 cps (1.925 cps per mrad/h) were measured for the Ag- and Sn-wrapped GM tubes respectively. The absolute uncertainties in each count rate are dominated by the 4.8% relative standard deviation in the ^{137}Cs air kerma rate. Based on counting statistics alone, the relative gamma response of the Sn-wrapped tube was therefore 1.256 ± 0.005 times higher than the Ag-wrapped tube for this HPI2080. This ratio is in very good agreement with the ratio of the background count rates mentioned above.

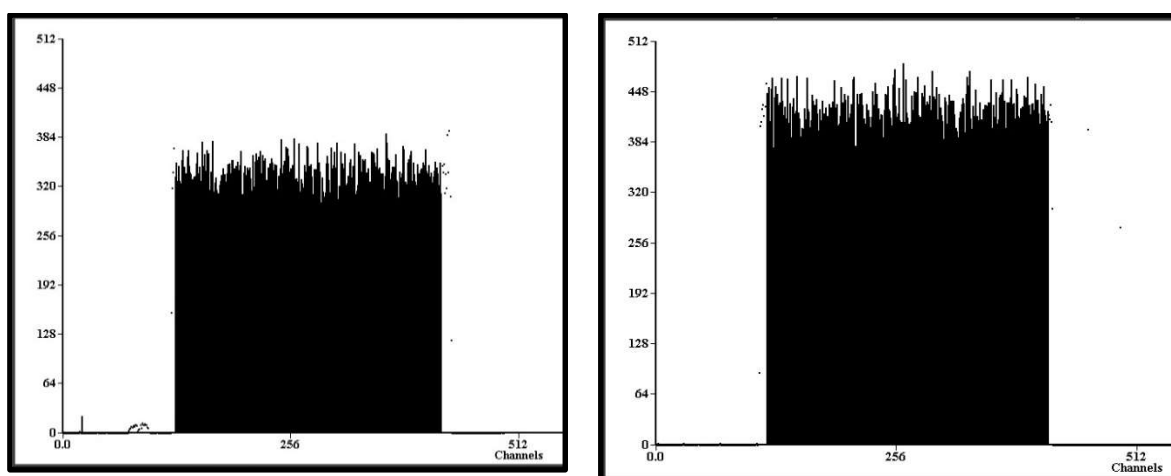


FIG. 9. MCS spectra in ^{137}Cs 220 mrad/h field a) neutron b) gamma detectors. Dwell times of 1 s used.

A similar measurement in an Am–Be reference field at $487 \mu\text{Sv/h}$ yielded the MCS spectra shown in Fig.10 for the neutron channel and Fig.11 for the gamma channel. Note the build-up in count rate at the start of the run and subsequent decay at the conclusion of the run for the Ag-wrapped tube. At equilibrium, gross count rates per unit $H^*(10)$ dose rate of 3.539 and 1.632 cps per $\mu\text{Sv/h}$ were recorded for the neutron and gamma GM tubes respectively. After accounting for the relatively higher gamma response of the Sn-wrapped tube, a net normalized neutron response of 0.0469 cps per $\mu\text{Sv/h}$ was calculated³. The uncertainty in this result was again mainly determined by the relative uncertainty (4.5%) in the Am–Be dose rate. Notwithstanding the changes in neutron dose quantities over the intervening years, the neutron sensitivity is in good agreement with the value of 0.65 cpm per mrem/h ($0.065 \mu\text{Sv/h}$) for Am–Be reported by Brown et al [7]. The gamma count rate of the current Sn-wrapped tube was about 47% of that given by Brown et al [7] in an Am–Be field.

³ When deployed in pulsed fields, the calibration constant would be set 18% lower or 0.0397 cps per $\mu\text{Sv/h}$

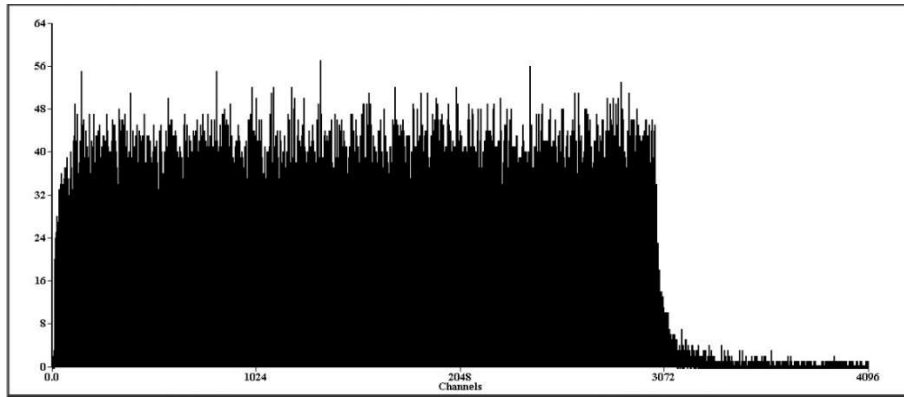


FIG. 10. MCS spectrum of the neutron channel in a 487 $\mu\text{Sv/h}$ Am-Be field.

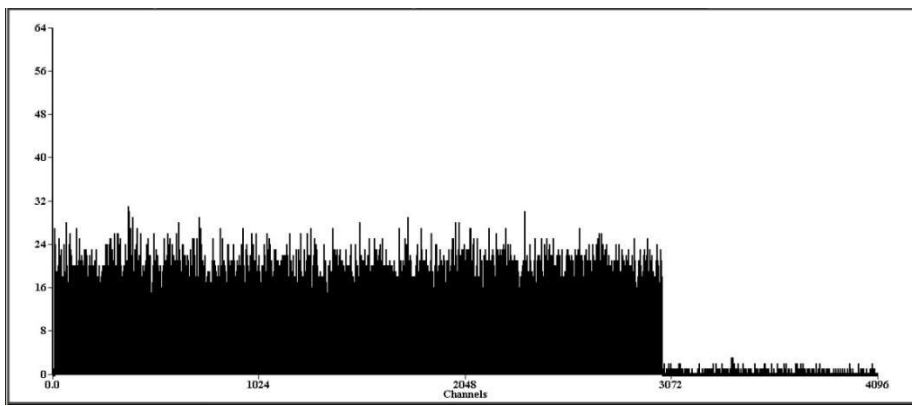


FIG. 11. MCS spectrum of the gamma channel in a 487 $\mu\text{Sv/h}$ field Am-Be field.

3.2 FIELD MEASUREMENTS

The Albatross and Eagle instruments using the HPI2080 and HPI2080B models have been used to make neutron measurements at various facilities at LANL and elsewhere in the Department of Energy complex. One interesting measurement was in support of a novel means of generating pulsed high-energy neutrons using LANL's TRIDENT laser facility [14]. Inside a vacuum chamber an 80 J, 600 fs long laser pulse ($\lambda = 1054$ nm) was focussed onto a thin (a few μm) deuterated polyethylene target to generate an ion beam that impinged upon a neutron converter such as Beryllium. Neutron yields of up to $1\text{E}10$ n/sr have been reported with energies ranging up to 100 MeV. This means of producing high neutron yields in short pulses of high energy has applications in fast time resolution imaging without the need for traditional but costly accelerators such as spallation facilities

These measurements were made with an Eagle rem meter (HPI2080 model) located 112cm from the exterior of the vacuum chamber. The individual GM tubes were again monitored separately in MCS mode. Figure 12 shows an MCS sweep of the neutron channel during the course of several hours (dwell times of 20 seconds were used). A total of three laser shots were done during this sweep and in each case the Eagle detected a neutron burst. The area beneath each peak was integrated manually and the gamma contribution subtracted (on the order of 2% as only the initial time bin had any significant counts). After applying the neutron calibration factor—corrected for pulsed field operation—doses of 13, 11 and 10 μSv were measured respectively for the three shots with uncertainties of perhaps as high as 30% due to the Eagle's dose response (Fig. 4). Had the new firmware been available at the time these measurements were made, the burst mode of operation would have automated the measurement process. Figure 13 shows a higher-resolution view of the neutron count rate following the second laser shot displayed in Fig.12. A single exponential least squares fit to this data yielded an effective decay time of 28.7 ± 0.3 seconds. Clearly, the higher yield, higher average energy ^{110}Ag betas are detected with greater efficiency than those from ^{108}Ag .

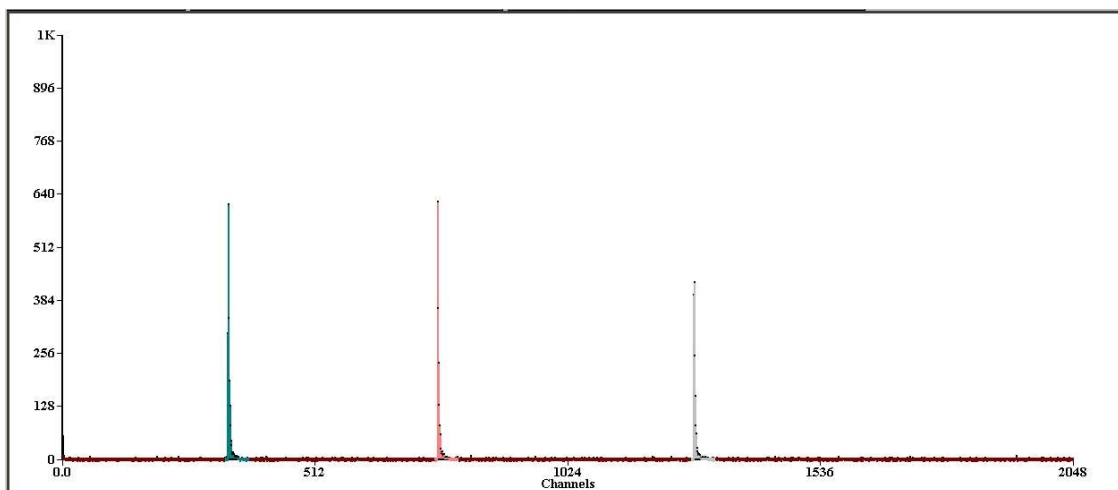


FIG. 12. MCS spectrum for neutron channel measurements at the Trident Facility. Each time channel is 20s in width.

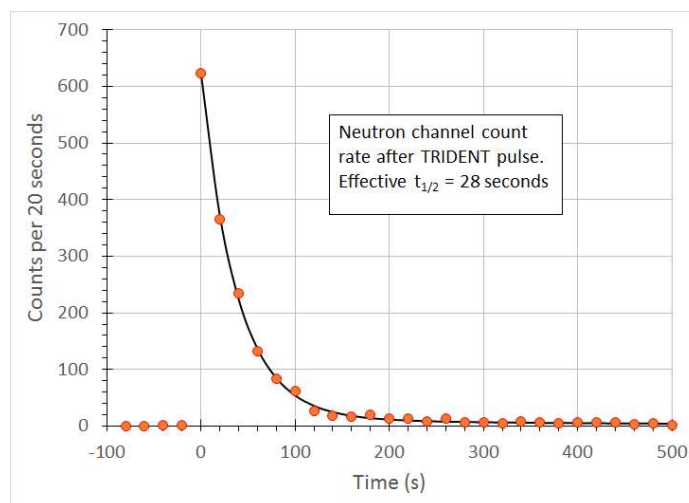


FIG. 13. Decay curve for the Ag-wrapped GM tube.

Measurements with a HPI2080B Albatross model have also been made at LANL’s Dual Axis Radiographic Hydrodynamic Test (DARHT) Facility. This facility images imploding objects using perpendicular and extremely short-duration, high-energy X-ray beams to produce two-dimensional images. The X-rays are energetic enough (up to 20 MeV) to create photoneutrons through interaction with surrounding materials. The Albatross, operated in burst mode, was used to monitor neutron dose levels in areas normally occupied during a test.

An upgraded Eagle instrument was also deployed at the Spallation Neutron Source (SNS) located at Oak Ridge National Laboratory. This accelerator produces microsecond-long neutron pulses at energies up to 1 GeV at a repetition rates of 60Hz. The burst mode of operation was used to integrate the neutron dose over a 30-minute period at locations where streaming had previously been identified. Based on this data, the average dose rate per kW at each location was calculated.

4 FUTURE UPGRADES

Other instrument improvements that have been discussed include adding two more GM tubes (Ag and Sn-wrapped) to double the sensitivity of the HPI2080. Also under consideration is placing the support paddle in a PE sleeve that can be easily inserted or removed from the bulk PE moderator. Only the sleeve would have to be transported back and forth to the calibration facility where it would be inserted into a matching PE moderator. Doing so, would address ergonomic issues associated with transporting the entire HPI2080. Finally, a spherical PE moderator to replace the current octagon-shaped assembly would improve the instrument’s angular dependence.

5 SUMMARY

Recent hardware and firmware upgrades to the HPI2080 pulsed neutron rem meter have been implemented and successfully demonstrated to function as intended. The modernization and capability enhancements of the instrument will ensure its continued use for many years to come.

ACKNOWLEDGEMENTS

This work has been authored by employees of Los Alamos National Security, LLC, operator of the Los Alamos National Laboratory under Contract No. DE-AC52-06NA25396 with the U.S. Department of Energy. The United States Government retains and the publisher, by accepting this work for publication, acknowledges that the United States Government retains a nonexclusive, paid-up, irrevocable, worldwide license to publish or reproduce this work, or allow others to do so for United States Government purposes.

REFERENCES

- [1] BUFFLER, A., et al., Towards a new compact scintillation spectrometer for 100 MeV Neutrons: A case study for reference neutron beams, paper presented at IAEA Technical Meeting on Modern Neutron Detection, 9/2017, Vienna, Austria.
- [2] ZAITSEVA, N., et al., New solid-state organic scintillators for wide-energy neutron detection, IAEA Technical Meeting on Modern Neutron Detection, 9/2017, Vienna Austria.
- [3] SHAH, K.S., Next generation neutron detectors, IAEA Technical Meeting on Modern Neutron Detection, 9/2017, Vienna, Austria.
- [4] SMITH, A.R., Measurement of radiation fields around high-energy accelerators, UCRL-10163, 1962.
- [5] CHADWICK, M.B., et al., ENDF/B-VII.1 Nuclear data for science and technology: cross sections, covariances, fission product yields and decay data, Nucl. Data Sheets **112** 12 (2011) 2887–2996.
- [6] AWSCHALOM, M., et al., Novel instrumentation for radiation monitoring at NAL, IEEE Trans. Nucl. Sci. **18** 3 (1971) 748–749.
- [7] BROWN, D., BUCHANAN, R.J., KOELLE, A.R., A microcomputer-based portable radiation survey instrument for measuring pulsed neutron dose rates, Health Phys. **38** (1980) 507–521.
- [8] FRANKLE, S.C., Neutron Energy Spectrum Measurements with Bonner Spheres and Neutron Dose Equivalent Rate (DER) Measurements Using Albatrosses, LA-UR-94-1281, (1994).
- [9] INTERNATIONAL COMMISSION ON RADIATION UNITS AND MEASUREMENTS, Conversion Coefficients for Use in Radiological Protection Against External Radiation, ICRU-57 (1998).
- [10] OLSHER, H.R., et al., WENDI: an improved neutron rem meter, Health Phys. **79** 2 (2000) 170–181.
- [11] AGOSTEO, S., SILARI, M., ULRICI, L., Improved response of bubble detectors to high energy neutrons, Rad. Prot. Dosim. **88** 2 (2000) 149–155.
- [12] WIEGEL, B., ALEVRA, A.V., NEMUS – the PTB neutron multisphere spectrometer: Bonner spheres and more, Nucl. Instrum. Methods A **476** 1 (2002) 36–41.
- [13] MCNPX, version 2.5.0, Los Alamos National Laboratory (2005).
- [14] ROTH, M., et al., A bright, laser-neutron source based on relativistic transparency of solids, Phys. Rev. Lett. **110** 4 (2013) 44802-1–44802-5.

NEUTRON SPECTROMETERS FROM THERMAL ENERGIES TO GeV BASED ON SINGLE MODERATORS

R. BEDOGNI

INFN – LNF, Via E. Fermi n. 40, 00044 Frascati (Rome)

Italy

Email: roberto.bedogni@lnf.infn.it

A. POLA

Politecnico di Milano – Dip. di Energia, Via La Masa, 34, 20156 Milano

Italy

J.M. GOMEZ-ROS

CIEMAT, Av. Complutense, 28040, Madrid

Spain

Abstract: Any practical workplace neutron spectrum spans in energy from the thermal domain up to the maximum production energy. Determining the whole neutron spectrum usually requires multiple devices covering different energy sub-intervals, and invariably constitutes a complex and time-consuming task. The Bonner sphere spectrometer (BSS) is still regarded as the state-of-art instrument for neutron spectrometry in radiation protection, but it requires multiple exposures and has no capability to operate as a real-time spectrometric monitor.

The INFN project NESCOFI@BTF (2011–2013) exploited the idea of an active spectrometer embedding several active thermal neutron detectors in a single moderator according to a well-defined geometry, thus resulting in a novel real-time monitor with spectrometric capabilities. Two separate instruments were developed, called SP² and CYSP, suited to cover the needs of different types of neutron producing facilities. SP² (SPHERICAL SPectrometer) consists of a spherical polyethylene moderator embedding thirty-one thermal neutron sensors arranged in symmetrical positions along the three axes. An internal 1cm thick lead shell, acting as (n, xn) radiator, allows response above 20 MeV. This device measures the neutron spectrum without regard for its directional distribution. The CYSP (CYLINDRICAL SPectrometer) is a cylindrical moderator embedding seven thermal neutron sensors at different depths along the cylindrical axis. An internal 1 cm thick lead shell allows detection of high-energy neutrons. The CYSP response is sharply directional and its collimating aperture defines the measurement direction. SP² and CYSP are similar to the BSS in terms of energy resolution, response curve and unfolding aspects, but only require a single exposure. This communication presents the design of SP² and CYSP and the experimental characterization of the corresponding prototypes.

1 INTRODUCTION

Neutrons play an established role in research, technology, and industry. As evidenced by current investments in advanced reactors, nuclear fusion, waste minimization and material science, their usage is increasing and will possibly extend to new fields, such as waste management in agriculture [1]. In any of the mentioned fields, monitoring devices are needed to detect neutrons ranging from the thermal domain up to tens of MeV, or higher energy domains. Due to this enormous variability in energy (ten orders of magnitude or more), the detection task is generally very complex [2]. Many applications need simple monitor devices responding in terms of spectrum-integrated quantities, or are just interested to specific energy sub-intervals. Other applications, like radiation protection, dosimetry and metrology, greatly benefit from neutron spectrometry. Before the introduction of SP² and CYSP (the new devices described in this work), no single device existed with the capability of simultaneously determine all energy components. The Bonner sphere spectrometer (BSS) was the only instrument able to respond over ten or more orders of magnitude in energy, although its energy resolution is limited [3]. In addition, it requires multiple exposures and has no capability to operate as a real-time monitor.

The NESCOFI@BTF project (2011–2013) exploited the idea of an active instrument embedding several active thermal neutron detectors in a single moderator according to a well-defined geometry, thus resulting in novel real-time monitors with spectrometric capabilities.

Two separate instruments were developed, called SP² and CYSP.

SP² (SPherical SPectrometer) consists of a spherical polyethylene moderator embedding thirty-one thermal neutron detectors arranged in symmetrical positions along the three axes. This device measures the neutron spectrum without regard to its directional distribution.

CYSP (CYlindrical SPectrometer) is a cylindrical moderator with seven thermal neutron detectors located at different depths along the cylindrical axis. Its response is sharply directional and its collimating aperture defines the acceptance solid angle.

Both devices can measure neutrons above 20 MeV relying on an internal lead shell (1 cm thick) acting as an (n,xn) radiator. The device geometry was studied [4,5] using MCNPX 2.6 [6] and verified using passive thermal neutron detectors [7].

The active prototypes were assembled by embedding active thermal neutron detectors in the previously studied spherical (SP²) or cylindrical (CYSP) geometries.

Although any cm-sized commercially available thermal neutron detector would have matched this objective, a dedicated sensor was developed to reduce costs. This is called TNPD (thermal neutron pulse detector) [8, 9] and is a one-cm² windowless p-i-n silicon diode covered with 30 μm of ⁶LiF. The deposition is done through evaporation. The detector signal is conditioned in a dedicated analog board formed by a charge preamplifier and a shaper amplifier. Two versions of this analog board were produced, acquiring respectively two or six TNPDs.

Data digitalization is done through a commercial USB digitizer National Instruments 6366. The pulses are analyzed in terms of their height distribution (spectrum). The discrimination between thermal neutron and photon signal is operated by means of a pulse height threshold.

This thermal neutron measurement chain proved to be linear up to at least 10⁵ cm⁻² s⁻¹ (thermal fluence rate) and to effectively reject photons up to tens of mSv h⁻¹ (⁶⁰Co).

Prior to their installation in the moderators, the TNPDs are individually calibrated in thermal neutron facilities traceable to primary standards [10].

2 THE SPHERICAL SPECTROMETER SP²

The SP² design relies on simulations performed with MCNPX 2.6 Monte Carlo code [6], using the ENDF/B-VII cross-section library [11] for neutrons with energies below 20 MeV and the room temperature cross-section tables in polyethylene, $S(\alpha,\beta)$. Neutron transport above 20 MeV has been modeled using Bertini intra-nuclear cascade model and Dresner evaporation model [12].

The SP² spectrometer consists of thirty-one TNPDs arranged along three perpendicular axes at five radial distances and at the centre of a high-density polyethylene sphere of diameter about 30 cm. The one-cm-thick high-energy lead radiator is located between radius 3.5 and 4.5 cm (Fig. 1). Although the response of a single TND in a given location is clearly not isotropic, a nearly isotropic response is obtained by summing the readings of the detectors located at the same radial position, as has been discussed in previously published papers [4, 5]. Experiments performed with a ²⁴¹Am-Be neutron source showed that the SP² radius-summed response is direction-independent within 2-3%.

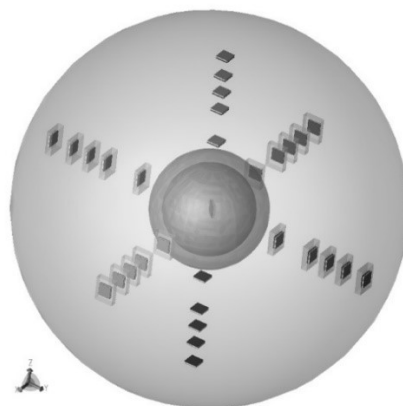


FIG. 1. 3D view of the SP². The TNPDs are arranged in symmetrical positions along the three axes. The one-cm thick lead shell is visible.

The response matrix of the device, defined as the summed reading of detectors located at the same radius, per unit fluence, as a function of the energy and of the radius, is very similar to that of a Bonner Sphere Spectrometer with sphere diameters from 8 to 30 cm. Validation tests have been performed with reference monoenergetic neutron beams at NPL (UK) at 144 keV, 565 keV, 1.2 MeV and 5 MeV. The experimental SP² response agreed with the simulated one within about 5%.

3 THE CYLINDRICAL SPECTROMETER CYSP

The CYSP mainly consists of a series of TNDs located along the axis of a polyethylene cylinder. A detailed 3D view of the instrument is shown in Fig. 2. It is a cylinder with overall dimensions 65 cm height × 50 cm diameter. The dimensions of the cylinder were optimized to practically eliminate the contribution from neutrons coming from other directions with respect to that identified by the collimator as well as the location of detectors. The internal locations of the TNDs were selected to achieve similar spectrometric capabilities as a Bonner Sphere spectrometer with diameters from 8 cm up to 30 cm.

CYSP consists of two main blocks:

- The collimator
- The detecting part

The collimator is 30 cm long with a 15 cm diameter collimating aperture. This is internally lined with 5 mm of borated rubber.

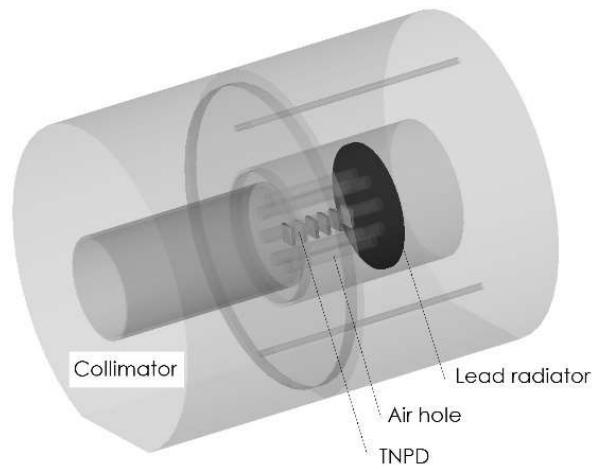


FIG. 2. 3D view of the CYSP. The TNDs are arranged along the cylindrical axis. The 7th detector (behind Pb) is not visible.

Seven TNDs are located along the axis of the cylinders at distances 4, 6, 8, 10, 12, 14 and 21 cm from the end of the collimator. A one-cm thick lead disk is located at 17 cm and serves as (n, xn) high-energy radiator. The cylindrical air holes around the TNDs enhance the response of the deeper detectors. The CYSP response matrix [13] was derived with MCNPX. Its accuracy was tested in reference monoenergetic neutron beams from 144 keV to 16.5 MeV at NPL (UK): an overall uncertainty of about 2% was derived in the mentioned energy range [14].

The CYSP was used in workplace already. A relevant example is the determination of the vertical component of the cosmic neutron field. With this purpose a first experiment was performed in Rome, near the sea level [15]. A further experiment is currently in progress at elevation 2650 m on the Zugspitze Mountain, in collaboration with the Helmholtz Zentrum Munchen, German Research Centre for Environmental Health (GmbH), Institute of Radiation Protection. Figure 3 shows a typical vertical neutron spectrum obtained with the CYSP, compared with an isotropic one, obtained with an extended range Bonner Sphere Spectrometer. The CYSP was oriented in the top-vertical direction, thus it does not register most of the medium- and low-energy neutrons, coming from the scattering (albedo) in the surrounding environment. The week-average fluence rate above 20 MeV measured by CYSP was, in this case, $(2.19 \pm 0.18)10^{-2} \text{ cm}^{-2}\text{s}^{-1}$.

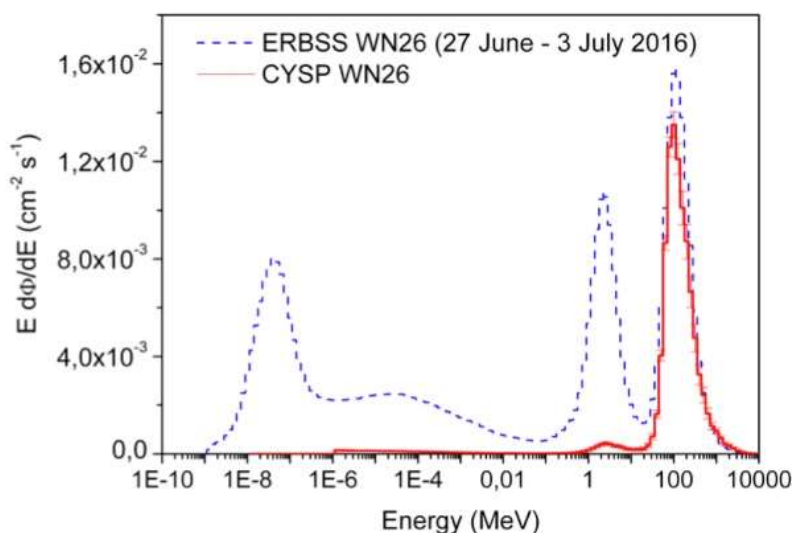


FIG. 3. Zugspitze mountain (2650 m). Typical vertical neutron spectrum obtained with the CYSP, compared with an isotropic one, obtained with an extended range Bonner Sphere Spectrometer (courtesy Vladimir Mares from HMGU).

4 CONCLUSIONS

Relying on an array of active thermal neutron detectors embedded in a moderating structure, the new neutron spectrometers, CYSP and SP², allow the determination of all energy components of a neutron spectrum in single exposure. The CYSP has cylindrical shape and exhibits a sharply directional response, whilst the SP² is spherical and shows isotropic response. Their overall responses are similar to that of a Bonner spheres spectrometer. The response matrices of these devices were derived with MCNPX and were evaluated in reference monoenergetic neutron beams at NPL (UK). For both instruments overall uncertainties in the order of few % were derived.

The CYSP and SP² offer new opportunities for real-time spectrometric monitoring of neutron fields in a variety of application. As a relevant example, the SP² has the size and the weight of an ordinary extended range remmeter, but can provide the neutron spectrum in addition to the dose equivalent. This means a dramatic improvement in the accuracy of workplace radiation protection measurements.

With its directional response, the CYSP can provide a great help in all workplaces where the direction is important, as in accelerator- or laser-based neutron fields.

ACKNOWLEDGEMENTS

This work was supported by projects NESCOFI@BTF and NEURAPID (INFN - Commissione Scientifica Nazionale 5, Italy) and FIS2012-39104-C02 (Spain). The staff of the neutron metrology group of NPL (Teddington, UK) is greatly acknowledged for the assistance provided during the irradiations with quasi mono-energetic neutrons. The staff of Helmholtz Zentrum Munchen, German Research Centre for Environmental Health (GmbH), Institute of Radiation Protection is also acknowledged for supporting the experiment on the Zugspitze Mountain.

REFERENCES

- [1] INTERNATIONAL ATOMIC ENERGY AGENCY, Nuclear Technology Review. GC(61)/INF/4 (2017).
- [2] INTERNATIONAL COMMISSION ON RADIATION UNITS AND MEASUREMENTS, Determination of Operational Dose Equivalent Quantities for Neutrons. Publication 66 (2001).
- [3] THOMAS, D.J., Neutron spectrometry. *Radiat. Meas.* 45 (2010) 1178–1185.
- [4] GOMEZ-ROS, J.M., et al., A multi-detector neutron spectrometer with nearly isotropic response for environmental and workplace monitoring. *Nucl. Instrum. Methods A* **613** (2010) 127–133.
- [5] GOMEZ-ROS, J. M., et al., Designing an extended energy range single-sphere multi-detector neutron spectrometer. *Nucl. Instrum. Methods A* **677** (2012) 4–9.
- [6] PELOWITZ D B (editor), MCNPX User's Manual Version 2.6. Report LA-CP-07-1473 (2008).
- [7] BEDOGNI, R., et al., Testing a newly developed single-sphere neutron spectrometer in reference monochromatic fields from 147 keV to 14.8 MeV. *Nucl. Instrum. Methods A* **714** (2013) 110–114.

- [8] BEDOGNI, R., et al., Experimental characterization of semiconductor-based thermal neutron detectors. *Nucl. Instrum. Methods A* **780** (2015) 51–54.
- [9] POLA, A., et al., Compact thermal neutron sensors for moderator-based neutron spectrometers. *Radiat. Prot. Dosim.* **161** (1–4) 229–232.
- [10] BEDOGNI, R., et al., Experimental characterization of HOTNES: A new thermal neutron facility with large homogeneity area. *Nucl. Instrum. Methods A* **843** (2017) 18–21.
- [11] CHADWICK, M.B., OBLOZINSKY, P., HERMAN, M., et al., ENDF/B-VII.0: Next Generation Evaluated Nuclear Data Library for Nuclear Science and Technology. *Nucl. Data Sheets* **107** (2006), 2931–3060.
- [12] PIOCH, C., MARES, V., RUHM, W., Influence of Bonner sphere response functions above 20 MeV on unfolded neutron spectra and doses. *Radiat. Meas.* **45** (2010) 1263–1267.
- [13] GOMEZ-ROS, J.M., et al., CYSP: A new cylindrical directional neutron spectrometer. Conceptual design, *Radiat. Meas.* **82** (2015) 47–51.
- [14] BEDOGNI, R., et al., Experimental test of a newly developed single-moderator, multi-detector, directional neutron spectrometer in reference monochromatic fields from 144 keV to 16.5 MeV, *Nucl. Instrum. Methods A* **782** (2015) 35–39.
- [15] GOMEZ-ROS, J.M., et al., The directional neutron spectrometer CYSP: Further developments for measuring low intensity fields. *Radiat. Meas.* **106** (2017) 580–584.

THE MEASUREMENT OF NEUTRON SOURCE TERMS USING THE NESTED NEUTRON SPECTROMETER

A. LICEA, Y. PICARD
Canadian Nuclear Safety Commission,
Ottawa, ON,
Canada

J. DUBEAU, S.S. HAKMANA WITHARANA
Detec,
Gatineau, QC
Canada

J. KILDEA, M. EVANS, R. MAGLIERI,
McGill University Health Centre,
Montreal, QC,
Canada

Abstract: The Canadian Nuclear Safety Commission (CNSC) regulates many different types of accelerator facilities across Canada. To fulfil its mandate, the CNSC evaluates the shielding design of proposed facilities prior to issuing a licence to construct each facility. For complex facilities, Monte Carlo simulations are used to validate the applicant's shielding design. Once facilities become operational, inspections are performed to verify compliance with applicable CNSC regulatory safety requirements. These inspections include verification of both photon and neutron dose rates in the facility. The neutron source term has a major impact on the shielding design and resulting dose rates, but often this information is not available in any of the literature for a particular type of accelerator, so on-site measurements of the spectrum may be required. Traditionally, Bonner Spheres Systems (BSS) with activation foils and TLDs are used for this type of measurement.

Recently, the CNSC has tested and used a new instrument called the Nested Neutron Spectrometer (NNS). It operates under the same principle as a Bonner Sphere Spectrometer; that is, the spectral information is based on the neutron energy response of a thermal neutron detector at the centre of moderating bodies. However, the NNS has modular cylindrical shells which make it lighter than the BSS, and easier to use in the field. The NNS can also be operated in ion chamber mode in order to measure high intensity neutron fluence rates, such as those found inside the vaults of accelerators. Finally, the NNS is accompanied by a user-friendly Windows™-based unfolding software. The results can be obtained in a very short period of time (within an hour) and immediately used in Monte Carlo simulations, benchmarking is in a very well agreement with the doses around the facilities, NNS is versatile and a useful tool in the assessment of neutron shielding facilities.

1 INTRODUCTION

The Canadian Nuclear Safety Commission (CNSC) regulates many different types of accelerator facilities and calibration facilities across Canada. To fulfill its mandate, the CNSC evaluates the shielding design of proposed facilities prior to issuing a licence to construct each facility. For complex facilities, Monte Carlo simulations are used to validate the applicant's shielding design. Once facilities become operational, inspections are performed to verify compliance with applicable CNSC regulatory safety requirements. These inspections include verification of both photon and neutron dose rates in the facility.

The neutron source term has a major impact on the shielding design and resulting dose rates, but often this information is not available in any of the literature for a particular type of accelerator or nuclear reaction, so on-site measurements of the spectrum may be required. Traditionally, Bonner Spheres Systems (BSS) with activation foils and TLDs are used for this type of measurement.

As an example, in a cyclotron operating at 24 MeV, 300 μA , the neutron flux can be as high as $10^8 \text{ n cm}^{-2} \text{ s}^{-1}$ at 1 m from a ^{100}Mo target due to the $^{100}\text{Mo}(p,2n)^{99\text{m}}\text{Tc}$ reaction. The neutron source term including the spectrum has been published.

In other cases, as in a medical linac accelerator operating at 15 MV, 600 MU, the flux can be as high as $7.85 \times 10^5 \text{ n cm}^{-2} \text{ s}^{-1}$ at 1.41 m from the target and 1 m from the isocentre on the patient plane. In recent models (last 15 years), no neutron source term is available.

2 THE NESTED NEUTRON SPECTROMETER

The Nested Neutron Spectrometer (NNS) is a recent invention by a Canadian company (DETEC, Gatineau, QC, Canada) [1]. Figure 1 shows the NNS with its ^3He counter and nested high-density polyethylene (HDPE) cylinders. The $^3\text{He}(n,p)^3\text{H}$ reaction in the ^3He counter detects thermal neutrons and the amount of moderator around the counter can be changed in an easy manner using the nested HDPE cylinders. This system is much less cumbersome than a typical BSS.



FIG. 1. NNS fully disassembled (left) and ready for use on a tripod (right). The small cylindrical ^3He counter is shown attached to a red LEMO cable.

2.1 NNS MEASUREMENT PRINCIPLES

By performing 8 measurements with the 7 HDPE moderators and one with no moderator, the neutron energy spectrum can be obtained, and the detection rate can be obtained by counting pulses.

Pulse counting is used for neutron fluxes less than $10^4 \text{ cm}^{-2} \text{ s}^{-1}$ using nuclear counting electronics. In addition, the NNS can operate in current-mode, which solves the problem of pulse pile-up in pulse-counting detectors for high neutron fluxes and for pulsed sources, since the current is measured in a manner analogous to that used in an ionization chamber. The current method is used for incident neutron flux $> 10^4 \text{ cm}^{-2} \text{ s}^{-1}$, such as those found near medical accelerators. The current is measured using an electrometer (Fig. 2).

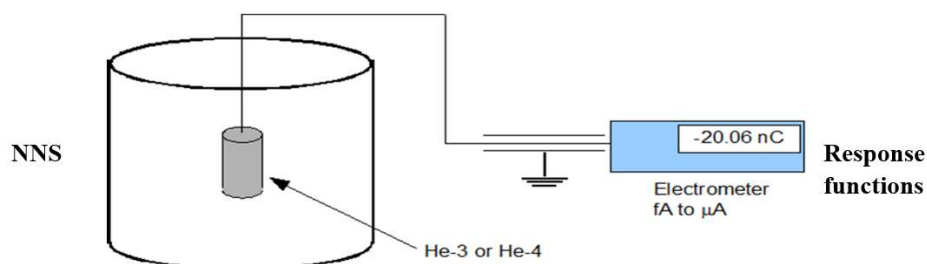


FIG. 2. The ^3He counter is operated at unity gain as an ion chamber. A neutron-insensitive ^4He ion chamber may also be used for the subtraction of the gamma-ray contribution to the current.

As in the BSS, the ability of the NNS to produce a neutron energy distribution is the result of changing energy-dependent neutron efficiency as a function of moderating HDPE mass around the ^3He counter. These efficiency curves, otherwise known as response functions, are shown in Figure 3 for the bare detector and for increasing amounts of HDPE from 200 g to more than 8 kg. The mean energy of the response function increases with the HDPE cylinder mass.

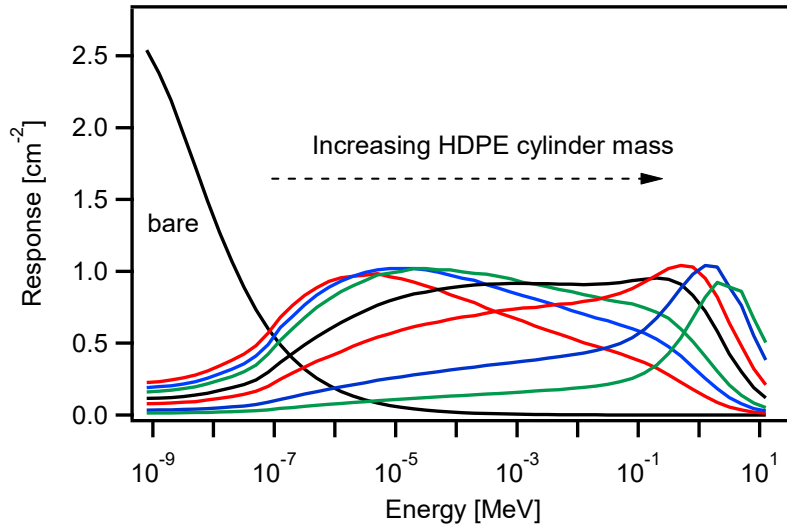


FIG 3. The shapes of the response functions (or energy dependent neutron counting efficiencies) are similar in appearance to those of the BSS.

2.2 NNS MEASUREMENT AND DATA UNFOLDING PROCESSES

In a given neutron field, 8 measurements are taken, with the bare ^3He counter and the same counter surrounded with the 7 combinations of cylindrical HDPE moderator. The observed variation of the counting rate, as a function of the amount of moderator, is then a direct consequence of the response functions of Figure 3 and the energy spectrum of the incident neutrons. Figure 4 shows two examples of the change in counting rate versus moderator amount for two very different neutron fields.

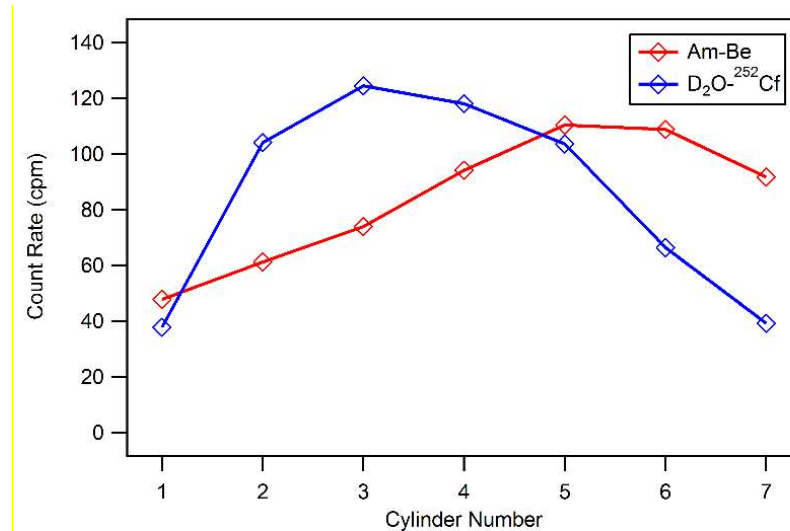


FIG 4. Counting rate dependence on the number of moderating cylinders for a 'hard' neutron spectrum (Am-Be) and a softer one (heavy-water-moderated ^{252}Cf).

Unfolding is the process by which one reconstructs the neutron energy distribution that led to the measured rates, such as those shown in Figure 4, based on the response functions of the spectrometer (Figure 3). This process is typically laborious and requires the insight of an experienced user. The NNS is provided with WindowsTM interface software (Figure 5) which greatly facilitates the unfolding process. It provides two unfolding algorithms. The first is a least square algorithm by Perey that was originally intended for the unfolding of foil activation data [2]. The second algorithm is called the Maximum Likelihood Expectation Maximization (MLEM), and although it is borrowed from the field of CT iterative image reconstruction, it has found applications in BSS and NNS unfolding [3–4].

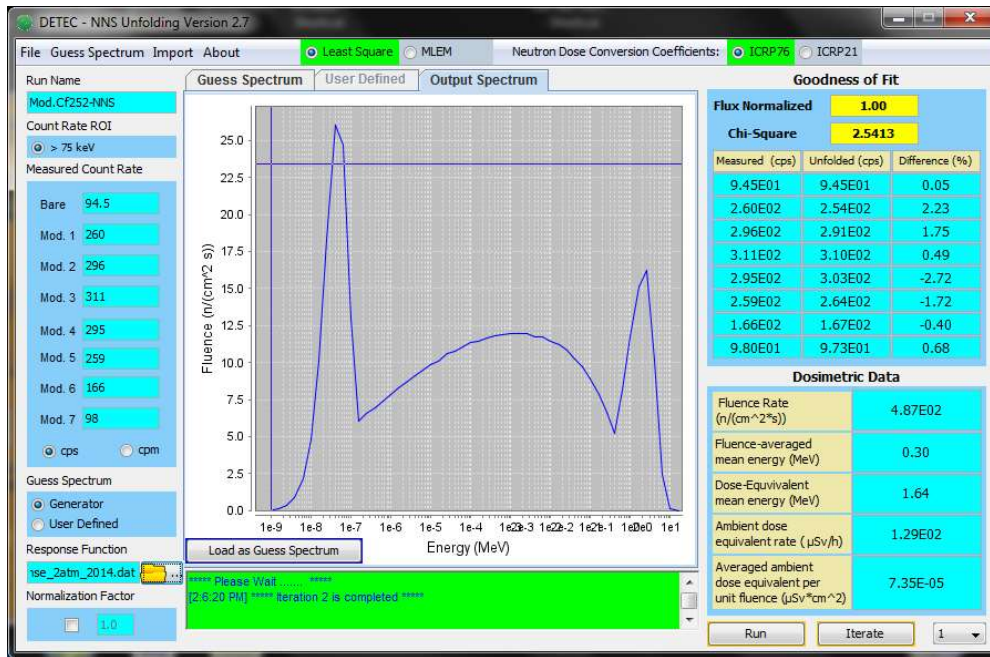


FIG. 5. In a given field, 8 measurements are performed with the 8 configurations of the NNS. The unfolding process creates an energy distribution over 52 energy bins. This requires a dedicated unfolding code. To this aim, a Graphical User Interface was created over the Least Square Minimization and MLEM algorithm

3 CNSC NEUTRON SPECTRUM MEASUREMENTS

3.1 NEUTRON SPECTRUM FROM THE REACTION $^{100}\text{Mo}(p,2n)^{99m}\text{Tc}$ IN A TR-24 CYCLOTRON

A 423 μm thick ^{100}Mo target, on an Aluminium holder, was mounted at the solid target port of an ACSI (Advanced Cyclotron Systems, Richmond, BC, Canada) TR-24 cyclotron at the Centre Hospitalier Universitaire de Sherbrooke and bombarded with 24 MeV protons. The distance between the NNS and the solid target was about 1.3 m (Fig. 6). The resulting neutron spectrum consisted of the neutrons from the $^{100}\text{Mo}(p,2n)^{99m}\text{Tc}$ reaction and 17.8 MeV residual energy, with the Al target holder (Fig. 7).

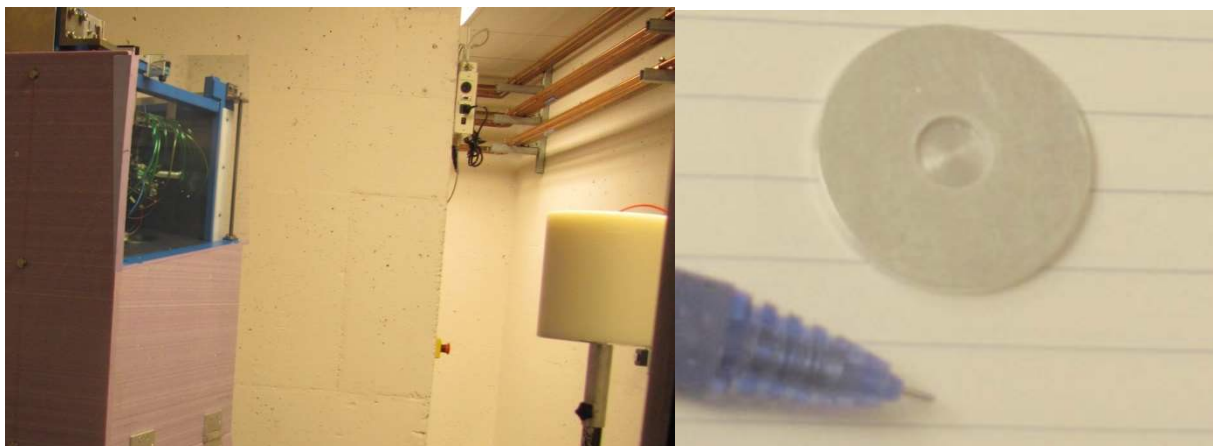


FIG. 6. Solid target station and NNS location at 1.3 m (left) and Al target holder (right)

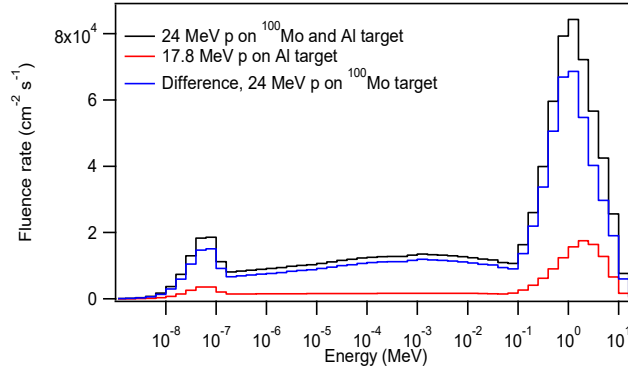


FIG. 7. Neutron energy spectrum measured at 1.3 m from the target of the TR-24 cyclotron. Separate measurements were performed for 24 MeV protons incident on ^{100}Mo and 17.8 MeV protons incident on the Al target holder. The difference, due to the $^{100}\text{Mo}(p,2n)^{99m}\text{Tc}$, is shown.

A second measurement was performed with 17.8 MeV protons directly on Al target holder in order determine the net neutron spectra from the $^{100}\text{Mo}(p,2n)^{99m}\text{Tc}$ reaction. The beam current was always $2.5 \mu\text{A}$, which is $\sim 1/120$ of its normal operating current during ^{99m}Tc production. Table 1 shows results for low operating current which includes low-energy neutrons due to room scatter.

TABLE 1. NEUTRON FIELDS PRODUCED IN A ^{100}Mo TARGET AND ALUMINIUM HOLDER AT $2.5 \mu\text{A}$ PROTON CURRENT

Quantity	Targets		
	Mo on Al – 24 MeV	Al – 17.8 MeV	Net $^{100}\text{Mo}(p,2n)^{99m}\text{Tc}$
Fluence rate [$\text{cm}^{-2} \text{s}^{-1}$]	9.31×10^5	1.65×10^5	7.66×10^5
H*(10) rate [mSv h^{-1}]	662.4	141.8	520.6
Average energy [MeV]	0.93	1.27	0.86

3.2 NEUTRON SPECTRUM IN A MEDICAL LINAC FACILITY OPERATED AT 15 MV

The NNS was operated in current mode to measure the neutron spectrum from the Varian TrueBeamTM medical linac (Figs. 8 and 9), at the new McGill University Health Centre (MUHC) facility (Glen site). The measurement distance was 1.41 m from the target and 1 meter from the isocentre on the patient treatment plan for different modes of operation (flattening filter free [FFF], flattening filter [FF] and electrons) and energies. The resulting unfolded neutron fluence rates are shown in Figure 10 and Figure 11 for the accelerator operated in photon and electron modes, respectively.

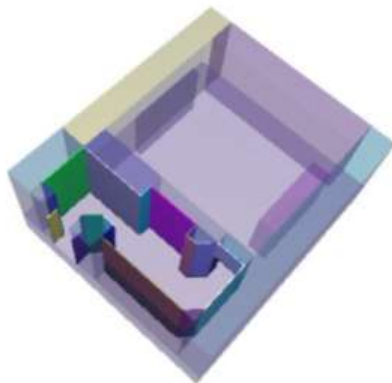


FIG. 8. Linac room depicting walls and borated polyethylene lined on the maze walls of the doorless facility.

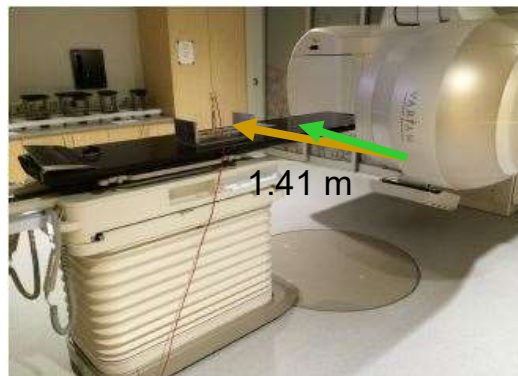


FIG. 9. NNS on the couch at 1.41 m from the target and 1 m from the isocentre in the patient plane.

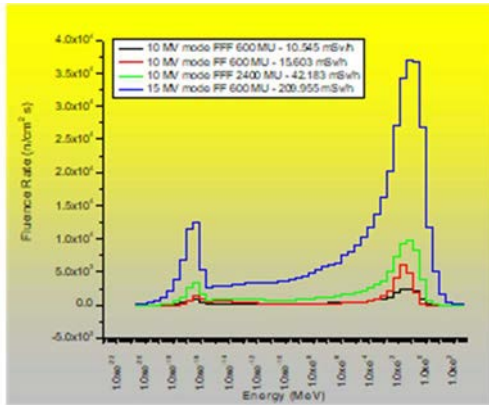


FIG. 10. Photon energies 10 and 15 MV, mode FFF and FF.

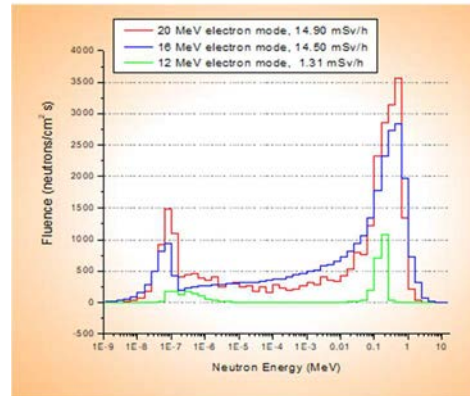


FIG. 11. Electron energies 20, 16 & 12 MeV, 1000 MU/min

3.3 NEUTRON SPECTRUM MEASUREMENTS IN PULSE MODE AT A NEUTRON GENERATOR FACILITY

In a neutron generator research facility at Bubble Technology Inc. (Chalk River, ON, Canada), NNS measurements were performed at 1 m from an Adelphi D-D neutron generator operated at 7.5×10^8 neutrons per second (Fig. 12). The NNS operated this time in pulse counting mode. The unfolded fluence spectral distribution is shown in Fig. 13.

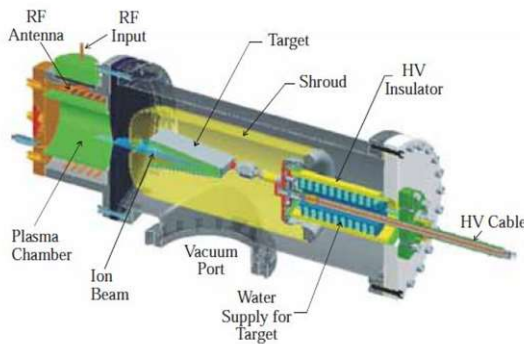


FIG. 12. Adelphi neutron generator

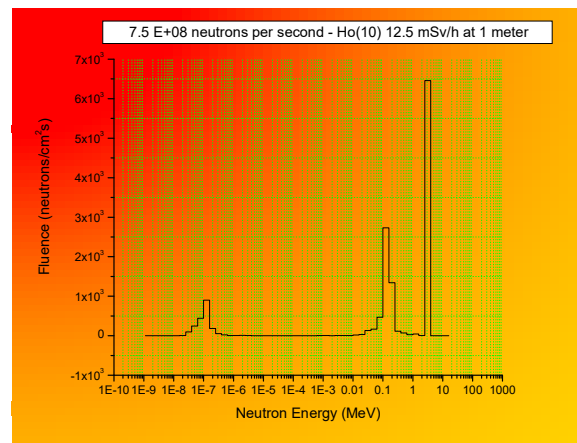


FIG. 13. D-D reaction at 7.5×10 n/s⁸

The epithermal region depicted in the neutron spectrum figures is due to the contribution of materials, accessories and object present in the bunkers during the measurements (wood, plastic, solid water, foam, etc).

4 CONCLUSION

The CNSC used the NNS to measure neutron energy spectra in the high flux environments near accelerators, the NNS was mainly operating in current mode. The instrument provided good characterization of the output (neutron source term) of these types of accelerators and the data obtained were used by the CNSC for its independent shielding assessment of the applicants. Measurements obtained in pulse mode showed similar results and have proved to be valuable in the measurement of high fluence rate sources and/or pulsed sources.

ACKNOWLEDGEMENTS

The CNSC would like to thank Centre Hospitalier Universitaire de Sherbrooke, QC, Canada, McGill University Health Centre (Glen site), Montreal, QC, Canada, Bubble Technology Inc. Chalk River, ON, Canada and Detect Inc, Gatineau QC, Canada, for their assistance and cooperation during the measurements.

REFERENCES

- [1] Dubeau, J., Hakmana Witharana, S.S., Atanackovic, J., Yonkeu, A., Archambault, J.-P., A neutron spectrometer using nested moderators, *Radiat. Prot. Dosim.* **150** 2 (2011) 217–222.
- [2] Perey, F.G. (1997) “Least Square Dosimetry Unfolding: The Program Stay’SL”, ORNL/TM 6062, ENDF 254, October 1977.
- [3] Tain, L., “GEANT4 Monte Carlo simulation school applied to neutron detection”, paper presented during summer school, April 10–11, CEIMAT, Spain (2007)
http://win.ciemat.es/despec/events/mc_school_9_10_april_2007/NeutDet.pdf
- [4] Maglieri, R., Lincea, A., Evans, M., Seuntjens, J., Kildea, J., Measuring neutron spectra in radiotherapy using the nested neutron spectrometer, *Med. Phys.* **42** 11 6162–6169.

NEUTRON SPECTROMETRY AROUND LINACS USING PASSIVE BONNER SPHERE SPECTROMETRY IN PLANETARY MODE

H.R. VEGA-CARRILLO

Unidad Academica de Estudios Nucleares y Unidad Academica de Ingenieria Electrica,
Universidad Autonoma de Zacatecas,

Mexico

E-mail: fermineutron@yahoo.com

J.L. BENITES-RENGIFO

Centro Estatal de Cancerologia de Nayarit

Mexico

E. GALLEGO, A. LORENTE, K.A. GUZMAN-GARCIA

Departamento de Ingenieria Energetica – ETSI Industriales

Universidad Politecnica de Madrid,

Spain

M.A.S. LACERDA

Laboratorio de Calibracion de Dosimetros

Centro de Desenvolvimento da Tecnologia Nuclear/Comissão Nacional de Energia Nuclear,

Brazil

R. MENDEZ

Laboratorio de Patrones Neutrónicos

CIEMAT,

Spain

L. HERNÁNDEZ-ADAME

CONACyT-Centro de Investigaciones Biológicas del Noroeste,

Mexico

Abstract: When linear accelerators operate above 8 MV, neutrons are produced in (γ, n) and ($e, e'n$) reactions in nuclei via the Giant Dipole Resonance. In linear accelerators for medical applications, the neutron contamination is a radiation protection issue where a non-negligible, and non-desired, dose is delivered to the patient. Moreover, neutrons around linear accelerators for medical applications have been associated with the cancer recurrence and the induction of new tumours. In the past decades several efforts to determine the neutron characteristics around linacs have been carried out; novel procedures and innovative measuring devices have been developed to perform such characterizations. The Bonner sphere spectrometer has been largely used to measure the neutron spectra around linacs; however, the time required to perform the measurements in the treatment hall is large, requiring many linac runs due to the number of spheres in the spectrometer. Aiming to reduce the measuring time, a procedure using a Bonner sphere spectrometer has been developed using a single linac exposure. The procedure was used to measure the photoneutron spectrum in a 15 MV linear accelerator.

1 INTRODUCTION

Genes in the deoxyribonucleic acid (DNA) of human cells produce proteins with specific functions. All types of cancer begin when one or several genes in a cell mutate and protein production is affected: abnormal proteins are produced or proteins are not produced. Thus, normal cells receive different information growing without control and become cancerous. Mutations are due to the genetic load (inherited), environmental factors, or from DNA replication errors [1].

All over the world, cancer kills more persons every year than those due to tuberculosis, malaria, and acquired immune deficiency syndrome (AIDS) combined. By 2030, it is expected that every year over 13 million persons will die from cancer, mostly from poor and low-income countries [2]. Procedures used to treat cancer include immunotherapy [3], surgery, chemotherapy, and radiotherapy. Radiotherapy is applied as curative or palliative treatment. Approximately 50–60% of cancer patients receive radiotherapy (alone or combined with surgery or chemotherapy) [4]. There are two modalities in radiotherapy: teletherapy and brachytherapy. In brachytherapy, radioactive seeds (sources) are placed near or in the tumor. In teletherapy, radiation is applied using units with

^{60}Co sources or linear accelerators (linacs). The main aim of radiotherapy is to deliver large doses to the tumor and minimal doses to the healthy organs and tissues around the tumor. Radiotherapy with linacs is the treatment most commonly used [5].

Linacs use high voltages, ranging from 4 to 25 MV, to accelerate electrons that are used to deliver the dose to tumors at low depth in the body, whereas for deep-seated tumors the electrons are used to produce bremsstrahlung photons. The use of high-energy x-rays offers several advantages, in comparison to use low-energy photons, such as a higher depth dose, a lower dose into tissues outside the target volume due to photon scattering, a reduced skin dose and less rounded isodose curves [6, 7]. Regardless of whether the dose is delivered with electrons or photons, when the linac operates above 8 MV neutrons are produced. Unwanted neutrons are produced through $(e, e' n)$ and (γ, n) nuclear reactions with elements in the accelerator head and structural materials whose nuclei cross-section have a giant dipole resonance [8–10].

The neutron contamination around linacs is a radiation protection issue for the facility because during neutron transport in the treatment hall, radioisotopes are produced through activation, and prompt and delayed γ -rays are emitted due to this induced radioactivity [11-13]. Without proper timing protocols, these photons contribute to the dose for the facility staff [14, 15]. Also neutrons, and activation photons, deliver an undesirable dose to the patient that can induce recurrence and secondary tumors [16, 17]. The information of the energy distribution of neutron fluence, also known as neutron spectrum ($\Phi_E(E)$), is important to determine radiation protection quantities using the neutron fluence-to-dose conversion coefficients ($\delta(E)$) through equation 1.

$$\Delta = \int_{vE} \Phi_E(E) \delta(E) dE \quad (1)$$

In equation (1) Δ is the dose rate of interest, and $\delta(E)$ are the conversion coefficients for the neutron fluence-to-dose of interest [18, 19].

The Bonner sphere spectrometer (BSS) [20], also known as multisphere spectrometer, is widely used to determine neutron spectra; however, it has several drawbacks such as the weight, the need of an unfolding procedure and poor resolution. Also, the BSS requires several exposures that imply time-consuming experimental sessions.

The measurement time depends upon the number of moderating spheres in the spectrometer. To overcome some of these drawbacks new spectrometers using a single moderator have been designed: Bedogni et al. [21] developed a new spectrometer using a single spherical moderator with several active thermal neutron detectors. Gómez-Ros et al [22] developed a single cylindrical moderator with seven active thermal neutron detectors. The performance of both spectrometers has been evaluated using a single exposure with a $^{241}\text{AmBe}$ source and the photoneutrons produced by a 15 MV linac [24].

The use of the BSS to determine the photoneutron spectrum around medical linacs has the inconvenience of the time required to perform all the measurements. Another way to overcome this difficulty is to use the BSS in planetary mode [25], where all moderator spheres are allocated around the isocentre. Thus, with a single exposure, the information obtained by the thermal neutron detectors in the centre of the spheres is used to unfold the neutron spectrum. The aim of this work is to describe the required conditions to use the BSS in planetary mode and to show the obtained results of measuring the photoneutron spectrum in the treatment hall with a 15 MV linac.

2 BSS IN PLANETARY MODE

In order to reduce the time required to measure the neutron spectrum around a linac the spectrometer spheres are placed around the circumference of a circle with its centre at the isocentre. Thus, the distance between the isocentre and the spheres' centres is the circle radius. In order to use this procedure, the neutron field has to be the same at the desired distance (symmetry condition) in all directions, and the spheres have to be allocated around the circle in such position where the crosstalk between the spheres is negligible. Both conditions can be determined using Monte Carlo methods. A passive BSS was used in planetary mode to determine the neutron spectrum in a treatment hall with a 15 MV linac. The Monte Carlo code MCNP5 [26] was used to evaluate the neutron field symmetry and the cross-talk between the moderating spheres. Measurements were carried out in a Varian iX 15-MV linac installed at the centre for cancer treatment in Tepic, Nayarit in Mexico.

2.1 SYMMETRY

In order to determine the distance from the isocentre where the neutron field is symmetric, a Monte Carlo model of the linac head, the solid water phantom, and the facility was built using the MCNP5 code. The linac head was

modelled using two concentric spheres: the inner sphere (vacuum) is of radius 5 cm, the outer sphere is of radius 15 cm, the 10-cm-thick shell being made of tungsten [27]. At the centre, the source term was defined for isotropically emitted neutrons according to the function reported by Tosi et al. [28] for a 15 MV linac.

The shell has a hole allowing to produce a 400 cm² irradiation area at the isocentre. The phantom is 30×30×15 cm solid water [29]; the isocentre was allocated to 100 cm from the source and at 5 cm-depth in the phantom. In the model, primary and secondary barriers were included, as well as the maze and the door. In the calculations, the treatment $S(\alpha, \beta)$ was included in the water content in the phantom and the concrete.

The door was modelled using lead (3.5 cm thick) and polyethylene (7.5 cm thick) plates covered by 0.5-cm-thick steel plates. In order to determine the neutron field symmetry in the treatment hall, detectors were placed in the plane of the isocentre, at every 45°, around the perimeter of circles whose radii from the isocentre were 25, 50, 100, and 150 cm. In each point the total neutron fluence per source neutron, the neutron spectrum, and the ambient dose equivalent ($H^*(10)$) per source neutron were calculated using a ring detector and fluence-to-ambient dose equivalent conversion coefficients [18]. In Figures 1–4, the neutron spectra are shown at 25, 50, 100, and 150 cm from the isocentre respectively. The neutron spectra show the evaporation neutrons and a small contribution of knock-on neutrons [28]. During transport in the linac system and around the room, the neutrons lose energy becoming epithermal and thermal. At 25 cm there is a strong influence of the solid water phantom, and there are differences among the spectra. As the distance is increased the differences between the spectra are reduced.

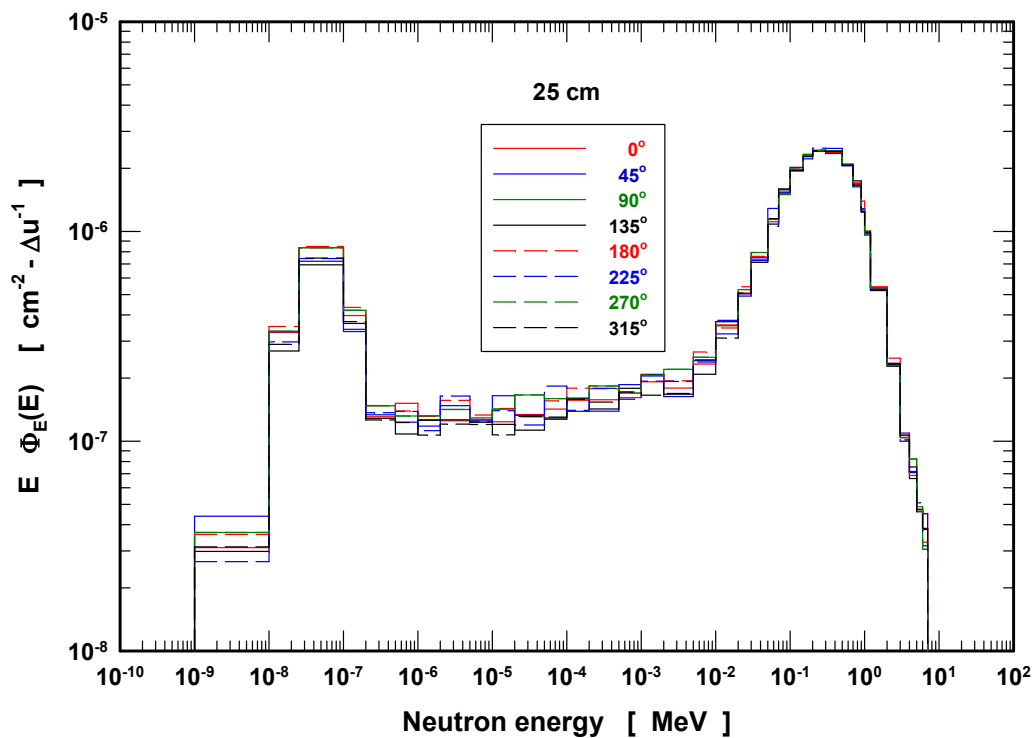


FIG. 1. Neutron spectra around a 25 cm-radius circle.

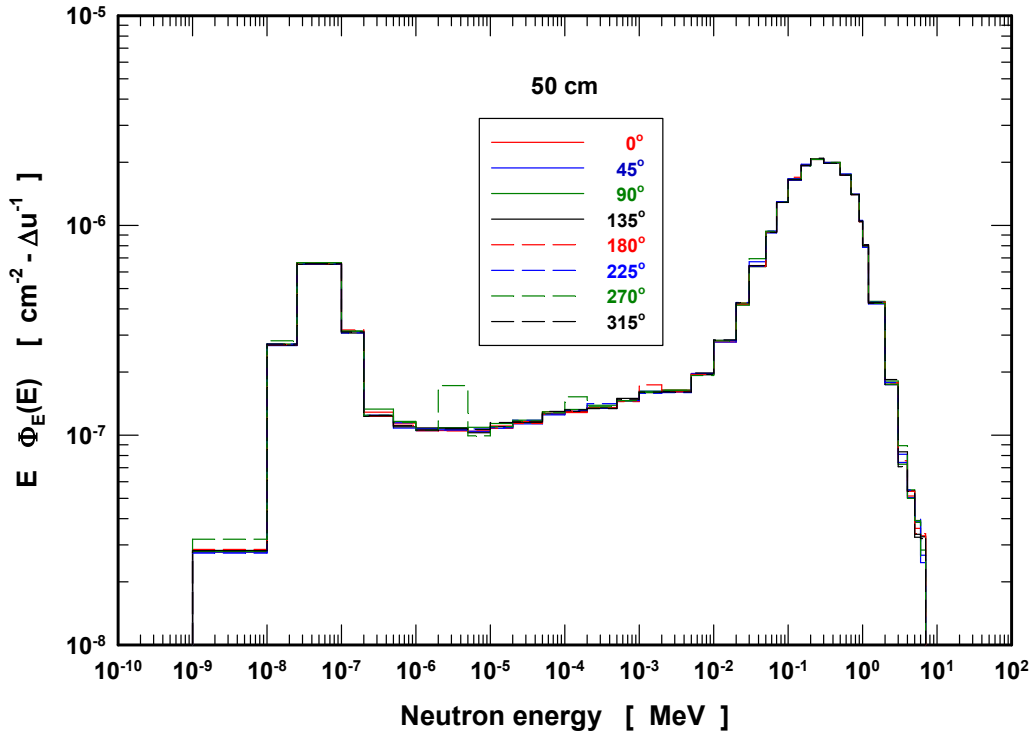


FIG. 2. Neutron spectra around a 50 cm-radius circle.

In Figure 5, the ratios between the $H^*(10)$ values at various angles to that of $H^*(10)$ at 0° are shown; here, the error bars include the error propagation of Monte Carlo uncertainties. In the figure, three parallel lines are included in order to highlight $\pm 0.5\%$. The $H^*(10)$ ratios measured at 100 cm are close to 1. Therefore, at 100 cm, the neutron field shows symmetry.

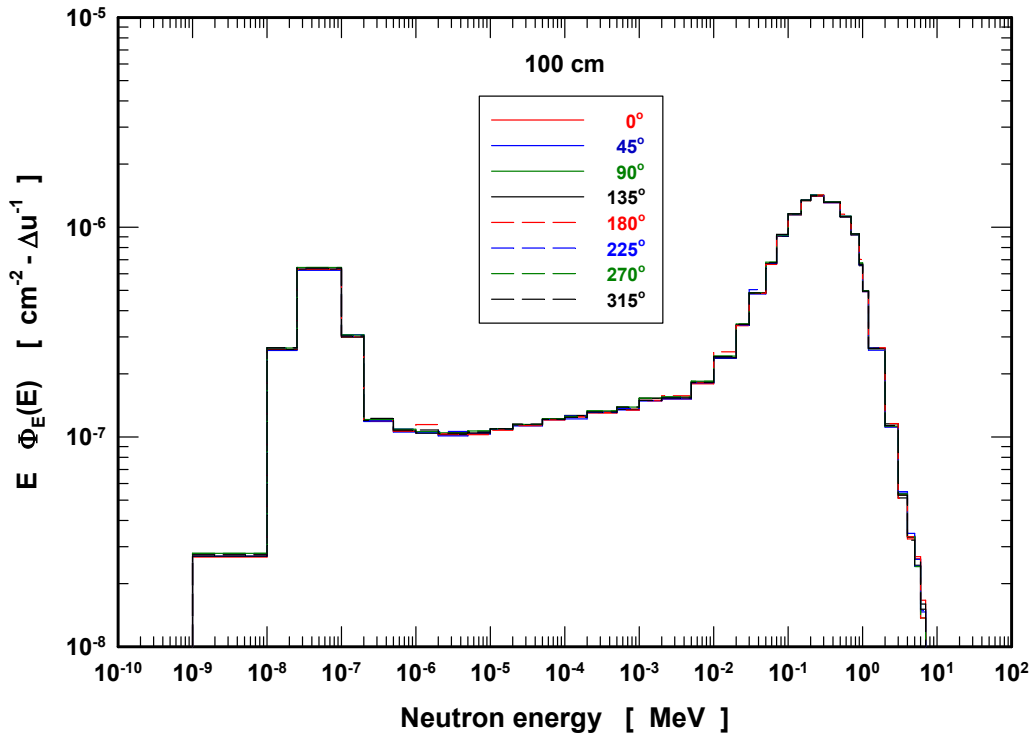


FIG. 3. Neutron spectra around a 100 cm-radius circle.

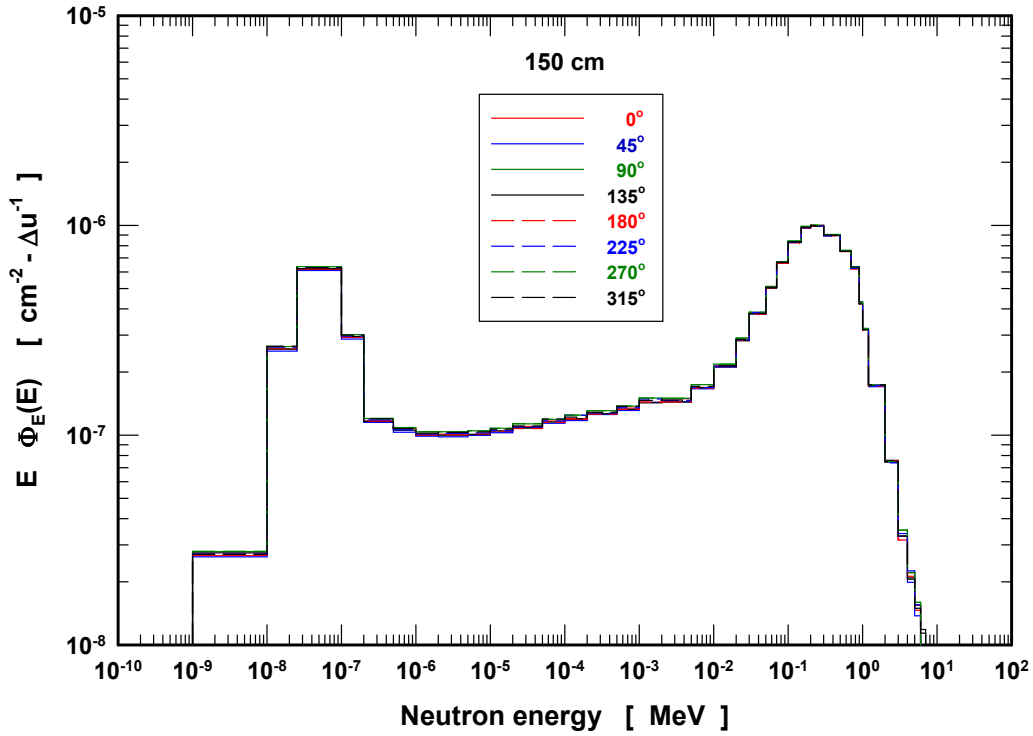


FIG. 4. Neutron spectra around a 150 cm-radius circle.

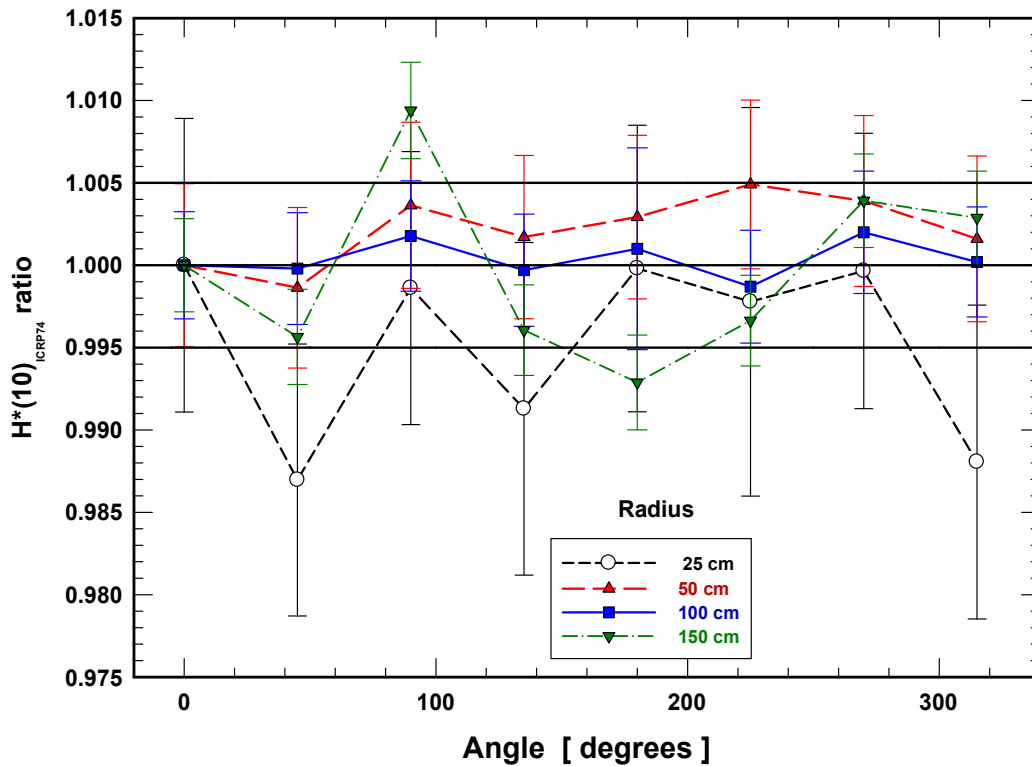


FIG. 5. $H^*(10)$ ratios for detectors placed at different distances and angles.

2.2 CROSS TALKING

A BSS has spherical moderators made of high-density polyethylene being 5.08, 7.62, 12.7, 20.32, 25.4, and 30.48 cm-diameter (2, 3, 5, 8, 10, and 12"). If the spheres are sited near each other inside a neutron field, their moderating features perturbate the neutron field at the location of other spheres. Thus, neutrons being scattered by one sphere

can reach another sphere that normally would not have reached it. In order to avoid this cross-talk, another computation was performed with the moderating spheres included at 100 cm. The space occupied by the treatment table and the gantry body put constraints on the BSS placement. Each sphere was placed at different angles based on the limited space available in the treatment hall. Several arrays were calculated, and we found that at 100 cm from the isocentre the spheres have to be separated by at least 17° [25].

In Figure 6, the contour plot of neutron fluence-per-history distribution around the isocentre is shown. The largest number of neutrons is in the phantom. The spheres clearly modify the neutron field, but in this set up the perturbation is in the vicinity of each sphere. In Figure 7, the contour plot of the $H^*(10)$ distribution per source neutron is plotted above the source plane. In both figures can be noticed that the perturbation depends upon the sphere size, but in this array the cross-talking is negligible. In Figure 8, the contour plot of neutron fluence-per-history in the facility is shown. Near the isocentre, the phantom modifies the neutron distribution. As the distance with respect to the isocentre increases the neutron distribution is reduced, but at larger distances the neutron distribution is modified by the walls. Along the maze, the neutron fluence is reduced, and the smallest neutron fluence is noticed outside the facility. In Figure 9, the contour plot of the $H^*(10)$ per source neutron is shown. This distribution is due the neutron spectrum, where the lowest dose is outside the facility and the largest dose is in the vicinity of the isocentre.

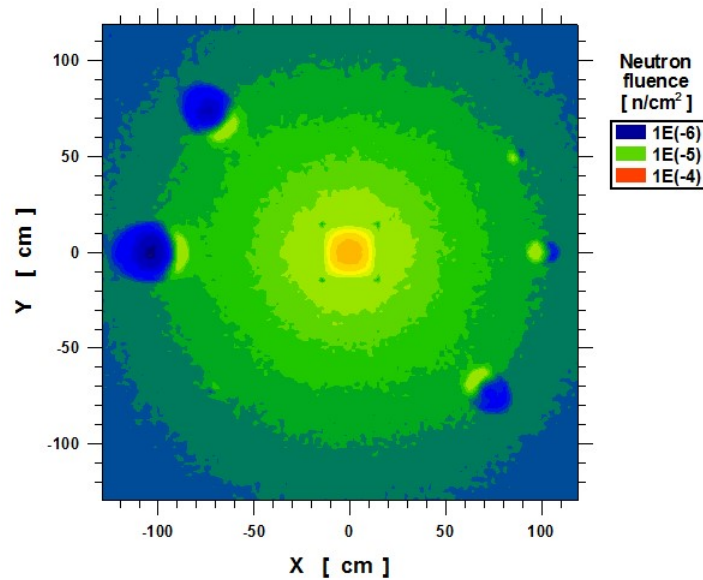


FIG. 6. Contour plot of neutron fluence per source neutron with the BSS at 100 cm.

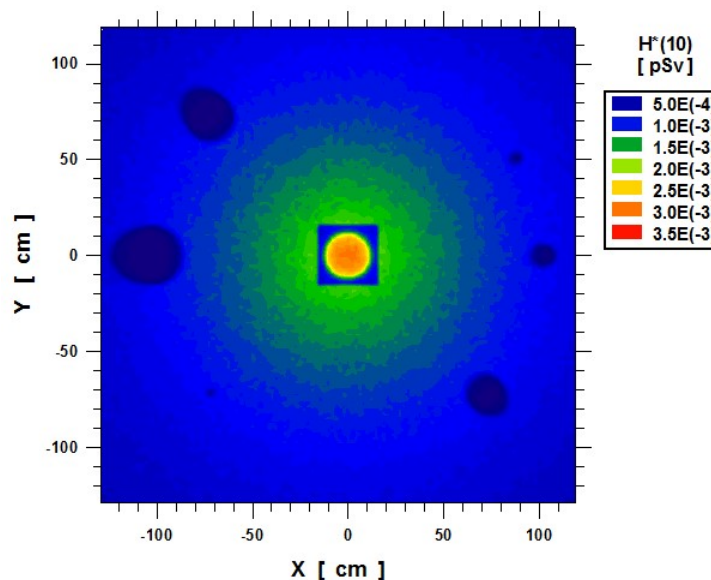


FIG. 7. Contour plot of $H^*(10)$ per source neutron with the BSS at 100 cm.

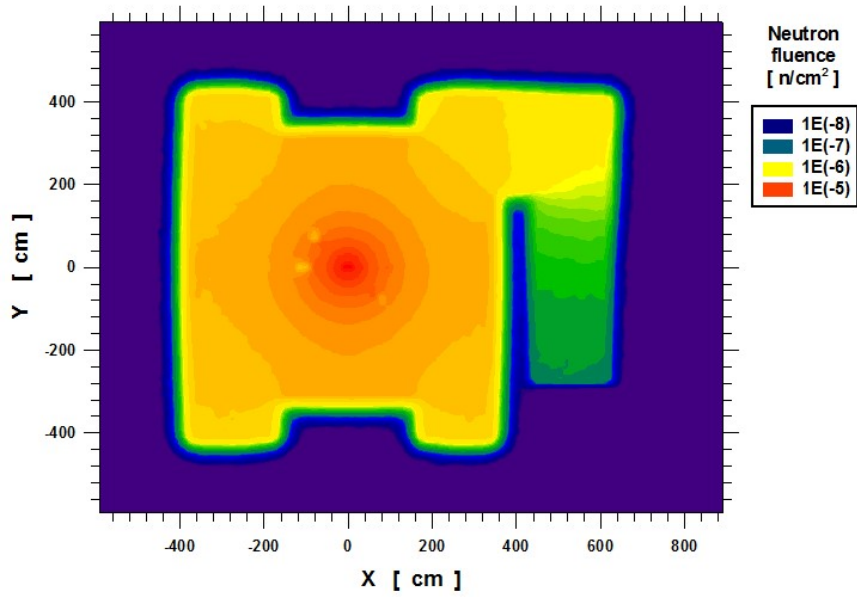


FIG. 8. Contour plot of neutron fluence per source neutron in the facility.

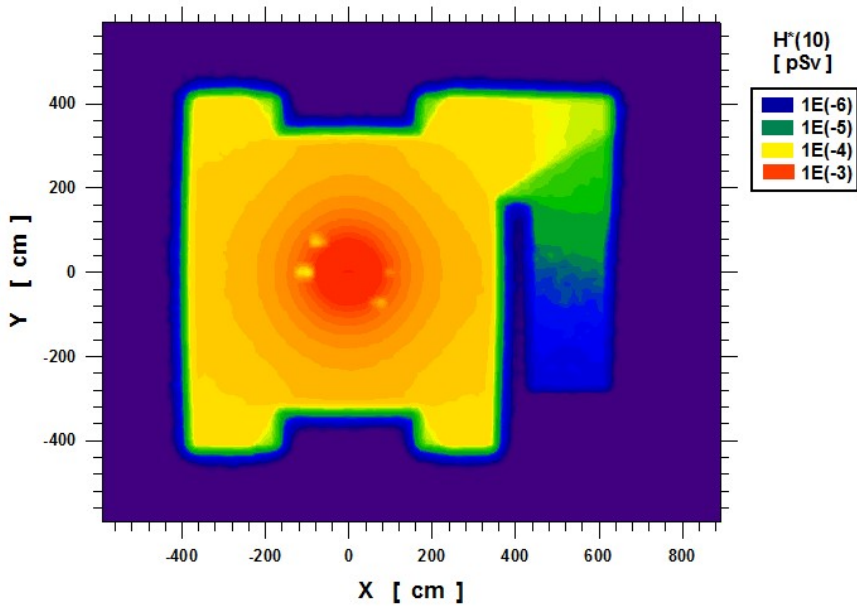


FIG. 9. Contour plot of $H^*(10)$ per source neutron in the facility.

3 MEASURING THE NEUTRON SPECTRUM

Once symmetry and cross-talking conditions were determined, measurements were carried out using a passive BSS. During the linac operation, the radiation field inside the treatment hall is an intense, pulsed, and mixed field of neutrons and photons which induces pulse pile-up and large dead time in any active detector. To overcome this problem, pairs of thermoluminescent dosimeters (TLDs) were used [30] in the centre of the spheres: specifically, two TLD600s and two TLD700s were used to detect the thermalized neutrons (BSS/TLDs) arriving at the sphere centres. In this measurement, the bare detector was also included and a set of 8 TLDs (4 TLD600s and 4 TLD700s) were used to measure the background. In Figure 10, the experimental set up is shown.



FIG. 10. Measuring the neutron spectrum with the BSS/TLDs in planetary mode.

TLDs were heated to 400 °C for 1 hour in order to eliminate any remnant signal. In the measurements, a single exposure resulting in 600 cGy of dose to the phantom at the isocentre was delivered by the x-rays using a 20×20 cm² radiation field. Both types of TLDs have approximately the same atomic number; therefore, their response to photons is approximately the same. However, TLD600 contains 95.6% of ⁶Li and 4.4% of ⁷Li while, TLD700 has 0.1% of ⁶Li and 99.9% of ⁷Li. The isotopic composition makes the TLD600s far more responsive to thermal neutrons than are the TLD700s. After the exposure, TLDs were read with a Harshaw 3500 reader in a high-purity nitrogen atmosphere, and the TLDs glow curves were obtained by heating each TLD from 50 to 300 °C using a temperature gradient of 10 °C/s. From each sphere (including the bare detector), the mean value of the readout of each type of TLD was calculated and corrected by the mean value of the readout of TLDs used to measure the background. The net neutron signal was used to unfold the neutron spectrum.

The neutron spectrum was unfolded using the NSDUAZ unfolding code [31] which provides the total fluence rate, the ambient dose equivalent rate, and the mean neutron energy. In Figure 11, the unfolded photoneutron spectrum at 100 cm from the isocentre is shown. The photoneutron spectrum calculated with the MCNP5 code, using 39 energy groups which match those from the NSDUAZ unfolding code, is also plotted. This calculation was carried out using the model used to determine the symmetry and the cross-talk impact.

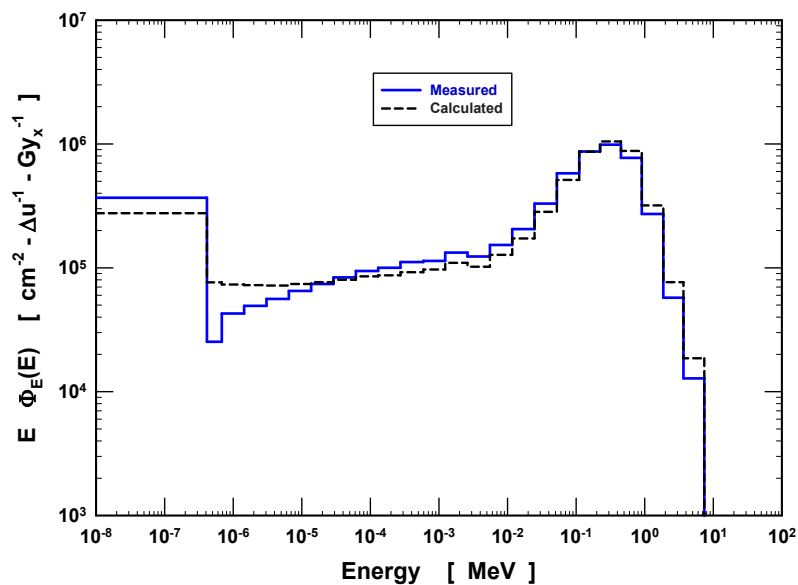


FIG. 11. Measured and calculated photoneutron spectrum.

Although a simple model of the linac head was used, both spectra look similar. The photoneutron spectrum has two peaks: the low energy one is due to thermal neutrons, and the larger one at higher energies is due to fast neutrons. Thermal and epithermal neutrons are due to the room return [32]. The difference between both spectra below 10^{-5} MeV neutrons is probably due to the over-iteration on the solution during unfolding and the elemental composition of concrete, particularly the amount of water. The neutron fluence is $5.20 \times 10^6 \text{ cm}^{-2} \cdot \text{Gy}_x^{-1}$. Using the criteria of the middle point and the median of the energy intervals of the unfolded spectrum, the mean neutron energy of the spectrum is 0.23 and 0.21 MeV, respectively, and the ambient dose equivalent are 633 ± 44 and $612 \pm 43 \text{ } \mu\text{Sv} \cdot \text{Gy}_x^{-1}$, respectively. These results are in agreement with those reported in the literature [32–34].

4 CONCLUSION

In order to reduce the measuring time of photoneutron spectra around linacs, the use of BSS in planetary mode has been demonstrated. Planetary mode requires determining the region in the treatment hall where the neutron field is symmetric and to evaluate the crosstalk among the moderating spheres of the BSS. In order to measure the photoneutron spectrum in the treatment hall with a 15 MV linac, both conditions were evaluated using Monte Carlo methods. The photoneutron spectrum was measured with a BSS/TLDs and it was compared with the photoneutron spectrum calculated with the MCNP5. The photoneutron spectrum was measured at 100 cm from the isocentre; the mean neutron energy, the ambient dose equivalent and the total neutron fluence were computed from the unfolded spectrum per dose delivered at the isocentre. The use of BSS in planetary mode requires a single exposure of the spectrometer instead of seven exposures. The unfolded spectrum compares well with the spectrum calculated with Monte Carlo methods.

REFERENCES

- [1] TOMASETTI, C., LI, L., VOGELSTEIN, B., Steam cell divisions, somatic mutations, cancer etiology, and cancer prevention, *Science* **355** (2017) 1330–1334.
- [2] INTERNATIONAL ATOMIC ENERGY AGENCY BULLETIN, Fighting Cancer in Developing Countries, Bulletin 52-1, IAEA, Vienna (2010).
- [3] GHASEMZADEH, A., BIVALACQUA, T.J., HAHN, N.M., DRAKE, C.G., New strategies in bladder cancer: a second coming for immunotherapy, *Clin. Cancer Res.* **15** (2016) 793–801.
- [4] WEICHSELBAUM, R.R., et al., Radiotherapy and immunotherapy: a beneficial liaison? *Nat. Rev. Clin. Oncol.* **14** (2017) 365–379.
- [5] MESBAHI, A., KESHTKAR, A., MOHAMMADI, E., MOHAMMADZADEH, M., Effect of wedge filter and field size on photoneutron dose equivalent for an 18 MV photon beam of a medical linear accelerator, *Appl. Radiat. Isot.* **68** (2010) 84–89.
- [6] HASHEMI, S.M., et al., A study of the photoneutrons dose equivalent resulting from a Saturne 20 medical linac using Monte Carlo method, *Nukleonika* **52** (2007) 39–43.
- [7] VEGA-CARRILLO, H.R., et al., Neutron and photon spectra in linacs, *Appl. Radiat. Isot.* **71** (2012) 75–80.
- [8] SOTO-BERNAL, T.G., et al., Neutron production during the interaction of monoenergetic electrons with a tungsten foil in the radiotherapeutic energy range, *Nucl. Instrum. Methods Phys. Res. A* **868** (2017) 27–38.
- [9] YUCEL, H., et al., Measurement of photo-neutron dose from an 18-MV medical linac using a foil activation method in view of radiation protection of patients, *Nucl. Eng. Tech.* **48** (2016) 525–532.
- [10] INTERNATIONAL ATOMIC ENERGY AGENCY TECDOC 1178 Handbook on Photonuclear Data for Applications. Cross-Sections and Spectra. IAEA, Vienna (2000).
- [11] KONEFAL, A., et al., W. Correlation between radioactivity induced inside the treatment room and the undesirable thermal/resonance neutron radiation produced by linac, *Phys. Med.* **24** (2008) 212–218.
- [12] POLACZEK-GRELIK, K., et al., Linear accelerator therapeutic dose-induced radioactivity dependence, *Appl. Radiat. Isot.* **68** (2010) 763–766.
- [13] POLACZEK-GRELIK, K., KARACZYN, B., KONEFAL, A., Nuclear reactions in linear medical accelerators and their exposure consequences, *Appl. Radiat. Isot.* **70** (2012) 2332–2339.
- [14] VEGA-CARRILLO, H.R., et al., Induced radioisotopes in a linac treatment hall, *Appl. Radiat. Isot.* **102** (2015) 103–108.
- [15] VEGA-CARRILLO, H.R., RIVERA-PEREZ, E., Moderator for neutron activation with the photoneutrons produced by a linac, *J. Radioanal. Nucl. Chem.* **299** (2014) 1499–1507.
- [16] STATHAKIS, S., LI, J., MA, C.C., Monte Carlo determination of radiation-induced cancer risk for prostate patients undergoing intensity-modulated radiation therapy, *J. Appl. Clin. Med. Phys.* **8** (2007) 14–27.

- [17] TRAVIS, L.B., et al., Second malignant neoplasms and cardiovascular disease following radiotherapy, *J. Natl. Cancer Inst.* **104** (2012) 357–370.
- [18] INTERNATIONAL COMMISSION ON RADIOLOGICAL PROTECTION, ICRP74. Conversion Coefficients for use in Radiological Protection Against External Radiation, *Ann. ICRP* **26** (1990) 1–201.
- [19] INTERNATIONAL COMMISSION ON RADIOLOGICAL PROTECTION, ICRP116. Conversion Coefficients for Radiological Protection Quantities for External Radiation Exposures, *Ann. ICRP* **40** (2010) 1–257.
- [20] BRAMBLETT, R.L., EWING, R.I., BONNER, T.W., A new type of neutron spectrometer, *Nucl. Instrum. Methods* **9** (1960) 1–12.
- [21] BEDOGNI, R., et al., A single-exposure, multidetector neutron spectrometer for workplace monitoring, *Radiat. Prot. Dosim.* **170** (2016) 326–330.
- [22] GÓMEZ-ROS, J.M., et al., CYSP: A new cylindrical directional neutron spectrometer. Conceptual design, *Radiat. Meas.* **82** (2015) 47–51.
- [23] GÓMEZ-ROS, J.M., et al., Designing an extended energy range single-sphere multi-detector neutron spectrometer, *Nucl. Instrum. Methods Phys. Res. A* **677** (2012) 4–9.
- [24] GÓMEZ-ROS, J.M., et al., Two new single-exposure, multi-detector neutron spectrometers for radiation protection applications in workplace monitoring, *Radiat. Prot. Dosim.* **173** (2017) 104–110.
- [25] BENITES-RENGIFO, J.L., VEGA-CARRILLO, H.R., VELAZQUEZ-FERNANDEZ, J., Photoneutron spectrum measured with Bonner sphere spectrometer in planetary method mode, *Appl. Radiat. Isot.* **83** (2014) 256–259.
- [26] X-5 MONTE CARLO TEAM. MCNP - A General Monte Carlo N-Particle Transport Code, Version 5, Report LA-UR-03-1987, Los Alamos National Laboratory. (2003).
- [27] NATIONAL COUNCIL ON RADIATION PROTECTION AND MEASUREMENTS (Bethesda, MD). Neutron Contamination from Medical Electron Accelerators, NCRP Rep. 79 (1984).
- [28] TOSI, G., et al., Neutron measurements around medical electron accelerators by active and passive detection techniques. *Med. Phys.* **18** (1991) 54–60.
- [29] HILL, R.F., BROWN, S., BALDOCK, C., Evaluation of the water equivalence of solid phantoms using gamma ray transmission measurements, *Radiat. Meas.* **43** (2008) 1258–1264.
- [30] VEGA-CARRILLO, H.R., TLDs pairs, as thermal neutron detectors in neutron multisphere spectrometry, *Radiat. Meas.* **35** (2002) 251–254.
- [31] VEGA-CARRILLO, H.R., ORTIZ-RODRIGUEZ, J.M., MARTINEZ-BLANCO, M.R., NSDUAZ unfolding package for neutron spectrometry and dosimetry with Bonner spheres, *Appl. Radiat. Isot.* **71** (2012) 87–91.
- [32] VEGA CARRILLO, H.R., et al., Study of room-return neutrons, *Radiat. Meas.* **42** (2007) 413–419.
- [33] KASE, K.R., et al., Neutron fluence and energy spectra around the Varian CLINAC 2100/2300C medical accelerator. *Health Phys.* **74** (1998) 38–47.
- [34] THOMAS, D.J., et al., Characterization and utilization of a Bonner sphere set based on gold activation foils. *Radiat. Prot. Dosim.* **126** (2007) 229–233.
- [35] KIM, H.S., LEE, J.K., Assessment and measurement of the photoneutron field produced in the Varian medical linear accelerator, *J. Nucl. Sci. Tech.* **44** (2007) 95–101.

ABSOLUTE NEUTRON COUNTING. THE INFLUENCE METHOD

R.E. MAYER, I.J. RIOS

Centro Atómico Bariloche and Instituto Balseiro

Comisión Nacional de Energía Atómica and Universidad Nacional de Cuyo
Argentina

Email: mayer@cab.cnea.gov.ar

Abstract: Absolute counting at energies where detectors are partially transparent to incident neutrons in a beam, usually leads to the numerical evaluation of detector efficiency or resort to comparison with standards. In many cases it will become possible to avoid this step through application of the 'Influence Method'. This method allows the absolute determination of a nuclear particle flux without the need to know detector efficiency and to register coincidences. The basic idea underlying the method is the influence of the presence of one detector in the count rate of another detector placed immediately behind the first one. The method defines statistical estimators for the absolute number of incident particles and for the efficiency. It also provides expressions for the uncertainty of the statistically correlated variables thus defined.

The philosophy of the method is to deal with a problem with a number k of unknowns, through the employment of k detectors (whenever possible), placed in such a way that their successive influences yield correlated measurements. Thus, for some needs, its expressions were extended for that arbitrary number k . It is particularly useful for time-of-flight determinations, given the fact that the efficiency measured for each of the approximately monoenergetic time bins is a particular constant for each of them. In other usual cases where there is a neutron spectrum involved, the method provides a weighted mean efficiency. Nevertheless, the efficiency is not needed because there is always an expression for the absolute number of neutrons in the beam.

The method was also implemented for the experimental assessment of the 'space charge effect', which diminishes gas multiplication in proportional counters undergoing irradiation by intense radiation bursts, where individual neutrons are not distinguished and, instead, the whole piled up electric charge is registered.

1. INTRODUCTION

When the need exists to determine the absolute number n of particles falling on a detector and the intrinsic efficiency is not known, methods have been devised along the time as it is the case of the coincidence method published in 1924 by Geiger and Werner [1] through the exploitation of the counting of coincident events (as in beta-gamma counting), or the coincident observation of each individual event.

But in the general case, when there is no possibility to apply a method which circumvents the need to know the intrinsic efficiency, for instance because there are no coincidences to be exploited, the usual solution is to theoretically evaluate or to employ standards to calibrate the efficiency. When resorting to the theoretical evaluation, the microscopic reaction cross section will be taken from nuclear data libraries, but the involved effective detector thickness will need to be determined relating detector shape and incident beam width and profile, which will have to be experimentally measured. Nuclear data for detector wall material will also play a part in the uncertainties of the calculation. Moreover, other contributions to uncertainty may end up dominating the results, as it is the case of the shape of the electric field at the ends of the electrodes in a gas ionization chamber, or the different light collection efficiency in a scintillator with respect to position of the detection event in the scintillator. Another contribution to the real detection efficiency value is the frequent presence of an electronic discriminator in the involved circuit, whose effect is uncertain to include in the theoretical model, as it depends on the shape of the pulse height spectrum of the detector and the uncertain value at which the particular discriminator circuit presents its selected cut-off.

In the face of such difficulties, a scientist will always prefer an experimental determination that naturally incorporates all these effects and any other not foreseen in a theoretical evaluation. Under such circumstances, the general method here described [2,3] allows the number n to be determined, without the need to know the efficiency ε and provides expressions for the statistical uncertainties and conditions for its application. In what follows, at first, ε is to be considered a constant. In the most general case, efficiency does not fulfil that condition as it is very often energy dependent. In the very particular case of time-of-flight spectrometry, the efficiency measured for each of the approximately monoenergetic time bins is a particular constant for each one of them. Another particular case is that of large neutron absorbing detectors constructed in the past in some laboratories, designed to absorb every neutron impinging on them in order to present constant detection efficiency over a certain energy range [4]. For such cases the method here proposed would not be useful. But in all the other usual cases, neutron efficiency is not constant, nevertheless it can be dealt with through particular evolutions of the basic method [5],

which provides an expression for the absolute number of neutrons in the beam and another expression for a weighted mean efficiency. These and other developments of the method [6,7] will be presented in the following sections. Other current developments of the Centro Atómico Bariloche group are the preparation and testing of nanoscintillators which through Gd doping are sensitive to neutrons [8], the development of large volume neutron detectors based in water (with and without dopants) derived from experience obtained in the Pierre-Auger large cosmic detection array installed in the argentinean province of Mendoza, and also, the testing of low cost CCD and CMOS cameras with neutron sensitive coatings as high resolution position sensitive detectors [9]. Development of an active interrogation non- intrusive container scanning method, employing a small electron accelerator driven neutron source, with large area neutron detectors and gamma scintillator banks, has also been tested at laboratory scale [10, 11].

The current text reviews several publications where the Influence Method has originally been introduced and, for the first time, presents an integrated view of the whole subject. Thus, the equations and Figures are the original ones and similitudes in parts of the texts are inevitable.

2 THE INFLUENCE METHOD

The influence method [2] is based on the influence introduced by a first detector, in the counting of a second detector. This influence consists in a modification in the detection probability of the second detector after the beam has passed through the first detector. Thus, a statistical estimator can be derived for the absolute number of incident events (particles) n , independent of the efficiency of the detectors ε . It is also interesting to note that a second estimator may also be derived from the same experiment for the detection efficiency.

2.1 CASE OF DETECTORS WITH SIMILAR EFFICIENCY

Let two detectors be placed one behind the other at a certain distance from the radiation source as schematized in Fig. 1. For the initial calculation let n be the number of neutrons arriving at the first detector and let both detectors have the same efficiency ε .

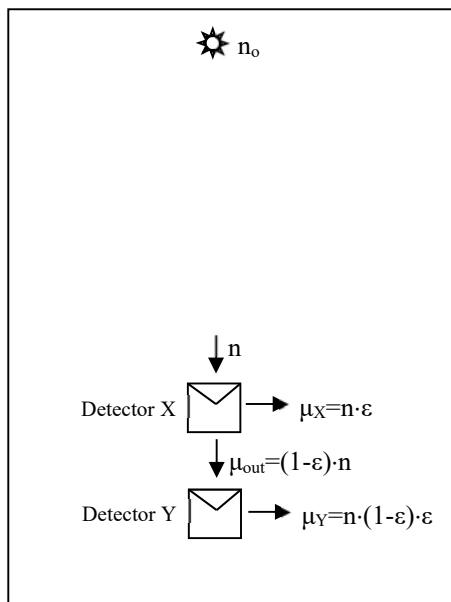


FIG. 1. Basic scheme of the Influence Method [2].

The number of particles counted by detector x is an aleatory variable (X) whose distribution is a binomial of parameters n and ε ($X \sim \text{Bi}(n, \varepsilon)$), and its expected value is

$$\mu_X = n \cdot \varepsilon \quad (1)$$

Let us now visualize in a schematic manner the detector array and the relation between the expected counting of each other. In this proposed detector array, particles not detected at X ($X_{out} = n - X$) impinge on detector Y. We have not yet considered, at this basic stage, scattering in the walls and by the detecting substance itself (which naturally has a scattering cross section of its own) and other effects. This is dealt with at a further step. Thus, the number of those particles detected by Y are an aleatory variable (Y) whose distribution is also a binomial of

parameters n and $\varepsilon(1 - \varepsilon)$ (demonstration that $Y \sim \text{Bi}(n, \varepsilon(1 - \varepsilon))$ in Appendix A of reference [3]). Then, the expected value for Y is

$$\mu_Y = n\varepsilon(1 - \varepsilon) = n\varepsilon - n\varepsilon^2 \quad (2)$$

As a consequence, an estimator for n can be proposed as

$$\hat{n} = \frac{x^2}{x-y} \quad (3)$$

This estimator results independent of detector intrinsic efficiency and, thus, allows an absolute determination of source activity. Analogously, it is possible to propose an estimator for detector intrinsic efficiency:

$$\hat{\varepsilon} = \frac{x-y}{x} \quad (4)$$

Eqs 1 and 2 allow us to check that the expected value of each estimator is precisely the parameter to be measured. This was the expected outcome when proposing both estimators, Eqs 3 and 4. It is important to mention, at this stage, that in the scheme proposed by the 'Influence Method' the two variables (X, Y) are not independent, but are instead correlated.

Ref.[3] studies this fact by starting to state the fact that the distributions are $X \sim \text{Bi}(n, \varepsilon)$ and $Y \sim \text{Bi}(n - X, \varepsilon)$, then the joint probability mass distribution function is:

$$\begin{aligned} P(X = x, Y = y) &= P(Y = y|X = x) \cdot P(X = x) \\ &= \binom{n-x}{y} \varepsilon^y (1 - \varepsilon)^{(n-x)-y} \cdot \binom{n}{x} \varepsilon^x (1 - \varepsilon)^{n-x} \\ P(X = x, Y = y) &= \binom{n-x}{y} \binom{n}{x} \varepsilon^{y+x} (1 - \varepsilon)^{2(n-x)-y} \end{aligned} \quad (5)$$

For $y \leq (n - x)$, and zero for the rest.

The expected values of the variables are $\mu_x = n\varepsilon$ and $\mu_y = n\varepsilon q = n\varepsilon(1 - \varepsilon)$, and their variances are $\sigma_x^2 = n\varepsilon q = n\varepsilon(1 - \varepsilon)$ and $\sigma_y^2 = n\varepsilon q(1 - \varepsilon q) = n\varepsilon(1 - \varepsilon)(1 - \varepsilon + \varepsilon^2)$. The covariance $\sigma_{XY} = -n\varepsilon^2(1 - \varepsilon)$ and the correlation coefficient $\rho = -\frac{\varepsilon}{\sqrt{1 - \varepsilon + \varepsilon^2}}$ between these variables are deduced in Ref.[3]. Finally, the complete expressions found for a pair of detectors with similar efficiencies are

$$\hat{n} = \frac{x^2}{x-y} \pm \left(\frac{xy\sqrt{(x+y)}}{(x-y)^2} \right) \quad (6)$$

$$\hat{\varepsilon} = \frac{x-y}{x} \pm \left(\sqrt{\frac{y(x+y)}{x^3}} \right) \quad (7)$$

A general condition is also found for the applicability of the method here introduced [3],

$$n \gg \frac{2}{\varepsilon^3} + \frac{5}{\varepsilon(1-\varepsilon)} \quad (8)$$

2.2 CASE OF DETECTORS WITH DIFFERENT EFFICIENCY

The treatment of this case was proposed in Ref. [2] and treated in detail in section 8 of Ref. [3].

The need will exist to measure the relation between the two efficiencies ($\varepsilon_x = k\varepsilon_y$) and proceed with a variable change. A first *comparison experiment* will have both detectors placed as to see the source with the same solid angle and avoiding interference with each other. This procedure will render an estimated factor k

$$\hat{k} = \frac{X'}{Y'} \quad (9)$$

Finally, the expressions obtained for the estimators with their statistical uncertainties (at the 68% confidence level) are

$$\hat{n} = \frac{x^2}{x-K \cdot y} \pm \left(\sqrt{x^2 \cdot Ky \cdot \frac{((K-1)x^2 + Kxy + K^2y^2)}{(x-Ky)^4}} \right) \quad (10)$$

and

$$\hat{\epsilon}_x = \frac{x - k \cdot y}{x} \pm \left(\sqrt{\frac{K^2 y \cdot (x + y)}{x^3}} \right) \quad (11)$$

In this case, the general condition found for the applicability of the method is,

$$n \gg \frac{2}{\epsilon_y \epsilon_x^2} + \frac{5}{\epsilon_y (1 - \epsilon_x)} \quad (12)$$

In practice, where detectors of high efficiency are employed, the condition for the applicability of the method translates itself simply into detector Y having sufficient counts.

It was also shown that for detectors of different efficiencies, the analysis of uncertainties led to the conclusion that the most efficient detector had to be placed in the front position

2.3 CASE OF COUNTS LOST DUE TO SCATTERING IN DETECTOR WALLS

Detector materials often have non-negligible scattering cross sections. This has to be accounted for in the influence method. As the number of scattered particles is proportional to the number of particles (n) incident upon the detector, then, the number of particles scattered out of the beam by the first detector would be ($s_x \cdot n$). If the scattering angle is not extremely small, these particles do not hit the second detector. Therefore, the second detector (Y) receives the number of original particles (n) less those detected by X ($\epsilon_x \cdot n$) and less those scattered out ($s_x \cdot n$).

This correction would also serve the case where, for any reason other than scattering, detector X does not count a certain particle while also impedes it to strike detector Y. One example could be that of a large scintillator which has absorbed the particle or a photon at a far end, but the light sensitive devices do not receive sufficient light to register a count. Another example would be that of an incident particle absorbed by the wall material of a proportional counter, preventing at the same time gas ionization and the particle proceeding to the second detector. Also, if the original particle penetrates the wall but the primary ionizing products hit the wall losing their kinetic energy, consequently generating a very small pulse which may not exceed the minimum discrimination level, this would constitute another case of a particle accounted for by this s_x correction.

A similar effect could be expected to arise from beam divergence. To summarize, constant s_x represents the proportion of particles not counted by detector X and that do not continue to hit detector Y. Such a parameter is highly case sensitive and as such, has to be defined for every particular circumstance. Its influence in statistical uncertainty will also have to be resolved for each case following the method described in Ref. [3].

Finally, when the case is that both detectors have different efficiency and that counts are lost by scattering or by other process, as described above, the general experimental estimator for n will be

$$\hat{n} = \frac{X^2}{X \cdot (1 - \hat{s}_x) - \hat{k} \cdot Y} \quad (13)$$

And the estimator for the efficiency

$$\hat{\epsilon}_x = \frac{X \cdot (1 - \hat{s}_x) - \hat{k} \cdot Y}{X} \quad (14)$$

Although when evaluating parameter s_x for the particular case, a simultaneous numerical evaluation for parameter k could also be implemented, as explained above, an experimental determination as described in section 4 of reference [2] will always be preferable.

2.4 CASE OF MULTIPLE DETECTORS

The complex case of a set-up of an arbitrary number k of detectors [5] was studied motivated by the possibility of low detection efficiency and the need to reduce statistical uncertainty. Figure 2 shows the results predicted by the model there developed.

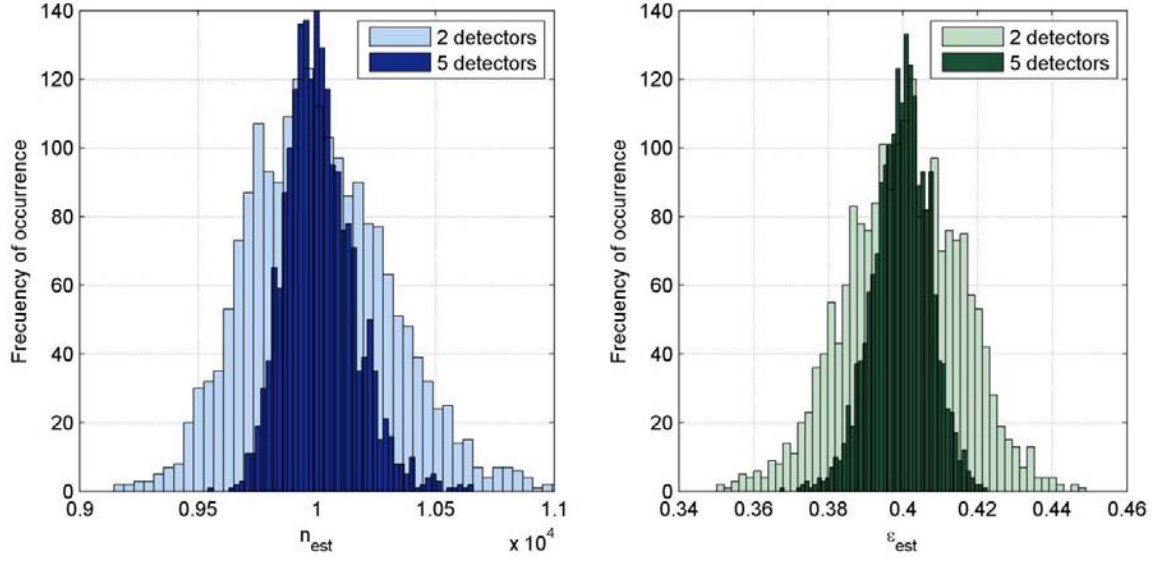


FIG. 2. Monte Carlo calculation of the distributions of values obtained for the two desired results, the number of particles in the beam and the estimated values for the efficiency, comparing results with 2 and with 5 similar detectors. The simulation carried out repetitively for initial $n=10000$ and $\varepsilon=0.4$ [5].

3 EXPERIMENTAL APPLICATION TO A NEUTRON SOURCE. INTRODUCTION OF A POISSON DISTRIBUTION

The extension of the method for its application to a radioactive source, which adds its natural statistical emission fluctuations, was published in Ref. [4].

In this case, the number of particles falling on the first detector (detector X), is an aleatory variable (Z) which is Poisson distributed with parameter $\lambda=n$ ($Z \sim Poi(n)$), where n is the expected value of Z , the number of particles incident upon the detector, which is related to the number of source particles (n_o) within the same time interval through the geometrical efficiency (ε_g). Thus, detector X obeys a binomial distribution of parameters Z and ε ($X \sim Bi(Z, \varepsilon)$), being ε the intrinsic efficiency of that detector. In the same Ref.[4] it is demonstrated that under these conditions X is also Poisson distributed ($X \sim Poi(n \cdot \varepsilon)$) and then, that Y is also Poisson distributed ($Y \sim Poi(n \cdot \varepsilon \cdot q)$). It has to be noticed that the variables being Poisson distributed, the expected values are the same as when the variables only obeyed binomial distributions, but the variances do change.

The effect of background (B) was also considered, yielding expressions with the corresponding uncertainties:

$$\hat{n} = \frac{(x-B)^2}{x-y} \pm \sqrt{\left(\frac{x^3((x-2y)^2+xy)}{(x-y)^4} + \frac{4x^2}{(x-y)^2} \sigma_B^2\right)} \quad (15)$$

$$\hat{\varepsilon} = \frac{x-y}{(x-B)} \pm \sqrt{\left(\frac{y(x+y)}{x^3} + \frac{(x-y)^2}{x^4} \sigma_B^2\right)} \quad (16)$$

In the experiment, a 1-Ci alpha Am–Be neutron source was placed in a light water sphere 30 cm in diameter contained in a steel sphere 1 mm thick. The neutrons emerging from the source were moderated in the light water sphere. Two successive ^3He detectors received moderated neutrons through a collimator (details in Ref. 4) at a variable distance from the source array. The repetitively obtained pairs of simultaneous measurements by those ^3He detectors were taken and recorded every 200 seconds (we will call a bin = 200 s) summing a total of 1250 samples. Thus, the experimental distributions turn out to be histograms of the number of times each individual result happened.

Background subtraction to the raw counting was later introduced in order to determine the final results, allowing for absorption in the moderating water sphere and attenuation in the air path from the source to the detectors.

The raw counting for each time bin is depicted in Figure 3, along with results for the absolute number of neutrons and that for the spectrum weighted effective efficiency.

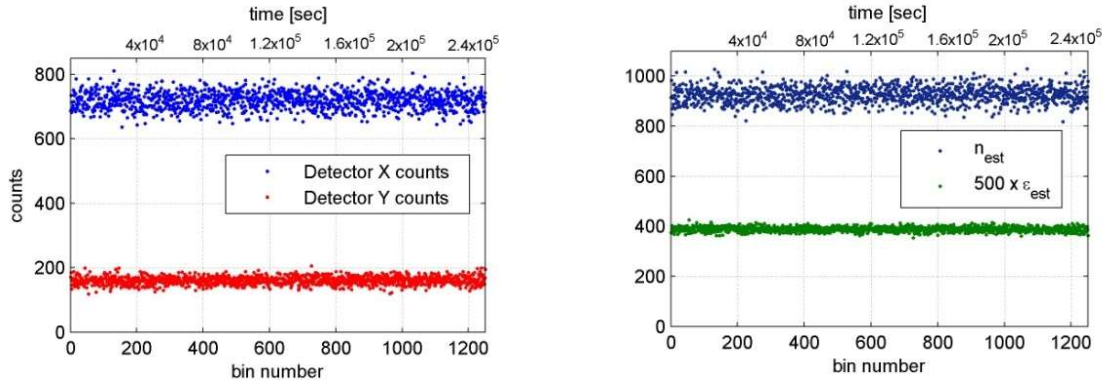


FIG. 3. Raw counts (left). Deduced number n and ϵ (right). Reprinted from Ref.4, with permission from Elsevier.

Figure 4 depicts the distribution of results shown in the lower graph of Figure 3 with the predictions of the theoretical continuous model developed in Ref. [4] superimposed for comparison purposes.

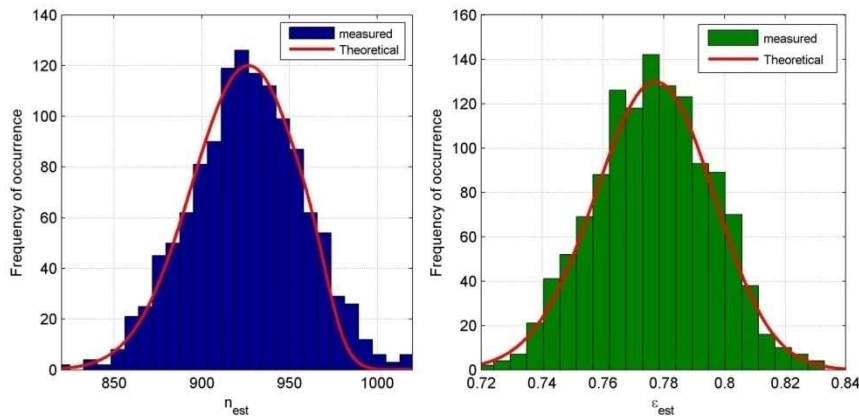


FIG. 4. Comparison of the continuous model with the experimental results obtained from the 1250 samples. Reprinted from Ref.4, with permission from Elsevier.

The effect of the magnitude of detector efficiency, for both detectors equally efficient, is shown in Figure 5, where the introduction of the Poisson distribution due to the source emission makes evident its influence, as compared with the case where the number n was a constant. In contrast with the latter, the Poisson statistical distribution of the source does not influence the uncertainty with which the spectrum weighted effective efficiency can be determined. Finally, it is to be said that the value of the commercial Am–Be source emission was determined to within 0.2% of the intensity granted by the vendor.

4 CONCLUSION

The ‘influence method’ has been tested in several possible scenarios and shows to be a useful tool for absolute radiation measurements in cases where detectors are partially transparent to incident radiation. It has also been adapted to the evaluation of the effect in proportional counters space charge accumulation during the absolute determination of neutron bursts [6]. It is most clearly useful for neutron measurements with detectors where each detected neutron disappears from the beam, thus excluding fast neutron detection with proton recoil detectors, except for the possibility to introduce an anticoincidence system that prevents the same neutron to be counted by both detectors. Predictions are given in the references for the minimum number of detections to make the method valid and, also, the most convenient efficiency range for each case.

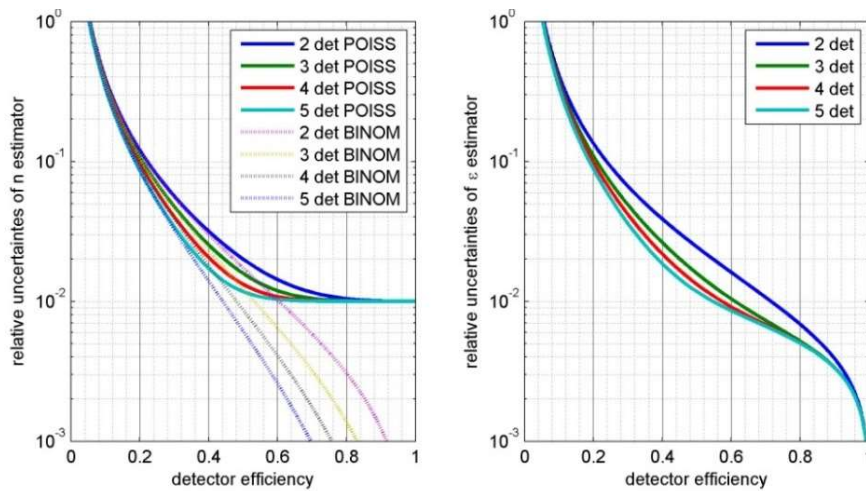


FIG. 5. Statistical uncertainties in relation to detector efficiency calculated for $n = 10000$. Left, for the n estimator, with and without the Poisson component introduced by the source. Right, for the effective efficiency, where the Poisson component does not extend its influence. Reprinted from Ref.5, with permission from Elsevier.

CREDITS

Figures 1 through 5 and Equations 1 through 16 are reproduced from references [2]; [3]; [4] and [5].

REFERENCES

- [1] GEIGER, H., WERNER, A., Z. Physik, **21** (1924) 187.
- [2] RIOS, I.J., MAYER, R.E., Absolute particle flux determination in absence of known detector efficiency. The "Influence Method", Nucl. Instrum. Methods Phys. Res., Sect. A **775** (2015) 99–104.
- [3] RIOS, I.J., MAYER, R.E., "Influence Method". Detailed mathematical description, Nucl. Instrum. Methods Phys. Res., Sect. A **788** (2015) 35–42.
- [4] POENITZ, W.P., The Black Neutron Detector, Nucl. Instrum. Methods **109** (1973) 413–420.
- [5] RIOS, I.J., MAYER, R.E., "Influence Method" applied to measure a moderated neutron flux, Nucl. Instrum. Methods Phys. Res., Sect. A **806** (2016) 231–239.
- [6] RIOS, I.J., MAYER, R.E., Multiple detectors "Influence Method", Appl. Radiat. Isot. **111** (2016) 92–103.
- [7] RIOS, I.J., MAYER, R.E., Absolute determination of radiation bursts and of proportional counters space charge effect through the Influence Method, Nucl. Instrum. Methods Phys. Res., Sect. A, **836** (2016) 61–66.
- [8] VARGAS, J.M., et al., Luminescent and scintillating properties of lanthanum fluoride nanocrystals in response to gamma/neutron" irradiation: codoping with Ce activator, Yb wavelength shifter, and Gd neutron captor, JINST **11** (2016) P09007.
- [9] PEREZ, M., et al., Thermal neutron detector based on COTS CMOS imagers and a conversion layer containing Gadolinium, Nucl. Instrum. Methods Phys. Res., Sect. A **893** (2018) 157–163, <https://doi.org/10.1016/j.nima.2018.03.032>.
- [10] MAYER, R.E., et al., Slow neutron interrogation for detection of concealed substances, third research coordination meeting on neutron based techniques for the detection of illicit materials and explosives, International Atomic Energy Agency, Coordinated Research Project F1.10.12, Johannesburg, South Africa 16–20 November (2009).
- [11] D'AMICO, N.M.B., MAYER, R.E., Development of neutron interrogation techniques to detect dangerous substances, Eur. Sci. J., Spec. Ed. **2** (2015) 306-313.

TOWARDS A NEW COMPACT SCINTILLATION SPECTROMETER FOR 100 MEV NEUTRONS: A CASE STUDY FOR REFERENCE NEUTRON BEAMS

A. BUFFLER, A.C. COMRIE, T. HUTTON

Department of Physics,
University of Cape Town, South Africa
Email: andy.buffler@uct.ac.za

F.D. SMIT

iThemba Laboratory for Accelerator-Based Sciences
Cape Town, South Africa

R. NOLTE

Physikalisch-Technische Bundesanstalt
Braunschweig, Germany

Abstract: Monoenergetic neutron beams up to energies of 100 MeV and beyond are important for benchmarking the response of instrumentation designed for monitoring neutrons around particle accelerators, and dosimetry in the upper atmosphere and in space. We describe the fast neutron beam facility of the iThemba Laboratory for Accelerator-Based Sciences (iTL) where time-of-flight measurements are possible across a wide energy range. We illustrate the need for such beams by presenting progress towards the realization of a new compact neutron spectrometer, designed for use over the neutron energy range 1 – 100 MeV. The detector is based on EJ299-33 plastic scintillator coupled to silicon photomultipliers, and a digital implementation of pulse shape discrimination.

1 INTRODUCTION

There is ongoing interest in developing neutron spectrometers for use at higher energies, particularly for use in monitoring around particle accelerators [1], and dosimetry in the upper atmosphere [2] and in space [3], where neutrons with energies up to several hundred MeV need to be measured [4]. Ionizing radiation in the atmosphere is due to the primary cosmic radiation (PCR) consisting of almost 99% of protons, and α -particles [5]. The PCR is only partially deflected by the earth's magnetic field, and those which strike the upper layers of the atmosphere induce nuclear reactions, producing a cascade of particles (secondary cosmic radiation (SCR)). Both low- and high-energy neutrons are produced as SCR, from the evaporation of highly energetic nuclei and as knock-on neutrons in peripheral collisions, or in charge exchange reactions [5]. A significant peak in the neutron energy spectrum occurs around 100 MeV, as illustrated in Fig. 1. This spectrum occurs especially at aviation altitudes, in heavier shielded spacecrafts, and of course on planetary or lunar surfaces where there is a lack of an atmosphere thick enough to attenuate this radiation source.

Fast neutron energy distributions can be determined via two main methods, time-of-flight or unfolding from the detector response. Time-of-flight methods require a nanosecond-long pulsed neutron beam, and a sufficiently long flight path, which is not always possible or practical. Alternatively, the neutron energy spectrum can be extracted from the measured detector response via the process of unfolding. Since the detection of fast neutrons is often complicated by the presence of gamma-rays, the discrimination between the two may be necessary.

Neutrons interact with matter in two broad categories, scattering and absorption. Fast neutron detectors utilise the different interaction types to generate charged particles, typically the elastic scatter from hydrogen, or fast fission of uranium. Novel methods for neutron detection have been developed [6,7], yet these two reaction channels remain the accepted metrology standards for fast neutron measurements [8]. Organic scintillators are often used for fast neutron spectrometry due to their fast timing and relatively high detection efficiency. Neutrons interact directly with the nuclei of the hydrogen and carbon within the detector, producing recoiling charged particles in the form of protons, deuterons and alphas. Fast neutron fields are often accompanied with gamma rays that may also interact within the detector. In organic scintillators Compton scattering is the primary gamma ray interaction mechanism resulting in a recoiling electron.

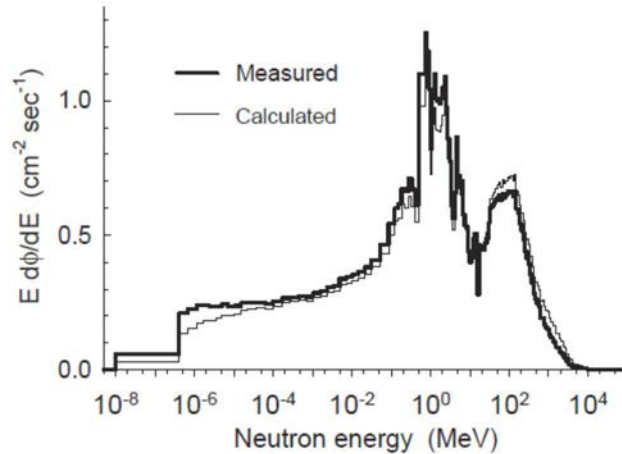


FIG. 1. Measured and calculated cosmic-ray neutron spectrum at high altitude (20 km, 56 g cm^{-2}) and latitude (54 N, 117 W, 0.8 GV cut-off) [4].

The ability to discriminate between neutron and gamma ray induced events lies in the time response of the scintillation output. It is possible to determine the difference between the recoiling charged particles by considering the ratio of the fast and slow decay components of the scintillation light, and as such separate the neutron and gamma ray induced events [10]. The identification of charged particles through their scintillation output is known as pulse shape discrimination (PSD) [9]. Many liquid and plastic organic scintillators are commercially available, and have been designed to maximise the PSD properties. Popular choices for fast neutron metrology are the liquid scintillators, NE213, BC501A and EJ301.

Additional considerations should be made for increasing neutron energy. It becomes more probable that the recoiling charged particles escape the detector volume resulting in partial energy deposition and a distorted detector response function. There are well documented approaches to compensate for the increased particle range [13], but there are further considerations. At neutron energies greater than approximately 6 MeV, charged particle production mechanisms become available in carbon [12]. At 100 MeV, approximately half of all n-C interactions will produce either recoiling protons or alpha particles. High-quality, measured cross-section data in this regime are severely lacking at this point in time, resulting in unreliable calculated detector response functions [14]. It is necessary to directly measure the response of a fast neutron spectrometer for energies above 20 MeV.

We present progress towards the realization of a new compact neutron spectrometer, designed for use over the neutron energy range 1–100 MeV. The detector is based on EJ299-33 plastic scintillator coupled to silicon photomultipliers, and a digital implementation of pulse shape discrimination. We also describe the fast neutron beam facility of the iThemba Laboratory for Accelerator-Based Sciences where time-of-flight measurements are possible across a wide energy range, and make the case for the importance of such reference beam facilities for the ongoing development of new detector systems which are designed for use above 20 MeV.

2 THE FAST NEUTRON BEAM FACILITY AT iTHEMBA LABS

The Separated-Sector Cyclotron (SSC) of the iThemba Laboratory for Accelerator-Based Sciences (iTTL), near Cape Town, South Africa, can accelerate protons in the energy range between 25 MeV to 200 MeV. A beam pulse selector is used to suppress a fraction of proton bunches to increase the time interval between beam pulses, which enables time of flight (TOF) measurements to be undertaken. At 100 MeV typical currents are about $5 \mu\text{A}$ in continuous mode and 500 nA at a repetition frequency of 2.5 MHz. At 200 MeV, a current of 300 nA can be provided at 26 MHz. The spread in time a proton bunch is around 1 ns.

A schematic of the fast neutron facility [15] is shown in Fig. 2. The ${}^7\text{Li}(p,n){}^7\text{Be}$ reaction is typically employed to produce quasi-monoenergetic neutrons from 25 MeV to 200 MeV. A steel collimator of thickness about 2 m has openings at 0° and 16° which shapes beams of profile $10 \text{ cm} \times 10 \text{ cm}^2$ at 8.0 m. The detector side of the collimator is lined by a layer of borated wax and polyethylene. Targets of ${}^{\text{nat}}\text{C}$ and ${}^{\text{nat}}\text{Be}$ have also been used from time to time. Background contributions due to proton interactions in the target station can be measured using an empty target. The unused protons are deflected into a well-shielded beam stop, with the current monitored continuously with a Faraday cup. Neutron flight paths range from 4.0 m to 10.0 m at 0° , and up to 8.0 m at 16° .

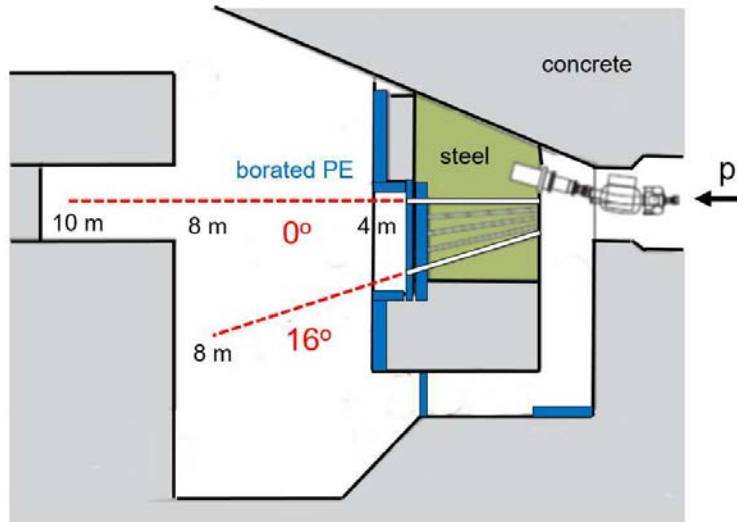


FIG. 2. Schematic of the fast neutron beam facility at iThemba LABS.

Neutron fluence measurements are usually carried out relative to a standard cross section. At iTL the preferred reference cross-section is the fast fission of ^{238}U implemented within a parallel-plate ^{238}U fission chamber (FC). This fission chamber was manufactured in 1988 at the Institute for Reference Materials and Measurements (IRMM), European Joint Research Centre in Belgium, and is now part of the permanent infrastructure of the facility. The $^{238}\text{U}_3\text{O}_8$ deposits, 76 mm in diameter, were produced by electronic spraying onto both sides of 6 tantalum backings. The distance between deposits and electrodes is 5.0 mm. A flux measurement performed with the fission chamber is insensitive both to gamma-rays and thermal neutrons since the ^{238}U fission cross section is almost negligible below 1 MeV [15].

An organic liquid scintillator, BC501A, with a 2" diameter and 4" length is used to measure the energy dependent neutron fluence with a timing resolution of about 1 ns. The large detection volume increases the sensitivity to high-energy and low intensity neutrons expected during ToF measurements. An additional disc-like NE102 detector, 2.0 mm in thickness, is operated in transmission mode as a fluence rate and ToF spectrum monitor. The pulse-height threshold on the anode and dynode signals is set such that gamma ray induced events largely suppressed. The gain on both scintillation detectors is stabilised with an internal LED pulser. For a typical metrology run, all three detectors are used (fission chamber, BC501A and NE102) to measure the energy dependent neutron fluence. The NE102 monitor is calibrated using the measured responses from the fission chamber and BC501A detector.

Figure 3 shows relative spectral fluences recorded with the BC501A detector for four proton energies [15]. The energy spread induced in the monoenergetic peak by the target thickness is indicated by the horizontal bars. The neutron energy spectra at emission angles of 0° and 16° generated by protons on a ^7Li target have two main components. First is a high-intensity, mono-energetic peak from the $^7\text{Li}(p, n)^7\text{Be}$ reaction with an energy equal to the incident proton energy minus the reaction Q-value. Second is a continuum from various neutron producing breakup reactions within the target which extends from low energies up to the primary peak [16]. The continuum is almost isotropic, meaning that the measured neutron energy spectrum will contain the continuum at both 0° and 16° . The primary high-energy peak is strongly forward biased and as such has a much-reduced intensity at 16° compared to 0° . After normalisation, the subtraction of the 16° from the 0° neutron energy spectrum results in a quasi-monoenergetic neutron energy.

As an illustration, Fig. 4 shows neutron energy spectra measured (for the same monitor count) at 0° and 16° for neutrons produced by a 100 MeV proton beam on a 6.0 mm $^{\text{nat}}\text{Li}$ target. The spectrum measured at 16° is normalized to that obtained at 0° by equalising the counts recorded in the continuum energy region. The difference spectrum is obtained by subtracting the normalized 16° spectrum from the 0° spectrum produces effectively a single line spectrum in which the line width is determined predominantly by the thickness (6 mm) of the Li neutron production target.

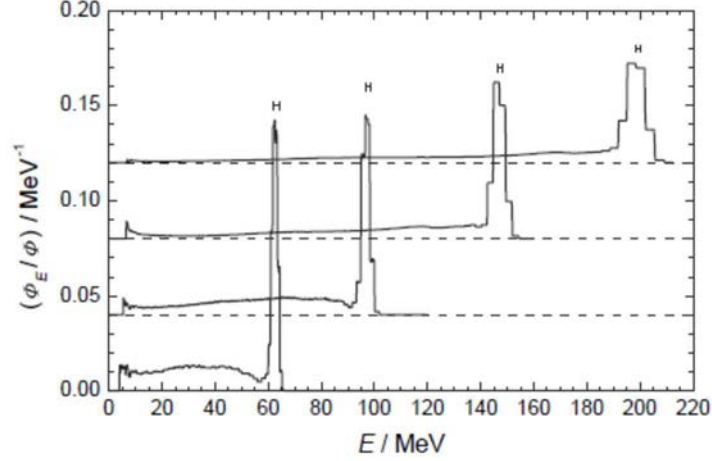


FIG. 3. Normalised spectral neutron distributions measured at 0° with a BC501A detector for proton energies of 66 MeV, 100 MeV, 150 MeV, and 200 MeV, using a 6 mm Li target. The intrinsic width, indicated by the horizontal bars, refers to the spread in neutron energy induced by the target thickness [15].

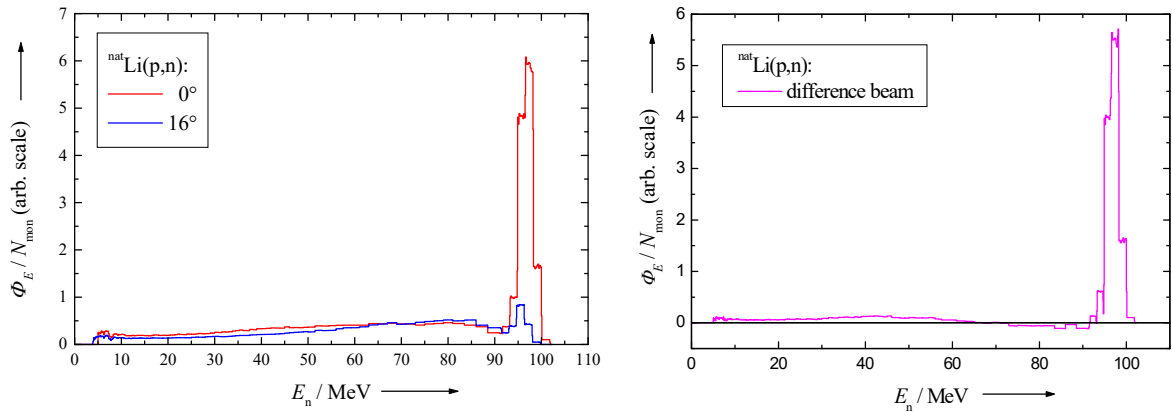


FIG. 4. Normalised spectral neutron distributions measured at 8.0 m at 0° and 16° (left) for a 100 MeV proton beam incident on a 6.0 mm thick Li target, and the difference spectrum (right).

The fast neutron facility at iTL has been widely used for detector development [17], cross section measurements [18, 19], radiation biology experiments [20], and detector calibrations, especially for dosimetry at flight altitudes and air crew dosimetry [21]. The neutron vault has remained virtually unchanged since it was first built thirty years ago, and a number of shortcomings have been identified [22], especially with regard to background radiation. Presently, a project is being discussed to upgrade the facility over the next three years with the goal of being recognised as an ISO-accredited reference facility for fast neutron beams.

3 A NEW COMPACT NEUTRON SPECTROMETER

As an example of the importance of quasi-monoenergetic neutron beams, we discuss a development of a compact neutron spectrometer, suitable for use up to 100 MeV. Three recent technological developments have assisted with the development of detectors requiring PSD for use in non-laboratory environments. Typical liquid scintillators such as the BC501A contain hazardous chemicals that are both toxic and flammable at room temperature limiting their use and transportability. However, PSD capabilities have been demonstrated in solid scintillators [23, 24] such as the EJ299-33 scintillator, which can be easily shaped and coupled to a photodetector. Traditional photomultipliers require high voltages to operate, and the development of silicon photomultipliers (SiPMs) offers a compact and robust alternative. Finally, the shift to digital data acquisition offers a level of flexibility in the implementation of pulse shape discrimination, either in software [25] or specialised hardware.

We are well-advanced in developing a compact neutron spectrometer suitable for measurements between 1 and 100 MeV [26]. The detector which has been developed (see Fig. 5) consists of 4 slabs of EJ299-33 plastic scintillator, each of dimension $6 \times 6 \times 50 \text{ mm}^3$, with each slab coupled to two SensL MicroFC-60035 SiPMs [27] using silicone grease. A cross-shaped length of polyethylene with thickness 15 mm separates the four scintillators. The SiPMs were operated at 3.5 V above the breakdown voltage of 24.6 V. Signals from the anodes of each SiPM are digitised by a CAEN Vx1761 10-bit digitiser, operating at 4 GS/s with a peak-to-peak range of 1 V. The digitised waveforms were recorded using custom-built, open-source software for offline analyses. Each scintillator was coupled to two SiPMs to maximise light collection and signal amplitudes. By taking the geometric mean of each pair, variations in light output can be mitigated.

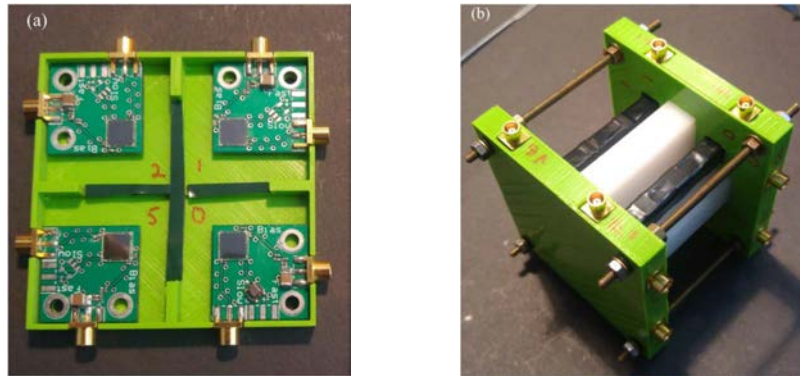


FIG. 5. The compact neutron spectrometer featuring 4 slabs of EJ299-33 plastic scintillator, each with dimensions $6 \times 6 \times 50 \text{ mm}^3$ and each coupled to two SensL MicroFC-60035 SiPMs.

For the purposes of illustration, we present measurements made with a $2.2 \text{ GBq } ^{241}\text{Am}^9\text{Be}$ (Am–Be) radioisotopic source producing about $1.4 \times 10^5 \text{ neutrons s}^{-1}$ with a complex energy spectrum with maximum energy at about 11 MeV, and 4.43 MeV gamma rays from the excitation of ^{12}C .

Figure 6 shows typical digitized pulses, each with the same total integral, for a single SiPM, compared to those from a reference detector. The reference detector was a cylindrical EJ299-33 scintillator (50 mm diameter \times 50 mm), optically coupled to an ETL 9214 12-stage photomultiplier tube (PMT) and base, supplied by Scionix, and operated at a negative bias of 950 V. The Am–Be neutron source provided a mixed field of neutrons and gamma rays. Exemplar detector pulses and their cumulative integrals are shown in Fig. 6. A baseline subtraction ensured any contributions due to voltage drift were removed.

Detector voltages were chosen such that the produced pulses peaked within the allowable range of the digitiser, with a digitisation uncertainty below 1 mV. The start time, t_0 , for each pulse was defined with respect to a digital constant fraction discriminator to minimise any effects due to noise, baseline shift and variations in pulse shape or amplitude. The detected pulses for the PMT typically decayed to 1% of their peak amplitude within 100 ns, whereas the SiPM pulses are much slower, taking 800 ns to drop below the 1% level.

For each recorded event, a parameter Q_L was calculated by integrating the digitised pulses over a time interval (t_L), starting from t_0 , chosen in order to capture as much of the entire pulse as possible, while still avoiding saturation of the available output transfer rate of the digitiser. Typical values for t_L are 250 ns for the PMT and 1200 ns for the SiPM. The detector response was calibrated with respect to a set of reference gamma ray energies from ^{22}Na , ^{137}Cs , ^{207}Bi and Am–Be sources, relating the integrated signal Q_L to the light output induced by known energies, L , in MeV electron equivalent (MeV_{ee}). This relationship was demonstrated to be linear for the range of energies considered, and subsequently extrapolated to the full energy range of the experiment. Scaling the long integral, Q_L to a reference energy is a requirement for the energy spectrum unfolding process. It was determined that coupling the $6 \times 6 \times 50 \text{ mm}^3$ scintillator to two SiPMs with a combined light output improved the PSD, energy resolution and linearity at higher L when compared to using single a SiPM.

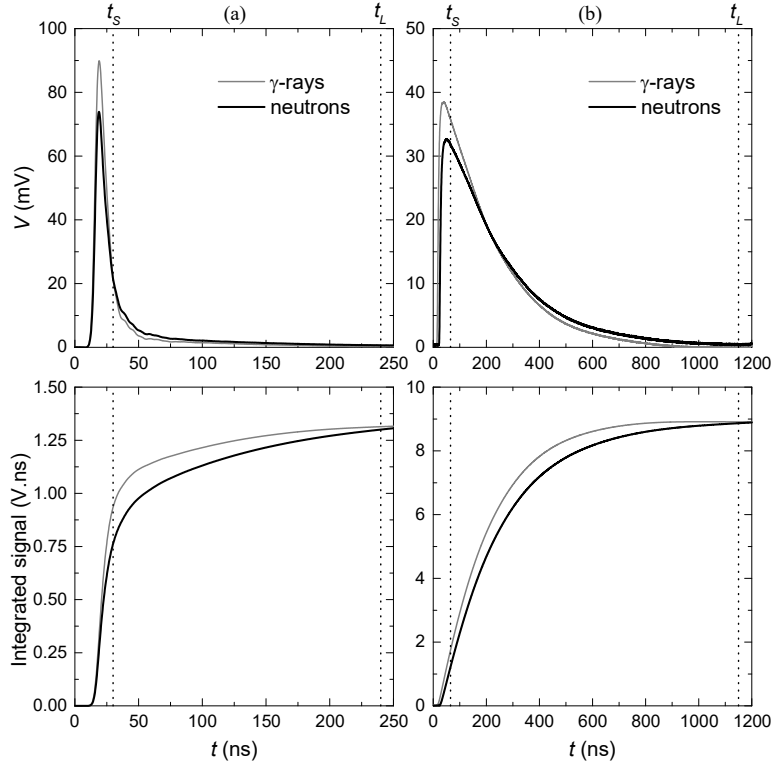


FIG. 6. Typical digitized pulses (above) and pulse integrals (below) for events arising from neutron and gamma-ray interactions in the EJ299-33 scintillators of dimensions: (a) 50 mm diameter \times 50 mm depth and (b) $6 \times 6 \times 50$ mm³. Integration times t_s and t_L are indicated.

To separate neutron and gamma ray induced events, pulse shape discrimination has to be implemented, in this case via the charge comparison method [28]. The pulse shape parameter S is defined as

$$S = k \frac{Q_S}{Q_L} + C \quad (1)$$

where Q_S is the integral of the pulse over a shorter time interval, around 30 ns for the PMT and 80 ns for the SiPM pulses, and the constants k and C are chosen to scale and offset the pulse shape parameter, S .

Signals generated from neutron induced events have a slower rise and more pronounced long decay component in comparison to the gamma ray induced events. For a neutron induced event, the ratio of short to long integral will be lower than a gamma ray induced event with the same long integral value.

The distribution of events as a function of the calibrated light output L , and the pulse shape parameter S can be seen in Fig. 7 for the Am-Be source. Two well separated loci can be identified, one associated with the recoiling electrons (e) from gamma ray interactions, and the other from the recoiling protons (p) from the neutron interactions. The slanted threshold at low values of L is a result of a pulse height trigger within the digitiser, which produces a more aggressive threshold on integrated signal parameters for neutron induced events compared to gamma ray induced events.

To quantify the quality of the PSD and the separation of the neutron and gamma ray induced signals, a range of L values can be selected and projected onto the S -axis. In Fig. 7 these cuts are represented with the dashed lines, with the region of interest between 1.9 and 2.1 MeV_{ee}. The projection of these data can be seen in Fig. 8(a).

To quantify the quality of the PSD and the separation of the neutron and gamma ray induced signals, a range of L values can be selected and projected onto the S -axis, and from here a figure of merit (FoM) can be extracted. In Fig. 7 the region of interest is represented with the dashed lines with L values between 1.9 and 2.1 MeV_{ee}, and then projected onto the S -axis as seen in Fig. 8(a).

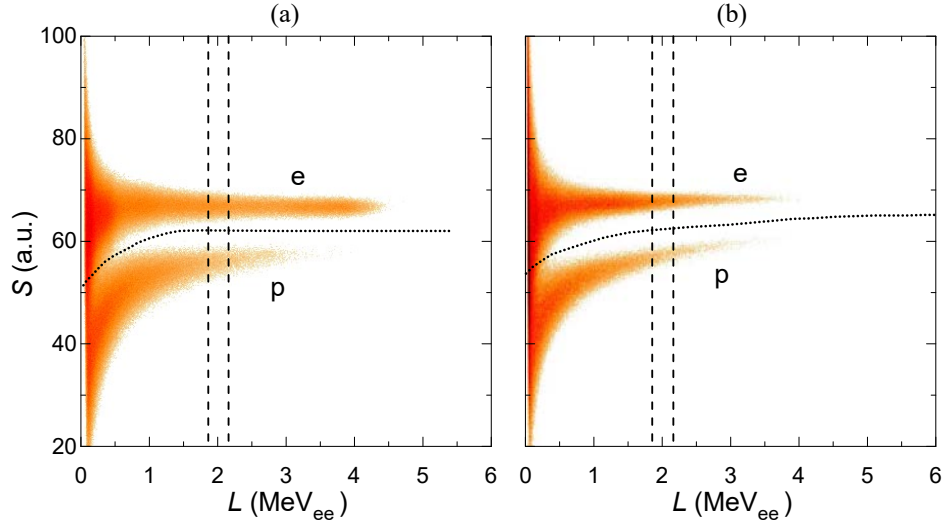


FIG. 7. Measured counts with respect to the calibrated light output, L , and the pulse shape parameter, S for the (a) 50 mm diameter \times 50 mm and (b) $6 \times 6 \times 50$ mm³ EJ299-33 scintillators when exposed to an Am-Be radioisotopic source. The gamma ray (recoiling electron, e) and neutron (recoiling proton, p) contributions are well separated. The dashed lines at $L=1.9$ MeV and 2.1 MeV indicate the cuts used to isolate events in this region.

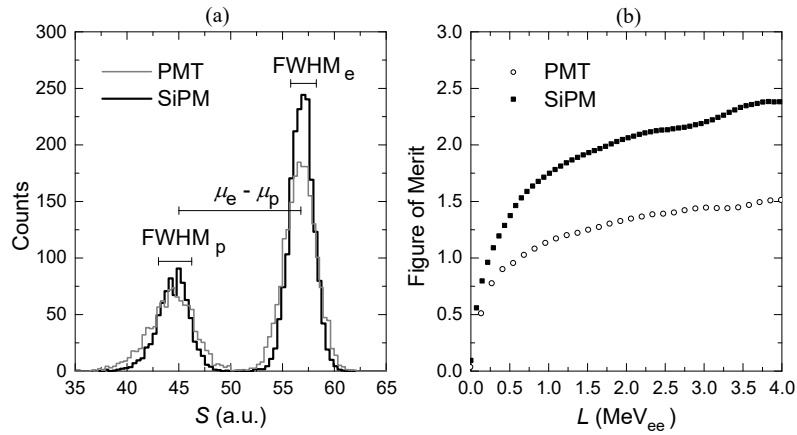


FIG. 8. (a) Measured counts versus pulse shape parameter, S , for events with L values between 1.9 and 2.0 MeV from Fig. 7, for the PMT and SiPM based detectors. (b) Calculated figure of merit over the full range of L values for the PMT and SiPM based detectors.

For two well defined Gaussian distributions, the FoM can be defined as the ratio of the difference between the mean values μ , and the sum of their full width half maxima (FWHM)

$$\text{FoM} = \frac{|\mu_e - \mu_p|}{\text{FWHM}_e + \text{FWHM}_p}. \quad (2)$$

The FoM is sensitive to the value of the short gate t_s and can be used to determine the value of t_s to maximise the separation. The FoM as a function of L for the data presented in Fig. 7 can be seen in Fig. 8(b), with the SiPM based detector demonstrating a far higher FoM than the PMT based detector.

The new detector geometry, with the $6 \times 6 \times 50$ mm³ plastic scintillator, and SiPM arrangement was simulated using GEANT4 [29] to determine the light response for various incident particle energies. Saturation effects in the SiPMs were included within the simulations, and scaling on light output and energy resolution was applied to match the measured spectra [25]. A comparison of the measured and simulated spectra can be seen in Fig. 9(a) for the example of a ¹³⁷Cs gamma ray source. The Compton edge is well defined, and aligns with the measured spectrum, however deviations can be seen towards lower values of L . The simulated spectrum does not include a

contribution to the spectrum from scattered gamma rays originating outside the detector. The simulations were repeated with mono-energetic neutrons from 0.2 MeV up to 12.0 MeV in steps of 0.2 MeV to construct a response matrix for this detector. A subset of these response functions can be seen in Fig. 9(b).

The simulated response matrix can be used by the HEPRO package [29] to unfold the neutron energy spectrum from the measured light output spectrum. Figure 10(a) shows the Am-Be neutron energy spectrum as unfolded from measured neutron light output spectra, in comparison to the expected neutron energy spectrum [31]. The key features are generally well replicated in the measured and unfolded neutron energy spectrum. The unfolded spectrum includes an additional contribution below 3 MeV due to the in-scatter of neutrons to the detector volume. Additional comparisons can be made with the measured and re-folded neutron light output spectra. Figure 10(b) shows that the two spectra are in excellent agreement, with a coefficient of determination of $R^2 = 0.998$.

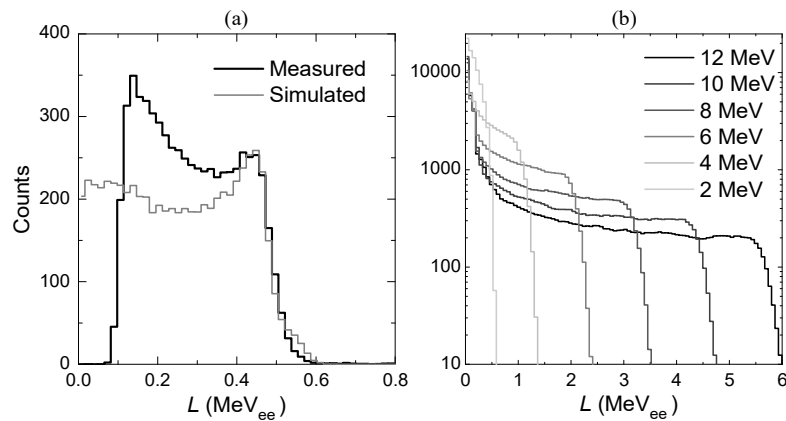


FIG. 9. (a) Lineshape for the $6 \times 6 \times 50 \text{ mm}^3$ scintillator (SiPM) measured for the 0.662 MeV gamma-ray from ¹³⁷Cs, and simulated using GEANT4. (b) Neutron lineshapes for the $6 \times 6 \times 50 \text{ mm}^3$ scintillator (SiPM) simulated using GEANT4

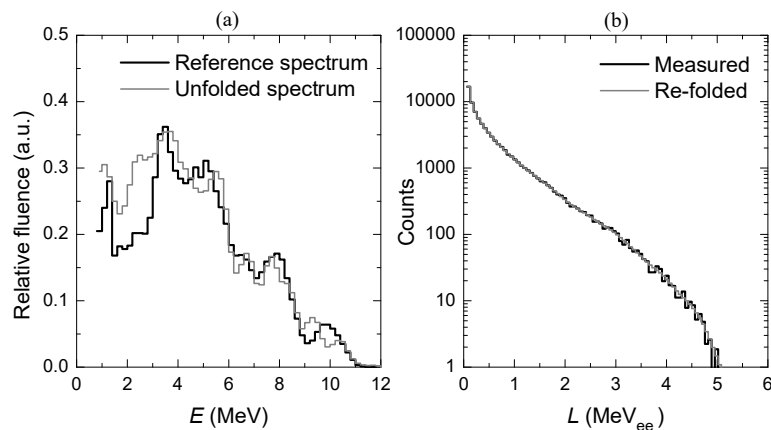


Fig. 10. (a) Unfolded neutron energy spectrum for neutrons from an Am-Be source for the EJ299-33 detector of dimension $6 \times 6 \times 50 \text{ mm}^3$ (SiPM) compared to the recommended spectrum [19]. (b) Re-folded light output spectrum, compared to the direct measurement.

4 FUTURE ACTION PLAN

The final version of the compact neutron detector features four ($6 \times 6 \times 150 \text{ mm}^3$) EJ299-33 scintillators, and 8 SiPMs, separated by the ‘cross-shaped’ high density polyethylene (HDPE) moderator (see Fig. 11). The additional length of the scintillators makes the device suitable for use for neutrons up to 100 MeV. Tests are underway with this detector using neutrons and gamma rays from an Am-Be source, a DT sealed tube neutron generator and neutron beams at iThemba LABS.



FIG. 11. The longer version of the compact neutron spectrometer featuring 4 slabs of EJ299-33 plastic scintillator, each with dimensions $6 \times 6 \times 150 \text{ mm}^3$ and each coupled to two SensL MicroFC-60035 SiPMs.

The pulse shape discrimination distribution for high energy neutrons is much more complex as more $n\text{-}^{12}\text{C}$ reactions channels open up resulting in recoiling protons, deuterons, tritons and alpha particles. The pulse shapes produced by recoiling charged particles are dependent on the energy loss of the particle and can be identified within an $L\text{-}S$ plot in order of increasing dE/dx . As the incoming neutron energy increases, the probability of a scattered proton escaping the detector also increases resulting in partial energy deposition. These events can clearly be identified due to their location within the $L\text{-}S$ plots between the well-defined proton and electron recoil loci. These features are useful for neutron spectrometry since they provide structure in the measured lineshapes comprising the response matrix produced from these data. This in turn improves the quality of unfolding achieved, thus reducing the uncertainty in the energy spectrum produced.

In parallel to this work, a significant upgrade to the fast neutron facility at iThemba LABS is presently underway, including the following:

- (i) An opening up of the available space within the vault;
- (ii) An increase of the flight path at 16° to at least 10 m;
- (iii) Reduction of the background radiation emanating from the passageway to the target area, and the slow neutron background generally;
- (iv) An improved proton beam monitoring system when high current beams are used; and
- (v) A new proton recoil telescope for fluence metrology.

ACKNOWLEDGEMENTS

The authors would like to thank the staff of iThemba LABS for assistance during experiments, and the staff of the UCT Physics Department workshop for constructing equipment used. We also acknowledge funding from the University of Cape Town, the Physikalisch-Technische Bundesanstalt, the National Research Foundation (South Africa) and the Technology Innovation Agency (South Africa).

REFERENCES

- [1] FIECHTNER, A., MAYER, S., BOSHUNG, M., Practical consequences for the use of a personal dosimeter for fast neutrons at high-energy accelerators based on PADC detectors exposed up to one year, *Radiat. Meas.* **45** (2010) 1557.
- [2] WISSMANN, F., Long-term measurements of at aviation altitudes in the northern hemisphere, *Radiat. Protect. Dosim.* **121** (2006) 347.
- [3] SMITH, M., et al., Measurements of the neutron dose and energy spectrum on the international space station during expeditions ISS-16 to ISS-21, *Radiat. Protect. Dosim.* **153** (2013) 509.
- [4] GOLDHAGEN, P., CLEM, J., WILSON, J., The energy spectrum of cosmic-ray induced neutrons measured on an airplane over a wide range of altitude and latitude, *Radiat. Protect. Dosim.* **110** (2004) 387.
- [5] GAISSER, T.K., *Cosmic Rays and Particle Physics*, Cambridge University Press (1990).
- [6] BROOKS, F.D., KLEIN, H., Neutron spectrometry—historical review and present status, *Nucl. Instrum. Methods A* **476** (2002) 1.
- [7] THOMAS, D.J., Neutron spectrometry from thermal energies to GeV, *Rad. Meas.* **45** (2010) 1178.
- [8] THOMAS, D.J., NOLTE, R., GRESSIER, V., What is neutron metrology and why is it needed? *Metrologia* **48** (2011) S225.
- [9] BROOKS, F.D., Development of organic scintillators, *Nucl. Instrum. Methods* **162** (1979) 477.

- [10] BIRKS, J.B., Scintillations from organic crystals: specific fluorescence and relative response to different radiations, Proc. Phys. Soc. **A64** (1951) 874.
- [11] WRIGHT, G.T., Scintillation decay times of organic crystals, Proc. Phys. Soc. **B69** (1956) 358.
- [12] KELLOGG, D.A., Cross sections for products of 90-MeV neutrons on carbon, Phys. Rev. **90** (1953) 224.
- [13] NOLTE, R., BROOKS, F.D., BUFFLER, A., et al., Quasi-monoenergetic neutron reference fields in the energy range from thermal to 200 MeV, Radiat. Protect. Dosim. **110** (2004) 97.
- [14] NOLTE, R., THOMAS, D.J., Monoenergetic fast neutron reference fields: II. Field characterization, Metrologia, **48** (2011) S274.
- [15] MOSCONI, M., MUSONZA, E., BUFFLER, A., et al., Characterisation of the high-energy neutron beam at iThemba Labs, Rad. Meas. **45** (2010) 1342.
- [16] IWAMOTO, Y., et al., Quasimonoenergetic neutron energy spectra for 246 and 389 MeV reactions at angles from 0 degrees to 30 degrees, Nucl. Instrum. Methods **A629** (2011) 43.
- [17] BROOKS, F.D., ALLIE, M.S., BUFFLER, A., et al., Measurement of neutron fluence spectra up to 150 MeV using a stacked scintillator neutron spectrometer, Rad. Prot. Dos. **110** (2004) 151.
- [18] SISTERSON, J.M., BROOKS, F.D., BUFFLER, A., et al., Cross section measurements for neutron-induced reactions in copper at neutron energies of 70.7 and 110.8 MeV, Nucl. Instrum. Methods B **240** (2005) 617.
- [19] NOLTE, R., et al., Cross sections for neutron induced fission of ^{235}U , ^{238}U , ^{209}Bi and $^{\text{nat}}\text{Pb}$ in the energy range from 33 MeV to 200 MeV measured relative to n-p scattering, Nucl. Sci. Eng. **156** (2007) 197.
- [20] NOLTE, R., et al., RBE of 200 MeV neutron radiation for the induction of chromosomal aberration in human lymphocytes, Proc. Sci. (FNDA2006) 082.
- [21] TROMPIER, F., BOSCHUNG, M., BUFFLER, A., et al., A comparison of the response of PADC neutron dosimeters in high-energy neutron fields, Rad. Prot. Dos. **161** (2014) 78.
- [22] POMP, S., et al., High-energy quasi-monoenergetic neutron fields: existing facilities and future needs, EURADOS Report 2013-02.
- [23] ZAITSEVA, N., et al., Plastic scintillators with efficient neutron/gamma pulse shape discrimination, Nucl. Instrum. Methods A **668** (2012) 88.
- [24] Eljen technology, EJ-299-33 plastic scintillator,
<http://www.eljentechnology.com/index.php/products/plastic-scintillators/114-ej-299-33>
- [25] LAWRENCE, C.C., et al., Neutron response characterization for the EJ299-33 plastic scintillation detector, Nucl. Instrum. Methods A **759** (2014) 16.
- [26] BUFFLER, A., COMRIE, A.C., SMIT, F.D., WOERTCHE, H., Neutron spectrometry with EJ299-33 plastic scintillator for En= 10-100 MeV, IEEE Trans. Nucl. Sci. **62** (2015) 1422.
- [27] SensL, C-Series silicon photomultipliers, <http://www.sensl.com/downloads/ds/DS-MicroCseries.pdf>.
- [28] COMRIE, A.C., BUFFLER, A., SMIT, F.D., WOERTCHE, H.J., Digital neutron-gamma discrimination with an organic scintillator at energies between 1 MeV and 100 MeV, Nucl. Instrum. Methods **A772** (2015) 43.
- [29] AGOSTINELLI, S., et al., Geant4 - a simulation toolkit, Nucl. Instrum. Methods **A506** (2003) 250.
- [30] MATZKE, M., Unfolding of Pulse Height Spectra: The HEPRO Program System, Physikalisch-Technische Bundesanstalt Report PTB-N-19 (1994).
- [31] KAWRAKOW, I., ROGERS, D.W.O, The EGSnrc Code System: Monte Carlo Simulation of Electron and Photon Transport, NRCC Report PIRS-701 (2000).

ROSPEC - A UNIQUE FAST NEUTRON SPECTROMETER

H. ING

Bubble Technology Industries Inc.
Chalk River, ON
Canada, K0J 1J0
Email: ingh@bubbletech.ca

Abstract: ROSPEC is an acronym for ROTating SPECTrometer. It consists of 6 spherical gas-filled proportional counters mounted on a round platform that rotates slowly, so that all the detectors sweep through essentially the same volume in space to minimize source – detector geometric variations during spectral measurements. ROSPEC measures neutrons from thermal to 4.5 MeV, with each of the counters covering a particular segment of the total energy span. This upper energy limit was chosen because ROSPEC was initially designed for the measurements of degraded fission spectra, of interest to the military. Subsequent applications of ROSPEC for higher energy neutrons led to the development of a companion spectrometer called the Simple Scintillator Spectrometer (SSS) to cover the energy range 4 MeV to 18 MeV. Thus, the simultaneous use of both spectrometers allows the measurements of neutrons from thermal to 18 MeV, which covers most neutron fields of interest for terrestrial applications.

ROSPEC was originally developed for NATO in 1989 and, after extensive testing by NATO, was adopted as the NATO reference spectrometer. However, since its development, ROSPEC has found wide-spread application in numerous large laboratories world-wide, involved in neutron physics or where accurate neutron dosimetry is desired. For the latter application, ROSPEC is often certified by NIST as part of the recommended quality assurance process. There are now many ROSPECs worldwide, used for a variety of applications and it is regarded as the state-of-the-art neutron spectrometer. Unlike Bonner Sphere Spectrometers, ROSPEC does not rely on the use of an accurate neutron spectrum as spectral input to generate the measured spectrum.

1 INTRODUCTION

ROSPEC [1] (ROTating SPECTrometer) is a unique, high-resolution neutron spectrometer originally built for NATO in 1989 [2] for accurate measurements of neutron spectra under various operational non-laboratory environments associated with nuclear warfare. After extensive evaluations by NATO, it was adopted [3] as the NATO reference neutron spectrometer. ROSPEC is designed for use by non-experts and produces neutron spectra using proven unfolding techniques as well as values of various dosimetric quantities, at the touch of a key, without any special input or prior spectral knowledge on the part of the user. ROSPEC has been extensively tested by many expert groups globally and proven to be a reliable, rugged and accurate neutron spectrometer. Many ROSPECs that are used mainly for accurate neutron dosimetry are individually calibrated by NIST as part of the recommended quality assurance, making them ‘NIST-traceable’.

A picture of ROSPEC is shown in Fig. 1. The neutron detectors are the 6 spherical counters that are mounted on the round platform that rotates at 3 rpm to minimize differences in source-detector geometries during spectral measurements.



FIG. 1. A picture of modern ROSPEC

2 HISTORICAL EVOLUTION OF ROSPEC

ROSPEC has its origins in the Chalk River Nuclear Laboratory (now CNL) in the 1970's, with the aim of characterizing neutron spectra associated with the various laboratory facilities that produced neutron radiation. The personal neutron dosimeter at that time was based on NTA film and it was recognized to be inadequate due to well-known problems of an excessively high-energy neutron threshold, fading after exposure and inadequate sensitivity. It was desirable to better characterize and quantify the various neutron fields for the protection of radiation workers.

Hydrogenous gas counters were extensively being studied at AWRE (UK) during that period and 5 cm diameter spherical gas counters were available from an associated company (20th Century Electronics) that was commercializing the technology developed at AWRE. Several such counters, filled with particular gas fillings to cover desired neutron energy ranges, were procured and these eventually led to the development of the ROSPEC prototype shown in Fig. 2. This prototype had only 4 counters, with one of them being a large 15 cm diameter counter to cover the highest energy interval, up to 4.5 MeV, especially made for our use. In this ROSPEC prototype, the pulse-height data from the counters were stored on a cassette-tape and the data were then transferred to cards for off-line processing at the CNL main computer using a modified version of the SPEC-4 unfolding program [4], developed by AWRE.

A similar version of this spectrometer was used to measure (for the first time) the neutron spectrum from a ^{238}Pu Li source [5]. Further development of ROSPEC was interrupted at CNL due to higher priority given to the Bubble Detector [6], also under development at the time, which led to the founding of Bubble Technology Industries (BTI).

Further evolution of ROSPEC continued at BTI under the support of NATO, which was interested in characterizing much more accurately, the neutron field from a fast burst reactor, used to assess the impact on military hardware under conditions of a nuclear explosion.

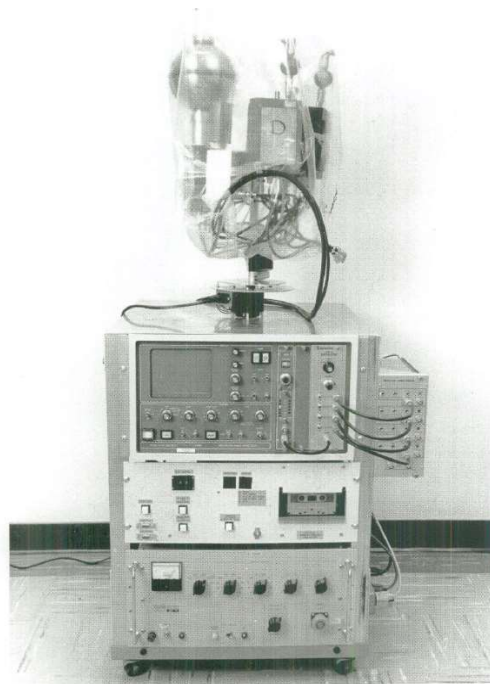


FIG. 2. A picture of a ROSPEC prototype, developed at CNL in the mid-1980's.

As a demonstration of the capability of the ROSPEC prototype, it was used to measure the neutron spectrum at various distances at close range from a fast burst reactor used by NATO. The results obtained by BTI are shown in Fig. 3. The results from these measurements were apparently in good agreement with theoretical predictions, made using early Monte Carlo and Discrete-Ordinate Codes, confirming the remarkable performance of the ROSPEC prototype.

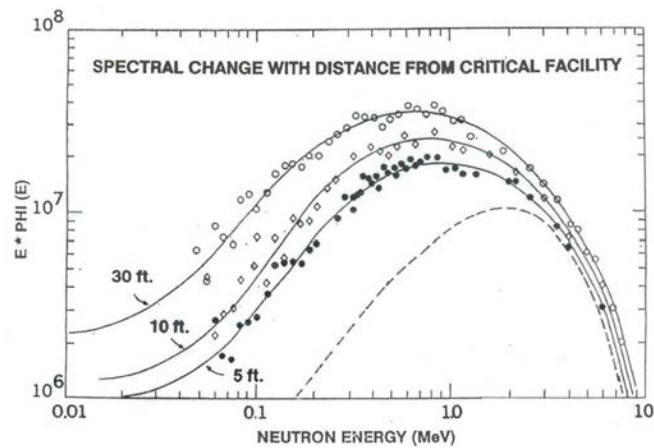


FIG. 3. Spectral changes at close range to a fast burst reactor measured using the ROSPEC prototype. For reference, a theoretical fission spectrum is shown by the dashed curve.

Following these measurements, NATO indicated that they would like a commercial version of the prototype that would be rugged enough for field use and could be operated by non-experts. Certain NATO measurements precluded the presence of non-military personnel; thus, measurements have to be made by military personnel. Specifications for 3 commercial ROSPECs were drawn up by NATO, to be delivered to the US Army, the French Army and the Canadian Department of National Defence.

The resulting commercial ROSPEC, meeting NATO specification, is shown in Fig. 4 and denoted here as 'Original ROSPEC'.



FIG. 4. A picture of the 'Original ROSPEC' as delivered to NATO members.

It still used 4 gas-filled counters identical to the prototype. However, the spectral unfolding was done using the accompanying lap-top, which was part of the ROSPEC system. The development of the ROSPEC entailed the development of spherical counters in-house (they were no-longer available from 20th Century Electronics) as shown in Fig. 5. This version of ROSPEC was then used to measure the neutron spectrum at 400 m from the fast burst reactor in free air (Fig. 6) and after shielding by a 10-cm wall of iron (Fig. 7) to simulate the neutron spectrum inside a military tank. These spectra were intensively assessed by NATO computational experts using various neutron transport codes and appeared to be in good agreement with the most reliable models used, confirming the reliability of ROSPEC for accurate spectral measurements. Thus, eventually leading to its general acceptance as the "reference NATO spectrometer" [3].

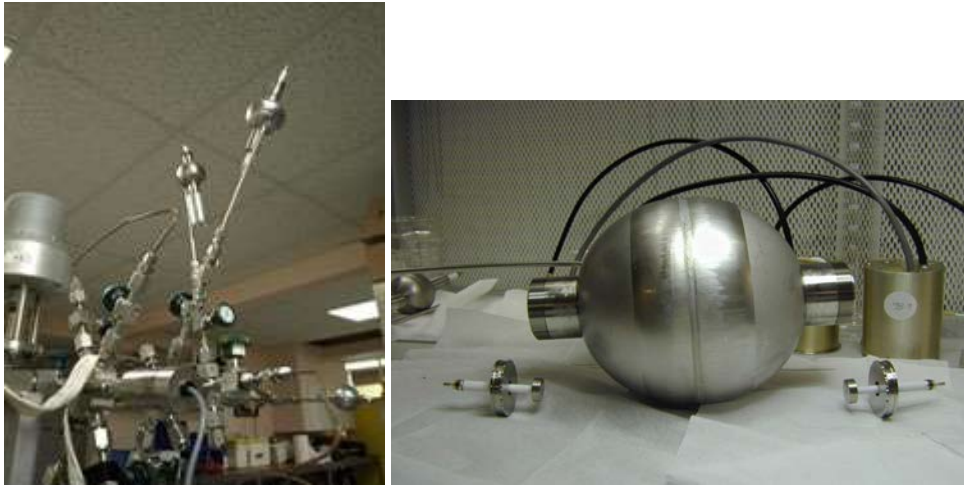


FIG. 5. Counters for ROSPEC were developed in-house.

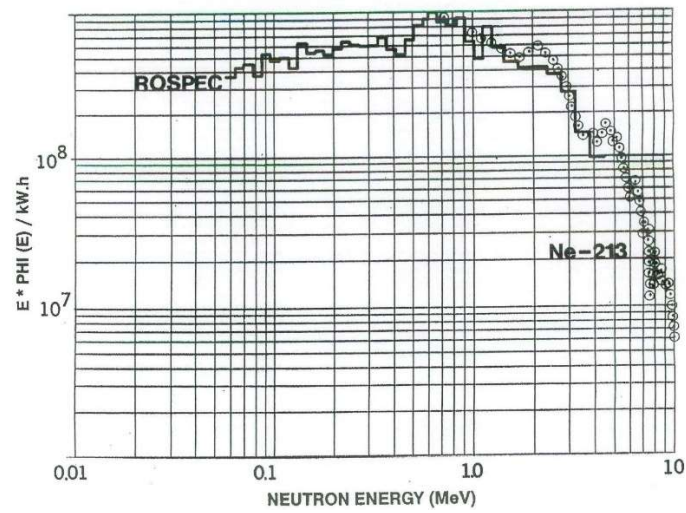


FIG. 6. The spectrum at 400 m from the fast burst reactor as measured by ROSPEC. Data above 4.5 MeV was obtained using a NE-213 liquid scintillator, which was a common spectrometer used by NATO. The fluence above 4.5 MeV is a small fraction of the neutron spectrum.

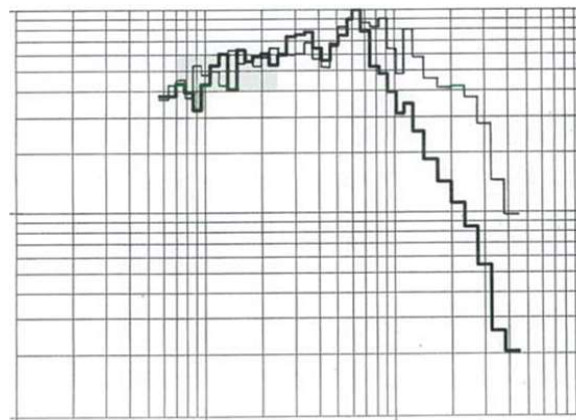


FIG. 7. The spectrum at 400 m from the fast burst, after filtration by 10 cm of iron, relative to the spectrum before filtration (lighter curve).

In the months following the development of the Original ROSPEC for the military, its existence became known to scientists at the DOE laboratories, mainly due to experts from NIST, who certified the Original ROSPEC, that was delivered to the US Army. NIST commented on the unprecedented performance of ROSPEC and expressed a desire for ROSPEC to be used throughout the DOE laboratories.

As more laboratories acquired their own ROSPECs, there were requests to extend its operational range down to thermal neutron energies. To meet this request, two more counters were added to ROSPEC, resulting in the modern ROSPEC (see Fig. 1), which is now the version that is commercially available.

3 THE GAS-FILLED COUNTERS USED IN ROSPEC

The 4 hydrogenous counters of ROSPEC for detection of fast neutrons are filled with different selected pressures of hydrogen gas. The three smaller (5 cm diam) counters are filled with 1, 4 and 10 atm (gauge) of H₂, while the large (15 cm diam) is filled with 5 atm of Ar-CH₄ gas. The need for a different gas for the large counter was dictated by the requirement for higher stopping power (for recoil protons) than provided by H₂. However, the use of the heavier gas increases the counter's response to gamma rays which is generally undesirable for neutron detectors. Furthermore, it introduces other neutron interactions that complicate the measured pulse-height spectrum relative to pure hydrogen recoil.

For each of the hydrogenous counters, its usable energy range is defined by the onset of gamma interference on its low-energy limit. On the high-energy side, the counter is limited by recoil protons escaping from the counter and not depositing its full energy within the gas, making energy determination of recoiling protons not possible.

These properties are well shown in Fig. 8. Figure 8a (left, main display) shows that when the recoiling protons are within the operating range of a counter, one gets a sharp edge in the pulse-height distribution. The neutrons shown here are 0.5 MeV, which are in the region of overlap for the 4-atm counter (Fig. 8a) and the 10-atm counter (Fig. 8b). Thus, the edge is also seen for the 10-atm counter. For the 4-atm counter, the response is close to its high-energy limit, while for the 10-atm counter, it is close to its low-energy limit. However, since 0.5 MeV neutrons are above the high-energy limit of the 1-atm counter, its response does not show a sharp edge, as can be seen in the top panel on the right side of Fig. 8a (denoted by cntr 0). Similarly, 0.5 MeV neutrons are below the lower limit of the large (15 cm diam) counter; thus they cannot be detected due to interference from gamma ray, as can be seen in the 4th panel (denoted cnte 3) on the right side of Fig. 8b. The neutron energy span of the 4 hydrogenous counters are shown in Fig. 9. Together, they span 50 keV to 4.5 MeV. Their approximate detection efficiencies (defined by gas volume and pressure) are shown relative to the dose-equivalent curve, used in radiation protection.



FIG. 8a.

FIG. 8b.

FIG. 8. Spectral data showing the pulse-height features for neutrons within a counter's operational range and above and below its range. The data are taken from a laptop display of ROSPEC after a measurement of 0.5 MeV monoenergetic neutrons.

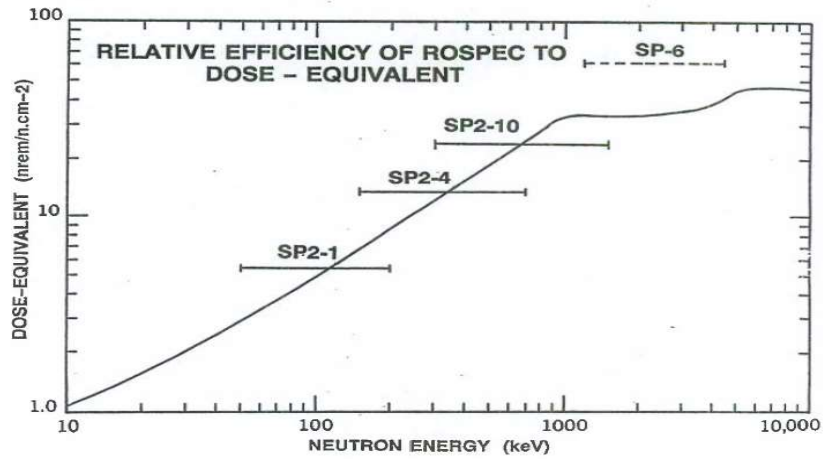


FIG. 9. The energy segment of coverage for each of the 4 hydrogenous counters of ROSPEC. The segments are vertically displaced in relation to their relative detection efficiency. The continuous curve is the fluence - to dose-equivalent conversion curve for neutrons.

Two additional (5 cm diam) counters are used to detect neutrons below 50 keV (ref. Fig. 1) down to thermal energies. One of the counters covers the range 50 keV down to 1 eV. To do this, a special boron shell [7] is used to embed a counter which is filled with ^3He gas, as shown on the right side of Fig. 10. The purpose of the shell is to suppress the increasing response of the ^3He counter with decreasing neutron energy as represented by the neutron cross-section in the Figure. The special shell design results in the final response shown, in comparison with the dosimetric curve ($^*\text{H}(10)$), which is the desired shape for neutron dosimetry. This final response of the boron-shielded ^3He counter is not a perfect replication of the dose-equivalent curve between 1 eV and 50 keV, but the use of algorithms in the spectral unfolding process compensates for some of the limitations.

The fluence of thermal neutrons is measured using a bare ^3He counter (as shown in Fig. 10). Its detection efficiency is determined using conventional Au and Cd-Au neutron activation measurements. It should be emphasized that the use of hydrogen recoil for fast neutron spectroscopy in ROSPEC makes it unnecessary to use an assumed input spectrum for spectral unfolding (unlike Bonner Spheres) since the responses for monoenergetic neutron are uniquely defined (see Fig. 8a).

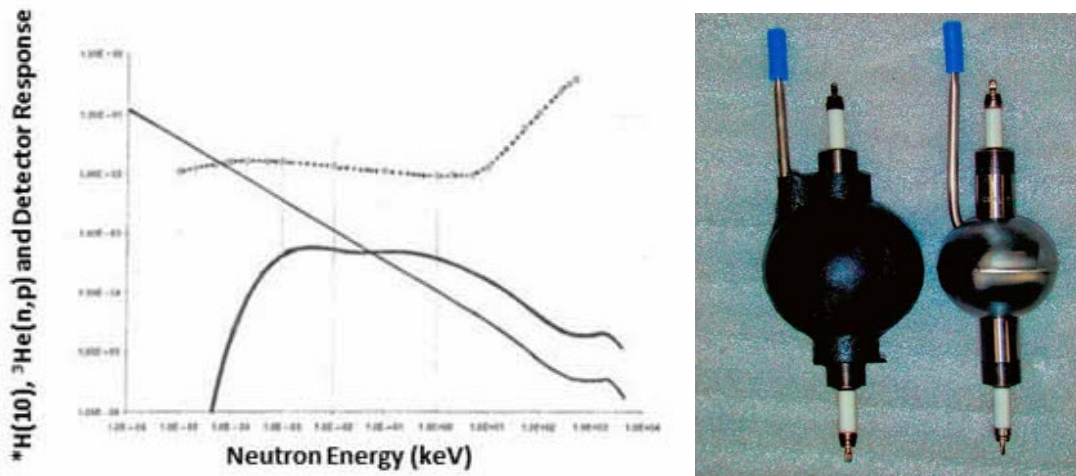


FIG. 10. The right side shows a picture of a ^3He counter bare and embedded in a boron shell. The left side (heavy curve) shows the response of the boron-covered detector as a function of neutron energy. The light curve shows the ^3He (n,p) cross-section. The dotted curve is the $^*\text{H}(10)$ dosimetric curve.

4 NEUTRON SPECTROSCOPY ABOVE 4.5 MEV

A companion spectrometer known as ‘Simple Scintillation Spectrometer’ (SSS) is used to measure neutrons above the 4.5 MeV limit of ROSPEC. A picture of SSS is shown in Fig. 11.

SSS covers the range 4 MeV to 18 MeV. To retain good robustness for military field operations, no pulse-shape discrimination techniques involving electronic circuitry is used. Ordinary plastic scintillators (using hydrogen recoil) are used as the neutron sensor.



FIG. 11. A picture of SSS, the companion spectrometer for the measurements of neutrons above the 4.5 MeV limit of ROSPEC

The sensors are shown in Fig. 12. They consist of an array of tiny scintillators, whose sizes are such that the maximum amount of light produced by electrons (due to gamma rays) is less than that by 4 MeV protons (due to neutrons). Thus, the separation of neutrons and gamma rays is done using simple pulse-height discrimination. The number of scintillators in the SSS was determined by having comparable detection efficiency as the ROSPEC itself.

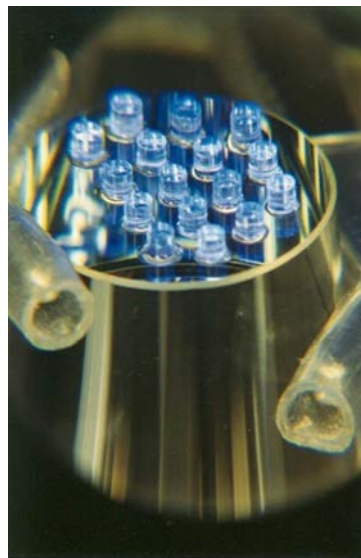


FIG. 12. The tiny scintillators that constitute the neutron sensors of the SSS.

Figure 13 shows unfolded spectra for 12 MeV and 14 MeV monoenergetic neutrons and a measured spectrum from an Am–Be neutron source, using a combination of the SSS and ROSPEC.

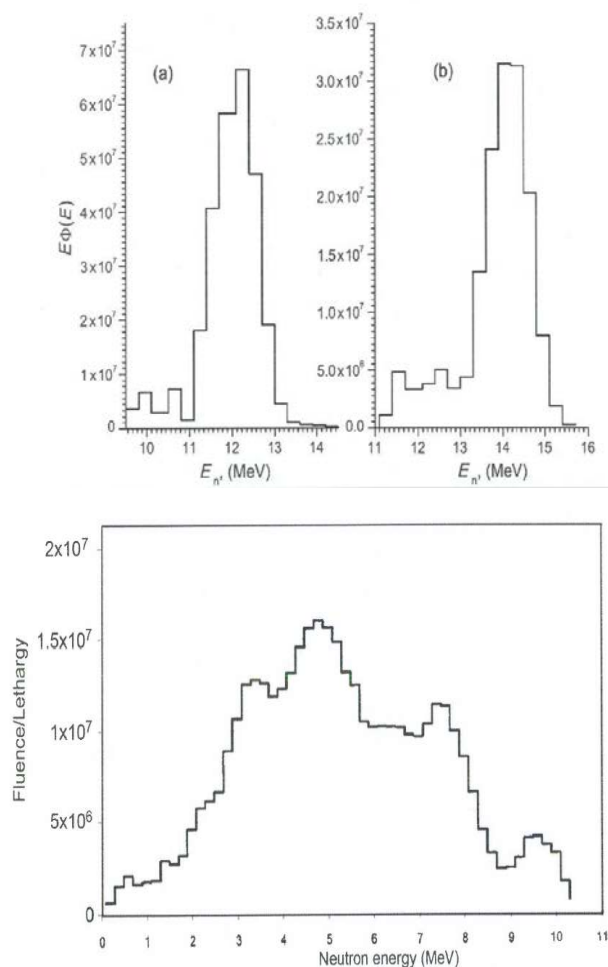


FIG. 13. Results for monoenergetic neutrons measured by SSS (left and middle). The right side shows a measured spectrum of an Am–Be source using both ROSPEC and SSS.

5 VALIDATION OF ROSPEC PERFORMANCE

Many eminent groups have evaluated the performance of ROSPEC. The earliest evaluation was by Schartz and Eisenhauer of NIST [8], comparing ROSPEC results with theoretical spectra for a bare Cf source, heavy-water moderated, iron-moderated and light-water moderated Cf sources. They concluded that “ROSPEC performed admirably” and they “were not aware of any other neutron spectroscopy system that performs at all comparably”. Comparable sentiments were expressed by subsequent NIST experts [9, 10].

Evaluations on the performance of ROSPEC were also done by groups in Germany [11] and in France [12] using mainly monoenergetic neutrons produced by accelerators. They obtained good agreement in energy measurements and fluence values to no worse than 8% with their standard reference instruments.

An extremely detailed assessment of ROSPEC was done by a group in the UK [13] using the The absolute fluences were determined using a shadow cone to enable the separate measurement of room-scattered neutrons. Their results for monoenergetic neutrons of 71 keV and 144 keV are shown in Fig. 14. Figure 15 gives the measured data for 565 keV neutrons (left) and for an ISO 8529 Am/B source (right). They also measured simulated workplace spectra that are used at NPL. They were extremely pleased with the good ROSPEC performance and praised the capability of ROSPEC to “generate data simply and routinely in minutes”.

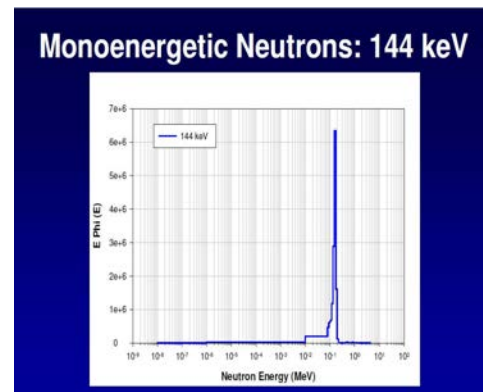
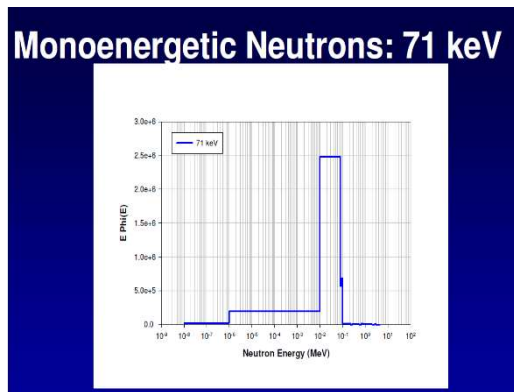


FIG. 14. Results for monoenergetic neutrons for 71 keV (left) and 144 keV (right)

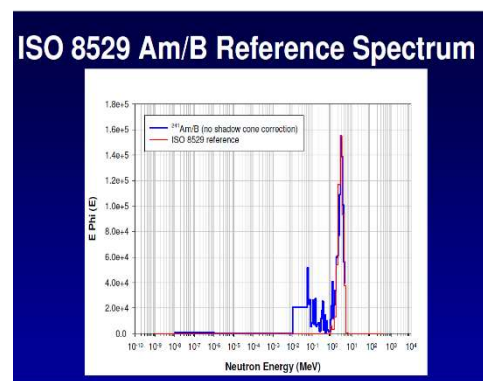
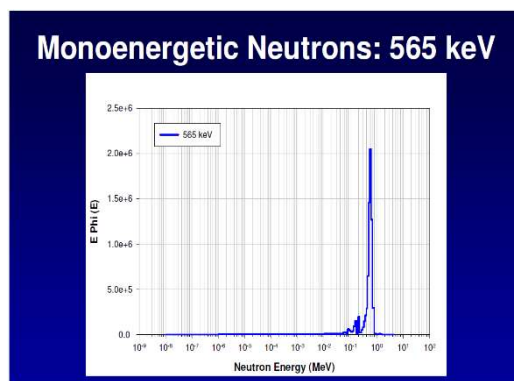


FIG. 15. Results for 565 keV neutrons (left) and for a Am-B neutron source (right). The theoretical spectrum for the Am-B source is also shown.

6 USES OF ROSPEC

ROSPEC is used for a variety of applications. ROSPEC is often used to measure radiation fields at a particular location from various sources that have been characterized only using theoretical computations or a variety of other spectroscopic techniques that may not be deemed completely reliable. For instance, Fig. 16 shows a spectrum at 1 m from a ^{252}Cf source [14] to establish the dose-rate and the impact of room scatter on the source spectrum. Figure 17 shows a spectrum at 1 m from a PuF4 source, used for calibrating personal neutron dosimeters at a large national laboratory. This spectrum is much softer than for a Cf source (also shown) and is much closer to the energies of neutrons that radiation workers are exposed to, at their site. Figure 18 (right) shows the measured results by ROSPEC in comparison with theoretical results for the source representing a Realistic Field at NPL (left). This source is often used for calibrating personal neutron dosimeters.

These results illustrate a particular character of spectral results generated by ROSPEC: it is sometimes difficult to be certain whether observed spectral features are real or a consequence of the unfolding process, which is inherently noisy. For good statistics (e.g. Fig. 16), the features over the region above 0.1 MeV are likely real, caused by resonances and anti-resonances in material in close proximity to the neutron source. Resonances in various materials have been used as a method of calibrating the different counters in the past [15]. However, for poor statistics (Fig. 17; > 2 MeV), the fluctuations are mainly due to the unfolding process itself. If the spectral features themselves are of interest, repeat measurements will provide a more definitive assessment. However, in general, these features from unfolding do not significantly impact the dose values provided by ROSPEC.

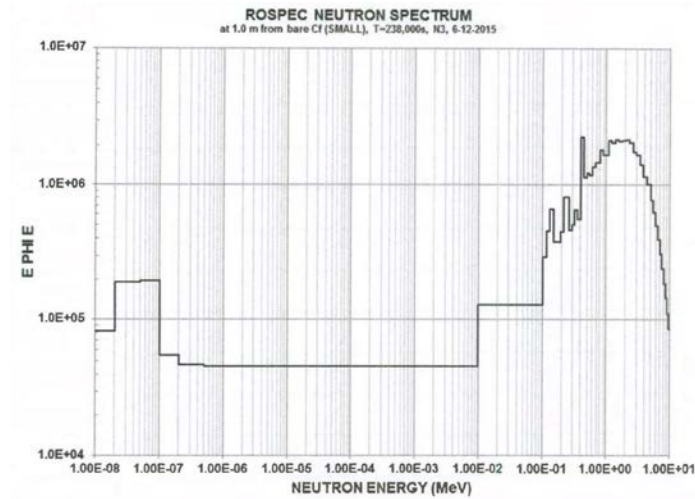


FIG. 16. A measured spectrum of Cf at 1 m distance in a facility, providing information on doserates from the source and from room scatter:

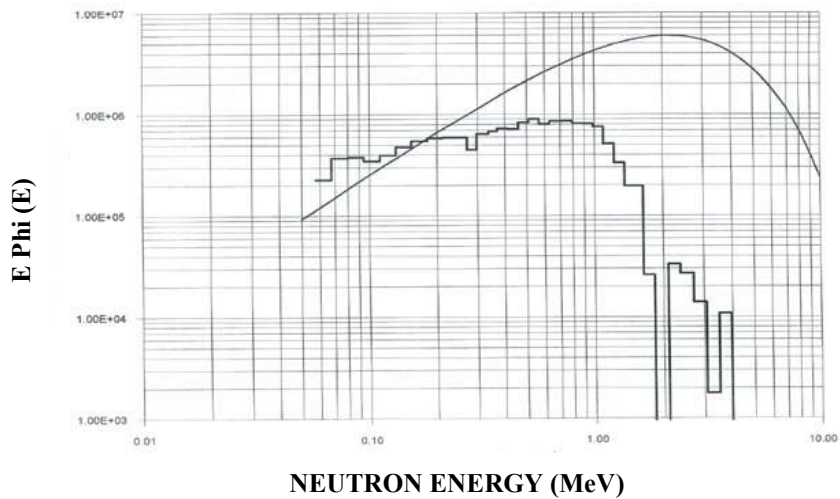


FIG. 17. A measured spectrum at 1 m from a PuF4 source, used for calibration. A fission spectrum (smooth curve) is shown for comparison.

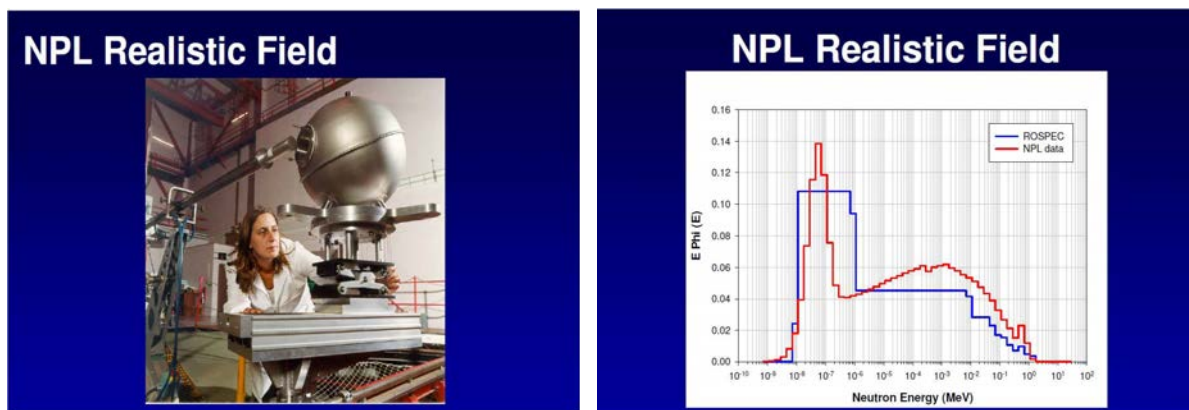


FIG. 18. ROSPEC results for a Realistic Field (shown on the right) produced by the NPL facility (left). The theoretical spectrum from the facility is also shown (finer bins) in the spectral data.

Sometimes, ROSPEC is used to determine the spectrum of neutrons from a source that is not easily to model, from a calculational viewpoint. For instance, Fig. 19 shows a ROSPEC spectrum in the maze of the CONSORT reactor [13] at the Imperial College in London (UK). These spectral features are likely real. Figure 20 shows a spectrum [16] outside a glove box for processing fissile materials; most of these features are likely real. Figure 21 shows spectra beside a waste cask, shielded and unshielded. The only reliable features in the unshielded spectrum are probably the dips at 1 MeV and ~ 450 keV. Figure 22 shows a measured spectrum [16] in a reactor facility; it is clearly dominated by thermal neutrons. Figure 23 shows spectra measured at two locations in the Service Area of a fuelling machine. It is surprising how much the neutron spectrum can change over a small distance in certain operational environments. The dose rate at these locations would be greatly different and calibrations of most personal neutron dosimeters would be extremely challenging to get reliable values for both these locations.

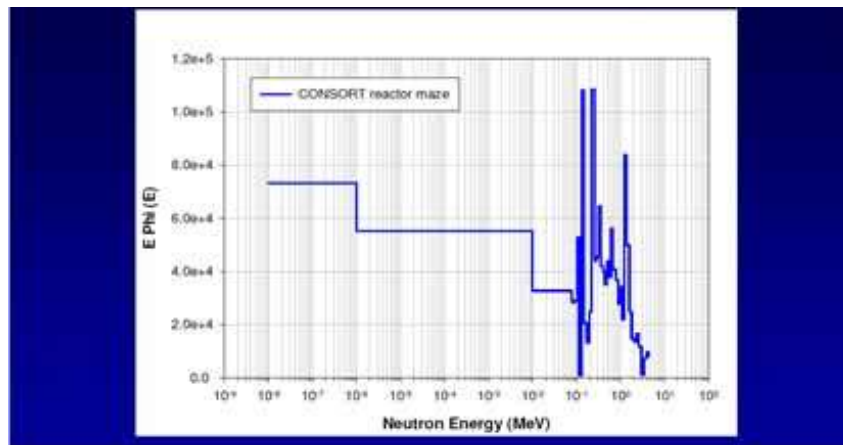


FIG. 19. ROSPEC spectrum in the maze of the CONSORT reactor.

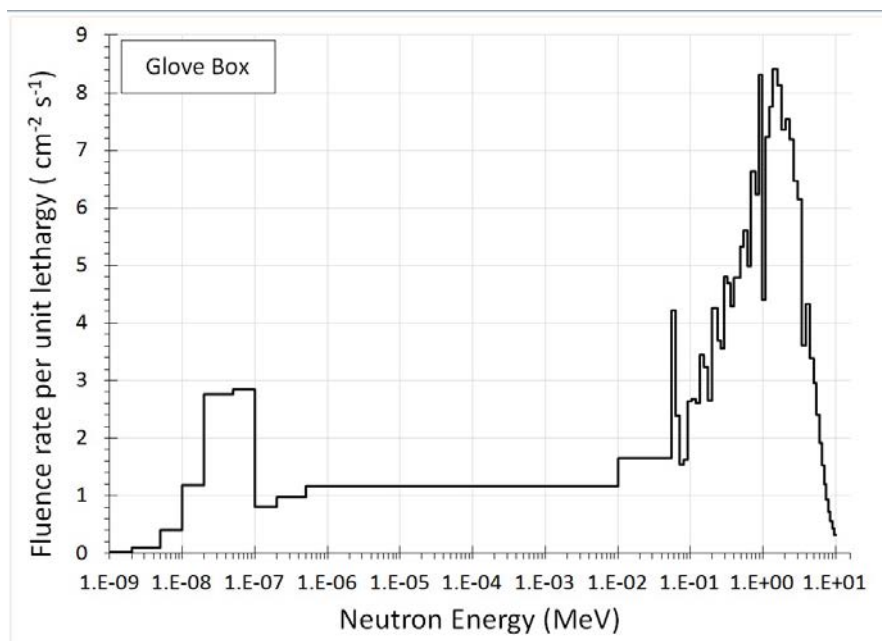


FIG. 20. Neutron spectrum outside a glove box for processing fissile materials.

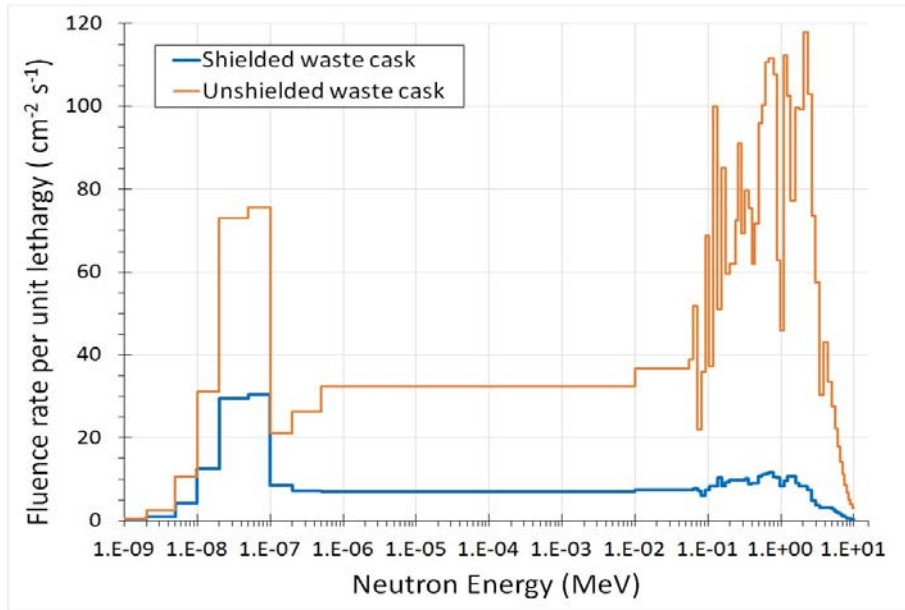


FIG. 21. Neutron spectrum beside a waste cask, unshielded and shielded.

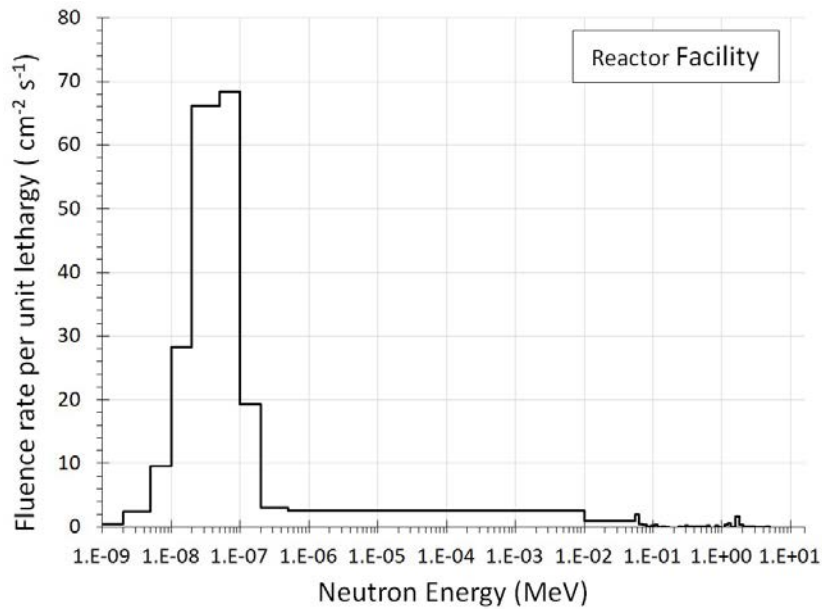


FIG. 22. Measured spectrum in a reactor facility.

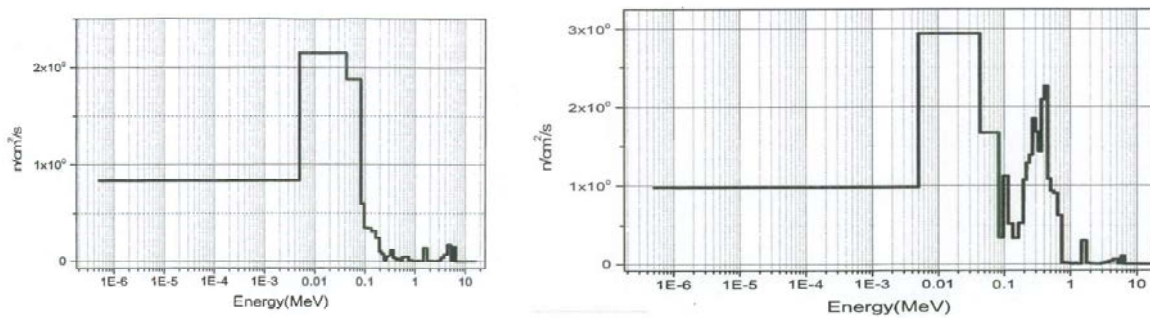


FIG. 23. Measured spectra at two locations in the Service Area of a fuelling machine, showing large spectral changed over a short distance.

Perhaps one of the most interesting applications of ROSPEC is its use for correcting the readings of personal neutron dosimeters at particular locations within a particular nuclear site. Figure 24 (left side) shows a picture [17] of ROSPEC located at a particular location to measure the neutron dose-rate. The right side of Fig. 24 shows a jug (acting as a phantom) located at the same location containing various mounted dosimeters to determine their respective readings. The ratio of reading of the ROSPEC dose to the reading of the particular type of dosimeter is used to ‘correct’ the dosimeter reading to yield the reported neutron dose at the particular site. This method of determining the ‘neutron dose correction factor’ for each location of interest is done across the site. This particular site had correction factors that ranged from 1.3 to 3.5. Such ROSPEC/phantom measurements are redone whenever there is a change at the location that could impact the neutron spectrum. Also, the measurements are redone periodically to reconfirm the neutron spectrum at a particular location.

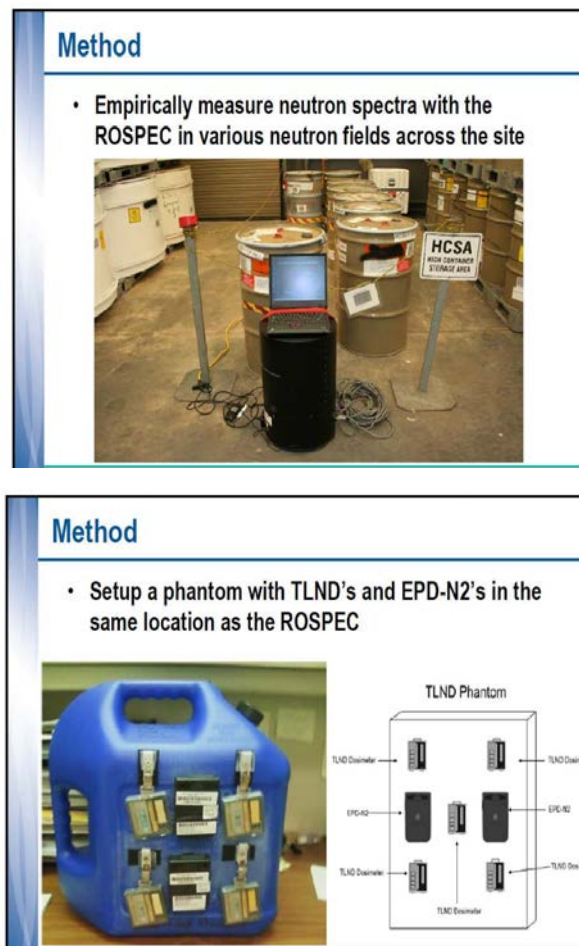


FIG. 24. The left side shows a ROSPEC measuring the neutron dose at a particular location within a nuclear facility. The right side shows a dosimetric set-up at the same location to get dosimeter readings. These readings are corrected using the ratios of ROSPEC dose to dosimeter readings.

7 NOTED DISCREPANCIES IN SPECTRAL RESULTS

Spectral results in the region below 50 keV, as measured by ROSPEC, has been noted to be high by at least 3 experts groups [10, 18, 19]. This is most easily seen in the results from NPL (Fig. 25) where the measured fluence is around 50% higher than the theoretical spectrum. For the intermediate energy region 1 eV – 50 keV, covered by the boron-covered ³He counter, it is simple for BTI to increase (artificially) the detection efficiency of this counter to bring the fluence in this region to be in better agreement with the theoretical spectrum. As for the thermal neutron fluence, it is difficult for us to understand how the ROSPEC thermal fluence can be significantly in error, since the detection efficiency of the bare ³He counter is established using the standard technique of Au and Cd-Au foil activation. We used the same foils and methodology, whose results have been well proven in our measurements in the IAEA program on the Intercomparisons of Criticality Accident Dosimetry Systems [20].

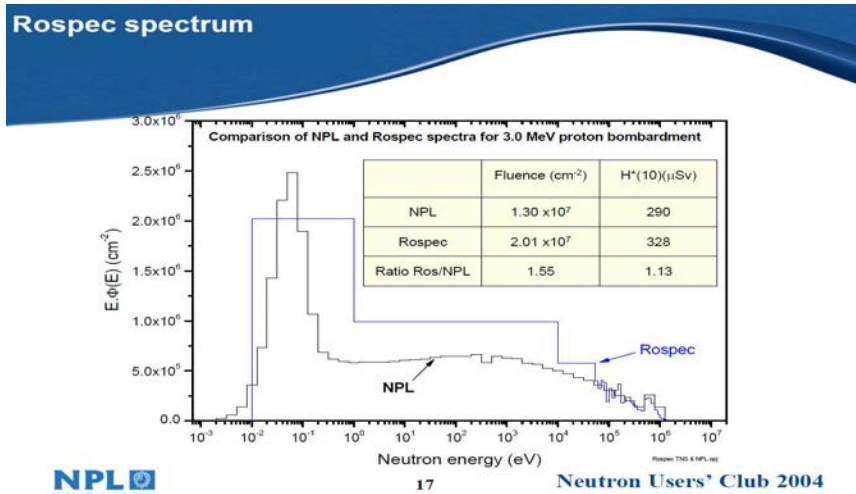


FIG. 25. Comparison of ROSPEC fluence with theoretical for a facility at NPL

It is possible that these noted discrepancies by the experts may be due to neutron scattering in ROSPEC itself. This could explain the thermal fluence discrepancy because our calibration is done with pairs of foils on both sides of the bare ³He counter before the counter is mounted on ROSPEC. Thus, the measured fluence by ROSPEC is the value including any scattering by ROSPEC itself. This value would therefore, be expected to be higher than that theoretical spectrum, since it would not include the effect of the measuring instrument.

If ROSPEC users can arrive a consensus on the exact reduction in thermal and epi-thermal fluences that they think is desired for agreement, it is simple for us to modify our calibrations of these two counters to yield results that they wish to obtain. Unfortunately, if the effect of scattering is due to an instrument itself, it is not a unique value and will vary (to some extent) depending on the actual source spectrum being measured.

There is some disagreement in the published literature by the various expert groups on the exact amount of discrepancy of their ROSPEC results relative to fluences that they believe are correct. For instance, measurements by experts from LANL [16] of the same facility at NPL show results (Fig. 26) that are in quite reasonable agreement with theoretical predications. In fact, here, the thermal fluence is actually lower (not higher) than the theoretical spectrum. It is difficult for us to remedy noted discrepancies in ROSPEC results, in view of disparate data that is currently available.

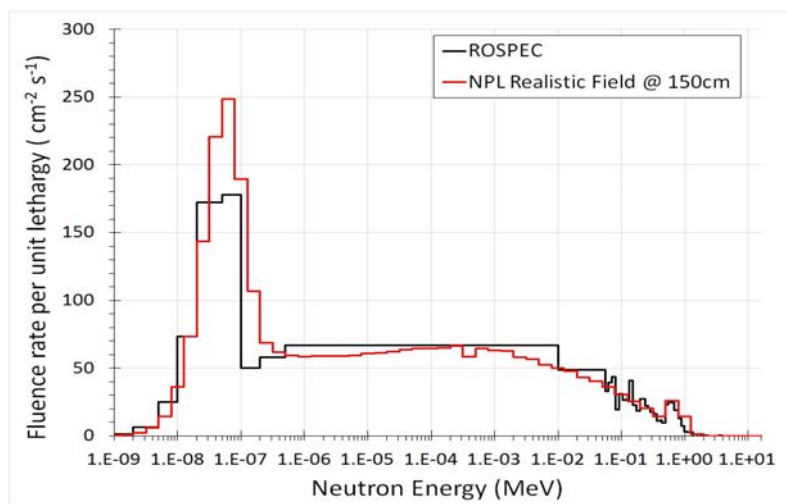


FIG. 26. ROSPEC results for the same facility as used for Fig.25, made by another expert group.

While the spectral results in Fig. 25 indicate fluence values that are over-estimated by more than 50%, it is worth noting that the dosimetric value (*H(10)) is only 13% higher than the theoretical. Thus, for operational neutron dosimetry, the values provided by ROSPEC are amply adequate, regardless of spectral uncertainties.

8 CONCLUSION

ROSPEC is a unique fast neutron spectrometer and is regarded as state-of-the-art for measurements of various neutron fields of main interest for radiation protection of personnel. It is a simple, rugged spectrometer designed for use by non-experts in neutron spectroscopy. It has been extensively tested by numerous expert groups world-wide and has been proven to be a reliable, accurate spectrometer and dosimeter. ROSPEC is designed for measurements of degraded fission spectra and covers the energy range thermal to 4.5 MeV. For measurements of higher-energy neutrons, a companion spectrometer (SSS) is available, allowing measurements of neutrons up to 18 MeV.

The historical evolution of ROSPEC over a period of over 30 years, from a NATO military spectrometer to a general purpose spectrometer used by numerous groups world-wide, has been given. Also, some of the technical reasons for the current design of ROSPEC has been presented, along with some representative samplings of data obtained by various users for a variety of applications.

Of course, ROSPEC is not a perfect spectrometer. There are many improvements that can be made to increase its ruggedness, reduction in size, increased detection sensitivity, improved spectral unfolding accuracy, improved spectral resolution, etc. However, these potential improvements do not appear to be important to many uses of ROSPECs, who in general seem to be pleased with the current product.

We encourage users of ROSPEC to contact us regarding any aspect of ROSPEC operation that is not satisfactory to their particular need. Only with such feedback would we be able to continue to improve ROSPEC to maintain its lead as a state-of-the-art instrument. There have been reports of spectral discrepancies between ROSPEC and theoretical spectra over the energy range thermal of 50 keV. Unfortunately, the extent of these discrepancies appear to vary among the groups that have reported them, making it difficult to correct this performances by modifying the detection efficiencies of the two ^3He counters. These discrepancies may be due to neutron scattering from ROSPEC itself and this can vary depending on the actual spectrum being measured. This behaviour was observed by the CEA group [18] that showed a dependence with spectrum softness. Fortunately, these spectral discrepancies have only a minor impact on the measured values of neutron dose by ROSPEC, needed for operational neutron dosimetry.

REFERENCES

- [1] ING, H., et al., ROSPEC - a simple reliable high-resolution neutron spectrometer, *Radiat. Prot. Dosim.* **70** (1997) 273–278.
- [2] ING, H., COUSINS, T., “Recent measurements of the APG neutron leakage spectrum using ROSPEC”. Proc. 1989 Workshop of the RSG5 Physical Dosimetry Subcommittee. ETCA Arcueil, France (1989) 1–15.
- [3] STANKA, M.B., “The ROSPEC neutron spectrometer, a NATO collaborative success”, in Proc. Workshop on biomedical aspects of nuclear defence, NATO technical proceeding AC/243 (Panel 8) TP/6 B3.1 - B3.11 (1995).
- [4] BENJAMIN, P.W., KEMSHALL, C.D., BRIKSTOCK, A., The analysis of recoil proton spectra. AWRE Report, Berkshire, UK, 0-9/68 (1968).
- [5] ING, H., CROSS, W.G., TYMONS, B.J., The spectrum of neutrons from a ^{238}Pu -Li source, *Health Phys* **40** (1981) 345–350.
- [6] ING, H., BIRNBOIM, H.C., A bubble-damage polymer for neutrons. *Nucl. Tracks Radiat. Meas.* **8** (1984) 285–288.
- [7] ING, H., et al., Modifications of ROSPEC to cover neutrons from thermal to 18 MeV. *Radiat. Prot. Dosim.* **126** (2007) 350–354.
- [8] SCHWARTZ, R.B., EISENHAEUER, C.M., Test of a neutron spectrometer in NIST standard fields, *Radiat. Prot. Dosim.* **55** (1994) 99–105.
- [9] DEVINE, R.T., et al., Evaluation of spectrum measurement devices for operational use. *Nucl. Instrum. Methods Phys. Res. Sect. A* **476** (2002) 416–422.
- [10] HEIMBACH, C., NIST calibration of a neutron spectrometer ROSPEC. *J. Res. Nat. Inst. Stand. Technol.* Nov–Dec **111** 6 (2006) 419–428.
- [11] ROSENSTOCK, W., KOBLE, T., KNIZINISKI, G., JAUNICH, G., Calibration of a nuclear spectrometer in the energy range 144 keV to 14.8 MeV with ISO energies. *Radiat. Prot. Dosim.* **70** (1997) 299–303.
- [12] BENMOSBAH, M., ASSELINEAU, B., Energy and fluence calibration of the neutron spectrometer ROSPEC at the IRNS AMANDE facility between 70 keV and 4.5 MeV. *Radiat. Prot. Dosim.* **135** (2009) 154–161.
- [13] NATIONAL PHYSICAL LABORATORY, www.npl.co.uk/ionising-radiation/rospec-irradiations.

- [14] RADEV, R., Measurements of the neutron spectrum and ambient neutron dose rate equivalent from a small ^{252}Cf source at 1 m. LLNL-TR-674298 Los Alamos, NM, USA (2015).
- [15] TYMONS, B.J., ING, H., Calibration of a Proportional Counter Neutron Spectroscopy System, *Health Phys.* **39** (1980) 561–564.
- [16] Data provided by Dr. T McLean, Los Alamos National Laboratory, Los Alamos, NM, USA.
- [17] WAGMER, D., “TLND Correction Factor Evaluation Using the ROSPEC”, paper presented in the Savannah River Chapter of the Health Physics Society 16th Annual Technical Seminar (2012).
- [18] CROVISIER, P., et al., French comparison exercise with the rotating neutron spectrometer "ROSPEC". *Radiat. Prot. Dosim.* **115** (2005) 324–328.
- [19] THOMAS, D., TAYLOR, G., A simulated neutron workplace field at NPL. Neutron Users Club (2004).
- [20] FLAKUS, F.N., “An international co-ordinated research programme on nuclear accident dosimetry”, *Proc. IRPA IVth International Congress, 24-30 April 1977, Paris, France* **1** (1977) 85–88.

TOPICAL SESSION 6
THERMAL NEUTRON DETECTORS FOR NEUTRON SCATTERING

DEVELOPMENT OF AREA DETECTORS FOR NEUTRON BEAM INSTRUMENTATION AT THE BUDAPEST NEUTRON CENTRE

J. ORBÁN, J. FÜZI and L. ROSTA¹

Wigner Research Centre for Physics of the Hungarian Academy of Sciences
POB 49, 1525 Budapest, Hungary
Email:rosta.laszlo@wigner.mta.hu

G. KISS

MIRROTRON Ltd.

Konkoly Thege út 29-33,
1121 Budapest, Hungary

Abstract: The Budapest Neutron Centre (BNC) is the research organisation enabling open access utilization in science and technology development of the 10 MW Budapest Research Reactor (BRR) facilities. The reactor has 10 horizontal beam tubes and a liquid hydrogen cold source with three neutron guides. On the supermirror guide system both thermal and/or cold spectra are available. BNC operates 15 experimental stations: diffraction, small angle scattering, inelastic scattering, radiography or irradiation, in-beam gamma capture and in-pile irradiation facilities are available. Instrumental development has been always in the focus of BNC research. Detectors are essential part of the instrumentation, thus a thorough programme on the development of 2D/area detectors was started in 2000. Multiwire counters have been chosen and they are likely to remain a reliable and cost-efficient option for a large class of instruments. Delay-line position encoding is widely used in multiwire position sensitive particle detectors. Improvement of several detector parameters is a continuous demand, such as count rate, position resolution, and energy resolution. Besides detector chambers, digitized/analogue signal acquisition systems have been also developed. In co-operation with spin-off companies at the reactor campus a standard detector family was produced with 20 cm × 20 cm active area, based on ³He gas as neutron converter. Six of the BNC experimental stations are equipped with this type of detector. This activity of developing ³He counters has remained in the scope of our detector programme by constructing prototypes of detectors with larger area and faster data acquisition system. Following the worldwide ³He crisis, however, we have turned our interest also towards systems based on solid boron converters. Typically, a converter can be created as a thin layer on a substrate by a sputtering process using pure ¹⁰B, or more practically, boron carbide (B₄C). In particular, the construction of a multiwire chamber with multiple boron layer converters is described here. The detector team also takes advantage of the flexibility of the BNC instruments to perform various kind of test measurements to probe and qualify detectors of new developments. Several beamlines/devices are available for test experiments to be used cold, thermal, as well as white or monochromatic neutron beams.

1 INTRODUCTION

1.1 NEUTRON RESEARCH IN HUNGARY

Neutron beam methods constitute an essential and unique part of the science tool kit for exploiting information about the properties and behaviour of matter at atomic and molecular level – this is also indispensable in order to design novel materials, devices, drugs and solve complex engineering problems. Neutrons can probe structure and dynamics of matter from mesoscale to nanoscale and from seconds to nanoseconds. Intense neutron beams are produced in nuclear reactors or accelerator-based neutron sources. Worldwide about 25 neutron source centres are those which provide high intensity neutron beams and give access for the multidisciplinary user community to about 350 various neutron spectrometers for materials research. The Budapest Neutron Centre (BNC) is one of these facilities.

BNC is the research organisation for the open access utilisation in science and technology development for the 10 MW Budapest Research Reactor, a unique infrastructure of this kind in the Central European region. BNC is a consortium of the *Wigner Research Centre for Physics* and the *Centre for Energy Research*. Both research centres with their staffs over 400 people each are part of the research network of the Hungarian Academy of Sciences and they have become important national hubs of their research fields.

1.2 THE BUDAPEST RESEARCH REACTOR

BRR has been utilized as a neutron source for basic and applied research or direct applications in various fields of industry, healthcare as well as in exploration and conservation for objects of cultural heritage. The reactor was first started in 1959. BRR is one of the leading research infrastructures in Hungary and in Central Europe [1]. The basic scientific activity at BRR is the use of neutron beam lines for neutron scattering investigations. The reactor was upgraded from 2 to 5 MW in 1967. Hungarian companies undertook a major refurbishment that started in 1986 in a project supported by IAEA and the European Union. The reconstruction was completed and the license for

reactor start-up was issued in 1992. The reactor reached its 10 MW nominal power in May 1993. At 10 MW power the reactor provides a maximum thermal neutron flux of 2.2×10^{14} n/cm²s and a fast neutron flux of 1×10^{14} n/cm²s in the core. The reactor has 10 horizontal beam tubes (eight radial and two tangential). At one of the tangential beam tubes a cold neutron source (CNS) has been installed. Three neutron guides transport neutrons to the measurement site in the guide hall adjacent to the reactor building. The neutron guides have bi-spectral nature, i.e. they can provide neutrons both with thermal or cold spectra [2]. Thanks to a continuous development the number of experimental stations now is 15 (Fig. 1 shows the lay-out of the horizontal beam-lines). The research staffs have grown by now to nearly 60 scientists. In 2010 a core conversion programme was completed, namely the change of the fuel from high enriched uranium to low (20 %) enriched uranium.



FIG 1. Layout of the horizontal neutron beam facilities at the Budapest Research Reactor:

1.3 PROGRESS IN NEUTRON SCIENCE

A review of some highlights from several decades of activities from the Budapest Research Reactor is given in Ref. [3]. Notable advancements were made by some of our leading scientists; e.g., development of neutron spin-echo spectroscopy (1972), supermirrors (1976), and the long-pulse spallation source concept by Ferenc Mezei, and of atomic-resolution neutron holography by László Cser (2002). Combined dynamic neutron-gamma radiography has become a widespread technique with industrial applications and BNC had a pioneering role in its development. A Prompt Gamma Activation Analysis (PGAA) instrument was installed in the mid-1990s on a cold guide at BNC. And more recently a second instrument was installed, making the PGAA station at Budapest a world-leading facility. The creation of a coherent PGAA library has been one of the major impacts of this group. They were also among the first to perform non-invasive neutron beam investigations of archaeological objects.

The history of neutron beam research is a continuous fight for intensity gain in order to compensate the drawback of the nature of neutron experiments, namely the poor intensity (weak interaction).

In most cases spatial or energy/time resolution of a measurement can be improved in expense to the intensity registered in the detector system. Thus, any improvement of the experimental conditions i.e. decreasing statistical

uncertainty due to gain in signal/background or achieving higher resolution is a crucially important part of neutron research. Progress in efficiency, sensitivity might be followed on two sides: enhancing neutron source intensity is one way and improving measuring instrumentation techniques is the other one. Below we list a few major steps in this progress (the date in brackets and the approximate improvement factor is indicated):

- Nuclear reactors for neutron beam research (~ 1950)
- Pulsed sources (~1960) $\times 10$
- Spallation sources (1960 - 70) $\times 10$
- Beam modulation techniques – time-of flight (TOF) (~1967) $\times 10$, special cases
- Neutron Spin Echo spectroscopy (1972) $\times 100$ in energy resolution
- Neutron supermirrors (1976) $\times 3$
- Long pulse spallation sources (1993) $\times 10$
- Repetition Rate Multiplication (1994) $\times 10$
- Ballistic neutron guides (1996) $\times 10$
- Atomic resolution neutron holography (2001) $\times 10$ in precision of atomic positions
- Multi-spectral beam extraction (2002) $\times 2$ in dynamic range
- Phase contrast imaging (2010) $\times 10$ in sensitivity
- Compact moderators (2012) $\times 3$ in cold neutron brightness

Concerning neutron detection, this is probably the most important factor in improving intensity issues in neutron experiments. Neutrons scattered from a sample usually cover a wide angular range. From the single point detectors in the early experiments, through multi-detectors and position sensitive counters to the development of large area position sensitive detectors covering space in the range of tens of square meters, the number of useful detected neutrons has increased by a factor of 10^3 – 10^6 by now. *This underlines the high importance of technical developments in the field of thermal and cold neutron detection applied to materials research.*

2 DETECTOR DEVELOPMENT AT BNC

2.1 INSTRUMENTATION AND DETECTORS AT BNC

The development of position sensitive detector (PSD) systems at BNC was started in 1986, when the medium resolution *powder diffractometer* was refurbished [4]. The instrument is now installed on the tangential thermal channel No.9 (see Fig.1), with $10^6 \text{ cm}^{-2}\text{s}^{-1}$ neutron flux at the sample position. This 2-axis diffractometer has been equipped with a linear position sensitive detector system: 5 pieces of half inch diameter and 60 cm length ^3He tubes form the detector assembly, which is mounted on the diffractometer arm and it spans a scattering angle range of 25° at a given detector position. The entire diffraction spectrum can be measured in five steps to cover 125° scattering angle. This diffractometer (Fig. 2) is still in use for atomic structure investigations of amorphous materials, liquids and crystalline materials where the resolution requirements are not very high.

2.1.1 High Resolution TOF Powder Diffractometer

The instrument has been installed on a radial thermal neutron beam in a new guide hall. Full diffraction spectrum can be recorded within a variable bandwidth with high resolution or with high intensity at conventional resolutions. In high-resolution mode, the very short (10 μs) neutron pulse and the 25 m total flight path allows us to obtain a diffractogram with an accuracy of 10^{-3}\AA in a single measurement on polycrystalline materials, while, in low-resolution mode, liquid diffraction can be performed at good neutron intensity up to 15\AA^{-1} . The diffractometer has been equipped by a multidetector system, the design and the data acquisition electronics has been developed at BNC (Figs 3–4).

2.1.2 SANS - Small Angle Neutron Scattering Instrument

The SANS instrument called ‘Yellow Submarine’ (Fig. 1) covers a Q -range from 0.003 – 0.5\AA^{-1} allowing the probing of structures at length scales from 5\AA to 1400\AA . The instrument is installed on the curved neutron guide No. 2, with $4 \times 4 \text{ cm}^2$ cross-section, made from supermirrors. It has a wide range of applications from studies of chemical aggregation, defects in materials, surfactants, colloids, ferromagnetic correlations in magnetism, alloy segregation, polymers, proteins, biological membranes and macromolecules. This instrument is equipped by a $64 \times 64 \text{ cm}^2$ grid area detector filled with BF_3 gas. The detector has a 6-m displacement path in the yellow vacuum tank in order to be able to vary the scattering angle range. The counter and its individual read-out electronic system

has been working properly in the past 25 years; it is, however, to be replaced by a similar ^3He detector with delay-line encoding electronics as soon as the budgetary situation will allow.

BNC operates altogether 15 experimental stations. Besides the 3 instruments described above another suit of 6 *scattering type* devices are equipped by PSD systems (see below). The remaining 6 instruments belong to the neutron/gamma capture and radiography types of instruments, the latter ones are also equipped by state-of-art 2D detector (neutron–photon conversion) and imaging systems (not described in this paper).



FIG. 2. The Powder Diffractometer at the Budapest Research Reactor with its triangular shape PSD detector bank.

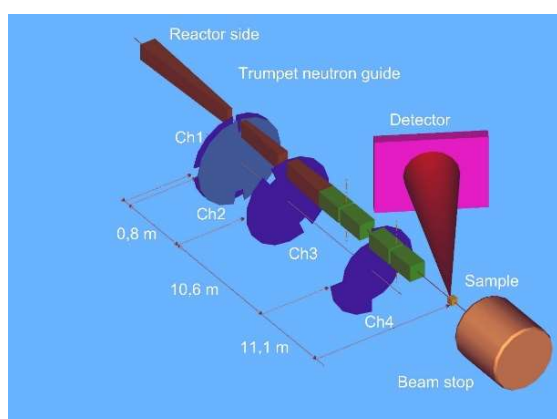


FIG. 3. The scheme of the TOF Diffractometer



FIG. 4. The multidetector bank of the TOF Diffractometer consisting of 150 ^3He tubes of 20 cm length.

2.2 DEVELOPMENT OF AREA DETECTORS FOR NEUTRON BEAM INSTRUMENTATION

In the 2000s, we started to develop a detector family based on the multiwire position sensitive (MWPC) gas chamber counters with delay-line encoding read-out electronic and data acquisition system. The basic design of this kind of detectors was well known [5, 6]. Together with small business companies (www.ante.hu, www.mirrotron.hu) at the BNC campus site, this technology has been developed, and several models of this type have been produced [7].

The principle of such a counter is the following: In a metallic chamber filled with a converter gas, grids of thin wires form an electrode system. When, by capturing a neutron, an ionising event occurs in the converter gas, free electrons are produced and they are accelerated towards the wire electrodes by the external electric field. In the vicinity of the wire, an electron avalanche occurs, a large amplification is provided, and an electric signal is picked up by a preamplifier. The amplitude of this signal is in correlation with the energy of the incident particle capture event and the position of the electron avalanche; i.e., the position of the incident event can be determined.

In the case of a two-dimensional (2D) counters, the anode consists of a central grid between the two cathode wire planes perpendicular to the anode wires. Each set of cathode wires is connected to a delay line read-out system. In

a detection event, the electric charge flow gives pulses at the end of the cathode wires. Then, the signals from each end of a delay line are pre-amplified then passing through fast amplifiers enter to low-level discriminators. The delay time differences are measured for each set of cathodes with time-pulse height converters and these analogue signals are digitized to give an XY position encoded output. Chambers with ^3He converter gas are used and CH_4 is added as stopping gas to limit the proton and triton ranges from the neutron capture. The complete 2D detector systems developed at BNC consist of three major components organically linked together: (i) *The detector chamber* is equipped with the gas filling valves and the electrical connections. The fast preamplifiers are also integrated to the chamber. The entrance window for neutrons is made of aluminium. (ii) The main components of the *Electronic control and data acquisition system* is a fast time-to-digital converter. Adjoining modules such as a constant fraction discriminator, high-voltage power supply, ratemeter, low-voltage power supplies make part of the system. (iii) A *Personal Computer configuration*, with integrated TDC (time digital convertor) card as well as the proper data processing and imaging software. Figure 5 shows the utilization of a MWPC detector for the verification of the brightness at a neutron guide exit by using the ‘camera obscura’ pin-hole imaging technique to feature the transmission imperfections of the neutron optical system [8]. Figure 6 shows some features of this type of detector.

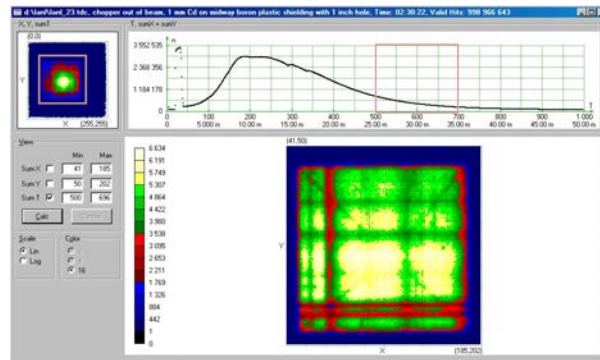


FIG. 5. Electronic testing of a $20 \times 20 \text{ cm}^2$ chamber (top) of an experiment to determine the intensity distribution over a guide exit. The $20 \times 20 \text{ cm}^2$ ^3He detector operates in TOF regime to obtain the neutron wave length distribution simultaneously.

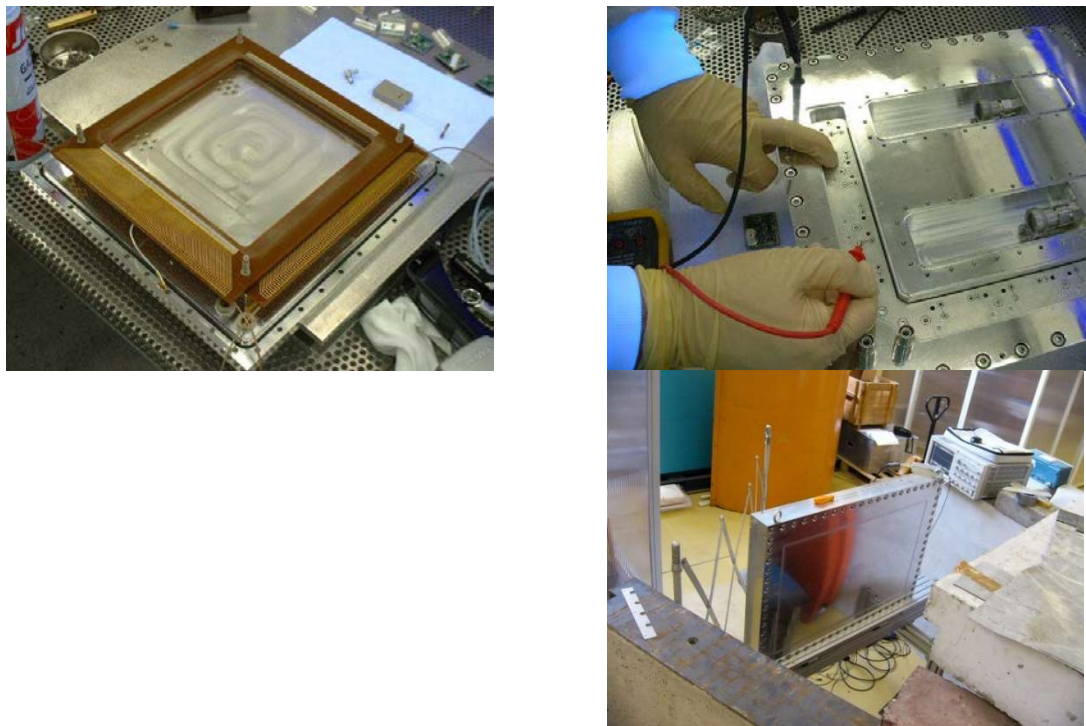


FIG. 6. The electrode system of a MWPC chamber (top left and right), neutron beam testing of a $60 \times 80 \text{ cm}^2$ detector at the BNC test-beamline (bottom)

This detector development activity has resulted at BNC in equipping most of the instruments with up-to-date detector systems. Each of the following instruments benefit from a $20 \times 20 \text{ cm}^2$ ^3He detector: TAST – Thermal Three-Axis Spectrometer, ATHOS – Cold Neutron Three-Axis Spectrometer, MTEST – diffractometer, GINA and REFL reflectometers and the FSANS – focusing small angle scattering spectrometer.

2.3 METHODOLOGY FOR DETECTOR DEVELOPMENT AND TESTING

As a part of the detector R&D activity at BNC, our laboratory has been a partner in a collaboration project on the development of MWPC detectors (EU FP6, NMI3/MILAND). Various types of chambers and readout methods based on ^3He as a gas converter were studied using state-of-the-art detector technologies. In particular, we have aimed to establish a protocol with the description of the parameters and procedures to be used for qualifying the detectors, for comparing counting performances of gas detectors, and in particular to help the decision for manufacturing, testing and utilisation of such detector systems [9].

The following parameters and procedures were considered for the design and fabrication of such kind of MWPC detectors:

- *Chamber design*: Overall dimensions, window thickness and material, weight; definition of the sensitive area, and useful area. Compact design for the overall dimensions, smooth faces for easy construction of shielding. *Detector vessel material*: A comparison of various materials should be made. Al-alloys with different properties should be considered. High-activation materials should be avoided. Zircalloy should be considered as an option. *Detector window thickness*: To be minimised for optimal neutron absorption. Finite element model calculations are to be performed for various geometries and materials. Pre-deformed window shapes can be modelled. The maximum allowed internal pressure is to be defined by model calculations.
- *Electrode system and detection conversion*: Field distortion correction (guard electrodes), Parallax error correction (electrostatic lens), gas mixture, pressure, and conversion gap, Detection conversion efficiency versus neutron wavelength. *Description* of the amplifying and sensing electrodes (wire dimensions and pitch, distance between electrode plans), readout method.
- *Vessel test under pressure (strain measurements)*: The detector vessel will be tested under normal and over-pressure. The window shape deformation will be measured in various directions and compared to the model calculations, strain values will be determined. *Cleaning procedure*: Before filling the detector with the appropriate gas mixture the chamber will be cleaned. Pumping procedures, vacuum values, outgassing by heat treatment, gas flushing are foreseen.

The tentative reference specification for a prototype MWPC was established as in Table 1.

TABLE 1. SPECIFICATION OF THE PROTOTYPE MWPC

Characteristic	Value
Overall dimensions	$450 \times 450 \times 80\text{-(}400\text{)} \text{ mm}^3$
Sensitive area	$320 \times 320 \text{ mm}^2$
Detector window thickness (average)	6 mm
Useful area	$314 \times 314 \text{ mm}^2$
Detector window/vessel material	Al-alloy (e.g. AlZnMgCu _{1.5})
Weight	32–45 kp
Gas mixture	$^3\text{He} + \text{CF}_4$
Gas pressure	3 bar $^3\text{He} + 4 \text{ bar CF}_4$
Conversion gap	30 mm
Field distortion correction	If required
Parallax error correction	If required
Anode wire grid	Au-W, 10 micron, 1 mm pitch
Cathode wire grids	Au-W, 30 micron, 1 mm pitch
X-Cathode-anode-Y-cathode grid distance	3.5–3.5 mm
Spatial (position) resolution (FWHM)	$1 \times 1 \text{ mm}^2$
Detection efficiency (at 0.24 nm wavelength)	70%
Readout method	Individual channels/delay line

Having manufactured a detector, two ways of testing procedure are to be followed:

a) Laboratory tests:

- First, the electronic properties of the system are to be tested:
- Shapes and amplitudes of anode and cathode signals are inspected. The range of amplitudes is determined
- Checking of the hum and noise on all amplifiers' signals, the discriminator thresholds have to be set and adjusted
- The CFD calculation has to be set-up for a minimal contribution of internal walk and thus for best position resolution.
- Control of the effective threshold setting
- Two-dimensional position spectrum homogeneity measurement (>12 hours) using a TDC
- Background measurements in shielding
- Diagrams of counting versus high voltage (HV) recorded with an isotope neutron (e.g. Am-Be) source.
- Gamma sensitivity test of the chamber (with isotope gamma sources).

b) Neutron beam tests

- 'Counting curve' measurements on the anode for a uniform irradiation (homogeneously distributed neutrons are created from the direct neutron beam widened with Plexiglas or a vanadium rod),
- The position resolution (PR) is to be measured in a collimated beam with a cadmium mask with holes of small diameters (0.5, 1, 1.5, 2 and 3 mm). Spots on the detector allow the measurement of PR and linearity
- The Cd mask is moved to get PR versus position on the detection area.
- Measurement of PR versus HV
- Measurement of PR versus inclination angle
- Efficiency test with cadmium mask (e.g. diameter < 1 cm) by comparison to a 'black' (100% absorbing) neutron detector
- Efficiency test for various wavelength values (a monochromatic beam with variable wavelength or white beam with TOF analysis)
- Local and global counting rate capability (use of attenuators).
- Measurements of counting uniformity, stability in time.

2.4 NEUTRON BEAM TESTING FACILITIES AT BNC

In order to perform neutron beam measurements as described above, several beam lines have been accommodated to detector test experiments at the Budapest reactor: The ATHOS 3-axis spectrometer provides monochromatic beam in the 0.2 – 0.6 nm wavelength range. The end position of the cold neutron guide No.3 is available for white beam measurements (see Fig.7), while the TOF diffractometer beamline can be used for thermal neutron white beam or pulsed beam measurements.

2.5 SOLID BORON LAYER DETECTOR PROTOTYPE

Due to its high cross section for neutron absorption and low sensitivity for gamma events, ^3He was an ideal choice as a converter material for neutron detectors up until the end of the 90's. Later on, the worldwide ^3He shortage resulted in a dramatic increase of price and added a strong motivation to find other alternative techniques and solutions.

A promising neutron converter material that can be applied in neutron detectors, typically by creating a thin layer on a substrate with a sputtering process, is ^{10}B . In fact, sputtering boron carbide (B_4C) instead is a much more efficient process; therefore, in most of the cases the latter material is used. Instead of using pure natural boron, a material enriched with ^{10}B is used in order to ensure a higher neutron absorption cross section. The neutron conversion reaction in the material is the following:

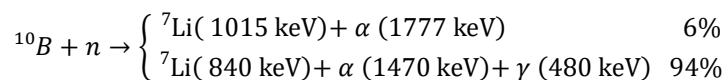




FIG. 7. A Multi-Blade Boron-10-based neutron detector for high intensity neutron reflectometry at ESS is in the testing set-up at the end position of the cold neutron guide No.3 of BNC [10].

The neutron absorption can be detected either by measuring the trace of the alpha particle or the lithium ion. As the ionization process inside the solid boron converter produces a low number of charge carriers, measuring it there is quite challenging task on its own. The applied solution is the well-known gas amplifying process.

A boron layer is placed in a gas-filled chamber. The thickness of the solid boron converter layer is limited in order to minimize the energy loss by ionization inside the solid layer. After reaching the gas volume the charged particle yields its remaining kinetic energy to the surrounding gas by ionization and creates free electron-ion pairs. The created primary electrons travel toward the anode layer. The charge cloud created by the primary electrons is amplified in the proximity of the anode surface by the gas amplification process (secondary ionization).

As the α and the ${}^7\text{Li}$ particles are emitted in the opposite directions, only one of them can escape from the boron layer and ionize the gas by its remaining energy.

Position sensitivity of the detector is based on the working principle of the multiwire proportional gas chambers. The position of the neutron absorption determines the position of the gas amplification that is sensed by cathode wires. The anode plane consists of anode wires, and it is surrounded by two, parallel cathode planes. The direction of the wires of one plane are parallel with the anode wires while the others are orthogonal. Signals are induced in the close cathode wires during the amplification process and based on this layout one cathode plane provides horizontal position while the other provides the vertical position of the event.

The readout method is delay-line based, as this cost-effective solution (compared to the individual readout) is sufficient to demonstrate the working principles of the prototype.

The thickness of the boron layer is limited by the expected average remaining kinetic energy of the escaped particle. We applied a similar thickness to that other detector laboratories have used before. The requirements, arguments, and calculations are published in several articles [11]. As a filling gas, CF_4 has been chosen: it has the highest stopping power compared to the other, commonly used detector gases.

2.5.1 Simulation and results

The main goal of the current development work was to analyze the limitations of position resolution using the described technology. A three-dimensional model was used for the simulation of the ionization process in order to specify the optimal pressure of the filling gas. The model (Fig. 8) considers the neutron penetration depth into the boron layer, the direction of the ionizing particles, the remaining kinetic energy and the pressure of the filling gas as an input parameter.

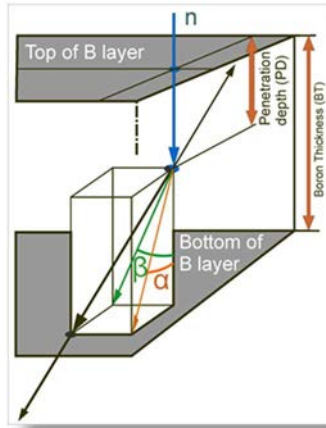


FIG. 8. Three-dimensional model of simulation.

The energy loss in the solid layer has been simulated by the SRIM software (Fig. 9). Li or alpha particle ionization occurs with the same probability. This principle comes from simple geometrical considerations of the opposite flying directions of the particles. A particle ionizes the CF_4 gas having escaped from the solid layer, and loses all of its remaining kinetic energy. Ionization lengths in CF_4 gas at different pressures are calculated by SRIM (Fig. 10). The end of the prolate shape ionization cloud is sensed by the delay-line readout. The position resolution can be simulated using this track-end method. The remaining energy and position resolution are simulated in Matlab.

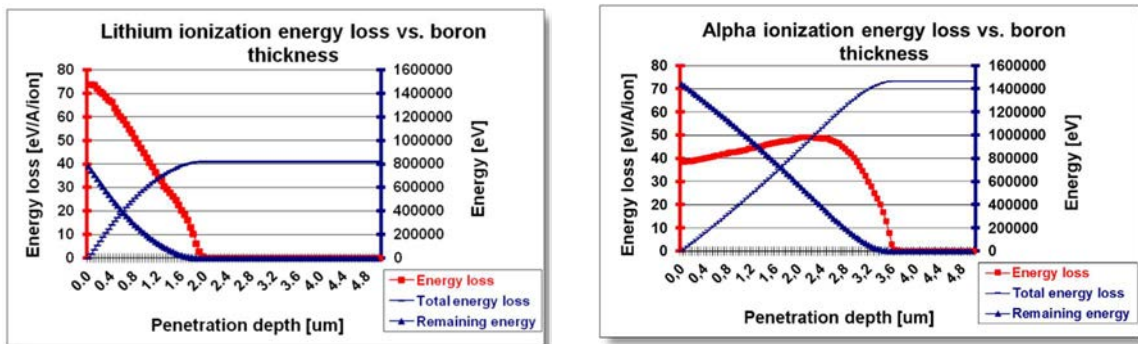


FIG 9. Remaining kinetic energy after escape from the solid layer

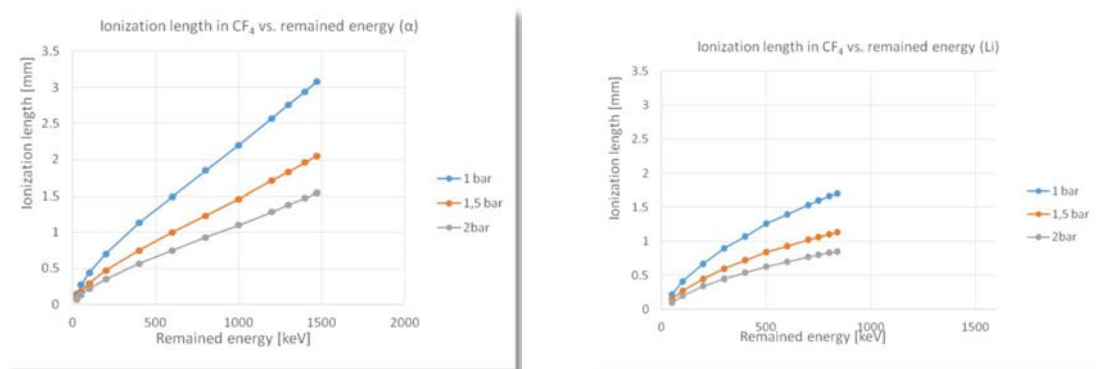


FIG. 10. Ionization length in CF_4 gas at different kinetic energies and gas pressures

The simulated position resolution at 2 bars of CF_4 filling gas is shown in Fig. 11. Theoretical position resolution characterized by the full width at half of maximum is expected about 0.4 mm. This is a fundamental limit and real position resolution of the detector will be modified by the dispersion of the noise and electronic measurement system.

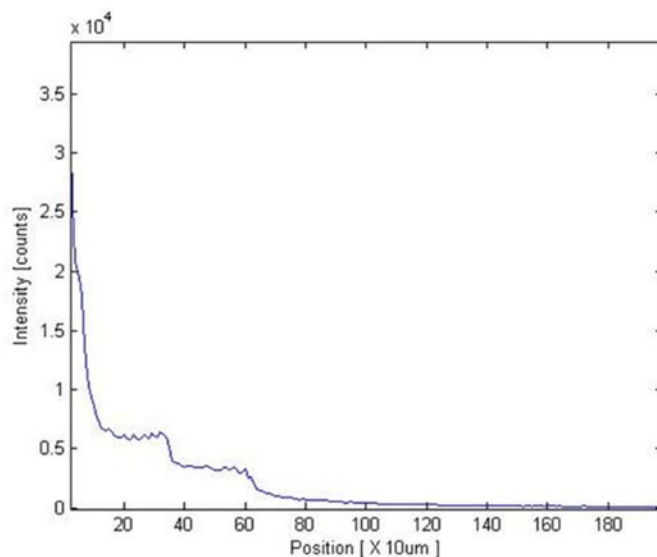


FIG. 11. Theoretical response of a pointwise neutron illumination at 2 bars of CF_4 .

2.5.2 Prototype detector details and experimental design

The simulation results are validated by experimental results on a prototype chamber (Fig. 12). The chamber is built from aluminium for low neutron absorption of the entrance window. The thickness of boron layer was $1.5 \mu\text{m}$ to ensure a high remaining energy and high probability of escaped ionizing particles. The detector was filled by 2 bars of CF_4 . The diameter of the anode wires was $10 \mu\text{m}$ for the high gas gain, while the diameter of the front cathode wires was $30 \mu\text{m}$ for more robust readout construction. The back cathode plane was a simple PCB with readout strips eliminating the elongation effect of the wires. The wire pitch was 0.8 mm.

Measurements were performed at the ATHOS instrument using a monochromatic collimated cold neutron beam. Position resolution has been measured at several anode high voltages as it has significant effect through changing the signal to noise ratio.

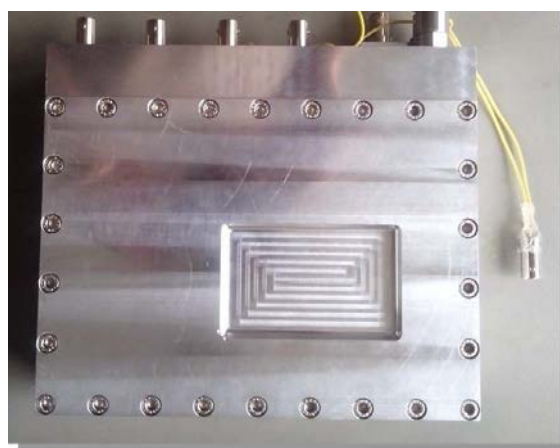


FIG. 12. Prototype detector with $80 \text{ mm} \times 50 \text{ mm}$ active area.

The full widths at half maxima are shown in Fig. 13. Extrapolation to higher voltages gives a limit for the position resolution of 0.68 mm (Fig. 14). A thin vertical slit has been used to collimate the direct, monochromatic neutron beam. The slit was positioned perpendicular to the anode wires to eliminate the effect of the discrete distribution of the anode wires. The two-dimensional results have been integrated vertically in order to get the horizontal distribution of the measured results. Anode high voltage was limited at 4500 V due to the risk of electrical breakdown.

In order to analyse the local dependency of the position resolution and the position linearity the detector has been moved behind the thin slit horizontally in 0.23 mm fine steps (Fig. 15). Measured positions are determined by centre of a fitted Gaussian curve. No local effect was observed due to the sensing wires. The average position linearity error is better than 1%.

A homogeneously distributed neutron beam was measured as a proof of concept as shown in Fig. 16. This result validates the detector as a two-dimensional neutron counter. The ratio between the length of the horizontal and vertical side is consistent with the real size of the detector. This demonstrates the distortion-free position mapping of the detector.

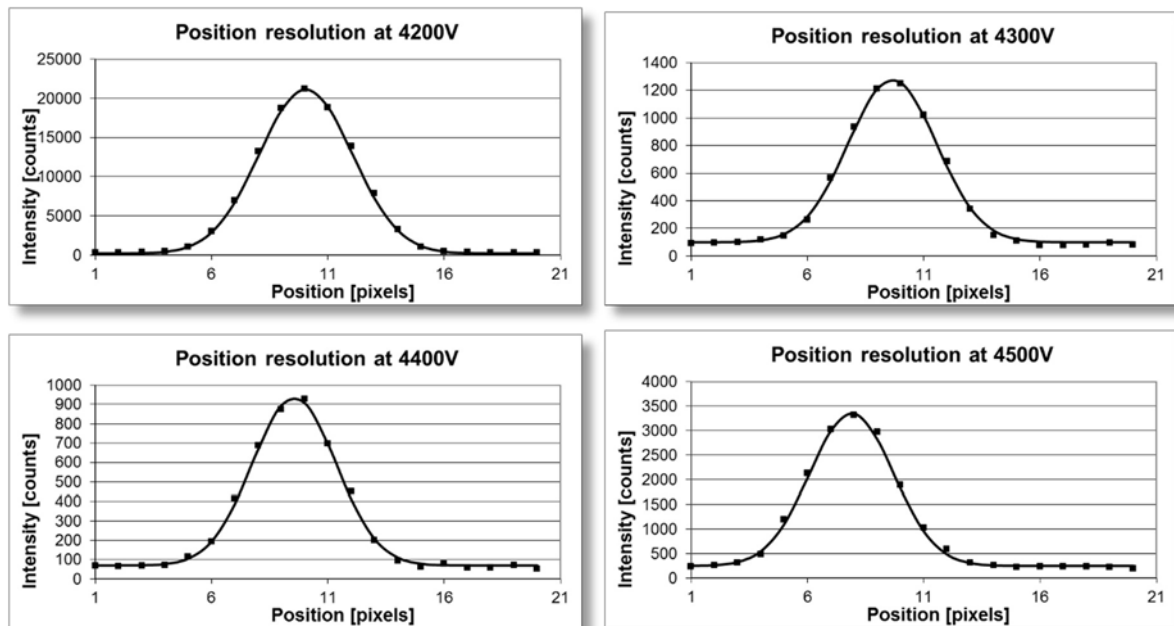


FIG. 13. Full width at half of maximum at different anode high voltages after deconvolution with the real slit size.

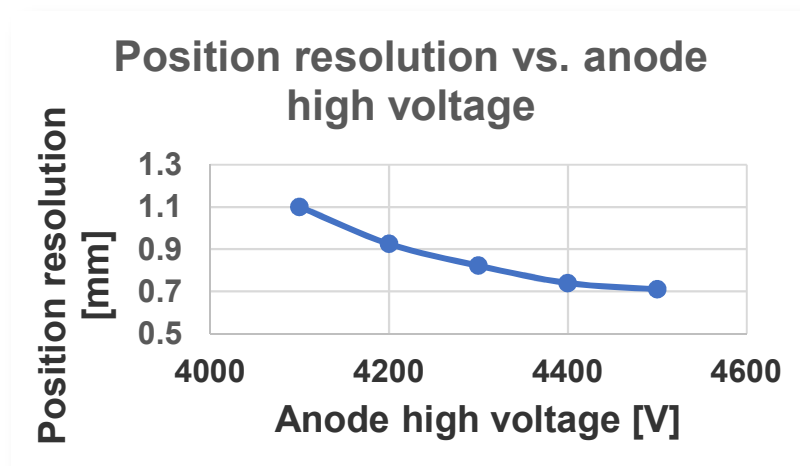


FIG. 14. Position resolution measured at different high voltages.

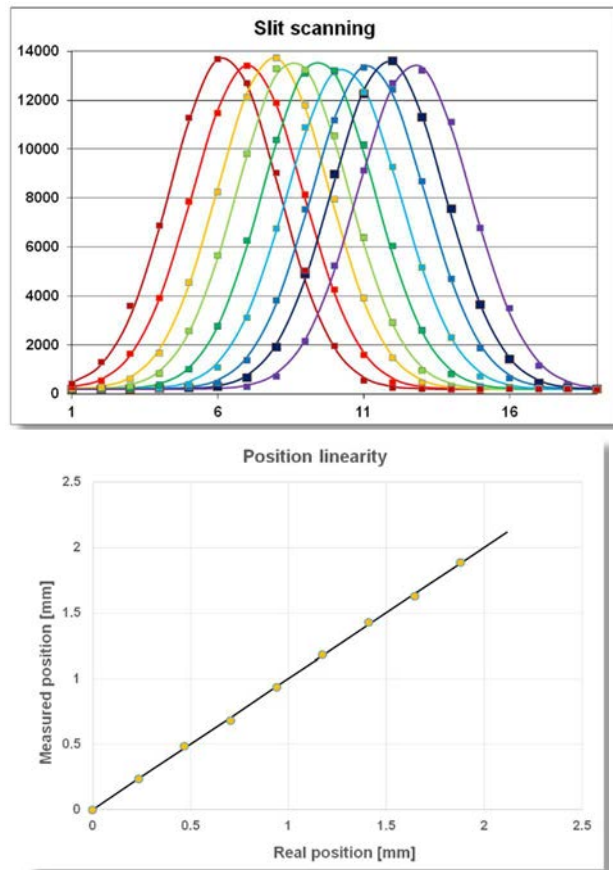


FIG. 15. Results of fine scanning.

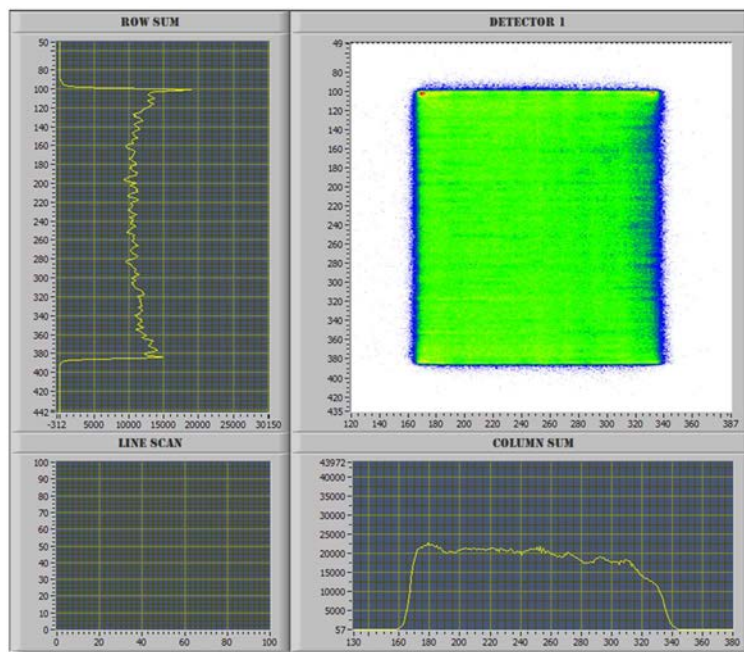


FIG. 16. Two-dimensional neutron beam test measurement.

3 CONCLUSIONS

A two-dimensional position sensitive neutron counter based on solid boron converter and optimized for position resolution has been simulated and experimentally validated. A three-dimensional model was developed for the simulation. A fundamental limit for position resolution is calculated at 2 bars of CF₄ filling gas. A prototype multiwire proportional chamber based on delay-line readout was built for experimental measurements. Position resolution, position linearity, and two-dimensional test measurements were carried out. For the future development programme we are going to work to decrease the noise level in order to improve the position resolution of the detector. A further improvement could be the use of boron multilayers to increase the efficiency of the detector.

ACKNOWLEDGEMENTS

Acknowledgment is made for the support of a part of this work from the EU H2020 BrightnESS project (GA No. 676548) and national grant TÉT_13_DST-1-2013-0017.

REFERENCES

- [1] ROSTA, L., BARANYAI, R., Budapest Research Reactor – 20 years of international user operation, *Neutron News*, **22**, 31-36 (2011)
- [2] ROSTA, L., Cold Neutron Research Facility at the Budapest Neutron Centre, *Appl. Phys. A* **74** (2002) S52–S54
- [3] ROSTA, L., Introduction to Neutron Beam Experiments, Research Instruments at the Budapest Neutron Centre, Füzi, J., Len, A., Bajnok, K. (Eds), Budapest (2017) p. 11–23
- [4] CSER, L., DEÁK, F., KOCSIS, M., Linear position sensitive detector at Budapest's WWR-SM Research Reactor. *Sci. Instrum.* **1** (1986) 21–28.
- [5] GABRIEL, A., *Rev. Sci. Instrum.* **48** (1977) 10.
- [6] FISCHER, J., RADEKA, V., BOIE, R.A., Position Sensitive Detection, Academic Press (1983) 129p.
- [7] CSER, L., et al., Neutron measurements on MK 200N-1 type 2-dimensional delay-line position sensitive detector with the new OTDCv1.11 time to digital converter, *Physica B* **276–278** (2000) 216.
- [8] FÜZI, J., et al., Neutron optical imaging study of neutron moderator and beam extraction system, *Physica B* **385–386** (2006) 1315–1317.
- [9] BUFFET, J.C., et al., Advances in detectors for single crystal neutron diffraction, *Nucl. Instrum. Methods A* **554** (2005) 392–405.
- [10] PISCITELLI, F., et al., The multi-blade boron-10-based neutron detector for high intensity neutron reflectometry at ESS, *J. Instrum.* **12** (2017) P03013.
- [11] PISCITELLI, F., et al., Study of a high spatial resolution ¹⁰B-based thermal neutron detector for application in neutron reflectometry: the Multi-Blade prototype, *J. Instrum.* **9** (2014) P03007.

STRATEGY OF EQUIPPING THE PIK REACTOR EXPERIMENTAL STATIONS WITH DETECTION SYSTEMS

A. KRIVSHICH

High Energy Physics Division,
Petersburg Nuclear Physics Institute (PNPI) of National Research Centre «Kurchatov Institute»,
Russia
Email: krivshich_ag@pnpi.nrcki.ru

D. ILYIN

High Energy Physics Division,
Petersburg Nuclear Physics Institute (PNPI) of National Research Centre «Kurchatov Institute»,
Russia

R. HALL-WILTON

European Spallation Source, Lund,
Sweden

Abstract: An analysis of the PIK reactor (PNPI, Russia) instrumental facility with regard to compliance of the neutron detectors with all the required operational parameters was performed based on analysis of detectors and strategic trends of their development in leading neutron research centres of the world and analogous centres in Russia over a period of more than 50 years. An attempt is made to estimate the development of neutron detector technologies for the next 10 years. A strategy outline as to how these requirements might be tackled by novel detector developments is shown. Despite the high price of ^3He , the global neutron community still considers gas-discharge ^3He -detectors to be the basic development direction for reactor-based sources for detectors with a detection area of up to 1 m^2 . The reason for this is a unique combination of such properties as high efficiency of neutron registration and low γ -background sensitivity. This strategy has at its basis to be able to produce optimally performing detectors that allow the PIK reactor instruments to be world leading.

1 INTRODUCTION

Due to the appearance of new high-intensity neutron sources and new high-performance neutron focusing optical systems, the intensity of neutron beams has increased significantly over the past 10–20 years. General technical progress and the new ideas implemented into the construction of the experimental stations and new detector systems has allowed performance in the field of neutron scattering research that until recently seemed impossible.

The necessity to develop and apply new research methods for both the study of the new class objects and search for solutions of experimental tasks at the highest level requires equipping the PIK reactor instrumental infrastructure with state-of-the-art neutron detection systems produced in Russia and worldwide. The PIK reactor is being constructed in Petersburg Nuclear Physics Institute named by B.P.Konstantinov of National Centre ‘Kurchatov Institute’ (hereafter referred to as PNPI).

The quality of information received within a modern experiment quite often depends directly on the practical realization of a combination of interconnected (and sometimes mutually contradictory) maximum attainable characteristics of the detection systems. Namely, large registration area, high neutron rate requirements and spatial resolution, low noise level, high performance within the whole required wavelength range of neutrons, very low sensitivity to background radiation, high stability of functional specifications, low cost, and maintainability.

The aim of the present work is to develop strategies of equipping the PIK reactor experimental stations with the detection systems based on three main factors:

- analysis of experience accumulated by the leading neutron research centres **over the last 40 years**;
- clear understanding of **the current state that has developed over the last 10 years** and ways to continue to realize the development trends of current detection technologies;
- estimation of the global trends of development of detection technologies and definition of concept of their further development **for the next 10-15 years**.

It is clear that the concept of development of neutron detectors for experimental stations of the PIK reactor should be based on the experience of the leading Russian and international neutron research centres, such as ILL (France), J-PARC (Japan), ESS (Sweden), FZ (Jülich, Germany) etc.

2 ANALYSIS OF THE EXPERIENCE OF WORLD-LEADING RESEARCH CENTRES IN NEUTRON DETECTOR CONSTRUCTION.

2.1 EXPERIENCE OVER THE LAST 40 YEARS: ANALYSIS OF ILL, FRANCE.

In order to produce neutron detectors for the experimental stations of the PIK reactor, it is essential to take into account the knowledge and experience of specialists working in the field of development of various types of neutron detectors around the world.

ILL is currently the unofficial world capital of neutron research [1]. Experience of neutron experiments has been accumulating in this Institute for over 40 years with world-leading experts from many different countries contributing to it. Unique world-class experimental stations were created, and their parameters were optimized based on simulations and experiments.

The structure of the instrumentation base in the main neutron centres of the world is approximately the same as in ILL. The neutron flux density of the PIK reactor is similar to that of the High-Flux Reactor (HFR) reactor at ILL, which essentially makes the PIK reactor a potential future successor of the HFR. For this reason, it would be reasonable to copy both the general instrumentation structure of ILL and appropriate types of neutron detectors, and to apply this knowledge to the PIK reactor installations. Various devices at ILL have been brought to perfection, and their parameters optimized based on simulations, testing, and experiments.

The classification of the types of detectors used for the ILL experimental stations and detection technologies are presented in Table 1.

TABLE 1. CLASSIFICATION OF THE TYPES OF DETECTORS USED AT ILL

Detection technology	Type of detector	Amount
Gas-discharge detectors based on ^3He converter	Proportional counters (^3He)	9
	Multidetectors and installations based on proportional counters	14
	Single- and multi-module microstrip detectors (MSGC)	6
	^3He 2D PSD	10
	Neutron beam monitors	4
Total		43
Scintillation detectors based on solid-state converters (^6Li and ^{10}B)	Scintillation detectors based on ZnS / LiF	2
	Scintillation detectors ImagePlates	2
Total		4

It is obvious that, despite the ^3He deficit, the leading European neutron research centre, ILL, uses detectors with ^3He as a converter gas in the vast majority of its experimental stations (43 out of 47).

2.2 CURRENT STATE OVER PAST 10 YEARS: ANALYSIS OF J-PARC, JAPAN

The MLF (Materials and Life Science Experimental Facility) neutron research centre was founded in J-PARC, Japan [2]. MLF uses a high-intensity pulsed spallation neutron source generated by a proton beam at 3 GeV, 333 μA current and 25 Hz operating frequency.

Implementation of new scientific and applied research programmes required new experimental stations equipped with new detectors. An analysis showed that in order to use ^3He -detectors it would be necessary to acquire more than 10 000 litres of this gas. Taking into account the rise in price, such an acquisition would require a serious financial investment – more than 20 million dollars for a period of 5 years.

It was, therefore, decided to use scintillation technologies for detectors having a complex surface geometry and a wider aperture (5 stations). In order to comply with the required detector parameters, standard scintillators based on ZnS / ^6LiF were dismissed in J-PARC and ceramic scintillators based on ZnS / $^{10}\text{B}_2\text{O}_3$ were put into operation. This allowed them to improve the parameters of existing scintillation detectors, enhancing their operational speed, efficiency, decreasing their afterglow and so on. With these enhancements, the efficiency of such scintillation detectors achieved about 70% of the efficiency of ^3He -detectors (4 bars). This work required creation of a new ‘scintillation’ infrastructure in J-PARC and more than 10 years of hard work.

Currently, it can be said that the situation with the application of different types of detectors is optimally balanced in J-PARC instruments. The proportion of experimental stations with different types of detectors is demonstrated in Fig. 1 (the stations with scintillation detectors are shaded yellow and the stations with ^3He -detectors are shaded red) [3]. It is obvious that most detectors are ^3He -detectors. They are used in order ‘to cover’ larger areas, to work in high-intensity neutron-beams – up to $1 \times 10^8 \text{ cm}^{-2} \cdot \text{s}^{-1}$, and to work with relatively small apertures (up to $300 \times 300 \text{ mm}$) when the delay line readout method is used (with only five channels of registration electronics), which significantly reduces the cost of the detector. The J-PARC centre is equipped with more than 21 experimental stations, most of which (about 75%) use gas-filled ^3He -detectors.

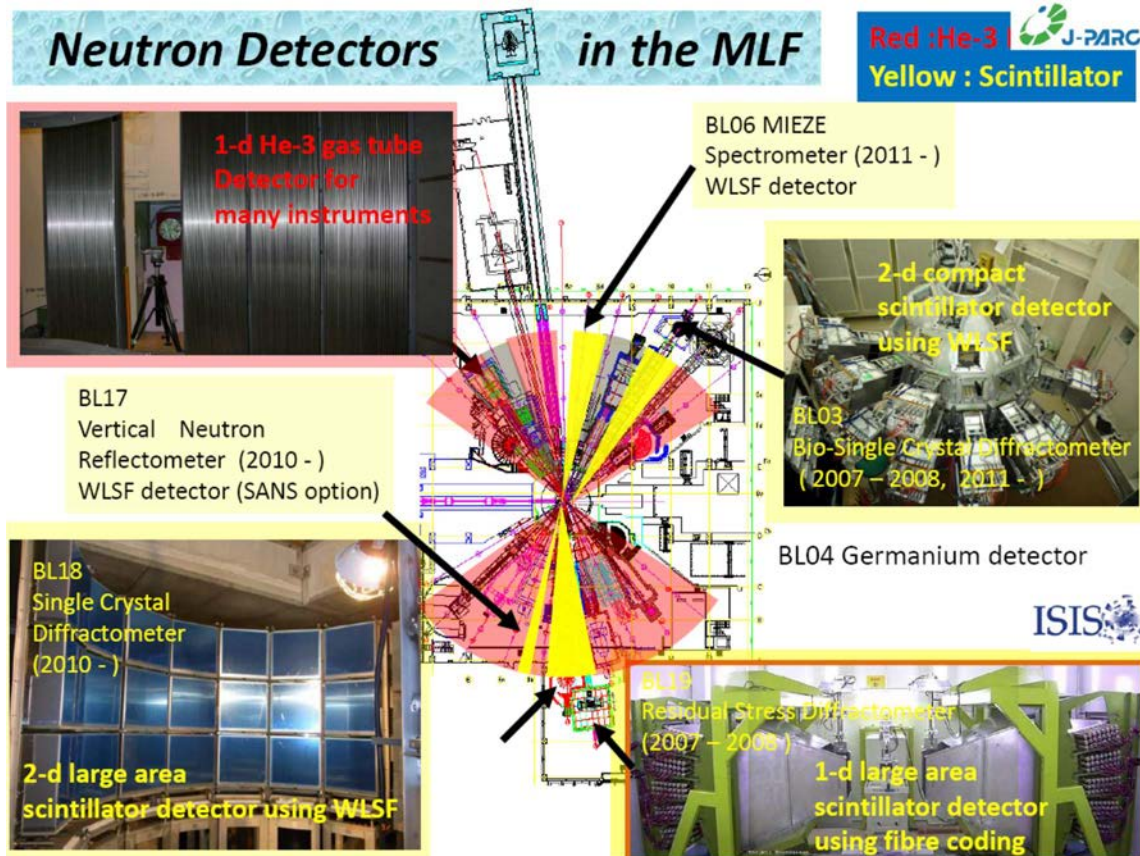


FIG. 1. Location and structure of neutron detectors at MLF experimental stations (J-PARC).

2.3 ESTIMATION OF THE GLOBAL TRENDS FOR THE NEXT 10–15 YEARS: EUROPEAN SPALLATION SOURCE (ESS, SWEDEN).

ESS is currently being built in Lund (Sweden). The first neutrons are planned to be generated in about 2020. It is also planned that ESS with its initial suite of experimental stations will be put into operation no later than 2025.

An international expert group was created in order to perform analysis of the technical requirements for ESS experimental stations and the neutron detectors required for them [4–6]. The analysis presented here is based on the initial suite of 22 instruments, put forward in the ESS Technical Design Report in 2013.

It appeared that the total area of neutron detectors exceeded 280 m^2 . More than half the area is reserved for three installations – 3 chopper spectrometer instruments (80 , 50 and 30 m^2). The total number of channels of registration electronics is quite large as well, it exceeds $60\,000$. It is worth noting that only two experimental stations should have a spatial resolution of 0.1 mm . The spatial resolution of other detectors should vary in the range of 1 – 10 mm , which is possible to achieve with existing technology. A major challenge for neutron detectors at ESS is the extreme instantaneous rate environment.

In the course of the analysis, all the detectors were divided into four categories according to their registration area: (i) large-area detectors (2 stations); (ii) high-resolution medium-area detectors (9 stations); (iii) small-area detectors $\leq 1 \text{ m}^2$ (9 stations) and (iv) ultrahigh-resolution detectors (2 stations).

The detectors from the first two categories occupy about 90% of the total area of all the detectors. In order to produce them using ^3He -technology, it would be necessary to acquire more than 25,000 litres of ^3He , which is quite a large sum at current European prices – about 50 million dollars. The need to decrease the expenses involved in ^3He acquisition essentially defined the choice of the strategy of detector production:

- Detectors in categories (i) and (ii) will not be based on ^3He ;
- Many of the nine small area detectors (category iii) are to be based on ^3He -detectors with the aim of ensuring the maximum attainable performance. This represents 9 of 22 experimental stations (40%).
- Ultrahigh-resolution detectors (category iv) can be produced based on scintillation detectors or gas-filled detectors GEM or Micromegas.

Production of detectors that do not use ^3He will be implemented in three basic directions. Their development requires significant financial investments and serious efforts from the international community [4–6]:

- $^6\text{LiF} / \text{ZnS}$ and $\text{B}_2\text{O}_3 / \text{ZnS}$ scintillation detectors with WLSF (wavelength-shifting fibre) readout;
- Gas detectors with a ^{10}B solid converter;
- Position-sensitive gas detectors based on BF_3 .

For ESS, the primary choice as ^3He -replacement technology has been decided to be gaseous detectors with a ^{10}B solid converter.

On the way to the creation of new detector technologies, there are a lot of open questions and difficult outstanding issues that have to be solved, so that the performance of new detectors comes as close as possible to that of modern ^3He -detectors.

The developers will have to take into account the following parameters for new detectors: the efficiency should be equivalent to that of ^3He -detectors; they should be capable of operating in high-intensity neutron beams; they should possess a low sensitivity to γ -background – the key factor for many experiments; there should be an essential reduction of costs of large area detectors.

2.4 SPECIFIC DETECTOR INFRASTRUCTURE IN SEVERAL OTHER WORLD LEADING NEUTRON CENTRES

2.4.1 Current state of neutron detectors and trends in their development at Russian research centres

The neutron detectors that are currently the most widely used in the Russian Federation can be divided into two main categories: gas-filled detectors and scintillation detectors.

Gas-filled detectors. Russian experts took notice of favourable conditions in Russia for the production of ^3He position-sensitive detectors (PSDs) up to $300 \times 300 \text{ mm}^2$. PNPI and JINR groups have been successfully developing and producing such detectors and are widely experienced in this field. A group from the Institute for Nuclear Research of the Russian Academy of Sciences (INR RAS, Troitsk) now works with such detectors as well. Many years of activity in this direction have allowed one to develop stable technologies for the production of gas-filled PSDs. The relatively easy availability of ^3He in Russia and its lower price (in comparison with global prices) act as a powerful motivator to continue working with ^3He gas-filled PSDs.

Detection systems based on helium counters operate at the IBR-2M reactor of JINR Laboratory of Neutron Physics (hereafter, LNP) as a part of the following experimental stations: NERA, SKAT EPSILON, DN-12, DIN-2PI, and at the reactor VVR-M of PNPI. The possibility to measure both coordinates by means of mutually orthogonal cathode planes in a proportional chamber allows one to use 2D PSDs to perform measurements for small-angle neutron scattering. Detectors of this type are used in the spectrometers REFLEX, GREINS, DN-2 at LNP JINR and at INR RAS (Troitsk) etc.

For neutron beam monitors, low efficiency is needed – typically in the region of one ten-thousandth of a percent. In order to reach such a low level of detection efficiency, the monitor was filled with a gas mixture of 50 mbar ^3He + 950 mbar CF_4 . The monitor was used to measure the profiles of the IBR-2M reactor beams. N_2 is added to the mixture as a converter gas in order to be able to work with ultra-high fluxes ($\geq 10^7 \text{ cm}^{-2} \cdot \text{s}^{-1}$).

Scintillation detectors. Scintillation methods are particularly attractive in time-of-flight neutron spectrometers. This is due to the fact that in scintillation detectors the detection layer is by an order of magnitude thinner than

and, consequently, their time-of-flight resolution is better than that of gas-filled detectors. A higher sensitivity of scintillation detectors to γ -background does not affect the results of time-of-flight experiments. In addition to a high efficiency of thermal neutron registration ($\lambda \leq 1 \text{ \AA}$) and time resolution of less than a few microseconds, such detectors are capable of a spatial resolution of about $100 \text{ }\mu\text{m}$.

JINR and PNPI developed scintillation detectors jointly already in the end of 1990s. This design solution was further developed in RASTR detector for the D7a diffractometer ($\lambda \leq 1.53 \text{ \AA}$, interplanar spacing resolution $\Delta d/d = 0.2\text{--}0.3 \%$) of IMP UB RAS. The experience in the production of modern scintillation detectors gained by LNP JINR is the basis for the future joint developments of PNPI and JINR physicists to be used in the PIK reactor

2.4.2 Forschungszentrum Jülich (FZ Jülich, Germany)

FZ Jülich possesses over 30 experimental stations, most of which are at FRM-II in Germany, three of which are in ILL, three in SNS, and two under construction [7]. Several instruments are planned as a contribution to ESS. The majority of these stations are designed for elastic (15 instruments) and inelastic (13 instruments) neutron scattering instruments.

The analysis shows that more than 70% of the stations use ^3He -detectors that are implemented as 2D PSDs (aperture – up to $500 \times 500 \text{ mm}$, spatial resolution – 2 mm) and proportional counters (from 100 to 1000 mm long).

2.4.3 Brookhaven National Laboratory (BNL, USA)

BNL no longer has a research reactor themselves, but previously implemented a research development programme focused on creation of high-precision thermal neutron PSDs and equipping experimental stations of national research centres (USA) with them, in particular for the SNS for structural biological and chemical research [8].

All the BNL detectors are ^3He -detectors based on proportional chambers with the data readout from cathode strips.

2.4.4 Some other centres

In other centres, for instance the Rutherford Appleton Laboratory (RAL, UK) at the ISIS source or Oak Ridge National Laboratory (ORNL, USA; SNS spallation source and the HFIR reactor), the correlation of gas-filled and scintillation detectors is a little more balanced. RAL has been successfully using scintillation technologies for neutron registration. The higher importance of time resolution at a pulsed spallation source, along with the better efficiency for lower wavelength neutrons is the primary motivation behind the higher proportion of scintillator detectors at spallation sources.

3 FINAL ANALYSIS OF THE GLOBAL TRENDS OF NEUTRON DETECTOR DEVELOPMENT

Based on the analysis of the most significant Russian and international neutron research centres and on their development trends drawn out in the course of the analysis (some of them were mentioned above), one can propose a strategy of development of neutron detectors and equipping experimental stations of the PIK reactor. The results of the analysis and prediction of detection technology development based on it demonstrate clearly the development strategies of neutron detectors over the period of more than 60 years (40 years of past + 'current' period of the last 10 years + about the next 10 years of the future) based on three main international neutron centres.

1. Analysis of the neutron detector structure established over the last 40 years is presented in the example of ILL experimental stations. In course of these 40 years, unique world-class experimental stations were created, and their parameters were optimized based on simulations and experiments. The vast majority of detectors (90%) are gas-filled devices using ^3He as a neutron converter.
2. A current state and practical implementation of 'current' development trends of detection technologies (over the last 10 years) were analysed using the example of the MLF centre (Materials and Life Science Experimental Facility) active as a part of Neutron research centre (J-PARC, Japan). About 75% are gaseous detector devices using ^3He as a neutron converter. Implementation of new scientific and applied programmes required creation of new complex experimental stations (5 units) equipped with the detectors based on scintillation technology.
3. The estimation of the global trends of detection technology development and generation of their development strategies (for the next 10 years) were considered based on the baseline ESS instrument suite from the Technical Design Report as an example.

The small-aperture detectors ($1 \times 1 \text{ m}^2$ and less) are in many cases planned to be produced based on ^3He -technology. These represent 9 of 22 experimental stations (40%).

Nine more detectors (40%) having medium and large aperture (from $1 \times 1 \text{ m}^2$ to $80 \times 80 \text{ m}^2$) will be created based on the following technologies: scintillation detectors and gaseous detectors based on ^{10}B solid converters. It is assumed that for the next 5–7 years these technologies will reach such a level that their performance could approach ^3He -detectors.

Therefore, the global neutron community still considers gas-discharge ^3He -detectors to be the basic development direction at least for the next 10 years. This is due to the outstanding combination of properties of detectors using ^3He as a neutron converter, which has defined the tendency of neutron centres to use such detectors throughout their history.

A transition to different detection technologies based on ^6Li and ^{10}B converters that are being currently developed is mostly caused by necessity and aims to reduce the costs of devices by abandoning the use of ^3He in large-volume detectors. At the same time, it should not cause an intention to upgrade all the detector nodes of the instruments, as, on one hand, it would require a significant financial investment, and on the other hand it would guarantee a change of a number of characteristics of devices for the worth: registration efficiency, spatial resolution, γ -background sensitivity and so on.

It is necessary to perform a detailed and thorough analysis of the applicability of different detection technologies to a specific physical task, and specific physical instrument. For instance, scintillation detectors are effective in cases when it is necessary to achieve a high spatial resolution ($\sim 100 \mu\text{m}$) and to build a complex geometry registration surface.

4 ANALYSIS OF THE ISSUE OF ^3HE DEFICIT

An analysis of the ^3He demand for neutron detectors operating in experimental neutron scattering centres has been presented [9–13], see Table 2. It should be noted that this is a minimum estimate of a global ^3He demand. For instance, the Table does not include the information of ESS detectors requiring more than 25 000 litres of ^3He .

Based on the comparative analysis of the data presented in Table 2, it is possible to state that the demand from the experimental facilities of the PIK reactor for ^3He is small, around 900 litres, which is a great deal less than the amount required by many major national or international centres.

TABLE 2. ANALYSIS OF ^3HE DEMAND IN THE LEADING NEUTRON CENTRES OF THE WORLD

Neutron centres	Exploitation of detectors and research	New small-aperture detectors	New large-aperture detectors
	l/g	[Litres]	[Litres]
ORNL (SNS)	100	1 300	25 000
ORNL (HFIR)	100	1 210	2 500
Los Alamos	100	1 994	12 362
NIST	100	560	40
BNL	50	180	
FRM-II	100	650	4 500
HZ Berlin	100	520	7 850
ILL	100	1 000	3 000
JCNS	40	15	7 200
LLB	50	600	600
PSI	50		2 000
STFC (ISIS)	100	400	11 300
J-PARC	100	40	16 100
JRR-3	31	71	
KAERI	150		2 000
CSNS	200		21 000
Total	1 431	8 540	115 372
The PIK reactor	10	900	0

One can see (see Tables 3 and 4) that about 70 % of neutron detectors are ^3He -detectors, which corresponds well with the global trends of development. The cost of ^3He for the PIK reactor is relatively low (one-time investments of ~ 900 000 USD) and the advantages gained by the international neutron research centre PNP based at the PIK reactor are positively significant, such as:

- Detectors based on ^3He have a generally accepted unique combination of performance characteristics;
- PNPI already possesses technologies necessary for development and production of neutron detectors with apertures up to 300×300 mm (and more), which guarantees compliance with the many requirements for modern neutron detectors. It does not require significant financial investment in technology. A technological modernization would, however, be required to create detectors with apertures of 1000×1000 mm;
- There are almost no sources of ^3He acquisition in Europe, and its price there is very high.
- For this reason, the European scientific community is actively searching for alternative neutron converters and conceptually new construction ideas in order to create detectors that could replace ^3He detectors.

TABLE 3. TYPES OF DETECTORS PROPOSED FOR APPLICATION AT THE PIK RESEARCH COMPLEX

Device/ detector	Gas neutron converter(^3He)		Solid neutron converters (^6Li and ^{10}B)	
	Proportional counters and 2D-modules based on LPSC (Linear Position Sensitive Counter)	2D PSD	Scintillators	Solid-state detector
Powder diffractometers	3 (D1, D2, D3)	–	–	–
Crystal diffractometers	–	3 (DC1, DC3, DC5)	3 (DC3, DC4, DC6)	–
Inelastic scattering spectrometers	2 (IN4)	1 (IN2)	3 (IN1, IN3, IN5)	–
Small-angle instruments	2 (S2, S3)	3 (S1, S4, S5)	–	–
Reflectometers	4 (R1–R4)	4 (R1–R4) 2 (R2, R3)	–	–
Total number	11	13	6	–

TABLE 4. DETECTORS OPERATING IN NEUTRON BEAMS OF DIFFERENT INTENSITIES AT PIK

Intensity of neutron beams, [neutron / s]	Experimental stations	No. detectors [units]	Detector technology
Up to 1×10^5	S1	1	2D PSD (^3He)
	D2, IN2, IN4 (2 un.)	3	^3He proportional counters and LPSC
	IN1, IN3	2	Scintillators
Up to 1×10^6	DC1–DC5, DC7, S3, S4, S5, R1, R2, R3, R4	12	2D PSD (^3He)
	D1, D3, S2, R1–R4	7	^3He proportional counters and LPSC
	DC3, DC6, IN5	3	Scintillators
	Beam monitor (R2, R3)	2	2D PSD (^3He -technology)
Up to 1×10^7	none	0	^3He proportional counters and LPSC
	none	0	Scintillators
Total number		30	

^3He is available in Russia, and its price is several times lower than the European one. For this reason, detectors based on ^3He are our competitive advantage over Europe, which certainly should be used to the fullest extent.

5 ANALYSIS OF THE PIK REACTOR PLANNED INSTRUMENTAL FACILITY AND RECOMMENDATIONS ON EQUIPPING THE EXPERIMENTAL STATIONS WITH NEUTRON DETECTORS

An analysis of the PIK reactor instrumental facility with regard to compliance of the neutron detectors with all the required operational parameters was performed based on analysis of detectors and strategic trends in their development at leading neutron research centres of the world and analogous centres in Russia [14].

The detectors that are planned to be used at the experimental stations of the PIK reactor are presented in a summary Table 3. Requirements for beam intensity requirements of detectors with ^3He -converter are presented in Table 4. A background level and γ -background sensitivity are stated as maximum loading capability / background count of $\geq 10^6$) and a lowest possible sensitivity to γ -background ($< 1 \times 10^{-7}$).

It is clear from Tables 3 and 4, which detection technologies should be given a high priority for development at PNPI.

Helium-3 detection technologies necessary for equipping the majority of experimental stations of the PIK reactor either exists in PNPI or can be produced there, as there is the technological capacity for their development and realization.

1. *Beam intensity: up to 1×10^5 neutron/s.* PNPI already possesses technologies necessary for development and production of neutron detectors with apertures up to 300×300 mm (and more), which comply with the requirements of current physical experiments (Fig. 2). Creation of such detectors does not require any significant financial investments in their development stage. Based on these technologies, one can create ^3He -detectors of different structural variations including the capacity to operate in vacuum.
2. *Beam intensity: up to 1×10^6 neutron/s.* For the existing 2D PSD ^3He -detectors to be able to work in intensive neutron fields, it is necessary to change the data readout method from a delay line readout to channel-by-channel readout from the cathode strips.
3. *Beam intensity: up to 1×10^7 neutron/s and higher.* If the experiment requires the detector to operate in a counting mode with efficiency close to 100 %, then it is necessary to perform a detailed analysis of a new detection technologies such as 2D LPSC; GEM-technology, pad-structural gas-discharge detectors, scintillation detectors, etc.

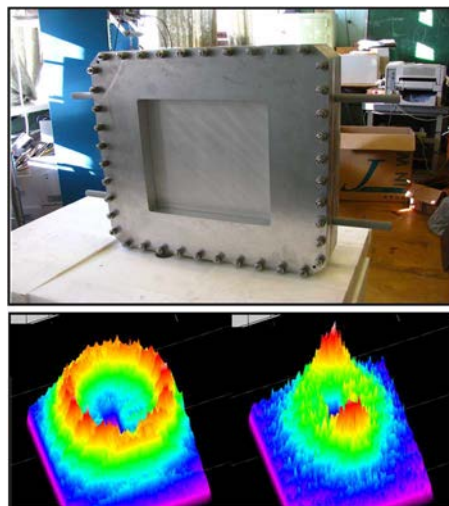


FIG. 2. Neutron detector (top). Asymmetric scattering of neutrons on a fluoroplastic film before its deformation and after (bottom).

Neutron beam monitors have a very low efficiency, which allows them to work in neutron beams of very high intensity (1×10^8 neutron / s) and density.

1. In order to create 2D detectors with aperture of $1\ 000 \times 1\ 000$ mm based on LPSC, it is necessary to update the technology line, to develop prototype models and registration electronics.
2. Production of banana-type detectors based on LPSC-technologies (or MSGC) requires separate development.

Special attention should be paid to development of scintillation detection technologies: the PIK reactor experimental stations are not yet fully equipped with such technologies, which are being actively developed around the world and have their own technological niches, such as:

- Creation of wide-aperture detectors of complex geometry;
- Neutron beam monitors.
- Applications such as neutron tomography requiring the creation of detectors with high spatial resolution at the level of 0.1 mm (and higher) etc.

Taking into account an insufficient technological capacity at PNPI in this field and the quite significant financial investments that would be needed, it is necessary to join efforts and support a joint activity of a developing collaboration of PNPI, JINR and INR RAS aimed at the development of scintillation technologies.

Neutron imaging for the purposes of tomography and radiography is a separate research field that has been widely developing in modern sources, but is still not listed among the PIK reactor research stations. The most advanced installations for neutron radiography and tomography in Europe are located at the FRM-II reactor in cold and thermal neutron beams and in PSI – cold and thermal neutrons. Analogous systems are in operation at NIST (USA).

Currently, further development of this field is possible only with the development of scintillation technologies.

Conclusions

1. An analysis of the PIK reactor instrumental facility with regard to compliance of the neutron detectors with all the required operation parameters was performed based on analysis of detectors and strategic trends of their development in leading neutron research centres of the world and analogous centres in Russia over the period of more than 60 years (40 years of past + 'current' period of the last 10 years + about the next 10 years of future) We have come to the conclusion that the global trends for the next 10 years of creation of new neutron detection technologies are developing in several main directions (they are arranged in priority order):
 - Modernization and development of gas detectors based on ^3He neutron converter.
 - Development of gas detectors based on ^{10}B solid converter.
 - Development of scintillation detectors based on spectrum-shifting optical fibres.
 - For specific cases another type of detectors, such as GEM, Micromegas, solid state semiconductor detectors and so on.
2. Despite the high price of ^3He , a global neutron community still considers gas-discharge ^3He -detectors to be the basic development direction, first of all, for detectors *with aperture of up to $1\ \text{m}^2$* . The reason for this is a unique combination of such properties as high efficiency of neutron registration and low γ -background sensitivity.

A possible transition to different detection technologies based on ^6Li and ^{10}B converters, which are being currently developed in Europe, is mostly caused by necessity and aims to reduce the costs of devices by abandoning the use of ^3He in large and medium volume detectors *with apertures from $1\ \text{m}^2$ to $80\ \text{m}^2$ and more*.

3. *He-3 detection technologies* necessary for equipping the majority (about 70%) of experimental stations of the PIK reactor either exist at PNPI or can be produced there as there is a technological capacity for their development and realization. Apertures of these detectors are no more than $1\ \text{m}^2$ and consequently do not require a large amount of ^3He (about 900 litres). ^3He is available in Russia, and its price is several times lower than the European one. For this reason, detectors based on ^3He is Russia's competitive advantage over Europe, which should be used to the fullest extent.
4. *Scintillation detection technologies*. Groups of experts professionally working with scintillation detectors and having some interesting activities in progress have been formed in PNPI, JINR and INR

RAS. The greatest experience in development of large-area ZnS(Ag) scintillation detectors was accumulated by JINR (LNP). Several such detectors have been created there and have been successfully put into operation at some Russia scientific centres. In order to succeed with any further activity in this area, it is necessary to join efforts at list Russia scientific centres and it is reasonable to base this joint activity on the experience of JINR (LNP) developments.

5. To perform a detailed and thorough analysis of applicability of different detection technologies (today's and future) to guarantee the best realization of its advantages, its competitive strengths in comparison with other neutron sources in Russia and abroad, it is important to organize fruitful collaborations across PNPI (NRC "KI", Russia) and world-leading scientific centres such as: European Spallation Source (ESS, Sweden), Institute Laue-Langevin (ILL, France), Forschungszentrum Jülich (Jülich, Germany), Japan Proton Accelerator Research Complex (J-PARC, Japan).
6. In the process of development of neutron detectors, it is necessary to apply widely the ideas and technologies developed for charged-particle detectors in high-energy physics (and other research fields). It is necessary to strive for unification of the equipment used and ready-made technological solutions. It is also reasonable to develop a unified detection electronics for the detection systems as well as electronics for data accumulation and processing. It is necessary to standardize interfaces and software at a lower level.

ACKNOWLEDGEMENTS

Special thanks for our colleagues from JINR (Dubna, Russia) and from PNPI (HEPhD and NRD, Russia) for their fruitful discussions and assistance during preparation of this article.

REFERENCES

- [1] INSTITUT LAUE-LANGEVIN, <https://www.ill.eu/instruments-support/instruments-groups>.
- [2] J-PARC (Japan Proton Accelerator Research Centre) <http://j-parc.jp/index-e.html>.
- [3] SOYAMA, K., Basic Energy Sciences Neutron & Photon Detector Workshop, August 1–3 2012, Holiday Inn Gaithersburg, USA (2012).
- [4] PEGGS, S., et al., European Spallation Source Technical Design Report, ESS-2013-001.
- [5] PEGGS, S., et al., European Spallation Source Conceptual Design Report, ESS-2012-001.
- [6] Kirstein, O., et al., "Neutron Position Sensitive Detectors for the ESS", PoS (Vertex2014) 029 (2014); arXiv:1411.6194.
- [7] FORSCHUNGSZENTRUM JÜLICH, http://www.fz-juelich.de/jcms/EN/Leistungen/InstrumentsNEW/_node.html.
- [8] YU, B., et al., Neutron detector development at Brookhaven. Nucl. Instrum. Methods Phys. Res. Section A **513** (2003) 362–366.
- [9] ZEITELHACK, K., Search for alternative techniques to helium-3 based detectors for neutron scattering applications, Neutron News **23** (2012) 10–13.
- [10] WILPERT, T., Boron trifluoride detectors, *ibid.*, p 14–19.
- [11] GUERARD, B., et al., ^{10}B multi-grid proportional gas counters for large area thermal neutron detectors, *ibid.* p 20–24.
- [12] RHODES, N.J., Scintillation detectors, *ibid.* p 26–30.
- [13] INTERNATIONAL COLLABORATION ON NEUTRON DETECTORS, <http://icnd.org>
- [14] KRIVSHICH, A., et al., Reactor complex PIK, Volume II, Scientific background for a complex of experimental stations at the PIK reactor, Detectors for the PIK reactor experimental stations, Gatchina (2014) p 164–196.

STATUS AND PROGRESS IN NEUTRON IMAGING DETECTION SYSTEMS

E. H. LEHMANN

Laboratory for Neutron Scattering & Imaging,
Paul Scherrer Institut, Switzerland
Email: eberhard.lehmann@psi.ch

Abstract: Neutron imaging has a long tradition since neutron sources with suitable beam ports became available in the late 1940s to the 1960s. Based on film in combination with neutron converters, this radiography approach attracted a lot of interesting applications in the industrial field, and in military and nuclear technologies. The alternative and complement to X-ray methods has been obvious from the beginning.

The real change in neutron imaging techniques and increase in scientific applications has been initiated by new detection systems which are nowadays digital. In this way, a much more efficient use of neutron beams has been enabled and sophisticated methods like neutron grating interferometers, diffractive imaging and imaging with polarized neutrons have been implemented at several places. A high level of quantification is enabled in this way: neutron tomography is nowadays a routine method in science and applications delivering voxel-wise values of attenuation coefficients.

However, dedicated neutron imaging beam lines need to be installed, where the detection systems are but one of the key components. Such attractive research facilities are established at only a few places world-wide, but several upcoming projects and installations are on the way to be realized at prominent sources like ESS (Lund, Sweden), SNS (Oak Ridge, USA) and other new neutron sources. The majority of neutron imaging detectors are based on the conversion of the neutrons into visible light—the scintillation process. Since neutron imaging enables the transmission through samples and objects on the macroscopic scale, the field-of-view has to be tuned according to their sizes. This can vary between about 40 cm and 1 cm with the inherent resolution of 500 to 2 μm . The development of suitable scintillation screens is still progressing with respect to inherent resolution, light output and stability. Scintillator solutions for even highly activated samples are under development.

The active sensor for the scintillation light can be either in direct contact (a-Si flat panels) or optically coupled via lenses (CCD or CMOS cameras). Due to their high performance and flexibility, cameras are presently the most used devices in neutron imaging. They can be tuned for very long or very short exposure times, be synchronized to repetitive processes, and enable a high dynamic range and a high signal/noise performance. Camera technology is still under development, and performance and prices follow this process in the usual manner.

Challenges for the next future are systems with ultimate spatial resolution to be competitive to X-ray methods, the most suitable systems for pulsed beams (in time-of-flight mode), and access to as many beam ports as possible to deliver neutron imaging as a routine method in science and for industry.

1 INTRODUCTION: WHAT IS NEUTRON IMAGING TODAY?

Transmission of neutron beams through objects or specific material samples is used in order to get information on their content in a non-invasive way. This approach is very comparable to X-ray investigations. However, the obtained image data differs quite significantly since the interaction with matter is different for neutrons and X-ray in principle (see below).

The first studies in radiography mode were already performed by the middle of the last century when the first sources of neutrons were available [2, 3]. This kind of investigation was done with X-ray films when a neutron converter based on a strong absorber like ^{10}B , Gd, Cd or Ag was placed in touch to the film. The secondary radiation (α , β or γ) from the capture process can be registered on film, while a direct neutron exposure without the converter gives nearly no signal. Figure 1 shows one of the first neutron radiography studies ever made; the comparison to the gamma radiation image was already given for comparison.

Today, the film method is practiced only in a few cases and for traditional applications which require a well-defined and certified process.

New detection systems are mostly based on **digital** sensors where the output is a two-dimensional pixel matrix of intensities. There are many advantages of the new class of neutron imaging detectors: linearity, high dynamic range, image processing options, easy data transfer, high frame rate and options for advanced data treatment (e.g. tomography, quantification, phase contrast and dark field imaging). A result of neutron tomography is given in Fig. 2 as the outer view of a fossilized animal. Its entire volume can be observed and analyzed ‘virtually’ with suitable software tools.

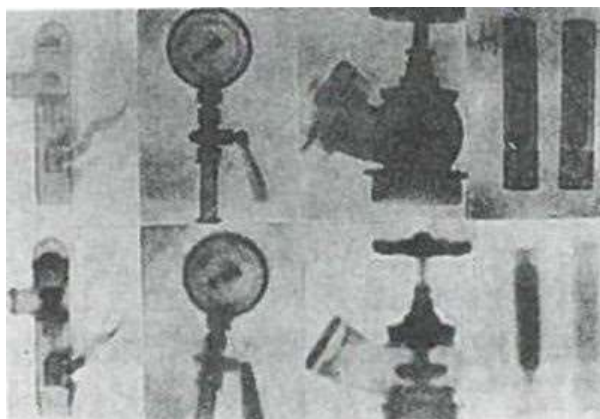


FIG. 1. One of the first neutron radiographs ever done (bottom): Comparison to gamma data (on top) both taken with film techniques [2, 3] for several common devices and structures.

In addition to the development of the detector technology, new and dedicated neutron imaging stations were designed and built in different countries around the globe. An overview of the state-of-the-art stations is given in Table 1. Although the number of facilities is quite limited, their use is shared among different users. This ‘user operation’ scheme is copied from neutron scattering facilities which can be booked via a proposal-based access procedure. The wide user community requires high flexibility in the operation of the neutron imaging facilities with respect to field-of-view, spatial and temporal resolution, and sample environment.



FIG. 2. Neutron tomography result (fossilized snail) taken with the micro-setup at the ICON facility at Paul Scherrer Institut (Switzerland); sample size about 2.5 cm; voxel size 13.5 μm .

There is still a lot of development in neutron imaging, which is described in more detail in the outlook of this paper. The link and interface to neutron scattering approaches and the combination with X-ray imaging are two new options—and detector development is quite essential for the progress of these topics.

2 NEUTRONS AND THEIR INTERACTION WITH MATTER

Both kinds of beams (X-rays/thermal neutrons) have the ability to transmit through materials of certain thicknesses. Comparing the intensities in the beam with (I) and without (I_0) a sample delivers information about its content, integrated over the thickness d in the beam direction. It has been demonstrated that the Beer-Lambert law is valid to first order:

$$I = I_0 \times e^{-\sigma \cdot N \cdot d} \quad (1)$$

N represents the nuclear density of the material with the interaction probability (microscopic cross-section) σ of the considered kind of radiation. These data are well known and tabulated (e.g. [4, 5]).

However, the interaction process of neutrons and X-rays, respectively, is completely different: neutrons interact with the nuclei of the atoms while X-rays mainly ‘see’ the electrons around. In both cases scattering and absorption happens, but in the case of neutron absorption a nuclear reaction is initiated with the creation of new isotopes, which can either be stable or radioactive. No activation can happen by X-ray absorption.

Since the number of electrons directly increases the interaction probability with X-rays, the attenuation contrast is much higher for heavy elements than for that of small mass. This is the reason why X-rays are the ideal tool for the study of the human body where the high amount of water (hydrogen) does not attenuate the beam much. Bones with materials of higher mass number (Ca, O, C) deliver higher contrast, while metals are often opaque.

For the attenuation of thermal neutrons, there is no clear and systematic rule. Even isotopes of one specific element can strongly differ in the interaction probability (e.g. $^1\text{H} \leftrightarrow ^2\text{H}$; $^{10}\text{B} \leftrightarrow ^{11}\text{B}$; $^6\text{Li} \leftrightarrow ^7\text{Li}$). As a general trend, heavy materials like Pb, Bi, W or even U are more transparent than for X-rays, while light elements deliver quite high contrasts. This behaviour is summarized in Fig. 3 by comparison of mass-attenuation coefficients. This difference can directly be seen in the images of both kinds of radiation as shown with the example of a mobile phone in Fig. 4.

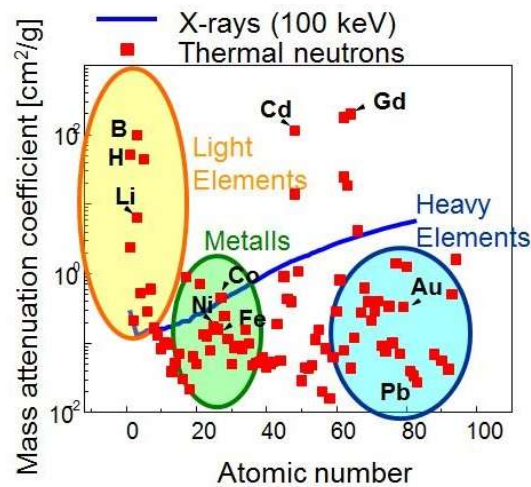


FIG. 3. Mass attention coefficients for thermal neutrons and 100 keV X-rays indicating the strong differences for light/heavy elements and many metals in particular.

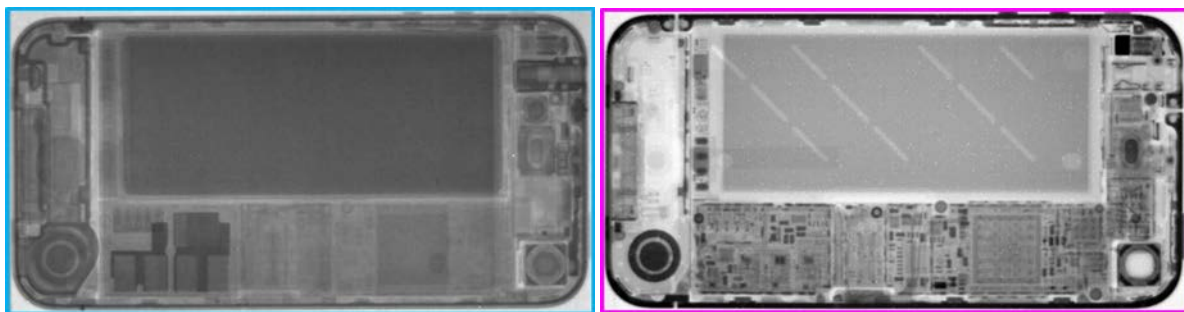


FIG. 4. Transmission images of a mobile phone obtained with thermal neutrons (left) and X-rays (right) showing similar image quality but very different contrast.

The Li-battery and plastic parts have higher contrast in the neutron image while metallic contacts are better visible with X-rays (same image quality in principle achieved).

The interaction properties with matter have also impact on the detector performance. Since neutrons can only be registered via a conversion reaction, the absorption probability should be high in order to be efficient. With respect to image blurring, e.g. within the scintillation process, the range of the secondary radiation also plays an important role if the highest possible spatial resolution is intended. A compromise has to be found between layer thickness (less blurring) and detection efficiency.

3 SETUP OF A NEUTRON IMAGING FACILITY

Although the neutron imaging detector is a key component for a neutron imaging facility, there are some other important parts to be considered for the most useful setup. Starting from the neutron source, the selection process of the beam has to be done in a manner such that the collimation is as high as possible (or reasonable with respect to low source strength and the needed exposure time). A key parameter which roughly describes the degree of collimation is the ratio between collimation length L and the aperture D next to the source. Another parameter is the beam dimension which influences the field-of-view (FOV) of the setup. Common values for imaging facilities are $L/D > 250$; FOV ~ 20 cm, while the neutron flux on sample should be $\phi > 10^6 \text{ cm}^{-2} \text{ s}^{-1}$.

A generic layout of a neutron imaging facility is given in Fig. 5. Along the beam line more than one setup with different detector options with respect to FOV and intensity are feasible. For radiation protection reasons it has to be enclosed into a shielded room (bunker) with strict access control. Further components are beam limiters, a beam dump and remotely controlled sample manipulators. Advanced installations have tools for energy selection, and setups for grating interferometry or for polarization of neutrons.

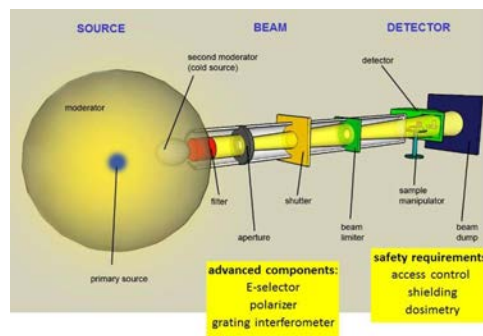


FIG. 5. Generic neutron imaging facility (not to scale) with components for tuning the beam and to manipulate samples with respect to the detection process.

4 EXAMPLES OF INSTALLATIONS

From the facilities given in Table 1 we highlight only two representatives. The beam lines of NEUTRA (thermal spectrum) [6] and ICON (cold spectrum) [7] are both arranged at the Swiss spallation neutron source, which is operated in a continuous mode with neutron intensities comparable to a 15 MW research reactor. They are both arranged tangentially to the spallation target so that the gamma background is low. Covered within a shielded bunker, the beam lines are very flexible with respect to collimation and intensity having at least two positions in the beam and options to tune the aperture and the beam size.

The different spectra of these facilities (in addition, access to a third one — BOA [8] — is possible) allows to choose between either higher sample transmission or higher sensitivity. These options are illustrated in Fig. 6 by the slope of the interaction probability of a common material with the wavelength.

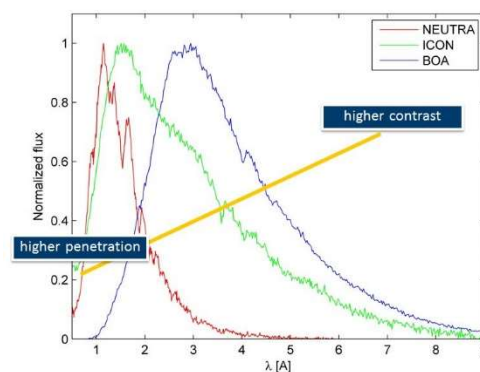


FIG. 6. Comparison of the normalized neutron spectra at three facilities at PSI which can be used for neutron imaging purposes: NEUTRA-thermal; ICON-cold; BOA-very cold and polarized.

TABLE 1. NEUTRON IMAGING USER FACILITIES WORLDWIDE

Country	Site	Institution	Facility	Neutron Source	Spectrum	Power (MW)	Status
Australia	Sydney	ANSTO	DINGO	OPAL reactor	Thermal	20	Operational
Germany	Munich-Garching	TU Munich	ANTARES	FRM-2 reactor	Cold	25	Operational
Germany	Munich-Garching	TU Munich	NECTAR	FRM-2 reactor	Fast	25	Operational
Germany	Berlin	HZB	CONRAD	BER-2 reactor	Cold	10	Operational
Hungary	Budapest	KFKI	NORMA	WWS-M reactor	Cold	10	Operational
Hungary	Budapest	KFKI	NRAD	WWS-M reactor	Thermal	10	Operational
Japan	Kyoto	Kyoto University	Imaging beamline	MTR reactor	Thermal	5	Standby
Japan	Tokai	JAEA	Imaging beamline	JRR-3m reactor	Thermal	20	Standby
Japan	Tokai	JAEA	RADEN	JPARC spallation	Cold	0.5	Operational
Korea	Daejon	KAERI	Imaging beamline	HANARO reactor	Thermal	30	Operational
Russia	Dubna	JINR	Imaging beamline	IBR-2M pulsed reactor	Thermal	2	Operational
Switzerland	Villigen	PSI	NEUTRA	SINQ spallation	Thermal	1	Operational
Switzerland	Villigen	PSI	ICON	SING spallation	Cold	1	operational
UK	Oxfordshire	Rutherford Lab	IMAT	ISIS spallation	Cold	0.3	Operational
USA	Gaithersberg	NIST	BT-2	NBSR reactor	Thermal	20	Operational
USA	Gaithersberg	NIST	NG-6	NBSR reactor	Cold	20	Operational
USA	Oak Ridge	ORNL	CG-1D	HFIR reactor	Cold	85	Operational
South Africa	NECSA	Pelindaba	SANRAD	SAFARI reactor	Thermal	20	Standby

5 DETECTOR OPTIONS IN THE PAST — AND TODAY

5.1 FILM BASED METHODS

As mentioned above, the initial detector for neutron imaging in radiography mode was **silver-halogenide film** in conjunction with converter layers. Due to the very high capture cross-section, Gd became preferred as a converter, and less than 50 μm thickness was enough for thermal neutrons to be absorbed completely. Several other converters like Dy, In or B were used for specific tasks like off-line conversion (for study of activated samples) or to make visible tracks in nitro-cellulose layers generated by absorption reaction products (see below).

A recent replacement of film by a digital system was provided by the introduction of **imaging plates** which are exposed in the beam and read out by means of a special laser scanner system. Although the imaging plates can be reused after erasure many times, their quality goes down by mechanical damage. While common imaging plates are mainly sensitive for X-rays — with huge potential in hospitals — they have to contain a neutron converter in the neutron case. The commercial devices are again Gd based. Some development for the transfer technique with Dy has been initiated by Tamaki [9]. The advantages of imaging plates are the high inherent spatial resolution (pixel size down to 25 μm), the high dynamic range, the high linearity, the large detector area (typically 20 cm \times 40 cm) and many image processing options. Disadvantages are the needs for the external read out that disables pixel-wise referencing, e.g. for ‘open beam’ comparison, the sensitivity for a gamma component in the beam and the low frame rate (1 picture within about 10 minutes). In some cases, ‘ghost images’ which do not vanish after erasure occur caused by activation in the image plate material.

So-called ‘**track etch foils**’ have been common to study highly activated samples like nuclear fuel after operation or damage. The nitro-cellulose layer has to be covered with boron-nitride as a converter and removed after exposure. The developing process is done by chemical means in a Na- or K-base, where the initial tracks made by the conversion α particles are etched until visible with an optical microscope. Due to the demanding developing process and the low contrast of the ‘images’, the method is only practiced at a few places.

5.2 CAMERA BASED SYSTEMS

The development of highly sensitive CCD cameras (mainly for astronomers) was also the kick-off for neutron imaging systems where a neutron sensitive scintillator screen has to be placed behind the object to be investigated. The camera has to be optically coupled with suitable highly light efficient lens systems, and the whole setup covered by a very light-tight box. Since direct exposure would damage the CCD electronics in a short time, the light from the scintillator is guided via one or more mirrors to the camera. Because the light emission from the scintillator is very low even under intense neutron exposure, all possible options have to be exploited to increase the signal at the camera detector.

First, the spectrum of the light emitted from the scintillator has to be tuned to the best spectral response of the CCD, which is in the green/blue region around 500 nm wavelength. Doping the very common scintillators (mixture of ^6LiF with ZnS) with Ag or Cu is most useful for this purpose.

Camera detectors are very flexible with respect to FOV and pixel size. Changing the lens system, a wide range can be covered where the limits are given also by the beam size and collimation. Figure 7 describes all camera-based systems at the PSI beam lines.

The development of suitable scintillator screens is still active [10]. The composition of ^6Li based scintillator materials has been known for a long time, but the optimization with respect to the light output and the inherent spatial resolution is still an important issue for neutron beam utilization. With the use of ^{157}Gd enriched screens, an expensive but ultimate solution was found for the highest possible spatial resolution in neutron imaging (see below).

It has to be mentioned that all cameras are operated under a low temperature regime in order to suppress the dark current and to enable long exposure times. Depending on the setup, the typical exposure is on the order of seconds while a high frame rate of 100 Hz is also possible to achieve. Specialized systems with trigger options enable stroboscopic imaging in a repetitive mode while images at identical positions are stacked in the camera main memory.

Recently, CMOS systems also became available; these have the advantage of much faster readout and much lower price compared to CCDs. However, image quality and the risk of camera crashes are still factors acting against widespread uptake of CMOS.

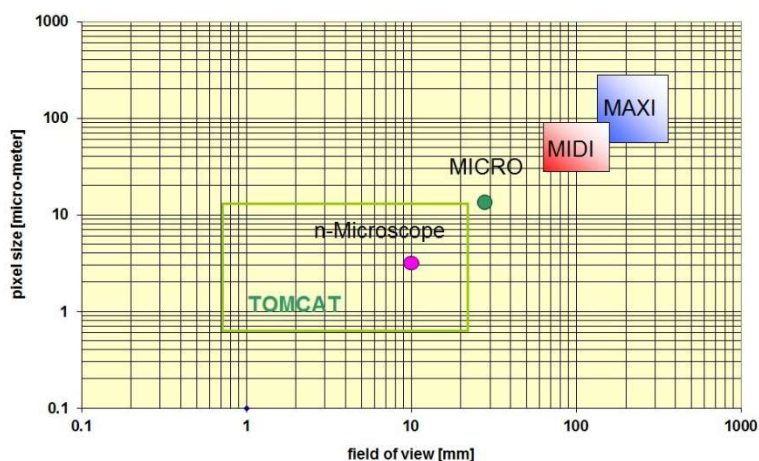


FIG. 7. Range of camera based systems with respect to FOV and pixel size (logarithmic scale to consider) MAXI (up to 40 cm); MIDI (up to 15 cm); MICRO (fixed to 27 mm FOV); n-Microscope (5–10 mm FOV).

5.3 FLAT PANELS WITH AMORPHOUS SILICON

Following the developments for medical imaging and computed X-ray tomography for industrial applications, where pixelated arrays of photo-diodes (flat panels) have been developed and optimized, neutron sensitive panels have also been tested [11]. The easiest approach is to exchange the scintillator screen, which is placed in direct contact with the pixel matrix, by a neutron sensitive one.

Since the panels operate in a continuous readout mode (like an old tube-type TV screen), only a readout frequency, but no explicit exposure time, is possible to define. The manufacturers of the screens handed over ‘raw products’ to companies which fixed the gap to the radio-medicine community and delivered customized devices. Therefore, it was hard to tune an ‘exotic’ neutron device for research purposes to the flexible exposure conditions required for many applications.

Although this technology is applicable for neutron imaging in principle, there are some drawbacks which hinder a wide usage in the community. First of all, the pixel size is given by the panel itself which is on the order of 50–200 μm . For small pixels the efficiency is quite low and the frame rate therefore limited. Furthermore, the dynamic range is less than the required 16 bits, the gamma sensitivity not negligible, and radiation damage (direct exposure) cannot be excluded.

5.4 PIXELATED DETECTORS

Integrating the readout electronics into each pixel by micro-structural techniques enables a very flexible operation of pixelated imaging systems. Compared to the amorphous Si systems where the pixels are just photo-diodes and the readout electronics is placed aside from the pixel matrix, the MEDIPIX and TIMEPIX architecture [12] has been used to build two lines of systems with integrated pixel-wise logics.

One approach is to use the X-ray sensitive systems together with a neutron converter (${}^6\text{Li}$, ${}^{10}\text{B}$ or Gd). These systems are not very efficient in the neutron detection but enable readout in the centroid mode where each capture event is registered individually and with sub-pixel resolution [13].

A more promising approach is to use micro-channel plates (MCP) which are placed in front of the readout chips, based on TIMEPIX. Since the MCPs are doped with ${}^{10}\text{B}$, the capture process initiates a charged particle emission, which is amplified by high voltage. Therefore, the system has to be operated under high vacuum conditions. Compared to the simpler pixel detector described above, the MCP device is more efficient [14]. Furthermore, the very fast readout can be used for the study of time dependent processes, in particular energy dispersive studies in TOF mode. This technique has particular potential at imaging facilities at the new pulsed spallation neutron sources. The current limitation is the relatively low number of pixels and the consequently small FOV. Table 2 gives an overview of detection systems for neutron imaging. The parameters can differ for any particular setup and facility.

TABLE 2. NEUTRON IMAGING DETECTORS IN COMPARISON

Detector system for digital neutron imaging	X-ray + transmission light scanner	Scintillator + CCD-camera	Neutron Microscope	Imaging Plates	Amorphous silicon flat panel	Pixel detector (MCP type)
Max spatial resolution (pixel size) [μm]	20–50	20–500	2–5	25–100	127–750	10–50
Typical exposure time for generation of valid images	5 min	10 s	600 s	20 s	0.1–10 s	20s
Detector area (typical)	18 \times 24 cm^2	25 \times 25 cm^2	7.5 \times 7.5 mm^2	20 \times 40 cm^2	30 \times 40 cm^2	40 \times 40 mm^2
Number of pixels per line (optimal conditions)	4000	2000	2000	6000	1750	512
Dynamic range	10 ² (non-linear)	10 ⁵ (linear)	10 ⁵ (linear)	10 ⁵ (linear)	10 ⁵ (non-linear)	Unlimited
Digital format	8 bit	16 bit	16 bit	16 bit	12 bit	Count rate/pixel
Special Features	Development lab needed	Various FOV by optics	Gd-157 scintillator	Converter Gd, Dy	Fixed pixel size/device	Few ns time resolution

6 THE NEUTRON MICROSCOPE PROJECT

There is a high demand to improve the spatial resolution in neutron imaging, following the similar trend in X-ray and synchrotron light imaging. Today it is possible to study sub- μm phenomena in 2D and 3D with the contrast features given by the X-ray–material interaction (see above).

It is a real challenge to compete with the X-ray world using neutrons. Since many samples contain large amounts of metals they are more transparent with neutrons and a high contrast can be obtained for light elements, hydrogen in particular.

From the detector side and by the beam properties there are limitations with respect to the spatial resolution: Neutrons can only be detected via a secondary (ionizing) radiation after a nuclear reaction (absorption, collision) takes place — the range of that radiation gives a physical limit on the order of a few μm . This could be overcome by ultra-thin detectors layers with the consequence of only limited efficiency.

1. The beam divergence induces optical blurring since the samples have to be at non-zero distance from the detector. The higher the collimation, the smaller is the beam intensity — and the longer is the exposure time.
2. The pixel array also has intrinsic limitations given by the pixel size (6–15 μm) where a direct link to the efficiency and full-well capacity is given. Only by magnification options (optically or with Wolter type lenses [21]) is a sub-10 μm achievement possible.

All three problems were tackled within the project ‘neutron microscope’ [15]. The development of a ¹⁵⁷Gd (capture cross-section 254 000 barns) Gadox scintillator with deposited layers of 5–10 μm was one important step [16]; a second one was the custom made, 5-times magnifying lens system. Now it is possible to study features in the range given in Table 2 within the mentioned conditions. Cameras with more than 4000 pixels will enable FOVs larger than 1 cm^2 . The overview picture of the setup is given in Fig. 8.

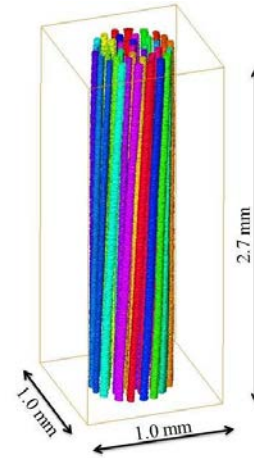


FIG. 8. The ‘neutron microscope’ prepared for superconducting investigations with the best possible spatial resolution: real setup and some first results –wires based on MgB_2 [17].

7 FUTURE DEVELOPMENTS

The improvement of components like scintillators (light output, resolution) or camera systems (increased pixel numbers, efficiency) will increase the performance of neutron imaging detection systems. With decreasing price levels, these detection systems will become more and more standard equipment at neutron sources.

There is still potential to make the detection systems ‘more intelligent’ by using the time structure of the beam and of the processes to be investigated. Increasing the FOV of pixelated detectors will make them more relevant for practical applications and for industry. An interesting approach to tune the light from the scintillator is the use of optical fibres, which can either focus or magnify. This approach has been already tested successfully [20].

Figure 9 gives an overview of the various detector options and underlines that either high time resolution OR high spatial resolution can be achieved with the same number of neutrons. Therefore, access to the most powerful beam ports enables improvement of both of these parameters, or the image quality in general.

There are upcoming new projects and upgrade initiatives as shown in Table 3. They will all use digital detectors with best performance under their particular conditions (including funding limitations). Which detection system is preferred depends very much on the beam conditions, the user profile, and the research and application fields.

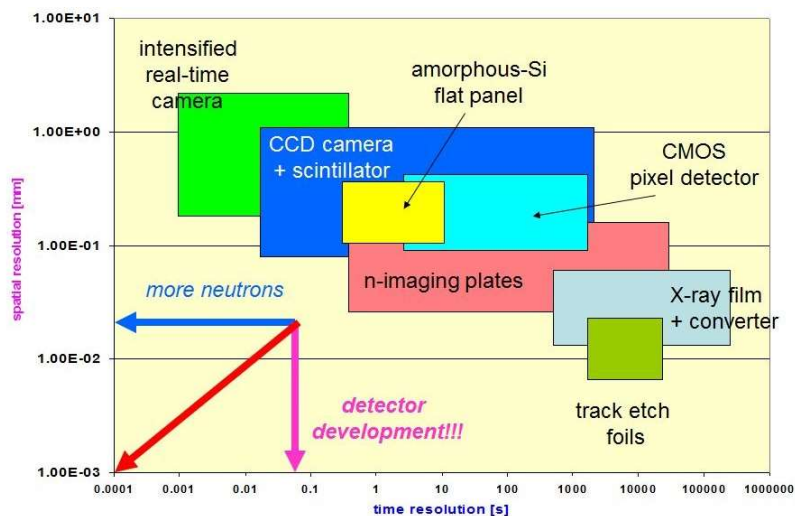


FIG. 9. Overview of neutron imaging detectors with respect to time and spatial resolution.

TABLE 3. NEUTRON IMAGING (NI) FACILITIES UNDER DEVELOPMENT (STATUS 2017)

Country	Source	Facility	Site	Status
USA	SNS	VENUS	Oak Ridge	Project
Europe	ESS	ODIN	Lund	Under construction
Argentina	RAIO	ASTOR	Buenos Aires	Project
Czech Republic	LVR-15	NI	Rez near Prague	Considerations
PR China	CARR	2N1	Beijing	Under installation
France	ORPHEE	IMAGINE	Saday	Operational
Europe	ILL	DSO	Grenoble	Shared with reflectometer
Norway	JEEP-II	NIMRAD	Kjeller	Upgrade
Netherlands	Delft RR	FISH	Delft	Project
Jordan	New reactor	NI	Amman	'Day one' project
South Africa	SAFARI	SANRAD-II	Pelindaba	Upgrade project
Russia	IBR-2	NI	Dubna	Improvements
South Korea	HANARO	NI	Daejon	Upgrade project
Germany	HBS	NI	Jülich	Project

8 SUMMARY AND CONCLUSIONS

Since the first trials of neutron imaging with films — about 60 years ago — there has been huge progress in the efficient usage of neutrons for imaging purposes. The various digital detection systems each enable new methods for different research fields using their inherent advantages in performance.

The most common neutron imaging device is camera based and applied together with a neutron sensitive scintillator. It has a high flexibility with respect to FOV and resolution, and can be tuned according to the requirement of the operators and users.

Recently, such detection systems have been introduced to perform neutron scattering experiments [18, 19]. Modern diffractometers will use neutron imaging detection systems at least as a comfortable in-situ monitor.

ACKNOWLEDGEMENTS

The author thanks all members of the Neutron Imaging & Activation Group at PSI and the users of the neutron imaging facilities who contributed to the methodical progress by motivation and excellent scientific work.

Funding for the detector development at PSI by Swiss Science Foundation and the CCMX network is acknowledged herewith.

REFERENCES

- [1] LEHMANN, E.H., et al., Neutron imaging — Detector options in progress, *J. Inst.* **6** (2011) C01050.
- [2] KALLMANN, H., *Research* **1** (1947) 254–260.
- [3] PETER, O., *Z. Naturforschung A* **1** (1946) 557–559.
- [4] NATIONAL INSTITUTE OF STANDARDS AND TECHNOLOGY, XCOM: Photon Cross Sections Database, <https://www.nist.gov/pml/xcom-photon-cross-sections-database>
- [5] INTERNATIONAL ATOMIC ENERGY AGENCY, Evaluated Nuclear Data File (ENDF), Database Version of 2017-10-27 <https://www-nds.iaea.org/exfor/endl.htm>.
- [6] PAUL SCHERRER INSTITUTE, NEUTRA: NEUtron Transmission Radiography, <https://www.psi.ch/sinq/neutra/parameters>.
- [7] PAUL SCHERRER INSTITUTE, ICON, <https://www.psi.ch/sinq/icon/icon>.
- [8] MORGANO, M., et al., Neutron imaging options at the BOA beamline at Paul Scherrer Institut, *Nucl. Instrum. Methods Phys. Res., Sect. A* **754**, (2014) 46–56.
- [9] TAMAKI, M., et al., Dy-IP characterization and its application for experimental neutron radiography tests under realistic conditions, *Nucl. Instrum. Methods Phys. Res., Sect. A* **542** (2005) 320–323.

- [10] RC TRITEC, Our selection of scintillators for neutron imaging, <http://www.retritec.com/en/scintillators/products.html>.
- [11] GRANFORS, P.R., AUFRICHTIG, R., Performance of a 41×41-cm² amorphous silicon flat panel X-ray detector for radiographic imaging applications, *Med. Phys.* **27** (2000) 1324–1331.
- [12] LLOPART, X., et al., Timepix, a 65k programmable pixel readout chip for arrival time, energy and/or photon counting measurements, *Nucl. Instrum. Methods Phys. Res., Sect. A* **581** (2007) 485–494.
- [13] JAKUBEK, J., et al., A coated pixel device TimePix with micron spatial resolution for UCN detection *Nucl. Instrum. Methods Phys. Res., Sect. A* **600** (2009) 651–656.
- [14] TREMSIN, A.S., et al., Detection efficiency, spatial and timing resolution of thermal and cold neutron counting MCP detectors, *Nucl. Instrum. Methods Phys. Res., Sect. A*, **604** (2009) 140–143.
- [15] TRTIK, P., LEHMANN, E.H., Isotopically-enriched gadolinium-157 oxysulfide scintillator screens for the high-resolution neutron imaging, *Nucl. Instrum. Methods Phys. Res., Sect. A* **788** (2015) 67–70.
- [16] TRTIK, P., et al., Improving the spatial resolution of neutron imaging at Paul Scherrer Institut—The Neutron Microscope Project, *Phys. Procedia* **69** (2015) 169–176.
- [17] ILES, G., PEETERMANS, S., SCHORR, S., LEHMANN, E., Laue diffraction using scintillator detectors, *Phys. Procedia* **69** (2015) 314–319.
- [18] PEETERMANS, S., LEHMANN, E.H., Simultaneous neutron transmission and diffraction contrast tomography as a non-destructive 3D method for bulk single crystal quality investigations, *J. Appl. Phys.* **114** (2013) 124905.
- [19] BETZ, B., GRÜNZWEIG, C., LEHMANN, E.H., Advances in neutron imaging with grating interferometry, *Mater. Eval.* **72** (2014).
- [20] MORGANO M., TRTIK P., Meyer M., Lehmann E., Hovind J. and Strobl M., Unlocking high spatial resolution in neutron imaging through an add-on fibre optics taper, *Optics Express* **26** 2 (2018) 1809–1816.
- [21] MILDNER, D., GUBAREV, M., Wolter optics for neutron focusing, *Nucl. Instrum. Methods Phys. Res., Sect. A* **634** (2010), Suppl. 1, S7–S11, <https://doi.org/10.1016/j.nima.2010.06.093>

MODERN NEUTRON DETECTORS WITH FAST TIMING RESOLUTION

B. SEITZ, J. R. M. ANNAND, L. BOYD
SUPA School of Physics and Astronomy,
University of Glasgow,
United Kingdom
Email: bjoern.seitz@glasgow.ac.uk

K. FISSUM
Nuclear Physics
University of Lund,
Sweden

Abstract: Thermal neutrons are a vital imaging modality with wide ranging applications, exemplified by worldwide endeavours to construct and operate the next generation of accelerator-driven neutron sources with significantly increased neutron flux and, hence, brightness and image contrast. In addition, a high spatial resolution and information about the neutron energy is often desired. The latter is commonly provided by a time-of-flight measurement. These user-driven demands to obtain the best possible image pose significant challenges to the design of the neutron sensor system. The neutron sensor needs to be highly efficient in detecting thermal neutrons, provide the desired spatial and temporal resolution, and has to operate at high count rates. Segmented photon sensors like Multi-Anode Photo Multiplier Tubes (MAPMT) or systems based on Micro Channel Plates (MCP) have been proven in other fields to meet the demands on efficiency, rates, spatial and temporal resolution. Combining these photon sensors with suitable neutron converters, e.g. Lithium-loaded glass scintillators, will provide a neutron detection system capable of meeting the requirements of the next generation of spallation neutron sources. One system based on GS-20 scintillator coupled to a Hamamatsu H12700 MAPMT will be described in detail, as will be the concept of a system based on gadolinium-coated silicon structures coupled to a segmented electron detector.

1 INTRODUCTION

Neutrons are a powerful tool to investigate the structure of materials. Neutron diffraction is an ever-growing tool for investigations in material science, condensed matter physics, chemistry and the life sciences. Many facilities worldwide (references here) offer neutron beams with a wide range of energies and intensities. Progress in imaging, however, is usually made with incident neutron beams of very high brilliance and well controlled energy spectrum. The time structure of the neutron beam is a further important factor. These requirements lead to the construction of neutron spallation sources, which offer pulsed neutron beams of unprecedented brilliance [1].

The European Spallation Source (ESS) is under construction at Lund, Sweden, and promises to become a world-leading facility in neutron imaging applications, offering 22 instruments with applications ranging from neutron imaging, small angle neutron scattering and crystallography to diffraction, reflectometry and spectroscopy. This wide range of applications requires detector areas ranging from 0.16 m² to 47.5 m², spatial resolutions from 0.001 mm to 25 mm, a neutron wavelength between 0.1 Å and 23 Å and time resolutions below the microsecond range. A wider ranging detector development program is underway to meet the demands of the upcoming experiments [2].

In view of the continuing shortage of ³He, the current *de facto* standard for large area neutron detectors, new sensor solutions are needed to meet the demands and requirements of future experiments planned at neutron facilities worldwide. Research concentrates on the development of sensors based on isotopically enriched boron carbide, ⁶Li-based scintillator detectors and Gd-based detectors for high resolution where requirements on high-energy photon (gamma) background can be relaxed. This paper introduces a sensor system based on a ⁶Li-glass scintillator coupled to a Multi-Anode Photo Multiplier Tube (MAPMT) for fast, high-rate neutron detection with moderate spatial resolution and outlines a concept for increased time- and position resolution in a vacuum based system using especially constructed Micro Channel Plates (MCP).

2 NEUTRON SENSITIVE SCINTILLATORS COUPLED TO MAPMT

The European Solid State Neutron Detector (SoNDe) project is a technology development project aimed at meeting the detector challenges posed by the ESS science programme [1]. The proposed technology is using a Multi-Anode Photo Multiplier Tube (MAPMT) coupled to lithium-glass scintillators to provide a fast, efficient, high-rate modular thermal neutron sensor system with position resolution exceeding that provided by conventional ³He tubes, and meeting the demanding specifications for ESS instrumentation. The thermal neutron detection will be provided by a thin, monolithic glass scintillator, enriched with ⁶Li. The scintillation light, in turn, will be detected by a MAPMT. The pixelization of the MAPMT allows operation at increased count rate and improved

position resolution. However, optical and electrical cross talk in MAPMTs remain a concern when discriminating the light distribution inside the scintillator and correlating it with the illuminated pixels.

Hamamatsu MAPMT H8500 is nowadays a prime candidate for large-area imaging applications [3–4]. It has proven to be capable to detect light down to the single-photon level [5]. The demand for low-level light detection, usually associated with the large areas and position resolution required for Ring Imaging Cherenkov Counters (RICH) led Hamamatsu to an improved model, H12700. The main difference between the two models is that the H12700 provides twice the gain between the photocathode and the first dynode, making it more effective for detecting low light levels. While the H8500 has been studied extensively, comparative results show a satisfactory performance of the H12700 and comparable mechanical dimensions and layout [3–5].

The H12700 is a 10-stage MAPMT with a bi-alkali photocathode yielding a peak photon detection efficiency of about 30% for a wavelength around 400 nm. Its external dimensions of $52 \times 52 \text{ mm}^2$. It features an 8×8 array of pixel, with each pixel being $6 \times 6 \text{ mm}^2$. The active area is $48.5 \times 48.5 \text{ mm}^2$ with a packing fraction of 87%. The typical gain for these devices is 2×10^6 at an operating voltage of -1000 V . The sensor and an assembled system are shown in Figure 1.

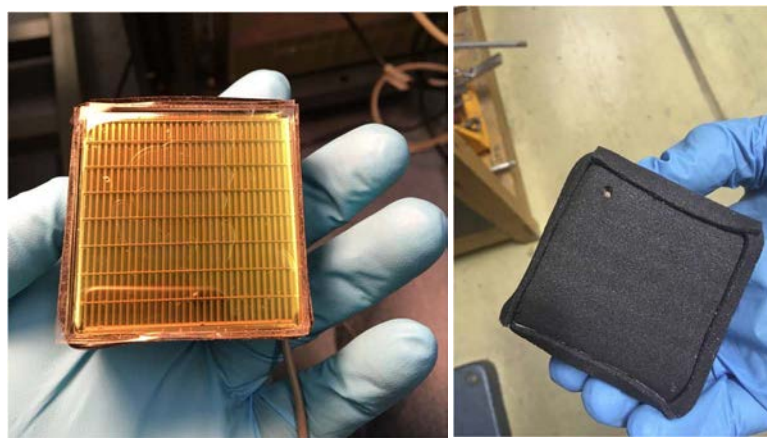


FIG. 1. Hamamatsu H12700 MAPMT (left) showing the pixel structure, and the assembled GS-20/MAPMT sensor system covered in MirroBor with one pixel open for neutron detection.

Detailed studies of the MAPMT have been performed to measure the gain per pixel and cross talk probabilities, usually about 10% at single-photon level. Both the gain variations and the potential cross talk have to be taken into account in the operation and data reconstruction when using a MAPMT. The gain map and cross talk probability are measured by systematically moving a laser with a sub-mm focal point across the MAPMT surface. The light level is adjusted to the single-photon level. A typical gain map is shown in Figure 2.

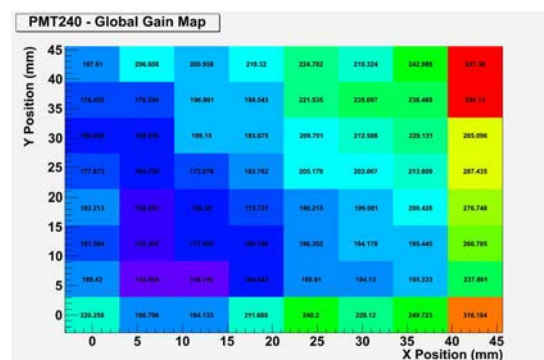


FIG. 2. Hamamatsu H12700 MAPMT gain map measured with a collimated laser beam at single photon level. A significant variation of gain across the MAPMP is visible and has to be taken into account in the offline analysis.

The proposed scintillator solution is GS-20 glass, provided by Scintacor. GS-20 is an established material for neutron detection [6–8]. GS-20 contains 6.6% lithium by weight, enriched to 95% ^6Li . The 1-mm thick GS-20 wafer used should, therefore, provide a detection efficiency of about 75% for thermal neutrons. The detection mechanism relies

on thermal neutron capture by ${}^6\text{Li}$, resulting in an alpha particle of 2.04 MeV and a triton of 2.72 MeV. Both particles are highly ionising and travel 5.3 μm and 34.7 μm in the material, respectively. Within the resolution required, this travelling distance is considered negligible. These ionising particles give rise to scintillation light with a maximum of emission of 390 nm, well matched to the chosen H12700 MAPMT's peak detection efficiency. The refractive index of GS-20 is $n = 1.55$ at 395 nm and hence relatively well matched to the refractive index of the MAPMT entrance window. Nevertheless, coupling should be done using an optical interface (e.g. EJ-560 silicone rubber). From tests reported in the literature [9], the expected photon signal will be about 6600 photons per neutron event with a peak at 390 nm, well within the detection range of the MAPMT and significantly above any background. The decay time is about 60 ns. While this does not classify GS-20 as a fast scintillator material, it is well within the requirements for timing resolution for a neutron imaging application at a spallation neutron source.

It should be noted, that GS-20 does not exhibit a significant difference in pulse shape between neutron events and absorbed gamma rays. It is possible to suppress low-energy gamma events using a threshold cut, but a background from high-energy gamma will be irreducible.

The setup has been assembled for testing with a MirroBor collimator of 3 mm opening that selects a single pixel on the MAPMT surface. The detector itself is shielded in a castle made from polyethylene and lead. A moderated ${}^{252}\text{Cf}$ neutron source has been used and a clear neutron signal has been observed at the irradiated pixel. Work on a detailed analysis of the pulse and position sensitivity is ongoing.

In recent years, soft photon sensors using silicon technology, often called Silicon Photo Multipliers (SiPM), have reached maturity and present a viable alternative to vacuum-based photon detection solutions. They can provide the time resolution and photon detection efficiency commonly associated with vacuum-based PMTs while adding the advantages of a small form factor allowing compact sensor design, relative cost effectiveness, being inherently insensitive to magnetic fields and operating at much lower voltages. A single module is usually limited in size to a few mm^2 , but with the advent of Through Silicon Vias, three- or even four-side buttable sensors are nowadays readily available, allowing for the construction of larger detection areas. The photon detection efficiency of SiPMs often exceeds vacuum-based solutions in performance. SiPMs have been successfully used in neutron/gamma counting, but care has to be taken to ensure linearity and pulse shape discrimination for bright scintillators [12]. The SiPM performance is also strongly temperature dependent and, depending on the operation mode and ambient temperature, will exhibit a strong dark count contribution. Furthermore, the radiation hardness of SiPM exposed to a high neutron flux remains a concern. MAPMT, as studied above, hence, remain a viable and preferable solution for neutron imaging detectors at high neutron flux.

3 NEUTRON SENSORS BASED ON MICROCHANNEL PLATES

An alternative approach to realise an efficient, fast neutron sensor with excellent timing properties is the use of microchannel plates (MCPs). These devices have a long and established history in the detection of photons, where they are commonly used for highly demanding timing applications, often with position sensitive readout [11,12]. Single-photon timing resolutions below 50 ps are reported [13]. A microchannel plate normally consists of a glass plate into which narrow channels have been etched. They are typically mounted with the channels at a shallow angle (8° – 15°) to the normal and operated at a potential difference of a few kV. Electrons entering a pore of the MCP will hit a wall, where they produce secondary electrons, which in turn get accelerated and multiply, generating a typical gain of 10^6 suitable for single photon detection. The narrow confinement of the electron avalanche inside a channel causes a small transit time spread (and hence excellent timing) and an inherent insensitivity to magnetic fields [13]. The diameter D of these channels range from 3 μm to about 50 μm and plate thicknesses l of about 2 mm. The aspect ratio D/l is crucial for the timing and amplification properties of the MCP. In the past, issues with the life-time and rate capabilities have been reported for these devices, but have been overcome by the introduction of atomic layer deposition technology in recent years [14].

The inherent properties of an MCP make it an attractive solution for neutron sensors as well. In its most simple application, a multi-channel MCP PMT could be used to improve the timing or performance in magnetic fields of the systems discussed above, replacing a conventional MAPMT. A promising and significant technological step further is to use the MCP directly as a converter for neutrons. This has been demonstrated by using borated glass to manufacture the MCP and couple it to a Medipix2 readout positioned 0.7 mm behind the MCP stack [17]. The detector shows a spatial resolution better than 15 μm and an efficiency of 43% and 16% for cold and thermal neutrons, respectively.

3.1 PLASMA-ETCHING FOR THE MANUFACTURE OF MICROCHANNEL PLATES

The manufacture of conventional MCP plates required the fusion of glass capillaries to a plate and then cutting and polishing this place to the desired dimensions and quality. An alternative way to produce MCPs has been investigated. This method aims at exploiting the advances made in nano-fabrication of silicon structures, which is mainly driven by the electronics industry. Etching methods, such as Deep Reactive Ion Etching (DRIE) can now be readily employed to etch structures of significant size, with limitations normally only imposed by the wafer size the etching tool can handle and the etching time available. It is important, however, to ensure excellent control of the process.

Two different approaches were developed by the authors together with Kelvin Nano Technology (KNT), Glasgow, U.K. The first replicates the shallow angle under which conventional MCP plates would be installed. The resulting MCP is shown in an electron microscope image in Figure 3. The quality of the etch is excellent, and was realised for a vacuum tube of 25 mm active diameter. The development of this process, while successful, showed that the manufacturing process is unnecessarily convoluted. A simpler process using straight channels and a funnel structure has been developed in a second step, again optimised for vacuum tubes of 25 mm active diameter. The resulting quality of the etched structures exceeds the specifications and precision of other manufacturing techniques.

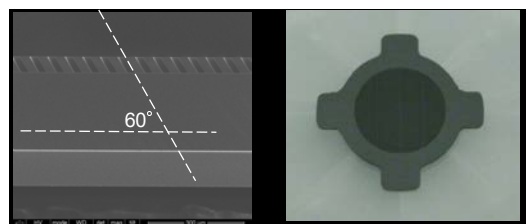


FIG. 3. Venetian blind geometry etched under an angle of 60° using DRIE (left) and the final Si dynode structure for implementation into a vacuum tube (right). The active diameter is 25 mm.

3.2 OUTLINE OF A NEUTRON SENSOR USING MICROCHANNEL PLATES

A silicon structure in itself is not an efficient neutron converter (nor an efficient secondary electron source). An application in a neutron sensor would, hence, require adding a significant amount of material capable of absorbing neutrons and emitting charged particles in the process. In the case of borated glass previously used [14], this is achieved by using a glass with a high boron content. Since a new manufacturing process is proposed, it would be ideal to replace silicon as a base material with a material of high boron content, e.g. BN or B_4C . Unfortunately, both materials are very hard and, therefore, do not lend themselves to easy etching at the desired thickness and aspect ratio. A promising, yet to be investigated avenue would be the use of heavily borated silicon substrates. An efficiency estimate, however, indicates that for current commercially available, highly borated substrates the upper limit of the efficiency would be a few percent, considered low compared to alternative technological solutions.

It is, however, reasonably straightforward to apply a metal coating, similar to ALD used in conventional MCP, to an etched silicon structure. A second-generation silicon MCP was successfully coated with gadolinium, the thickness varying from 20 nm at the top of the microchannel to 3 nm at the bottom. The variation in thickness is solely due to the manufacturing process. A SEM picture (Figure 4) shows the resulting quality with a poorly etched silicon wafer.

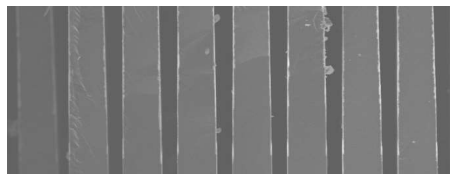


FIG. 4. Gadolinium-covered MCP with a channel diameter of $10\mu\text{m}$. The coated layer is 20 nm thick.

Natural gadolinium exhibits a high neutron capture cross section in the relevant neutron energy range. In most cases, the neutron capture is followed by the emission of a high-energy gamma-photon. But in a significant number of cases, electrons will be emitted, suitable for amplification and detection. An efficiency estimate yields an expected efficiency in excess of 50%. Replacing natural gadolinium with isotopically enriched ^{157}Gd will further increase the efficiency. A gadolinium coating has been already successfully used in a complementary

technique, coating GEM foils with a 250 μm sheet of Gd. The prototype achieved a measured efficiency of 11.8% and a position resolution better than 250 μm [17].

Following the conversion of a neutron into a charged particle, the detection task now is to efficiently detect this charged particle. For an MCP-based detector, this would most naturally be within the vacuum vessel housing the MCP. Several candidate systems exist, mostly notably the Medipix family, in particular the Timepix3 chip [16]. The chip is designed in 130 nm CMOS and contains 256×256 pixel channels ($55 \times 55 \mu\text{m}^2$). It provides a timing resolution of 1.6 ns as well as Time-over-Threshold and Time-of-Arrival measurements. The pixel size is well matched to the pore size of an MCP and Time-over-Threshold allows for an energy measurement and hence rudimentary particle identification and background rejection as well. A combination of modern detection and read-out chips, like the Timepix3 with new developments in neutron efficient MCP production will enable the next generation neutron imaging sensors with excellent spatial resolution.

4 CONCLUSIONS

The advanced neutron sources currently under construction require a new generation of neutron imaging sensors capable of imaging at high instantaneous neutron flux and with sufficient spatial and temporal resolution. As the time resolution contributes to both, the rate capacity but crucially the energy resolution of the scattered neutrons, optimising the sensor system for best time resolution is advantageous.

Modern neutron converters coupled to either visible light detectors or incorporated into an MCP-type structure and semi-conductor sensor for charge particle detection provide the necessary technological advance to realise neutron sensor systems meeting the performance demands of future neutron imaging applications. The initial estimates and tests performed indicate that the necessary performance will be realised in the final detector system.

A sensor arrangement based on neutron sensitive scintillators coupled to MAPMT is in an advanced stage of development. The realisation of an MCP-type neutron sensor with new manufacturing techniques is in the early stages of development and will enter the proof-of-concept stage soon.

REFERENCES

- [1] PEGGS, S., ESS Technical Design Report (2013).
- [2] KIRSTEIN, O., et al., Neutron position sensitive detectors for the ESS, Proceedings of Science. The 23rd International Workshop on Vertex Detectors, 15-19 September 2014 Macha Lake, The Czech Republic, (2014).
- [3] MONTGOMERY, R.A., et al., Multianode photomultiplier tube studies for imaging applications, *J. Nucl. Instrum. Methods Phys. Res. A* **695** (2012) 326–329.
- [4] CONTALBRIGO, M., et al., The large-area hybrid optics CLAS12 RICH detector: Tests of innovative components, *J. Nucl. Instrum. Methods Phys. Res. A* **766** (2014) 22–27.
- [5] MONTGOMERY, R.A., et al., Investigation of Hamamatsu H8500 phototubes as single photon detectors, *J. Nucl. Instrum. Methods Phys. Res. A* **790** (2015) 28–41.
- [6] FIRK, F., SLAUGHTER, G., GINTHER, R., *Nucl. Instrum. Methods* **13** (1961) 313.
- [7] SPOWART, A.R., *Nucl. Instrum. Methods* **135** (1976) 441.
- [8] SPOWART, A.R., *Nucl. Instrum. Methods*. **140** (1977) 19.
- [9] KEMMERLING, G., JAKSCH, S., Solid-State Neutron Detector INFRADEV-1-2014/H2020, Grant Agreement Number: 654124.
- [10] PRESTON, R.M., EBERHARDT, J.E., TICKNER, J.R., Neutron–gamma pulse shape discrimination using organic scintillators with silicon photomultiplier readout, *Trans. Nucl. Sci.* **61** (2014) 2410–2418.
- [11] SEITZ, B., et al., Development of DIRC counters for the PANDA experiment at FAIR, *J. Nucl. Instrum. Methods Phys. Res. A* **628** (2011) 304–308.
- [12] CONNEELY, T.M., et al., The TORCH PMT: a close packing, multi-anode, long life MCP-PMT for Cherenkov applications, *J. Instrum.* **10** (2015) C05003.
- [13] LEHMANN, A., et al., Performance studies of microchannel plate PMTs in high magnetic fields *J. Nucl. Instrum. Methods Phys. Res. A* **595** (2008) 173–176.
- [14] LEHMANN, A., et al., Lifetime of MCP-PMTs, *J. Instrum.* **11** (2016) C05009.
- [15] TREMSIN, A.S., et al., Detection efficiency, spatial and timing resolution of thermal and cold neutron counting MCP detectors, *J. Nucl. Instrum. Methods Phys. Res. A* **604** (2009) 140–143.
- [16] POIKELA, T., et al., Timepix3: a 65K channel hybrid pixel readout chip with simultaneous ToA/ToT and sparse readout, *J. Instrum.* **9** (2014) C05013.
- [17] PFEIFFER, D., et al., First measurements with new high-resolution Gadolinium-GEM Neutron Detectors, *J. Instrum.* **11** (2016) P05011

DEVELOPMENT OF NEUTRON DETECTORS FOR THE SPECTROMETERS OF THE IBR-2 REACTOR

S.A. KULIKOV, A.V. CHURAKOV, V.V. KRUGLOV, A.A. BOGDZEL, V.M. MILKOV, V.V. ZHURAVLEV, S.M. MURASHKEVICH, E.I. LITVINENKO, TS.TS. PANTELEEV

Frank Laboratory of Neutron Physics,
Joint Institute for Nuclear Research,
Russia
Email: churakov@nf.jinr.ru

Abstract: The variety of research being conducted at the instruments on the external beams of the IBR-2 pulsed research reactor in Frank Laboratory of Neutron Physics of Joint Institute for Nuclear Research (FLNP JINR) leads to a variety of requirements for detectors. This leads to the necessity of developing a variety of detectors in the Laboratory (gaseous ^3He -based detectors: 1D and 2D multi-wire proportional chambers (MWPC), ‘ring’ detectors; ^6Li -scintillator-based detectors with wavelength shifting fibers, detectors and monitors with solid ^{10}B converters etc.). This article describes the neutron detection systems developed and used at the instruments, as well as the current status and projects carried out at FLNP on the development of detectors and data acquisition systems.

1 INTRODUCTION

Research on modern high-flux neutron sources requires a variety of diverse experimental equipment. Neutron detectors, as well as detector systems are important components of the experimental equipment. Detectors include neutron counters, position sensitive detectors, neutron calorimeters, neutron flux monitors, etc. The detector system carries out data acquisition and accumulation and transfers the data for processing and storage. It includes one or several detectors, front-end electronics, data acquisition system and software. The detector systems are usually included in the structure of more complex automated systems. They can interact with other scientific equipment, for example, receiving a start signal in Time-Of-Flight (TOF) mode. In turn, the detector system itself constantly transfers information to the experimental control system.

2 DETECTOR DEVELOPMENTS

A variety of devices operating on different physical principles can be used to detect neutrons. The scientists of department of the IBR-2 spectrometer complex (DSC) at Frank Laboratory of Neutron Physics (FLNP JINR) develop new types of detectors, as well as create detector systems on the basis of already existing devices. Most of these detectors are gaseous proportional devices that use ^3He as a neutron converter. Scintillation detectors and gaseous position-sensitive detectors (PSD) with a solid-state boron converter are also put in operation, as well as fast neutron spectrometric detectors working on the principle of recoil nuclei.

2.1 MULTI-COUNTER SYSTEMS

Historically, industrial proportional counters such as SNM-17 (Russia) have been widely used in experiments with neutrons. Individual counters are used on most experimental IBR-2 channels [1] as a complementary neutron detector. They have good efficiency for thermal and cold neutrons, and can work in time-of-flight mode. Proportional counters are relatively easy to operate and well mastered by commercial manufacturers.

The multi-counter detector systems, consisting of proportional helium counters, operate at the spectrometers NERA [2], SKAT [3], EPSILON [4], DN-12 [5], DIN-2PI [6], RTD [7] and DN-6 of the IBR-2 reactor. Multi-counter systems are simple to design, can be relatively quickly developed and put into operation (Fig. 1). The disadvantages of multi-counter systems are the diverse efficiency of individual counters, caused by variations in the gas mixture pressure and the lack of coordinate sensitivity over the sensitive area. For experiments in which these deficiencies are significant, specialized devices had to be developed, for example, ring detectors or position-sensitive detectors.



FIG. 1. Multi-counter systems of IBR-2 spectrometers EPSILON(left), SKAT(centre) and DN-12(right).

2.2 RING DETECTORS

Gaseous ring detectors unite several independent detector elements in one sealed body. These devices are used at FLNP JINR for condensed matter investigations along with industrial proportional neutron counters. Detectors are designed to measure the angular distribution of scattered neutrons relative to the direction of the incident beam. In the centre of the ‘ring’ detector, an opening is usually made for the transmission of the direct neutron beam. All gas ring detectors developed by FLNP JINR use ^3He as a neutron converter.

The multisectional annular thermal-neutron detector (Fig. 2) operates at the DN-6 spectrometer for the study of diffraction on microsamples in axial geometry [8]. The input window for scattered neutrons is the surface of the inner ring of the detector. The sensitive volume of the detector is divided into 16 sectors in a plane perpendicular to the beam axis. Each of the sectors is further divided into 6 sections along the generatrix of the cylindrical surface, so the detector contains 96 independent counting elements located in a single gas volume. A common hermetic volume for all counting elements makes it possible to obtain practically uniform efficiency for all sections. The detector has smaller ‘dead zones’ and better angular resolution than the ring of individual counters used previously. The body of the detector is made of an aluminum alloy that provides tightness and mechanical durability of the device. Preamplifiers are also located inside the hermetic volume to provide maximum protection against noise. Individual readout of information from each counting element provides the necessary flexibility for adjustments of the detector. Signals from the preamplifiers of the detector are fed to the inputs of a MPD-32 data acquisition unit [9].

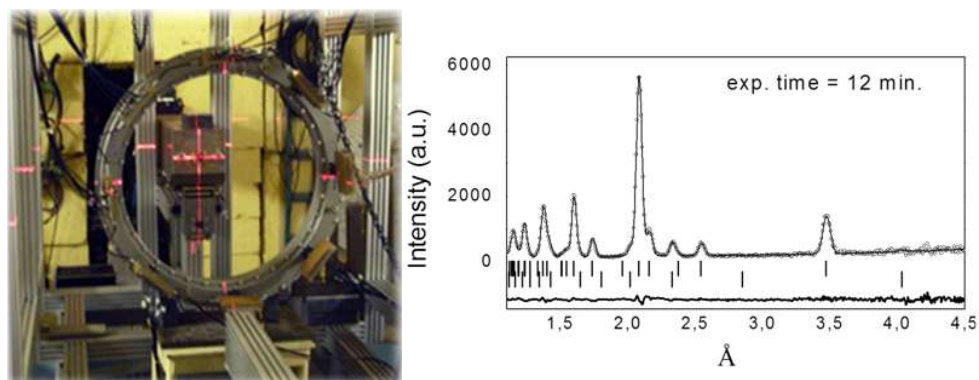


FIG. 2. Multisectional, annular, thermal-neutron detector for the study of diffraction on microsamples in axial geometry located at DN-6 spectrometer.

Ring detectors are also used at FLNP JINR for experiments on small-angle neutron scattering (SANS). The small-angle spectrometer YuMO, located at beam №4 of IBR-2, uses a detector system consisting of two ring detectors and a direct beam monitor [10]. The design of the gaseous 8-section ring detector was originally developed by Yu. M. Ostanevich, B. N. Ananiev, and E. Ya. Pikelner. Copper cathodes divide the inner volume of the detector into 8 rings. In the centre of each ring an anode wire is fixed by the supporting columns. The scattering angle is determined by the number of the ring in which a neutron was registered. A similar detector was manufactured and put into operation at the RTD spectrometer in 2014 (Fig. 3, left).

Based on the construction of the old 8-section detector [12], a new ring detector for small-angle scattering of thermal neutrons was developed. It is designed for measurements of biological samples and nanodispersed polymer objects containing functionally significant heterogeneities of various structural complexities at the RTD diffractometer. An important feature of this detector is the ability to determine the second angular coordinate of neutrons in the plane perpendicular to the beam. This can be useful for carrying out measurements in which angular or axial inhomogeneity of thermal neutron beam is observed. The cathodes separating the detector into 9 rings are made of double-sided copper-coated fiberglass. Each ring has inner and outer cathodes, and the anode wire is fixed in the middle between them. The outer cathode of each ring is divided into 16 independent electrically isolated segments, giving a total number of 144. The induced signals are read from these cathode segments, and the signals from the anodes are also registered. Each segment covers an angle of ~ 22.5 degrees of the corresponding ring. One detector of this type has been made, shown in Fig. 3 (right).



FIG. 3. Ring detectors for SANS. Old 8-section ring detector (left) and new 9-section two-coordinate ring detector (right).

2.3 POSITION-SENSITIVE DETECTORS (PSD)

Position-sensitive detectors (PSDs) are versatile instruments for various neutron diffraction experiments. They have the possibility to determine the coordinates of the neutron registration point with accuracy much smaller than the size of the detector. At FLNP JINR two types of universal PSDs have been developed – a one-coordinate (1D) detector of thermal neutron with a sensitive area of $200 \times 80 \text{ mm}^2$ [11] and a two-coordinate (2D) version with a sensitive area of $200 \times 200 \text{ mm}^2$. These devices have a similar construction, made on the principle of the multiwire proportional camera (MWPC). A hermetic volume encloses an electrode system consisting of 2 cathode grids and an anode grid, as well as 2 drift planes. Drift planes that limit the sensitive thickness of the detector are fed with a negative potential, while the anode is under a positive high voltage potential. There is no gas gap between the input window and the first drift plane, so neutrons are not absorbed uselessly outside the sensitive volume. The time information is determined by the anode signal, coordinate information received from cathodes using delay lines. The coordinate resolution is 2 mm for a 1D PSD and $2 \times 2.3 \text{ mm}^2$ for a 2D PSD. Standardized data acquisition system DeLiDAQ [12] or DeLiDAQ-2 [13] is used for processing and storage of data for both types of detector. The efficiency of the detectors for thermal neutrons (2\AA) is $\sim 65\%$. The neutron converter is ^3He . Photos of the 1D and 2D PSD are shown in Fig. 4.



FIG. 4. 1D (left) and 2D (right) PSD.

One-coordinate PSDs developed by FLNP JINR worked on the HRFD diffractometer of FLNP JINR, at the Kurchatov Institute (Moscow, Russia) and at the branch of the Karpov Institute of Physical Chemistry (Obninsk, Russia). Two-coordinate PSDs are used on the REFLEX, REMUR, GRAINS, RTD spectrometers of FLNP JINR, at the Institute for Nuclear Research of the Russian Academy of Sciences (INR RAS) (Moscow, Russia) and the Institute of Nuclear Physics of the Czech Academy of Science (Rez, Czech Republic) [14] The Kurchatov Institute has a slightly modified version of a two-coordinate detector with a sensitive area of $150 \times 250 \text{ mm}^2$.

2.4 NEUTRON MONITORS

In experiments on modern research neutron sources, the problem of measuring the neutron flux profile before the sample often arises, and the changes in the incident beam from the detector have to be minimal. Specially developed neutron monitors solve this problem. In order to measure the spatial distributions of neutron beams on the neutron guides of the IBR-2 reactor, a 2D PSD monitor was developed [15]. The monitor is a multiwire proportional chamber with external dimensions of $320 \times 320 \times 23 \text{ mm}^3$ and a sensitive area of $100 \times 100 \text{ mm}^2$. The thickness of input and output windows are 1 mm. This value selected in order to have the least possible attenuation of the neutron flux while maintaining an acceptable reliability of the device. The appearance of the monitor is shown in Fig. 5 (left). The monitor has an extremely low efficiency, estimated at $\sim 10^{-5}$, which makes it possible to operate in a direct beam of the reactor without overloading. Some of direct external beam profiles of the IBR-2 reactor measured with this 2D monitor are shown in Fig. 6.



FIG. 5. 2D PSD monitors: 100×100 (left), 'Troitsk' (right).

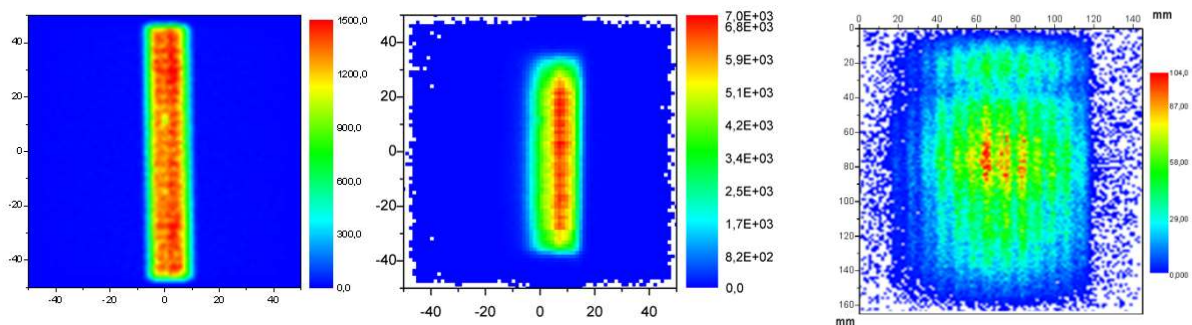


FIG. 6. Profiles of RTD (left), HRFD (centre) and DIN-2PI (right) spectrometers of IBR-2.

To measure the spatial distribution of the thermal and cold neutron beams of the IN-06 source [16], a similar two-coordinate neutron monitor, 'Troitsk', was designed and manufactured (Fig. 5, right). The device allows monitoring the profile of the beam incident on the sample and the position of the sample. This is especially important when the position of the sample cannot be determined visually, for example, when using a cryostat, furnace, or high-pressure chamber. The input and output windows of the monitor are interchangeable, which allows working not only in the thermal, but also in the cold energy region with a thin input window. When working with standard parameters (input and output windows thickness: 1 mm; efficiency: 0.1%) losses in the input beam for thermal neutrons (1.8 \AA) are less than 3%. The electronic system for data collection and acquisition has been unified with the standard FLNP electronics for position-sensitive detectors.

2.5 2D PSD PROTOTYPE WITH B₄C CONVERTER

Boron-10 is a promising converter for thermal neutron detectors. The European Spallation Source (ESS), using the advanced thin film evaporation technology, has developed gas detectors [17] [18] with a B₄C converter enriched with ¹⁰B. Position-sensitive detectors with this type of converter can be of interest both as direct beam monitors and as detectors for neutron diffraction. The localization of the interaction point in a thin converter layer may yield better coordinate resolution than resolution of the ³He gas detectors.

In cooperation with the detector department of ESS, a 2D PSD prototype with B₄C converter was developed and created. The prototype shown in Fig. 7 has the following design. An aluminum plate, 0.1 mm thick, with a deposited layer of B₄C, 0.5 μm thick, is fixed on the entrance window. The plate with the converter is under zero potential and serves as a drift electrode. The cathode is a two-sided printed circuit board with copper pads used to collect the induced signal. Anode wires, 10 μm thick, are located in the middle between the drift electrode and the cathode. Half of the cathode pads are connected to each other by conductors running parallel to the anode; the other half of the pads are connected by conductors, perpendicular to the cathode. The conductors are connected through a delay line, which are used to determine the coordinate. The prototype parameters were measured on channel No. 13 of the IBR-2 reactor. The measured coordinate resolution of the detector was 0.9 mm in the coordinate perpendicular to the anode. The detector showed good stability. Despite a rather long operating time in the direct beam, there was no degradation or shedding of the neutron converter layer over time.

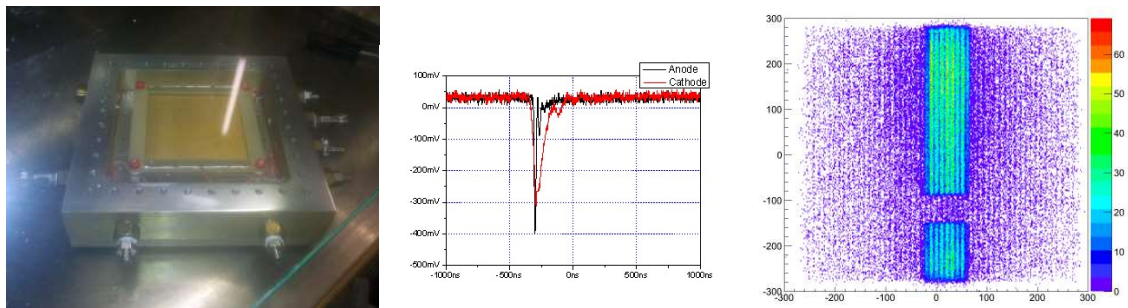


FIG. 7. 2D PSD with B₄C converter (left), its amplitude (middle) and coordinate (right) spectra.

2.6 SCINTILLATOR DETECTORS

Along with gaseous detectors, scintillation systems based on a proven combination of ZnS (Ag) scintillator, ND screen with ⁶Li neutron converter and wavelength shifting fibers (WLS) are also being developed. In FLNP JINR, this technique is used for the detector system ‘ASTRA’ [19] located at the neutron Fourier stress diffractometer FSD [20]. The detector system consists of two symmetrical banks centred on a scattering angle of ±90 degrees. Each bank is planned to compose of 7 modules with 4 counters per module. The counters are designed and arranged to approximate a time-focusing surface. At present, 4 modules are installed in each bank. Module №4 and typical diffraction spectra from the ‘ASTRA’ detector system are shown in Fig. 8.

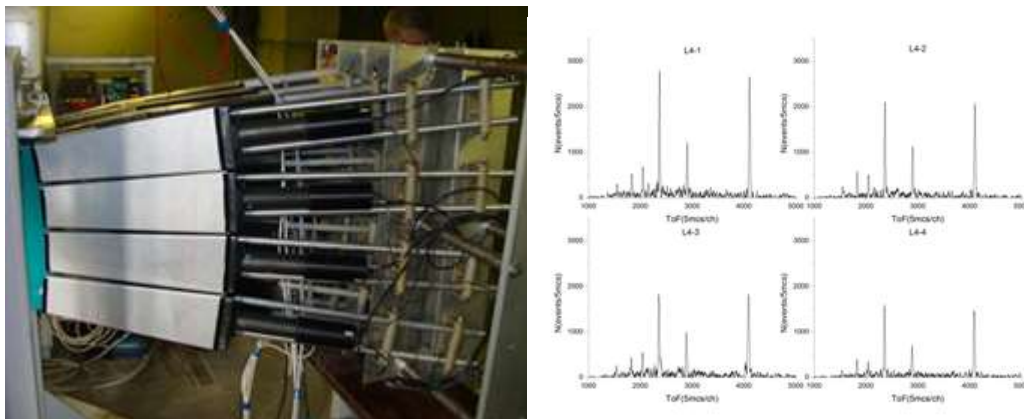


FIG. 8. ‘ASTRA’ scintillator detector (left), diffraction spectra of α-Fe, measured with ‘ASTRA’ detector system (right).

Implementation of the initial phase of the ‘ASTRA’ project showed that the selected design of the individual counter provides the required characteristics of the detector system. The shielding against the background of scattered neutrons, made of epoxy with a boron carbide, works quite effectively. However, the general scheme of the detector system based on a set of individual counters severely complicates the assembly of the system and does not allow high accuracy in the installation of individual meters. The design of the shielding significantly reduces active solid angle of the detector and is difficult to manufacture. To eliminate these drawbacks, a new version of the detector system, the ASTRA-M, was developed. In this version, the geometry of the surfaces was changed. The dimensions of the detector elements were standardized, which significantly reduced the cost of component materials. Detecting elements consisting of a scintillator and optical fibers are fixed closely to the surface of counters without a gap between them. All optical fibers from one block are combined into one photomultiplier. Thus, each block actually represents a single scintillation counter of a complex shape. The proposed design of the ‘ASTRA-M’ (Fig. 9) detection system has significant advantages over the original version of the system. The possibility of adjusting the detectors as part of the Fourier stress diffractometer FSD has been radically improved. It was possible to approximate the time-focusing surface as closely as possible without complicating the design of the detector. The number of registration channels significantly decreased. Currently, the updated version of the system ‘ASTRA-M’ is in the process of assembly.

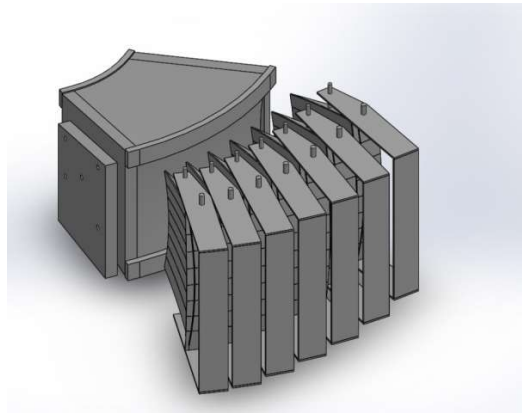


FIG. 9. Design of improved detector system ‘ASTRA-M’.

2.7 SPECTROMETRY DETECTORS

To determine the energy spectra of fast neutron with energy >100 keV, the recoil nuclei method is used. The energy of the recoil protons produced by elastic scattering of neutrons in hydrogenous material is measured in this method. For experimental studies with fast neutrons, a neutron spectrometer based on a proton telescope with electronic collimation of recoil protons is created [21]. The design of the telescope is based around a hermetical case that encloses an anode wire and two cylindrical cathodes. The inner volume of the telescope is filled with hydrogen-containing gas mixture. The first cathode limits the target area and the second cathode collimates the recoil protons in the required solid angle. The region from the end of the second cathode to the end of the detector body creates a volume in which the energy of the recoil protons is completely absorbed. The choice of signals is realized by the coincidence of the pulses from the recoil protons in both cathodes. The efficiency and dynamic energy range of the device can be adjusted by varying the pressure of the gas mixture. The device was used to determine the spectra of fast neutrons on neutron-producing targets of electrostatic generator EG-5 of the FLNP JINR.

A new version of proton telescope (Fig. 10) has been designed, manufactured and tested. It can measure the kinetic energies of neutrons with better efficiency in a large dynamic range. The device is used to measure the plasma temperature from the D (d, n) ^3He reaction at the KSTAR thermonuclear reactor facility at the National Nuclear Fusion Research Institute (NIJAS, Daejeon, Korea).



FIG. 10. New proton telescope.

3 DATA ACQUISITION

Standardized electronic systems [22] are used for data acquisition from detectors at the IBR-2 reactor. These systems represent a unified set of identical modules developed in the Department of the IBR-2 spectrometers complex (the first DeLiDAQ boards developed in collaboration with HZB, Berlin). For gaseous or scintillation counters and multi-counter systems, as well as for ring detectors, DAQ systems based on MPD-16 and MPD-32 units are used. These blocks have a NIM form factor. The maximum number of detection channels is 16 for MPD-16 and 240 for MPD-32. For 1D and 2D position-sensitive detectors the PCI board DeLiDAQ or new DeLiDAQ-2 NIM units are used. All electronic systems can operate in the TOF mode.

4 CONCLUSION

The employees of FLNP JINR carried out work on providing the IBR-2 experimental facilities with modern detectors and maintaining old systems in working condition. The detector systems on all commissioned instruments of the IBR-2 reactor successfully function and allow conducting the experiments for which they are intended. At the same time, new challenges require joint efforts and collaboration of leading neutron centres to create detector systems, electronics and software.

ACKNOWLEDGEMENTS

The authors are grateful to all of the DSC staff, who participated in the development of new detectors, as well as to all their colleagues from FLNP JINR, who helped with the deployment and testing.

The authors would also like to express gratitude to our colleagues from the detector department of ESS, Sweden, and the detector group HZB, Germany for assistance in our development.

REFERENCES

- [1] DRAGUNOV, Y.G., et al., Modernization of the IBR-2 pulsed research reactor, *At. Energy* **113** (2012) 29–38.
- [2] NATKANIEC, I., et al., Parameters of the NERA spectrometer for cold and thermal moderators of the IBR-2 pulsed reactor, *J. Phys. Conf. Series* **554** (2014) 012002.
- [3] ULLEMEYER, K., et al., The SKAT texture diffractometer at the pulsed reactor IBR-2 at Dubna: experimental layout and first measurements, *Nucl. Instrum. Methods Phys. Res. A* **412** (1998) 80–88.
- [4] WALTHER, K., SCHEFFZUEK, C., FRISCHBUTTER, A., Neutron time-of-flight diffractometer Epsilon for strain measurements: layout and first result, *Phys.B* **276–278** (2000) 130–131.
- [5] AKSENOV, V.L., et al., DN-12 time-of-flight high-pressure neutron spectrometer for investigation of microsamples, *Phys. B* **265** (1999) 258–262

- [6] KALININ, I.V., et al., Characteristics of the DIN-2PI spectrometer with a neutron concentrator, *Tech. Phys. Russian J. Appl. Phys.* **59** (2014) 307–310.
- [7] BALAGUROV, A.M., et al., Neutron diffractometer for real-time studies of transient processes at the IBR-2 pulsed reactor, *J. Surf. Investig. X-ray Synchr. Neutr. Tech.* **10** (2016) 467–479.
- [8] BELUSHKIN, A.V., et al., A multisectional annular thermal-neutron detector for the study of diffraction on microsamples in axial geometry, *Phys. Part. Nucl. Letters* **10** (2013) 436–441.
- [9] LEVCHANOVSKIY, F.V., MURASHKEVICH, S.M., A data acquisition system for neutron spectrometry—the new approach and the implementation, in *Proc. XXIV Int. Symp. on Nuclear Electronics and Computing NEC'2013* (Varna, Bulgaria), (Dubna, JINR), (2013) 176–179.
- [10] KUKLIN, A.I., ISLAMOV, A.KH., GORDELIY, V.I., Two-Detector system for small-angle neutron scattering instrument, *Neutr. News* **16** 3 (2005) 16–18.
- [11] BELUSHKIN, A.V., et al., A one-dimensional position-sensitive detector for thermal neutrons, *Instrum. Exp. Tech.* **50** (2007) 737–743.
- [12] LEVCHANOVSKIY, F.V., et al., A PCI DAQ board for MWPC detectors with delay line position readout, *Nucl. Instrum. Methods Phys. Res., A* **529** (2004) 413–416.
- [13] LEVCHANOVSKIY F.V., MURASHKEVICH S.M., DE-LI-DAQ-2D — a new data acquisition system for position-sensitive neutron detectors with delay-line readout, *Phys. Part. Nucl. Letters* **13** (2016) 591–594.
- [14] LITVINENKO, E.I., et al., Upgrade of detectors of neutron instruments at Neutron Physics Laboratory in Řež, *Nucl. Instrum. Methods Phys. Res. A* **841** (2017) 5–11.
- [15] BELUSHKIN, A.V., et al., Two-coordinate position-sensitive monitor-detector of thermal neutrons, *Tech. Phys. Russian J. Appl. Phys.* **53** (2008) 117–121.
- [16] KUZNETSOV, S. P., et al., Multifunctional pulsed neutron spectrometer IN-06 of INR RAS, *Bull. Lebedev Phys. Inst.* **40** (2013) 245–250.
- [17] PISCITELLI, F., et al., The Multi-Blade Boron-10-based neutron detector for high intensity neutron reflectometry at ESS, *J. Inst.* **12** (2017) P03013.
- [18] ANASTASOPOULOS M., et al., Multi-Grid detector for neutron spectroscopy: Results obtained on Time-of-Flight spectrometer CNCS, *J. Inst.* **12** (2017) P04030.
- [19] KUZMIN, E.S., et al., Detector for the FSD Fourier-diffractometer based on ZnS(Ag)⁶LiF scintillation screen and wavelength shifting fibers readout, *J. Neutr. Res.* **10** (2002) 31–41.
- [20] BOKUCHAVA, G.D., BALAGUROV, A.M., SUMIN, V.V., PAPUSHKIN, I.V., Neutron Fourier diffractometer FSD for residual stress studies in materials and industrial components, *J. Surf. Investig. X-ray Synchr. Neutr. Tech.* **4** (2010) 879–890.
- [21] MILKOV, V.M., et al., Neutron spectrometer based on a proton telescope with electronic collimation of recoil protons, *Phys. Part. Nucl. Letters* **9** (2012) 508–516.
- [22] KULIKOV, S.A., PRIHODKO, V. I., A new generation of data acquisition and data storage systems of the IBR-2 reactor spectrometers complex, *Phys. Part. Nucl.* **47** (2016) 702–710.

THE NEUTRON-TAGGING FACILITY AT LUND UNIVERSITY

F. MESSI, H. PERREY, K. FISSUM, D.D. DIJULIO, E. KARNICKIS, V. MAULEROVA, N. MAURITZSON, E. ROFORS

Division of Nuclear Physics, Lund University and
European Spallation Source ERIC
Lund, Sweden

Email: francesco.messi@nuclear.lu.se

A. HUUSKO, T. ILVES, A. JALGÉN, S. KOFIGAR, H. SÖDERHJELM, D. SÖDERSTRÖM

Division of Nuclear Physics, Lund University
Lund, Sweden

R. HALL-WILTON

European Spallation Source ERIC

Lund and
Mid-Sweden University
Sundsvall, Sweden

P.M. BENTLEY, C.P. COOPER-JENSEN, J. FREITA-RAMOS, F. ISSA, K. KANAKI, A. KHAPLANOV, G. MAURI, F. PISCITELLI, I. STEFANESCU

European Spallation Source ERIC
Lund, Sweden

J. SCHERZINGER

Department of Physics, University of Pisa
Pisa, Italy

R. AL JEBALI

European Spallation Source ERIC
Lund, Sweden and
School of Physics and Astronomy, Glasgow University,
Glasgow, UK

J.R.M. ANNAND, L. BOYD

School of Physics and Astronomy, Glasgow University,
Glasgow, UK

M. AKKAWI, W. PEI

University of Toronto
Toronto, Canada

Abstract: Over the last decades, the field of thermal neutron detection has overwhelmingly employed He-3-based technologies. The He-3 crisis together with the forthcoming establishment of the European Spallation Source have necessitated the development of new technologies for neutron detection. Today, several promising He-3-free candidates are under detailed study and need to be validated. This validation process is in general long and expensive. The study of detector prototypes using neutron-emitting radioactive sources is a cost-effective solution, especially for preliminary investigations. That said, neutron-emitting sources have the general disadvantage of broad, structured, emitted-neutron energy ranges. Further, the emitted neutrons often compete with unwanted backgrounds of gamma-rays, alpha-particles, and fission-fragments. By blending experimental infrastructure such as shielding to provide particle beams with neutron-detection techniques such as tagging, disadvantages may be converted into advantages. In particular, a technique known as tagging involves exploiting the mixed-field generally associated with a neutron-emitting source to determine neutron time-of-flight and thus energy on an event-by-event basis. This allows for the definition of low-cost, precision neutron beams. The Source-Testing Facility, located at Lund University in Sweden and operated by the SONNIG Group of the Division of Nuclear Physics, was developed for just such low-cost studies. Precision tagged-neutron beams derived from radioactive sources are available around-the-clock for advanced detector diagnostic studies. Neutron measurements performed at the Source Testing Facility are thus cost-effective and have a very low barrier for entry. In this paper, we present an overview of the project.

1 INTRODUCTION

Neutrons of all energies are important probes of matter. The precise detection of neutrons emerging from a sample under study is crucial to the quality of the resulting experimental data. Until recently, He-3-based technologies were essentially the only method used for neutron detection. The recent He-3-crisis [1,2] and the proposal of the European Spallation Source (ESS) [3,4] have led to an aggressive search for alternative technologies [5]. Together, the prohibitive cost of He-3 and the design goals for the new facility with its extremely high flux of neutrons call for completely new concepts for detectors [6] and shielding [7]. Strong candidates for new detector technologies exist, but few of these have been characterized properly. Most are still in their developmental infancy and need to be precisely validated. In general, the validation of a new detector technology is a two-step process: first, wide-ranging irradiations are performed using neutron-emitting radioactive sources, where the cost per neutron is low; and second, promising technologies are then precisely irradiated at neutron-beam facilities, where the cost per neutron is substantially higher. We note that the cost per neutron at a neutron-beam facility can be so high that it may be prohibitively expensive. A facility based upon neutron-emitting radioactive sources is thus a cost-effective solution to this problem with a relatively low entry threshold. Once the sources and necessary infrastructure are in place, ‘natural’ neutrons are available around the clock. Thus, the overhead for initially benchmarking new technology will not be dominated by beam-time associated costs. Further, by instrumenting a source facility with well understood shielding and equipment to take advantage of nuclear-physics knowledge associated with the particular radioactive decay in question, low-cost polychromatic beams of neutrons may be created.

At the Division of Nuclear Physics at Lund University [8], the internationally accessible Source-Testing Facility (STF) [9] facility has been constructed to provide precision beams of neutrons from radioactive sources. Thus, a cost-effective solution for performing advanced detector diagnostics already exists and is in fact routinely employed by its users. The STF has been instrumented to provide all the tools necessary for the initial characterization of newly developed detectors and shielding materials to its users.

2 THE SOURCE TESTING FACILITY

Constructed at the Division of Nuclear Physics at Lund University in collaboration with the Detector Group [10] at ESS, the STF is operated by the SONNIG group [11]. It is a fully equipped user facility. The STF boasts a complete range of neutron and gamma-ray sources for the characterizations of detectors and is also equipped with several detectors, detector-associated infrastructure and IT, as well as the electronic components essential to the needs of a user-focused laboratory. As there are no reactors or accelerators involved, the STF is available continuously for prototype development and commissioning. Figure 1 shows an overview of the facility.

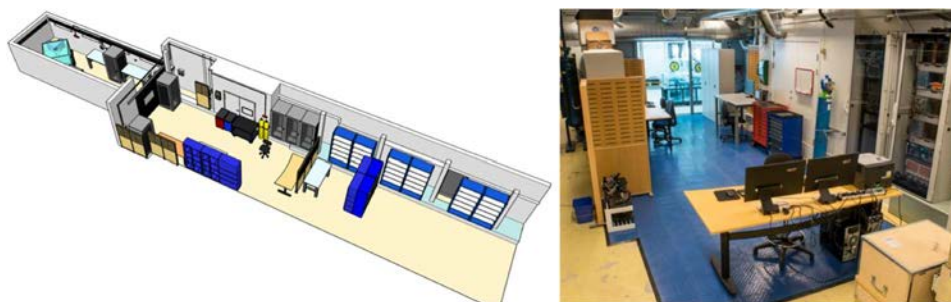


FIG. 1. The STF. On the left, a 3D-rendering and on the right, a photo.

The key infrastructure available at the STF includes:

- **Sources:** several mixed-field Actinide-Beryllium sources, a fission neutron source as well as gamma-ray sources. In particular, $^{241}\text{Am-Be}$, $^{238}\text{Pu-Be}$ and ^{252}Cf (thin window) sources are available as well as ^{57}Co , ^{60}Co , ^{137}Cs , ^{22}Na and ^{133}Ba sources for gamma-ray radiation.
- **Detectors:** - a full set of detectors, both commercially provided and in-house developed, for background monitoring, gamma-ray detection and fast- and thermal-neutron detection. The detector pool of the STF includes plastic and liquid scintillators, gas detectors (He-3 tube, He-4 cells), solid-boron detectors, inorganic crystal scintillators (such as 1.5” CeBr₃ and LaBr₃ as well as a 12” NaI) and boron-straw tubes, to name a few. Example of detectors available at the STF are shown in Fig. 2.



FIG 2. Example of detectors available at the STF. From the left, two plastic scintillator paddles read out by PMTs, one He-4 cell (operated at 5 atm) read out by a 2" PMT, a He-3 tube (calibrated efficiency of 96.1% at 2.5Å) and two NE213 liquid scintillator (0.43 and 4.5 l) read out by a 3" PMT.

- The Aquarium:** a custom-designed shielding apparatus for neutron sources, delivering if desired beams of ‘tagged’ neutrons¹ (see Fig. 3). The Aquarium consist of a 3-section cube of Plexiglas (~1.4 m side), filled with about 2650 l of high-purity water. It is designed to host a neutron source in its centre, together with four gamma-ray sensitive detectors. The designed goal for the equivalent dose rate on the external surface of the cube is <math><0.5 \mu\text{Sv/h}</math> when an industry standard 18.5 GBq ²⁴¹Am–Be source is encapsulated. Four horizontal cylindrical apertures of ~17 cm in diameter act as ‘beam guides’, one perpendicular to each of the four vertical faces of the cube, providing four uniform but combined beams of gamma-rays and neutrons from the source.
- A black-box:** a light-tight enclosure for testing light-sensitive detectors such as open photo-multiplier tubes (PMTs) (see Fig. 4). The enclosure will eventually contain an optical Table with a 1 m² work surface. One end of the enclosure will house servo stages which can either carry a calibrated laser emitter or radioactive sources. These servo stages will allow for the mapping of the topological response of areal detectors such as multi-anode PMTs.
- Electronics and computers:** the STF is equipped with a comprehensive set of electronics modules and computers. The facility is designed to be modular and flexible, so that users can bring their own equipment or use the available infrastructure in any combination. This includes analog NIM, CAMAC and VME modules (discriminators, QDCs, TDCs, visual scalers, etc...) as well as more modern digitisers (see Fig. 5). Several computers are also available to be connected to the experimental setup under consideration to acquire data from the detectors.
- Shielding materials:** such as plastic or lead bricks, as well as borated-Al plates and various geometries of borated-plastic material. These may be used to optimise experimental setups.
- Acquisition and analysis software** are both available, in particular a pair of ROOT-based DAQs [12]. The DAQs may be employed to collect data and to provide a first analysis (see Fig. 6). Commercial software is also available for various MCA and Digitiser modules.

¹The neutron-tagging technique is described in detail in Sec. □.

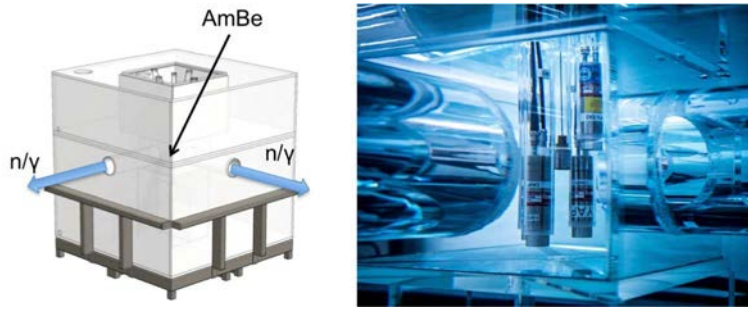


FIG. 3. The Aquarium. On the left, a CAD drawing and on the right, a photo of the inner chamber of the Aquarium. The neutron source surrounded by four gamma-ray detectors as well as two of the four beam ports may be seen.



FIG. 4. The black-box at the STF. On the left, a CAD drawing of the apparatus under construction and on the right, a photo of the existing prototype. The light-tight box may be surrounded by modular shielding.



FIG. 5. A subset of the electronics modules available at the STF.

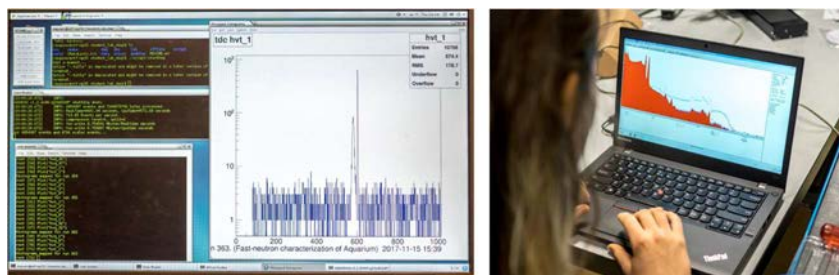


FIG. 6. DAQs running at the STF. On the left, a screen shot of a ROOT-based DAQ and on the right, a student using the MCA software.

- **Simulation tools**, based on GEANT4 [13] and included in the simulation framework of the ESS [14, 15, 16], have been developed to characterize the Aquarium and the sources. They are intended to be used to facilitate understanding of features within data that would be difficult to study in real life.
- **SONNIG expertise**. The group members are available for consulting and support. They are highly experienced with the set-up of the experiment and/or the optimization of the DAQs and with how to use the analysis software. Experience with the setup is gladly shared and help with optimizing acquisition software as well as data analysis can be provided.

3 TAGGING NEUTRONS

Employing radioactive sources for detector characterizations can be advantageous to the user. For example, once the setup is optimised and the acquisition of data is started, in contrast to accelerator-based measurements, no further assistance is needed and no night shifts are required. A disadvantage of employing radioactive sources is that the emitted neutrons have a wide range of energies that are not uniform. The ISO 8529-2 recommended neutron-energy spectrum from $^{241}\text{Am-Be}$ is shown in Fig. 7. As can be seen, the emitted neutrons are definitely not mono-energetic. Moreover, any neutron-emitting source likely emits a mixed field of γ -rays, α -particles and neutrons.

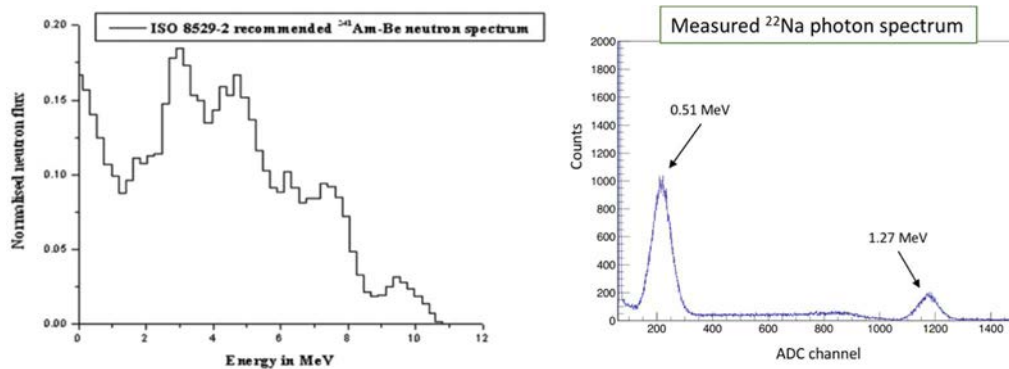
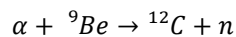


FIG. 7. Spectra from sources. On the left, the ISO 8529-2 recommended neutron spectrum for a $^{241}\text{Am-Be}$ source and on the right, a measured gamma-ray-spectrum for a ^{22}Na source.

Further, neutron sources generally radiate mixed field isotropically. Due to the mixed field, the wide energy spectrum of the released neutrons, and the randomness of the underlying decay processes, direct-exposure irradiations offer a less controlled environment compared to a reactor beam line. Clearly, such a beam line may be carefully tuned to provide a continuous mono-energetic beam of neutrons. However, by precisely measuring the radiation field on an event-by-event basis, one can reconstruct the properties of each individual neutron and thereby ‘tag’ the neutrons. The process involves determining the time-of-flight (ToF) and thus the energy of each detected neutron [17, 18].

In a source, such Am–Be, fast neutrons are emitted via the reaction



The recoiling ^{12}C is left in its first excited state about 55% of the time and the emitted neutron is accompanied by the prompt emission of a 4.44 MeV gamma-ray from the instantaneous de-excitation of the ^{12}C to its ground state. If both the neutron and the gamma-ray are detected, the ToF and thus kinetic energy of the neutron may be determined on an event-by-event basis (see Fig. 8). Note that the emission rate of such a source is $\sim 1.1 \cdot 10^6$ n/s over the 4π . The solid angle decreases for larger distances between source and detector and thus the neutron irradiation rate depends directly on the neutron flight path.²

² Note that the emission rate of such a source is $\sim 1.1 \cdot 10^6$ n/s nearly isotropically. As the solid angle decreases for larger distances between the source and detector, the neutron irradiation rate depends directly on the neutron flight path. By placing the detector in question close to the source, the rate may be increased. By placing the detector in question further away from the source, the rate will decrease.

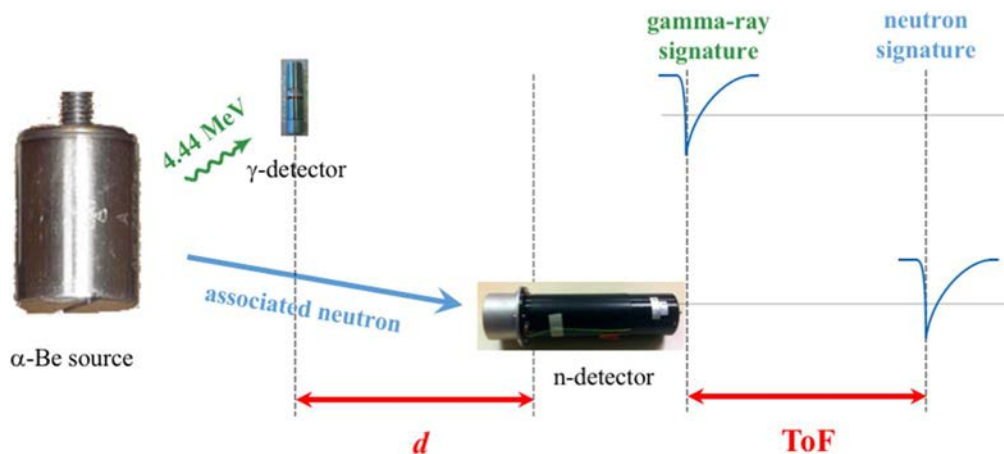


FIG. 8. Neutron-Tagging technique. A 4.44 MeV gamma-ray is measured in conjunction with the associated emitted neutron. From the time difference between the detection of the two particles, the ToF of the neutron can be determined and thus its energy may be calculated.

In our case, the relative timing between the detection of the gamma-ray by an Yttrium Aluminum Perovskite (YAP) inorganic crystal-scintillator detector and the detection of the neutron by an organic liquid-scintillator detector is measured, resulting in the spectrum shown in Fig. 9. For every event, the ToF of the detected neutron can be determined and thus, knowledge of the source-to-detector distances facilitates the calculation of the neutron energy.

The setup is self-calibrating thanks to physical events where two gamma-rays are emitted simultaneously by the source³. These events both travel the well-known distances involved at the speed of light, and result in a gamma-flash in the ToF spectrum. The gamma-flash provides a reference point from which the instant of the double gamma-ray emission may be determined. In general, the source and YAP detectors are placed inside the central chamber of the Aquarium, while the neutron detector is placed at one of the beam ports.

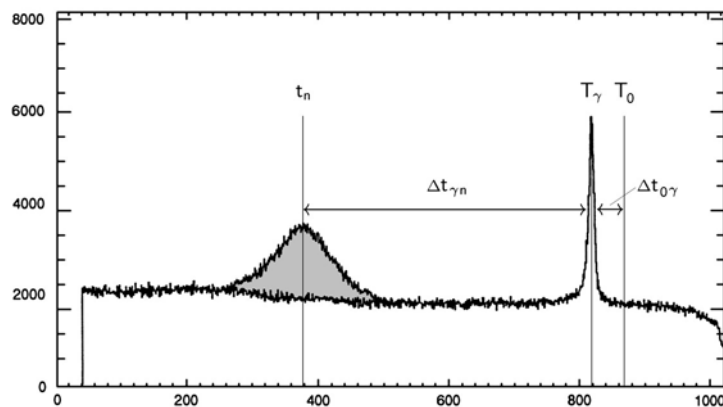


FIG 9. TDC spectrum of tagged fast neutrons (TDC channels vs number of counts). An entry is the time between the start signal from the neutron detector and the stop signal from the gamma-ray detector. The gamma-flash is at T_γ , while the neutron distribution is at t_n . The indicated T_0 -position is the reconstructed time of the actual decay. Figure from [19]

With these techniques, the STF is presently capable of measuring the response of detectors to fast neutrons, fast-neutron detection efficiency and the neutron and gamma-ray attenuation properties of shielding materials (tagged neutron energy between 1 and 6 MeV). Note that a major upgrade of the Aquarium and the electronics available at the facility have recently been funded via the Lund University Natural Science Faculty. Together with a corresponding upgrade of the data-acquisition systems, we anticipate a first attempt to tag neutrons of energies in the thermal region (~ 25 meV) to commence very soon.

³For example, the alpha decay of Am-241 leaves the daughter nucleus Np-237 in an excited state, which decays to the ground state via the emission of multiple gamma-rays (see <http://www.nndc.bnl.gov/nudat2/>).

4 EXAMPLES FOR RECENT STUDIES PERFORMED AT THE STF

Highlights of recent results obtained by various user groups of the STF are presented below.

4.1 CHARACTERIZATION OF SOURCES

All of our neutron sources have been systematically characterized in-situ (see Fig. 10), providing important validation benchmarks for our experimental infrastructure [20, 21]. Note that the difference between our measurements and the reference measurements for the Am–Be source at high energy are due to limitations in the tagging technique. Differences at low energy come from detector thresholds. The difference to the ISO recommended Am–Be spectrum at both low and high energies to our measurements comes from the limitation of the tagging technique. We only tag neutrons corresponding to the first excited state of C*-12 limiting neutron energy to the range of our tagged-neutron spectra. This program of systematic characterization was deemed important since the sources were to be provided to a user community. Requiring each group in this user community to individually study the sources they were provided was felt to be unreasonably inefficient. The tagging technique has been extended to a Cf-252 fission fragment source [22]. For this, the single-sided Cf-252 source was positioned within a gaseous He-4 scintillator detector in which light and heavy fission fragments corresponding to neutron emission were detected as tags. Since the emission spectrum for Cf-252 is exceptionally well-known, an excellent benchmark exists from which it is anticipated the neutron-detection efficiency of a detector can be unfolded.

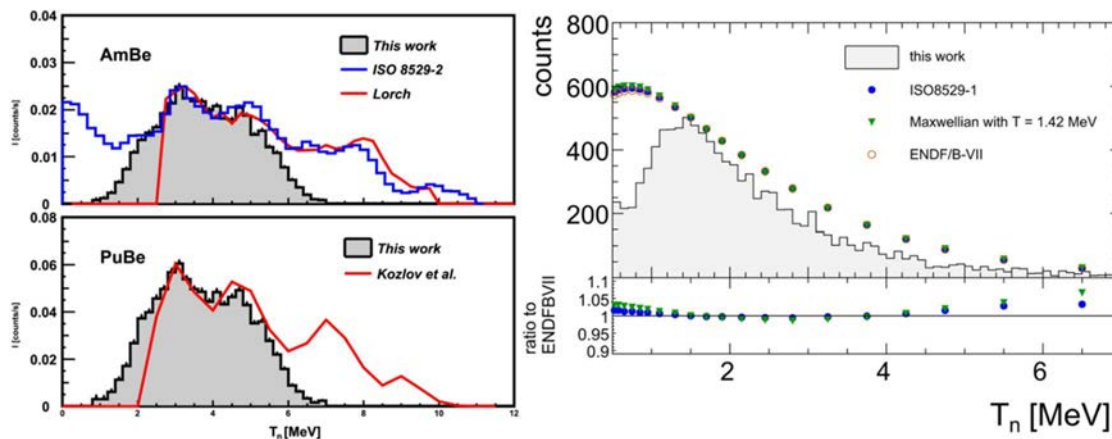


Fig. 10. Spectra of sources measured at the STF. On the left, the measured spectra of the Am–Be (top) and PuBe (bottom) sources (plots from [21]) and on the right, the measured spectrum of the Cf source (plot from [22]). In these publications, we have demonstrated that we are able to reproduce the general shape of the spectra.

4.2 CHARACTERIZATION OF DETECTORS

The STF is ideal for the development of prototypes in preparation for tests at nuclear reactors or on real spallation instruments. It is anticipated that a very large subset of ESS detector prototypes will see the neutrons of the STF at some stage of their development (as the case for the Multi-Grid [23], to cite one). Using either direct irradiation or the tagging technique, simple functionality tests of detector prototypes may be performed. Further, the sensitivity of a prototype to fast-neutron or gamma-ray backgrounds may be investigated. Examples of the latter are recent studies performed on commercially available beam monitors [24] or on the Multi-Blade [25] detector (see Fig. 11). The Multi-Blade detector is being developed for reflectometry instruments at ESS.

A recently developed black-box (see Fig. 12), to be equipped with a servo stages on an optical Table, has been used to characterize Multi-Anode PMTs for the SoNDe project [26]. The SoNDe project is focused on the development of pixelated, solid-state neutron detectors for ESS.

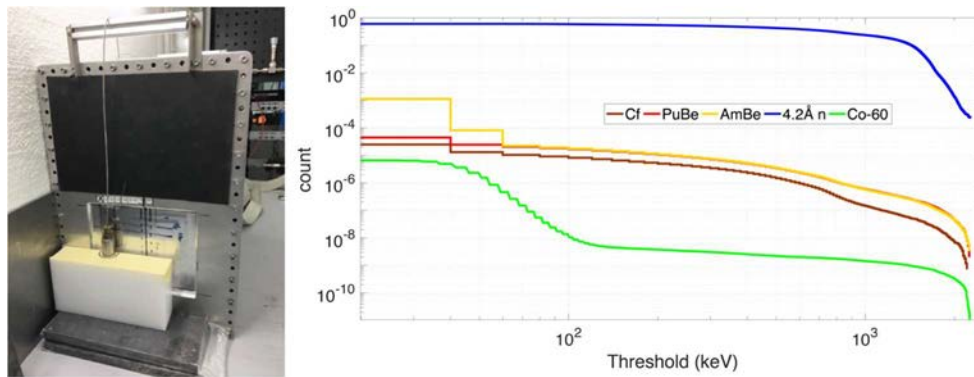


FIG. 11. Fast-neutron sensitivity measurement on the Multi-Blade detector: an example of untagged irradiation measure for detector characterization at STF. On the left, a photo of the detector irradiated by the PuBe source at STF and on the right, the cumulative number of counts as function of an energy threshold for different incoming radiations, normalised to the sensitivity of the detector to thermal neutrons (4.2\AA). (Plot from [27]).

4.3 CHARACTERIZATION OF SHIELDING

The potential of the STF is not limited to the development of new neutron instrumentation. Using its tagged-neutron beams, the behaviour of materials under neutron or gamma-ray irradiation may be studied in detail [28]. This is a research domain traditionally addressed at reactors or spallation sources which has recently been invigorated with the promise of proton therapy in treating cancer. We investigated radiation attenuation in steel, copper, Polyethylene (PE) and both regular and PE/B₄C-enriched concrete samples using the Aquarium (see Fig. 12). To understand the scattering inside the concretes, measured ToF transmission spectra of tagged neutrons were compared to simulation with a very high level of agreement (see Fig. 13). We note that the correlation between ToF and neutron energy is not conserved for all events, if a sample is irradiated. Nonetheless, the shape of the neutron-energy spectrum measured downstream from the concrete shielding block can be unfolded from the data using the simulation.



FIG. 12. Radiation attenuation in shielding material measurements. Transmission measurements were performed.

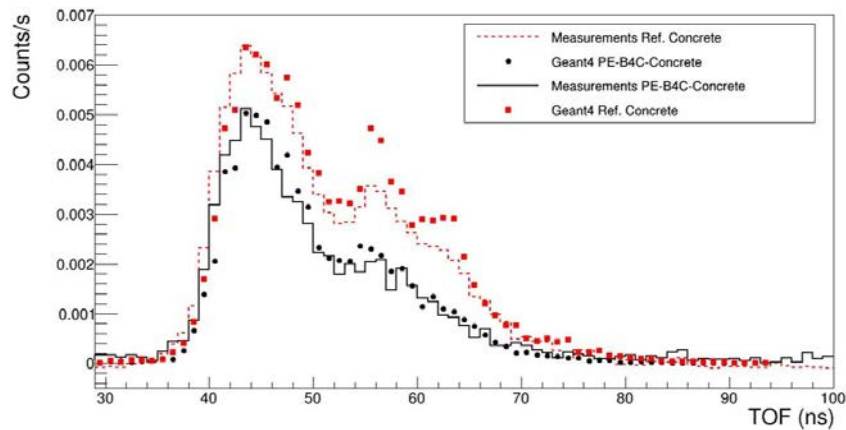


FIG 13. A comparison of measurements and simulations for reference concrete and PE-B₄C-concrete. (Plot from [28]).

4.4 EDUCATION

As part of Lund University infrastructure, the STF has been used extensively for student training at all levels. Table 1 shows a list of thesis work performed to date.

TABLE 1: STF THESES

Name of Student	Type of thesis	Institution	Date	Title
Tõnu Ilves	Master	LU	February 12, 2018	<i>2D Imaging with 10B-Based Multi-Blade Neutron Detector</i>
Amanda Jalgén	Master	LTH	September 12, 2017	<i>Initial Characterizations of a Pixelated Thermal-Neutron Detector</i>
Laura Boyd	Summer	University of Glasgow	September 8, 2017	<i>Initial Testing of the Response of a Pixelated Thermal-Neutron Detector</i>
Mohamad Akkawi	Summer	University of Toronto	June 13, 2017	<i>Photon Detection Using Cerium Bromide Scintillation Crystals</i>
Nicholai Mauritzson	Master	LU	June 9, 2017	<i>Design, Construction and Characterization of a portable Fast-Neutron Detector</i>
Henrik Söderhielm	Undergraduate	LU	February 3, 2017	<i>Two-Dimensional Radiation Field Map of a Be-based Source</i>
Julius Scherzinger	PhD	LU	December 16, 2016	<i>Neutron Irradiation Techniques</i>
Emil Rofors	Master	LTH	March 14, 2016	<i>Fast Photoneutron Production</i>
Sharareh Koufigar	Undergraduate	LU	October 21, 2015	<i>The Radiological Footprint of a Be-based Source</i>
Julius Scherzinger	Licentitate	LU	March 20, 2015	<i>A Source-Based Testbed for Fast-Neutron Irradiation</i>

NOTE: For a complete description please visit <http://www.nuclear.lu.se/english/research/neutronfysik/>.

5 SUMMARY

Located at the Department of Physics of Lund University, the Source-Testing Facility has been designed for advanced detector and material diagnostics. Being a user facility, the STF offers a complete set of infrastructure, including gamma-ray and neutron sources, shielding, detectors, computers and IT. Furthermore, acquisition, analysis, and simulation software, and support are offered by the SONNIG group, who operate the facility. Until now, the STF has been used almost exclusively for the development of He-3 free neutron detectors and the study of advanced neutron shielding. The STF offers the potential of a low cost, low barrier to entry, and low flux neutron source, that has potential applications beyond those utilised presently. The hands-on training of the next generation of neutron scientists is a high priority. If you are in need of neutrons, contact us. We are happy to provide access to the STF and support your measurements with consultations and hands-on support during beam-time.

- Source Testing Facility c/o
Lund University
Department of Physics
Division of Nuclear Physics
P.O Box 118
SE-221 00 Lund
Sweden
- <http://www.nuclear.lu.se/english/research/neutronfysik/>
- <https://europeanspallationsource.se/workshops-facilities#source-testing-facility>
- stf@nuclear.lu.se

ACKNOWLEDGEMENTS

This work has been funded by:

- the BrightnESS project, Work Package (WP) 4.4. BrightnESS is funded by the European Union Framework Program for Research and Innovation Horizon 2020, under grant agreement 676548.
- The Faculty of Science at Lund University (Grant for Infrastructure 2017, V2016/1949).
- The UK Science and Technology Facilities Council (Grant nos. STFC 57071/1 and STFC 50727/1).

REFERENCES

- [1] SHEA, D.A., MORGAN, D., The Helium-3 shortage: supply, demand, and options for congress, Technical Report R41419, Congressional Research Service (2010).
- [2] KOUZES, R.T., The ^3He Supply Problem. PNNL-18388 Pacific Northwest National Laboratory, Richland, WA, (2009).
- [3] LINDROOS, M., et al., The European Spallation Source, Nucl. Instrum. Methods Phys. Res. Sect. B **269** 24 (2011) 3258–3260.
- [4] PEGGS, S., et al., European Spallation Source Technical Design Report, ESS-2013-001.
- [5] HALL-WILTON, R., et al., Detectors for the European Spallation Source, IEEE Nucl. Sci. Symp. Conf. Rec. (2012) 4283–4289.
- [6] KIRSTEIN, O., et al., Neutron Position Sensitive Detectors for the ESS, (2014), PoS (Vertex2014) 029 arXiv:1411.6194.
- [7] CHERKASHYNA, N., et al., High energy particle background at neutron spallation sources and possible solutions, J. Phys. Conf. Ser. **528** (2014) 012013.
- [8] LUNDUNIVERSITY, <http://www.nuclear.lu.se/english/>.
- [9] EUROPEAN SPALLATION SOURCE, <https://europeanspallationsource.se/workshops-facilities#source-testing-facility>.
- [10] EUROPEAN SPALLATION SOURCE, <https://confluence.ess.lu.se/display/DG/Detector+Group+link+needs+ESS+account>.
- [11] LUND UNIVERSITY, <http://www.nuclear.lu.se/english/research/neutronfysik/>.

- [12] BRUN, R., RADEMAKERS, F., ROOT - an object oriented data analysis framework, Nucl. Instrum. Methods A **389** (1996) 81–86 url: <http://root.cern.ch/>.
- [13] AGOSTINELLI, S., et al., Geant4 - a simulation toolkit, Nucl. Instrum. Methods Phys. Res. Sect. A, **5-6 3** (2003) 250–303.
- [14] KITTELMANN, T., et al., “Geant4 Based Simulations for Novel Neutron Detector Development”, paper presented at the 20th International Conference on Computing in High Energy and Nuclear Physics, CHEP. J. Phys. Conf. Ser. **513 2** (2013) 022017.
- [15] KITTELMANN, T., BOIN, M., Polycrystalline neutron scattering for Geant4: NXSG4, Comput. Phys. Commun. **189** (2015) 114–118.
- [16] CAI, X.X., KITTELMANN, T., “NCrystal : A library for thermal neutron transport in crystals”, [http://mctools.github.io/ncrystal/ v0.9.1](http://mctools.github.io/ncrystal/v0.9.1).
- [17] SCHERZINGER, J., Neutron Irradiation Techniques, Lund University, Faculty of Science, Department of Physics, (2016).
- [18] SCHERZINGER, J., et al., The light-yield response of a NE-213 liquid-scintillator detector measured using 2–6 MeV tagged neutrons, Nucl. Instrum. Methods Phys. Res. Sect. A: **840** (2016) 121–127.
- [19] NILSSON B., “High-resolution Measurement of the $^4\text{He}(\gamma, n)$ Reaction in the Giant Resonance Region”, Lund University, Faculty of Science, Department of Physics, (2003).
- [20] SCHERZINGER, J., et al., Tagging fast neutrons from an $^{241}\text{Am}/^9\text{Be}$ source, Appl. Radiat. Isot. **98** (2015) 7479.
- [21] SCHERZINGER, J., et al., A comparison of untagged gamma-ray and tagged-neutron yields from ^{241}Am –Be and ^{238}Pu –Be sources, Appl. Radiat. Isot. **127** (2017) 98–102.
- [22] SCHERZINGER J. et al., Tagging fast neutrons from a ^{252}Cf fission-fragment source, Appl. Radiat. Isot. **128** (2017) 270–274.
- [23] KHAPLANOV, A., et al., ^{10}B multi-grid proportional gas counters for large area thermal neutron detectors, Nucl. Instrum. Methods A **720** (2013) 116–121.
- [24] ISSA, F., et al., Characterization of thermal neutron beam monitors, Phys. Rev. Accel. Beams **20** (2017) 092801.
- [25] PISCITELLI, F., et al., The multi-blade boron-10-based neutron detector for high intensity neutron reflectometry at ESS, J. Instrum. **12** (2017) P03013.
- [26] JAKSCH, S., et al., “Cumulative Reports of the SoNDe Project July 2017”, arXiv:1707.08679 (2017).
- [27] MESSI, F., et al., “Gamma- and Fast Neutron- Sensitivity of ^{10}B -based Neutron Detectors at ESS”, paper presented at 2017 IEEE Nuclear Science Symposium and Medical Imaging Conference (2017 NSS/MIC).
- [28] DIJULIO, D., et al., A polyethylene-B₄C based concrete for enhanced neutron shielding at neutron research facilities, Nucl. Instrum. Methods Phys. Res. Sect. A **859** (2017) 41–46.

TOPICAL SESSION 7
NEUTRON DETECTORS FOR FUSION ENERGY

NOVEL NEUTRON ACTIVATION DETECTOR FOR FUSION

I.E. STAMATELATOS*, M.I. SAVVA, T. VASILOPOULOU, K. TRIANTOU, K. MERGIA,
S. MESSOLORAS

Institute of Nuclear and Radiological Sciences and Technology, Energy and Safety,
National Centre for Scientific Research 'Demokritos'
Greece

*Email: ion@ipta.demokritos.gr

L.W. PACKER, C.R. NOBS, Z. GHANI

Nuclear Technology Department,
Culham Centre for Fusion Energy
United Kingdom

P. BATISTONI, M. PILLON, S. LORETI

Department of Fusion and Technology for Nuclear Safety and Security
ENEA- Agenzia Nazionale per le Nuove Tecnologie, l'Energia e lo Sviluppo Economico Sostenibile
Italy

Abstract: For future fusion plants, such as DEMO, there is a great need for detectors capable of accurately monitoring neutrons under the harsh conditions imposed by the fusion environment. In particular, it is required to utilize detectors that are capable of accurately measuring neutron fluence under high and variable neutron count rates, high gamma background, high temperature, and high and variable magnetic fields encountered during the measurement. A novel neutron activation detector providing a robust approach for accurate neutron fluence measurements under the harsh environment conditions encountered in a fusion plant is developed. The detector comprises a composite low activation matrix compound capsule containing a defined concentration of added metallic elements (targets). The key novelty is provided by the robust matrix which is enabling measurements to be performed under the extreme conditions encountered in a fusion plant, while the capsule itself does not interfere with the gamma spectrum of the active metallic elements. The capsule is fabricated by graphite or Ceramic Matrix Composite (CMC) enabling the detector not to interfere with the strong magnetic fields and to withstand high temperatures encountered in a fusion plant. The neutron fluence and energy spectrum is evaluated by analysis of the gamma lines produced by the activation reactions in the metallic elements. In this work, the progress in the development of the Novel Neutron Detector for Fusion (VERDI) with respect to the selection of the active elements and the matrix material is discussed. Moreover, the results of a test experiment performed at the ENEA Frascati Neutron Generator to demonstrate the feasibility of using a VERDI detector for measuring neutrons in a reference fusion relevant field are also presented.

1 INTRODUCTION

For future fusion plants, such as DEMO, there is a great need for detectors capable of accurately monitoring neutrons under the harsh conditions imposed by the fusion environment. It is required to utilize detectors that are capable of accurately measuring neutron fluence under high and variable neutron count rates, high gamma background, high temperature, and high and variable magnetic fields encountered during the measurement.

A novel neutron activation detector providing a robust approach for accurate neutron fluence measurements under the harsh environment conditions encountered in a fusion plant is being developed. The detector comprises a graphite or ceramic matrix composite being of low activation and containing a defined concentration of added metallic elements (targets). The neutron detection method is based on the well-known multiple foil activation technique [1–2]. The neutron detection method is based on multiple foil activation [1], [2], where the neutron fluence and energy spectrum are inferred from the gamma rays produced by the activation reactions using computational unfolding. The novel aspect is a capsule matrix that is sufficiently robust to allow measurements under the harsh conditions of a fusion plant.

The proposed detector provides the flexibility to tailor the sampled neutron energy range to that of most interest in fusion, based upon the plasma neutron source, physical conditions and processes to be studied in a particular experiment. It allows measurement of integral neutron fluence and reconstruction of the neutron energy spectrum at the position of measurement. Therefore, it will allow monitoring the neutron fluence on components and materials, tritium breeding rates, nuclear heating, and a variety of other parameters in fusion reactors such as ITER and DEMO, as well as future fusion plants [2–4].

In this work the progress in the development of the VERDI detector with respect to the selection of the active elements and capsule matrix material is discussed and the results of a test experiment performed at the ENEA

Frascati Neutron Generator (FNG) in order to demonstrate the feasibility to measure neutron fluence in a fusion relevant neutron spectrum are presented.

2 ACTIVE ELEMENTS

2.1 SELECTION CRITERIA

The selection criteria for the active metallic elements were their activation cross-section (thermal, threshold), product half-life, melting point, intensity of emitted gamma lines, interferences between gamma lines, material hazard information, flammability and cost. The most promising candidate metallic elements that fulfil these criteria are presented in Table 1 together with their respective data regarding the physical and nuclear characteristics. In particular, for each element, the melting point is given together with its natural isotopes and their abundance. In addition, for each isotope, the reactions of interest that can be used for the purposes of the VERDI detector are given, as well as the product isotopes nuclear characteristics (i.e. half-life and main photon energy and emission probability/yield).

2.2 RADIONUCLIDE INVENTORY CALCULATIONS

Radionuclide inventory calculations were performed using the FISPACT-II code [5] for specified fusion relevant neutron spectra. The FISPACT-II code is part of the EASY package developed by CCFE and predicts how materials evolve under irradiation and through radioactive decay processes. The input data required are the neutron spectrum, the target material and the mass to be irradiated, as well as the irradiation scheme and the cooling time. In this study the EAF-2010 nuclear data library was used with VITAMIN-J 175 group energy bin structure [6]. The output data are given in terms of specific activity (Bq/g) for each isotope.

Calculations were performed for the ENEA FNG quasi mono-energetic reference neutron field [7]. The FNG based on the $T(D, n)\alpha$ fusion reaction produces a nearly isotropic source of 14–15 MeV (Fig. 1) (Colangeli A., priv. comm.). Moreover, the position B of the JET Long Term Irradiation Station (LTIS) was also considered. The neutron energy spectrum at the LTIS position was calculated using a detailed MCNP model of the JET tokamak (Conroy S. and Lengar I., priv. comm.) and is shown in Figure 2. The cooling times selected for each irradiation represented a realistic estimate of the actual time between the end of the irradiation and the start of the γ -spectroscopic analysis. The irradiation schemes examined are presented in Table 2.

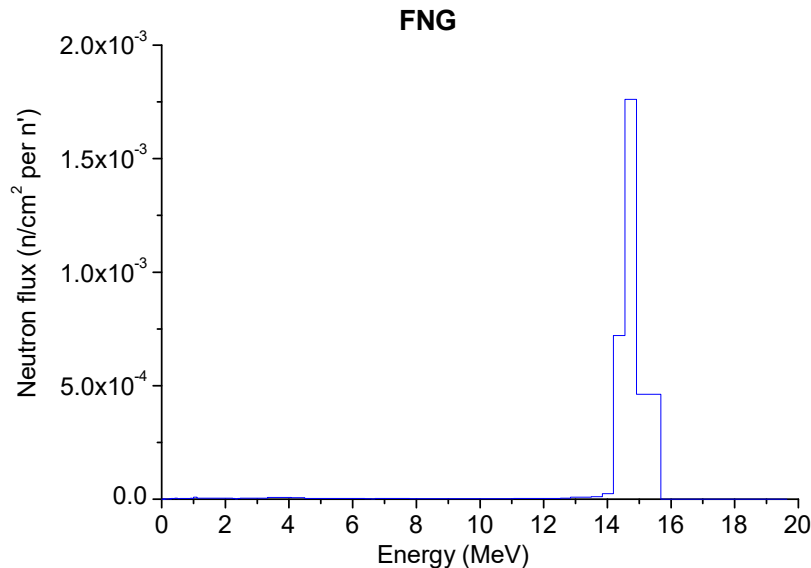


FIG. 1. MCNP evaluated neutron energy spectrum at the FNG source.

TABLE 1. CANDIDATE METALLIC ELEMENTS (TARGETS)

Element	Melting	Isotopic		Reaction	Threshold	Product Half-life	E_γ (keV)	Yield (%)
	point (°C)	Isotope	Abundance (%)		energy (MeV)			
Ag	962	^{107}Ag	51.84	$^{107}\text{Ag} (n, \gamma) ^{108}\text{Ag}$	--	2.37 min	633.0	1.8
		^{109}Ag	48.16	$^{109}\text{Ag} (n, \gamma) ^{110m}\text{Ag}$	--	249.8 d	657.7	94.7
Al	660	^{27}Al	100.00	$^{27}\text{Al} (n, \gamma) ^{28}\text{Al}$	--	2.24 min	1778.9	100.0
				$^{27}\text{Al} (n, p) ^{27}\text{Mg}$	1.90	9.46 min	843.7	71.8
				$^{27}\text{Al} (n, \alpha) ^{24}\text{Na}$	3.24	14.95 h	1368.6	100.0
Au	1064	^{197}Au	100.00	$^{197}\text{Au} (n, \gamma) ^{198}\text{Au}$	--	2.69 d	411.8	95.5
				$^{197}\text{Au} (n, 2n) ^{196}\text{Au}$	8.13	6.18 d	355.7	87.0
Mn	1246	^{55}Mn	100.00	$^{55}\text{Mn} (n, \gamma) ^{56}\text{Mn}$	--	2.57 h	846.8	98.9
				$^{55}\text{Mn} (n, 2n) ^{54}\text{Mn}$	10.50	310 d	834.8	100.0
				$^{55}\text{Mn} (n, \alpha) ^{52}\text{V}$	0.64	3.7 min	1434.1	100.0
Nb	2469	^{93}Nb	100.00	$^{93}\text{Nb} (n, 2n) ^{92m}\text{Nb}$	9.00	10.15 d	934.5	99.1
Ni	1455	^{58}Ni	68.08	$^{58}\text{Ni} (n, p) ^{58m}\text{Co}$	0.40	9.04 h	×	
				$^{58m}\text{Co} (\text{IT}) ^{58}\text{Co}$	--	72 d	810.8	99.4
				$^{60}\text{Ni} (n, p) ^{60m}\text{Co}$	2.20	10.5 min	×	
				$^{60m}\text{Co} (\text{IT}) ^{60}\text{Co}$	--	5.27 y	1332.5	100.0
Rh	1963	^{103}Rh	100.00	$^{64}\text{Ni} (n, \gamma) ^{65}\text{Ni}$	--	2.52 h	1481.8	23.6
				$^{103}\text{Rh} (n, 2n) ^{102}\text{Rh}$	9.50	2.9 y	475.1	38.4
				$^{103}\text{Rh} (n, \gamma) ^{104}\text{Rh}$	--	42.3 s	555.8	2.00
Ta	3020	^{181}Ta	99.99	$^{103}\text{Rh} (n, p) ^{103}\text{Ru}$	0.20	39.3 d	497.1	90.9
				$^{181}\text{Ta} (n, \gamma) ^{182}\text{Ta}$	--	111 d	1121.3	35.0
				$^{181}\text{Ta} (n, 2n) ^{180}\text{Ta}$	7.62	8.15 h	93.3	4.5
Ti	1668	^{46}Ti	8.00	$^{46}\text{Ti} (n, p) ^{46m}\text{Sc}$	1.62	18.8 s	142.5	62.0
				$^{46m}\text{Sc} (\text{IT}) ^{46}\text{Sc}$	--	85 d	889.2	100.0
				$^{47}\text{Ti} (n, p) ^{47}\text{Sc}$	0.66	3.43 d	159.4	68.0
				$^{48}\text{Ti} (n, p) ^{48}\text{Sc}$	3.29	44 h	983.5	100.0
				$^{50}\text{Ti} (n, p) ^{50}\text{Sc}$	6.40	102.5 s	1553.8	100.0
Y	1526	^{89}Y	100.00	$^{50}\text{Ti} (n, \gamma) ^{51}\text{Ti}$	--	5.76 min	320.0	93.0
				$^{89}\text{Y} (n, \gamma) ^{90m}\text{Y}$	--	3.19 h	202.5	97.3
				$^{89}\text{Y} (n, n) ^{89m}\text{Y}$	(1.00)	16.1 s	908.9	99.0
				$^{89}\text{Y} (n, \alpha) ^{86}\text{Rb}$	3.03	18.63 d	1076.6	9.0
				$^{89}\text{Y} (n, \alpha) ^{86m}\text{Rb}$	3.03	1.02 min	556.1	98.0
				$^{89}\text{Y} (n, 2n) ^{88}\text{Y}$	12.00	106.6 d	1836.1	99.2
Zn	419	^{64}Zn	48.60	$^{64}\text{Zn} (n, p) ^{64}\text{Cu}$	0.10	12.7 h	1345.8	0.5
				$^{64}\text{Zn} (n, 2n) ^{63}\text{Zn}$	12.50	38.5 min	669.6	8.0
				$^{66}\text{Zn} (n, p) ^{66}\text{Cu}$	1.90	5.12 min	1039.2	9.0
				$^{68}\text{Zn} (n, \gamma) ^{69m}\text{Zn}$	--	13.76 h	438.6	94.8
				$^{68}\text{Zn} (n, p) ^{68}\text{Cu}$	3.80	31.1 s	1077.3	64.0
				$^{68}\text{Zn} (n, \alpha) ^{65}\text{Ni}$	0.10	2.52 h	1481.8	23.6

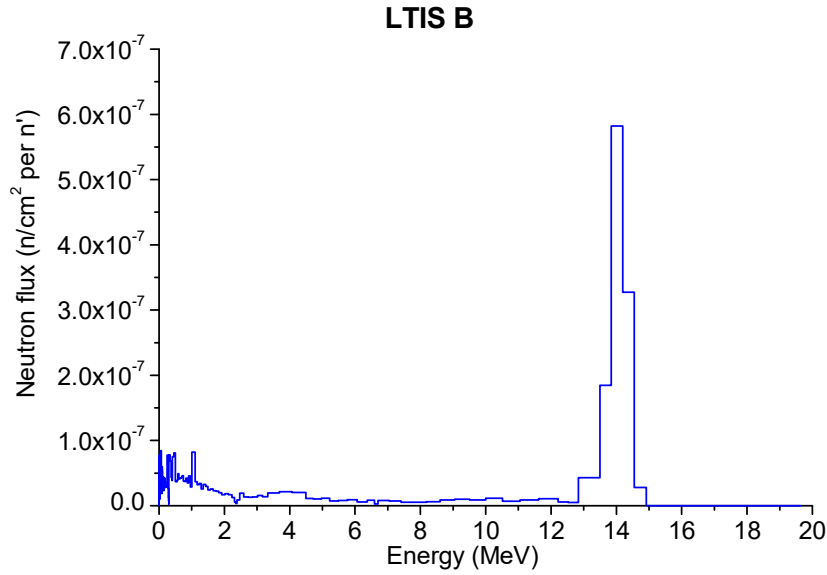


FIG. 2. MCNP evaluated neutron energy spectrum at the position B of the JET Long Term Irradiation Station (LTIS).

It is noted that for the duration of the irradiation at JET, the assumption of 1 s pulse is made, although the actual JET pulses can extend up to several seconds. Nevertheless, this assumption can be considered as adequate for the purposes of the pre-analysis, since only long-lived products are examined in the present work. In addition, in order for the assumption to be more realistic, the average fluence rate was obtained from the total fluence of the 2015–2016 JET campaign divided by the total pulses.

TABLE 2. EXAMINED IRRADIATION/DETECTION SCHEMES

Position	Neutron flux (n/cm ² /s)	Irradiation	Cooling time
FNG	1.78×10^8	5 hours	10 d
JET LTIS B	3.69×10^{10}	3682 pulses of 1 s	90 d

For the gamma-ray measurements a high-purity coaxial germanium semiconductor detector of 85% relative efficiency was considered. For the calculation of the target elements mass, a desired count rate needs to be chosen. The criterion is to get sufficient counting statistics at the photo-peaks at a given measurement time. Since in LTIS only long-lived radionuclides can be measured, the counting time can be long (24 h or even more), allowing for a lower count rate to be selected, i.e. *0.01 cps*. The same applies for the experiments at FNG facility, where the measurement will take place approximately 10 days after the irradiation. To this end, it should be noted that the calculated target mass is the minimum required mass to achieve the set count rate at the specified gamma ray detector.

2.3 RADIONUCLIDE CALCULATIONS RESULTS

The results for the FNG in terms of induced activity per produced isotope as a function of time post-irradiation after DT irradiation of 5 h are presented in Figure 3. The results for the LTIS B in terms of induced activity per produced isotopes after irradiation of 3682 pulses of 1 s for DT plasma source as a function of time post-irradiation are presented in Figure 4.

The results in terms of required mass of each element for all irradiation positions are presented in Table 3. For the determination of the minimum required mass for the VERDI detectors, the cooling times presented in Table 2 were applied and the desired count rate was considered for a distance of 6 cm from the reference HPGe detector. For each reaction the minimum mass required to get the desired count rate is calculated. For the determination of the final mass of the candidate elements a compromise is made between the different reactions. Table 4 shows the final proposed masses for the test experiment at FNG.

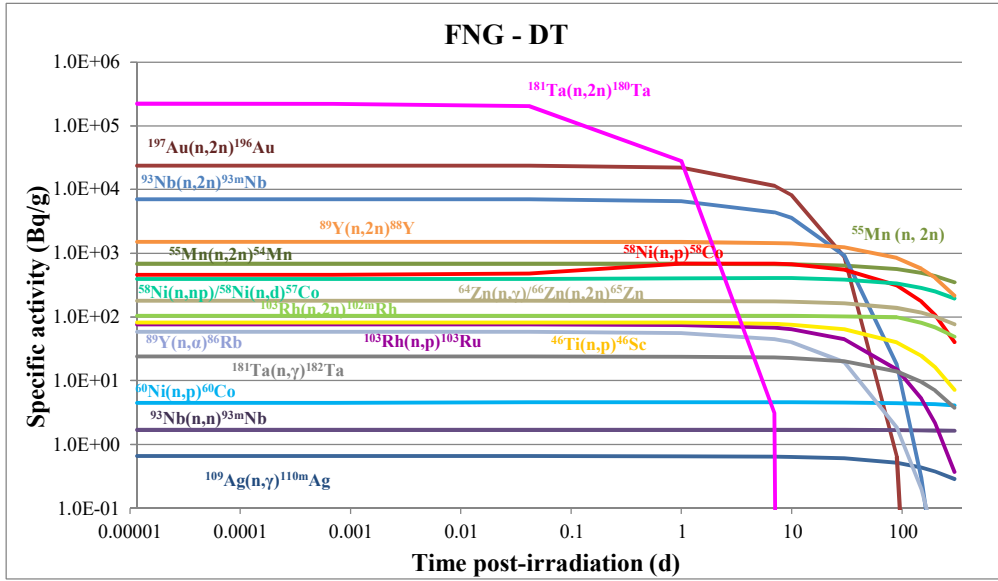


FIG. 3. Induced activity as a function of time post-irradiation for FNG.

TABLE 3. PRELIMINARY ACTIVE ELEMENTS DETECTOR COMPOSITION

Material	Threshold energy (MeV)	Reaction	Required mass for LTIS (mg)	Required mass for FNG (mg)
Ag	--	$^{109}\text{Ag} (n, \gamma) ^{110m}\text{Ag}$	0.3	3
Al	--	$^{27}\text{Al} (n, \gamma) ^{28}\text{Al}$	--	--
	1.90	$^{27}\text{Al} (n, p) ^{27}\text{Mg}$	--	--
Au	--	$^{197}\text{Au} (n, \gamma) ^{198}\text{Au}$	--	5
	8.13	$^{197}\text{Au} (n, 2n) ^{196}\text{Au}$	1500	0.1
Nb	9.00	$^{93}\text{Nb} (n, 2n) ^{92m}\text{Nb}$	350	0.3
Ni	0.40	$^{58}\text{Ni} (n, p) ^{58}\text{Co}$	1	1.7
	2.20	$^{60}\text{Ni} (n, p) ^{60}\text{Co}$	92	800
	9.24	$^{58}\text{Ni} (n, np) ^{57}\text{Co} (67.8\%^1)$	0.3	1.1
	6.08	$^{58}\text{Ni} (n, d) ^{57}\text{Co} (32.2\%)$		
Rh	--	$^{103}\text{Rh} (n, \gamma) ^{104}\text{Rh}$	--	--
	9.50	$^{103}\text{Rh} (n, 2n) ^{102}\text{Rh}$	2	13
	0.20	$^{103}\text{Rh} (n, p) ^{103}\text{Ru}$	1	9
Ti	1.62	$^{46}\text{Ti} (n, p) ^{46}\text{Sc}$	100	138
	3.29	$^{48}\text{Ti} (n, p) ^{48}\text{Sc}$	--	7.7
	--	$^{50}\text{Ti} (n, \gamma) ^{51}\text{Ti}$	--	--
	6.40	$^{50}\text{Ti} (n, p) ^{50}\text{Sc}$	--	--
Y	3.03	$^{89}\text{Y} (n, \alpha) ^{86}\text{Rb}$	0.4	0.6
	12.00	$^{89}\text{Y} (n, 2n) ^{88}\text{Y}$	2000	40
Zn	--	$^{64}\text{Zn} (n, \gamma) ^{65}\text{Zn}$	4	24
	11.32	$^{66}\text{Zn} (n, 2n) ^{65}\text{Zn}$	7	41
	12.50	$^{64}\text{Zn} (n, 2n) ^{63}\text{Zn}$	--	--

¹ Percentage of contribution of each reaction to the production of ^{57}Co as per FISPACT-II results.

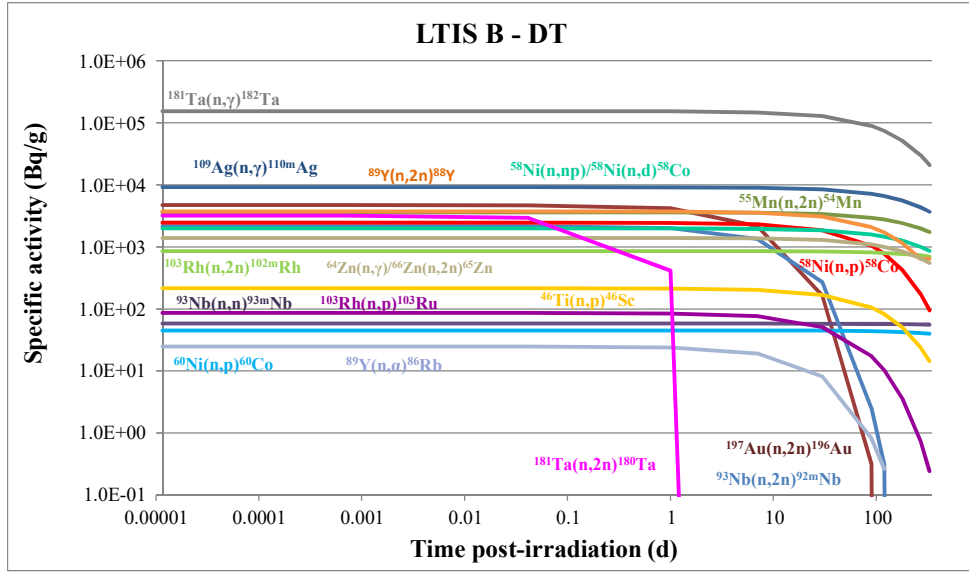


FIG. 4. Induced activity as a function of time post-irradiation for JET LTIS B.

TABLE 4. PROPOSED ELEMENTS AND MASSES FOR THE FNG TEST EXPERIMENT

Material	Threshold energy (MeV)	Reaction	Proposed mass (mg)
Ag	--	$^{109}\text{Ag} (n, \gamma) ^{110m}\text{Ag}$	3
Au	--	$^{197}\text{Au} (n, \gamma) ^{198}\text{Au}$	5
	8.13	$^{197}\text{Au} (n, 2n) ^{196}\text{Au}$	
Mn	--	$^{55}\text{Mn} (n, \gamma) ^{56}\text{Mn}$	2
	0.64	$^{55}\text{Mn} (n, \alpha) ^{52}\text{V}$	
	10.50	$^{55}\text{Mn} (n, 2n) ^{54}\text{Mn}$	
Nb	9.00	$^{93}\text{Nb} (n, 2n) ^{92m}\text{Nb}$	0.3
Ni	0.40	$^{58}\text{Ni} (n, p) ^{58}\text{Co}$	2
	2.20	$^{60}\text{Ni} (n, p) ^{60}\text{Co}$	
Rh	9.50	$^{103}\text{Rh} (n, 2n) ^{102}\text{Rh}$	13
	0.20	$^{103}\text{Rh} (n, p) ^{103}\text{Ru}$	
Ti	1.62	$^{46}\text{Ti} (n, p) ^{46m}\text{Sc}$	200
	3.29	$^{48}\text{Ti} (n, p) ^{48}\text{Sc}$	
	--	$^{50}\text{Ti} (n, \gamma) ^{51}\text{Ti}$	
	6.40	$^{50}\text{Ti} (n, p) ^{50}\text{Sc}$	
Y	3.03	$^{89}\text{Y} (n, \alpha) ^{86}\text{Rb}$	40
Zn	--	$^{64}\text{Zn} (n, \gamma) ^{65}\text{Zn}$	80
	11.32	$^{66}\text{Zn} (n, 2n) ^{65}\text{Zn}$	
	12.50	$^{64}\text{Zn} (n, 2n) ^{63}\text{Zn}$	

3 CAPSULE MATERIAL

3.1 SELECTION CRITERIA

The specifications for the capsule matrix material were resistance to high temperatures (the required service temperature was set at 700 °C), ability to introduce metallic elements in a robust construction, very low concentration of impurities which can be activated and interfere with the gamma ray lines of the target elements and no interference with magnetic fields.

The materials that meet the specifications and were used for the fabrication of detector capsules were graphite and Ceramic Matrix Composite (CMC). The graphite material has a purity of 99.997% and was supplied by Goodfellow. The CMC material is a carbon fibre reinforced silicon carbide, C/C–SiC, supplied by the German Aerospace Centre (DLR). It is manufactured by the Liquid Silicon Infiltration (LSI) technique in which the SiC matrix is obtained by a reaction of residual carbon and liquid silicon [8]. The residual carbon is produced on a preform after a pyrolysis step on a CFRP (Carbon Fibre Reinforced Plastic) preform and the liquid silicon is infiltrated into this preform. Typical properties of the two selected materials are presented in Table 5.

TABLE 5. TYPICAL PROPERTIES OF GRAPHITE AND C/C–SiC MATERIALS

Properties	Graphite	C/C–SiC
Maximum service temperature (°C)	<ul style="list-style-type: none"> • neutral or reducing atmosphere: -200 up to 3000 °C • oxidizing atmosphere: -200–525 °C (oxidation resistant grades) 	1600 °C general stability of the mechanical properties at high temperatures
Machinability	easily machinable	requires diamond tools
Purity	Ultra high (up to 99.997%)	High (>99%)
Density (g/cm ³)	2.25	1.9–2.0
Tensile strength (MPa)	6.2 (along length & width)	80–190
Strain to failure (%)		0.15–0.35
Young's modulus (GPa)	8–15	50–70
Compression strength (MPa)	20–200	210–320
Flexural strength (MPa)	6.9–100	160–300
Fibre content (vol.%)		55–65
CTE Coefficient of thermal expansion (10 ⁻⁶ K ⁻¹)	0.6-4.3	-1–2.5 (2) ⊥ 2.5–7 (2)
Thermal conductivity (W/mK)	25–470 along length and width: 140 through thickness: 5	17.0–22.6 (3) ⊥ 7.5–10.3 (3)
Specific heat (J/kgK)	710–830	690–1550

|| and ⊥ = Fibre orientation; (2) RT–1500 °C; (3) 200–1650 °C

Figure 5 shows the microstructure of the graphite and the C/C–SiC materials. For the C/C–SiC material the carbon fibres are depicted in cross section and the grey area is the SiC matrix.

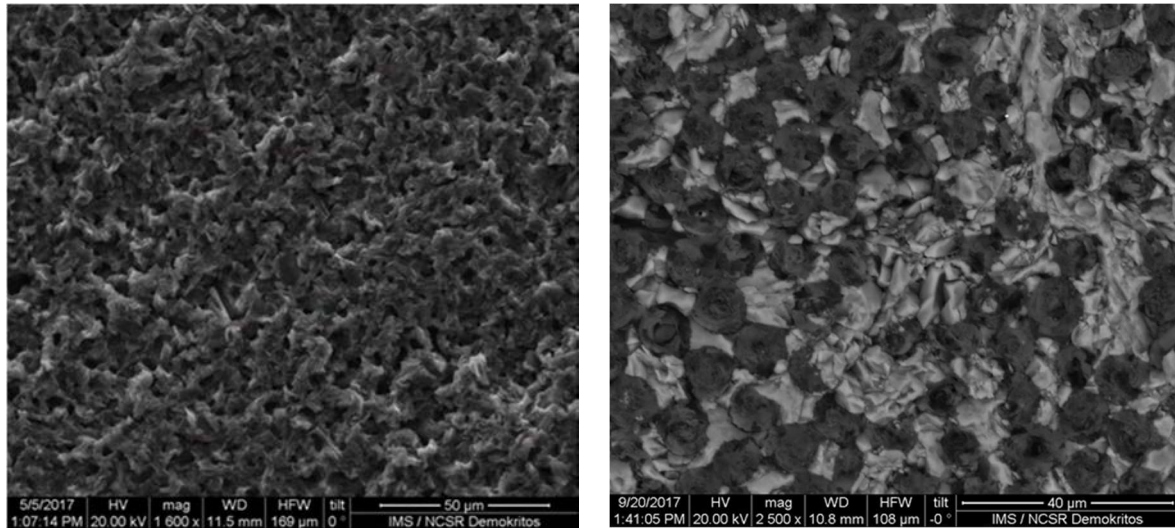


FIG.5. SEM micrographs of the graphite (left) and the C/C-SiC (right) materials.

3.2 CAPSULE DESIGN AND PERFORMANCE

Different design geometries and process routes were investigated for the fabrication of the VERDI detectors. Capsules of two types were fabricated: (a) with adhesive-based joining of the parts of the capsule and (b) with mechanical enclosure of the active elements using a threaded cover. The joining of the adhesive based capsules was performed using the high temperature adhesive Graphi-Bond™ 669 which has a service temperature of 760 °C.

The adhesive based capsule is advantageous when available space in height is limited and in case good sealing of the metallic elements is required. Also, the use of such a capsule can minimize the thickness of the required capsule walls. The threaded capsule design offers the possibility to remove the active elements out of the capsule and measure them separately, besides measuring the whole system.

Regarding the adhesive based capsules, the curing conditions of the adhesive included curing at room temperature for 2 hours and at 120 °C in air for 5 hours. Pull off tests showed that the adhesive based capsule has an average pull-off strength of 0.65 ± 0.05 MPa with the fracture taking place inside the adhesive (cohesive failure). The pull off strength increases almost five times after thermal treatment at 500 °C in vacuum and reaches the value of 3.0 ± 0.4 MPa.

Also, shear tests of graphite/graphite adhesive joints having dimensions of 10×10 mm² were performed at room temperature using the configuration shown in Figure 6. The tests were carried out on an INSTRON 5982 Universal Testing Machine at a displacement rate of 100 µm/min. The values of maximum load and displacement at maximum load were obtained from the load-displacement curves. In addition, the ultimate shear strength (the ratio of the maximum load to the area under shear) and the % ultimate shear strain (the ratio of displacement at ultimate shear strength to the original length) were determined. The results are presented in Table 6. The ultimate shear strength was on average (2 ± 0.4) MPa with the % ultimate shear strain being 1.3 ± 0.4 . In all the joints tested, the fracture took place inside the graphite adhesive layer.

TABLE 6. SUMMARY RESULTS OF THE SHEAR TESTS OF GRAPHITE/GRAPHITE JOINTS USING GRAPHITE ADHESIVE.

	Maximum Load (N)	Ultimate Shear Strength (MPa)	Displacement at maximum load (mm)	Ultimate Shear Strain (%)
Average value ± STDEV	200 ± 41	2.0 ± 0.4	0.13 ± 0.04	1.3 ± 0.4

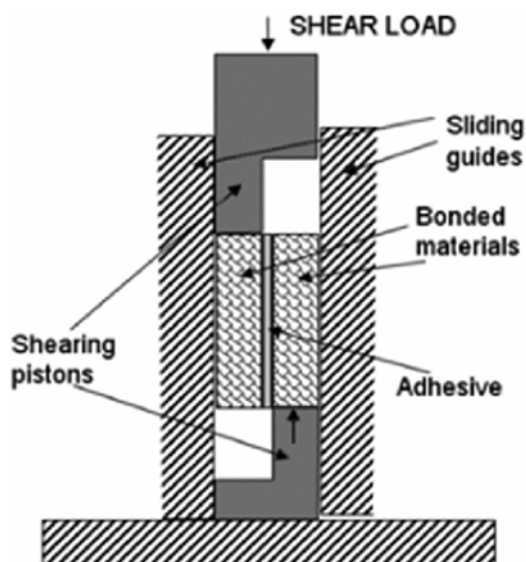


FIG. 6. Schematic drawing of the jig and the joint geometry for the mechanical shear tests.

A set of prototype detectors were fabricated with the adhesive-based design and a set with the threaded design using graphite material in order to be tested at ENEA Fast Neutron Generator facility. The active elements were encapsulated in the form of foils. One detector of each design was also fabricated with no metallic elements added (blank detectors) in order to check for interferences from the matrix material.

4 EXPERIMENT AT FRASCATI NEUTRON GENERATOR

Six prototype detectors, including two blanks, composed of graphite capsule were fabricated and tested at ENEA Frascati Neutron Generator (FNG). The detectors were placed on an Al holder (99.0% purity, 100 mm width, 50 mm height, 1.5 mm thickness), as shown in Figure 7. The detectors' assembly was irradiated at the reference 14 MeV neutron field of the FNG for 2.956 h at 5.3 cm distance from the neutron source.

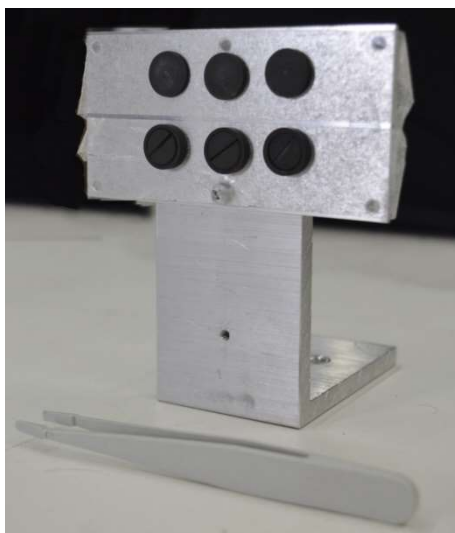


FIG.7. The prototype detectors attached to the sample holder prepared for the irradiation at ENEA FNG.

The neutron source strength at the FNG target is determined absolutely by counting the α -particle associated with the neutrons produced by the $T(D, n)\alpha$ reaction. Using the associated particle technique, the achieved total neutron yield at the source was measured to be 4.96×10^{14} neutrons. Taking into account the MCNP model of the source the neutron flux at the detectors' irradiation position was estimated (Table 7). The statistical error of the calculation was of 0.04%. Induced activity was calculated for all detectors at the end of irradiation.

TABLE 7. NEUTRON FLUXES AT THE DETECTORS' IRRADIATION POSITION

Detector	Neutron flux [n/cm ² /s]
1	1.55×10 ⁸
2	1.69×10 ⁸
3	1.57×10 ⁸
4	1.61×10 ⁸
5	1.72×10 ⁸
6	1.60×10 ⁸

The irradiated VERDI detectors were analysed by means of gamma spectrometry both at ENEA, immediately after irradiation, using a 60% HPGe, and at NCSR, approximately 7 days after the end of irradiation, using an 85% HPGe. Spectra collected at ENEA provided data for short-lived isotopes, while spectra collected at NCSR allowed for the detection of isotopes with longer half-lives. Excellent agreement was found between the analyses at ENEA and at NCSR.

A typical γ -spectrum of the analyses performed at ENEA is presented in Figure 8 (acquisition time 79 000 s). The respective typical spectrum of the analyses performed at NCSR is presented in Figure 9 (acquisition time 86 400 s). In the spectrum collected at NCSR additional photopeaks are detected, corresponding to isotopes with longer half-lives: ⁵⁷Co, ⁵⁸Co, ¹⁰²Rh, ¹⁰³Ru, ^{92m}Nb.

As far as the blank detectors are concerned, no induced activity due to the neutron irradiation was detected. The only photopeaks detected, both at ENEA and at NCSR, correspond to natural background peaks (²¹⁴Bi, ²¹⁴Pb, ²¹²Pb, ²²⁸Ac, ²⁰⁸Tl, ⁴⁰K, ²³⁴Th, ²²⁶Ra), mainly due to radon and thoron progeny. No differences were observed between the two different enclosure types, which lead to the conclusion that the graphite based adhesive used does not affect the neutron activation results. Therefore, minimizing the capsule mass is not considered as a major requirement for the fabrication of the detectors.

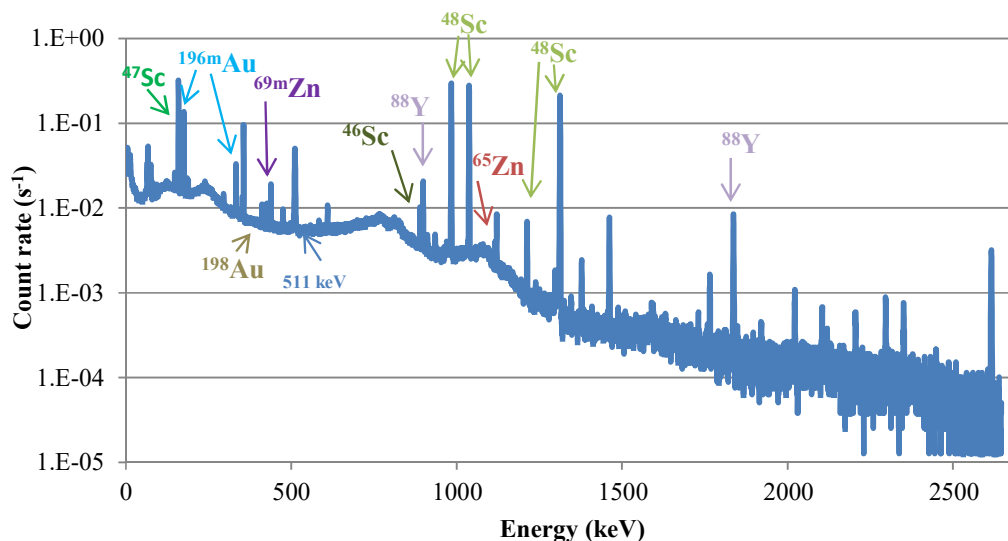


FIG. 8. Typical γ -spectrum collected at ENEA for 79 000 s.

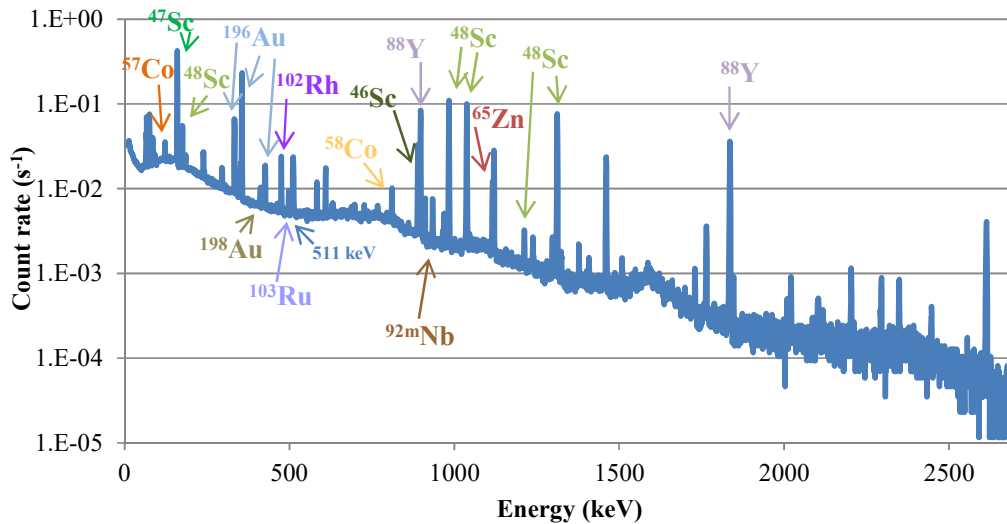


FIG. 9. Typical γ -spectrum collected at NCSR D for 86 400 s.

5 DISCUSSION AND FURTHER WORK

Neutron monitoring (fluences and spectra) is of crucial importance for fusion devices such as ITER and DEMO. Activation methods are one of the few available options for measuring fusion power and quantify the neutron energy spectrum at the measurement location. Existing neutron monitoring techniques might not work in demanding DEMO and future fusion plants conditions. In this work, the neutron activation technique was advanced by providing a composite activation target and implementing the activation analysis method based on high sensitivity gamma-ray detection. The proposed neutron monitoring method under the VERDI project is based on the standard foil activation dosimetry, but it adds a very innovative step to adapt the technique to the harsh DEMO and future fusion power plant conditions. A set of relevant metallic particles (which will be activated) are introduced in a ceramic matrix with suitable physical, chemical and mechanical properties to withstand high temperatures, high magnetic fields and severe radiation fields. This approach delivers a robust technique for determining neutron fluence in the demanding fusion environment and could replace or complement existing neutron monitoring methods. In particular, it would provide an absolutely calibrated basis for comparison of time-integrated neutron yield measurements from other types of detectors, and also of other neutron spectrometry diagnostics. It will therefore allow monitoring the neutron fluence on components and materials, tritium breeding rates, nuclear heating, and a variety of other parameters in fusion reactors such as ITER, DEMO as well as future fusion plants.

A number of prototype detectors was fabricated and tested at ENEA FNG to demonstrate the feasibility of the VERDI detector to measure neutron fluence in a fusion relevant neutron spectrum. It was shown that the complexity of the gamma spectra from the activation products (different gammas from various activation products) is disentangled by careful selection of active elements in the detector in order to have minimum overlapping of the emitted photons. Moreover, interference from the matrix material composition was found to be minimal. The induced activity data, in conjunction with cross section data, will provide the required information for the unfolding process in order to evaluate the neutron energy spectrum.

Further experiments are planned to test detectors both at ENEA's fusion neutron source and at JET tokamak during the forthcoming DD as well as TT and DT campaigns taking most particularly advantage of those tritium-based experiments that are not going to be repeated in the foreseeable future. Therefore, the new detector will contribute scientific data for the JET research program as well.

ACKNOWLEDGEMENTS

This work has been carried out within the framework of the EUROfusion Consortium and has received funding from the Euratom research and training programme 2014–2018 under grant agreement No 633053. The views and opinions expressed herein do not necessarily reflect those of the European Commission. The help of Dr Amalia Marinou in the lap shear tests is acknowledged.

REFERENCES

- [1] LOUGHLIN, M., FORREST, R., EDWARDS, J., Neutron activation studies on JET, *Fusion Eng. Des.* **58–59** (2001) 967–971.
- [2] PROKOPOWICZ, R., et al., Measurements of neutrons at JET by means of the activation methods, *Nucl. Instrum. Methods Phys. Res., Sect. A* **637** 1 (2011) 119–127.
- [3] ANGELONE, M., et al., Neutronics experiments, radiation detectors and nuclear techniques development in the EU in support of the TBM design for ITER, *Fusion Eng. Des.* **96–97** (2015) 2–7.
- [4] KLIX, A., et al., Neutronics diagnostics for European ITER TBMs: Activation foil spectrometer for short measurement cycles, *Fusion Eng. Des.* **87** 7–8 (2012) 1301–1306.
- [5] SUBLET, J.-C., EASTWOOD, J., MORGAN, J., The FISPACT-II User Manual, CCFE-R (11), (2013) UK Atomic Energy Authority.
- [6] SUBLET, J.-C., et al., The European Activation File: EAF-2010 neutron induced cross section library, CCFE-R (10) 05 (2010) UK Atomic Energy Authority.
- [7] MARTONE, M., ANGELONE, M., PILLON, M., The 14 MeV Frascati neutron generator, *J. Nucl. Mater.* **212–215** (1994) 1661–1664.
- [8] HEIDENREICH, B., “Manufacture and Applications of C/C–SiC and C/SiC Composites”. *Processing and Properties of Advanced Ceramics and Composites IV* (SINGH, J., et al., Eds.), **234** (2012) 183–198, USA: John Wiley & Sons.
- [9] GOORLEY, T., et al., Initial MCNP6 Release Overview, *Nucl. Technol.* **180** (2012) 298–315.

NEUTRON DETECTION TECHNOLOGIES AND MEASUREMENT CHALLENGES AT JET AND ITER

L. W. PACKER*, Z. GHANI, M.R. GILBERT, S. POPOVICHEV

United Kingdom Atomic Energy Authority

Culham Centre for Fusion Energy

United Kingdom

*Email: lee.packer@ukaea.uk

V. KRASILNIKOV^{a,b}

^aITER Organization

Route de Vinon-sur-Verdon - CS 90 046 - 13067 St

Paul Lez Durance Cedex

France

^bTokamak Energy Ltd

120A Olympic Avenue

Oxfordshire

OX14 4SA

UK

M. CECCONELLO

VR Association,

Uppsala University,

Department of Physics and Astronomy,

PO Box 516, SE-75120 Uppsala,

Sweden

M. TARDOCCHI, M. REBAI, D. RIGAMONTI

Istituto di Fisica del Plasma ‘P. Caldirola’

Via R. Cozzi 53,

20125, Milano

Italy

and JET Contributors*

*See the author list of “X. Litaudon et al 2017 Nucl. Fusion 57 102001”.

Abstract: In the development of nuclear fusion energy technologies based on deuterium–tritium (DT) reaction, which releases a high energy neutron around 14.1 MeV, robust and accurate neutron detection technologies are needed. These are required for monitoring and control of plasma conditions, tritium accountancy, and for the measurement of fusion power itself. The JET device, based at Culham in the UK and funded by the EU, is currently the largest operating fusion tokamak device operating worldwide, also with the capability and infrastructure to operate with fusion plasmas containing tritium. A new DT experiment is scheduled over the next few years, which presents a unique opportunity to gain further knowledge and experience in fusion technologies, including the nuclear metrology and technological aspects of neutron detection for fusion. JET operations and experience are now strongly oriented to provide input into the preparations for the ITER device, being constructed in Cadarache, France—an international endeavour comprising seven members: China, the European Union, India, Japan, Korea, Russia and the United States—and expected to be operational by the 2025. This paper gives an overview of the range of neutron detection and diagnostic systems currently employed at JET and those being designed, built and considered for ITER, including neutron spectrometers, magnetic proton recoil spectrometers, fission yield counters, diamond detectors and activation foil-based systems and other systems. We identify the key technologies and challenges for neutron detection systems in fusion environments.

1 INTRODUCTION

Controlled thermonuclear fusion is a promising, yet technologically challenging, route to low carbon power generation. To create the necessary fusion conditions, a plasma containing fusion fuel ions has to be arranged to meet a minimum required value of the so-called triple product, comprising the quantities confinement time, plasma ion density and plasma temperature. One of the most successful types of device in meeting these requirements and in providing a stable plasma configuration over long periods of time is via the tokamak concept, which achieves these conditions through the creation of a magnetic bottle in a toroidal form to contain a hot plasma. This is done via the introduction of two magnetic field components: one via magnetic coils and a central solenoid and the other by passing a strong axial current through the plasma itself. This creates resultant helical magnetic field lines which wind around the toroidal plasma shape, serving to confine the fuel ions by preventing charge separation and ion losses which lead to plasma cooling. Heating to the plasma, typically to achieve typical temperatures of 150 million Kelvin, is provided through three main modes: Ohmic heating provided via the plasma current, through RF heating tuned to the electron and ion gyro frequencies and finally by neutral deuteron beam heating systems. The most suitable fuel ions to achieve these conditions are via the hydrogen isotopes, deuterium (D) and tritium (T); the DT

fusion reaction has the highest fusion cross section at typical plasma temperatures achieved in magnetic confinement fusion devices or via inertial confinement experiments compared with alternative fuel types. Each DT fusion reaction releases 17.6 MeV energy carried by two ejectiles: a neutron, which carries 80% of the energy (14.1 MeV), and an alpha particle (3.5 MeV) which carries the remaining 20%. In fusion power plant concepts, the alpha particle energy is partly used to heat the plasma itself; the degree to which the alpha energy is retained depends on the level of the plasma confinement and this reduces reliance on external heating systems to provide heating. The neutron readily escapes from the plasma—its energy is deposited in a blanket structure surrounding the plasma and ultimately transferred to a coolant via a heat exchanger to drive turbines and thus to produce electricity, the main goal of the endeavour in this research field. The fact that nuclear fusion is a neutron rich energy source, significantly more so than nuclear fission, means that the accurate measurement of neutrons is essential to the success of the technology itself, with impact on control, performance and safety.

This paper provides an overview of neutron detection systems that are in use and being developed at JET [1] and at ITER [2], devices that are at the forefront of the development of fusion energy, with contrasts being made between the conditions and requirements for detection systems in those devices. ITER is currently being constructed in Cadarache in Aix en Provence in the South of France via the combined resources of seven members: China, the European Union, India, Japan, Korea, Russia and the United States. Its first plasma is scheduled for December 2025. It is being designed to operate with a nominal 500 MW fusion power and a fusion gain of $Q = 10$ —hence it will be the first fusion device to produce net energy. ITER will also be the first fusion device to maintain a fusion plasma for long periods of time, typically with 400 second pulses, through the use of superconducting magnetic field coils. ITER will be the first fusion device to test the integrated technologies, materials, and physics regimes necessary for the commercial production of fusion-based electricity.

JET is currently the largest and most powerful tokamak in the world. It is currently the only machine capable of operating with the deuterium-tritium fuel mix of future commercial reactors. The device has been in operation since 1983 and was designed to study the plasma behaviour in conditions approaching those required for a fusion reactor. In 1997, JET produced 16 MW of fusion power from a total input power of 24 MW (a fusion gain of $Q = 0.67$) and to date this stands as the record for controlled fusion power production in an experimental device. It is important to note that the measurement of fusion power and gain, the most important measures of fusion success, are derived directly from the measurement of neutron yield. Due to the flexible original design the JET machine has been able to evolve over the years with the experimental programme and research remaining at the forefront of fusion research. The main focus of the current JET experimental programme is to support the construction and operation of ITER, acting as a test bed for ITER technologies and plasma operating scenarios. The main components of the JET machine are the vacuum vessel, where the fusion plasma is confined by means of strong magnetic fields and plasma currents (up to 4 T and 5 MA current), surrounded by magnetic field coils and shielding materials. The major radius of JET is 2.96 m and minor radius 0.9 m. The vacuum vessel itself is made of Inconel and double walled with a total thickness of 2 cm. The machine is made up of eight octants, with each of these having a horizontal access port through the shielding. A divertor at the bottom of the vacuum vessel allows escaping heat and gas to be exhausted in a controlled way. Since 2011 the first wall of the vacuum vessel has been made of beryllium and tungsten, mirroring the material choices of ITER.

1.1 RADIATION FIELD MEASUREMENT ENVIRONMENT IN TOKAMAKS

A challenging range of conditions for nuclear measurements exist in tokamak devices operating with significant fusion power, such as ITER and in next step conceptual power plant demonstrators, referred to as DEMO concepts. The neutron fluxes in these tokamak devices are predicted to span several orders of magnitude in flux level; in ITER for example, which is designed to operate with 500 MW fusion power, neutron fluxes are predicted to be up to 10^{14} n/s/cm² at the plasma-facing first wall materials and below 10^4 n/s/cm² in surrounding tokamak building maintenance areas. One is required to measure the spatial, temporal and spectral neutron emissivity from the plasma as well as the fluxes of neutrons at various locations within the device and tokamak complex. Since sufficiently high flux, high energy neutron irradiation and testing facilities at the aforementioned levels do not currently exist, though some have been proposed, such as IFMIF and CTF for example, the development of fusion technologies including instrumentation relies significantly on models and simulations. Computational tools such as MCNP6 [3] together with nuclear data libraries such as FENDL-3.1 [4] play a crucial role in predicting the nuclear fields in which technologies operate. Figure 1 shows an MCNP6 calculation of the neutron spectra in ITER and JET during DT operations at first wall locations, which are compared to corresponding spectra during DD plasma operations, and against a spectrum DEMO fusion power plant conditions, where the neutron flux levels are predicted to be a factor ranging between two and six greater than those in ITER DT operations - the factor depends on the particular design power of the DEMO concept, of which there are many under consideration.

Figure 2 shows a spatial prediction of neutron flux distribution through an $X-Z$ cross-section of an ITER model performed at 500 MW fusion power in DT operation using MCNP6. A range of neutron detection systems are needed to measure this fusion environment with the appropriate dynamic range, energy, temporal and directional response; radiation, temperature and magnetic field resilience; and sensitivity to, and system ability to discriminate from, the significant prompt and residual gamma background fields.

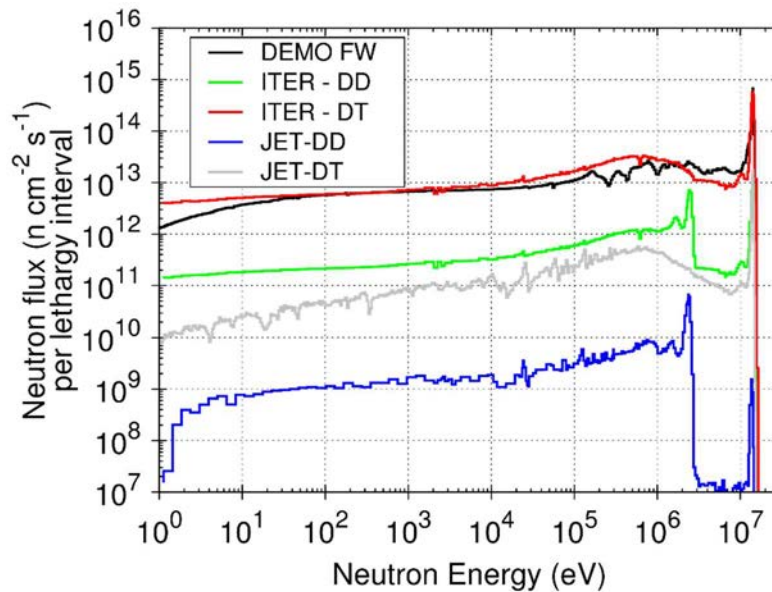


FIG. 1. Calculated neutron flux spectra at the first wall in a DEMO power plant with ITER and JET DT and DD plasma operations at locations near the first wall.

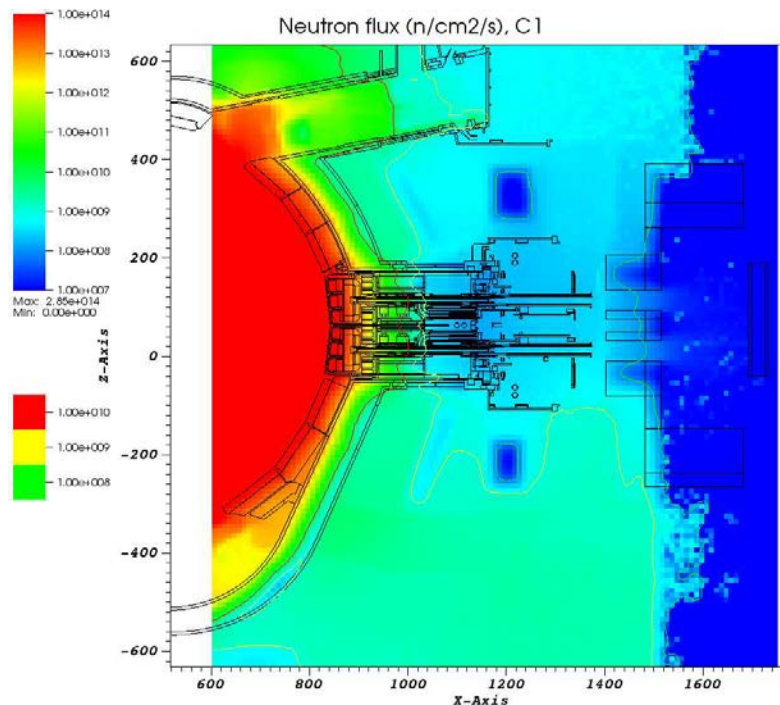


FIG. 2. Simulated neutron flux map through an $X-Z$ slice of an ITER model containing an ion cyclotron resonance heating system in an equatorial port. Calculations were performed using MCNP6 and show a neutron flux range spanning seven orders of magnitude.

The residual photon fields that are present during and following operations due to neutron induced activation of materials comprising the device itself, are an important consideration for neutron instrumentation in fusion devices. Instrumentation systems have to be able to satisfactorily discriminate gamma background from the neutron signal. In DEMO environments within the tokamak vessel directly following significant power operations gamma dose rates due to activation of materials are typically predicted to be in the several 10's kSv/h range, though this reduces over time following operations, and with the major radial distance through the tokamak device beyond the first wall due to the effect of neutron shielding. Computational tools such as FISPACT-II [5, 6] with nuclear data libraries EAF-2010 [7] and TENDL-2015 [8] are widely used to predict the full complexity and temporal behaviour of such fields and may be coupled with radiation transport codes to determine 3D activation gamma fields [9]. Figure 3 shows an example of a FISPACT-II output calculation. The data is represented on a section of the nuclide chart, displaying a range of isotopes (defined by proton number, Z , and neutron number N). The plot predicts the contact gamma dose rate distribution across isotopes for pure tungsten material exposed to five years of neutron irradiation under fusion DEMO conditions. Tungsten, prior to irradiation, contains five stable isotopes and one can see in this plot the complexity in the isotopic distribution of the material following the irradiation phase.

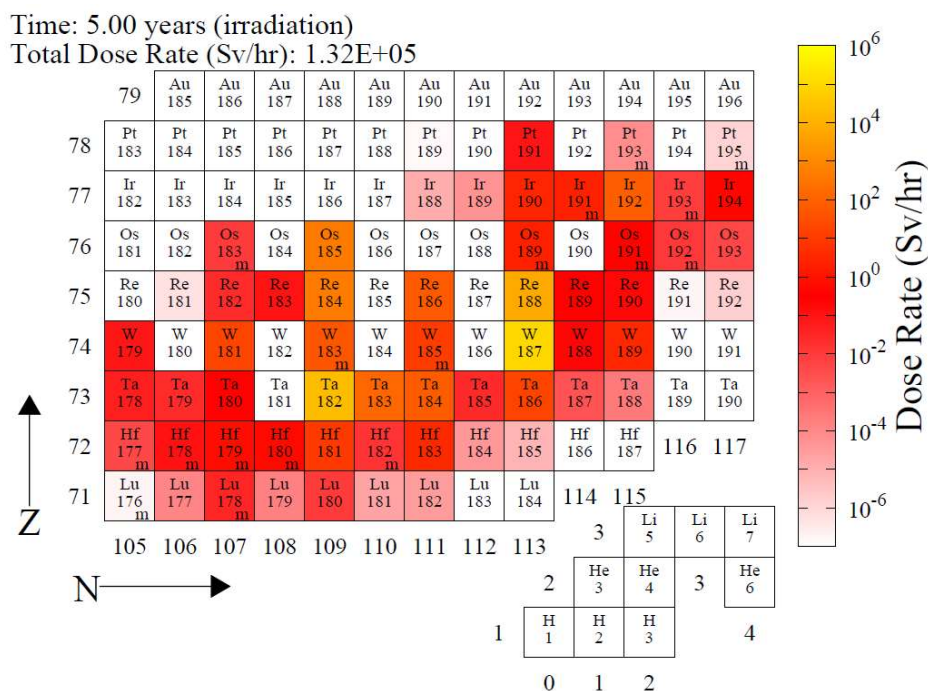


FIG. 3. Nuclide chart section showing the output from a FISPACT-II calculation of the nuclide distribution of gamma dose rate from W exposed to a neutron irradiation field in a DEMO first wall environment over a period of 5 years. See [10–12] for details on the methodology and further examples.

1.2 NEUTRON EMISSION MEASUREMENTS AND DETECTION

The measurement of the neutron emission in fusion devices can be divided in the three broad categories: counters, cameras and spectrometers. Time resolved neutron yield monitors (counters) measure the instantaneous neutron emission strength providing information on the efficiency of different heating schemes and the fusion power achieved. In addition, the signal from neutron yield monitors is often affected by rapid fluctuations which can be related to plasma instabilities. This can be exploited both for the real-time control of plasma operations and for physics studies. Arrays of collimated, time resolved neutron yield profile monitors (usually called cameras) provide in addition spatial information on the neutron emission enabling the reconstruction of the neutron emissivity profiles via inversion (tomographic) techniques and the measurements of the plasma column radial and vertical position inside the vacuum vessel. If fast enough, cameras can also contribute to the study of fast ion confinement, where fast ions are generated by the fusion reactions themselves (both DD and DT) or the result of external heating. Of particular interest is the interplay between fast ions and plasma instabilities that can interact non-linearly resulting in the redistribution and loss of fast ions from the hot central part of the plasma thus potentially reducing the fusion power. Time resolved neutron spectrometers can provide information on the

neutron energy spectrum, measure the fuel ions temperature and velocity distribution, study the effect of different heating schemes and plasma rotation as well as the fuel ratio nD/nT which is a key parameter for the optimization of the fusion power which requires $nD = nT$.

Neutron detection methods rely on two main interaction mechanisms of neutron with matter: firstly, via nuclear reactions and secondly via scattering interactions. Nuclear reactions result in the emission of prompt energetic particles. The cross-section for these nuclear reactions changes with neutron energy, and for many reactions of interest is often lower at high energies (above a few eVs) resulting in a low detection efficiency and therefore in a low time resolution (relevant for time of flight spectrometry systems discussed in later sections). In addition, information relating to the original neutron energy is lost since the signal generated by the fission products is linked to the Q of the reaction and not the energy of the incoming neutron and therefore of limited spectroscopy interest. Some spectroscopic capabilities are retained in the case of threshold reactions such as in the case of activation foils and diamond-based detectors. Elastic neutron scattering with atoms in the detector medium typically results in an energetic recoil proton (or other charged particle) which then deposits its energy in the medium via Coulomb interactions thus providing the required signal. The amplitude of the signal is proportional to the energy deposited by the recoil proton thus providing some spectroscopic capabilities which are limited by the detector response function not always being straightforward.

Neutron detectors which are routinely employed in present day devices, such as JET, and planned to be used in ITER and DEMO, can be divided in those relying on nuclear reactions such as fission chambers, activation foils and diamonds and on those relying on elastic scattering such as scintillator, diamond, GEM, He-4 gas filled chambers detectors, and super-heated bubble detector types, for example. Neutron spectrometers, discussed in more detail in later sections, are most frequently based on time of flight or magnetic spectrometry techniques.

2 JET NEUTRON DETECTION SYSTEMS

This section describes the features and technologies of neutron detection systems, either currently deployed in JET or are under development. Brief, key details on each of the systems are provided in this overview and, where further details are required, readers are referred to some of the papers provided as references; these are by no means comprehensive, though we nevertheless aim this section to serve as a helpful starting point of reference for those interested in researching the current status of neutron diagnostics deployed in tokamaks.

2.1 FISSION YIELD COUNTERS

One of the most important measurements at JET is the total neutron yield from the plasma. Due to the wide range of possible plasma operations, the measurement requirements for the neutron detection system have to span 10 orders of magnitude in intensity, with total neutron emission rates from the plasma ranging from 10^{10} to 10^{20} n/s. Additional requirements are that the system should be insensitive to gamma and X-rays, have a relatively flat neutron energy response and insensitive to fluctuating magnetic field and RF interference. JET has adopted pairs of fission chambers for this purpose, one fission chamber based on U-235 as the sensitive element and the other based on U-238 [13]. Figure 4 shows an image of the paired fission chamber configuration.

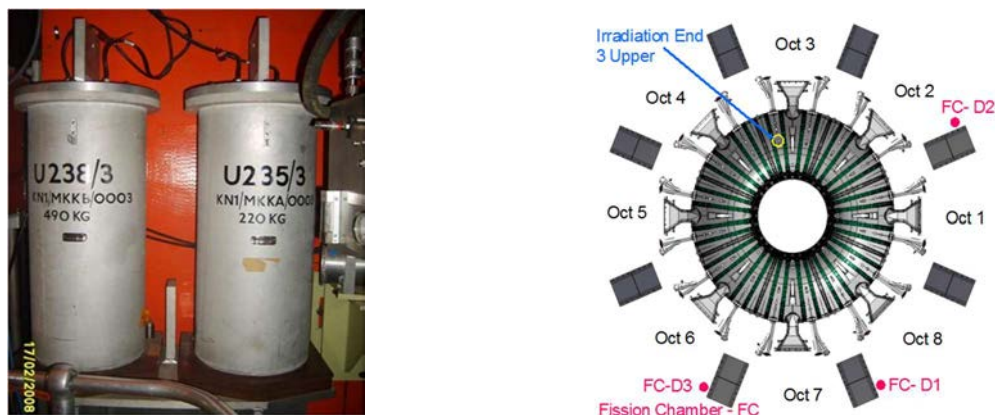


FIG. 4. (LHS) Neutron yield measurement system at JET, based on a pair of fission chambers. (RHS) Octant locations of the three pairs of fission chambers at JET D1, D2 and D3.

A schematic of a U-235 based system is shown in Figure 5. The U-235 fission chamber is surrounded by a layer of low antimony lead followed by surrounding polyethylene and cadmium layers of 50 mm and 1 mm respectively. The U-238 fission chamber configuration contains a thick layer of lead (95 mm) and slightly thinner layer of Cd compared to the U-235 configuration of 0.25 mm. Each fission chamber assembly is enclosed in aluminium casing of 1.3 cm thickness. Three pairs are used at JET to measure the neutron yield at different locations, each pair is mounted on a transformer limb at radius of $R = 7.82$ m in the equatorial plane, outside the vacuum vessel at the mid-plane height. The fission chamber electronics are designed to operate in both pulse counting and current modes, so that each detector has an operational range of more than 8 orders of magnitude. Since there is overlap in the operational range of each fission chamber type, cross calibration of the detectors can be performed.

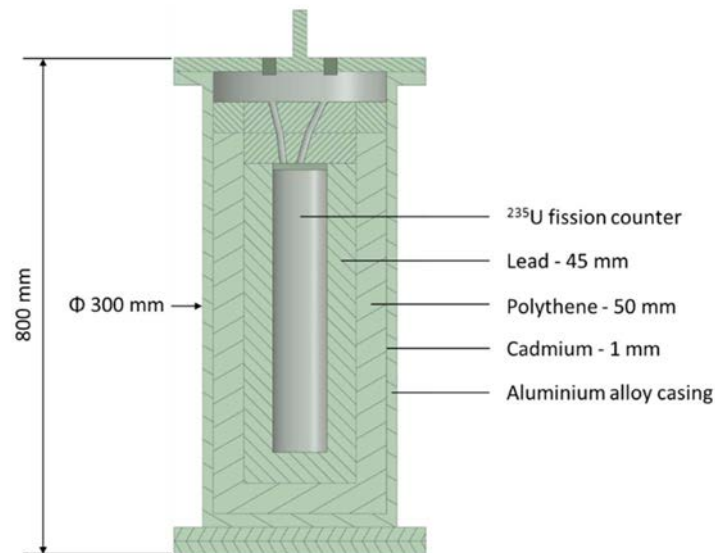


FIG. 5. Schematic showing the U-235 based fission yield counter used at JET.

The system has been absolutely calibrated to 10%. This was performed in-situ using a Cf-252 source in 1984 [14] and in 2013 [16] with a numerical study being performed between these periods [15]. Most recently the system was calibrated, for the first time, using a well characterised DT neutron generator placed inside the torus vessel [17]. The main reason for repeating the calibration exercise is because the JET device itself has changed over the years with installation of several new large systems in the torus hall out-side the JET vacuum vessel which had led to a reduction in response per source neutron [16]. The system is also periodically cross calibrated by the activation technique.

2.2 PNEUMATIC ACTIVATION FOIL TRANSFER DIAGNOSTIC SYSTEMS

To perform integrated measurements of neutron flux over individual experimental shots JET operates a pneumatic capsule transfer system, deployed via a carousel system, able to transport via a plastic capsule activation dosimetry foils to a range of irradiation ends in the machine (see Figure 6). In these irradiation ends the foils are exposed to significant fluxes of neutrons as a result of JET plasma experiments inducing characteristic neutron induced reactions in the selected foils. The JET activation foil system, known as KN2, has eight irradiation ends. Seven of these ends are located behind the tokamak shield, and one, the 3 upper irradiation end position (3U) is located in Octant 3, placed inside the vacuum vessel itself. Because of the high temperatures at this location, about 300 degrees Celsius, the 3U irradiation end is water cooled [18]. Following irradiation, the capsules are pneumatically retrieved from the irradiation ends to a radiometric laboratory, where the foil activities are measured by calibrated HPGe or NaI detection systems.

Dosimetry reactions commonly used include: Al-27(n, α)Na-24, Si-28(n,p)Al-28, In-115(n,n')In-115m, Fe-56(n,p)Mn-56. For DT neutron energies in particular the Nb-93(n,2n)Nb-92m and Y-89(n,2n)Y-88 reactions are used, due to their high energy threshold.

The KN2 pneumatic transfer system has also been used to test the development of neutron spectrometers and associated spectrum unfolding methodologies that may be used in ITER test blanket modules [19, 20].

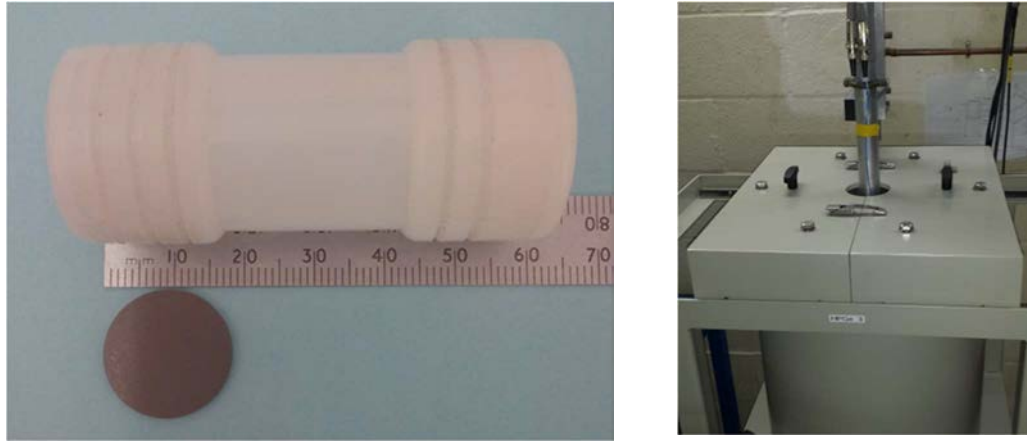


FIG. 6. (LHS) KN2 plastic dosimetry foil transfer capsule alongside a Nb dosimetry foil. (RHS) capsule retrieval location inside a low background lead shield housing a HPGe detector.

2.3 DELAYED NEUTRON COUNTING SYSTEM

Samples of Th-232 or U-238 may be transferred to irradiation ends and exposed to JET neutrons, which induce fission events in the samples, before being transferred to a well counting station based on He-3 gas filled proportional counters arranged in a polyethylene moderator [21, 22]. The delayed neutrons that are emitted from the sample following fission are efficiently measured in the counter and may be used to derive a total neutron yield measurement, which may be compared to other total neutron yield systems.

2.4 NEUTRON EMISSION PROFILE MONITOR

The primary function of the neutron emission profile monitor, also known as the neutron camera instrument at JET (see [23–25]), is to measure the neutron emission as a function of both position and time in a poloidal (vertical along major radius) section through the torus. It is composed of 19 collimated lines of sight in fan shaped arrays, ten horizontal and nine vertical (see Figure 7). Each collimated line of sight contains a NE213 liquid scintillator, used for the detection of both DD and DT neutrons, and BC418 plastic scintillator for the detection of DT neutrons. In addition, CsI(Tl) photodiodes detection systems are used to measure hard X-rays and gamma emissions in range $0.2 < E_\gamma < 6$ MeV.

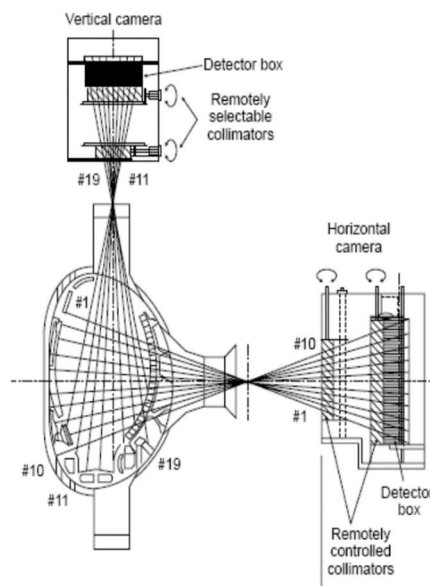


FIG. 7. Schematic showing the 19 lines of sight for the JET neutron emission profile monitor comprising the horizontal and vertical neutron camera.

2.5 NEUTRON EMISSION SPECTROSCOPY SYSTEMS

The spectrum of neutrons from the plasma carries useful information about the state of the triton and deuteron fuel ions undergoing fusion reactions, and such measurements thus offer an important diagnosis of plasma conditions. Neutron emission spectroscopy (NES) measurements have been developed at JET for this purpose, but are also deployed in various other tokamaks, notably TFTR and JT60 for example, as well as in inertial confinement fusion experiments. Whilst the focus of NES is often on observations of the main spectral neutron emissions as a result of ion kinematics with distributions around 2.45 and 14.1 MeV, in the cases of DD and DT fusion plasmas respectively, the effects of alpha and external ion beam interactions within the plasma as well as triton burn up through the $D + D \rightarrow T + P$ reaction may be observed through such measurements.

Neutron spectrometers can be divided in two major categories: compact spectrometers, whose response function is determined by the physical process governing the neutron interaction in the medium, and spectrometer whose response function is designed to match specific measurements requirements (usually the energy resolution). Examples of neutron spectrometers belonging to the second category are the 2.45 and 14.1 MeV spectrometer TOFOR a MPRu at JET while the VCN is an example of a compact spectrometer. All the spectrometers rely on the elastic scattering between neutron and proton in hydrogen rich materials. Figure 8 shows schematically the elastic processes involved in the three major types of neutron spectrometers.

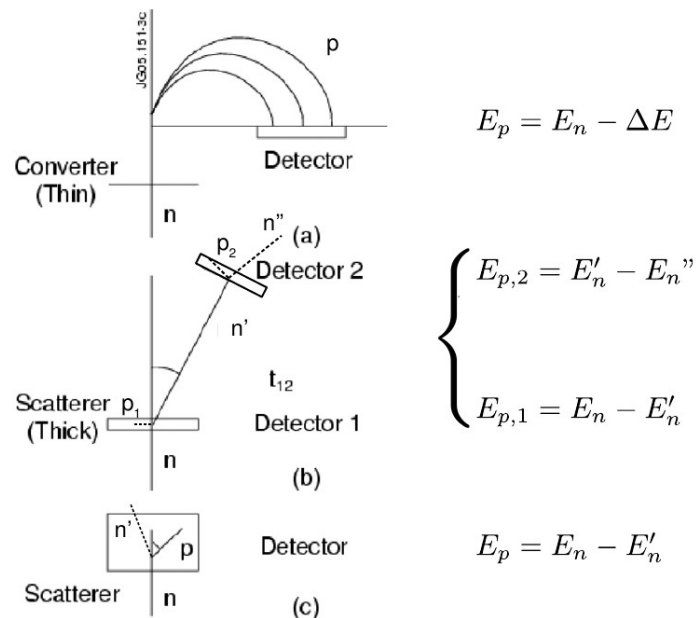


FIG. 8. (a) Proton-recoil magnetic spectrometer; (b) time-of-flight; (c) compact spectrometer.

In a magnetic spectrometer the neutron is converted into a proton whose energy for a head on collision is equal to that of the neutron minus a minor energy loss fraction in the converter foil. The recoil proton is then energy and momentum analysed in a magnetic field providing information on the incoming neutron energy. The proton recoil telescope works in a similar manner. Both the MPR and TPR require a vacuum chamber in which the proton can travel unencumbered between the converter and the detector. In a neutron time-of-flight spectrometer the incoming neutron collides elastically with a proton twice. The time difference between the detection of the recoil protons in the first and second detector together with the accurate knowledge of the system geometry allows calculating the incoming neutron energy. In a compact spectrometer, only the recoil proton that deposits its energy in the detector is measured. Its energy depends on the scattering angle and ranges from zero to the incoming neutron energy. The response function of a compact spectrometer is therefore much broader than that of either recoil or time-of-flight spectrometers. In addition, compact spectrometers cannot distinguish between a uncollided neutron scattering elastically at a certain angle and a scattered neutron making a head-on collision resulting in recoil protons of the same energy. For these reasons, compact spectrometers have limited spectroscopic capabilities and the extraction of the incoming neutron energy spectrum is more complicated and usually affected by a poorer energy resolution.

2.5.1 TOFOR

One of the major NES systems deployed at JET is the neutron time-of-flight (TOF) spectrometer, which has been optimized for operation at high rates (TOFOR) [26] (see Figure 9). The TOFOR system determines the incident neutron energy via a TOF measurement between two arrays of plastic scintillator detectors, S1 and S2. The S1 detector assembly is made up of a stack of five BC-418 scintillator units and the S2 detector is made of 32 modules consisting of Bicron BC-420 scintillator. Both detector arrays are coupled to photomultiplier tubes via optical guides. The first detector, S1, is placed in a collimated beam of neutrons and a fraction of these are detected through the proton recoil events causing scintillations in the detector which are then detected by the photomultiplier tube. A second detector array positioned a known distance and angle from S1 records a fraction of the scattered neutrons, again through proton recoils. The time of flight time is used to determine the spectrum. For example, for a flight path of approximately 1.2 m and scattering angle of 30 degrees the TOF time is around 65 ns for DD neutrons of 2.45 MeV and 27 ns for DT neutrons of 14.1 MeV [ref M. Gatu Johnson].

The efficiency of TOFOR is approximately in the range of $10^{-2}/10^{-3}$ per DD/DT neutron and it has an energy resolution of about 7% at 2.45 MeV for count rates of about 0.5 MHz. A typical example of a time-of-flight spectrum is shown in Figure 10 where both DD and DT contributions can be seen. Forward modelling is used to model the measurements including the contribution from emissions from T burn-up reactions (long-dashed blue line), thermal DD reactions (solid red line), beam-thermal DD reactions (solid black line), beam-beam reactions (broken black line) and scattered neutron (short-dashed black line) components. Since the neutron emission from the plasma depends on the physical processes affecting the fuel ions, forward modelling allows to infer their properties when the scattered contribution is correctly accounted for (in this case with MCNP-derived correction factors).

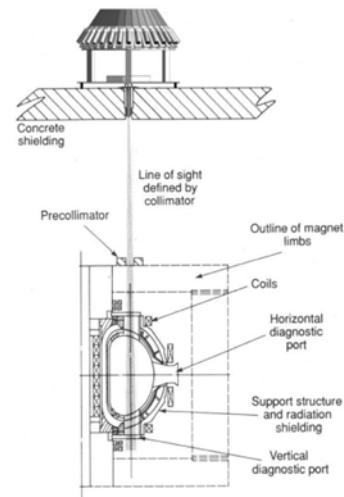


FIG. 9. LHS photo of TOFOR system; (RHS) schematic image showing the vertical TOFOR line-of-sight from the roof laboratory into the JET tokamak through the collimator in the concrete and precollimator, which can be used to constrain the viewed plasma volume.

2.5.2 Magnetic proton recoil spectrometer

The Magnetic Proton Recoil (MPR) at JET is used to measure the neutron spectrum by a well characterized energy conversion of the incoming neutron energy into a recoil proton energy optimized for DT neutrons (14 MeV). The MPR, originally installed in JET in 1996 with the focus to measure neutron energies around 14 MeV, was upgraded, called MPRu, in 2006, to improve the signal to background ratio and to provide a capability for 2.5 MeV neutron measurement [27]. The principal mode of operation is based on the conversion of a collimated beam of neutrons originating from the JET plasma, incident onto a thin CH₂ foil target (different thicknesses in the range 8–50 mg/cm² can be selected) to recoil protons (see Figure 11). The CH₂ target acts as a recoil proton source that is imaged onto the focal plane of a magnetic spectrograph. The image is spatially dispersed according to proton momentum; the momentum distribution is then used to infer the incoming neutron energy distribution. The MPR has an energy resolution of 2.5% at 14 MeV and an efficiency of about 10^{-4} – 10^{-5} cm². The MPR has been successfully used at JET to measure for example the presence of alpha particles via the knock-on effect as well the plasma rotation as shifts in the emitted neutron energy spectrum.

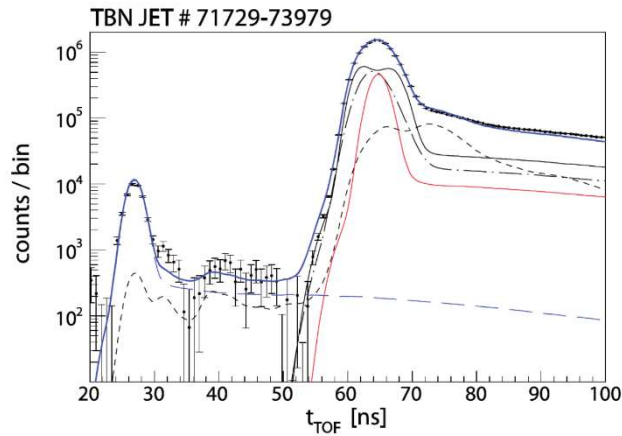


FIG. 10. example of time of flight spectrum from the TOFOR instrument on JET with DD and DT (burn-up) neutron emission.

2.5.3 Thin film proton recoil spectrometers

In the thin foil proton recoil (TPR) detection technique a collimated neutron flux interacts with a thin hydrogen-rich foil (CH_2), where elastic neutron-proton scattering takes place like the MPR method described previously, but unlike MPRs no magnetic field is here used. The recoil proton is instead detected in thin silicon CMOS detectors (usually between 10 to 20 μm). The thickness of the neutron-proton converter foil, the distance between the foil and the detector and the geometry of the system affect the achievable energy resolution and efficiency with typical values of 2% at 14 MeV and 10^{-3} to 10^{-5} protons per neutron and cm^2 . In order to reduce background signal, two Si detectors can be used in a $\Delta E/E$ configuration where the first detector measures the energy deposited by the proton traversing it and the second, thick detector fully stops the neutron and measures its energy. This configuration allows, through the coincidence method, to ensure that the proton is indeed coming from an elastic scattering with a neutron originating in the target. By exploiting the energy relation between the two detectors it is possible to discriminate against other particle types. To increase the efficiency of such systems, usually the Si detectors are installed in an annular region of a plane perpendicular to the incident neutron flux. On JET, TPR have been used to infer the fuel ion density in DT discharges, the fuel ion temperature and the fraction of fusion power coming from thermal reactions. The TPR was mounted outside the JET torus hall looking at the plasma through a collimated hole in tangential direction on the equatorial plane. More recently TPRs with improved resilience to neutron damage (though poorer signal to background) compared to Si, based on $\text{LaBr}_3(\text{Ce})$ and $\text{YAP}(\text{Ce})$, have been developed and reported here [29].

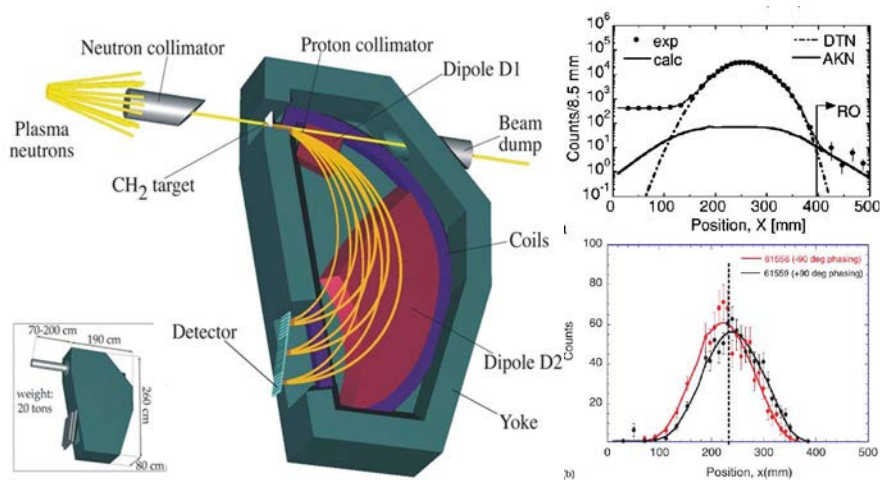


FIG. 11. (LHS) schematic of the principle features of the MPR diagnostic. (RHS) example of MPR measured data.

2.5.4 Compact Neutron Spectrometers

Compact neutron spectrometers are based on the elastic collision of the incoming neutron with the proton in a hydrogen rich material. The recoil proton deposits its energy in the medium by exciting the molecules which de-excite by emitting light in the UV region of the spectrum. These detectors are therefore known as scintillators. Scintillators are also sensitive to gamma-ray radiation which interacts with the medium via the Compton scattering on electrons (photo-electric absorption is very unlikely due to the low Z of the scintillation materials). Typical scintillators are NE213 or more recently EJ301. The light output is then converted into a voltage signal via a photo-multiplier. The light output response for recoil electrons depends linearly on the gamma-ray energy while the light output function for recoil protons has a non-linear dependence on the neutron energy. Discrimination between gamma-rays and neutrons is possible due to the different decay constants of the light pulse generated by recoil electrons and protons. The elastic scattering process results in a recoil proton whose energy depends on the scattering angle and ranges from the incoming neutron energy for a head-on collision to zero for a grazing collision. As a result, the response function to a mono-energetic neutron beam has the well-known ‘box-like’ shape. The response function is further complicated by the role of multiple scatterings of the same neutron on both the hydrogen and the carbon atoms in the scintillator material and by the non-linearity in the light response function. The use of scintillator detectors for spectroscopy use in fusion devices is further complicated by two factors: one is due to the fact that the emission spectrum from a fusion plasma is far from mono-energetic and that scattered neutrons are always present at some level in the observed signal. The first issue can be addressed by forward modelling of the detector response function to multiple ‘mono-energetic’ neutrons in the energy range of interest. The second aspect is more difficult to address as scattered neutrons are indistinguishable from direct neutrons interacting with the protons with a larger than zero scattering angle. Usually, their contribution is estimated via MCNP simulations of the direct to scattered ratio and by setting high energy acquisition thresholds to reduce their contribution. Forward modelling of a compact spectrometer is relatively straightforward and standard Monte Carlo-based codes such as NRESP & NEFF, MCNP and GEANT4 have been successfully used to match experimental neutron light output pulse spectra. Reconstruction of the neutron energy spectrum from the light output pulse height spectrum is however more complicated and relies on inversion techniques based on least-squares fitting or maximum entropy-type algorithms. Compact spectrometers have the advantage of a high efficiency (usually of the order of 5–10%) and energy resolutions from 20 to 5% for neutron energies from 2.45 MeV to 14 MeV. Compact spectrometers however face a series of issues such as their sensitivity to stray magnetic fields (due to the presence of the PMT), their limited temperature range (which might require cooling) and the non-linearity in the PMT gain at high count rates (above few hundreds of kHz). Compact neutron spectrometers have been used on JET to measure the neutron emission in trace-Tritium experiments and to determine the neutron energy spectrum using a maximum entropy unfolding algorithm [28] where an energy resolution as low as 2% at 14 MeV was claimed. A new compact neutron spectrometer is under development for JET in combination with a diamond matrix for the measurement of neutron energy spectra in different JET scenarios, specifically aimed at testing its performances according to ITER requirements. This system, based on the NE213 scintillator, is expected to operate at count rates of 400 kHz and above with energy resolutions below 5% for both DD and DT neutrons. Energy spectra are estimated using both forward and inverse methods. An image of the vertical compact spectrometer installed at JET on top of TOFOR is shown in Figure 12.

Recently, a series of novel materials have led to the development of new scintillators both liquid (EJ309) and solid (plastic, EJ-299-33) with good gamma-ray/neutron discrimination capabilities that are able to operate at higher temperatures compared to EJ301/NE213 ones. These detectors are of high interest for ITER and will be tested as part of the detector prototyping for the ITER radial neutron camera.

Two new compact neutron spectrometers have been recently developed and installed along the vertical line of sight of JET within the EUROFUSION enhancement program. The two detectors (see Figure 12), namely a NE213 scintillator crystal and a diamond-based system, share the same line of sight of the TOFOR providing high resolution neutron spectroscopy measurements of 14 MeV neutrons in DT plasmas.

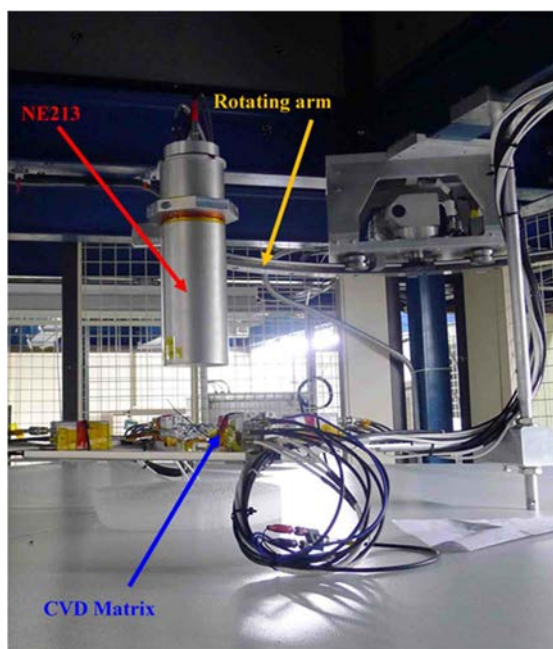


FIG. 12. Vertical Compact Neutron Spectrometer [VCNS].

2.5.5 Diamond detector-based systems

Diamond detectors operate as neutron detectors on the diode detector principle where a combination of doped/not-doped diamond layers exploit the large energy gap (5.5 eV) to provide a voltage signal. Diamond detectors have the advantage of being highly radiation hard and insensitive to magnetic fields which makes them interesting for ITER and DEMO. However, the active volume is very small resulting in very low efficiencies of the order of 10^{-4} to 10^{-7} counts/cm²/s. For these reasons, matrices of diamond detectors are usually employed (see the later discussion below on the DVNS). Neutron spectroscopy with diamond detectors is based on the collection of the electron-hole produced by charged particles generated by the neutron interaction with ¹²C carbon nuclei. The main nuclear reaction channels between ¹²C and neutrons in the energy range of interest for plasma diagnostics are the following elastic and inelastic scattering reactions: (i) ¹²C(n,n')¹²C which produces a continuum in the spectrum, mainly used in present day fusion devices; (ii) the carbon breakup reaction ¹²C (n,n')3 α with Q_{value} of -7.23 MeV; and (iii) the ¹²C (n, α)⁹Be reaction with a Q_{value} of -5.702 MeV. The latter reaction is the best candidate reaction for high resolution spectroscopy of 14 MeV neutrons, since it leads to a well-defined peak centred at $E_{\text{dep}} = E_n - 5.702$ MeV. It provides a direct relationship between the incoming neutron energy and the measured deposited energy from the charged product (the energy calibration of diamond detectors is usually performed with mixed triple α -sources). The shape of the measured spectrum is due to the intrinsic statistical broadening through the detector response itself and an additional kinematic broadening due to the energy distribution of the incoming neutrons. Due to the enhanced energy resolution of diamonds for 14 MeV neutrons (which is approximately 120–140 keV FWHM), the analysis of the peak that is present in the spectrum due to the alpha in the ¹²C(n, α)⁹Be reaction allows retrieval of information on the DT plasma, such as the ion temperature, and to diagnose the supra-thermal fraction and behaviour of fuel ions.

Similar considerations can be applied to the shape of the elastic edge produced by 2.5 MeV neutrons emitted by D plasmas. In this case neutrons interact in the carbon via elastic collision in which only part of the neutron energy is transferred to the recoiling ¹²C atom. The resulting energy deposited spectrum is a continuum and features an elastic edge placed at $E_{\text{d,max}} = 0.284 E_n$. In this case the energy resolution is lower with respect to the values obtained at 14 MeV and it is in the range 80–90keV at 2.5 MeV (FWHM). Therefore, although diamond offers moderate energy resolution for 2.5 MeV neutrons, the analysis of the shape of the elastic edge can still provide information on the incoming neutron spectrum in D plasma. It has demonstrated the possibility to carry out neutron spectroscopy measurements in discharges heated by neutral beam injection and radio-frequency waves.

A prototype single crystal diamond detector (SDD) consisting of a matrix of 12 independent SDDs (see Fig. 13), called the Diamond Vertical Neutron Spectrometer (DVNS) is installed at JET and has demonstrated the possibility to carry out neutron spectroscopy measurements in discharges heated by neutral beam injection and radio-frequency waves. It offers increased detection efficiency of a single SDD simply through the linear scaling

of the number of detectors in the instrument and it combines the enhanced energy resolution with the MHz counting rate capabilities. This reference [33] describes the main features of the DVNS, including the detector design, energy resolution, and data acquisition system for on-line processing. The detector is shown in Figure 13. Diamond detectors are also being considered for the ITER radial neutron camera, and radiation hardness tests in mixed fields (neutrons and gamma-rays) are in progress.

In preparation for the forthcoming DT JET campaign, expected around 2020, the excellent spectroscopic capabilities of the diamond detector for 14 MeV neutrons have been explored during the characterization of the 14 MeV neutron generator [17, 31, 32]. The latter is based on DT reactions and used for the JET 14 MeV neutron calibration. As shown in Figure 14, the high resolution neutron spectroscopy measurements performed by the diamond detector, allows one to resolve the complex features of the neutron energy spectra resulting from the mixed D/T beam ions reacting with the T/D nuclei present in the target [31, 32]. These results open up potential new prospects for diagnosing DT plasmas on both JET and ITER. The enhanced energy resolution of diamond detectors would allow accurate identification of different neutron components (NBI components, RF components, thermal components) in DT plasma operations.

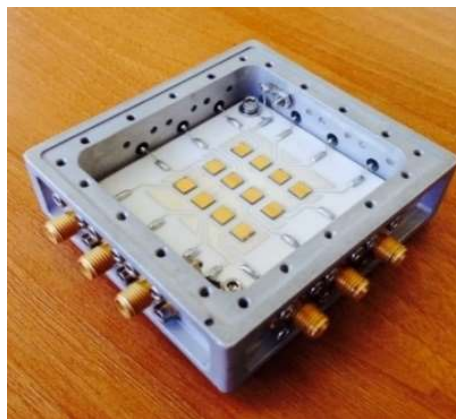


FIG. 13. Photograph showing the matrix of SDDs comprising the Diamond Vertical Neutron Spectrometer [DVNS]

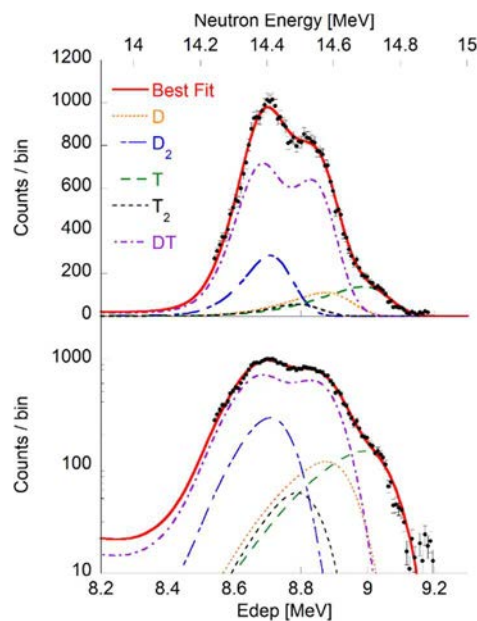


FIG. 14. Pulse height spectrum recorded at zero degrees by the single crystal diamond detector; shown in linear (left) and logarithmic (right) scales. Measured data are shown as black dots without the low energy tail being due to partial charge collection. The neutron beam components with their weights and their sum correspond to the best fit to the data. The lower x-axis represents the neutron deposited energy inside the detector whilst the upper x-axis represents the energy of the incoming neutrons [31, 32].

3 ITER NEUTRON DETECTION SYSTEMS

3.1 OVERVIEW OF ITER DEVICE AND DIAGNOSTIC SYSTEMS

ITER is an experimental nuclear reactor, aiming to demonstrate the feasibility of nuclear fusion power. It is a tokamak based plasma device operating with a magnetic toroidal field of 5.3 T, plasma current of 15 MA, pulse duration ranging from 300 s up to 500 s, and producing operating power of 500 MW, ranging up to 700 MW fusion power [34]. Some of the main component features of ITER are shown in Figure 15. These parameters are contrasted to the peak fusion power of 16 MW and a 4 MW production lasting 4 seconds, which were obtained at JET in 1997 [35].

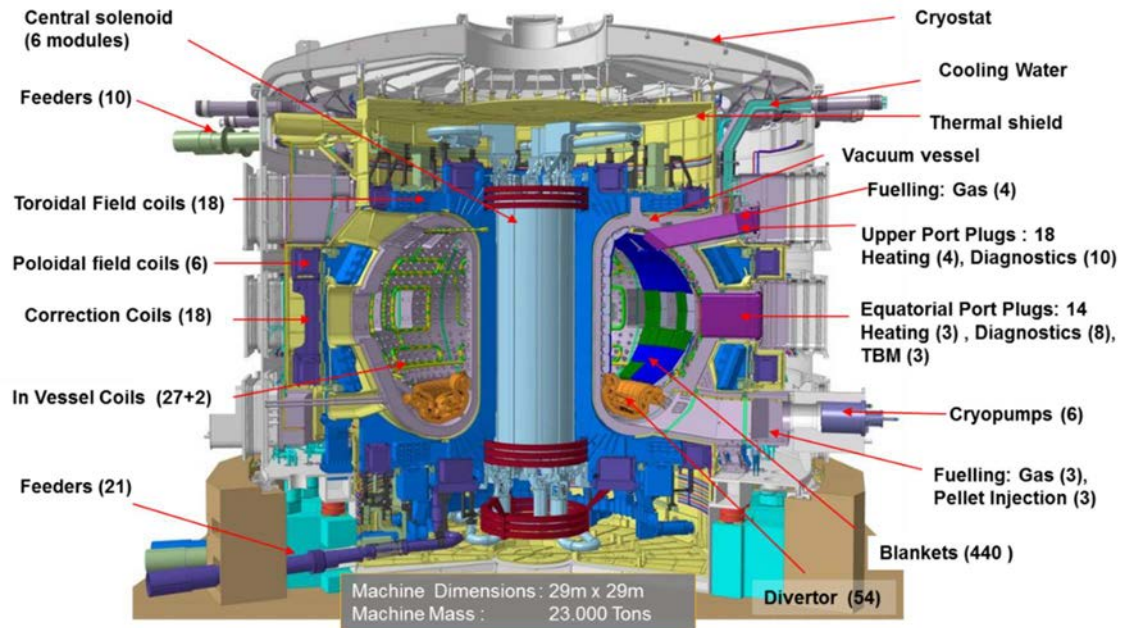


FIG. 15. A section of ITER Tokamak 3D model showing the variety of technology systems comprising the machine (with numbers in parenthesis). The toroidal vacuum vessel is surrounded by helium-cooled cryostat. The upper, equatorial, and lower ports are occupied by cryopumps, additional plasma heating systems, and diagnostics.

ITER members China, European Union, India, Japan, Korea, Russia, and the United States support the ITER project via domestic agencies (DA) which provide various components/systems including the vacuum vessel, magnets, blanket modules, divertor cassettes, and diagnostics.

About 100 plasma parameters [34] for plasma control and performance, machine protection, and physics studies will be measured. The diagnostic systems are to be placed in divertor cassettes as well as in the vacuum vessel in the following locations: the equatorial and upper ports, and on the inner surface.

The ITER environment is expected to experience fluxes up to 10^{14} n/cm²s of 14.1 MeV neutrons, temperatures up to 1000 C and up to 6 T magnetic fields. Electromagnetic noise from the auxiliary RF heating systems complicates measurement further [36]. Maintainability has to be considered especially carefully for those diagnostic systems within the vessel that face the highest electromagnetic (EM) and nuclear loads [37].

Neutron emission relates to the fusion power –important in machine protection, plasma optimization, and physics understanding [38–40]. Neutron diagnostics will also be valuable for determining the densities of D and T in the plasma core, neutron fluence at the first wall, neutron and alpha source profiles, fusion power density, and ion temperatures.

Figure 16 shows the relationship between primary measurement parameters and various neutron system and the domestic agencies involved in the design and operation of the measurement system.

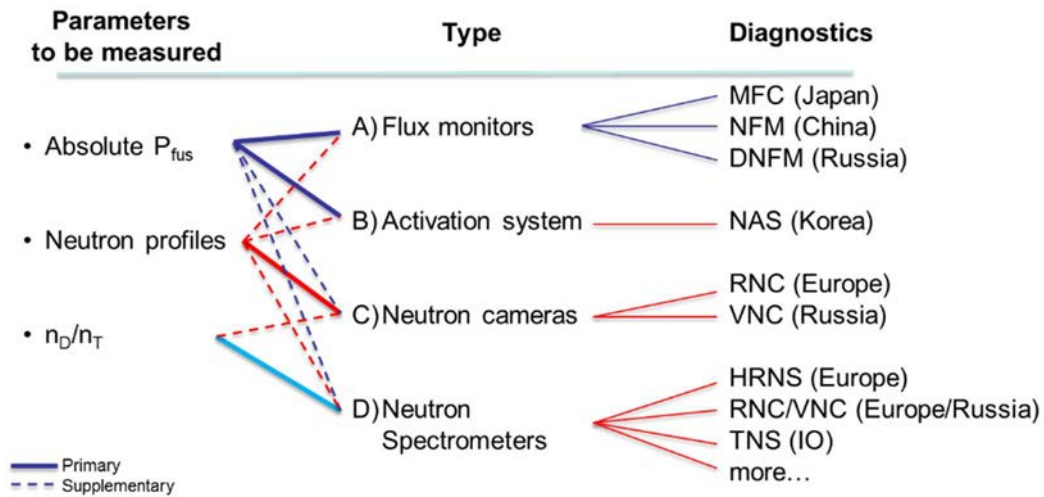


FIG. 16. The distribution roles of primary and supplementary roles for neutron diagnostics at ITER. Primary role means that diagnostic is well suited to perform the measurement; Supplementary role means that diagnostic performs the measurement with limitations; it validates or calibrates the primary measurement but is not complete in itself.

Neutron emission rates are expected to range from 1014 ns⁻¹ for DD up to 1021 ns⁻¹ for DT plasmas [41]. Specifications for the diagnostics require accuracy better than 10% for neutron emissions with a temporal resolution of 10–3 seconds. In addition to a high-resolution neutron spectrometer (HRNS), a neutron spectrometer in the Neutral Particle Analyzer complex, and the tangential neutron spectrometer. a wide variety of neutron diagnostic systems is planned and will be distributed at various locations within ITER (Table 1) [41, 43]: Neutron flux monitors (NFM) installed in radial diagnostic ports;

TABLE 1. NEUTRON DIAGNOSTIC SYSTEMS PLANNED AT ITER

Type	Location
Neutron flux monitors (NFM)	Radial diagnostic ports
Divertor neutron flux monitors (DNFM)	Under the divertor
Micro-fission chambers (MFC)	between the vacuum vessel 's inner shell and the blanket modules
Neutron activation system (NAS)	Within the vacuum vessel
Neutron cameras	Radial (RNC) and vertical (VNC)

3.2 NEUTRON EMISSION MEASUREMENT AND RELATED NEUTRON DIAGNOSTICS

Knowledge of the absolute neutron emission rate from the whole plasma is important as a fusion power monitor. This requires calibrated neutron flux monitors, usually ionization chambers (also known as fission chambers) containing ²³⁵U or ²³⁸U isotopes and Argon gas at a few atmospheres pressure. Time-resolved neutron detection systems of various kinds and at multiple locations (in-vessel and ex-vessel) provide redundancy and may compensate for changes in plasma shape or position. From their measurements of the global neutron source strength, the total fusion power can be obtained. Research and development of diagnostic systems and components that will withstand the ITER environment is underway [42]. The diagnostics systems used to determine the total neutron emission are outlined below.

3.2.1 Neutron Flux Monitors (NFM, DNFM and MFC)

The measurement of the total neutron emission during all phases of ITER operation will be carried out by these diagnostic systems.

During ITER's low fusion power phase, NFMs in ports #1 and #7 will measure neutron emission from DD reactions; during full power DT operation, NFMs in ports #8 and #17 will monitor neutron flux [44]. The most sensitive fission

chamber is the NFM unit in equatorial port plug # 1 (Figure 17). Various moderators (Be, B₄C, graphite) of different thicknesses can be used to tune the NFMs' sensitivities for measurements of total neutron strength over a wide range. A variety of signal acquisition and data processing techniques will be used for different operational modes: at low flux, pulse counting; at intermediate fluxes, Campbell; and at high flux, current mode [44].

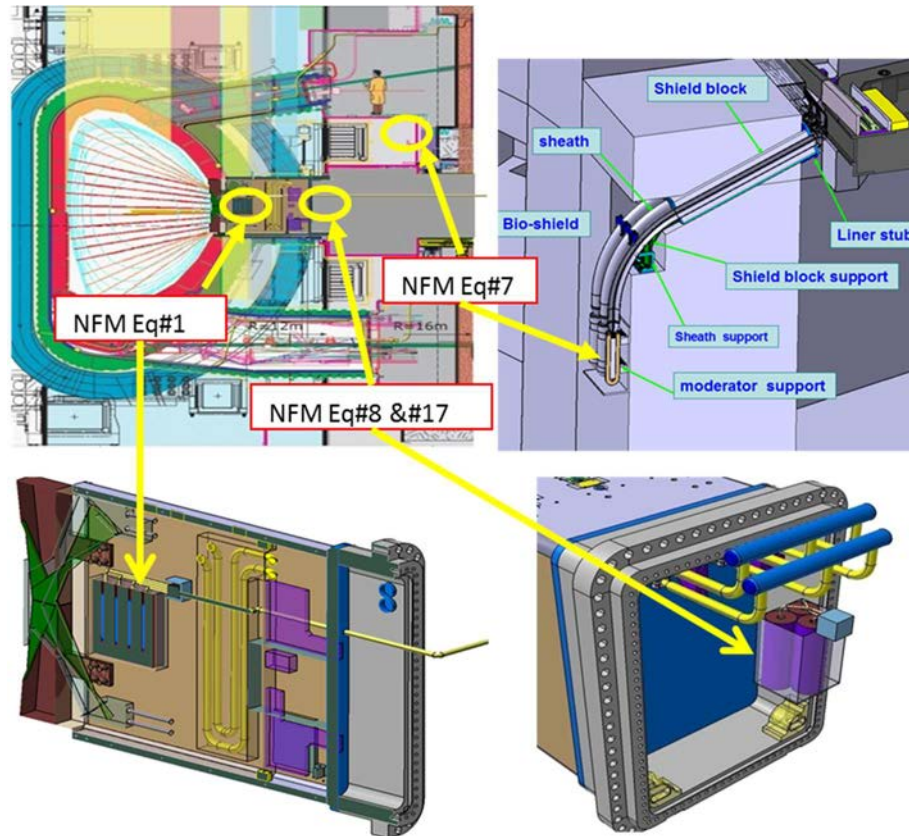


FIG. 17. Distribution of NFM units ITER equatorial ports.

The Divertor Neutron Flux monitors (DNFM) provide additional measurements [45]. Three DNFM's at different toroidal positions are located at the bottom of the vacuum vessel, under the dome of the divertor cassettes. Each DNFM is composed of six fission chambers (FC) identical size but with different U coatings. The six FCs are wrapped in two cylinders; three ²³⁵U FCs in one and three ²³⁸U FCs in the other, to create a DNFM module (Figure 18). Water jackets in the stainless-steel cylinder permit temperature control of the modules.

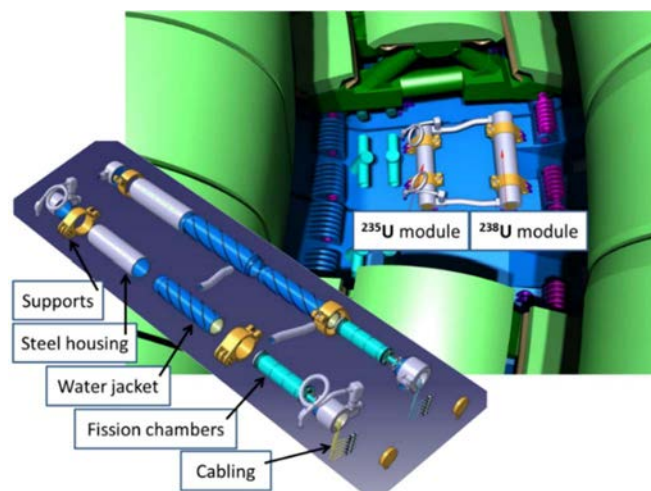


FIG. 18. DNFM modules location and exploded (DNFM modules are located under the dome of ITER divertor).

During DT operation phases, particularly high levels of fusion power require the micro-fission chamber (MFC) system, which are ‘pencil sized’ FCs. They typically contain only a few tens of milligrams of U and installed between the outboard inner shell of the vacuum vessel and the blanket modules. Each module contains two U-containing MFCs and a third U-free MFC, used for noise/gamma measurement. Two modules are placed in two different poloidal locations (upper and lower outboard) at two different toroidal positions, see Figure 19 [46]. The two particular poloidal were shown, using neutron transport calculations, to show that the averaged output of the two MFCs modules is insensitive to plasma position change. Issues including clearance tolerance between the MFC components and the blanket modules, high operating temperatures, and the vacuum leak rate of the MFC have been considered as well as the functioning of the chambers during vibration and shock effects [47].

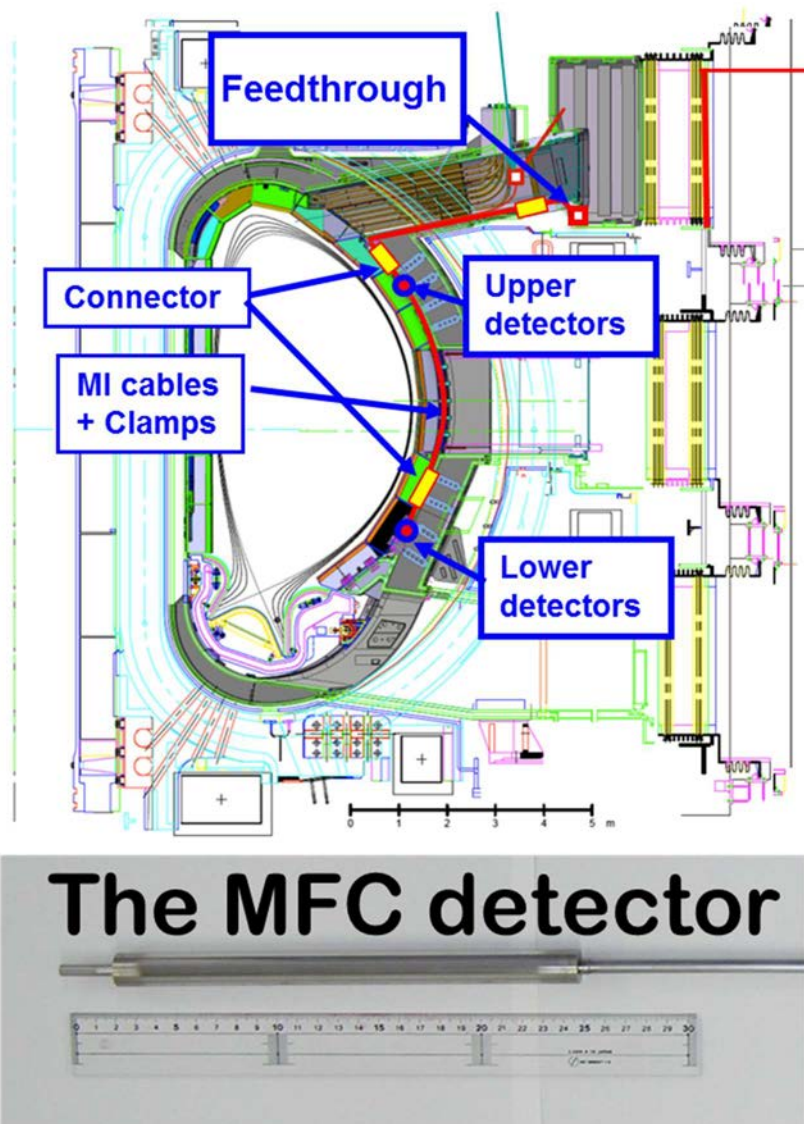


FIG. 19. MFC detector modules allocation under blanket modules inside ITER vacuum vessel.

3.2.2 ITER Neutron Activation System (NAS)

A neutron activation system will be used to performed time-integrated neutron fluence measurements of total fusion power and neutron fluence at the first wall of the blanket modules [48]. Similar to JET, this will be done by measuring induced gamma radiation from activated samples. Pneumatic systems transfer encapsulated samples between irradiation ends near the first walls to a counting station in the Tritium Building.

Several irradiation ends are placed on the vacuum vessel inner wall, between various Blanket Modules and Equatorial Ports (Figure 20). They will face temperatures up to 800 °C due to the plasma radiation and nuclear heating, and will experience plasma-induced electromagnetic forces.

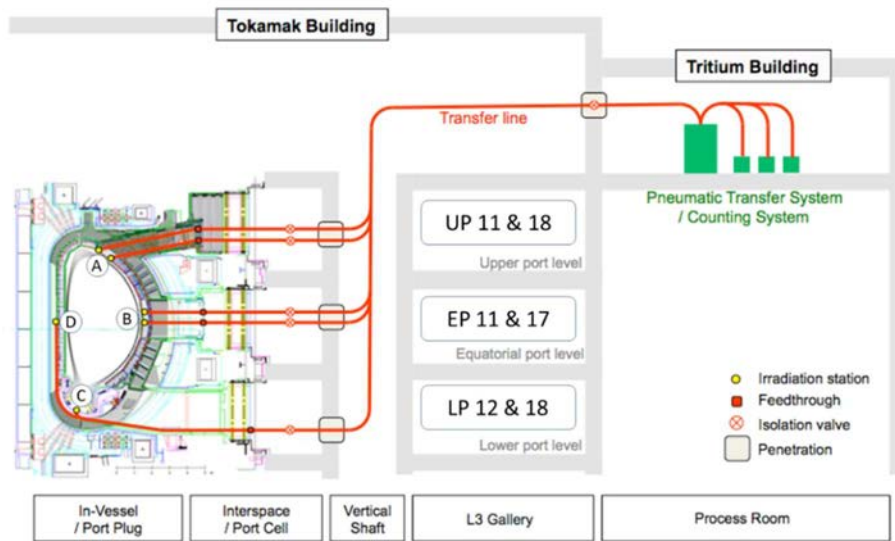


FIG. 20. Distribution of ITER NES irradiation ends. A and B – inside upper and equatorial port plugs; C and D – in vessel with transfer lines entering the vessel in lower port zones.

Detailed design and the selection of gamma spectrometry systems are currently ongoing. NaI and HPGe detectors are the most obvious candidates, but other detectors including gas chambers, scintillators, and semiconductor detectors are also considered. The following reactions are considered in calculations for the NAS performance assessment: $^{28}\text{Si}(n,p)^{28}\text{Al}$, $^{63}\text{Cu}(n,2n)^{62}\text{Cu}$, and $^{48}\text{Ti}(n,p)^{48}\text{Sc}$.

The NAS diagnostic has an intrinsic dynamic range of 10 orders of magnitude. This is achieved by appropriate selection of mass and materials [48]. The NAS diagnostic is unique at ITER, and will be absolutely calibrated during in situ neutron calibration, as well as during DD and DT phases by JOG discharges (well-known plasma reference discharges). Other neutron diagnostic systems will be cross-calibrated to this [49,50]. The dynamic range of all the flux monitors (EP1-EP8), DNFM, MC1 and MC2) for a 1 ms response time in counting mode are shown in Figure 21.

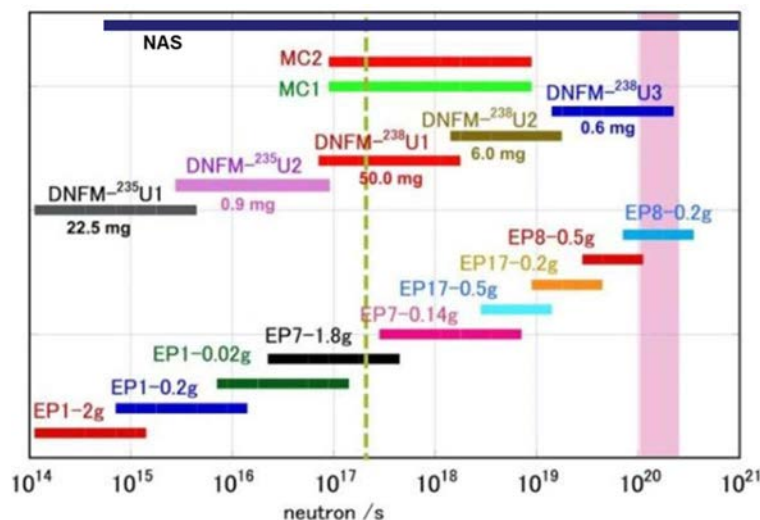


FIG. 21. The overall dynamic range of all neutron flux monitors and neutron activation system in counting mode for a 1 ms response time. The pink shaded area corresponds to 500 MW fusion power. The in-vessel calibration is expected to calibrate the detectors to the left of the vertical broken line. Collectively these systems span the entire ITER neutron emission range. The pink shaded area corresponds to 500 MW fusion power. The in-vessel neutron calibration is expected to calibrate all the detectors to the left of the broken line.

3.2.3 Radial and Vertical Neutron Cameras (RNC and VNC)

The Radial Neutron Camera (RNC) [51] consists of a fan-shaped array of collimators with detectors located in the port-plug (in-port subsystem, for plasma edge measurements) and in the port inter-space (ex-port subsystem, for core plasma measurements) of Equatorial Port #1 (EP01) (see Figure 22). The main role of the RNC is the measurement of the local profile of the plasma neutron emission for real-time plasma burn control with a time resolution of 10 ms, an accuracy of 10% and a spatial resolution of $a/10$ where a is the ITER plasma's minor radius. Each collimator culminates in a set of detectors chosen to cover the ITER large range of neutron emissivity, from 10^{14} to $10^{19} \text{ s}^{-1} \text{ m}^3$. The final design consists of 20 ex-port collimators of length varying from 1.4 to 3.0 m and with a diameter of 1.1 cm divided in two fans of 10 lines of sight each and of 6 in-port collimators (3 in the upper/lower in-port plug each) of length varying from 0.95 to 1.5 m and with 3.2 cm diameter. The lines of sights are purely radial on a poloidal plane with roughly equal angular separation of approximately 1.4 degrees. The RNC detector modules (defined as the combination of one or more detectors per line of sight) should satisfy a series of very demanding conditions. They should be capable to withstand ITER environmental constraints in terms of the local temperature up to 250 °C, stray magnetic fields (from few Tesla in the in-port region down to few mT in the ex-port region) and neutron fluxes and fluences up to $10^{12} \text{ n/cm}^2 \text{ s}$ and $\sim 10^{16} \text{ n/cm}^2$ and doses up to 10^5 Gy . In addition, they should have a dynamic range of 10^4 . The detector modules should be sensitive to both 2.5 and 14 MeV neutrons with a selectable energy threshold for background rejection and the minimization of the scattered neutrons contribution. The detector modules should be able to discriminate between 2.5 and 14 MeV neutrons and to discriminate between neutrons and γ -rays. The envisaged detectors to be used are 1 cm thick single unit scintillators with neutron/gamma discrimination capability (SC), a matrix of single crystal diamond detectors (D) with 500 μm active layer and parallel-plate multilayer ^{238}U fission chambers (FC). The RNC has been optimized so that the count rate does not exceed 1 MHz in each detector in ITER scenario with the highest neutron emissivity ensuring a statistical uncertainty in the counts of about 1% which allows to reconstruct the neutron emissivity profile with an accuracy better than the required 10%. Although the RNC is considered neutron spectrometer, diamonds and scintillator with provide some limited neutron energy resolving capabilities. In order to allow the measurement of the plasma temperature of about 5 keV, the detector modules should have an energy resolution of approximately 3% at 14.1 MeV and of 7.5% at 2.5 MeV. The calibration of the detectors consists in a combination of individual detector calibration (efficiency, energy resolution) and of Monte Carlo radiation transport simulations for the cross-calibration of the RNC with other ITER absolutely calibrated neutron diagnostics such as the activation system. This in combination with embedded calibration sources together with reference ITER plasma discharges would allow to track the RNC calibration for ITER life time.

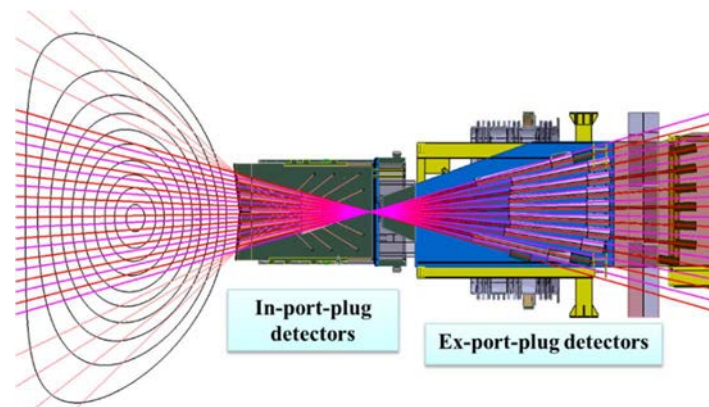


FIG. 22. Layout of the ITER Radial Neutron Camera [RNC].

Because ITER does not have vertical ports it is difficult to measure the neutron emission in the vertical direction (necessary for combination with the radial measurements for tomographic reconstructions of the neutron source profile). A concept for the vertically viewing neutron camera (VNC) has been designed [52] representing two sets of detectors with vertical collimators alignment—one in a lower port and one in upper port [53] (see Figure 23). The lower detector cassette will be installed in port 14. The plasma will be observed through collimators in dedicated shielding modules in the divertor cassette and in the blanket module. The detectors will be hosted in a secondary vacuum container in order to avoid the risk of gas leakage to the torus vacuum. Another set of detectors for the VNC will be installed inside the port plug of upper port #18. The challenges for these detectors are similar to those of the in-port-plug detectors of the RNC.

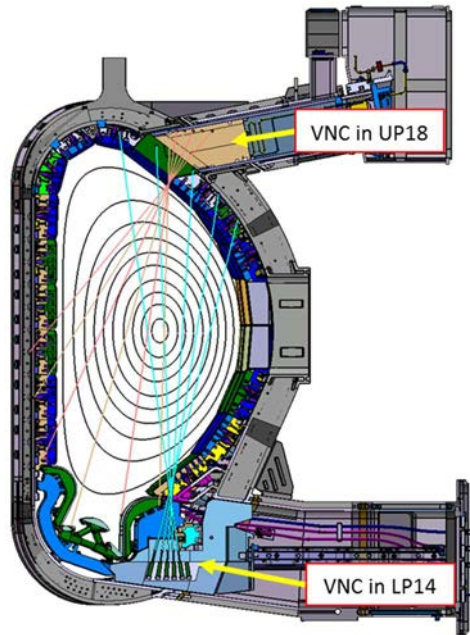


FIG. 23. Arrangement of VNC collimators in lower port 14 and upper port 18 represented on one effective cross section of the ITER tokamak.

3.2.4 High resolution neutron spectrometer (HRNS)

Presently in ITER a dedicated neutron spectrometer is being considered for an enhanced neutron spectrometer diagnostics. Facility space allocation has been reserved for the diagnostic and conceptual studies are being carried out. One concept under investigation is the High Resolution Neutron Spectrometer (HRNS), a single-channel 2.45 and 14 MeV combined spectrometer detailed in [54]. The HRNS will share the same equatorial port plug of the RNC and will be installed behind it outside the bio-shield. The main interfacing requirements for the HRNS is a 10-cm diameter aperture in the ITER first wall resulting in a neutron flux of the order of 10^9 n/cm²/s spanning an area of 10 cm² at a distance of 16 m from the first wall. The proposed HRNS consists of three neutron spectrometer sub-systems with the primary function to provide measurements of the fuel ion ratio nT/nD , in the plasma core. The ITER requirement for the HRNS primary function is to measure the fuel ion ratio with a 20% uncertainty and a time resolution of 100 ms for full power DT plasmas. Supplementary functions of the diagnostic are to assist or provide information on fuel ion temperature, the energy distribution of fuel ions, and the confined alpha-particle and neutron emission profiles. In order to cover the full dynamic range required, three spectroscopic systems are placed one after the other along the line of sight. The first is a thin-foil proton recoil telescope with segmented annular Si detectors in $\Delta E/E$ configuration, followed by a single crystal CVD diamond detector after which two time of flight spectrometers are located, in forward and back-ToF configurations. The forward ToF subsystem employs H-rich organic scintillators in the usual forward scattering configuration, as TOFOR on JET, whilst the back-ToF is based on a deuterated organic scintillator in the backward scattering configuration [55]. The forward-ToF and the back-ToF can then measure simultaneously the 2.45 and 14 MeV neutron emission respectively in a relatively compact system. It has been shown that the system fulfils the ITER requirement for the measurements of the fuel ion ratio nT/nD spanning over an order of magnitude in fusion power, $40 < P_{\text{fus}} < 500$ MW when background contributions, due to neutron scattering in the vessel walls, collimator and beam dump were included together with a component of neutron induced gamma-rays [54].

4 DISCUSSION ON CHALLENGES FOR DETECTION SYSTEMS IN FUSION ENVIRONMENTS

The fusion environment itself poses a formidable range of challenges for operation of neutron detection systems, high temperature environments, high and transient magnetic fields, high radiation fields, intense RF fields and low vacuum conditions; many of these challenging environments are experienced in combination. During ITER operations, for example, the vacuum vessel and the port plugs will be kept at the temperature of 100 °C and in

magnetic fields ranging between 1 and 2 T (depending on where in the port plug). Diagnostic components in these areas need to routinely and reliably operate at this temperature and in these magnetic fields. In some areas, such as on the vacuum vessel surface under gaps between blanket modules and in the divertor region, nuclear heating may cause the temperature of components rise to several hundred degrees Celsius. Such areas require particular attention in detector design. At the end of every shut-down period the vacuum vessel and port plugs will be baked at the temperature of 240 °C and divertor cassettes will be baked at 360 °C. Magnetic fields in the divertor locations during operations can reach up to 6 T. Besides the temperature and magnetic field operational environments, the radiation resilience and maintenance issues are extremely important. In ITER operational conditions neutron flux levels ranging as high as 10^{14} n/cm²·s in some locations need to be measured reliably and accurately. Whilst the neutron fluences experienced by neutron detection systems at JET are significantly lower than those predicted at ITER, JET has been the leading developmental test bed for tokamak diagnostics and has demonstrated successful operation over many years of a variety of neutron detection systems in some ITER-relevant conditions, more so than any other facility. It is important to note however that testing technologies in JET operational conditions do not absolutely qualify detection systems for ITER, especially for those factors affecting the long-term behaviour and performance of detector technologies, such as radiation resilience of detection materials and electronics, reliability and maintainability factors. The high neutron fluence levels at ITER results in high residual gamma radiation fields post operations, due to neutron induced activation of materials, which impacts on human access for maintenance operations. Many of JET's systems can be maintained using human access during shut-down periods as the residual dose rates are acceptably low. In many neutron detector locations in ITER detection systems will need to be maintained remotely due to the very high gamma fields (and due to tritium considerations for in-vessel locations), presenting challenges to be overcome by dedicated design solutions. For some of the ITER neutron detection systems, such as the MFC and DNFM systems, maintenance operations are not expected to be possible. Human access to the diagnostic components will be extremely limited with any required maintenance performed by means of remote handling in the majority of cases. Neutron fluxes in the location of many detector modules in ITER will exceed 10^9 n/cm²·s, and in some particular cases such as DNFM and MFC this may reach fluxes as high as 10^{14} n/cm²·s. In the high flux locations, which are inside the vacuum vessel, there is a need for monitored double-containers for in-vacuum fission chambers, redundant safety valves and shutters on NAS transfer tubes penetrating confinement barriers. Furthermore, special considerations to the neutron activation system capsule positioning and stuck recovery scenarios have been developed to assure nuclear safety during all potential and foreseeable off-normal events. In the domain of radiation resilience diamond detectors have proven to be applicable for high-resolution DT-neutrons spectroscopy, yet their projected lifetime sets significant limitations on their application at ITER. A number of R&D activities is ongoing in this area; if they succeed, the area of application of this kind of detectors may be broadened in the future. Of particular interest are tests that are at presently being carried out for the ITER radial neutron camera where prototype detectors (fission chambers, diamonds and scintillators) are being tested to radiation levels (neutron and gamma-rays mixed fields) equal to those expected on ITER.

5 CONCLUSIONS

Accurate measurement of neutrons is essential to the success of fusion technology, an inherently neutron-rich energy source, with impact on control, performance and safety. JET—the EU experimental tokamak facility based in the UK and currently the largest device of its type worldwide with the infrastructure to operate with plasmas containing tritium—has provided an important testing facility to further research and development of a range of neutron diagnostic systems, with further activities planned for testing in DT operations expected in early 2020. This paper provides a current overview of the range of neutron detection and diagnostic systems currently employed at JET and those being designed, built and considered for ITER, which is expected to begin operations in 2025. The key systems we cover include neutron spectrometers, magnetic proton recoil spectrometers, fission yield counters, diamond detectors and activation foil-based systems along with a few others. Summary details on each of the systems have been provided in this paper and some key papers are referred to for readers to discover more comprehensive information.

ACKNOWLEDGEMENTS

This work has received funding from the Euratom research and training programme 2014–2018 under grant agreement No 633053 and from the RCUK Energy Programme [grant number EP/P012450/1]. The work on JET has been carried out within the framework of the EUROfusion Consortium and has received funding from the Euratom research and training programme 2014–2018 under grant agreement No 633053. The views and opinions expressed herein do not necessarily reflect those of the European Commission or the ITER organisation.

REFERENCES

- [1] JOINT EUROPEAN TORUS, website <https://www.euro-fusion.org/jet/>
- [2] ITER, <https://www.iter.org/>
- [3] GOORLEY, T., et al., Initial MCNP6 release overview, *Nucl. Technol.* **180** (2012) 298–315.
- [4] FORREST, R.A., et al., FENDL-3 library—Summary document, INDC(NDS)-628 (2012).
- [5] SUBLET, J.-Ch., et al., FISPACT-II: an advanced simulation system for activation, transmutation and material modelling, *Nucl. Data Sheets* **139** (2017) 77–137.
- [6] SUBLET, J.-Ch., et al., FISPACT-II User Manual, Tech. Rep. UKAEA-R(11)11 Issue 8, UKAEA, Dec. 2016. Available from: <http://fispact.ukaea.uk>
- [7] SUBLET, J.-Ch., et al., The European Activation File: EAF-2010 neutron induced cross section library, CCFE-R(10)05 (2010) UK Atomic Energy Authority.
- [8] KONING, A.J., “TENDL-2015,” Release Date: January 18, 2016. Available from: https://tendl.web.psi.ch/tendl_2015/tendl2015.html
- [9] DAVIS, A., PAMPIN, R., Benchmarking the MCR2S system for high-resolution activation dose analysis in ITER, *Fusion Eng. Des.* **85** 1 (2010) 87–92.
- [10] GILBERT, M.R., et al., Automated inventory and material science scoping calculations under fission and fusion conditions, *Nucl. Eng. Technol.* **49** 6 (2017) 1346–1353.
- [11] GILBERT, M.R., SUBLET, J.-Ch., Handbook of Activation, Transmutation, and Radiation Damage Properties of the Elements Simulated Using FISPACT-II & TENDL-2015; Magnetic Fusion Plants, Tech. Rep. CCFE-R(16)36, CCFE, 2016 Available from: <http://fispact.ukaea.uk>
- [12] GILBERT, M.R., et al., Handbook of Activation, Transmutation, and Radiation Damage Properties of the Elements and of ITER Materials Simulated Using FISPACT-II & TENDL-2015; ITER FW Armour Focus, Tech. Rep. CCFE-R(16)37, CCFE, 2016. Available from: <http://fispact.ukaea.uk>
- [13] SWINHOE, M.T., JARVIS, O.N., Calculation and measurement of U-235 and U-238 fission counter detection efficiency, *NIM* **221** (1984) 460–465.
- [14] JARVIS, O.N., et al., Calibration of the neutron yield detectors in the JET tokamak, 1984, JET-IR(84)02.
- [15] LAUNDY, B.J., JARVIS, O.N., Numerical study of the calibration factors for the neutron counters in use at the Joint European torus, *Fusion Technol.* **24** (1993) 150 (also JET-P(92)60).
- [16] SYME, D.B., et al., Fusion yield measurements on JET and their calibration, *Fusion Eng. Des.* **89** 11 (2014) 2766–2775.
- [17] BATISTONI, P., et al., 14 MeV calibration of JET neutron detectors—phase 1: calibration and characterization of the neutron source, *Nucl. Fusion* **58** (2018) 026012.
- [18] PROKOPOWICZ, R., et al., Measurements of neutrons at JET by means of the activation methods, *Nucl. Instrum. Methods A* **637** 1 (2011) 119–127.
- [19] COLLING, B., et al., Testing of tritium breeder blanket activation foil spectrometer during JET operations, *Fusion Eng. Des.*, article in press 2018.
- [20] ANGELONE, M., et al., Neutronics experiments, radiation detectors and nuclear techniques development in the EU in support of the TBM design for ITER, *Fusion Eng. Des.* **96–97** (2015) 2–7.
- [21] TOURWE H, et al., “Delayed Neutron Counting System for Jet Plasma Neutron Yields Diagnostics”, *Reactor Dosimetry* (GENTHON, J.P., RÖTTGER, H. Eds). Springer, Dordrecht (1985).
- [22] ANGELONI, M., et al., derivation of nuclear parameters for delayed neutron detector measurements for D–D and D–T plasma operation at the Joint European Torus, *Fusion Technol.* **24** 1 37–49 (1993).
- [23] ADAMS, J.M., et al., The JET neutron emission profile monitor, *Nucl. Instrum. Methods Phys. Res. A* **329** (1993) 277–290, [http://dx.doi.org/10.1016/0168-9002\(93\)90947-G](http://dx.doi.org/10.1016/0168-9002(93)90947-G)
- [24] RIVA, M., et al., The new digital electronics for the JET neutron profile monitor: Performances and first experimental results, *Fusion Eng. Des.* **86** (2011) 1191–1195.
- [25] BINDA, F., et al., Calculation of the profile-dependent neutron backscatter matrix for the JET neutron camera system, *Fusion Eng. Des.* **123** (2017) 865–868.
- [26] GIACOMELLI, L., et al., Advanced Neutron Diagnostics for JET and ITER Fusion Experiments, EFDA–JET–PR(05)13.
- [27] SUNDEN, E.A., et al., The thin-foil magnetic proton recoil neutron spectrometer MPRu at JET, *Nucl. Instrum. Methods Phys. Res. A* **610** 3 (2009) 682–699.
- [28] ZIMBAL, A., et al., Compact NE213 neutron spectrometer with high energy resolution for fusion applications, *Rev. Sci. Instrum.* **75** 10 (2004) 3553–3555.

- [29] CAZZANIGA, C., et al., Thin YAP:Ce and LaBr₃:Ce scintillators as proton detectors of a thin-film proton recoil neutron spectrometer for fusion and spallation sources applications, *Nucl. Instrum. Methods Phys. Res. A* **751** (2014) 19–22.
- [30] NEMTSEV G., et al., Diagnostic of fusion neutrons on JET tokamak using diamond detector, *AIP Conf. Proc.* **1612** (2014) 93.
- [31] RIGAMONTI, D., et al., Neutron spectroscopy measurements of 14 MeV neutrons at unprecedented energy resolution and implications for deuterium–tritium fusion plasma diagnostics, *Meas. Sci. Technol.* **29** (2018) 045502.
- [32] RIGAMONTI, D., Development of neutron and gamma-ray spectrometers for fusion plasma applications, Phd Thesis, Università di Milano-Bicocca, 2017.
- [33] MURARO, A., et al., First neutron spectroscopy measurements with a pixelated diamond detector at JET, *Rev. Sci. Instrum.* **87** 11D833 (2016).
- [34] DONNE, A.J.H., et al., Chapter 7: diagnostics, *Nucl. Fusion* **47** 6 (2007) 337–384.
- [35] JACQUINOT, J., The JET team, JET results in D/T divertor plasmas, *Nucl. Fusion* **38** 9 (1998) 1263–1273, JET Preprint JET-P(98)05.
- [36] VAYAKIS, G., HODGSON, E.R., VOITSENYA, V., Chapter 12: generic diagnostic issues for a burning plasma experiment, *Fusion Sci. Technol.* **53** (2008) 699–750.
- [37] ENCHEVA, A., BERTALOT, L., MACKLIN, B., VAYAKIS, G., WALKER, C., Integration of ITER in-vessel diagnostic components in the vacuum vessel, *Fusion Eng. Des.* **84** (2009) 736–742.
- [38] KRASILNIKOV, A.V., et al., Status of ITER neutron diagnostic development, *Nucl. Fusion* **45** (2005) 1503–1509.
- [39] SASAO, M., et al., Chapter 9: Fusion product diagnostics, *Fusion Sci. Technol.* **53** (2008) 604–639.
- [40] ORSITTO, F.P., et al., “Burning plasmas diagnostics,” in *AIP Proc.*, Varenna, Italy, 2007, vol. 988.
- [41] BERTALOT, L., et al., “Fusion neutron diagnostics on ITER tokamak,” in *Proc. FNDA 2011*, Ein Gedi, Israel, Nov. 2011.
- [42] KRASILNIKOV, V., BERTALOT, L., BARNSLEY, R., WALSH, M., Neutron detector needs for ITER, *Fusion Sci. Technol.* **71** 2 (2017) 196–200.
- [43] SASAO, M., et al., Issues on the absolute neutron emission measurement at ITER, *Plasma Fusion Res.* **8** (2013) 2402127.
- [44] YANG, J., et al., Fusion neutron flux monitor for ITER, *Plasma Sci. Technol.* **10** (2008) 141.
- [45] KASHCHUK, Y.A., KRASIL'NIKOV, A.V., PROSVIRIN, D.V., A conceptual project for a divertor monitor of the neutron yield in the ITER, *Instrum. Exp. Technol.* **49** (2006) 179–186
- [46] ISHIKAWA, M., et al., Design of microfission chamber for ITER operations, *Rev. Sci. Instrum.* **79** (2008) 10E507.
- [47] ENCHEVA, A., et al., Structural integrity report for ITER micro-fission chamber, *ITER Doc. ITER_D_3TDURL*.
- [48] CHEON, M.S., et al., In-vessel design of ITER diagnostic neutron activation system, *Rev. Sci. Instrum.* **79** (2008) 10E505.
- [49] BERTALOT, L., et al., “A strategy for calibrating the neutron systems at ITER,” in *Proc. 35th Plasma Phys. Conf. 2008*, EPS Europhys. Conf. Abstracts, Oral Contribution O2001, vol. 32D.
- [50] SASAO, M., BERTALOT, L., ISHIKAWA, M., POPOVICHEV, S., Strategy for the absolute neutron emission measurement on ITER, *Rev. Sci. Instrum.* **81** (2010), 10D329.
- [51] L. PETRIZZI et al., Neutronic design of the ITER radial neutron camera, *Fusion Sci. Eng.* **82** (2007) 1308.
- [52] KRASILNIKOV, A.V., WALKER, C.I., KASHCHUK, Y.A., PROSVIRIN, D.V., A multichannel neutron collimator for the ITER tokamak, *Instrum. Exp. Technol.* **47** (2004) 139.
- [53] ENCHEVA, A., et al., Engineering aspects of integration of ITER divertor diagnostics, *Fusion Eng. Des.* **86** (2011) 1323.
- [54] ERICSSON, G., et al., Conceptual design of a high resolution neutron spectrometer system for ITER, 26th IAEA Fusion Energy Conference Kyoto (2016).
- [55] HELLESEN, C., et al., Conceptual design of a BackTOF neutron spectrometer for fuel ion ratio measurements at ITER, *Nucl. Fusion* **57** (2017) 066021.

ACTIVATION FOIL CANDIDATES FOR INTENSE D-LI NEUTRON MEASUREMENT UP TO 60 MEV

S. KWON*, M. OHTA, K. OCHIAI, H. SUZUKI

National Institutes for Quantum and Radiological Science and Technology (QST)

Rokkasho-mura, Kamikita-gun, Aomori-ken 039-3212,

Japan

Email: kwon.saerom@qst.go.jp

Abstract: In order to assess a radiation damage of a fusion material before a decision of Japanese fusion DEMO reactor construction, we have been designing an intense d-Li neutron source facility, Advanced Fusion Neutron Source (A-FNS) in Japan. A-FNS will be constructed before 2025. The main purpose of A-FNS is to acquire radiation damage data of the fusion material under fusion-like neutron irradiation testing. One of the characteristics of A-FNS is that large amounts of high energy neutrons (> 1 MeV) are produced with an expected intensity around 6.8×10^{16} n/s. In this study, we propose a neutron measurement system that is configured with multiple threshold reaction activation foils which are sensitive to high energy neutrons. The need to measure the cross-section data for the threshold reactions is also discussed.

1 INTRODUCTION

1.1 RADIATION DAMAGE OF FUSION MATERIAL

Neutrons can damage materials such as a displacement per atom (dpa) and a gas production in the materials. The cross section for neutron-induced dpa is large in the low energy region. The gas production, however, is a type of threshold reaction. Figure 1 shows the cross section for (a) dpa and (b) helium-4 production in ^{56}Fe . Currently the radiation damage of the fusion materials is being predicted by the observed results of light and heavy ion irradiation tests. In order to assess the radiation damage of the fusion materials by d-t fusion neutrons, the neutron irradiation test should be performed at the d-t neutron source or neutron source facilities which reproduce fusion-relevant radiation damages.

Figure 2 shows the ratio of helium-4 production to dpa for ^{56}Fe , and can be used to compare the characteristics of different irradiation fields such as those from fusion reactors and neutron sources. The d-t fusion neutrons result in a ratio of around 10 appm/dpa. So, to obtain initial data for the fusion DEMO reactor design, irradiation tests are needed up to at least 10 dpa/fpy. The existing d-t neutron sources including ITER are not quite sufficient for such testing. Also, fission reactor and spallation neutron sources are not appropriate for the verification based on the ratio of helium-4 production to dpa. Hence, a key point for decisions concerning the DEMO reactor construction is the need to prepare a proper neutron irradiation facility and perform the radiation damage assessments for the fusion materials.

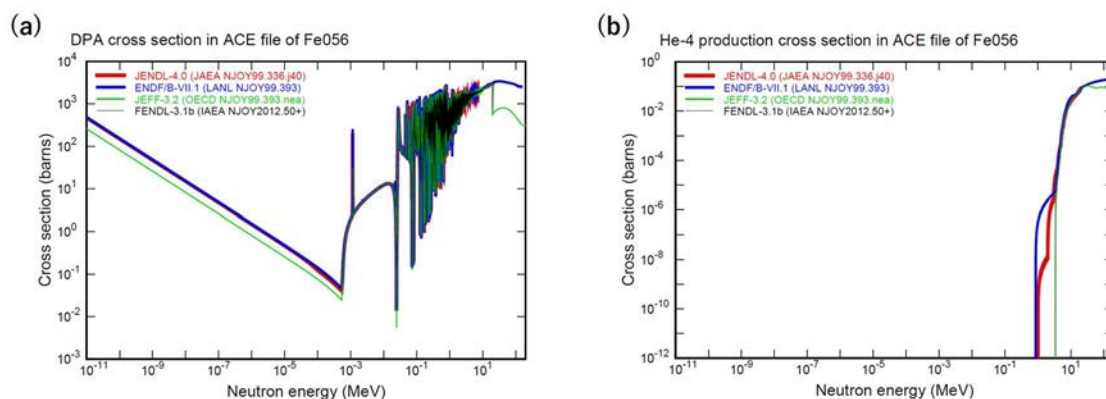


FIG. 1. (a) DPA and He-4 cross sections in various ACE files of ^{56}Fe .

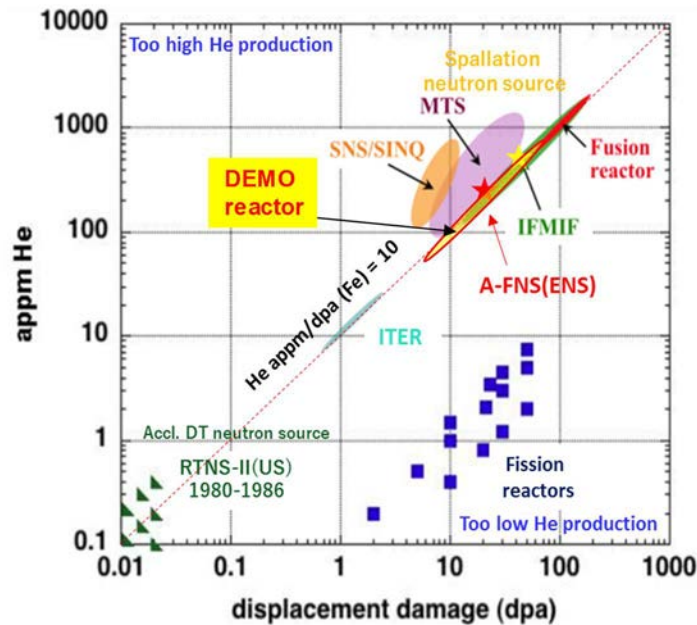


FIG. 2. Radiation damages and fusion-related facilities.

1.2 IRRADIATION TEST FACILITY FOR FUSION MATERIAL

Since the late 1970s, the irradiation facilities based on a deuteron-lithium (d-Li) neutron source have been proposed for the fusion materials: Fusion Materials Irradiation Test (FMIT) facility in the US (1978–1984) [1–2], Energy Selective Neutron Irradiation Test Facility (ESNIT) in Japan (1988–1992) [3–4], and International Fusion Materials Irradiation Facility (IFMIF) in EU and Japan (1995–Present) [5–6]. IFMIF is currently ongoing its Engineering Validation and Engineering Design Activities (EVEDA) phase under the Broader Approach Agreement between EU and Japan [7]. The Intermediate IFMIF Engineering Design Report (IIEDR) was released in 2013 [8]. It outlined the major systems of IFMIF, the accelerator facility, the lithium target facility, the test facility, and the post irradiation examination facility. As the results of the IFMIF/EVEDA project, a long-term stability of high-speed liquid flow of lithium target was validated at EVEDA Lithium Test Loop (ELTL) at Japan Atomic Energy Agency (JAEA), Japan in 2014, and a prototype of High Flux Test Module was manufactured and its remote handling was tested at Karlsruhe Institute of Technology (KIT), Germany in 2015. Now, the Linear IFMIF Prototype Accelerator (LIPAc) achieves 9 MeV (CW) operation at National Institutes for Quantum and Radiological Science and Technology (QST), Japan. From the viewpoint of the early realization of the fusion neutron source, a facility producing a fusion-like neutron spectrum with a half flux of IFMIF is considered as DEMO Oriented Neutron Source (DONES) in the EU [9] and Advanced Fusion Neutron Source (A-FNS) in Japan [10–11] based on achievements of IFMIF/EVEDA.

1.3 ADVANCED FUSION NEUTRON SOURCE IN JAPAN

We are carrying out the conceptual design activity of the A-FNS. The engineering design of the A-FNS needs to be performed before 2025; the construction site of A-FNS is planned for Rokkasho-mura, Japan. Then, the necessary data for decisions related to construction of the DEMO will be acquired before 2035 using the irradiation test at A-FNS facility. The schedule for the A-FNS construction is shown in Fig. 3. As opposed to IFMIF (125 mA \times double beam line), the A-FNS has a single deuteron beam line. The accelerated deuterons up to 40 MeV with 125 mA beam current are normally incident upon the liquid lithium target (25 mm in thickness) as shown in Fig. 4. The parameters of the A-FNS is shown in Table 1. The neutron relevant parameters were calculated by the Monte Carlo method using values that were obtained theoretically and experimentally. In order to evaluate the irradiation impact for the fusion materials at the A-FNS facility, the neutrons or photons which can affect directly the radiation damage are precisely measured in energy and intensity using a neutron measurement module.

In this paper, we present the description of the neutron spectrum measurement system which uses an activation method for high energy neutrons. The required dosimetry reactions and the experimental approach related to measurement of the reaction cross sections are among our current activities and are of interest in predicting the neutronics calculations for the design of A-FNS.

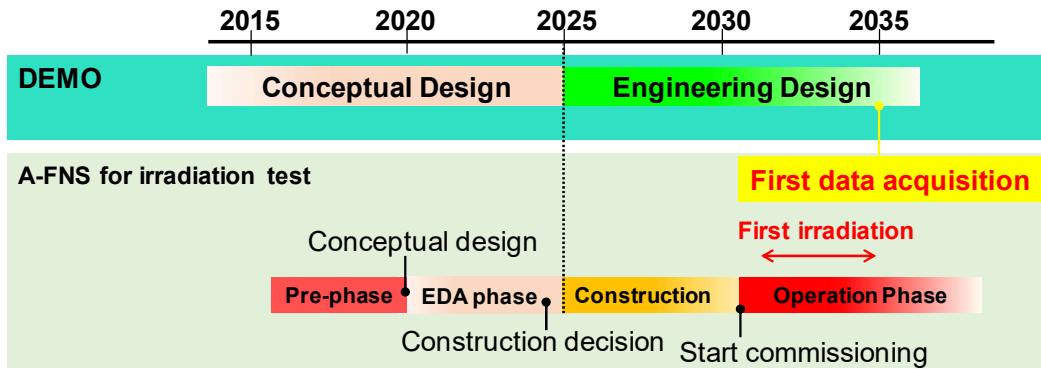


FIG. 3. Time schedule of A-FNS and Japanese DEMO reactor.

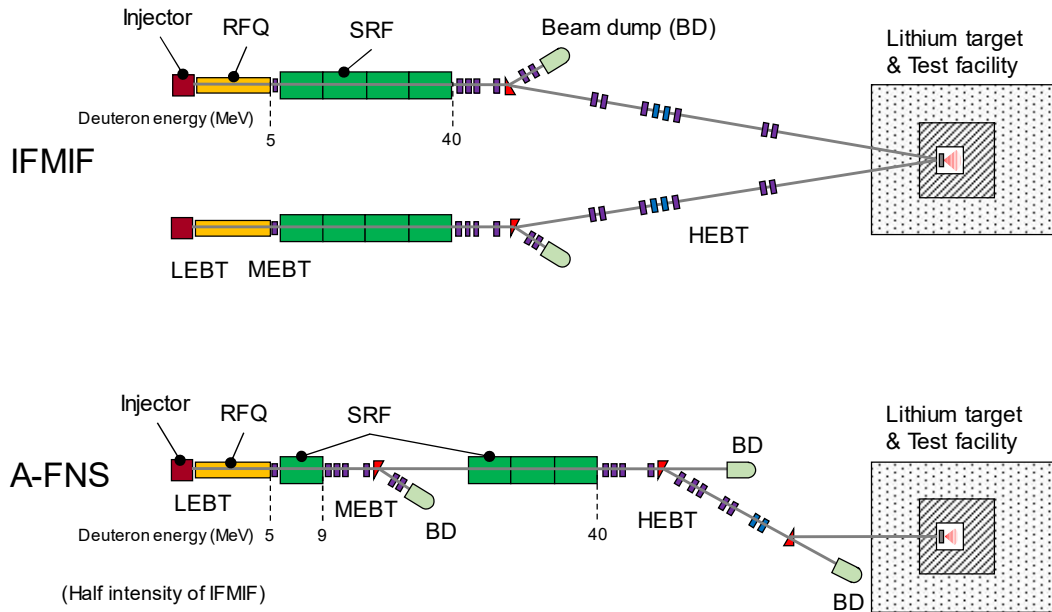


FIG. 4. Schemes of IFMIF and A-FNS.

TABLE 1. PARAMETERS OF A-FNS

Accelerator	Particle	Deuteron
	Energy	40 MeV
	Current	125 mA (CW)
	Beam foot print	200 × 50 mm ²
	Incident angle	Normal
	Availability	33% at least
Target	Material	Liquid lithium target (jet)
	Temperature	200–270 °C
	Velocity	10–15 m/s at target
	Thickness	25 mm
	Window	Free surface
Neutron	Intensity (at back plate)	6.8×10^{16} n/s
	Averaged flux	6.0×10^{14} n/cm ² /s
	Helium production rate (He P.R.)	3.12×10^2 appm/fpy
	Displacement (dpa)	24.7 dpa/fpy
	HeP.R./dpa	12.6

2 NEUTRON MEASUREMENT OF A-FNS

The A-FNS has a large population of high energy neutrons ranging up to 55 MeV as shown in Fig. 5. The high-energy neutrons dominate the value of the helium production to dpa ratio since helium production is the threshold reaction. Thus, the neutron measurement system for use at the A-FNS should cover a wide-energy range from thermal up to 60 MeV. In order to measure the spectrum of neutrons, we are designing a neutron spectrum measurement system which uses multiple activation foils with threshold reactions sensitive to high energy neutrons above a few MeV. The selected reaction candidates should satisfied the following conditions: (a) the reaction elements should be monoisotopic or mononuclidic elements to avoid unnecessary isotope production, (b) the produced isotopes should emit strong photons with good detection efficiency, (c) the produced isotopes has quite long half-life above a few days due to considering of A-FNS operation scenario (continuous operation over dozens of days), and (d) have an evaluated nuclear data library for the reactions, if possible, dosimetry cross section data are desirable.

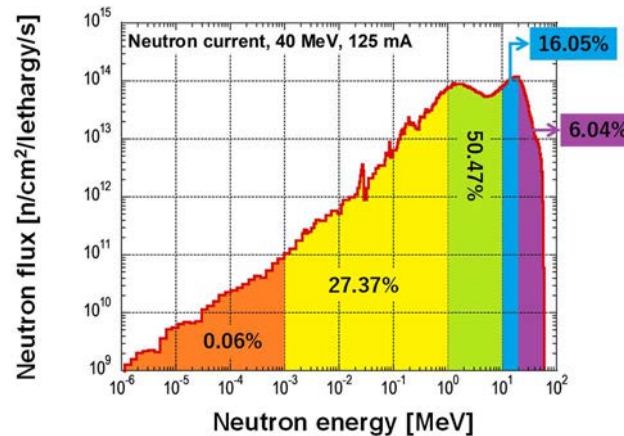


FIG. 5. Calculated Neutron Spectrum of A-FNS.

The candidate threshold foils are summarized in Table 2. Among the reactions, especially the bismuth ones are expected to be used due to their multiple threshold reactions. We are also investigating other elements and reactions even if they are not monoisotopic or mononuclidic but have multiple threshold reactions like the bismuth.

TABLE 2. DOSIMETRY THRESHOLD REACTIONS FOR APPLICABLE A-FNS NEUTRON SPECTRUM MEASUREMENT SYSTEM

Dosimetry reaction	Melting point (°C)	Half-life	Photons (keV)**	Threshold (MeV)	Typical nuclear data library available (Upper energy, MeV)			Experimental data EXFOR (MeV)
					IRDF-1.05	EAF-2010	FENDL-3.1c	
$^{55}\text{Mn}(n,2n)^{54}\text{Mn}$	1246	312.1 d	835	10.5	< 60	< 60	< 60	11.14–38.5
$^{59}\text{Co}(n,p)^{59}\text{Fe}$	1495	44.5 d	1099 1291	1.75	< 60	< 60	< 150	2.5–35.5
$^{59}\text{Co}(n,2n)^{58}\text{Co}$	1495	70.9 d	811	10.63	< 60	< 60	< 150	10.9–38.3
$^{59}\text{Co}(n,3n)^{57}\text{Co}$	1495	271.7 d	122 136	19.35	< 60	< 60	-	17.5–38.3
$^{75}\text{As}(n,2n)^{74}\text{As}$	615*	17.8 d	596 635	10.5	< 60	< 60	-	10.9–19.76
$^{89}\text{Y}(n,2n)^{88}\text{Y}$	1526	106.6 d	443 1836	11.8	< 60	< 60	< 200	11.38–59
$^{93}\text{Nb}(n,2n)^{92\text{m}}\text{Nb}$	2469	10.2 d	935	9	< 20	< 60	< 150	8.92–35.63
$^{169}\text{Tm}(n,2n)^{168}\text{Tm}$	1545	93.1 d	198 816	8.3	< 60	< 60	-	8.44–30.09
$^{169}\text{Tm}(n,3n)^{167}\text{Tm}$	1545	9.3 d	208	15	< 60	< 60	-	15.09–30.09
$^{197}\text{Au}(n,2n)^{196}\text{Au}$	1064	6.2 d	148 356	8.25	< 60	< 60	< 150	8.44–151.6
$^{209}\text{Bi}(n,3n)^{207}\text{Bi}$	271	32.9 y	570 1063	14.6	< 60	< 60	< 200	14.6–35.9
$^{209}\text{Bi}(n,4n)^{206}\text{Bi}$	271	6.2 d	803 881	23	-	< 60	-	24.5–94
$^{209}\text{Bi}(n,5n)^{205}\text{Bi}$	271	15.3 d	703 1764	30	-	< 60	-	34.25–94

*Sublimation point. **if ≥ 3 gamma energies existed, only the two energies which have the highest intensities are given.

Most parameters of the neutron and photon fields of A-FNS are predicted based on Monte Carlo radiation transport calculation. The neutronics calculations of the A-FNS, including the neutron spectrum as shown in Fig. 5, were carried out using the Monte Carlo calculation code, McDeLicious-11 [12]. Figure 6 shows the calculation model of A-FNS used in the simulation. The calculation model was modified to match A-FNS conditions from IFMIF neutronics model “mdl69 [13]”. The McDeLicious was developed by KIT for the proper representation of the d-Li neutron source term in the Monte Carlo calculation. We used the latest version of Fusion Evaluated Nuclear Data Library, FENDL-3.1b [14] for the neutron and photon transport calculations, and International Reaction Dosimetry Fusion File, IRDFF-1.05 [15] and European Activation File, EAF-2010 (same as FENDL/A-3.0) [16] for the reaction rate calculations. The FENDL is developed by the International Atomic Energy Agency (IAEA) Nuclear Data Section (NDS) and is a comprehensive nuclear data library for fusion applications. The IRDFF is a standardized evaluated cross section library of neutron dosimetry reactions and the EAF is an activation file for the response of materials to irradiation.

Figure 7 (a) shows the calculated reaction rates of the selected foil candidates. As shown in the plot, some foil reactions have similar reaction rates as other which can be covered the same energy range. Thus, Fig. 7. (b) shows the eliminated reaction rates from all the selected candidates. The reaction rates of $^{209}\text{Bi}(n, 4n)^{206}\text{Bi}$ and $^{209}\text{Bi}(n, 5n)^{205}\text{Bi}$ reactions were calculated using EAF-2010 (FENDL/A-3.0), since there were no cross section data for them in the IRDFF-1.05. In the neutronics calculations of the A-FNS, we have found that the measured cross section data at incident neutron energy higher than 20 MeV are extremely scarce. Figure 8 shows several examples of cross section data of the reaction candidates obtained from the IRDFF-1.05 and the Experimental Nuclear Data Library (EXFOR) [17]. The EXFOR library contains an extensive compilation of experimental nuclear reaction data. We have experimental work to measure and investigate cross sections of the dosimetry reactions related to the design activity for the neutron measurement system of the A-FNS.

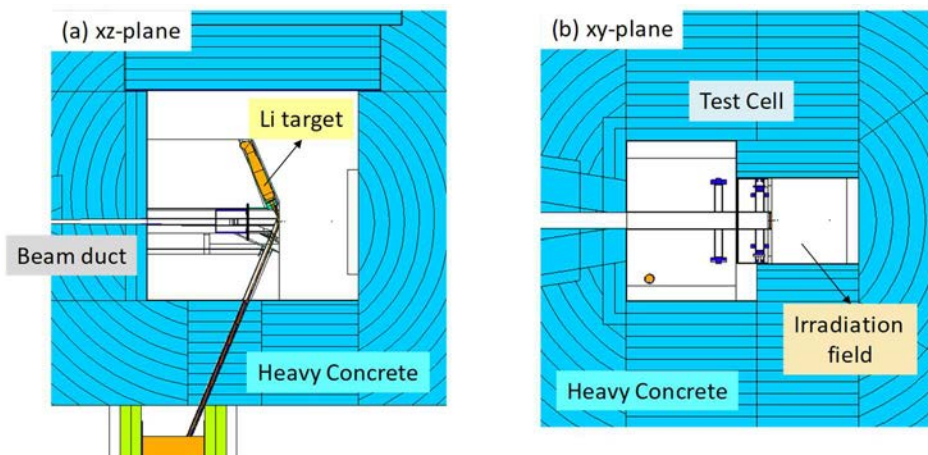


FIG. 6. Neutronics calculation model of A-FNS.

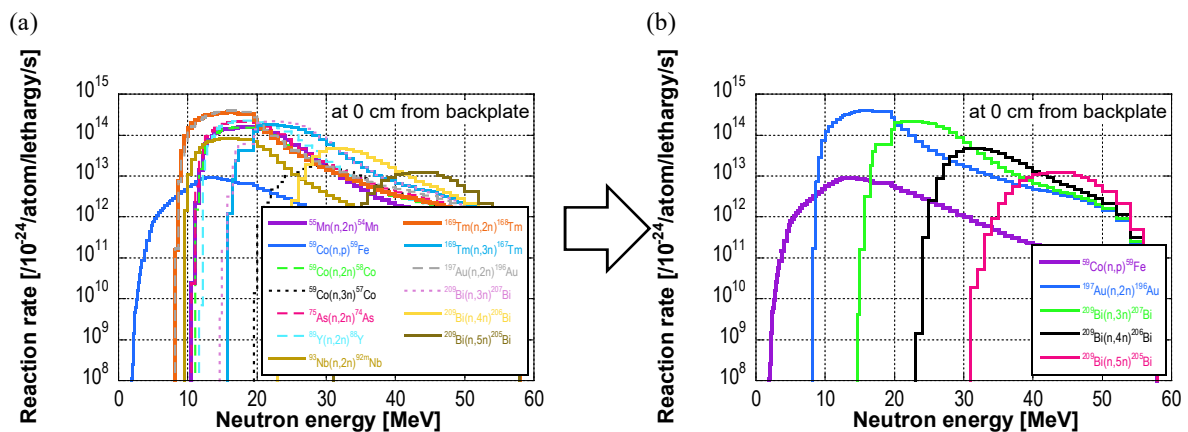


FIG. 7. (a) Reaction rates of the dosimetry threshold reactions, (b) Reaction rates of eliminated similar energy cover reactions.

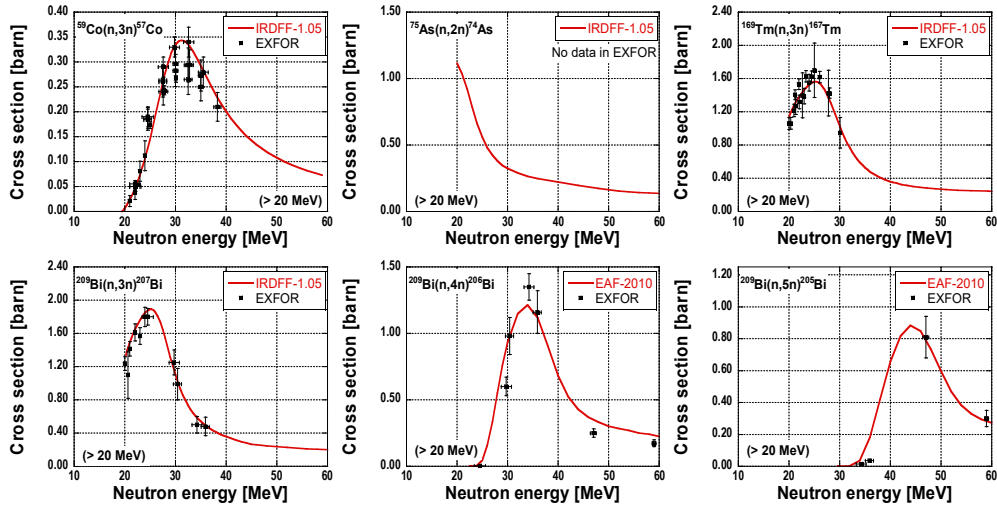


FIG. 8. Example reaction cross sections with scarce experimental data above 20 MeV in EXFOR and IRDFF-1.05.

3 DOSIMETRY CROSS SECTION MEASUREMENT FOR THE CANDIDATES

As shown in Fig. 8, the measured cross section data of the dosimetry reactions above 20 MeV neutrons are very scarce, because there has been no strong demand for experimental data at these higher energies in contrast to the measurements that are readily performed with 14.1 MeV d-t neutrons. At present, however, the intense neutron source facilities which provide similar radiation damage to that of the fusion reactor are highly desirable and are needed for design activities, such as IFMIF, DONES and A-FNS, respectively. Thus, the cross-section data should be measured in the energy regions where limited experimental data exists to evaluate the nuclear data library currently available.

Here we have been considering the experiment for the dosimetry cross section measurement under the same neutron spectrum as the A-FNS using the d-Li reaction. The deuterons (d) are accelerated up to 40 MeV by a cyclotron. A cylindrical lithium target 25 mm thick with a 20 mm radius is set in a pure aluminium holder which is prepared to prevent unnecessary long-lived activation products. The thickness of the lithium target was estimated as a stopping distance of 40 MeV deuteron in a solid lithium with Stopping and Range of Ions in Matter code, SRIM-2013 [18]. The irradiation material samples to measure the (n,xn) cross section measurement are located at behind the aluminium holder. The materials are in the form of foils with dimensions from $10.0 \times 10.0 \times 1.0 \text{ mm}^3$ to $20.0 \times 20.0 \times 1.0 \text{ mm}^3$ or $10.0 \varnothing \times 1.0 \text{ mm}$. Typical experimental conditions expected are a 4–5 hour irradiation period with a current of 1–2 μA . This should be sufficient to obtain measurable radioactivity using HPGe detector with 1% accuracy. After the irradiation with proper cooling time, the emitted photons from the radionuclides produced by the (n,xn) reactions are measured and the reaction rates derived from the measured values. Then the neutron spectrum is determined by unfolding method. Figure 9 illustrates the experimental configuration. The results from the experiment can make contribute to a new measurement (e.g. $^{75}\text{As}(n,2n)^{74}\text{As}$ in Fig. 8) and benchmark of the existing dosimetry cross section data (e.g. $^{59}\text{Co}(n,3n)^{57}\text{Co}$ or $^{209}\text{Bi}(n,xn)$ reactions in Fig. 8 also). We are currently preparing the experiment at AVF cyclotron facility of Tohoku University (Japan) in December 2017. The results will be reported in the near future.

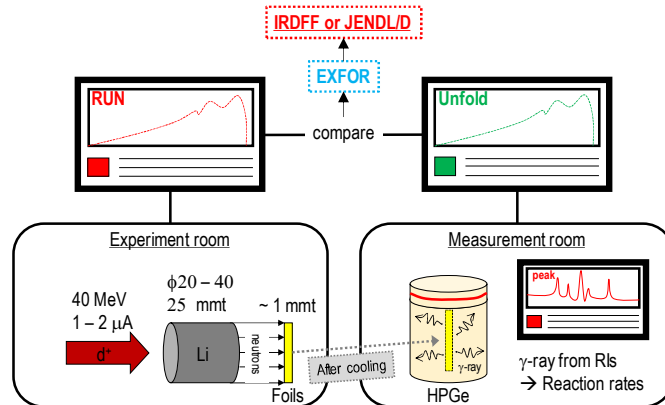


FIG. 9. A schematic diagram of the experimental configuration.

4 CONCLUSION

We have outlined the intense fusion neutron source facility, A-FNS, to study and test the neutron irradiation characteristics of the fusion materials for DEMO reactor construction decision before 2035. The neutron measurement system of the A-FNS will use multiple activation foils which are sensitive to high energy neutrons as discussed, because the A-FNS has large population of high energy neutrons above a few MeV ranging up to 55 MeV. In the neutronics analysis of the neutron measurement system of the A-FNS, it has been found that the neutron dosimetry cross section data above 20 MeV are very scarce. The scarce data issue can affect the neutronic analyses of the A-FNS, and its neutron measurement system design. Hence, we have proposed cross section measurements of the dosimetry foil candidates as the experimental approach related to the design activity for the neutron measurement system. The part of the experiment is going to be carried out at AVF cyclotron facility of Tohoku University in December 2017.

As for future work, other neutron measurement methods and their feasibilities are being investigated in detail to design the neutron measurement module of A-FNS: (a) activation method by capture reactions as a fluence monitor, (b) fission chambers such as ^{235}U , ^{238}U , ^{232}Th and ^{237}Np as online neutron monitor, (c) other neutron detectors such as the SiC detector, liquid/crystal scintillators for radiation hazards and precautions for embodiment of safety design.

ACKNOWLEDGEMENTS

A part of this work was obtained on the supercomputer system, Selene (QST), and ICE-X (JAEA).

REFERENCES

- [1] POTTMEYER, E.W., The fusion materials irradiation test facility at Hanford, *J. Nucl Mater* **85** (1979) 463–465.
- [2] HAGAN, J.W., OPPERMAN, E.K., TREGO, A.L., The fusion materials irradiation test (FMIT) facility, *J. Nucl Mater* **123** (1984) 958–964.
- [3] KONDO, T., OHNO, H., MIZUMOTO, M., ODERA, M., Selective energy neutron source based on the D-Li stripping reaction, *J. Fusion Energy* **8** (1989) 229–235.
- [4] NODA, K., et al., Characteristics of and energy selective neutron irradiation test facility (ESNIT) for material irradiation studies, *J. Nucl Mater* **179–181** (1991) 1147–1150.
- [5] EHRLICH, K., MOSLANG, A., IFMIF – An international fusion materials irradiation facility, *Nucl Instrum Methods Phys Res B* **139** (1998) 72–81.
- [6] KNASTER, J., et al., IFMIF, a fusion relevant neutron source for material irradiation current status, *J. Nucl Mater* **453** (2014) 115–119.
- [7] YAMANISHI, T., et al., Recent technical progress on BA program: DEMO activities and IFMIF/EVEDA, *Fusion Eng Des* **109–111** (2016) 1 272–1279.
- [8] IFMIF/EVEDA Integrated Project Team, IFMIF Intermediate Engineering Design Report (IIEDR), 2013.6.
- [9] IBARRA, A., et al., A stepped approach from IFMIF/EVEDA toward IFMIF, *Fusion Sci Technol* **66** (2014) 252–259.
- [10] NISHITANI, T., et al., DEMO activities in the broader approach and beyond, *Fusion Sci Technol* **66** (2014) 1–8.
- [11] OCHIAI, K., KONDO, K., KASUGAU, A., O'HIRA, S., IFMIF/EVEDA activity of broader approach and future plan, *J. Plasma Fusion Res* **92** (2016) 271–277.
- [12] SIMAKOV, S.P., FISCHER, U., KONDO, K., PERESLAVTSEV, P., Status of the McDeLicious approach for the D-Li neutron source term modelling in IFMIF neutronics calculations, *Fusion Sci Technol* **62** (2012) 233–239.
- [13] KONDO, K., et al., Neutronics analysis for the IFMIF EVEDA reference test cell and test facility, *Fusion Eng Des* **89** (2014) 1758–1763.
- [14] INTERNATIONAL ATOMIC ENERGY AGENCY, Fusion Evaluated Nuclear Data Library, <https://www-nds.iaea.org/fendl/>.
- [15] INTERNATIONAL ATOMIC ENERGY AGENCY, International Reactor Dosimetry and Fusion File, <https://www-nds.iaea.org/IRDF/>.
- [16] SUBLET, J.C., et al., EASY Documentation Series CCFE-R 5 (2010).
- [17] SEMKOVA, V., et al. EXFOR – a global experimental nuclear reaction data repository: Status and new developments, *EPJ Web Conf* 146 (2017) 07003.
- [18] ZIEGLER, J.F., SRIM-2013, <http://www.srim.org>.

LIST OF ABBREVIATIONS

Abbreviation	Full Name
ACNS	American Conference on Neutron Scattering
ADCs	Analog-to-Digital Converter
A-FNS	Advanced Fusion Neutron Source
ANIMMA	Advancements in Nuclear Instrumentation Measurement Methods and their Applications
ASDEX	Axially Symmetric Divertor Experiment
AWRE	Atomic Weapons Research Establishment
BARC	Bhabha Atomic Research Centre
BB	Bibenzyl
BCS	Boron-Coated Straw
BGO	Bismuth Germanate
BNC	Budapest Neutron Centre
BNCT	Boron Neutron Capture Therapy
BRR	Budapest Research Reactor
BSS	Bonner Sphere Spectrometer
BTI	Bubble Technology Industries
CAMAC	Computer Automated Measurement and Control
CCD	Charge Coupled Device
CCRI	Consultative Committee for Ionizing Radiation
CFRP	Carbon Fibre Reinforced Plastic
CIPM	International Committee for Weights and Measures
CLLB	$\text{Cs}_2\text{LiLa}(\text{Br})_6$
CLLC	$\text{Cs}_2\text{LiLa}(\text{Cl})_6$
CLYC	$\text{Cs}_2\text{LiYCl}_6$
CMC	Ceramic Matrix Composite
CMOS	Complementary Metal–Oxide–Semiconductor
CNL	Chalk River National Laboratory
CNS	Cold Neutron Source
CNSC	Canadian Nuclear Safety Commission
CT	Computed Tomography
CV curve	Capacitance–Voltage (CV) curve
CVD	Chemical Vapour Deposition
CYSP	CYlindrical SPectrometer
DAQ	Data AcQuisition system
DARHT	Dual Axis Radiographic Hydrodynamic Test
DD	Deuterium–Deuterium
DEMO	DEMOstration power plant,
DLC	Diamond-Like Carbon
DNFM	Divertor Neutron Flux Monitors
DOE	US Department of Energy
DONES	DEMO Oriented Neutron Source
DPAC	diphenylacetylene
DRIE	Deep Reactive Ion Etching
DT	Deuterium–Tritium
DVNS	Diamond Vertical Neutron Spectrometer
EAf	European Activation File
EAST	Experimental Advanced Superconducting Tokamak
ENDF	Evaluated Nuclear Data File
ESNIT	Energy Selective Neutron Irradiation Test facility
ESS	European Spallation Source
FEE	Front-End Electronics
FENDL	Fusion Evaluated Nuclear Data Library
FLNP	Frank Laboratory of Neutron Physics
FMIT	Fusion Materials Irradiation Test
FOM	Figure of Merit

FOV	Field of View
FWHM	Full Width at Half Maximum
GEM	Gas Electron Multiplier
GEM	Generalized Expectation Maximization
GM	Geiger-Muller
HDPE	High Density PolyEthylene
HRNS	High Resolution Neutron Spectrometer
IEEE	Institute of Electrical and Electronics Engineers
IFMIF	International Fusion Materials Irradiation Facility
INR RAS	Institute for Nuclear Research of the Russian Academy of Sciences
IRDF	International Reaction Dosimetry Fusion File
ISO	International Organization for Standardization
ISRD	International Symposium on Radiation Detectors
JET	Joint European Torus
JET LTIS	JET Long Term Irradiation Station
JINR	Joint Institutes of Nuclear Research
J-PARC	Japan Proton Accelerator Research Complex
KSTAR	Korea Superconducting Tokamak Advanced Research
LAMPF	Los Alamos Meson Physics Facility
LANL	Los Alamos National Laboratory
LIPAc	Linear IFMIF Prototype Accelerator
LO	Light Output
LSI	Liquid Silicon Infiltration
LYSO	($\text{Lu}_{1.8}\text{Y}_{0.2}\text{SiO}_5:\text{Ce}$) Lutetium Yttrium Silicate
MAP	Maximum A Posteriori Probability
MAPMT	Multi-Anode Photo Multiplier Tube
MC	Monte Carlo
MCA	MultiChannel Analyser
MCNP	Monte Carlo N-Particle
MCP	Micro-Channel Plates
MCS	MultiChannel Scaler
MeSA	MethylSalicylic Acid
MFC	Micro-Fission Chamber
MIP	Minimum Ionizing Particle
ML	Maximum Likelihood
MLEM	Maximum Likelihood Expectation Maximization
MLF	Materials and Life science experimental Facility
MPR	Magnetic Proton Recoil
MSGC	Micro-Strip Gaseous Chamber
MUHC	McGill University Health Centre
MWPC	MultiWire Proportional Counter
NAA	Neutron Activation Analysis
NAS	Neutron Activation System
NATO	North Atlantic Treaty Organisation
NFM	Neutron Flux Monitors
NIST	National Institutes of Standards and Technology
NMI	National Metrological Institute
NNS	Nested Neutron Spectrometer
NPL	National Physical Laboratory
NSTX	National Spherical Torus EXperiment
ORNL	Oak Ridge National Laboratory
PCR	Primary Cosmic Radiation
pCVD	Polycrystalline Chemical Vapour Deposition
PCz 9	PhenylCarbazole
PGAA	Prompt Gamma Activation Analysis
PLC	Precision Long Counter
PM	PhotoMultiplier

PMT	PhotoMultiplier Tube
PNNL	Pacific Northwest National Laboratory
PNPI	St Peterburg Nuclear Physics Institute
PPO	2,5-diphenyloxazole
PSD	Position-Sensitive Detector
PSD	Pulse shape discrimination
QDC	Charge-to-Digital Converter
RAL	Rutherford Appleton Laboratory
RCT	Radiological Control Technician
RF	RadioFrequency
RNC	Radial Neutron Camera
ROE	Read-Out Electronics
ROSPEC	ROtating SPECTrometer
SANS	Small Angle Neutron Scattering
SCR	Secondary Cosmic Radiation
SDD	Single-crystal Diamond Detector
SEE	Single Event Effects
SPND	Self-Powered Neutron Detectors
SiPM	Silicon PhotoMultiplier
SNM	Special Nuclear Material
SNS	Spallation Neutron Source
SORMA	Symposium on Radiation Measurements and Applications
SP ²	SPherical Spectrometer
SRIM	Stopping and Range of Ions in Matter
STAG	Standard Thermal Assembly in Graphite
TDCs	Time-to-Digital Converter
TENDL	TALYS-based Evaluated Nuclear Data Library
TLD	ThermoLuminescent Detector
TNPD	Thermal Neutron Pulse Detector
TOF	Time Of Flight
USB	Universal Serial Bus
UV	UltraViolet
VDC	Voltage-to-Digital Converter
VNC	Vertical Neutron Camera
YAP	Yttrium Aluminum Perovskite

CONTRIBUTORS TO DRAFTING AND REVIEW

The IAEA would like to thank all participants, and in particular

Scientific Chairs

Harry Ing	Bubble Technology Industries Inc., Canada
Lee Packer	United Kingdom Atomic Energy Authority, UK
Richard Hall-Wilton	European Spallation Source, Sweden

Reviewers of Papers

Mike Squillante	RMD Inc., USA
Thomas Mclean	Los Alamos National Laboratory, USA
David Thomas	National Physical Laboratory, UK
Nolan Hertel	Georgia Institute of Technology, USA
Vincent Gressier	Institut de Radioprotection et de Sûreté Nucléaire, France

Technical Meeting

Vienna, Austria, 4–8 September 2017

Consultants' Meeting

Vienna, Austria 8-9 February 2017



IAEA

International Atomic Energy Agency

No. 26

ORDERING LOCALLY

IAEA priced publications may be purchased from the sources listed below or from major local booksellers.

Orders for unpriced publications should be made directly to the IAEA. The contact details are given at the end of this list.

NORTH AMERICA

Bernan / Rowman & Littlefield

15250 NBN Way, Blue Ridge Summit, PA 17214, USA

Telephone: +1 800 462 6420 • Fax: +1 800 338 4550

Email: orders@rowman.com • Web site: www.rowman.com/bernan

REST OF WORLD

Please contact your preferred local supplier, or our lead distributor:

Eurospan Group

Gray's Inn House
127 Clerkenwell Road
London EC1R 5DB
United Kingdom

Trade orders and enquiries:

Telephone: +44 (0)176 760 4972 • Fax: +44 (0)176 760 1640

Email: eurospan@turpin-distribution.com

Individual orders:

www.eurospanbookstore.com/iaea

For further information:

Telephone: +44 (0)207 240 0856 • Fax: +44 (0)207 379 0609

Email: info@eurospangroup.com • Web site: www.eurospangroup.com

Orders for both priced and unpriced publications may be addressed directly to:

Marketing and Sales Unit

International Atomic Energy Agency

Vienna International Centre, PO Box 100, 1400 Vienna, Austria

Telephone: +43 1 2600 22529 or 22530 • Fax: +43 1 26007 22529

Email: sales.publications@iaea.org • Web site: www.iaea.org/publications

**International Atomic Energy Agency
Vienna**